I. Iervolino
editor

reluis

EUCENTRE
European Centre for Training and Research in Earthquake Engineering

This book is the 2015-2017 report of the RINTC project, which has been a joint project of ReLUIS and EUCENTRE. The project intended to assess the seismic risk of code-conforming structures in Italy. The results presented herein are, in some cases, different from those presented in the previous years and from preliminary literature derived from this project. This is because, as discussed in the body of text, hypotheses and choices have been continuously revised until consolidation; this process might be continuing even after the end of the project. In general, all computed annual structural failure rates closely reflect specific assumptions on design, modeling and analysis of the considered structures, and this has to be always taken into account when discussing the results of this project.

The working group of the project consisted of the following six sub-groups, each of which explores (i) seismic risk assessment of code-conforming structures, designs, modelling, and analyses of (ii) masonry buildings, (iii) precast reinforced concrete buildings, (iv) reinforced concrete buildings, (v) steel buildings, and (vi) base-isolated reinforced concrete buildings.

The book is structured such that each chapter presents the research results from the corresponding sub-group: Chapter (i) introduces the objectives and framework of the project; Chapters (ii)-(vi) develop code-conforming designs, modelling and analyses of buildings for each structural type; Chapter (vii) concludes the study presenting the final results of the computed failure rates for the structures examined in the preceding chapters. Moreover, readers can refer to Appendices A to C for the details of the considerations on (a) usability-preventing limit state, (b) soil-structure interaction, and (c) model-uncertainty, respectively.

The implicit risk of code-conforming structures in Italy
A joint ReLUIS-EUCENTRE project

# The implicit risk of code-conforming structures in Italy

## A joint ReLUIS-EUCENTRE project

Iunio Iervolino
editor
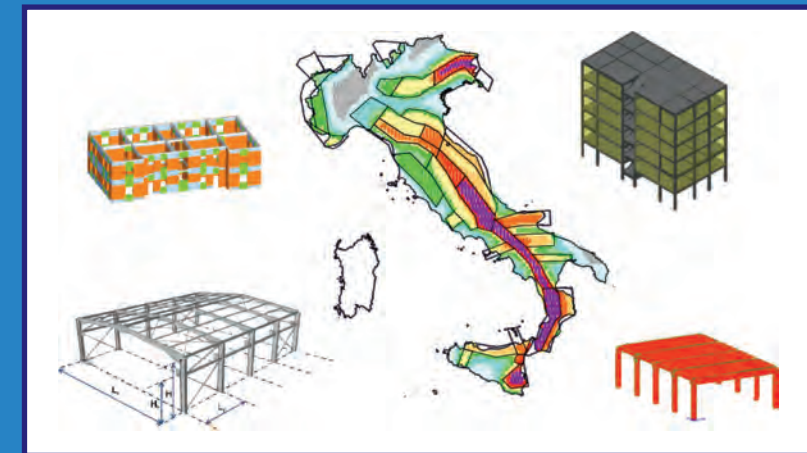
# The implicit risk
# of code-conforming structures
# in Italy

## A joint ReLUIS-EUCENTRE project

Iunio Iervolino
editor

**AT II – *Temi territoriali***

**RISCHIO IMPLICITO NTC – RINTC (2018)**

**Coordinators – for ReLUIS Iunio Iervolino, for EUCENTRE Paolo Bazzurro**

# Contents

# FOREWORD

This report collects the 2015-2017 deliverables of the RINTC project, which has been a joint project of ReLUIS and EUCENTRE. The project intended to assess the seismic risk of code-conforming structures in Italy. This report replaces the previous versions (2015 and 2016) thus the results presented herein are, in some cases, different from those presented in the previous years and from preliminary literature derived from this project. This is because, as discussed in the body of text, hypotheses and choices have been continuously revised until consolidation; this process might be continuing even after the end of the project. In general, all computed annual structural failure rates closely reflect specific assumptions on design, modeling and analysis of the considered structures, and this has to be always taken into account when discussing the results of this project.

The working group of the project (listed below) consists of the following six sub-groups, each of which explores (i) seismic risk assessment of code-conforming structures, designs, modelings, and analyses of (ii) masonry buildings, (iii) precast reinforced concrete buildings, (iv) reinforced concrete buildings, (v) steel buildings, and (vi) base-isolated reinforced concrete buildings. The remainder of this report is structured such that each chapter presents the research results from the corresponding sub-group: Chapter (i) introduces the objectives and framework of the project; Chapters (ii) – (vi) develop code-conforming designs, modelings and analyses of buildings for each structural type; Chapter (vii) concludes the study presenting the final results of the computed failure rates for the structures examined in the preceding chapters. Moreover, readers can refer to Appendices A to C for the details of the considerations on (a) usability-preventing limit state, (b) soil-structure interaction, and (c) model-uncertainty, respectively.

# WORKING GROUP

The results discussed in this report and the report itself are contributed by the following working group (in alphabetical order):

*Research units:* EUCENTRE, University of Chieti-Pescara Gabriele D'Annunzio (UniCh), University of Basilicata (UniBas), University of Camerino (UniCam), University of Genoa (UniGe), University of Naples Federico II (Unina-M, Unina-V), University of Padua (UniPd), Sapienza University of Rome (UniRm), University School for Advanced Studies Pavia (IUSS).

Paolo Bazzurro and Iunio Iervolino (coordinators), Davide Bellotti, Stefano Bracchi, Guido Camata, Daniela Camilletti, Serena Cattari, Donatello Cardone, Francesca Celano, Maddalena Cimmino, Nadia Conte, Mariana Ercolino, Andrea Dall'Asta, Francesa da Porto, Gaetano Della Corte, Luca de Sanctis, Antonio Di Cesare, Amedeo Flora, Paolo Franchin, Giovanni Guidi, Sergio Lagomarsino, Raffaele Landolfo, Gianmarco Leccese, Guido Magenes, Gennaro Magliulo, Vincenzo Manfredi, Martina Mandirola, Carlo Filippo Manzini, Angelo Masi, Fabio Micozzi, Claudio Modena, Fabrizio Mollaioli, Roberto Nascimbene, Fabrizio Noto, Andrea Penna, Crescenzo Petrone, Felice Ponzo, Laura Ragni, Paolo Ricci, Maria Rota, Fabrizio Scozzese, Enrico Spacone, Andrea Spillatura, Akiko Suzuki, Giusy Terracciano, Marco Terrenzi, Gerardo Verderame, Alessandro Zona.

Technical editor: Akiko Suzuki.

Document date: May 2018.

# CHAPTER I – INTRODUCTION AND PROJECT COMMONS

## 1.1 Scope of the project

The current Italian code provisions, i.e. Norme Tecniche per le Costruzioni 2008 (NTC08), allow engineers to design seismic resistant structures with a certain amount of safety with respect to the onset of given limit states (e.g., Collapse – SLC – or Life Safety – SLV). These safety margins against collapse and therefore against potential loss of life are implicitly assumed to be adequate, i.e.,comparable to those adopted for other risks. However, said safety margins are not directly computed but are rather implicitly embedded into the code requirements that prescribe the way engineers design structures to withstand rare and severe levels of ground shaking associated with long return periods, $T_R$, at each building site. In particular, the design values of $T_R$ depend not only on the limit state but also on the importance, the use and the expected life span of the structure to be designed. For example, for an ordinary structure[1] the SLV and SLC Limit States have to be verified for ground motion levels with return periods of 475 and 975 years, respectively, (i.e., respective probabilities of exceedance of 10% and 5% in 50 years).

Although compliance to these requirements guarantees a certain level of safety, the designer does not know the probability that the structure under design will reach (or exceed) a given limit state during its life span. Moreover, there is no explicit assurance in the code provisions that different structures designed for the same site, or similar structures at different sites, have the same margin of safety with respect, for example, to the SLC limit state. As of today, no studies have systematically addressed the issue of estimating such probabilities for several classes of buildings designed according to the current code provisions in Italy. Knowledge of these probabilities would form a sound basis for further considerations regarding the acceptability of the safety margin of current-code-conforming structures. The present project intends to start filling the existing gap by developing a systematic methodology for the estimation of collapse probabilities of buildings designed according to the current code and by applying it to different classes of buildings.

It is emphasized that the probabilities computed here do not account for the presence of errors that may sometimes lie in real buildings and for some sources of uncertainty. For example, the collapse of a building during an earthquake could be observed at a lower level of ground motion than anticipated in this study as a consequence of a mistaken implementation of code provisions or of human errors during construction. Moreover, the uncertainty in the capacity of such buildings is not considered. This means that collapse of these buildings has been assumed to occur when specific, deterministically chosen thresholds of selected structural response measures (i.e. maximum inter-story drift) are exceeded. In reality, however, collapse may occur at lower values of response or may not occur until higher levels of response than the threshold assumed here. Similarly, uncertainty about the characteristics of the material or of the dimensions of the structural members is neglected. Finally, it is assumed that the structure is not affected by any soil failure that may occur during an earthquake.

The definition of collapse considered here also deserves an additional clarification. Reaching, or even exceeding, the response measures' threshold values associated with collapse does not necessarily imply that the structure is expected to become a completely destroyed mass of debris. It may be the case that the structure is still standing but the level of damage in structural and non-structural elements is such that the building is irreparable and may have to be demolished.

The methodology devised here was applied to test bed buildings belonging to the major structural types of the Italian portfolio. According to the previous considerations, five main structural types (i.e., unreinforced masonry; URM, reinforced concrete; RC, precast reinforced

---

[1] E.g., Classe d'uso (building usage class) II and Vita Nominale (building expected life) ≥ 50 years.

concrete; PRC, steel; S, and base-isolated reinforced concrete; BI) located in five sites with different levels of seismic hazard (i.e., Milan, Caltanissetta, Rome, Naples and L'Aquila) were selected (see Figure 1.1.1 and Table 1.1.1). These buildings were designed and analyzed for Soil Type A and C (defined according to NTC08, Table 1.1.2). In order to cover a wider variety of structures, various configurations in terms of structural details and number of stories were selected for each structural type.

Table 1.1.2 summarizes some general characteristics of the analyzed buildings; additional details will be supplied later in this document while Figure 1.1.2 shows a few models for each structural type.



Figure 1.1.1 Location of the five selected cities. Legend: AQ=L'Aquila; NA=Naples; RM = Rome; CL=Caltanissetta; MI=Milan.

Table 1.1.1 Location and design PGA levels (for Soil Types A and C) of the five selected cities.

| City | Longitude | Latitude | PGA (475 years) (Soil A) [g] | PGA (475 years) (Soil C) [g] | Seismic Zone |
|---|---|---|---|---|---|
| Milan | 9.186 | 45.465 | 0.0495 | 0.0743 | IV |
| Caltanissetta | 14.060 | 37.480 | 0.0762 | 0.11428 | III-b |
| Rome | 12.479 | 41.872 | 0.1204 | 0.1806 | III-a |
| Naples | 14.268 | 40.854 | 0.1668 | 0.24338 | II |
| L'Aquila | 13.399 | 42.349 | 0.2607 | 0.3451 | I |

Table 1.1.2 Soil Type A and C defined as a function of the average shear wave velocity in the top 30m of soil, $V_{s,30}$ (from Table 3.2II, NTC08).

| Soil Type | $V_{s,30}$ [m/s] |
|---|---|
| A | > 800 |
| C | 180< $V_{s,30}$< 360 |

Table 1.1.2 Main characteristics of the selected structural type[2]

| | Soil Type | Milan | Caltanisse-tta | Rome | Naples | L'Aquila |
|---|---|---|---|---|---|---|
| **RC** | *Soil A* | --- | --- | --- | --- | 9-story (BF/PF/IF) |
| | *Soil C* | 3/6/9-story (BF/PF/IF) 9-story SW | 6-story (BF/PF/IF) | 6-story (BF/PF/IF) | 3/6/9-story (BF/PF/IF) Mod.Unc. 9-story SW (also w/ SSI) | 3/6/9-story (BF/PF/IF) Mod.Unc. 9-story SW 3-story existent (WP7) |
| **URM** | *Soil A* | 2/3-story, regular/irregular | 2/3-story, regular | 2/3-story, regular Mod. Unc. | 2/3-story, regular/ irregular | 2/3-story, regular ModUnc |
| | *Soil C* | 2/3-story, regular/irregular | 2/3-story, regular/ irregular | 2/3-story, regular/ irregular | 2/3-story, regular/ irregular 5-story existent (WP7) | 2/3-story, regular/irregular 2/3-story existent (WP7) |
| **PRC** | *Soil A* | 1-story, geometry 1/2/3/4 | --- | --- | 1-story, geometry 1/2/3/4 | 1-story, geometry 1/2/3/4 |
| | *Soil C* | 1-story, geometry 1/2/3/4 | --- | --- | 1-story, geometry 1/2/3/4 | 1-story, geometry 1/2/3/4 |
| **S** | *Soil A* | 1-story, geometry 1/2/3/4 w/ and w/o panels | --- | --- | 1-story, geometry 1/2/3/4 w/ and w/o panels | 1-story, geometry 1/2/3/4 w/ and w/o panels |
| | *Soil C* | 1-story, geometry 1/2/3/4 w/ and w/o panels | --- | --- | 1-story, geometry 1/2/3/4 w/ and w/o panels | 1-story, geometry 1/2/3/4 w/ and w/o panels 1story-existent (WP7) |
| **BI** | *Soil A* | --- | --- | --- | --- | --- |
| | *Soil C* | --- | --- | --- | 6-story, HDRB/HDRB+Slider | 6-story, HDRB/HDRB+Sli-der/DCFP (11 configurations) Mod.Unc. |

[2]The acronyms used in the table are explained below:
- BF, IF and PF are respectively Bare/Infilled/Pilotis frames,
- SW are Shear Walls
- ModUnc: Modelling Uncertainty (see Appendix C)
- SSI: soil-structure interaction (see Appendix B)
- WP7: indicates the working package related to existing buildings
- HDRB: High damping rubber bearing
- DCFP: Double-curvature friction pendulum system (FPS in Chapter 6)

(a)

(b)

(c)

(d)

(e)
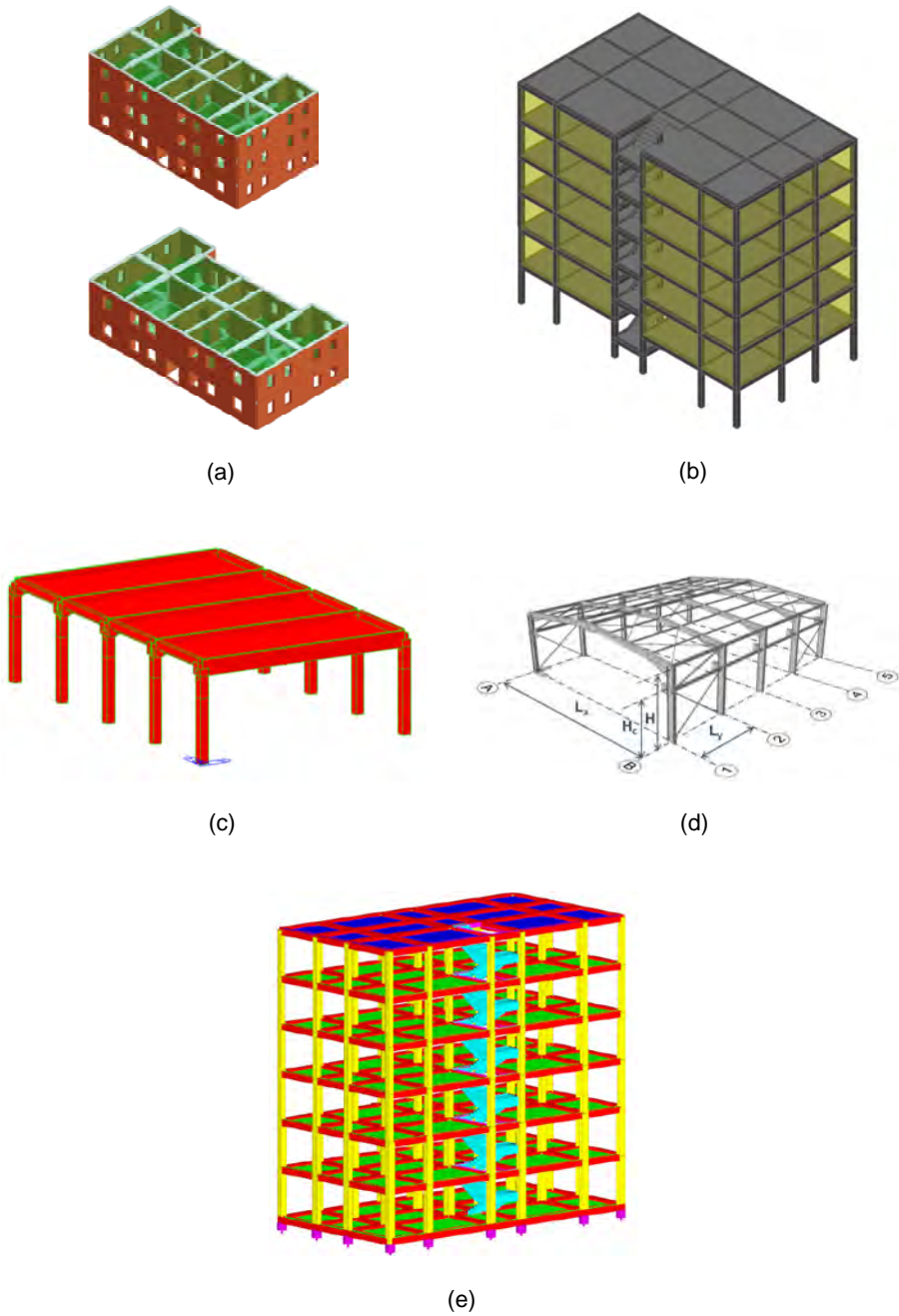
Figure 1.1.2 Examples of models for URM (a), RC (b), PRC (c), Steel (d) and BI reinforced concrete (e) buildings.

## 1.2   Seismic hazard

As previously stated, the final goal of this study is to estimate the nominal probability of failure for test bed buildings designed according to the current Italian Code (Normativa Tecnica delle Costruzioni, NTC08). The estimation procedure is necessarily supported by the assessment of the seismic hazard at the sites where the test bed buildings are assumed to be located. The adopted seismic hazard model is the one developed by Istituto Nazionale di Geofisica e Vulcanologia (INGV): Convenzione INGV-DPC 2004 – 2006, which is the model underlying current code provisions. The hazard estimates are freely available online (http://esse1-gis.mi.ingv.it/), however, they are not sufficient for the scope of this study, which needs hazard estimates in terms of spectral acceleration, Sa, at several oscillator periods both on rock and different reference soil conditions and at many values of annual probability of exceedance. In addition, for reasons to be clarified later, we needed to know which scenario earthquakes (i.e., magnitude, M, and source-to-site distance, R) contributed the most to the hazard at different return periods. Therefore, the core of the INGV seismic hazard model was implemented in the Openquake platform (Global Earthquake Model, 2012) to meet the objectives of this study. More specifically, we implemented Branch 921 of the MPS04 source model of the INGV study together with the Ambraseys et al. 1996 Ground Motion Prediction Equation (GMPE). This combination of the source model and the GMPE was selected because it provides hazard estimates that are very close to the median hazard estimates from Strucchi et al. (2011).

This additional effort allowed us to compute Sa hazard curves and the contributing earthquakes in terms of M and R for any combination of:

- Oscillator Period, *T*;
- Soil Type, as defined in terms of average shear wave velocity in the top 30m of soil, $V_{s30}$, in the NTC08;
- Annual Exceedance Probability or its reciprocal, namely the return period ($T_R$).

The Openquake (OQ) hazard estimates were compared to the hazard for rock conditions (i.e., Soil Type A) from INGV and from the NTC08 code provisions. A hazard comparison for Type C soil was, of course, not possible. Figure 1.2.1 and Figure 1.2.2 show a very favorable comparison of uniform hazard spectra (UHS) and hazard curves for *T*=1.0s for the city of Rome. The discrepancies are in part due to the exclusive use of branch 921 instead of the entire logic tree and in part to a slight mismatch in site coordinates: Openquake performs its computation at the exact longitude and latitude that a user specifies, while the INGV spectra are computed for the grid point closest to the location of interest (Figure 1.2.1b).
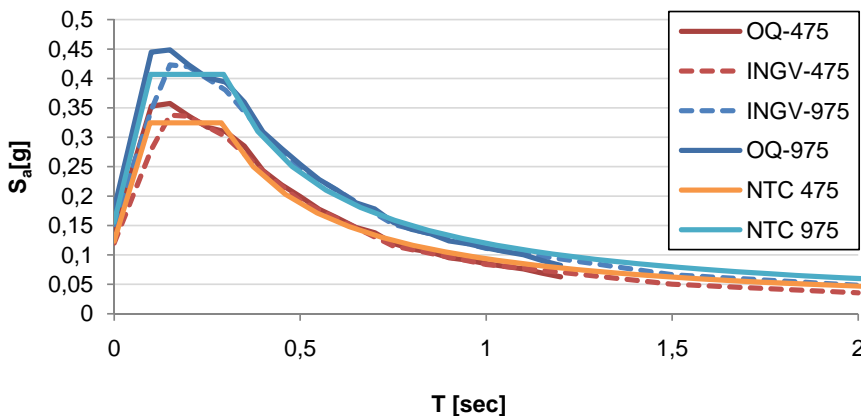


(a)
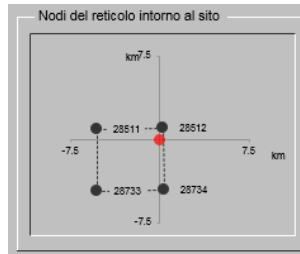
(b)

Figure 1.2.1 (a) UHS for Rome, Soil Type A, $T_R$ values of 475 and 975 years computed according to INGV, Openquake and NTC08. (b) The OQ and NTC08 hazard values are computed at the location (red dot) while the INGV hazard is computed at the grid point #28512.
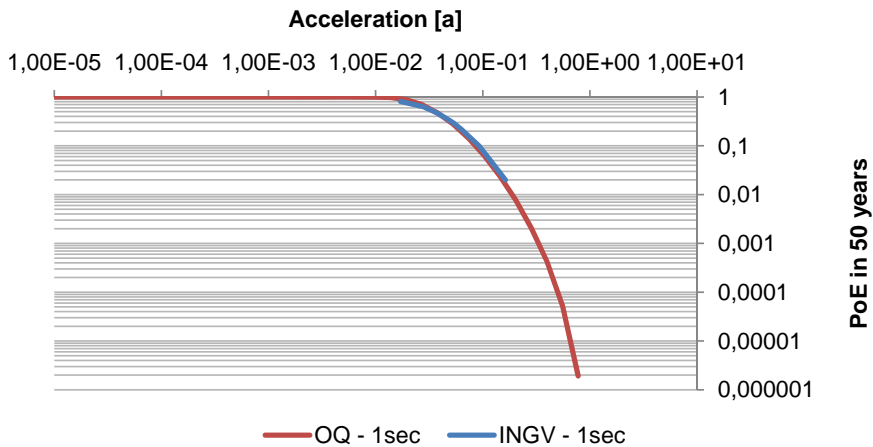


Figure 1.2.2 PGA hazard curve comparison for Rome, Soil Type A, T=1.0s. Acceleration is expressed in g. Legend: PoE: Probability of Exceedance.

Figure 1.2.3 shows a set of hazard curves computed using OQ for the five selected sites (i.e., L'Aquila, Naples, Rome, Caltanissetta and Milan), Soil Type A ($V_{s,30}$ > 800 m/s) and Type C (180 < $V_{s,30}$ < 360 m/s), and oscillator period of 0s (i.e., PGA), T=0.5s and T=2.0s.

Since long-period structures (e.g., base-isolated) were included in the project, it has been necessary to extend the hazard study to periods higher than two seconds (the upper limit considered in the adopted GMPE of Ambraseys, 1996). In particular, the attenuation law of Akkar and Bommer (2010) has been used to compute hazard and disaggregation which are the fundamental data for the record selection procedure and the following risk calculation. A comparison between these two models in terms of hazard curve and Uniform Hazard Spectrum (UHS) is presented in Figure 1.2.4 and Figure 1.2.5.

The influence of vertical component of the ground motion in the response was investigated particularly for base-isolated and steel structures. However, it was not performed in an ad-hoc record selection: the existent database was integrated with the vertical component related to the already selected horizontal records.
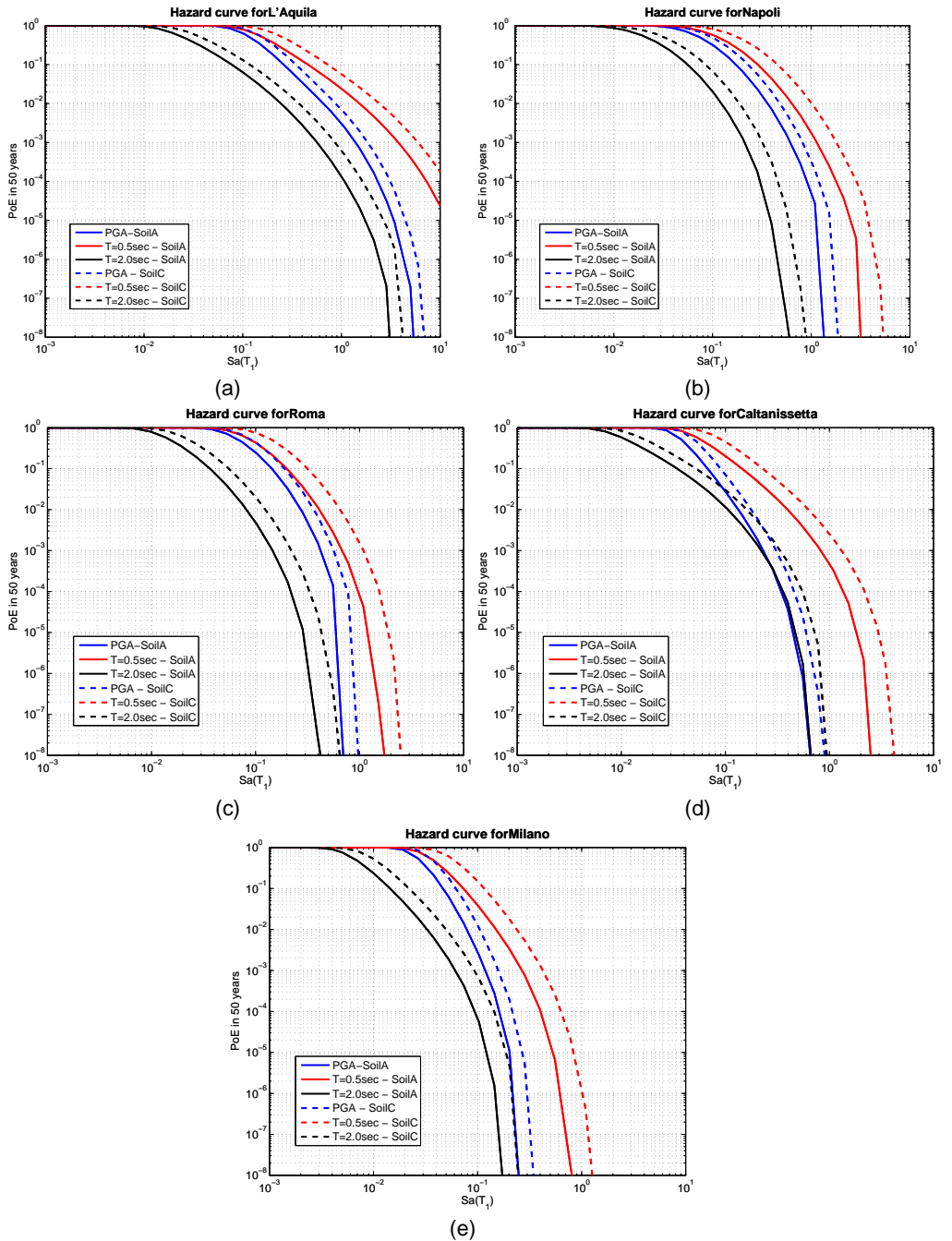
Figure 1.2.3 Hazard curves for PGA, and $S_a$'s at T=0.5s and T=2.0s computed for Soil Type A conditions for L'Aquila (a), Naples (b), Rome (c), Caltanissetta (d) and Milan (e).
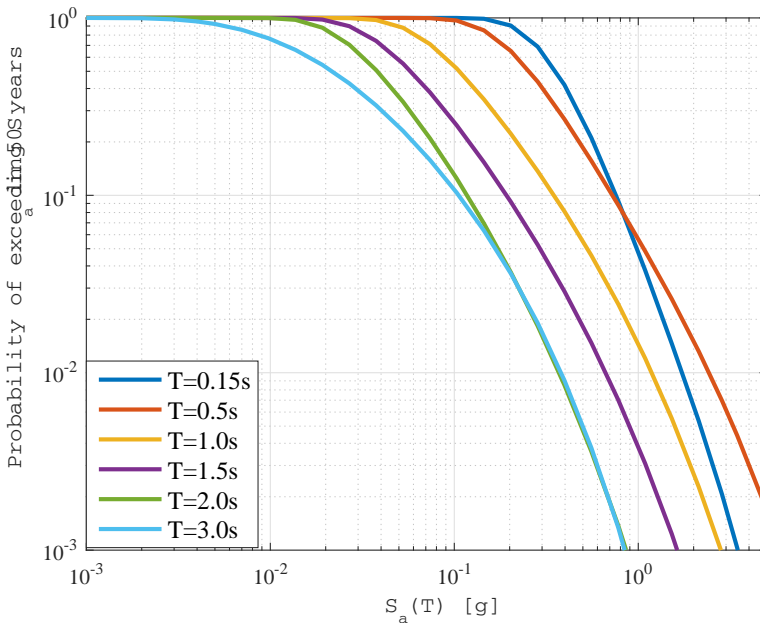
Figure 1.2.4 Hazard curves at L'Aquila for Soil Type C; the curve at T=3.0s was computed according to the model of Akkar and Bommer (2010).
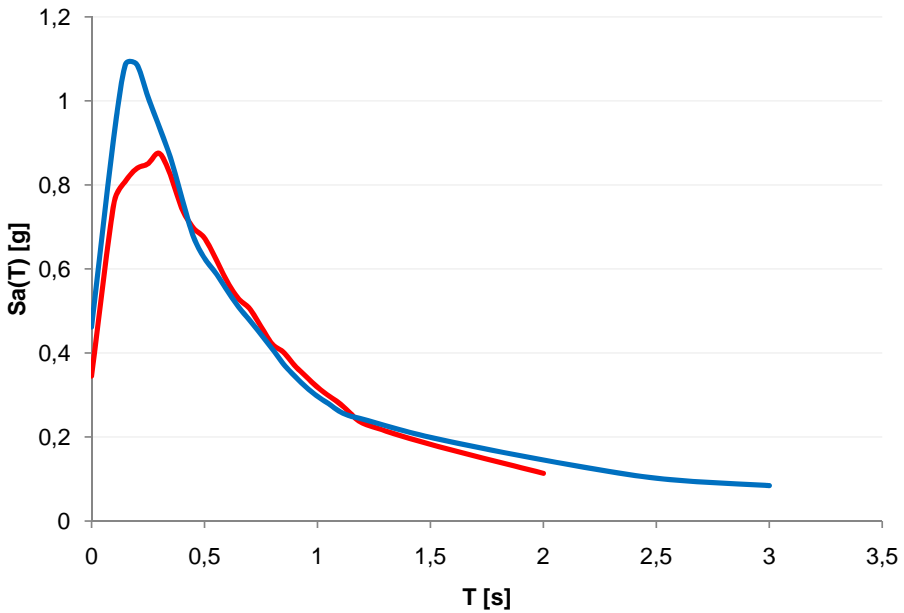


Figure 1.2.5 UHS, for Soil A, at L'Aquila according to Ambraseys (1996), red line, and Akkar and Bommer (2010), blue line.

## 1.3    Record selection

Since the structural assessment method of choice is non-linear dynamic analysis, the input ground motion selection is an essential step. The ITACA record database (http://itaca.mi.ingv.it), which includes accelerograms from Italian earthquakes, is the preferred source for ground motion acceleration time histories for this study. However, the particular restrictions and conditions imposed by the record selection procedure were such that an additional dataset had to be added to augment the pool of available accelerograms. For this reason, when the ITACA database did not provide enough records for our purposes, the missing records were selected from the NGAwest2 database (http://ngawest2.berkeley.edu/), which includes accelerograms from earthquakes that occurred in different parts of the world. NGAwest2 records were needed especially for high ground shaking intensity levels.

The selection algorithm utilized in this study is based on the Conditional Spectrum (CS) approach (Baker, 2011, Jayaram and Baker, 2011, Lin et al., 2013). The CS provides the distribution of Sa at any period, $T_i$, conditioned on a given value of Sa at a fixed period of interest, $T_j$ (e.g., the fundamental period of the structure, $T_1$). The CS approach is often used, as done in this study, in Multiple Stripe Analysis (MSA) framework (Jalayer, 2003; Jalayer and Cornell, 2002). MSA is a methodology aimed at computing the distributions of one (or more) engineering demand parameters (EDPs) for many different levels of $Sa(T_j)$ experienced by the structure under consideration. A set of response analyses is carried out for any selected level of $Sa(T_j)$ using a suite of ground motion records having the same $Sa(T_j)$ level either naturally or, more often, artificially via amplitude scaling. Each set of response analyses provides a stripe of EDP values. The CS procedure allows to select a set of ground motion records with a given level of $Sa(T_j)$ and the following features:

- The records are statistically consistent with the distribution of Sa values at any given period $T_i \neq T_j$ conditioned on the given level of $Sa(T_j)$.
- The records are "linked" to
  - o the dynamic characteristics of the structure through a selection of the conditioning period $T_j$ in such a way that $Sa(T_j)$ is a good predictor of the EDP of choice, and
  - o the site, favoring records consistent with the earthquake scenarios, (expressed in terms of M and R), that are more likely to cause the $Sa(T_j)$ level at the site (obtained via hazard disaggregation, Bazzurro and Cornell, 1999).

An automatic procedure for record selection based on the CS approach is freely available online (http://web.stanford.edu/~bakerjw/research/conditional_spectrum.html). The main steps of this approach can be summarized as follows:

1. Definition of the distribution of $Sa(T_i)$ conditioned on $Sa(T_j)=x$ for any $T_i \neq T_j$. The original version of the code identifies a reference M-R scenario (either the mode or the mean of the M-R distribution conditional on observing the $Sa(T_j)=x$ at the site obtained via disaggregation) and use it to define the conditional spectrum (i.e., both the mean and variability). This approach is approximate and, in line with the suggestions of Lin et al. (2013), the original code was successively modified to account for multimodal M-R distributions.
2. Simulation of *n* response spectra, where *n* is the desired number of records for that stripe, according to the CS previously defined at bullet 1.
3. Selection of *n* records which, if needed, are individually scaled in such a way as to minimize the difference between each response spectrum and a simulated one. To assess failure probability of buildings in Italy, the records were first extracted from the ITACA database and, if no records with similar spectra were available there, the additional missing records were extracted from the NGAwest2 database.

### 1.3.1    Adopted record selection procedure

Note that both in the original and in the modified approaches discussed in the previous section, the record selection (step #3) is performed without regard to the characteristics of the causative earthquake. In other words, the M and R values associated with each record are not

considered. This implies that the structural response to a given record is affected mostly by spectral shape and nothing else. Although this may be true in many practical cases, the duration or the energy content of records, which may be correlated with M and R of the causative earthquake, could play a non-negligible role in the prediction of structural response. Hence, the existing algorithms have been further improved in order to include the M-R distribution suggested by the disaggregation into the record selection. This enhancement aims at accounting, albeit implicitly, for other characteristics of the records other than their spectral shape when computing structural responses.

Therefore, step #3 of the above procedure was modified to explicitly account for the M-R distribution associated with the observation of $Sa(T_j)=x$ at the site. For example Figure 1.3.1a below shows the M-R characteristics of the record set selected according to the original CS methodology for the city of Rome, T=1s at Intensity Measure Level (IML) 5 (see Table 1.3.1). Since the CS methodology does not explicitly account for the M and R characteristics of the selected records but only for their spectral shape the distribution of M and R of this set (Figure 1.3.1a) is not in agreement with the M-R distribution obtained via disaggregation of the $S_a(T_1)$ at the given IML for the city of Rome shown in Figure 1.3.1b.



(a)                                                                (b)
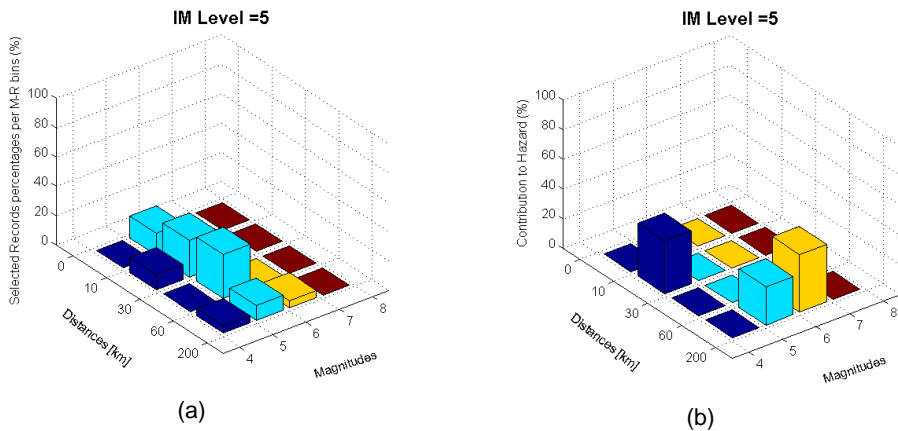
Figure 1.3.1 M-R characteristics of records selected for Rome, T=1.0s, IML5 according to the original CS method (a), Disaggregation at IML5 of seismic hazard related to $S_a$(T=1.0s) (b).

In this case, since about 30% of the contribution (Figure 1.3.1(b)) came from a bin with M between 4 and 5 and R between 10 and 30 km, 6 out of 20 records were selected with M and R in this bin. Practically speaking, the records selected by the original CS methodology with M and R belonging to bins with zero or negligible contributions are screened out from the set. The final set of records selected by the modified procedure adopted in this study contains a number of records in each M and R bin whose contribution is proportional to the occurrence of the $S_a$ level at the site.

As previously mentioned this enhanced selection procedure is integrated in a multiple stripe analysis framework (see Jalayer, 2003). Ten different values of $Sa(T_j)=x$ were considered according to given hazard levels. The hazard levels at each one of the five cities of Milan, Caltanissetta, Rome, Naples, and L'Aquila were selected to be corresponding to the mean return periods listed in Table 1.3.1. Hence, each set of records corresponding to one value of $Sa(T_j)=x$ will be different for each:

- City of interest
- Natural period of the structure
- Soil Type

Table 1.3.1 Return periods for 10 Intensity Measure Levels.

| # IML | Return Period [years] |
|:---:|:---:|
| 1 | 10 |
| 2 | 50 |
| 3 | 100 |
| 4 | 250 |
| 5 | 500 |
| 6 | 1000 |
| 7 | 2500 |
| 8 | 5000 |
| 9 | 10000 |
| 10 | 100000 |

Note that the GMPE used in the hazard formulation (Ambraseys et al., 1996) provides the maximum horizontal component and not the geometric mean of the two horizontal components. Therefore, for the sake of consistency, the selection has been done here on the basis of the maximum horizontal component, which is not necessarily used in common practice. Figure 1.3.2 shows, as an example, the spectra of 20 pairs of records for the case of L'Aquila, Soil Type C and $S_a(T_1=1.0s)=0.139g$, and $S_a(T_1=1.0s)=0.558g$ which are the $3^{rd}$ and the $6^{th}$ IMLs, respectively.
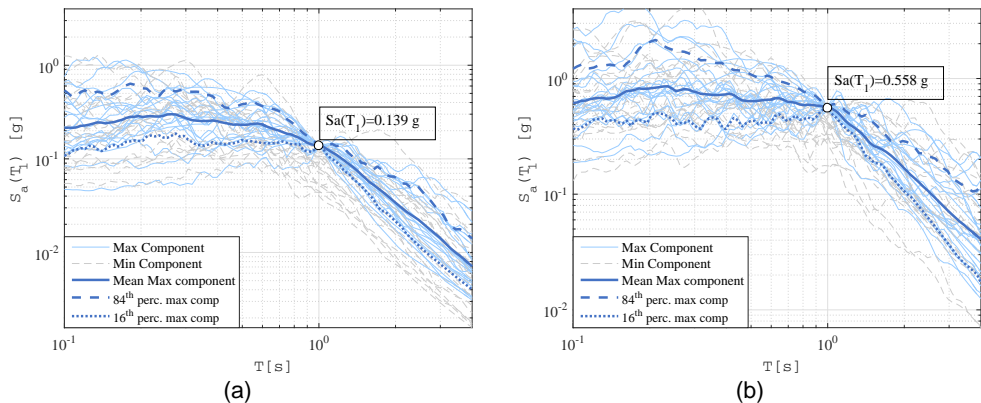


Figure 1.3.2 Response spectra of both horizontal components of selected records for the case of L'Aquila, Soil Type C, and IMLs 3(a) and 6(b).

The values of the reference period $T_j$ were selected to be appropriate for the structures whose response will be evaluated. In the end, in order to cover a satisfactory range, five periods have been chosen: 0.15s, 0.5s, 1.0s, 1.5s and 2.0s. Consequently, the record selection has been performed for 500 cases given by the combination of five cities (L'Aquila, Naples, Rome, Caltanissetta and Milan), two Soil Types (A and C), five oscillator periods, and ten $S_a(T_j)=x$ levels. It should be pointed out that for Soil Type A the $V_{s,30}$ limits were relaxed in order to increase the pool of candidate records on hard soil so that both the matching with spectral shape and M-R characteristics could be achieved. For each case, 20 different accelerograms were selected.

As an aside, note that to reduce the computational effort, all the selected records have been post processed prior to using them in the response analyses. The post-processing involved removing parts of the signal that, when omitted, do not cause any significant change in the response. The main steps of the post-processing procedure are summarized below:

- Computation of Normalized Arias Intensity (Husid, 1969, and Arias, 1970)

$$I_{a,N} = \frac{\int_0^t a(t)^2 dt}{\int_0^T a(t)^2 dt} \tag{1.1}$$

Computation of $t_{0.05\%}$ and $t_{99.95\%}$, which represents the times that bracket $I_{a,N}$ between 0.05% and 99.95% of the total value of $I_{a,N}$

- Cut off the parts of the signal outside of the $t_{0.05\%}$ and $t_{99.95\%}$ range.

This procedure is completely independent of the scaling factor that is applied to the record to match the CS as described above. Figure 1.3.3 compares the original and the cut records for two cases extracted from the selected set for Milan, T=1.0s and Soil Type C.
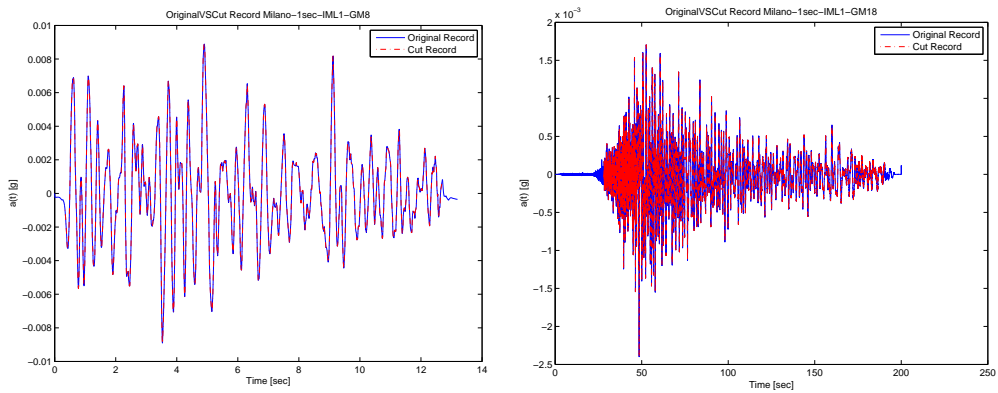


Figure 1.3.3 Original vs cut records

## 1.4   Summary of methodology, working hypotheses and uncertainty

- The final results of the project are represented by the annual failure rates ($\lambda_f$) of the considered sample of structures. Such failure rates are obtained by integration of structural fragility and seismic hazard for the sites where the structures are supposed to be located. In particular, equation (1.2) is considered.

$$\lambda_f = \lambda \cdot \int_0^{+\infty} P\big[ failure|IM = x \big] \cdot f_{IM}(x) \cdot dx \tag{1.2}$$

where: $\lambda$ is the rate of earthquakes above a magnitude of interest at the site of the construction, $f_{IM}(x)$ is the distribution of the considered ground motion intensity measure (IM, spectral acceleration herein) given an earthquake event and $P\big[ failure|IM = x \big]$ is the fragility of the building. Equation (1.2) , may be rewritten in the more familiar format of in Equation (1.3), with obvious meanings of the symbols.

$$\lambda_f = \int_0^{+\infty} P\big[ failure|IM = x \big] \cdot \big| d\lambda_{IM}(x) \big| \tag{1.3}$$

In fact, structural fragility has been computed by discretizing the domain of the IM at the same ten levels at which hazard was computed. At each of these levels fragility was evaluated as per Equation (1.4) where EDP is a response measure (engineering demand parameter), the lower case C indicates structural capacity and 'col' indicates collapse cases (global instability) according to the terminology of Shome and Cornell (2000).

$$P\left[\,failure\big|IM_i\right] = \left[1 - \Phi\left(\frac{\log\left(EDP_C\right) - \mu_{\log\left(EDP|IM_i\right)}}{\sigma_{\log\left(EDP|IM_i\right)}}\right)\right]\cdot\left(1 - \frac{N_{col,i}}{N_{tot}}\right) + \frac{N_{col,i}}{N_{tot}} \tag{1.4}$$

The preferred method for structural analysis is the multi-stripe nonlinear dynamic analysis. The procedure to select records for the ten considered stripes was described earlier in this chapter.

- The EDP is the maximum, between the two horizontal directions of the structure, demand over capacity ratio (in terms of interstory drift angle or roof drift angle).

- All models are lumped plasticity 3D models (except masonry and steel structures). The analyses neglected the vertical component of ground motion. Soil structure-interaction is neglected except specific cases (see Appendix B).

- The buildings are designed for the life-safety limit states and accounting for damage preventing code limitations; the annual rate of failure will be quantified both in terms of global collapse and onset of damage preventing usability (see Appendix A).

- Uncertainty is, in general, related only to hazard and to record-to-record variability reflecting on the structural response. Structural models and capacity thresholds are deterministic except some cases where modeling uncertainty is considered (see Appendix C).

- All models with the same typology are analyzed with the same software: the TREMURI software (Lagomarsino et al., 2013) was adopted for the masonry buildings while OpenSees (McKenna, 2011) for all the other structural types.

## 1.5   References

Akkar, S. and Bommer, J.J. (2010) "Empirical Equations for the Prediction of PGA, PGV, and Spectral Accelerations in Europe, the Mediterranean Region, and the Middle East", Seismological Research Letters, 81(2), 195-206.

Arias, A. (1970). "A measure of earthquake intensity", in Seismic design for nuclear power plants, (R.J. Hansen, ed.) MIT Press, Cambridge MA, pp. 438-483. Baker, J. W., and Cornell, C. A. (2006). "Spectral shape, epsilon and record selection." Earthquake Engineering & Structural Dynamics, 35(9), 1077–1095.

Baker, J.W. (2007). "Probabilistic structural response assessment using vector valued intensity measures" Earthquake Engng Struct. Dyn., 36:1861–1883.

Baker, J.W. (2011). "Conditional Mean Spectrum: Tool for ground motion selection", Journal of Structural Engineering, 137(3), 322-331.

Baker, J.W. (2015). "Efficient Analytical Fragility Function Fitting Using Dynamic Structural Analysis", Earthquake Spectra, 31(1), 579–599.

Bazzurro P., Cornell C.A. (1999). "On disaggregation of seismic hazard." Bulletin of Seismological Society of America, BSSA; 89(2), 501–520.

Bradley, B. A., and Dhakal, R. P., (2008). "Error estimation of closed-form solution for annual rate of structural collapse", Earthquake Engineering & Structural Dynamics 37, 1721–1737.

Convenzione INGV-DPC (2004 – 2006), "Progetto S1 Proseguimento della assistenza al DPC per il completamento e la gestione della mappa di pericolosità sismica prevista dall'Ordinanza PCM 3274 e progettazione di ulteriori sviluppi" (http://esse1.mi.ingv.it/deliverable.html).

Global Earthquake Model (2012). Available from: http://www.globalquakemodel.org/ [12 September 2012].

Husid, L. R. (1969) "Características de Terremotos, Análisis General." Revista del IDIEM 8, Santiago, Chile, 21–42.

Iervolino, I., Galasso, C., Cosenza, E., (2010). "REXEL: computer aided record selection for code-based seismicstructural analysis." Bulletin of Earthquake Engineering 8, 339-362.

Jalayer, F. (2003). "Direct probabilistic seismic analysis: Implementing non-linear dynamic assessments." Ph.D. Dissertation, Stanford University.

Jalayer, F., Cornell C.A., (2002), "Alternative Nonlinear Demand Estimation Methods for Probability-Based Seismic Assessments", Earthquake Engng Struct. Dyn., 00, 1–6

Jayaram N., Lin T., Baker J. (2011), "A Computationally Efficient Ground-Motion Selection Algorithm for Matching a Target Response Spectrum Mean and Variance", Earthquake Spectra, 27(3), 797–815.

Lagomarsino S., Penna A., Galasco A., Cattari S. (2013) "TREMURI Program: An equivalent frame model for the nonlinear seismic analysis of masonry buildings. Engineering Structures", 56: 1787-1799.

Lin T., Harmsen S.C., Baker, J.W., and Luco N. (2013) "Conditional Spectrum Computation Incorporating Multiple Causal Earthquakes and Ground-Motion Prediction Models", Bulletin of the Seismological Society of America, 103(2A), 1103-1116.

Lin T., Haselton C. B. and Baker, J.W. (2013), "Conditional spectrum-based ground motion selection. Part I: Hazard consistency for risk-based assessments", Earthquake Engng Struct. Dyn., 42(12), 1847-1865. DOI: 10.1002/eqe

McKenna, F. (2011) "OpenSees: a framework for earthquake engineering simulation", Computing in Science & Engineering, 13(4), 58-66.

Meletti C., Montaldo V. (2007) "Stime di pericolosità sismica per diverse probabilità di superamento in 50 anni: valori di ag. Progetto DPC-INGV S1", Deliverable D2, http://esse1.mi.ingv.it/d2.html

Montaldo V., Meletti C. (2007) "Valutazione del valore della ordinata spettrale a 1sec e ad altri periodi di interesse ingegneristico." Progetto DPC-INGV S1, Deliverable D3, http://esse1.mi.ingv.it/d3.html

NTC08 (2008) "Norme Tecniche per le Costruzioni", Decreto Ministeriale del 14/1/2008, Suppl. ord. n. 30 alla G.U. n. 29 del 4/2/2008.

Spallarossa D., Barani S. (2007). "Disaggregazione della pericolosità sismica in termini di M-R-ε. Progetto DPC-INGV S1, Deliverable D14", http://esse1.mi.ingv.it/d14.html

Shome, N., Cornell, C.A. (2000). "Structural seismic demand analysis: Consideration of collapse", In Proceedings of the 8th ASCE Specialty Conference on Probabilistic Mechanics and Structural Reliability (pp. 1-6). South Bend, Indiana: University of Notre Dame.

Stucchi M, Meletti C, Montaldo V, Crowley H, Calvi GM, Boschi E (2011). "Seismic hazard assessment (2003–2009) for the Italian building code". B. Seismol. Soc. Am., 101: 1885-1911.

# CHAPTER II – MASONRY STRUCTURES

## 2.1 Case study structures

Masonry buildings with eight different (in plan) architectural configurations were analyzed in the course of the project. Since these configurations were defined to be representative of typical Italian residential buildings, they have some common features concerning materials, structural details, number and typologies of diaphragms. Keeping in line with the main objective of the project, they were designed according to the Italian code provisions (named in the following as NTC 2008) for new buildings.

In particular, all the designed configurations are two- or three-story unreinforced masonry buildings made of perforated clay units with mortar joints characterized by mechanical properties consistent with the prescriptions of the NTC 2008. Some of these buildings (in particular the "E" type configurations) were also designed assuming they were made of concrete blocks instead of perforated clay units. As far as the diaphragm is concerned, slabs made of combined concrete and hollow clay blocks were assumed, as the most common practice in new residential masonry buildings in Italy. Some of them were designed also for the case of reinforced masonry buildings, as discussed in section 2.2.5.

In particular, the architectural configurations examined can be divided into three main categories, hereinafter denoted as:

- ''C'' type (regular) and ''I'' type (irregular) configurations, designed by the Genoa Research Unit (RU);
- "E'' type (regular and irregular) configurations, designed by the Pavia RU;
- ''F'' type and ''G'' type (both irregular) configurations, designed by the Padua RU.

### 2.1.1 Description of the "C" and "I" type configurations

The UR of Genoa was responsible for the design and modelling of regular (''C'' type) and irregular (''I'' type) buildings described in the following. In both cases, two or three-story configurations were considered with slabs made of a combination of concrete and hollow clay blocks (20+4 cm solution); moreover, in all the defined configurations the roof was assumed as plane.

2.1.1.1 "C" type –regular configuration

In Figure 2.1.1, the plan and 3D views of a ''C'' configuration building (referring to the three-story building) are provided. The inter-story height of the building is 3.1 m.



<table>
<tr><td>(a)</td><td>(b)</td></tr>
</table>
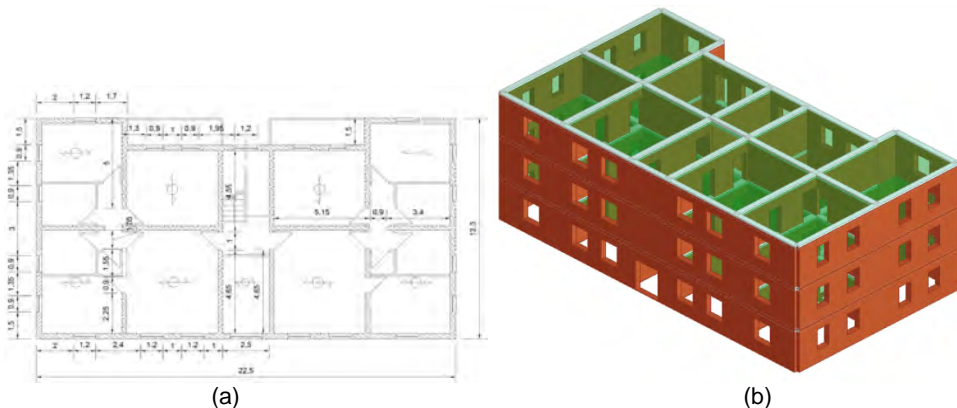
Figure 2.1.1 Plan view (a) and 3D view (b) of the considered ''C'' type configuration.

The assumed design loads are summarized in Table 2.1.1.

Table 2.1.1 Design loads for "C" type configurations.

|                    | $G_{1k}$ [kN/m²] | $G_{2k}$ [kN/m²] | $Q_k$ [kN/m²] |                    |
|--------------------|------------------|------------------|---------------|--------------------|
| Intermediate floor | 3.0              | 2.5              | 2.0           | Cat. A             |
| Roof               | 3.0              | 1.1              | (*)           | snow ≤ 1000 m a.s.l. |
| Stairs/Balcony     | 3.0              | 2.5              | 4.0           |                    |

2.1.1.2  "I" type irregular configuration

According to the definitions of 'regularity in plan' and 'regularity in elevation' provided by the NTC 2008 (§ 7.2.2), the ''I'' type configurations are irregular as illustrated in Figure 2.1.2



(a)                                                                                           (b)



(c)                                                                                           (d)
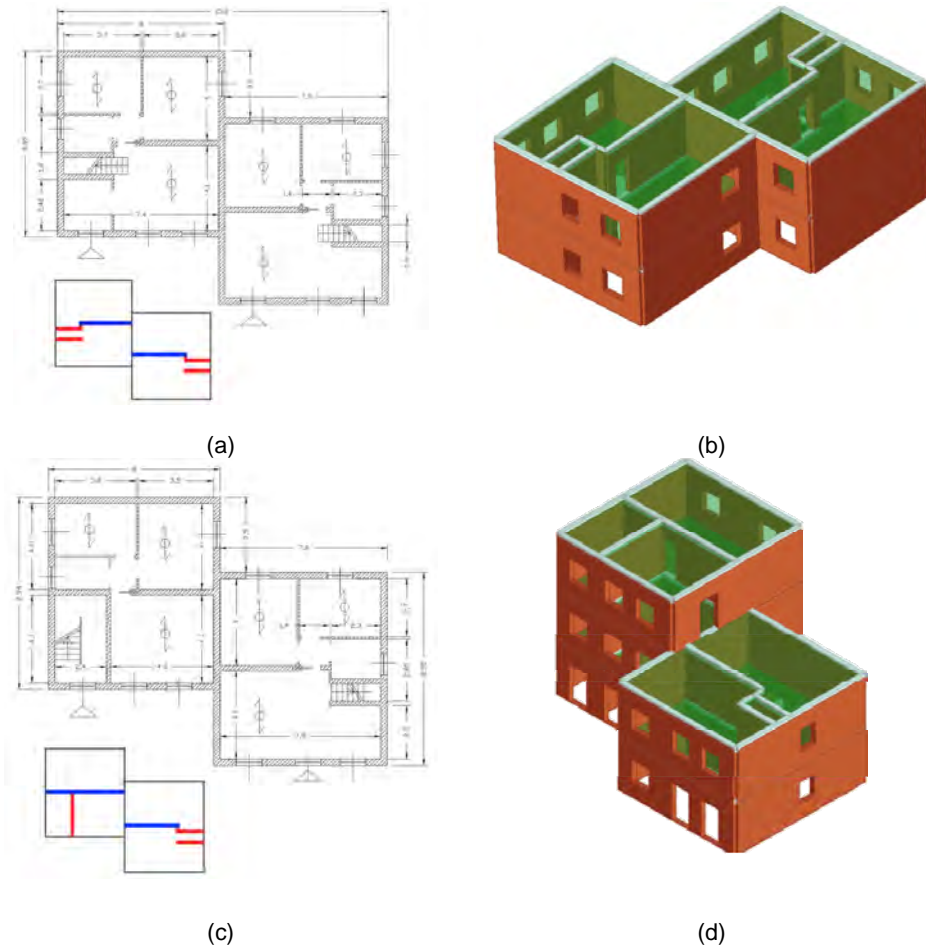
Figure 2.1.2 Plan views and 3D views of the ''I'' type configurations: 2-story building tagged ''I1''(a-b) and 3-story building tagged ''I2'' (c-d). Next to each plan view a scheme about the structural role of the internal walls is provided: the walls only bearing vertical loads are marked in red while walls bearing both horizontal and vertical loads are marked in blue.

The two-story building presents only plan irregularity and inter-story height of 3.3 m, while the three story building presents irregularity both in plan and in elevation since it is composed by two units, with a different number of stories (one building with two stories and the other one with three stories). In this case the inter-story height is 3.1 m.

For each of these two buildings the internal bearing walls play a different role: the two walls bearing the staircase carry only vertical loads (the red ones in Figure 2.1.2 with a thickness equal to 0.2 m) while the other internal bearing walls carry both vertical and horizontal loads (the blue ones in Figure 2.1.2 with a thickness equal to 0.25 m). In Figure 2.1.2 the plan views and some 3D views of the two configurations (referred to as I1 for the two-story building and I2 for the three-story one) together with an explanation of the different role of each internal bearing wall are provided. The external walls are charactherized by the thickness equal to 0.3 m.

The assumed design loads are summarized in Table 2.1.2.

Table 2.1.2 Design loads for "I" type configurations.

|  | $G_{1k}$ [kN/m$^2$] | $G_{2k}$ [kN/m$^2$] | $Q_k$ [kN/m$^2$] |  |
|---|---|---|---|---|
| Intermediate floor | 3.0 | 2.5 | 2.0 | Cat. A |
| Roof | 3.0 | 1.1 | (*) | snow ≤ 1000 m a.s.l. |
| Stairs | 3.0 | 2.5 | 4.0 |  |

### 2.1.2    Description of the "E" type configurations

The Pavia RU was responsible for the design and modelling of four ''E'' type building configurations, defined with reference to different structural typologies. Among these, three are regular in plan and elevation, whereas one is irregular in plan. For each configuration in plan, two different cases were considered, with either two or three stories. Also, two different masonry typologies were considered, namely, concrete blocks and perforated clay blocks (with a percentage of vertical holes below 45%).

Figure 2.1.3 shows plan views and isometric views of the 3D models of the four alternative "E" type plan configurations under consideration (referring to the three-story building case).

The following design options were selected for all considered cases:

- Each inter-story height of 3.10 m was assumed for all configurations, with the floor thickness of 0.25 m at all stories, leading to a clearance of 2.85 m.
- All ceilings consist of unidirectional floors, made by combining concrete and hollow clay blocks (0.20+0.05 m solution)
- The roof was assumed pitched, sloping at 19° with eaves protruding 1.30 m from of the external side of the outer walls.

The assumed design loads are summarized in Table 2.1.3.

Table 2.1.3 Design loads.

|  | $G_{1k}$ [kN/m$^2$] | $G_{2k}$ [kN/m$^2$] | $Q_k$ [kN/m$^2$] |  |
|---|---|---|---|---|
| Intermediate floor | 3.5 | 2.5 | 2.0 | Cat. A |
| Attic + Roof | 6.0 | 1.5 | (*) | snow ≤ 1000 m a.s.l. |
| Roof gutter | 4.0 | 1.0 | (*) | snow ≤ 1000 m a.s.l. |
| Stairs/Balcony | 5.0 | 1.0 | 4.0 |  |

The characteristic value of the snow load naturally varies depending on each building's location. In any case, this load does not need to be combined with the seismic action.

The thickness of load-bearing walls vary in each configuration; in particular, external and internal walls' width is assumed, respectively, 30 cm and 25 cm for "E2" type, 35 cm and 30 cm for "E5" type and 30 cm each for both "E8" and "E9" types.



(a)



(b)



(c)



(d)

(e)



(f)



(g)



(h)
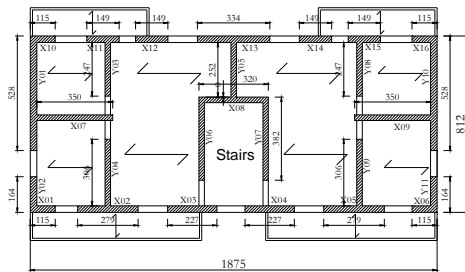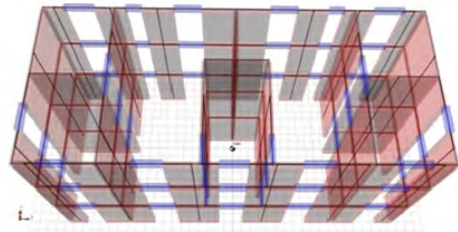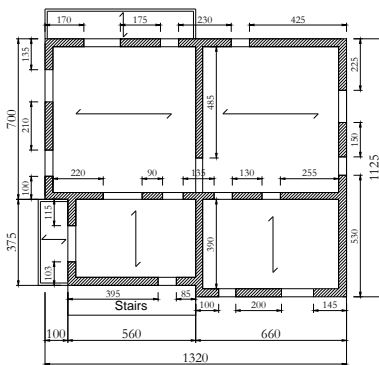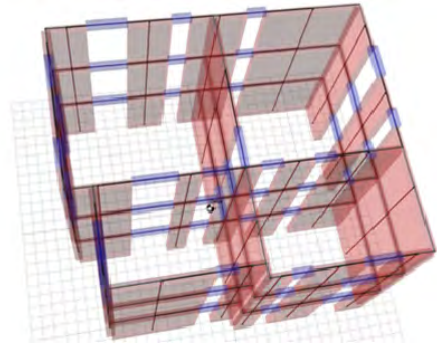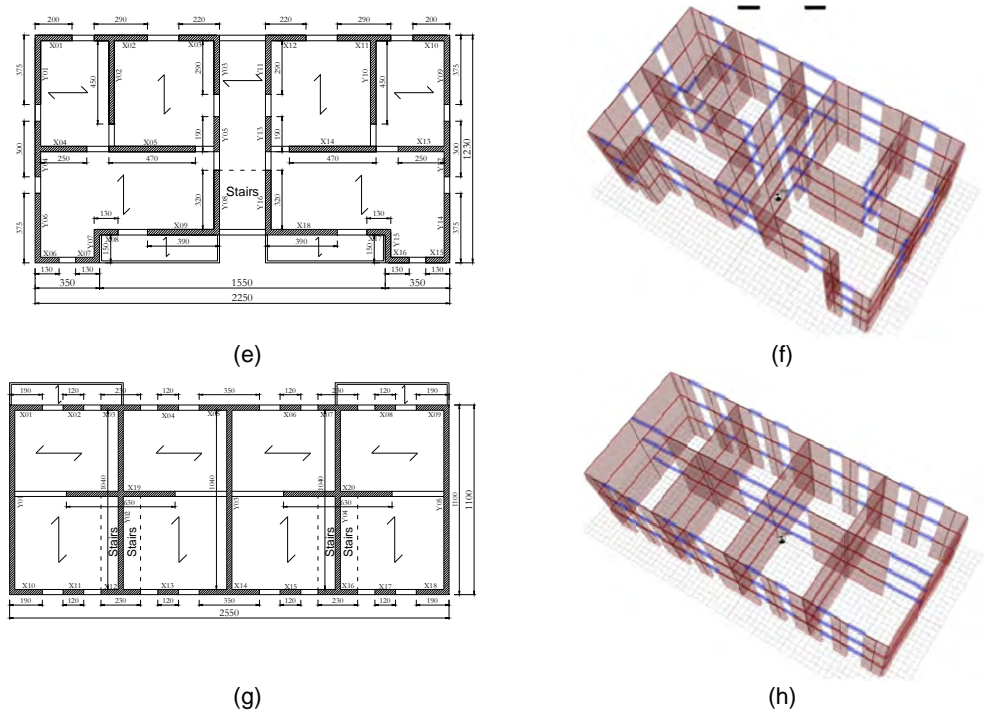
Figure 2.1.3 Plan views and 3D models of the 4 considered ''E'' type configurations, named ''E2''(a-b), ''E5'' (c-d), "E8" (e-f), "E9" (g-h).

### 2.1.3    Description of the "F" and ''G'' type configurations

The Padua RU was responsible for the design and modelling of irregular buildings designed, as mentioned earlier, according to the criteria of NTC 2008. The two basic building configurations with load-bearing masonry made of clay blocks, are described in the following.

2.1.3.1  ''F'' type - single family building with two stories

The first analyzed building configuration is a single-family, two-story residential building, which is irregular both in plan and in elevation (Figure 2.1.4). It was designed with a load-bearing structure made of clay unit unreinforced masonry. The body of the building consists of the main residential areas on two different floors and a garage at the ground floor.

The ceilings consist of a combination of concrete and hollow clay blocks (0.20+0.04 m solution), while composite action between the wooden truss of the roof and a lightweight concrete slab ensures rigid diaphragm conditions.

*Building characteristics.*

The gross ground floor areas of the buildings are 132.4 $m^2$ and 90.4 $m^2$ at the ground and first floor areas, respectively. As mentioned earlier, the load-bearing walls are made of clay units and the ground floor net height is 2.70 m, when first floor height is calculated as average height between the intrados of roof and slab. All the described characteristics are summarized in Table 2.1.4.

Table 2.1.4 Principal characteristics of two-story, single-family building.

| SINGLE-FAMILY BUILDING DATA | |
|---|---|
| ground floor height | 2.70 m |
| average height of first floor | 2.93 m |
| height of first slab | 0.24 m |
| height of second slab | 0.23 m |
| eave offset | 1.00 m |
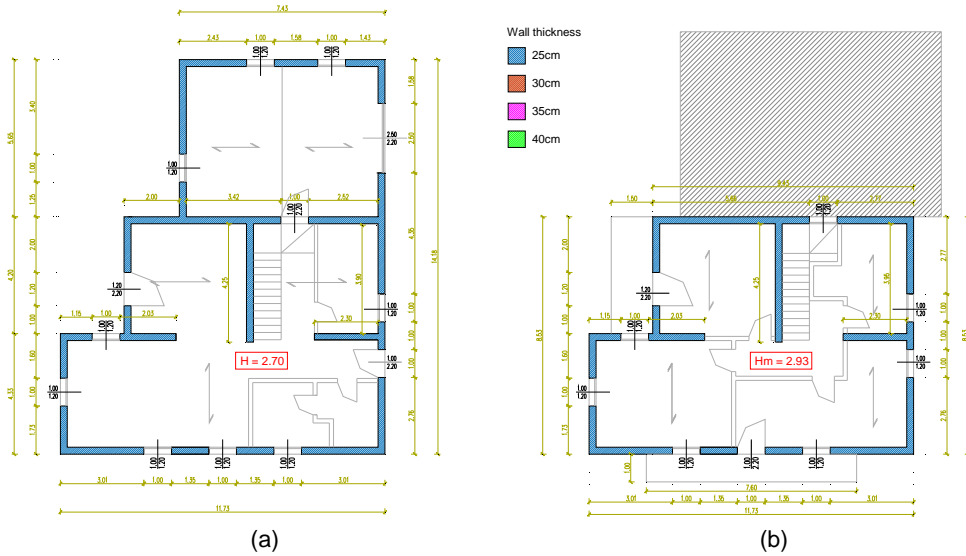


Figure 2.1.4 Plan views of ground floor (a) and first floor (b) of ''F'' type configuration.

2.1.3.2  ''G'' type configuration - two-family, three-floor building

The second analyzed building configuration is a two family, three-story residential building (Figure 2.1.5). The two building units are connected to each other only on one side, forming a L-shaped building floor plan. The two units are identical in plan in terms of shape, area and rooms' layout. The building is irregular both in plan and in elevation. The roofs at the first and second floor levels is made of 0.04 m thick concrete slabs, supported on masonry parapets. At the both floor levels, the assumption of rigid plane condition is valid. The roof at the third level is realized as a composite wood-lightweight concrete roof.

(a)                                    (b)                                    (c)
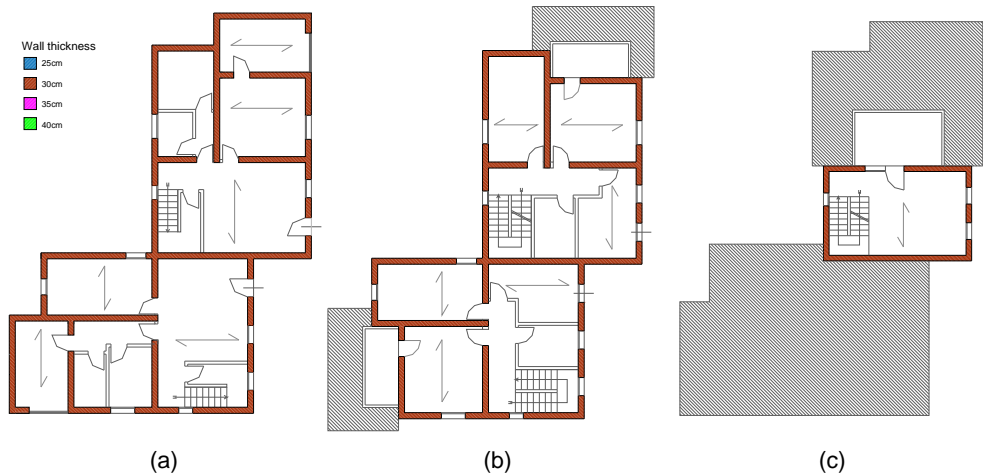
Figure 2.1.5 Plan view of ground floor (a), first floor (b) and second floor (c) of ''G'' type configuration.

*Building characteristics*

The building has a gross ground floor area of 184.5 m$^2$, first floor area of 156.5 m$^2$ and second floor area of 40.8 m$^2$. The load-bearing walls are made of clay units. The story height of all three floors is 2.70 m. All the described characteristics are summarized in Table 2.1.5.

Table 2.1.5 Principal characteristics of with three-story two-family building.

| TWO-FAMILY BUILDING DATA | | |
| --- | --- | --- |
| Ground floor height | 2.70 | m |
| Average height of first floor | 2.70 | m |
| Average height of second floor | 2.70 | m |
| Height of first slab | 0.24 | m |
| Height of second slab | 0.24 | m |
| Height of third slab | 0.23 | m |
| Eave offset | 0.60 | m |

## 2.2   Design of masonry buildings

The configurations described in the previous section were designed using different methods, among those proposed by NTC 2008. Keeping in mind the main purposes of the project, the methods most often used in engineering practice were selected, namely:

- linear static analysis (LSA), without force redistribution, with equivalent frame and cantilever models (NTC § 7.8.1.5.2);
- linear static analysis (LSA), with force redistribution, with cantilever models (NTC § 7.8.1.5.2);
- nonlinear static analysis (NLSA) with equivalent frame models (NTC § 7.8.1.5.4);
- so-called 'simple masonry building' rules (NTC §7.8.1.9).

For each of these methods, the provisions of NTC 2008 were respected, by ensuring compliance with the safety checks at the SLV limit state.

In particular, recalling the main aspects related to the use of these methods, it should be noted that: for linear static analysis, the verification has to be performed at the individual structural element level in terms of strength, while for nonlinear static analysis the verification has to be performed at a global scale, since the displacement demand is required to be lower than the corresponding capacity (evaluated by considering the displacement corresponding to the fixed 20% threshold on total base-shear reduction). While both the LSA and the NLSA require the definition of a structural model, the rules for the so-called 'simple masonry building' rules are based on complying with code provisions related to certain structural aspects, in terms of geometry, materials, structural details and minimum resistant area (NTC §7.8.1.9).

With regard to the methods requiring a structural model, the design of the configurations has been carried out by using two different computer programs: 3 Muri program (distributed by S.T.A. Data s.r.l., Lagomarsino et al. 2013) and ANDILWall (Manzini et al. 2013). Both these programs are based on the use of the equivalent frame modelling approach, according to which in each masonry walls piers and spandrels have to be defined, as well as regions idealized as rigid nodes. Only the in-plane response of masonry walls is considered.

In case of LSA, since the code provisions allow to use cantilever models, this type of approach was also used. Five sites (Milan, Caltanissetta, Rome, Naples, and L'Aquila) were analyzed and each of them was evaluated with two different types of soil (A and C), for a total of 10 different design acceleration values.

As already mentioned, all the defined configurations (types "C", "E", "F", "G", and "I") have some common or similar features. In particular, all the configurations are provided with reinforced concrete ring beams at each level; according to the prescriptions of NTC 2008 (7.8.5.1), the ring beams of the internal walls should be as large as the wall itself, while the length of those of the external walls is 0.05 m smaller than the thickness of the wall, in order to accommodate thermal insulation elements. The reinforcement is the minimum allowed by the code, both in case of longitudinal reinforcements (4Φ16) and stirrups (Φ8 every 0.25 m).

The mechanical properties of the materials used for the defined configurations are summarized in Table 2.2.1. These mechanical properties are consistent with the prescriptions of NTC 2008 for new buildings in seismic areas (§ NTC 7.8.1). The table shows that the same values of shear and Young modulus for masonry are used for all configurations, while the other mechanical properties, even if very similar, present slight differences depending on the type of configuration (i.e., class of concrete, characteristic compressive strength and specific weight of units, class of mortar). In particular, for ''C'' and ''I'' type configurations mortar type M10 and units with a strength of 8 MPa were used, while for the RC elements the class of concrete is C20/25and B450C reinforcements steel bars were used. Similarly, for "E" type configurations with clay units, mortar type M10 and units with strength of 8 MPa were used, with concrete class C25/30 for RC elements and B450C reinforcement. On the other hand, for "E" type configurations with concrete units, mortar type M5 and units with strength of 5 MPa were used, always with C25/30 concrete class for RC elements and B450C reinforcement. For all buildings derived from ''G'' type configuration, masonry unit strength ($f_{bk}$) of 15 MPa and mortar type M10 were used. For RC elements (curbs, floor, etc.) concrete class C25/30 and B450C reinforcing steel bars were used. Finally, for ''F'' type configurations the mechanical characteristics of the masonry were changed: masonry unit strength ($f_{bk}$) ranged between 8 and 15 MPa and mortar type M5 or M10 was used. For the RC elements (ring beams, floor diaphragms, etc.) C25/30 concrete class and B450C reinforcing steel bars were used.

The following sub-sections discuss the design of the different structural configurations derived from the architectural configurations presented in the previous section.

Table 2.2.1. Mechanical properties of the materials used in the defined configurations.

| Configuration type | | C/I | E clay | E concr. | F | G |
|---|---|---|---|---|---|---|
| Masonry | | | | | | |
| Young modulus | $E$ | 1000 $*f_k$ | 1000 $*f_k$ | 1000 $*f_k$ | 1000 $*f_k$ | 1000 $*f_k$ |
| Shear modulus | $G$ | 0.4*E | 0.4*E | 0.4*E | 0.4*E | 0.4*E |
| Characteristic compressive strength of units | $f_{bk}$ [MPa] | 8 | 8 | 5 | 8 ÷ 15 | 15 |
| Characteristic horizontal compressive strength of units | $f'_{bk}$ [MPa] | 1.5 | 1.5 | 1.5 | 1.5 | 1.5 |
| Specific weight | $W$ [N/m³] | 9000 | 9000 | 11000 | 11000 | 11000 |
| Mortar class | | M10 | M10 | M5 | M5-M10 | M10 |
| Characteristic strength of masonry | $f_k$ [MPa] | 4.66 | 4.66 | 3.30 | * | * |
| Design strength for gravity loads | $f_d$ [MPa] | $f_k$/3 | $f_k$/3 | $f_k$/3 | $f_k$/3 | $f_k$/3 |
| Design strength for seismic loads | $f_d$ [MPa] | $f_k$/2 | $f_k$/2 | $f_k$/2 | $f_k$/2 | $f_k$/2 |
| Characteristic shear strength without vertical load | $f_{vk0}$ [MPa] | 0.2 | 0.2 | 0.1 | 0.2 | 0.2 |
| Concrete | | | | | | |
| Concrete class | | C20 /25 | C25 /30 | C25 /30 | C25 /30 | C25 /30 |
| Characteristic compressive strength | $f_{ck}$ [MPa] | 20 | 25 | 25 | 25 | 25 |
| Design compressive strength | $f_{cd}$ [MPa] | 11.33 | 14.17 | 14.17 | 14.17 | 14.17 |
| Steel reinforcements B450C | | | | | | |
| Characteristic yielding strength | $f_{yk}$ [MPa] | 450 | 450 | 450 | 450 | 450 |
| Design yielding strength | $f_{yd}$ [MPa] | 391 | 391 | 391 | 391 | 391 |

* the value of $f_k$ was obtained by linear interpolation of the data in Table 11.10.V (§NTC 11.10.3.1.2).

### 2.2.1    Design of the "C" and "I" type configurations

The ''C'' type configurations were designed by using both the rules for the so-called 'simple buildings' and NLSA, since they are regular both in plan and in elevation, according to the definitions of regularity provided by NTC 2008 (§ 7.2.2). Furthermore, the "C" type configurations were also verified in each site with the LSA. The ''I'' type configurations, on the other hand, were designed using exclusively NLSA, because they present irregularity features (only in plan or both in plan and in elevation) that do not allow the use of other approaches.

2.2.1.1  ''C'' type configurations

According to the criteria provided by NTC 2008, seven different plan configurations of "simple masonry building" were designed for the ''C'' type base configuration. These seven plan configurations will be denoted hereafter as C1…. C7 (Figure 2.2.1) and they differ in terms of the percentage of resisting area, which gradually increases from 4% to 7%, in order to respect the limits required by the code (§ NTC, Tab. 7.8.III), as a function of the seismic input ($a_gS$) and the number of stories.
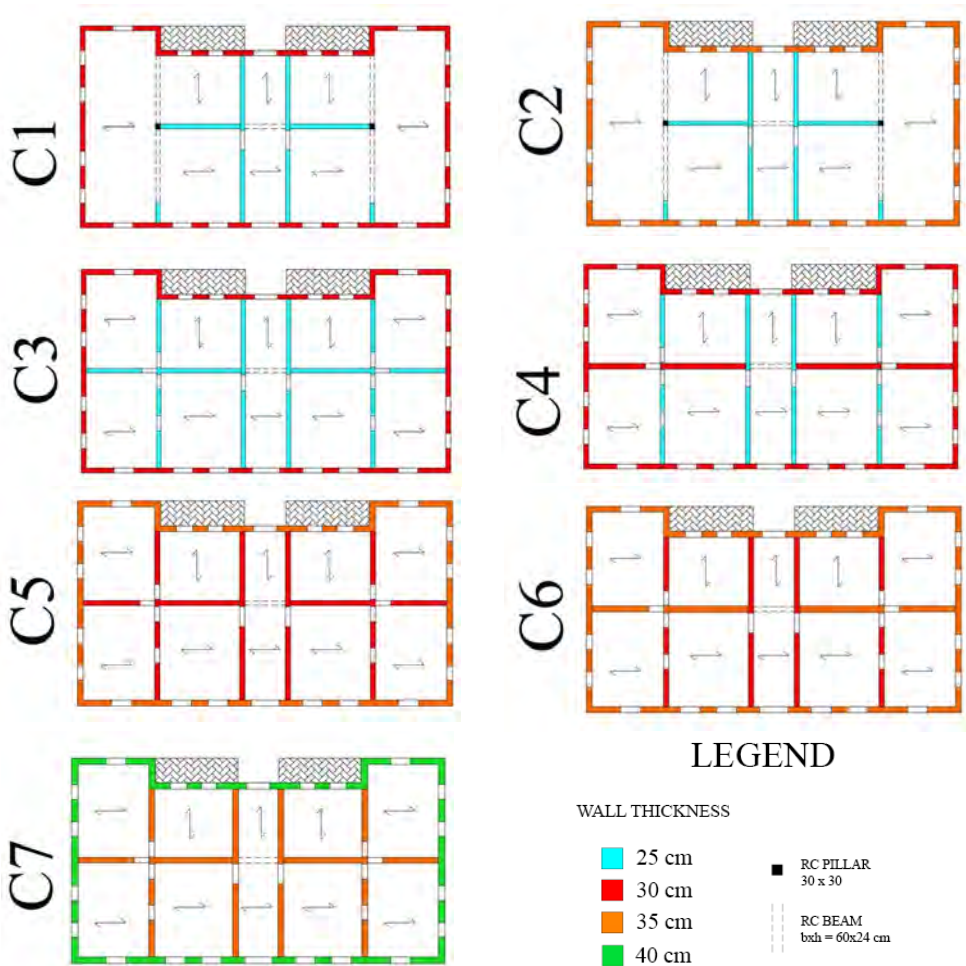


Figure 2.2.1 Plan configurations of the ground floor of the ''C'' type buildings.

The different percentages of resistant area characterizing the different plan configurations were obtained by varying the thickness of the masonry walls (both internal and external) from the minimum of 0.25 m to the maximum of 0.40 m. Furthermore, in the configurations denoted as C1 and C2, some internal walls were replaced by RC beams and columns, to obtain an even lower percentage of resistant area that barely complies with the minimum requirement by code provisions.

As far as the thickness of masonry walls is concerned, considering that in the NTC 2008 a minimum thickness of 0.24 m (Tab. 7.8.II) is imposed, it was assumed that the external walls need to have a thickness of at least 0.30 m (also for thermal insulation requirements) while the internal ones can have a lower thickness (but necessarily larger than 0.24 m).

The different values of resistant area associated to each of these buildings are provided in Table 2.2.2; they are computed as the smaller resistant area between the *x* and *y* direction. Since the second floor is identical to the first floor, these values are the same as those of the first floor for the two- and three-story buildings.

Table 2.2.2. Percentage of resistant area associated to each defined configuration.

| | Ground floor | | | | First Floor | | | | | |
|---|---|---|---|---|---|---|---|---|---|---|
| | $A_x$ | $\%A_x$ | $A_y$ | $\%A_y$ | $A_x$ | $\%A_x$ | $A_y$ | $\%A_y$ | $Min(\%A_{res})$ | |
| | [m$^2$] | | [m$^2$] | | [m$^2$] | | [m$^2$] | | | |
| C1 | 11.34 | 4.40 | 11.85 | 4.60 | 11.34 | 4.40 | 11.35 | 4.40 | 4.40 | $4\%<A_{res}<4.5\%$ |
| C2 | 12.91 | 5.00 | 13.08 | 5.08 | 12.91 | 5.00 | 12.58 | 4.88 | 4.88 | $4.5\%<A_{res}<5\%$ |
| C3 | 13.34 | 5.18 | 14.78 | 5.73 | 13.34 | 5.18 | 14.28 | 5.54 | 5.18 | $5\%<A_{res}<5.5\%$ |
| C4 | 14.25 | 5.53 | 14.78 | 5.73 | 14.25 | 5.53 | 14.28 | 5.54 | 5.53 | $5.5\%<A_{res}<6\%$ |
| C5 | 15.78 | 6.12 | 17.72 | 6.87 | 15.78 | 6.12 | 17.12 | 6.64 | 6.12 | $6\%<A_{res}<6.5\%$ |
| C6 | 16.77 | 6.51 | 17.72 | 6.87 | 16.77 | 6.51 | 17.12 | 6.64 | 6.51 | $6.5\%<A_{res}<7\%$ |
| C7 | 18.44 | 7.15 | 20.72 | 8.04 | 18.44 | 7.15 | 20.02 | 7.77 | 7.15 | $A_{res}>7\%$ |

By comparing the data in Table 2.2.2 for the percentage of resistant area required by the code, it is possible to establish which of the defined plan configurations can be used, with either two or three stories, at each site.

Table 2.2.3 and Table 2.2.4 show, for the two- and three- story buildings respectively, all the configurations that can be used in the ten different sites under consideration. The final choice was to consider, for each site, the configuration with the minimum percentage of resisting area complying with the requirements of NTC 2008, without being excessively over-dimensioned. In the end, eight different buildings and sixteen different building – site combinations have been defined by following the 'simple masonry building' rules.

Table 2.2.4 shows that the three-story C1 configuration cannot be designed as a simple building, not even in Milan, since its resistant area is lower than 4.5%, which is the minimum requested by the code for a three-story building.

These configurations were subsequently verified using NLSA as well. In this case they have been modelled with the equivalent frame technique, by using the 3Muri software (the commercial version of TREMURI used later on for performing the nonlinear dynamic analyses), in order to verify which configuration can be used in each of the ten sites defined in the project, considering both the two and the three-story solutions. With regard to the masonry panels, both piers and spandrels were modelled. Moreover, the full coupling among the connected walls was assumed and orthotropic membrane finite elements were introduced to model the diaphragms; the

properties of the diaphragms were assumed consistently with the diaphragm types, thus representative of a "rigid" behavior.

Table 2.2.3. Two-story ''C'' type configurations that can be used in the different sites, according to the criteria of NTC 2008 for 'simple buildings': bright green indicates the configurations with the minimum resistant area among all the configurations that respect the percentage of resistant area requested for that site, while the light green those "oversized".

| SIMPLE MASONRY BUILDING | | | | | | | | | | |
|---|---|---|---|---|---|---|---|---|---|---|
| 2_LEVELS | | | | | | | | | | |
| | | | | CONFIGURATIONS | | | | | | |
| SEISMIC AREA | SITE | $a_gS$ [g] | Ares$_{min}$ | 1 | 2 | 3 | 4 | 5 | 6 | 7 |
| IV | Mi_A | 0.049 ≤ 0.1 | 4% | | | | | | | |
| IV | Mi_C | 0.074 ≤ 0.1 | 4% | | | | | | | |
| III-b | Ca_A | 0.073 ≤ 0.1 | 4% | | | | | | | |
| III-b | Ca_C | 0.109 ≤ 0.15 | 4.5% | - | | | | | | |
| III-a | Ro_A | 0.121 ≤ 0.15 | 4.5% | - | | | | | | |
| III-a | Ro_C | 0.182 ≤ 0.2 | 5% | - | - | | | | | |
| II | Na_A | 0.168 ≤ 0.2 | 5% | - | - | | | | | |
| II | Na_C | 0.245 ≤ 0.25 | 5.5% | - | - | - | | | | |
| I | Aq_A | 0.261 ≤ 0.3 | 6% | - | - | - | - | * | * | * |
| I | Aq_C | 0.347 ≤ 0.35 | 6.5% | - | - | - | - | - | * | * |

*these buildings have not been analyzed since they were treated as if they were located in seismic area I; however, it has to be observed that L'Aquila, even if associated to PGA > 2.5 m/s$^2$, are not classified in seismic area I at an administrative level.*
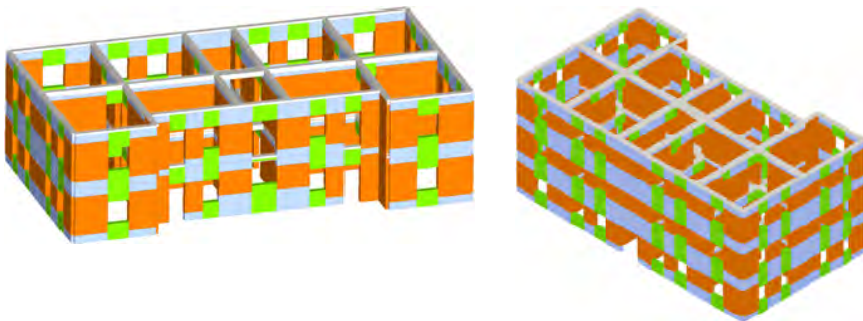


Figure 2.2.2 3D views of the equivalent frame idealisation of the two and three-story buildings.

Table 2.2.4. Three-story ''C'' type configurations that can be used in the different sites, according to the criteria of NTC 2008 for 'simple buildings': dark green indicates the configurations with the minimum resistant area among all the configurations that respect the percentage of resistant area requested for that site, while the light green indicates those "oversized".

| SIMPLE MASONRY BUILDING | | | | | | | | | | |
|---|---|---|---|---|---|---|---|---|---|---|
| 3_LEVELS | | | | | | | | | | |
| | | | | CONFIGURATIONS | | | | | | |
| SEISMIC AREA | SITE | $a_gS$ [g] | $Ares_{min}$ | 1 | 2 | 3 | 4 | 5 | 6 | 7 |
| IV | Mi_A | 0.049 ≤ 0.1 | 4.5% | - | | | | | | |
| | Mi_C | 0.074 ≤ 0.1 | 4.5% | - | | | | | | |
| III-b | Ca_A | 0.073 ≤ 0.1 | 4.5% | - | | | | | | |
| | Ca_C | 0.109 ≤ 0.15 | 5% | - | - | | | | | |
| III-a | Ro_A | 0.121 ≤ 0.15 | 5% | - | - | | | | | |
| | Ro_C | 0.182 ≤ 0.2 | 5.5% | - | - | - | | | | |
| II | Na_A | 0.168 ≤ 0.2 | 5.5% | - | - | - | | | | |
| | Na_C | 0.245 ≤ 0.25 | 6% | - | - | - | - | | | |
| II | Aq_A | 0.261 ≤ 0.3 | 6.5% | - | - | - | - | - | * | * |
| | Aq_C | 0.347 ≤ 0.35 | 7% | - | - | - | - | - | - | * |

*these buildings have not been analyzed since they were treated as if they were located in seismic area I; however, it has to be observed that L'Aquila, even if associated to PGA > 2.5 m/s$^2$, are not classified in seismic area I at an administrative level.*

Figure 2.2.3 and Figure 2.2.4 report some of the pushover curves of the buildings. The pushover analyses were carried out in both the x and y directions and by using both the inverted triangular and the uniform load patterns. It may be seen that the curves referring to the C1 and C2 configurations present a lower strength with respect to the curves related to the other ones (C3, C4, C5, C6, C7): this evident difference is due to the fact that, as mentioned before, in C1 and C2 some internal masonry walls were replaced by RC beams and pillars, as to greatly reduce the percentage of resistant area, especially in the y direction.
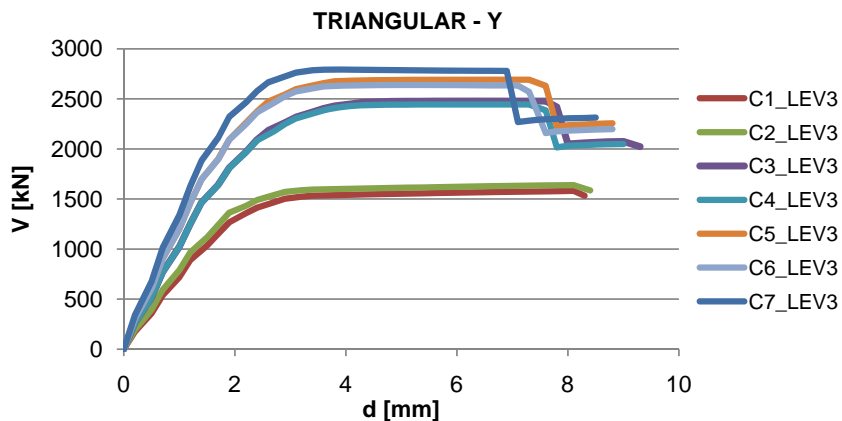


Figure 2.2.3 Pushover curves of the three-story ''C'' type configurations: the analysis was performed by using the inverse triangular distribution and pushing the buildings in the *y* positive direction.
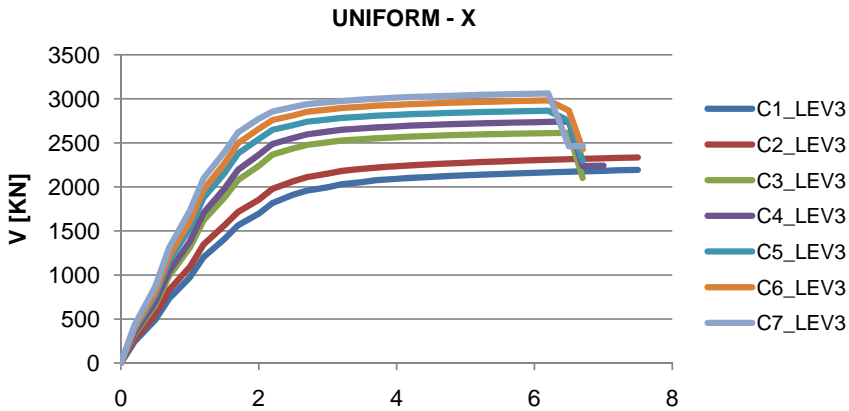
Figure 2.2.4 Pushover curves of the three-story ''C'' type configurations: the analysis was performed by using the uniform distribution and pushing the buildings in *y* positive direction.

Aiming to obtain code-compliant yet not over-dimensioned buildings, a global safety factor *α,* which is defined as the ratio between the PGA corresponding to the attainment of the ultimate capacity and the design PGA for return period of 475 years, was used to find one or more configurations associated with the safety factor only slightly higher than 1 (i.e., *α* <1.5), for each site, among the buildings that satisfied the verification with NLSA. Following this criteria, four configurations (C1 and C3 with two- or three- story) were chosen, resulting in five building-site combinations in total.

In particular, referring to the two-story buildings, the C3 configuration is sufficient in L'Aquila (soil type C) while the C1 configuration can be used both in L'Aquila- soil type A and in Naples- soil type C; in all the other sites, the seismic hazard is lower and the safety factor for this configuration is higher than 1.5.

For the case of three-story buildings, none of the considered configurations is verified with NLSA in L'Aquila- soil type C (even C7 is not verified in this case), while the C1 configuration can be used in L'Aquila- soil type A and Naples- soil type C; in all the other sites the defined configurations present a safety factor higher than 1.5. It can also be seen that the three-story C1 configuration, which, as mentioned above, cannot be considered in any site as a simple building, according to NLSA-based design can be located even in L'Aquila, soil type A.

The "C" type configurations have also been checked in each site with LSA without force redistribution in collaboration with Pavia RU. The numerical models of the buildings were created and analyzed with the program ANDILWall using assumptions compatible with the characteristics of the program 3Muri , used to carry out the NLSA. Both equivalent frame and cantilever models were considered.

The results of the analyses were elaborated to define the global safety factor. Table 2.2.5 summarizes the results of the design, in terms of return period $T_{R(C,SLV)}$ and global safety factor α. Red cells indicate buildings whose design does not comply with the requirements, buildings largely complying with them are in yellow, and buildings that are considered as satisfactory for each reference site are in green. Empty cells correspond to cases in which a specific building is not even verified for the return period $T_R$ = 30 years.

Table 2.2.5. Results of the design by means of LSA: type "C" configurations – clay blocks.

$T_R(d_{SLV,d} = d_{SLV,c})$

| site | zone | $a_g S$ [g] | $a_g SF_0$ [g] | C3_CLAY_2ST FRAME | C3_CLAY_2ST CANT | C3_CLAY_3ST FRAME | C3_CLAY_3ST CANT | C4_CLAY_2ST FRAME | C4_CLAY_2ST CANT | C4_CLAY_3ST FRAME | C4_CLAY_3ST CANT | C5_CLAY_2ST FRAME | C5_CLAY_2ST CANT | C5_CLAY_3ST FRAME | C5_CLAY_3ST CANT | C6_CLAY_2ST FRAME | C6_CLAY_2ST CANT | C6_CLAY_3ST FRAME | C6_CLAY_3ST CANT | C7_CLAY_2ST FRAME | C7_CLAY_2ST CANT | C7_CLAY_3ST FRAME | C7_CLAY_3ST CANT |
|---|---|---|---|---|---|---|---|---|---|---|---|---|---|---|---|---|---|---|---|---|---|---|---|
| AQ_C | II | 0.347 | 0.820 | - | - | - | - | - | - | - | - | - | - | - | - | - | - | - | - | - | - | - | - |
| AQ_A | II | 0.261 | 0.616 | - | - | - | - | - | - | - | - | - | - | - | - | - | - | - | - | - | - | - | - |
| NA_C | II | 0.245 | 0.582 | - | - | - | - | - | - | - | - | 33 | - | - | - | 33 | - | - | - | 41 | - | - | - |
| RM_C | III | 0.182 | 0.479 | - | - | - | - | - | - | - | - | 32 | - | - | - | 32 | - | - | - | 42 | - | - | - |
| NA_A | II | 0.168 | 0.398 | - | - | - | - | 59 | 47 | - | 35 | 70 | 45 | - | 37 | 70 | 59 | - | 47 | 87 | 54 | - | 47 |
| RM_A | III | 0.121 | 0.319 | - | - | - | - | 57 | 50 | - | 40 | 83 | 48 | - | 39 | 83 | 67 | - | 50 | 109 | 60 | - | 50 |
| CL_C | III | 0.109 | 0.283 | - | - | - | - | 82 | 59 | - | 46 | 104 | 55 | - | 42 | 104 | 82 | - | 58 | 141 | 72 | - | 58 |
| MI_C | IV | 0.074 | 0.197 | - | - | - | - | 204 | 138 | - | 102 | 270 | 127 | - | 93 | 270 | 204 | - | 136 | 397 | 175 | - | 136 |
| CL_A | III | 0.073 | 0.189 | - | - | - | - | 244 | 173 | - | 134 | 317 | 162 | - | 123 | 317 | 244 | - | 171 | 454 | 212 | - | 171 |
| MI_A | IV | 0.049 | 0.131 | - | - | - | - | 606 | 520 | - | 389 | 1102 | 473 | - | 355 | 1102 | 806 | - | 511 | 1672 | 681 | - | 511 |

$\alpha$

| site | zone | $a_g S$ [g] | $a_g SF_0$ [g] | C3_CLAY_2ST FRAME | C3_CLAY_2ST CANT | C3_CLAY_3ST FRAME | C3_CLAY_3ST CANT | C4_CLAY_2ST FRAME | C4_CLAY_2ST CANT | C4_CLAY_3ST FRAME | C4_CLAY_3ST CANT | C5_CLAY_2ST FRAME | C5_CLAY_2ST CANT | C5_CLAY_3ST FRAME | C5_CLAY_3ST CANT | C6_CLAY_2ST FRAME | C6_CLAY_2ST CANT | C6_CLAY_3ST FRAME | C6_CLAY_3ST CANT | C7_CLAY_2ST FRAME | C7_CLAY_2ST CANT | C7_CLAY_3ST FRAME | C7_CLAY_3ST CANT |
|---|---|---|---|---|---|---|---|---|---|---|---|---|---|---|---|---|---|---|---|---|---|---|---|
| AQ_C | I | 0.347 | 0.820 | - | - | - | - | - | - | - | - | - | - | - | - | - | - | - | - | - | - | - | - |
| AQ_A | I | 0.261 | 0.616 | - | - | - | - | - | - | - | - | - | - | - | - | - | - | - | - | - | - | - | - |
| NA_C | II | 0.245 | 0.582 | - | - | - | - | - | - | - | - | 0.29 | - | - | - | 0.29 | - | - | - | 0.33 | - | - | - |
| RM_C | III | 0.182 | 0.479 | - | - | - | - | - | - | - | - | 0.36 | - | - | - | 0.36 | - | - | - | 0.41 | - | - | - |
| NA_A | II | 0.168 | 0.398 | - | - | - | - | 0.39 | 0.34 | - | 0.31 | 0.42 | 0.33 | - | 0.30 | 0.42 | 0.39 | - | 0.34 | 0.48 | 0.37 | - | 0.34 |
| RM_A | III | 0.121 | 0.319 | - | - | - | - | 0.50 | 0.44 | - | 0.40 | 0.54 | 0.43 | - | 0.39 | 0.54 | 0.50 | - | 0.44 | 0.61 | 0.48 | - | 0.44 |
| CL_C | III | 0.109 | 0.283 | - | - | - | - | 0.55 | 0.49 | - | 0.44 | 0.60 | 0.48 | - | 0.43 | 0.60 | 0.55 | - | 0.49 | 0.67 | 0.52 | - | 0.49 |
| MI_C | IV | 0.074 | 0.197 | - | - | - | - | 0.78 | 0.70 | - | 0.64 | 0.85 | 0.68 | - | 0.62 | 0.85 | 0.78 | - | 0.70 | 0.95 | 0.75 | - | 0.70 |
| CL_A | III | 0.073 | 0.189 | - | - | - | - | 0.81 | 0.72 | - | 0.66 | 0.88 | 0.71 | - | 0.64 | 0.88 | 0.81 | - | 0.72 | 0.99 | 0.77 | - | 0.72 |
| MI_A | IV | 0.049 | 0.131 | - | - | - | - | 1.14 | 1.02 | - | 0.94 | 1.24 | 1.00 | - | 0.92 | 1.24 | 1.14 | - | 1.02 | 1.37 | 1.10 | - | 1.02 |

Final results are summarized in Table 2.2.6, where, for each site, the ''C'' type configurations defined according to NLSA are compared to those obtained with the criteria for 'simple buildings' and LSA.

Table 2.2.6. Configurations obtained for each site with the different design methods considered (rules for 'simple masonry buildings', LSA with frame and cantilever models and NLSA).

| Considered buildings (safety factor slightly higher than 1) | | Oversized buildings (safety factor higher than 1.5) | | No verified buildings among those defined |
|---|---|---|---|---|

| Site | $a_g S$ [g] | TWO-STORY BUILDINGS | | | | | THREE-STORY BUILDINGS | | | | |
|---|---|---|---|---|---|---|---|---|---|---|---|
| | | Simple building | LSA (FRAME) | LSA (CANT) | NLSA | $\alpha_{min}$ | Simple building | LSA (FRAME) | LSA (CANT) | NLSA | $\alpha_{min}$ |
| Mi_A | 0.049 | C1 | C4 | C4 | C1 | > 1.5 | C2 | | C6 | C1 | > 1.5 |
| Mi_C | 0.074 | C1 | C7 | | C1 | > 1.5 | C2 | | | C1 | > 1.5 |
| Ca_A | 0.073 | C1 | C7 | | C1 | > 1.5 | C2 | | | C1 | > 1.5 |
| Ca_C | 0.109 | C2 | | | C1 | > 1.5 | C3 | | | C1 | > 1.5 |
| Ro_A | 0.121 | C2 | | | C1 | > 1.5 | C3 | | | C1 | > 1.5 |
| Ro_C | 0.182 | C3 | | | C1 | > 1.5 | C4 | | | C1 | 1.28 |
| Na_A | 0.168 | C3 | | | C1 | > 1.5 | C4 | | | C1 | >1.5 |
| Na_C | 0.245 | C4 | | | C1 | 1.22 | C5 | | | C3 | 1.17 |
| Aq_A | 0.261 | - | | | C1 | 1.15 | - | | | C1 | 1.01 |
| Aq_C | 0.347 | - | | | C3 | 1.22 | - | | | | |

By considering the ''C'' type configurations defined with the logic of the three designed methods considered (rules for 'simple masonry building', LSA and NLSA), 11 different buildings and 26 combinations site – building were defined.

### 2.2.1.2 ''I'' type configuration

The ''I'' type configurations cannot be designed according to the 'simple buildings' rules, since, as already mentioned, they were defined as irregular. Therefore, they have only been verified by using NLSA, checking that the corresponding safety factor is larger than 1 and lower than 1.5, in order to consider the corresponding configuration as acceptable (i.e., not over-dimensioned). As in the previous case, the adopted modelling technique is that of the equivalent frame, together with the use of bilinear constitutive laws for masonry panels. Figure 2.2.5 shows some images of the equivalent frame idealization of the modelled building.



(a)                                                                                          (b)
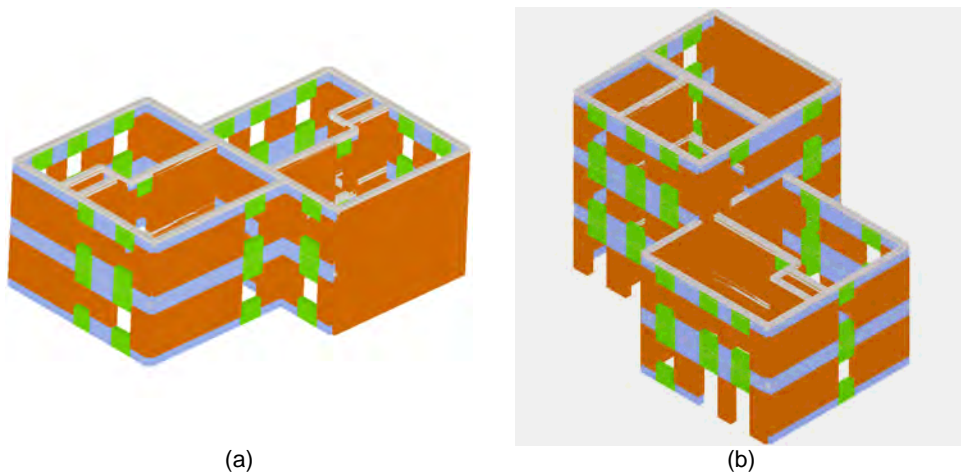
Figure 2.2.5 3D views of the structural models of the ''I'' type configurations: two-story (a) and three-story (b) building.

As a result of the analyses performed, it came out that the two-story irregular building (I1) can be considered only in L'Aquila soil type C, since it is excessively oversized in the other sites (safety factor higher than 1.5). On the other hand, the three-story irregular building can be used only in Naples soil type C: it is not code-compliant for the sites with higher seismic hazard, while it is too over-dimensioned for the sites with lower seismic hazard (Table 2.2.6).

In conclusion it may be said that, by considering both the 'C' and the 'I' type configurations and by using the different design approaches ("simple buildings" rules and NLSA), thirteen buildings with two- or three- stories were defined, for twenty-seven building-site combinations, in total, to be analyzed by means of NLDA.

Table 2.2.7. Configurations obtained for each site with NLSA for "I" type configuration.

| | Considered buildings (safety factor slightly higher than 1). | | Oversized buildings (safety factor higher than 1.5). | | No verified buildings among those defined. |
|---|---|---|---|---|---|
| | | **TWO-STORY BUILDINGS** | | **THREE-STORY BUILDINGS** | |
| **Site** | **$a_gS$ [g]** | **NLSA** | **$\alpha_{min}$** | **NLSA** | **$\alpha_{min}$** |
| Mi_A | 0.049 | I1 | > 1.5 | I2 | > 1.5 |
| Mi_C | 0.074 | I1 | > 1.5 | I2 | > 1.5 |
| Ca_A | 0.073 | I1 | > 1.5 | I2 | > 1.5 |
| Ca_C | 0.109 | I1 | > 1.5 | I2 | > 1.5 |
| Ro_A | 0.121 | I1 | > 1.5 | I2 | > 1.5 |
| Ro_C | 0.182 | I1 | > 1.5 | I2 | > 1.5 |
| Na_A | 0.168 | I1 | > 1.5 | I2 | > 1.5 |
| Na_C | 0.245 | I1 | > 1.5 | I2 | 1.27 |
| Aq_A | 0.261 | I1 | > 1.5 | | <1 |
| Aq_C | 0.347 | I1 | 1.28 | | <1 |

## 2.2.2    Design of the "E" type configurations

The "E" type buildings were designed according to three code approaches, consisting of LSA, with both "cantilever" and "equivalent frame" modelling, NLSA and "simple buildings" rules (with the exception of building E5, which is irregular).

Numerical analyses necessary for designing the different building configurations were carried out using the program ANDILWall.

The numerical models of the buildings to be analyzed with the program ANDILWall were created on assumptions that they are compatible with the characteristics of the program 3Muri , which was used in the following phases of the work to carry out dynamic analyses, in order to avoid variability in the models that could create incompatibility among the results. In particular, the following modelling assumptions were adopted:

- The distribution of the loads transferred by the floors to the vertical load-bearing elements was based on the assumption that the unidirectional concrete-brick floors transfer the loads both to the walls perpendicular to the direction spanned by the joists and, partially, to those parallel to it. To this aim, the width of the floor portion pertaining to these elements was assumed equal to 0.50 m starting from the internal edge and the angle of distribution between perpendicular walls was assumed equal to 45° (Figure 2.2.6)
- No masonry spandrels were included in the numerical models. It was therefore assumed that the deformable edge portion of the vertical structural elements coincides with the net inter-story height and thus, at the end of each element, rigid segments with a length equal to half thickness of the corresponding floor were considered. For the horizontal elements, the deformable portion was assumed equal to the net width of the corresponding openings.
- The roof structure was not explicitly considered in the numerical model, apart from the load transfer.
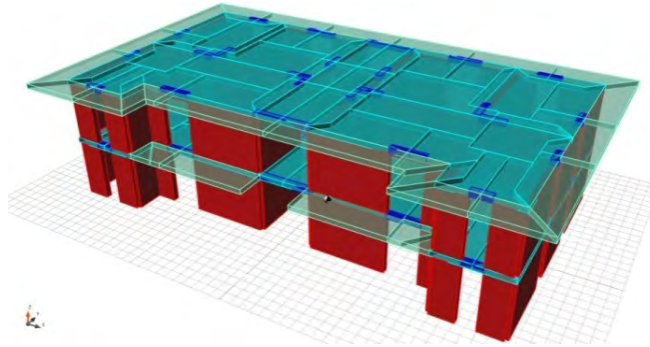
Figure 2.2.6 Identification of the floor areas resting on each load-bearing structural element.

As already mentioned, two different modelling approaches were considered for linear analysis, namely the equivalent frame approach and the cantilever approach. Concerning equivalent frame modelling, the following additional assumptions were made:

- the contribution of masonry spandrels (above/below openings) to the global structural capacity was neglected, similarly to the out-of-plane contribution of masonry panels;
- floors were modelled as infinitely rigid diaphragms within their plane;
- the connection between wall panels constituting flanged walls was realized by infinitely rigid links (at the floor levels), aiming at guaranteeing the compatibility of vertical and horizontal displacements of intersecting walls. The presence of a continuous reinforced concrete tie beam and the connection of the panels in the intersection area, thanks to interlocking of staggered masonry blocks, provide this internal constraint.

On the other hand, regarding cantilever modelling, the infinitely rigid diaphragm condition was kept as the only restraint among structural nodes of the same story. In fact, all horizontal elements (story tie beams and infinitely rigid links) were removed from the numerical model.

The adopted mechanical properties of the materials are summarized in Table 2.2.8. The hypothesis of cracked sections was adopted in the calculations, by assuming a reduction coefficient equal to 0.5.

In order to define the set of meaningful designs for each site, two different criteria were adopted (Table 2.2.8). The first one is based on the value of return period $T_{R(C,SLV)}$, while the second is based on the value of the global safety factor α. Using this approach, it was possible to optimize the choice of design (i.e., of the combinations of structural configuration and design method) for each reference site. This consisted of identifying, for each site, a set of designs (at least one for each site) either satisfying the requisites of "simple buildings" and/or characterized by the minimum values of return period ($T_{R(C,SLV)}$) or global safety factor among the values obtained.

Table 2.2.8. Adopted criteria for the identification of the meaningful designs by means of linear and nonlinear static analysis.

|  | $T_{R(C,SLV)}$ | α |
|---|---|---|
| Non-compliant building | $T_{R(C,SLV)}$< 400 | α < 0.95 |
| Over-dimensioned building | $T_{R(C,SLV)}$> 700 | α > 1.15 |
| Barely compliant building | 400 ≤ $T_{R(C,SLV)}$≤ 700 | 0.95 ≤ α ≤ 1.15 |

Table 2.2.9 illustrates the total number of buildings that turned out to be barely compliant with the requirements according to the discussed criterion. The information is reported both considering the total amount of buildings and subdividing the results based on the number of stories. The results are reported both with reference to the entire set of structural configurations under consideration and subdivided based on the masonry typology (concrete and clay blocks). Red cells indicate cases in which it was not possible to identify any complying buildings for the corresponding site, whereas yellow cells indicate cases in which $\alpha$ was larger than the defined significant threshold, for all the code-compliant buildings.

Table 2.2.9. Type "E" configurations – meaningful cases for each site and for each design method.



All material types — Concrete units — Clay units

Table 2.2.10 reports in detail the results obtained by designing according to the rules for "simple buildings". For each site, the green, yellow, and red colors indicate the structural configurations that comply with the limitations in terms of average compressive stress and minimum percentage of masonry in the two main directions (provided that it has been previously checked that all other code requirements are satisfied), those that largely comply, and those that do not comply, respectively.

It should be noted that building E5, which is irregular in plan, was not considered among the "simple buildings". Nevertheless, since the performed modal analyses showed that the participating mass associated with the principal modes in X and Y directions are higher than 80% and 60%, respectively, it was decided to consider it in the building set subjected to linear static analysis.

Table 2.2.10. Results of the design according to "simple buildings" rules.



* Building not taken in count, having been treated as located in seismic area I.

Finally Table 2.2.11 and Table 2.2.12 summarize the results of the designs carried out with linear static and nonlinear static analyses in terms of return period $T_{R(C,SLV)}$ and global safety factor α. For each of these criteria, red cells indicate buildings whose design does not comply with the requirements, buildings largely complying with them are in yellow, and buildings that are considered as satisfactory for each reference site are in green. Empty cells correspond to cases in which a specific building does not even comply for the return period $T_R$ = 30 years.

Table 2.2.11. Results of the design by means of LSA and NLSA: type "E" configurations – concrete blocks.

| $T_R(d_{SLV,d}=d_{SLV,c})$ | | | | E2_CONCR_2ST. | | | E2_CONCR_3ST. | | | E5_CONCR_2ST. | | | E5_CONCR_3ST. | | | E8_CONCR_2ST. | | | E8_CONCR_3ST. | | | E9_CONCR_2ST. | | | E9_CONCR_3ST. | | |
|---|---|---|---|---|---|---|---|---|---|---|---|---|---|---|---|---|---|---|---|---|---|---|---|---|---|---|---|
| site | zone | $a_gS$ [g] | $a_gSF_0$ [g] | LSA (FRAME) | LSA (CANTILEVER) | NLSA | LSA (FRAME) | LSA (CANTILEVER) | NLSA | LSA (FRAME) | LSA (CANTILEVER) | NLSA | LSA (FRAME) | LSA (CANTILEVER) | NLSA | LSA (FRAME) | LSA (CANTILEVER) | NLSA | LSA (FRAME) | LSA (CANTILEVER) | NLSA | LSA (FRAME) | LSA (CANTILEVER) | NLSA | LSA (FRAME) | LSA (CANTILEVER) | NLSA |
| AQ_C | I | 0.347 | 0.820 | - | - | 342 | - | - | 95 | - | - | 248 | - | - | 128 | 47 | - | 365 | 34 | - | 94 | 33 | - | 283 | - | - | 146 |
| AQ_A | I | 0.261 | 0.616 | 44 | - | 1224 | 32 | - | 515 | - | - | 1357 | - | - | 343 | 119 | 57 | 1886 | 82 | 38 | 516 | 80 | 55 | 1593 | 32 | 44 | 753 |
| NA_C | II | 0.245 | 0.582 | 59 | 32 | 840 | 44 | - | 320 | 35 | 30 | 1002 | - | - | 360 | 140 | 73 | 2011 | 100 | 51 | 323 | 98 | 72 | 1276 | 44 | 59 | 484 |
| RM_C | III | 0.182 | 0.479 | 67 | 31 | 2475 | 47 | - | 820 | 36 | - | 2475 | - | - | 1020 | 197 | 88 | 2475 | 131 | 56 | 962 | 127 | 85 | 2475 | 47 | 67 | 1592 |
| NA_A | II | 0.168 | 0.398 | 131 | 67 | 2475 | 95 | 55 | 2139 | 75 | 64 | 2475 | 39 | 42 | 2475 | 353 | 168 | 2475 | 242 | 112 | 2475 | 235 | 163 | 2475 | 95 | 131 | 2475 |
| RM_A | III | 0.121 | 0.319 | 182 | 79 | 2475 | 122 | 61 | 2475 | 91 | 75 | 2475 | 42 | 44 | 2475 | 644 | 250 | 2475 | 397 | 149 | 2475 | 384 | 240 | 2475 | 122 | 181 | 2475 |
| CL_C | III | 0.109 | 0.283 | 242 | 98 | 2475 | 158 | 74 | 2475 | 116 | 93 | 2475 | 46 | 49 | 2475 | 829 | 338 | 2475 | 565 | 195 | 2475 | 521 | 325 | 2475 | 158 | 243 | 2475 |
| MI_C | IV | 0.074 | 0.197 | 806 | 253 | 2475 | 459 | 180 | 2475 | 309 | 236 | 2475 | 102 | 113 | 2475 | 2475 | 1215 | 2475 | 2158 | 612 | 2475 | 2067 | 1157 | 2475 | 459 | 801 | 2475 |
| CL_A | III | 0.073 | 0.189 | 835 | 298 | 2475 | 520 | 217 | 2475 | 359 | 279 | 2475 | 134 | 146 | 2475 | 2475 | 1185 | 2475 | 1951 | 663 | 2475 | 1879 | 1137 | 2475 | 520 | 831 | 2475 |
| MI_A | IV | 0.049 | 0.131 | 2475 | 1023 | 2475 | 1959 | 702 | 2475 | 1274 | 948 | 2475 | 388 | 424 | 2475 | 2475 | 2475 | 2475 | 2475 | 2475 | 2475 | 2475 | 2475 | 2475 | 1959 | 2475 | 2475 |

| α | | | | E2_CONCR_2ST. | | | E2_CONCR_3ST. | | | E5_CONCR_2ST. | | | E5_CONCR_3ST. | | | E8_CONCR_2ST. | | | E8_CONCR_3ST. | | | E9_CONCR_2ST. | | | E9_CONCR_3ST. | | |
|---|---|---|---|---|---|---|---|---|---|---|---|---|---|---|---|---|---|---|---|---|---|---|---|---|---|---|---|
| site | zone | $a_gS$ [g] | $a_gSF_0$ [g] | LSA (FRAME) | LSA (CANTILEVER) | NLSA | LSA (FRAME) | LSA (CANTILEVER) | NLSA | LSA (FRAME) | LSA (CANTILEVER) | NLSA | LSA (FRAME) | LSA (CANTILEVER) | NLSA | LSA (FRAME) | LSA (CANTILEVER) | NLSA | LSA (FRAME) | LSA (CANTILEVER) | NLSA | LSA (FRAME) | LSA (CANTILEVER) | NLSA | LSA (FRAME) | LSA (CANTILEVER) | NLSA |
| AQ_C | I | 0.347 | 0.820 | - | - | 0.92 | - | - | 0.60 | - | - | 0.84 | - | - | 0.67 | 0.43 | - | 0.93 | 0.36 | - | 0.60 | 0.36 | - | 0.87 | - | - | 0.71 |
| AQ_A | I | 0.261 | 0.616 | 0.37 | - | 1.38 | 0.31 | - | 1.03 | - | - | 0.89 | - | - | 0.67 | 0.59 | 0.42 | 1.59 | 0.50 | 0.34 | 1.03 | 0.49 | 0.41 | 1.50 | 0.31 | 0.37 | 1.17 |
| NA_C | II | 0.245 | 0.582 | 0.40 | 0.28 | 1.16 | 0.34 | - | 0.88 | 0.30 | 0.28 | 1.20 | - | - | 0.91 | 0.62 | 0.45 | 1.40 | 0.53 | 0.37 | 0.88 | 0.52 | 0.44 | 1.28 | 0.34 | 0.40 | 1.01 |
| RM_C | III | 0.182 | 0.479 | 0.50 | 0.35 | 1.54 | 0.43 | - | 1.17 | 0.37 | - | 1.54 | - | - | 1.24 | 0.75 | 0.56 | 1.54 | 0.65 | 0.46 | 1.22 | 0.64 | 0.55 | 1.54 | 0.43 | 0.50 | 1.39 |
| NA_A | II | 0.168 | 0.398 | 0.58 | 0.42 | 1.67 | 0.50 | 0.37 | 1.60 | 0.44 | 0.41 | 1.67 | 0.31 | 0.32 | 1.67 | 0.89 | 0.66 | 1.67 | 0.77 | 0.54 | 1.67 | 0.76 | 0.65 | 1.67 | 0.50 | 0.58 | 1.67 |
| RM_A | III | 0.121 | 0.319 | 0.73 | 0.53 | 1.66 | 0.63 | 0.48 | 1.66 | 0.57 | 0.52 | 1.66 | 0.40 | 0.42 | 1.66 | 1.10 | 0.81 | 1.66 | 0.94 | 0.68 | 1.66 | 0.93 | 0.80 | 1.66 | 0.63 | 0.73 | 1.66 |
| CL_C | III | 0.109 | 0.283 | 0.81 | 0.59 | 1.60 | 0.70 | 0.53 | 1.60 | 0.63 | 0.58 | 1.60 | 0.44 | 0.46 | 1.60 | 1.18 | 0.90 | 1.60 | 1.05 | 0.75 | 1.60 | 1.03 | 0.89 | 1.60 | 0.70 | 0.81 | 1.60 |
| MI_C | IV | 0.074 | 0.197 | 1.14 | 0.83 | 1.51 | 0.99 | 0.75 | 1.51 | 0.88 | 0.81 | 1.51 | 0.64 | 0.66 | 1.51 | 1.51 | 1.27 | 1.51 | 1.46 | 1.07 | 1.51 | 1.45 | 1.25 | 1.51 | 0.99 | 1.14 | 1.51 |
| CL_A | III | 0.073 | 0.189 | 1.18 | 0.86 | 1.60 | 1.03 | 0.78 | 1.60 | 0.91 | 0.84 | 1.60 | 0.66 | 0.68 | 1.60 | 1.60 | 1.31 | 1.60 | 1.50 | 1.10 | 1.60 | 1.48 | 1.29 | 1.60 | 1.03 | 1.18 | 1.60 |
| MI_A | IV | 0.049 | 0.131 | 1.51 | 1.22 | 1.51 | 1.43 | 1.10 | 1.51 | 1.28 | 1.19 | 1.51 | 0.94 | 0.97 | 1.51 | 1.51 | 1.51 | 1.51 | 1.51 | 1.51 | 1.51 | 1.51 | 1.51 | 1.51 | 1.43 | 1.51 | 1.51 |

Table 2.2.12. Results of the design by means of LSA and NLSA: type "E" configurations – clay blocks.

| $T_R(d_{SLV,d}=d_{SLV,c})$ | | | | E2_CLAY_2ST. | | | E2_CLAY_3ST. | | | E5_CLAY_2ST. | | | E5_CLAY_3ST. | | | E8_CLAY_2ST. | | | E8_CLAY_3ST. | | | E9_CLAY_2ST. | | | E9_CLAY_3ST. | | |
|---|---|---|---|---|---|---|---|---|---|---|---|---|---|---|---|---|---|---|---|---|---|---|---|---|---|---|---|
| site | zone | $a_gS$ [g] | $a_gSF_0$ [g] | LSA (FRAME) | LSA (CANTILEVER) | NLSA | LSA (FRAME) | LSA (CANTILEVER) | NLSA | LSA (FRAME) | LSA (CANTILEVER) | NLSA | LSA (FRAME) | LSA (CANTILEVER) | NLSA | LSA (FRAME) | LSA (CANTILEVER) | NLSA | LSA (FRAME) | LSA (CANTILEVER) | NLSA | LSA (FRAME) | LSA (CANTILEVER) | NLSA | LSA (FRAME) | LSA (CANTILEVER) | NLSA |
| AQ_C | I | 0.347 | 0.820 | - | - | 562 | - | - | 123 | - | - | 654 | - | - | 115 | 57 | - | 783 | 40 | - | 180 | 44 | - | 712 | - | - | 362 |
| AQ_A | I | 0.261 | 0.616 | 44 | - | 2370 | 35 | - | 732 | - | - | 2359 | - | - | 143 | 145 | 62 | 2475 | 98 | 38 | 1071 | 111 | 62 | 2475 | 39 | 44 | 1785 |
| NA_C | II | 0.245 | 0.582 | 59 | 35 | 2475 | 48 | - | 493 | 38 | 32 | 2475 | - | - | 83 | 168 | 79 | 2475 | 118 | 51 | 779 | 131 | 79 | 2475 | 53 | 59 | 1539 |
| RM_C | III | 0.182 | 0.479 | 67 | 36 | 2475 | 51 | - | 2133 | 39 | 31 | 2475 | - | - | 144 | 250 | 97 | 2475 | 160 | 56 | 2475 | 182 | 97 | 2475 | 59 | 67 | 2475 |
| NA_A | II | 0.168 | 0.398 | 131 | 75 | 2475 | 103 | 55 | 2475 | 81 | 67 | 2475 | 47 | 42 | 477 | 432 | 183 | 2475 | 292 | 112 | 2475 | 329 | 183 | 2475 | 117 | 131 | 2475 |
| RM_A | III | 0.121 | 0.319 | 182 | 79 | 2475 | 135 | 61 | 2475 | 100 | 79 | 2475 | 50 | 44 | 1521 | 842 | 280 | 2475 | 499 | 149 | 2475 | 586 | 280 | 2475 | 157 | 181 | 2475 |
| CL_C | III | 0.109 | 0.283 | 242 | 116 | 2475 | 176 | 74 | 2475 | 128 | 98 | 2475 | 58 | 49 | 1537 | 1049 | 380 | 2475 | 716 | 195 | 2475 | 764 | 380 | 2475 | 205 | 243 | 2475 |
| MI_C | IV | 0.074 | 0.197 | 806 | 309 | 2475 | 530 | 180 | 2475 | 351 | 253 | 2475 | 136 | 113 | 2475 | 2475 | 1398 | 2475 | 2475 | 612 | 2475 | 2475 | 1398 | 2475 | 656 | 801 | 2475 |
| CL_A | III | 0.073 | 0.189 | 835 | 359 | 2475 | 589 | 217 | 2475 | 405 | 298 | 2475 | 171 | 146 | 2475 | 2475 | 1339 | 2475 | 2475 | 663 | 2475 | 2475 | 1339 | 2475 | 703 | 831 | 2475 |
| MI_A | IV | 0.049 | 0.131 | 2475 | 1274 | 2475 | 2263 | 702 | 2475 | 1463 | 1023 | 2475 | 511 | 424 | 2475 | 2475 | 2475 | 2475 | 2475 | 2475 | 2475 | 2475 | 2475 | 2475 | 2475 | 2475 | 2475 |

| α | | | | E2_CLAY_2ST. | | | E2_CLAY_3ST. | | | E5_CLAY_2ST. | | | E5_CLAY_3ST. | | | E8_CLAY_2ST. | | | E8_CLAY_3ST. | | | E9_CLAY_2ST. | | | E9_CLAY_3ST. | | |
|---|---|---|---|---|---|---|---|---|---|---|---|---|---|---|---|---|---|---|---|---|---|---|---|---|---|---|---|
| site | zone | $a_gS$ [g] | $a_gSF_0$ [g] | LSA (FRAME) | LSA (CANTILEVER) | NLSA | LSA (FRAME) | LSA (CANTILEVER) | NLSA | LSA (FRAME) | LSA (CANTILEVER) | NLSA | LSA (FRAME) | LSA (CANTILEVER) | NLSA | LSA (FRAME) | LSA (CANTILEVER) | NLSA | LSA (FRAME) | LSA (CANTILEVER) | NLSA | LSA (FRAME) | LSA (CANTILEVER) | NLSA | LSA (FRAME) | LSA (CANTILEVER) | NLSA |
| AQ_C | I | 0.347 | 0.820 | - | - | 1.04 | - | - | 0.66 | - | - | 1.08 | - | - | 0.65 | 0.47 | - | 1.12 | 0.40 | - | 0.76 | 0.42 | - | 1.10 | - | - | 0.93 |
| AQ_A | I | 0.261 | 0.816 | 0.37 | - | 1.71 | 0.33 | - | 1.16 | - | - | 1.71 | - | - | 0.63 | 0.64 | 0.44 | 1.73 | 0.54 | 0.34 | 1.32 | 0.57 | 0.44 | 1.73 | 0.35 | 0.37 | 1.56 |
| NA_C | II | 0.245 | 0.582 | 0.40 | 0.30 | 1.45 | 0.35 | - | 1.01 | 0.31 | 0.28 | 1.45 | - | - | 0.48 | 0.67 | 0.47 | 1.45 | 0.57 | 0.37 | 1.14 | 0.60 | 0.47 | 1.45 | 0.38 | 0.40 | 1.33 |
| RM_C | III | 0.182 | 0.479 | 0.50 | 0.37 | 1.54 | 0.44 | - | 1.49 | 0.39 | 0.35 | 1.54 | - | - | 0.67 | 0.81 | 0.58 | 1.54 | 0.70 | 0.46 | 1.54 | 0.73 | 0.58 | 1.54 | 0.47 | 0.50 | 1.54 |
| NA_A | II | 0.168 | 0.398 | 0.58 | 0.44 | 1.67 | 0.52 | 0.37 | 1.67 | 0.46 | 0.42 | 1.67 | 0.34 | 0.32 | 1.00 | 0.96 | 0.68 | 1.67 | 0.83 | 0.54 | 1.67 | 0.87 | 0.68 | 1.67 | 0.55 | 0.58 | 1.67 |
| RM_A | III | 0.121 | 0.319 | 0.73 | 0.57 | 1.66 | 0.66 | 0.48 | 1.66 | 0.59 | 0.53 | 1.66 | 0.44 | 0.42 | 1.44 | 1.20 | 0.84 | 1.66 | 1.02 | 0.68 | 1.66 | 1.07 | 0.84 | 1.66 | 0.69 | 0.73 | 1.66 |
| CL_C | III | 0.109 | 0.283 | 0.81 | 0.63 | 1.60 | 0.73 | 0.53 | 1.60 | 0.65 | 0.59 | 1.60 | 0.49 | 0.46 | 1.40 | 1.26 | 0.93 | 1.60 | 1.13 | 0.75 | 1.60 | 1.15 | 0.93 | 1.60 | 0.76 | 0.81 | 1.60 |
| MI_C | IV | 0.074 | 0.197 | 1.14 | 0.88 | 1.51 | 1.03 | 0.75 | 1.51 | 0.91 | 0.83 | 1.51 | 0.70 | 0.66 | 1.51 | 1.51 | 1.31 | 1.51 | 1.51 | 1.07 | 1.51 | 1.51 | 1.31 | 1.51 | 1.09 | 1.14 | 1.51 |
| CL_A | III | 0.073 | 0.189 | 1.18 | 0.91 | 1.60 | 1.07 | 0.78 | 1.60 | 0.95 | 0.86 | 1.60 | 0.72 | 0.68 | 1.60 | 1.60 | 1.35 | 1.60 | 1.60 | 1.10 | 1.60 | 1.60 | 1.35 | 1.60 | 1.12 | 1.18 | 1.60 |
| MI_A | IV | 0.049 | 0.131 | 1.51 | 1.28 | 1.51 | 1.48 | 1.10 | 1.51 | 1.33 | 1.22 | 1.51 | 1.02 | 0.97 | 1.51 | 1.51 | 1.51 | 1.51 | 1.51 | 1.51 | 1.51 | 1.51 | 1.51 | 1.51 | 1.51 | 1.51 | 1.51 |

The obtained results show that buildings designed with LSA often comply only for lower seismicity sites. In many cases, buildings do not even satisfy the requirements for the site of Milan and for soil type A, due to the occurrence of localized failures in a limited number of elements, from the very first analysis steps. On the other hand, if the same buildings are designed with nonlinear static analyses, they result to largely comply with the requirements, often even for higher seismicity sites, with α higher than the assumed limit value of 1.15, corresponding to very high values of the return period $T_{R(C,SLV)}$.

It can be noticed that the target of obtaining, for each site and for each analysis method, at least one building barely complying with the requirements was not reached for some of the ten selected sites, typically for those with medium-high seismicity.

Table 2.2.13 summarizes the sites for which it is possible to design the different masonry building configurations (clay blocks), with either two or three stories. It should be noted that the figures into brackets indicate the return period of the action corresponding to the SLV, whereas the sites in italic are those in which the building would be slightly under-designed or largely over-designed.

These results showed that, depending on the selected analysis method, a building could comply with the requirements on either one or all the sites. One example is building E5 with two stories, which complies only for Milan soil type A (MI-A) for LSA, and for all the sites with NLSA. Based on this, it was decided to analyze all the buildings for all the sites, leading to 80 building-site combinations (160000 nonlinear dynamic analyses with the seismic action simultaneously applied in two horizontal directions). By only considering the combinations corresponding to the results of design with the different methods, the number goes down to thirty-nine (Table 2.2.14) and it can be further reduced to thirty, by considering only buildings barely complying with requirements.

Table 2.2.13. Buildings designed at each site according to the different analysis methods.

| Config. | No. of stories | Simple building | LSA (frame) | LSA (cantilever) | NLSA |
|---|---|---|---|---|---|
| E2 | 2 | AQ-A | MI-C ($T_{r,slv}$ = 806) CL-A ($T_{r,slv}$ = 835) | MI-A ($T_{r,slv}$ = 1274) | AQ-C ($T_{r,slv}$ = 562) |
| E2 | 3 | NA-C | MI-C ($T_{r,slv}$ = 530) CL-A ($T_{r,slv}$ = 589) | MI-A ($T_{r,slv}$ = 702) | AQ-A ($T_{r,slv}$ = 732) NA-C ($T_{r,slv}$ = 493) |
| E5 | 2 | - | *CL-A ($T_{r,slv}$ = 405)* MI-A ($T_{r,slv}$ = 1463) | MI-A ($T_{r,slv}$ = 1023) | AQ-C ($T_{r,slv}$ = 654) |
| E5 | 3 | - | MI-A ($T_{r,slv}$ = 511) | *MI-A ($T_{r,slv}$ = 424)* | NA-A ($T_{r,slv}$ = 477) *RM-A ($T_{r,slv}$ = 1521)* *CL-C ($T_{r,slv}$ = 1537)* |
| E8 | 2 | RM-C NA-A | *NA-A ($T_{r,slv}$ = 432)* RM-A ($T_{r,slv}$ = 842) CL-C ($T_{r,slv}$ = 1049) | *MI-C ($T_{r,slv}$ = 1398)* *CL-A ($T_{r,slv}$ = 1339)* | AQ-C ($T_{r,slv}$ = 783) |
| E8 | 3 | RM-A CL-C | RM-A ($T_{r,slv}$ = 499) CL-C ($T_{r,slv}$ = 716) | MI-C ($T_{r,slv}$ = 612) CL-A ($T_{r,slv}$ = 663) | NA-C ($T_{r,slv}$ = 779) AQ-A ($T_{r,slv}$ = 1071) |
| E9 | 2 | RM-A CL-C | RM-A ($T_{r,slv}$ = 586) CL-C ($T_{r,slv}$ = 764) | *MI-C ($T_{r,slv}$ = 1398)* *CL-A ($T_{r,slv}$ = 1339)* | AQ-C ($T_{r,slv}$ = 712) |
| E9 | 3 | CL-A MI-C | MI-C ($T_{r,slv}$ = 656) CL-A ($T_{r,slv}$ = 703) | MI-C ($T_{r,slv}$ = 801) CL-A ($T_{r,slv}$ = 831) | *NA-C ($T_{r,slv}$ = 1539)* *AQ-A ($T_{r,slv}$ = 1785)* |

Table 2.2.14. Building-site combinations corresponding to the different analysis methods.

| Configuration | No. of stories | Sites | Building-site combination |
|---|---|---|---|
| E2 | 2 | AQ-A, AQ-C, Mi-A, MI-C, CL-A | 5 |
| E2 | 3 | AQ-A, NA-C, MI-A, MI-C, CL-A | 5 |
| E5 | 2 | AQ-C, *CL-A*, MI-A | 3 (1 underdesigned.) |
| E5 | 3 | MI-A, NA-A, *RM-A, CL-C* | 4 (2 overdesigned.) |
| E8 | 2 | AQ-C, RM-A, RM-C, NA-A, *MI-C*, *CL-A*, CL-C | 7 (2 overdesigned.) |
| E8 | 3 | AQ-A, NA-C, RM-A, CL-A, CL-C, MI-C | 6 |
| E9 | 2 | AQ-C, RM-A, *CL-A*, CL-C, *MI-C* | 5 (2 overdesigned.) |
| E9 | 3 | *AQ-A*, CL-A, MI-C, *NA-C* | 4 (2 overdesigned.) |
| | | Total combinations | 39 (9 over/underdes.) |

### 2.2.2.1 LSA with force redistribution

A semi-automatic procedure was implemented for the design of unreinforced masonry buildings with LSA and with force redistribution, following the approach of NTC 2008. This procedure was used for re-designing all the structural configurations proposed by the Pavia RU, for the case of clay units with two or three stories. The results of the cantilever models were used, as they present less critical points with respect to equivalent frame models (the absence of horizontal elements connecting masonry piers guarantees a constant level of axial compression in the elements).

The results of numerical analyses were elaborated in order to:

1) Obtain the stress and strength distribution among the structural elements, for each of the 32 load combinations indicated by the seismic code and for each of the sites in which the considered building would not comply with the requirements for the case of LSA without any force redistribution.

2) Evaluate the story strength distribution in the principal directions of the building and determine the "critical" story. Under the hypothesis that the story resistance is reached in one of the stories, the corresponding strength demand at the other stories, required to satisfy the profile of the story forces' distribution, is calculated

3) For each site and for each load combination, determine the maximum difference between the applied and the resisting shear in the structural elements; this difference can be redistributed if it does not exceed the maximum allowed by the code.

The application of points 2) and 3) allows the automatic identification of the sites in which the elements' strength and the shear variation required to comply with the flexural and shear strength checks of the elements are such as to potentially allow the application of the force redistribution.

For each site of interest at which the force redistribution turns out to be applicable, it is hence necessary to apply the design method, with a trial and error approach, acting on the data regarding each of the thirty-two load combinations of the code, for which at least an element does not comply with the requirements for flexure and/or shear. Table 2.2.15 reports an example of the results obtained when checking if the criterion is applicable.

Table 2.2.15. Check of the applicability of the force redistribution criterion.

| | AQ_C | AQ_A | NA_C | RM_C | NA_A | RM_A | CL_C | MI_C | CL_A | MI_A | |
|---|---|---|---|---|---|---|---|---|---|---|---|
| $V_{Rd,X}$ | KO | KO | KO | OK | OK | OK | OK | OK | OK | OK | (1) |
| $V_{Rd,Y}$ | KO | KO | KO | KO | OK | OK | OK | OK | OK | OK | (1) |
| $dV_{Ed}$ | OK | OK | OK | OK | OK | OK | OK | - | - | - | (2) |
| | KO | KO | KO | KO | OK | OK | OK | - | - | - | |

(1) Identification of the "critical" story in each direction, evaluation of story strength distribution and comparison with story shear demand distribution corresponding to the design force.

(2) Comparison of maximum difference between shear resistance and demand in the structural elements and limit to the force redistribution imposed by the code

| KO | Force redistribution not applicable |
| OK | Force redistribution applicable |
| - | Force redistribution not necessary |

The results obtained with the LSA with force redistribution for the entire set of two-story and three-story configurations are summarized in Table 2.2.16. The force redistribution was applied with the aim of guaranteeing the compliance with the strength requirements in the structural elements, while satisfying the global story equilibrium condition.

Under these hypotheses, the global safety factor α associated to each design (and hence to a specific redistribution of the story forces) can be conventionally assumed to be equal to 1.

Table 2.2.16. Results of the design with LSA with force redistribution.

**E2 – 2 stories**

|            | AQ_C | AQ_A | NA_C | RM_C | NA_A | RM_A | CL_C | MI_C | CL_A | MI_A |
|------------|------|------|------|------|------|------|------|------|------|------|
| $V_{Rd,X}$ | KO | KO | KO | KO | KO | KO | KO | OK | OK | OK |
| $V_{Rd,Y}$ | KO | KO | KO | OK | OK | OK | OK | OK | OK | OK |
| $dV_{Ed}$  | OK | OK | OK | OK | OK | OK | OK | OK | OK | - |
|            | KO | KO | KO | KO | KO | KO | KO | OK | OK | - |

|            | AQ_C | AQ_A | NA_C | RM_C | NA_A | RM_A | CL_C | MI_C | CL_A | MI_A |
|------------|------|------|------|------|------|------|------|------|------|------|
|            | KO | KO | KO | KO | KO | KO | KO | OK | OK | OK |

**E2 – 3 stories**

|            | AQ_C | AQ_A | NA_C | RM_C | NA_A | RM_A | CL_C | MI_C | CL_A | MI_A |
|------------|------|------|------|------|------|------|------|------|------|------|
| $V_{Rd,X}$ | KO | KO | KO | KO | KO | KO | KO | OK | OK | OK |
| $V_{Rd,Y}$ | KO | KO | KO | KO | OK | OK | OK | OK | OK | OK |
| $dV_{Ed}$  | KO | KO | KO | OK | OK | OK | OK | OK | OK | - |
|            | KO | KO | KO | KO | KO | KO | KO | OK | OK | - |

|            | AQ_C | AQ_A | NA_C | RM_C | NA_A | RM_A | CL_C | MI_C | CL_A | MI_A |
|------------|------|------|------|------|------|------|------|------|------|------|
|            | KO | KO | KO | KO | KO | KO | KO | OK | OK | OK |

**E5 – 2 stories**

|            | AQ_C | AQ_A | NA_C | RM_C | NA_A | RM_A | CL_C | MI_C | CL_A | MI_A |
|------------|------|------|------|------|------|------|------|------|------|------|
| $V_{Rd,X}$ | KO | KO | KO | KO | KO | KO | OK | OK | OK | OK |
| $V_{Rd,Y}$ | KO | KO | KO | OK | OK | OK | OK | OK | OK | OK |
| $dV_{Ed}$  | KO | KO | KO | KO | KO | KO | KO | OK | OK | - |
|            | KO | KO | KO | KO | KO | KO | KO | OK | OK | - |

|            | AQ_C | AQ_A | NA_C | RM_C | NA_A | RM_A | CL_C | MI_C | CL_A | MI_A |
|------------|------|------|------|------|------|------|------|------|------|------|
|            | KO | KO | KO | KO | KO | KO | KO | OK | OK | OK |

**E5 – 3 stories**

|            | AQ_C | AQ_A | NA_C | RM_C | NA_A | RM_A | CL_C | MI_C | CL_A | MI_A |
|------------|------|------|------|------|------|------|------|------|------|------|
| $V_{Rd,X}$ | KO | KO | KO | KO | KO | KO | KO | OK | OK | OK |
| $V_{Rd,Y}$ | KO | KO | KO | KO | KO | OK | OK | OK | OK | OK |
| $dV_{Ed}$  | KO | KO | KO | KO | KO | KO | KO | OK | OK | OK |
|            | KO | KO | KO | KO | KO | KO | KO | OK | OK | OK |

|            | AQ_C | AQ_A | NA_C | RM_C | NA_A | RM_A | CL_C | MI_C | CL_A | MI_A |
|------------|------|------|------|------|------|------|------|------|------|------|
|            | KO | KO | KO | KO | KO | KO | KO | OK | OK | OK |

**E8 – 2 stories**

|            | AQ_C | AQ_A | NA_C | RM_C | NA_A | RM_A | CL_C | MI_C | CL_A | MI_A |
|------------|------|------|------|------|------|------|------|------|------|------|
| $V_{Rd,X}$ | KO | KO | KO | OK | OK | OK | OK | OK | OK | OK |
| $V_{Rd,Y}$ | KO | KO | KO | KO | OK | OK | OK | OK | OK | OK |
| $dV_{Ed}$  | OK | OK | OK | OK | OK | OK | OK | - | - | - |
|            | KO | KO | KO | KO | OK | OK | OK | - | - | - |

|            | AQ_C | AQ_A | NA_C | RM_C | NA_A | RM_A | CL_C | MI_C | CL_A | MI_A |
|------------|------|------|------|------|------|------|------|------|------|------|
|            | KO | KO | KO | KO | OK | OK | OK | OK | OK | OK |

**E8 – 3 stories**

|            | AQ_C | AQ_A | NA_C | RM_C | NA_A | RM_A | CL_C | MI_C | CL_A | MI_A |
|------------|------|------|------|------|------|------|------|------|------|------|
| $V_{Rd,X}$ | KO | KO | KO | KO | OK | OK | OK | OK | OK | OK |
| $V_{Rd,Y}$ | KO | KO | KO | KO | KO | OK | OK | OK | OK | OK |
| $dV_{Ed}$  | OK | OK | OK | OK | OK | OK | OK | - | - | - |
|            | KO | KO | KO | KO | KO | OK | OK | - | - | - |

|            | AQ_C | AQ_A | NA_C | RM_C | NA_A | RM_A | CL_C | MI_C | CL_A | MI_A |
|------------|------|------|------|------|------|------|------|------|------|------|
|            | KO | KO | KO | KO | KO | OK | OK | OK | OK | OK |

**E9 – 2 stories**

|            | AQ_C | AQ_A | NA_C | RM_C | NA_A | RM_A | CL_C | MI_C | CL_A | MI_A |
|------------|------|------|------|------|------|------|------|------|------|------|
| $V_{Rd,X}$ | KO | KO | KO | OK | OK | OK | OK | OK | OK | OK |
| $V_{Rd,Y}$ | OK | OK | OK | OK | OK | OK | OK | OK | OK | OK |
| $dV_{Ed}$  | KO | KO | KO | OK | OK | OK | OK | - | - | - |
|            | KO | KO | KO | OK | OK | OK | OK | - | - | - |

|            | AQ_C | AQ_A | NA_C | RM_C | NA_A | RM_A | CL_C | MI_C | CL_A | MI_A |
|------------|------|------|------|------|------|------|------|------|------|------|
|            | KO | KO | KO | OK | OK | OK | OK | OK | OK | OK |

**E9 – 3 stories**

|            | AQ_C | AQ_A | NA_C | RM_C | NA_A | RM_A | CL_C | MI_C | CL_A | MI_A |
|------------|------|------|------|------|------|------|------|------|------|------|
| $V_{Rd,X}$ | KO | KO | KO | KO | OK | OK | OK | OK | OK | OK |
| $V_{Rd,Y}$ | OK | OK | OK | OK | OK | OK | OK | OK | OK | OK |
| $dV_{Ed}$  | KO | KO | KO | KO | OK | OK | OK | - | - | - |
|            | KO | KO | KO | KO | OK | OK | OK | - | - | - |

|            | AQ_C | AQ_A | NA_C | RM_C | NA_A | RM_A | CL_C | MI_C | CL_A | MI_A |
|------------|------|------|------|------|------|------|------|------|------|------|
|            | KO | KO | KO | KO | OK | OK | OK | OK | OK | OK |

### 2.2.3    Design of the "F" and ''G'' type configurations

As explained in a previous section, two model-building configurations with load-bearing masonry made of clay blocks were the starting reference point. The other analyzed configurations differ from them as a function of the following characteristics:

- number of floors;
- type of analysis used for the design: linear static (LSA) or non-linear static (NLSA);
- modelling methodology: equivalent frame or cantilever;
- seismic design input.

The labels used to identify configurations depending on the variants are summarized in Table 2.2.17. Each of them was analyzed for all design accelerations provided, thus two hundred and ninety different configurations were analyzed in total.

Table 2.2.17. Analyzed configurations and applied labels.

| Number of floors | Building type | Analysis type | Analysis scheme | Label |
|---|---|---|---|---|
| 2 stories | Single-family | Linear | Equivalent Frame | 2P_L_F |
| | | | Cantilever | 2P_L_C |
| | | Non linear | Equivalent Frame | 2P_NL_F |
| | | | Cantilever | 2P_NL_C |
| | Two-family | Linear | Equivalent Frame | 2P_L_F |
| | | | Cantilever | 2P_L_C |
| | | Non linear | Equivalent Frame | 2P_NL_F |
| | | | Cantilever | 2P_NL_C |
| 3 stories | Two-family | Linear | Equivalent Frame | 3P_L_F |
| | | | Cantilever | 3P_L_C |
| | | Non linear | Equivalent Frame | 3P_NL_F |
| | | | Cantilever | 3P_NL_C |

2.2.3.1 ''F'' type configurations

Five different building configurations were designed for the base ''F'' type configuration, considering the following variations:

- width of the walls (varying from 0.25 m to 0.40 m);
- mechanical characteristics of masonry (block and mortar strength);
- length and position of door and window openings (maintaining the functionality of the building);
- possible addition of load bearing walls in place of internal partitions (maintaining the functionality of the building).

The aim of these variations was to design structures with gradually increasing structural resistance against external loads, all the while trying to keep mass participation factor just above 60%, which is the minimum value for which nonlinear static analysis can be applicable for masonry buildings, according to the code provisions. To achieve this aim, the irregularities of each building were accentuated. In the main characteristics of different analyzed building configurations are shown. In order to get a safety index as close as possible to 1, a further configuration (F1-a) with less internal load-bearing walls, was considered. These walls were replaced with either RC elements for vertical load bearing function (e.g., columns and beams),

and with internal partition walls for dividing function among rooms. reports several plan views of the different configurations.

Table 2.2.18. Wall characteristics and ratio of load-bearing walls over gross floor area for each "F" type configuration.

| | Wall width | $f_{bk}$ | Mortar Type | Ground floor | | | | First Floor | | | |
|---|---|---|---|---|---|---|---|---|---|---|---|
| | | | | $A_x$ | $\%A_x$ | $A_y$ | $\%A_y$ | $A_x$ | $\%A_x$ | $A_y$ | $\%A_y$ |
| | [cm] | [MPa] | | [m$^2$] | | [m$^2$] | | [m$^2$] | | [m$^2$] | |
| F1 | 25 | 8 | M5 | 6,78 | 5,12 | 6,10 | 4,61 | 5,70 | 6,31 | 4,18 | 4,62 |
| F2 | 30 | 15 | M10 | 8,59 | 6,49 | 7,53 | 5,69 | 6,99 | 7,73 | 5,16 | 5,71 |
| F3 | 40 | 15 | M10 | 11,81 | 8,92 | 10,7 | 8,08 | 9,31 | 10,30 | 7,18 | 7,94 |
| F4 | 30 | 15 | M10 | 8,59 | 6,49 | 7,53 | 5,69 | 7,73 | 6,99 | 3,83 | 4,24 |
| F1-a | 25 | 8 | M5 | 6,20 | 4,68 | 5,04 | 3,80 | 5,12 | 5,66 | 3,11 | 3,44 |



F1

F2

F3

F4

F1-a

25cm

30cm

35cm

40cm

Wall widths
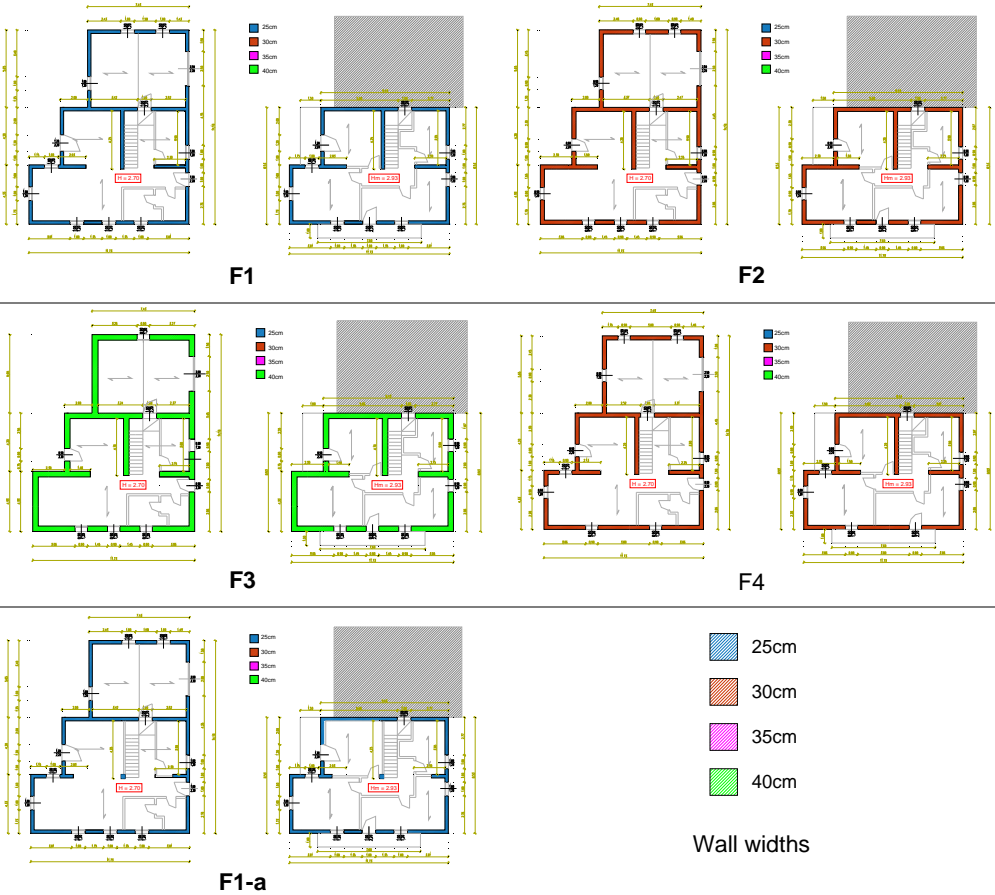
Figure 2.2.7 Plan views of the different "F" type configurations.

2.2.3.2 ''G'' type configuration

Four different building configurations were designed for the base ''G'' type configuration, considering the same variations of section 2.2.3.1 for width of the walls (varying from 0.30 to 0.40 m) and length and position of door and window openings (maintaining the functionality of the building). In addition, the possible addition of load bearing walls in place of internal partitions (maintaining the functionality of the building) was considered. The aim of these variations was to design structures with gradually increasing strength. To get a safety index as close as possible to 1, a further configuration (G1-a) with less internal load-bearing walls was considered. These walls were replaced with either RC elements for vertical load bearing function (e.g., columns and beams) and with internal partition walls for dividing function among rooms. Variations are made only at the ground floor and first floor. Plan views of different configurations and corresponding characteristics are reported in Figure 2.2.8, Figure 2.2.9, and Table 2.2.19.



**Wall widths** 30cm   40cm

Figure 2.2.8 Plan views of configurations G5 and G6.

Table 2.2.20 reports the values of safety index, calculated as the ratio between capacity and demand of different configurations depending on the spectral accelerations of the ten considered sites. For linear analysis, the table shows the smaller ratio between the two principal directions in terms of PGA (capacity over demand) calculated at the Ultimate Limit State. For NLSA the safety index was calculated in terms of PGA ratios at the attainment of the ultimate displacement, as the minimum value for the 16 load combinations.

Values greater than or equal to 1 mean the building is safe (in green), whereas values less than 1 mean that structure is vulnerable (in red) respect to Ultimate Limit State.

**G7**



**G5-a**



**Wall widths** [ ] 30cm   [ ] 40cm

Figure 2.2.9 Plan views of configurations G7 and G5-a.

Table 2.2.19. Wall characteristics and ratio of load-bearing walls over gross floor area for each "G" type configuration.

| | Wall width | $f_{bk}$ | Mortar Type | Ground floor | | | | First Floor | | | | Second Floor | | | |
|---|---|---|---|---|---|---|---|---|---|---|---|---|---|---|---|
| | | | | $A_x$ | $\%A_x$ | $A_y$ | $\%A_y$ | $A_x$ | $\%A_x$ | $A_y$ | $\%A_y$ | $A_x$ | $\%A_x$ | $A_y$ | $\%A_y$ |
| | [cm] | [MPa] | | [m$^2$] | | [m$^2$] | | [m$^2$] | | [m$^2$] | | [m$^2$] | | [m$^2$] | |
| **G5** | 30 | 15 | M10 | 13,11 | 7,10 | 13,32 | 7,22 | 11,05 | 7,06 | 11,21 | 7,16 | 11,05 | 2,13 | 5,22 | 3,93 |
| **G6** | 40 | 15 | M10 | 19,06 | 10,33 | 17,82 | 9,65 | 16,19 | 10,34 | 14,95 | 9,55 | 16,19 | 4,30 | 10,54 | 5,24 |
| **G7** | 30 | 15 | M10 | 14,36 | 7,78 | 13,38 | 7,25 | 12,20 | 7,79 | 11,27 | 7,20 | 12,20 | 3,98 | 9,75 | 3,69 |
| **G5-a** | 30 | 15 | M10 | 10,56 | 5,72 | 12,06 | 6,53 | 8,50 | 5,43 | 9,95 | 6,36 | 8,50 | 2,13 | 5,22 | 3,93 |

The following summarizes the obtained results, as far as the type of analysis is concerned:

- in case of LSA applied with medium to high design acceleration (above NA, soil A), the analyzed configurations do not comply with the requirements.
- On the other hand, NLSA leads to high values of the safety index. Most likely, this fact is exacerbated by the irregularity of the buildings.

With regard to the variation of parameters:

- The variation of the wall thickness leads to small increases of capacity.
- To improve building capacity, it is much more effective to modify the geometry by increasing the lengths of the masonry walls, or by adding other resistant walls.

In the end, as far as the analysis scheme is concerned, it has to be observed that cantilever models have both stiffness and capacity lower than equivalent frame models.

Table 2.2.20. Results of the analyses performed on the defined configurations. The results are expressed in terms of safety factors associated to each analysis performed at ULS.

| Building with a safety factor slightly higher than 1 | | | Oversized building (safety factor higher than 1.5) | | | | Building not verified | | |
|---|---|---|---|---|---|---|---|---|---|
| **CONFIGURATION** | **DESIGN SITES AND SOILS** | | | | | | | | |
| | **AQ_ C** | **AQ_ A** | **NA_ C** | **RM_ C** | **NA_ A** | **RM_ A** | **CLT_ C** | **MI_ C** | **CLT_ A** | **MI_ A** |
| $a_gS$ [g] | 0.347 | 0.261 | 0.245 | 0.182 | 0.168 | 0.121 | 0.109 | 0.074 | 0.073 | 0.049 |
| $a_gsF_0$ [g] | 0.820 | 0.616 | 0.582 | 0.479 | 0.398 | 0.319 | 0.283 | 0.19 | 0.189 | 0.131 |
| F1_2P_L_C | 0.154 | 0.206 | 0.217 | 0.265 | 0.318 | 0.396 | 0.447 | 0.633 | 0.671 | 0.964 |
| F2_2P_L_C | 0.161 | 0.215 | 0.227 | 0.277 | 0.333 | 0.414 | 0.468 | 0.662 | 0.702 | 1.008 |
| F3_2P_L_C | 0.252 | 0.336 | 0.355 | 0.434 | 0.517 | 0.648 | 0.732 | 1.035 | 1.098 | 1.577 |
| F4_2P_L_C | 0.217 | 0.290 | 0.306 | 0.373 | 0.448 | 0.558 | 0.630 | 0.892 | 0.945 | 1.358 |
| G7_2P_L_C | 0.224 | 0.299 | 0.318 | 0.385 | 0.462 | 0.580 | 0.643 | 0.924 | 0.974 | 1.398 |
| F1_2P_L_F | 0.207 | 0.276 | 0.291 | 0.355 | 0.427 | 0.531 | 0.600 | 0.849 | 0.900 | 1.292 |
| F2_2P_L_F | 0.266 | 0.355 | 0.375 | 0.458 | 0.549 | 0.684 | 0.773 | 1.093 | 1.159 | 1.167 |
| F3_2P_L_F | 0.396 | 0.528 | 0.557 | 0.680 | 0.812 | 1.018 | 1.149 | 1.625 | 1.723 | 2.475 |
| F4_2P_L_F | 0.235 | 0.313 | 0.330 | 0.403 | 0.485 | 0.603 | 0.681 | 0.964 | 1.022 | 1.468 |
| G5_2P_L_F | 0.259 | 0.346 | 0.368 | 0.445 | 0.535 | 0.670 | 0.751 | 1.068 | 1.126 | 1.617 |
| G6_2P_L_F | 0.294 | 0.393 | 0.417 | 0.505 | 0.607 | 0.761 | 0.852 | 1.212 | 1.279 | 1.835 |
| G7_2P_L_F | 0.315 | 0.421 | 0.447 | 0.541 | 0.650 | 0.815 | 0.904 | 1.299 | 1.370 | 1.966 |
| F1-a_2P_NL_F | 0.316 | 0.389 | 0.462 | 0.553 | 0.637 | 0.837 | 1.151 | 1.711 | 1.780 | 2.691 |
| F1_2P_NL_F | 0.881 | 0.998 | 1.417 | 1.858 | 1.822 | 2.257 | 10.792 | 14.978 | 12.319 | 12.757 |
| F2_2P_NL_F | 1.025 | 1.203 | 1.720 | 2.388 | 2.364 | 3.118 | 17.714 | 20.615 | 17.000 | 17.762 |
| F3_2P_NL_F | 1.492 | 1.846 | 2.791 | 4.579 | 4.493 | 7.500 | 27.381 | 34.267 | 29.267 | 29.500 |
| F4_2P_NL_F | 1.098 | 1.290 | 1.860 | 2.631 | 2.582 | 3.450 | 18.694 | 18.214 | 18.481 | 13.917 |
| G5_2P_NL_F | 1.902 | 2.152 | 3.711 | 5.239 | 5.134 | 6.333 | 21.549 | 25.079 | 20.974 | 21.469 |
| G6_2P_NL_F | 2.579 | 3.051 | 6.021 | 12.587 | 9.683 | 9.906 | 30.938 | 35.440 | 29.231 | 30.800 |
| G7_2P_NL_F | 2.383 | 2.738 | 5.233 | 9.640 | 7.855 | 8.594 | 26.395 | 31.063 | 25.656 | 26.692 |
| F4_2P_NL_C | 0.500 | 0.571 | 0.750 | 0.921 | 0.969 | 1.301 | 2.583 | 3.691 | 3.891 | 5.460 |
| G7_3P_L_C | 0.215 | 0.286 | 0.301 | 0.369 | 0.440 | 0.553 | 0.623 | 0.875 | 0.935 | 1.344 |
| G5_3P_L_F | 0.153 | 0.203 | 0.216 | 0.262 | 0.315 | 0.396 | 0.443 | 0.625 | 0.664 | 0.954 |
| G6_3P_L_F | 0.169 | 0.225 | 0.237 | 0.291 | 0.347 | 0.436 | 0.491 | 0.690 | 0.737 | 1.059 |
| G7_3P_L_F | 0.235 | 0.313 | 0.330 | 0.404 | 0.482 | 0.606 | 0.683 | 0.959 | 1.024 | 1.473 |
| G5-a_3P_NL_F | 0.069 | 0.110 | 0.108 | 0.149 | 0.194 | 0.286 | 0.396 | 0.684 | 0.729 | 1.259 |
| G5_3P_NL_F | 0.250 | 0.284 | 0.363 | 0.444 | 0.455 | 0.561 | 0.988 | 1.516 | 1.401 | 1.985 |
| G6_3P_NL_F | 0.283 | 0.464 | 0.497 | 0.764 | 0.960 | 1.241 | 2.930 | 4.780 | 4.509 | 5.829 |
| G7_3P_NL_F | 0.154 | 0.247 | 0.273 | 0.415 | 0.510 | 0.756 | 1.716 | 2.309 | 2.190 | 2.761 |

### 2.2.4   Design of unreinforced masonry buildings according to the draft of NTC18

The regular "C" type configurations and the irregular "I" type configurations were also designed with NLSA according to the prescriptions contained in the draft of the new NTC18 (the ongoing updated version of NTC 2008).

As far as the seismic design with nonlinear static analysis for masonry structures concerns, some differences arise with respect to the previous version of the document (NTC 2008). In particular, the changes introduced by the draft of the new NTC18 deal with the following issues:

1) the definition of updated values for the ultimate drift to be considered in the constitutive laws of the masonry panels (both for flexural and shear behaviors);
2) the definition of an updated limit value for the q* factor, to be considered for the verification together with the condition that the expected seismic demand displacement is lower than the capacity displacement;
3) the need to consider the bi-directional effect of the seismic action.

As far as the first point is concerned, the draft of NTC18 states that, at the scale of the single masonry panel, the behavior can still be represented by a bilinear elastic-perfectly plastic (EPP) constitutive law (§NTC18, 7.8.1.5.4). However updated values are defined for the ultimate drift, which has to be representative of the collapse limit state (SLC). The proposed values are higher than the ones previously proposed in NTC 2008, which are assumed to be representative of the life-safety limit state (SLV), even if this is not explicitly stated. In particular, for the flexural behavior of URM buildings (§NTC18, 7.8.2.2.1), the ultimate drift is assumed to be 1% (the value proposed in NTC 2008 was instead 0.8%) while for shear behavior (§NTC18, 7.8.2.2.1) it is assumed to be 0.5% (the value proposed in NTC 2008 was instead 0.4%).

Regarding the second point, it is recalled that the $q*$ factor is defined as the ratio between the total base-shear of the equivalent SDOF system calculated with the elastic response spectrum, and the total base-shear of the equivalent SDOF system obtained through the nonlinear analysis. The limit value for q* introduced in the code represents the limit beyond which the verification is not satisfied; this value is increased in the new document from 3 (§NTC 2008, 7.8.1.6) to 4 (§NTC18, 7.8.1.6).  Even if it is not clearly stated in the document, this increased value of the $q*$ factor has probably been introduced to match this parameter to the collapse limit state rather than the life-safety limit state, similarly to the ultimate drift values for the masonry panels.

Finally regarding the third point on the draft of NTC18, it is no longer explicitly stated that, in case of NLSA, it is possible to uncouple the two horizontal components of the seismic action (§NTC18, 7.3.5). Therefore, in order to take into account the simultaneity of the seismic action in the two horizontal directions, it is necessary, for each direction, to consider also 30% of the action in the orthogonal direction. In the absence of a well-defined criterion to be adopted in the case of nonlinear static analysis, the resultant of the load pattern was then determined based on the rule of the square root of the sum of the squares (SRSS).

From these considerations, it can be seen that the draft of NTC18 introduces several explicit modifications for the analyses and the verifications with NLSA of masonry structures. However, while NTC 2008 explicitly states that it can be considered safe with respect to all the ultimate limit states (§NTC 2008, 7.1) as long as structural safety is verified with respect to the SLV, NTC18 does not specify which ultimate limit state has to be checked (SLV or SLC).

Since, as seen above, the only certain elements provided by the new draft of the code (in terms of ultimate drift values and $q*$) are referring to the collapse limit state, it is implied that SLC becomes the new reference for design and verification at the ultimate limit state conditions: for the SLV, indeed, no sufficient data are provided to univocally define the verification criteria.

According to this logic, it was decided to finalize the design phase with respect to the collapse limit state. Therefore, the reference spectrum was associated with this higher return period (975 years).

Regarding the constitutive laws for masonry panels, since in the draft no specific indications are given, it was assumed to extend the plastic branch from the value of the ultimate drift defined in NTC 2008 (referred to SLV) to the value of the ultimate drift defined for SLC in the draft of NTC18 without assuming any strength degradation between the two conditions. This, indeed, was considered as the most probable choice that a professional engineer would adopt, even if the actual behavior of piers – in particular in case of a prevailing shear failure mode – should be characterized by a softening phase (as proved by many experimental campaigns and also adopted in the assessment phase through nonlinear dynamic analyses).

Finally, in order to complete the verification, it is necessary to define on the global curve the displacement capacity related to the SLC, that has to be compared with the seismic displacement demand. In NTC 2008 the displacement capacity corresponding to SLV was defined in the commentary of the code (Circolare n.617/2009) as the displacement corresponding to a decay of 20% of the global base-shear (§C7.8.1.5.4). Since the commentary of the NTC18 has not been yet completed, and therefore no specific indications are included in the draft about this point, it was assumed to use the same criterion also for the SLC.

Following the new rules explicitly introduced in the draft of NTC18, together with the aforementioned assumptions in the cases for which no sufficient explanations are given in the code, the nonlinear static analyses on the "C" and "I" type configurations were repeated, as well as the procedure for outlining the configurations to be used in each one of the examined sites. In particular, for each building-site combination, the related safety factor $\alpha$ was checked. As mentioned before, $\alpha$ was established to be lower than 1.5 in order to consider the correspondent configuration acceptable (i.e., not over-dimensioned), was checked.

The results deriving from the design with NLSA according to the draft of NTC18, compared with the results obtained according to NTC 2008, are illustrated in Table 2.2.21 for the regular ''C'' type configurations (with two and three stories) and in Table 2.2.22 for the irregular ''I'' type configurations (with two and three stories). For the cases in which, for a given site, the design procedure according to NTC18 provides the same configuration as the one obtained with NTC 2008 (indicated in bold in Table 2.2.21 and 2.2.22), it is also indicated the ratio between the new and the previous safety factor $\alpha$ associated with that building-site combination.

From these results, it turns out that, according to the design procedure introduced in the draft of NTC18, in general, it is more demanding to satisfy the requirements: indeed, for a given building-site combination, lower values of the safety factor $\alpha$ have been obtained. On one hand this result can be expected, because the seismic action is referred to a higher return period (Tr =975 years) and hence the demand is higher. On the other hand, the reduction of the safety factor $\alpha$ was not so obvious, because also the parameters related to the capacity was changed: both the ultimate drift values at the scale of masonry panels and the limit value for the $q^*$ factor increased. Moreover, the necessity of taking into account the simultaneity of the seismic action in the two horizontal directions (while according to NTC 2008 they were uncoupled) leads to a further amplification of the seismic action itself, hence resulted in a further reduction of the obtained safety factors.

The consequences of these stricter requirements on the design of the "C" and "I" type configurations are the following:

- some building-site combinations verified according to NTC 2008 with a very low safety factor (slightly higher than 1) are no longer verified;
- some building-site combinations verified according to NTC 2008 are still verified but with a lower safety factor (as it can be seen from Table 2.2.21 and 2.2.22, in these cases α decreases by approximately 15%);
- the NTC18-based design provided new building-site combinations to be analyzed; this is because configurations which were over-dimensioned in a site according to the NTC08 are found to have a safety factor lower than 1.5, thus consistent with the criteria for selecting building-to-site combinations (building verified but not over-dimensioned).

In particular, considering the case of three-story "C" type configurations, for example, it can be seen that:

- the C1 configuration, according to the draft of NTC18, is no longer verified in L'Aquila soil type A and, in addition, it is no more possible to have a three-story "C" type configuration in L'Aquila A;
- in Rome soil type C, the presence of C1 configuration is confirmed, but the associated safety coefficient $\alpha$ is lower than before (it decreases by 13.2%);
- the C3 configuration, before located in Naples soil type C, is no more verified and the first configuration that can be used at this site is C5; in this way there is a new building-site combination to analyze (C5 with three-stories in Naples soil type C).

In conclusion, from the results presented in Table 2.2.21 and 2.2.22, it turns out that, when following the design procedure introduced in the draft of NTC18, ten new building-site combinations have to be analyzed (six regular "C" type configurations and four irregular "I" type configurations).

Table 2.2.21. Regular "C" type configurations obtained for each site with NLSA: comparison between building-site combinations obtained according to the draft of NTC18 and to NTC08.

| Considered buildings (safety factor slightly higher than 1). | | Oversized buildings (safety factor higher than 1.5). | | No verified buildings among those defined. | | | |
|---|---|---|---|---|---|---|---|
| **REGULAR "C" TYPE CONFIGURATIONS** | | | | | | | |
| | | **TWO STORY BUILDINGS** | | | **THREE STORY BUILDINGS** | | |
| **Site** | **a$_g$S [g]** | **NTC 18** | **NTC08** | $\dfrac{\alpha NTC18}{\alpha NTC08}$ | **NTC 18** | **NTC08** | $\dfrac{\alpha NTC18}{\alpha NTC08}$ |
| Mi_A | 0.049 | | | | | | |
| Mi_C | 0.074 | | | | | | |
| Ca_A | 0.073 | | | | | | |
| Ca_C | 0.109 | | | | | | |
| Ro_A | 0.121 | | | | | | |
| Ro_C | 0.182 | C1 | | | **C1** | **C1** | 0.868 |
| Na_A | 0.168 | C1 | | | C1 | | |
| Na_C | 0.245 | C2 | C1 | | C5 | C3 | |
| Aq_A | 0.261 | C3 | C1 | | | C1 | |
| Aq_C | 0.347 | **C3** | **C3** | 0.873 | | | |

Table 2.2.22. Irregular "I" type configurations obtained for each site with NLSA: comparison between building-site combinations obtained according to the draft of NTC18 and to NTC08.

| Considered buildings (safety factor slightly higher than 1). | | Oversized buildings (safety factor higher than 1.5). | | No verified buildings among those defined. | |
|---|---|---|---|---|---|

| IRREGULAR "I" TYPE CONFIGURATIONS | | | | | | | |
|---|---|---|---|---|---|---|---|
| | | TWO STORY BUILDINGS | | | THREE STORY BUILDINGS | | |
| Site | $a_gS$ [g] | NTC 18 | NTC08 | $\dfrac{\alpha NTC18}{\alpha NTC08}$ | NTC 17 | NTC08 | $\dfrac{\alpha NTC18}{\alpha NTC08}$ |
| Mi_A | 0.049 | | | | | | |
| Mi_C | 0.074 | | | | | | |
| Ca_A | 0.073 | | | | | | |
| Ca_C | 0.109 | | | | | | |
| Ro_A | 0.121 | | | | | | |
| Ro_C | 0.182 | | | | I2 | | |
| Na_A | 0.168 | | | | I2 | | |
| Na_C | 0.245 | I1 | | | | I2 | |
| Aq_A | 0.261 | I1 | | | | | |
| Aq_C | 0.347 | **I1** | **I1** | 0.842 | | | |

## 2.2.5   Design of reinforced masonry "E" type configurations

Two "E" type building configurations ("E2" and "E8", Figure 2.2.10) and one "F" type configuration (already designed for the case of unreinforced masonry) were considered for the design of reinforced clay masonry buildings. The results obtained will be discussed in this section.

Regarding the "E" type configurations, the reader is referred to section 2.1.2 for the adopted design choices and for the analysis of the applied loads, whereas the selected modelling options are reported in section 2.2.2.

The following assumptions on the material mechanical characteristics were adopted:

- H-shaped clay unit masonry, with a characteristic compressive strength $f_{bk}$ = 10 MPa
- M10 mortar
- C25/30 concrete tie beams at the story level
- B450C steel reinforcement

Sections were assumed to be cracked, by applying 50% reduction of the geometrical properties of the structural elements' section. Table 2.2.23 summarizes the values of the mechanical properties, with reference to the case of uncracked sections.

E2
Thickness of external walls: 30 cm
Thickness of internal walls: 25 cm

E8
Thickness of external walls: 30 cm
Thickness of internal walls: 30 cm
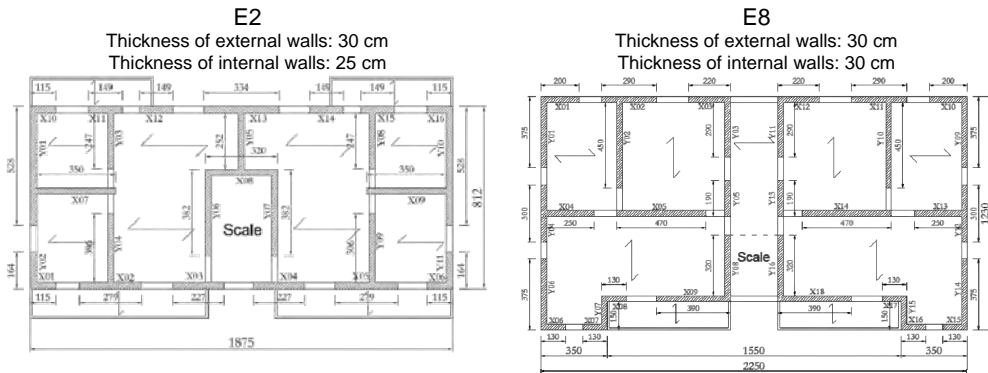


Figure 2.2.10 Design of "E" type reinforced masonry buildings: plan views of the two different configurations considered.

Table 2.2.23. Mechanical properties of the materials.

| Masonry | | | Concrete C25/30 | | | Steel B450C | | |
|---|---|---|---|---|---|---|---|---|
| $\omega$ | 9 | [kN/m$^3$] | $\omega$ | 25 | [kN/m$^3$] | $f_{yk}$ | 450 | [MPa] |
| $f_{bk}$ | 10 | [MPa] | $R_{ck}$ | 30 | [MPa] | | | |
| $f_m$ | 10 | [MPa] | $f_{ck}$ | 24.9 | [MPa] | | | |
| $\mu$ | 0.4 | [-] | $f_{ctk}$ | 1.8 | [MPa] | | | |
| $f_k$ | 5.3 | [MPa] | E | 31447 | [MPa] | | | |
| $f_{hk}$ | 0.9 | [MPa] | G | 13103 | [MPa] | | | |
| $f'_{bk}$ | 2.0 | [MPa] | $\nu$ | 0.2 | [-] | | | |
| $f_{vk0}$ | 0.2 | [MPa] | | | | | | |
| $f_{vk,lim}$ | 1.5 | [MPa] | | | | | | |
| $f_{tk}$ | 0.3 | [MPa] | | | | | | |
| E | 5300 | [MPa] | | | | | | |
| G | 2120 | [MPa] | | | | | | |

For all the elements, the minimum reinforcement according to NTC08 was initially assumed (Table 2.2.24). When necessary based on the results of the analysis, this reinforcement was locally increased to comply with the strength requirements.

Table 2.2.24. Minimum reinforcement according to NTC08 for reinforced masonry.

| Rinforcement | R.c. story tie beams | Wall panels |
|---|---|---|
| Longitudinal | 2+2Ø16 | 1Ø16 at each end or wall intersection, with a distance not larger than 4 m (0.05% ≤ $\rho_l$ ≤ 1.00%) |
| Transversal | stirrups Ø8/25 cm | stirrups Ø6/40 cm, every two courses (0.04% ≤ $\rho_w$ ≤ 0.50%) |

The design was carried out according to the following scheme:

1. Evaluation of the global safety factor of the buildings with minimum reinforcement by means of:
   • Nonlinear Static Analysis (NLSA) on equivalent frame models;
   • Linear Static Analysis (LSA) without any force redistribution on both equivalent frame and cantilever models.
2. Redesign of the reinforcement to comply with the requirements at each site.

The reinforcement was redesigned for the case of the three-story building "E8", by means of LSA without any force redistribution on an equivalent frame model (Figure 2.2.11). The increase in the reinforcement regarded some wall elements (typically at the lowest building levels) and some story tie beams, whose longitudinal reinforcement was increased to 3+3Ø16, whereas closer stirrups were adopted (Ø8|15 cm).

The design according to NLSA was carried out with the software ANDILWall, using an equivalent frame modelling of the buildings with the following assumptions:

- fully coupled orthogonal walls, by means of infinitely rigid links at the floor level, connecting the end nodes of the elements;

- diaphragms infinitely rigid in their plane.
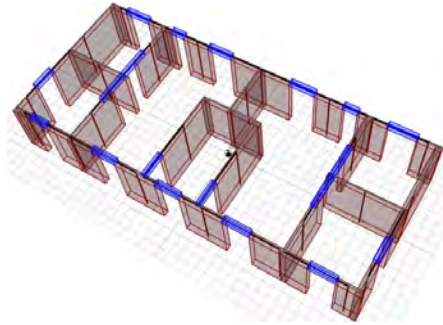


Figure 2.2.11 Design by means of NLSA: equivalent frame model.

The design of both buildings resulted in high values of *α*, even with the minimum reinforcement of the code. In almost all sites, buildings comply with the requirements for values of the return period close to the maximum value of the code (2475 years). For these reasons, it was decided to also consider a four-story configuration. Figure 2.2.12 shows, as an example, the capacity curves obtained from two of the considered analyses for the four-story "E8" configuration and the corresponding comparison (for the highest seismicity site, AQ soil type C) between displacement capacity and demand at the ultimate limit state (SLV).

The design by LSA was carried out using the software ANDILWall, with both cantilever and equivalent frame models (Figure 2.2.13). Numerical models were defined according to the following hypotheses:

- Cantilever model:
    - longitudinal bars at the T and L intersections assigned to each of the incident masonry piers;
    - diaphragms infinitely rigid in their plane.
- Equivalent frame model:
    - longitudinal bars at the walls' intersections assigned to each of the incident masonry piers;
    - no coupling at the story level at the walls' intersections between incident masonry piers;
    - diaphragms infinitely rigid in their plane.

Analysis X+|e$_a$+|G$_{1modal}$



Analysis Y+|e$_a$+|G$_{1modal}$
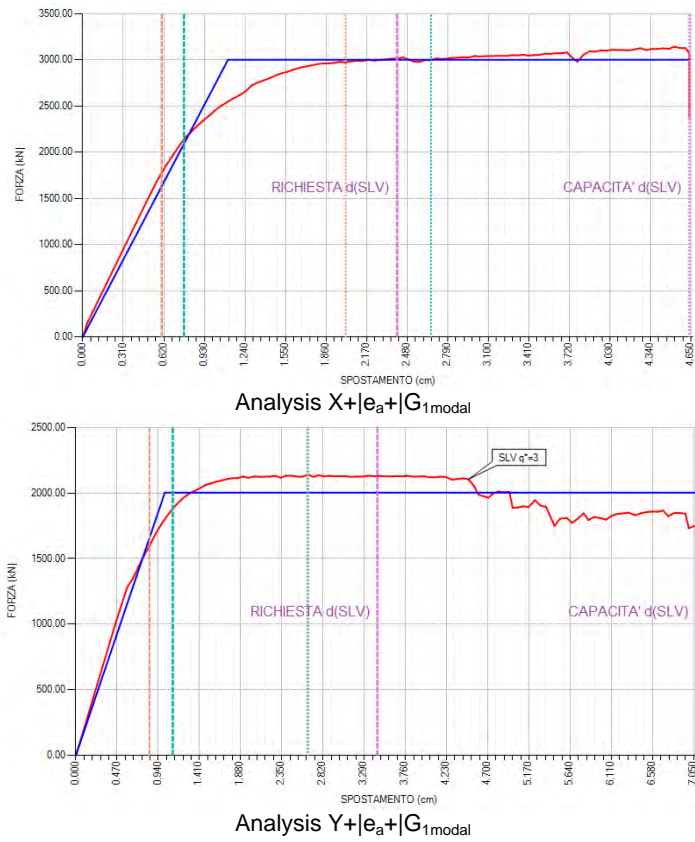
Figure 2.2.12 Examples of the capacity curves obtained from NLSA in the *x* and *y* direction (four-story "E8" configuration).



(a)



(b)
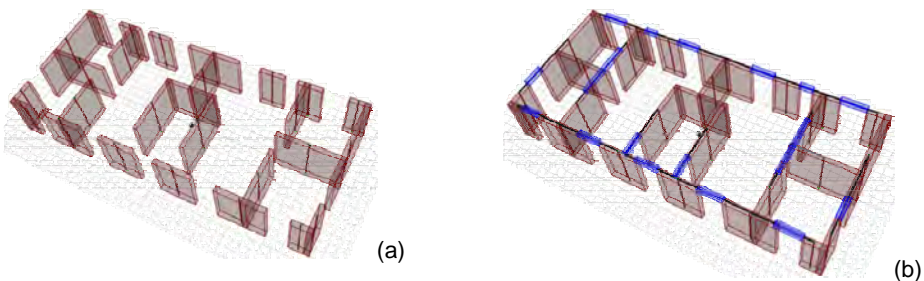
Figure 2.2.13 Design by LSA: (a) cantilever model; (b) equivalent frame model.

Table 2.2.25 summarizes the results of the design of the two configurations with the different adopted criteria (red highlights the results of the reinforcement redesign for the considered case).

Table 2.2.25. Results of the design of three-/four-story configurations "E2" and "E8" with reinforced masonry.

| $T_R(d_{SLV,d} = d_{SLV,c})$ | | | | E2_CLAY_3ST_RM | | | E2_CLAY_4ST_RM | | | E8_CLAY_3ST_RM | | | E8_CLAY_4ST_RM | | | LSA (FRAME) |
|---|---|---|---|---|---|---|---|---|---|---|---|---|---|---|---|---|
| site | zone | $a_gS$ [g] | $a_gSF_0$ [g] | LSA (FRAME) | LSA (CANTILEVER) | NLSA | LSA (FRAME) | LSA (CANTILEVER) | NLSA | LSA (FRAME) | LSA (CANTILEVER) | NLSA | LSA (FRAME) | LSA (CANTILEVER) | NLSA | |
| AQ_C | I | 0.347 | 0.820 | 163 | 68 | >2475 | 46 | <30 | 1358 | 170 | 109 | >2475 | 56 | 41 | >2475 | 495 |
| AQ_A | I | 0.261 | 0.616 | 420 | 174 | >2475 | 134 | 79 | >2475 | 435 | 288 | >2475 | 160 | 122 | >2475 | 1070 |
| NA_C | II | 0.245 | 0.582 | 490 | 199 | >2475 | 136 | 77 | >2475 | 514 | 334 | >2475 | 165 | 122 | >2475 | 1682 |
| RM_C | III | 0.182 | 0.479 | 993 | 313 | >2475 | 189 | 94 | >2475 | 1058 | 582 | >2475 | 245 | 166 | >2475 | >2475 |
| NA_A | II | 0.168 | 0.398 | 1380 | 528 | >2475 | 341 | 178 | >2475 | 1438 | 908 | >2475 | 426 | 303 | >2475 | >2475 |
| RM_A | III | 0.121 | 0.319 | >2475 | 1096 | >2475 | 863 | 390 | >2475 | >2475 | 2263 | >2475 | 1137 | 746 | >2475 | >2475 |
| CL_C | III | 0.109 | 0.283 | >2475 | 1509 | >2475 | 874 | 374 | >2475 | >2475 | >2475 | >2475 | 1162 | 751 | >2475 | >2475 |
| MI_C | IV | 0.074 | 0.197 | >2475 | >2475 | >2475 | >2475 | 1333 | >2475 | >2475 | >2475 | >2475 | >2475 | >2475 | >2475 | >2475 |
| CL_A | III | 0.073 | 0.189 | >2475 | >2475 | >2475 | >2475 | 1285 | >2475 | >2475 | >2475 | >2475 | >2475 | >2475 | >2475 | >2475 |
| MI_A | IV | 0.049 | 0.131 | >2475 | >2475 | >2475 | >2475 | >2475 | >2475 | >2475 | >2475 | >2475 | >2475 | >2475 | >2475 | >2475 |

| α | | | | E2_CLAY_3ST_RM | | | E2_CLAY_4ST_RM | | | E8_CLAY_3ST_RM | | | E8_CLAY_4ST_RM | | | LSA (FRAME) |
|---|---|---|---|---|---|---|---|---|---|---|---|---|---|---|---|---|
| site | zone | $a_gS$ [g] | $a_gSF_0$ [g] | LSA (FRAME) | LSA (CANTILEVER) | NLSA | LSA (FRAME) | LSA (CANTILEVER) | NLSA | LSA (FRAME) | LSA (CANTILEVER) | NLSA | LSA (FRAME) | LSA (CANTILEVER) | NLSA | |
| AQ_C | I | 0.347 | 0.820 | 0.735 | 0.515 | -sup- | 0.426 | -inf- | 1.244 | 0.745 | 0.636 | -sup- | 0.471 | 0.403 | -sup- | 1.010 |
| AQ_A | I | 0.261 | 0.616 | 0.956 | 0.688 | -sup- | 0.616 | 0.489 | -sup- | 0.969 | 0.833 | -sup- | 0.665 | 0.593 | -sup- | 1.321 |
| NA_C | II | 0.245 | 0.582 | 1.009 | 0.730 | -sup- | 0.609 | 0.460 | -sup- | 1.022 | 0.891 | -sup- | 0.669 | 0.579 | -sup- | 1.350 |
| RM_C | III | 0.182 | 0.479 | 1.234 | 0.874 | 1.065 | 0.741 | 0.573 | -sup- | 1.254 | 1.065 | -sup- | 0.808 | 0.707 | -sup- | -sup- |
| NA_A | II | 0.168 | 0.398 | 1.408 | 1.036 | -sup- | 0.879 | 0.674 | -sup- | 1.425 | 1.242 | -sup- | 0.959 | 0.839 | -sup- | -sup- |
| RM_A | III | 0.121 | 0.319 | -sup- | 1.307 | -sup- | 1.214 | 0.938 | -sup- | -sup- | 1.619 | -sup- | 1.321 | 1.158 | -sup- | -sup- |
| CL_C | III | 0.109 | 0.283 | -sup- | 1.395 | -sup- | 1.199 | 0.926 | -sup- | -sup- | -sup- | -sup- | 1.299 | 1.146 | -sup- | -sup- |
| MI_C | IV | 0.074 | 0.197 | -sup- | -sup- | -sup- | -sup- | 1.298 | -sup- | -sup- | -sup- | -sup- | -sup- | -sup- | -sup- | -sup- |
| CL_A | III | 0.073 | 0.189 | -sup- | -sup- | -sup- | -sup- | 1.335 | -sup- | -sup- | -sup- | -sup- | -sup- | -sup- | -sup- | -sup- |
| MI_A | IV | 0.049 | 0.131 | -sup- | -sup- | -sup- | -sup- | -sup- | -sup- | -sup- | -sup- | -sup- | -sup- | -sup- | -sup- | -sup- |

The "F5" building configuration (already designed for the case of unreinforced masonry) was designed as a two-story reinforced clay masonry building (Figure 2.2.14). For the adopted design choices and for the analysis of the applied loads, the reader is referred to section 2.1.3.1 whereas the selected modelling options are reported in section 2.2.3.1.
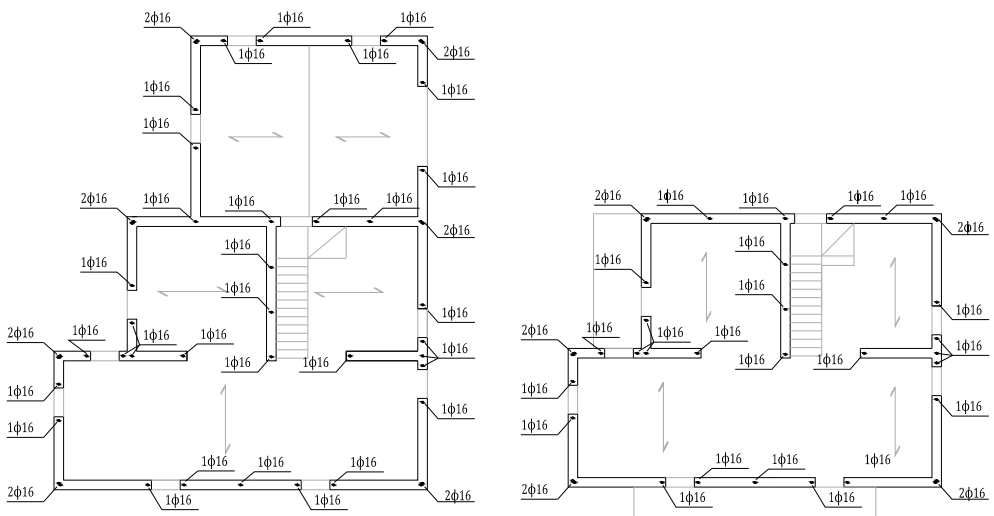


Figure 2.2.14 Design of reinforced masonry buildings: plan views with vertical reinforcement at the two floor levels of the "F5" configuration.

The assumptions on the mechanical characteristic of masonry elements were the same of other "F" type configurations: M10 mortar, B450C steel for reinforcement. Vertical reinforcement was placed according to NTC08 prescriptions (Figure 2.2.14) with a bar diameter of 16mm; horizontal reinforcement was placed every 3 bed-joints (spacing of 600mm) with a bar diameter of 5mm.

The design according to NLSA was carried out with the software ANDILWall, using an equivalent frame modelling of the buildings with the following assumptions:
- fully coupled orthogonal walls, by means of infinitely rigid links at the floor level, connecting the end nodes of the elements;
- diaphragms infinitely rigid in their plane;
- longitudinal bars at the walls' intersections assigned to each of the incident masonry piers.

The design of building resulted in a high value of $\alpha$ (>14), even with the minimum reinforcement quantity indicated by the code. In all the sites, buildings resulted to comply with the code requirements (Table 2.2.26).

Table 2.2.26. Results of the analyses performed on the defined F5 configuration. The results are expressed in terms of safety factors associated to each analysis.

| | Building with a safety factor slightly higher than 1 | | | Oversized building (safety factor higher than 1.5) | | | Building not verified | | |
|---|---|---|---|---|---|---|---|---|---|---|
| **CONFIGURATIONS** | **DESIGN SITES AND SOILS** | | | | | | | | | |
| | **AQ_C** | **AQ_A** | **NA_C** | **RM_C** | **NA_A** | **RM_A** | **CLT_C** | **MI_C** | **CLT_A** | **MI_A** |
| $a_gS$ [g] | 0.347 | 0.261 | 0.245 | 0.182 | 0.168 | 0.121 | 0.109 | 0.074 | 0.073 | 0.049 |
| $a_gsF_0$ [g] | 0.820 | 0.616 | 0.582 | 0.479 | 0.398 | 0.319 | 0.283 | 0.19 | 0.189 | 0.131 |
| **F5_2P_NL_T_RM** | 14.39 | 15.68 | 20.09 | 23.78 | 23.95 | 28.79 | 45.40 | 56.39 | 58.27 | 67.74 |

Figure 2.2.15 shows, as an example, the capacity curve obtained from the considered analyses for the F5 configuration.
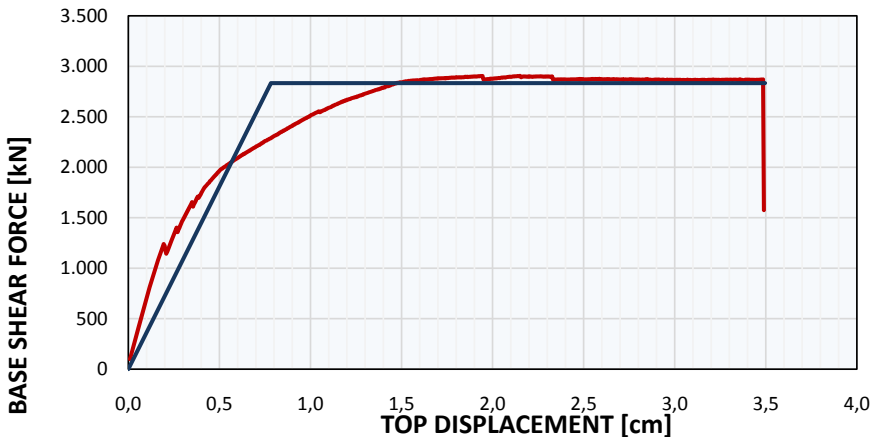


Figure 2.2.15 Examples of the capacity curve obtained from NLSA of F5 configuration.

From this preliminary design, it can be concluded that the use of reinforced masonry increases significantly both displacement and strength capacity of the building. Thus, to reach a global safety factor close to 1, it would be necessary to completely redesign the configuration.

## 2.3   Modelling issues and strategies

### 2.3.1   Description of the constitutive laws adopted for masonry elements

Since the main purpose of the project is to assess the "structural collapse" in the most reliable way permissible by current state-of-the-art research knowledge, passing from NLSA to Non-Linear Dynamic Analyses (NLDA), more refined constitutive laws were adopted in the simulations:

- stiffness and strength degradation more reliable in describing the actual response of masonry panels composed by hollow clay blocks and cement mortar;
- cyclic hysteretic behavior able to capture the differences in the various failure modes that may occur (rocking, diagonal cracking, sliding and mixed, when possible) and in the response of piers and spandrels to the highest possible degree of accuracy.

This required a review of the experimental data available in the literature for such masonry type, in order to calibrate the constitutive laws and in particular drift limits and strength degradation. Table 2.3.1 summarizes the median values that served as the basis for the calibration of the adopted constitutive laws; all of which refer to piers' response. Experimental tests on spandrels composed by modern blocks are indeed too limited to permit meaningful statistical evaluations. Usually, experimental tests refer to the attainment of 20% loss in peak strength as "ultimate state". However, in some cases, tests were performed going even further in order to provide information on a more severe damage state, called "near collapse" in the table. The table reports values for the case of either shear or flexural failure modes. In case of mixed failure modes experimental tests suggest the adoption of intermediate drift limits.

Finally, for the case of spandrels, the limited availability of experimental tests and the consequent increased uncertainty in the definition of their drift limits does not affect the performed analyses in a relevant way, since the contribution provided by reinforced concrete beams in coupling piers was dominant in the analyzed buildings. Moreover, differently from existing buildings, the interaction with RC elements promotes the "strong spandrels" behavior, with nonlinearity mainly concentrated in piers.

Table 2.3.1 Data obtained from available experimental tests adopted as a reference for the calibration.

| Drift limits obtained for hollow bricks and cement mortar masonry piers | | | |
|---|---|---|---|
| Shear failure mode [*] | | Flexural failure mode [**] | |
| 20% peak strength loss | "near collapse" | 20% peak strength loss | "near collapse" |
| 0.24% | 0.54% | 1.22% | 1.6% |

[*] *Magenes et al. (2008), Morandi et al. (2015, 2016)*
[**] *Such values come from statistical processing of data available in Petry and Beyer (2014). Indeed, the collapse condition was not available and thus conventionally assumed as 4/3 of the displacement capacity at 20% peak strength loss as proposed in EC8-3 (2005) passing from SD to NC limit state (§C.4.2.2.)*

More details on the adopted constitutive laws are described in the following. In particular, two different approaches were used to model masonry panels: one approach based on a phenomenological nonlinear beam in the case of the Genoa RU and the other approach based on the macroelement mechanical model in the case of the Pavia RU. Both are implemented in the TREMURI program (Lagomarsino et al. 2013) adopted for performing NLDA.

2.3.1.1 Nonlinear beam with piecewise-linear force-deformation relationship

According to this model (Cattari and Lagomarsino, 2013), masonry panels are modelled as nonlinear beam elements with lumped inelasticity idealization and a piecewise-linear behavior. The constitutive law allows to consider the nonlinear response until very severe damage levels

(from 1 to 5) through progressive strength degradation in correspondence of assigned values of drift (see Figure 2.3.1a that also clarifies the damage legend). Moreover, a hysteretic response (Figure 2.3.1b) is also formulated, through a phenomenological approach, in order to capture the differences among the various possible failure modes (of prevalently flexural type, shear type or even mixed) and the different response of piers and spandrels.
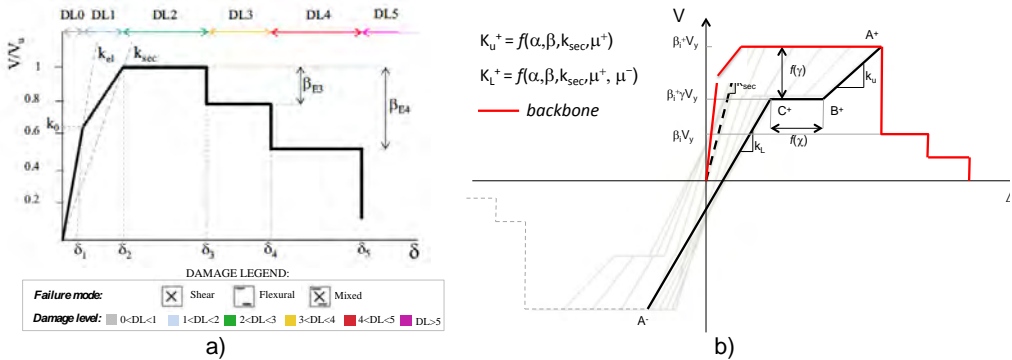


Figure 2.3.1 Piecewise linear constitutive law in TREMURI (a) and hysteretic response (b).

The parameters required to completely define these laws may be grouped in two sets (as summarized in Table 2.3.2): the first one serves to describe the backbone, while the second one defines the hysteretic response. Regarding the first set of parameters, the principal ones may be grouped in: those used to define the initial stiffness of the panel and its progressive degradation (computed in an approximate way starting from the secant stiffness and by assigning two coefficients $k_r$ and $k_0$); those used to define the maximum strength of the panel ($V_u$); those used to describe the progressing of nonlinear response for increasing damage levels ($\delta_{Ei}$, $\beta_{Ei}$). The maximum strength of the panel ($V_u$) is computed according to some simplified criteria that are consistent with those most commonly proposed, in both the literature and codes, for the prediction of masonry panel strength as a function of different failure modes (flexural or shear). The final $V_u$ value is computed as the minimum between the prediction provided by the strength domains associated to the failure criteria considered on the basis of the current axial stress acting on the element; in this way, the current prevailing behavior ruling the hysteretic response of the element is also determined. Different values of $\theta_{E,i}$ and $\beta_{E,i}$ may be defined for describing the prevailing flexural or shear response of the panel. Moreover, they may be differentiated in case of spandrel and pier elements as well. In the case of a mixed failure mode, average values for $\theta_{E,i}$ and $\beta_{E,i}$ are computed by the program starting from those assigned in the case of a prevailing flexural or shear response (as defined by a user). The occurrence of a mixed mode is established by assigning in the input of the panel a given admissible range in the $V - N$ domain (close to the points in which the flexural and shear domains intersect with one another). Figure 2.3.2 clarifies the criterion adopted to define the occurrence of a mixed failure mode.

Table 2.3.2 Summary of parameters that define the piecewise-linear constitutive laws.

| | | |
|---|---|---|
| **Backbone** | **Initial stiffness and its degradation** | **E** Young modulus; **G** shear modulus; **η** stiffness reduction coefficient; geometry of the panel (**l, h, t**: length, height and thickness of the panel); **$k_r$** ratio between the initial $k_{el}$ and secant $k_{sec}$ stiffness at the point in which the maximum strength is reached; **$k_0$** ratio between the shear at the end of the elastic phase and the shear strength |
| | **Maximum strength $V_u$** | **Strength material parameters** aimed at describing the flexural and shear strength domain. They vary as a function of the criteria adopted for the examined masonry ($f_m$, $τ_0$ (or $c$ and $μ$), $f_{bt}$ etc.) **$w_1$** and **$w_2$** aimed at defining the admissible range of mixed failure mode |
| | **Degradation for increasing DLi** | drift $δ_{E,i}$ and percentages of strength reduction $β_{E,i}$ corresponding to DLi (with $i$=3,4,5) *they have to be defined for the two failure modes (flexural and shear)* |
| **Hysteretic response** | | $α$ and $β$ aimed at defining $K_u$ $γ$: aimed at defining the extension of branch A⁺B⁺ $χ$: aimed at defining the extension of branch C⁺B⁺ *they have to be defined for the two failure modes (flexural and shear)* |

The second set of parameters describing the hysteretic response refers to the slope of unloading and loading branches of the hysteresis loops. In particular, the unloading branch from A+ to C+ is ruled by the stiffness $K_u$ (Figure 2.3.1b). It is computed as indicated in the equation 2.2 (for example in the case of a positive quadrant):

(2.2)

$$K_u^+ = K_{sec} \left(μ^+\right)^α \left[1 - ζ\left(1 - β_i^+\right)\right]$$

where: $μ^+$ is the maximum value of ductility reached in the backbone of positive quadrant; $α$ is a parameter aimed to degrade the value of $K_u$ with respect to the secant stiffness $K_{sec}$ (the values from 0 - elasto-plastic law- to 1 -secant stiffness may be assumed); $ζ$ aims to further degrade the value of $K_u$ by taking into account the progressing strength decay reached on the backbone, described by the maximum damage level the structure reached, which corresponds to a specific value of strength decay $β_E$ (it may assume values from 0 to 1). An analogous expression may be defined for the negative quadrant.

After a first branch (A+ B+) ruled by $K_u$, the unloading branch may also exhibit a horizontal branch (B+ C+) where: the point B⁺ is determined by the $γ$ coefficient that varies from 0 (A⁺ B⁺ branch until the abscissa axis) to 1 (elastic nonlinear condition). The extension of B⁺ C⁺ is determined by the $χ$ coefficient: although it may vary from 0 to ∞, the suggested values range from 0 to 1. Finally, the loading branch from C+ to A- is ruled by the stiffness $K_L$. It is computed by taking into account $K_u$ and the maximum ductility value reached in both positive and negative quadrant ($μ$+,$μ$-).
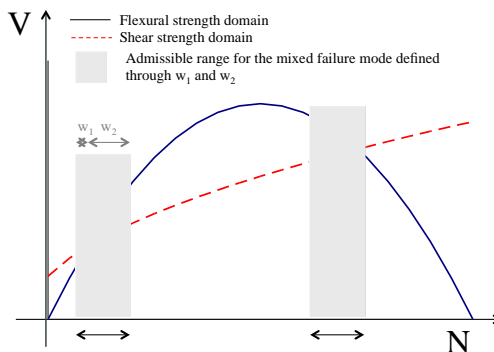


Figure 2.3.2 Schematic representation of the criteria assumed to define the occurrence of a mixed failure.

Table 2.3.3 summarizes the parameters adopted in NLDA. It is possible to observe how the drift limits of piers at damage levels 3 and 4 correspond to those calibrated on the basis of the experimental tests available in the literature. In particular, for shear failure, a larger strength degradation is assumed for the first drift limit (40% instead of 20%) and a very limited residual strength (20%) was maintained until DL5 (actual collapse), conventionally assumed for the drift of 0.7%. In the case of flexural failure, the drop down of 20% is considered as DL4, because for this mechanism the strength degradation occurs quite close to the actual collapse (DL5).

Table 2.3.3 Parameters adopted for piers and spandrels in case of piecewise linear constitutive laws.

| Pier | SHEAR | | | | FLEXURAL | | | |
|------|-------|---|---|---|----------|---|---|---|
| | | | Hysteretic response | | | | Hysteretic response | |
| | Drift [%] | Residual Strength | α | 0.8 | Drift [%] | Residual Strength | α | 0.9 |
| DL3 | 0.24 | 0.6 | β | 0.8 | 0.6 | 1 | β | 0.8 |
| DL4 | 0.54 | 0.2 | γ | 0 | 1.22 | 0.85 | γ | 0.6 |
| DL5 | 0.7 | 0 | | | 1.6 | 0 | χ | 0.5 |

| Spandrel | SHEAR | | | | FLEXURAL | | | |
|----------|-------|---|---|---|----------|---|---|---|
| | | | Hysteretic response | | | | Hysteretic response | |
| | Drift [%] | Residual Strength | α | 0.2 | Drift [%] | Residual Strength | α | 0.2 |
| DL3 | 0 | 0.7 | β | 0 | 0.6 | 1 | β | 0 |
| DL4 | 0.4 | 0.7 | γ | 0.3 | 0.8 | 0.7 | γ | 0.3 |
| DL5 | 0.7 | 0 | | | 1.2 | 0 | χ | 0.8 |



| Geometry of the panels | | | | |
|------------------------|-------|-------|-------|--------------|
| | b [m] | h [m] | t [m] | Bound. Cond. |
| P_01 | 2.5 | 2.6 | 0.3 | Double fixed |
| P_02 | 3 | 2.6 | 0.3 | Double fixed |
| P_03 | 3.5 | 2.6 | 0.3 | Double fixed |

Figure 2.3.3 Example of the cyclic response simulated with the piecewise linear constitutive laws.

Figure 2.3.3 shows the resulting hysteretic responses for three single panels with fixed-fixed boundary conditions subjected to a compressive state equal to 7% of the masonry compressive strength; they are characterized by the same masonry but three different slenderness ratios, such as to induce three different failure modes (flexural, shear or mixed one). These hysteretic responses clarify those simulated in the NLDA.

### 2.3.1.2  Macroelement mechanical model

The adopted equivalent-frame modelling strategy implemented in the TREMURI program (Lagomarsino et al., 2013) is based on the effective nonlinear macroelement modelling approach.

The macroelement model represents the cyclic nonlinear behavior associated with the two main in-plane masonry failure modes, bending-rocking and shear mechanisms, with a limited number of degrees of freedom (8) and internal variables which describe the damage evolution (Penna et al., 2014). The two-node mechanics-based macroelement, suitable for modelling piers and spandrel beams, can be ideally subdivided into three parts (Figure 2.3.4): a central body where only shear deformation can occur and two interfaces where the external degrees of freedom are placed, the latter being able to exhibit relative axial displacements and rotations with respect to those of the extremities of the central body. In the two interfaces, infinitely rigid in shear, the axial deformations are due to a distributed system of zero-length springs with no-tension and limited compression behavior.

Involving a nonlinear shear stress–strain cyclic relation derived by the macroscopic integration of the Gambarotta and Lagomarsino (1996) continuum model for masonry, the macroelement formulation can represent both the cyclic shear and flexural response of masonry panels. The nonlinear description of the coupled relation between the flexural and axial degrees of freedom allows the explicit evaluation of how cracking affects the rocking motion. The macroelement model includes a nonlinear degrading model for rocking damage, which accounts for the effect of limited compressive (i.e., toe-crushing) strength.
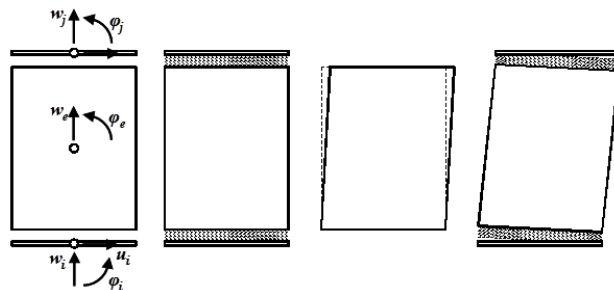


Figure 2.3.4 Kinematics of the macro-element model (Lagomarsino et al., 2013).

In addition to geometrical characteristics, the macroelement model is defined by eight parameters representative of an average behavior of the masonry panel: density $\rho$, elastic modulus in compression $E$, shear modulus $G$, compressive strength $f_m$, shear strength (i.e., cohesion) $c_{eff}$, global equivalent friction coefficient $\mu_{eff}$, and two coefficients $\beta$ and $c_t$. The parameter $\beta$ governs the slope of the softening branch of the nonlinear shear model, whereas the parameter $c_t$ signifies non-dimensional shear deformability. Depending on the macroscopic cohesive behavior, the amplitude of the inelastic displacement component in the displacement–shear relationship is proportional to the product $Gc_t$ (Figure 2.3.5).
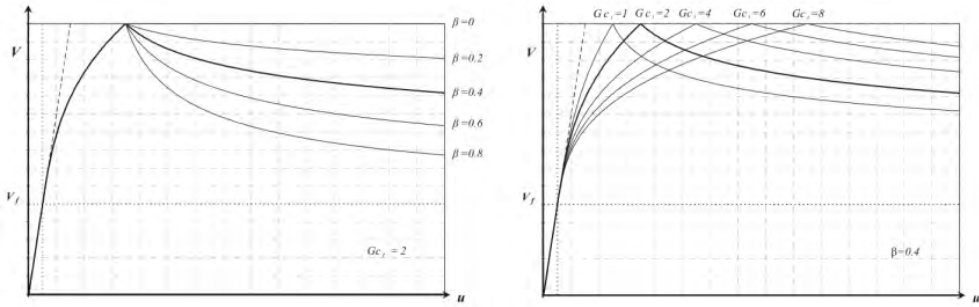
Figure 2.3.5 Roles of parameters $\beta$ (left) and $c_t$ (right) on the shape of the nonlinear shear model (Penna et al., 2014).

Due to the concentration of the axial and flexural deformations in the interfaces, the spring stiffness equal to $k = 2E'/h$, where $E'$ is an effective elastic modulus and $h$ is the element length (height in case of pier elements), is defined differently, depending on whether axial or lateral stiffness needs to be more accurately reproduced ($E' = 1 \div 3E$ depending on the boundary conditions). The macroscopic shear model is based on a combination of equivalent cohesion, $\bar{c}$, and friction, $\bar{\mu}$, parameters. The determination of the model parameters from the "local" mechanical parameters derives from characterization tests and depends on the governing shear failure mode.

The parameters of the masonry type used in the numerical models for dynamic analyses were calibrated to be representative of typical unreinforced masonry with perforated clay blocks. The parameters were compared with some literature experimental data, many of which derived from tests on masonry piers carried out at the Eucentre laboratory (Magenes et al., 2008, Figure 2.3.6).

For the analysis of entire buildings, with boundary conditions intermediate between cantilever and double-fixed, the Young modulus was taken equal to $E' = 2E = 9320$ MPa. The shear modulus $G$ was taken equal to $G' = G/1.2 = 1553$ MPa.

Regarding the shear strength model parameters, the criterion reported in Eurocode 6 was considered:

$$V_{res} = l't f_v \qquad\qquad (2.3)$$

with $f_v = f_{vmo} + \mu \frac{N}{l't} \leq 0.065 f_b$.
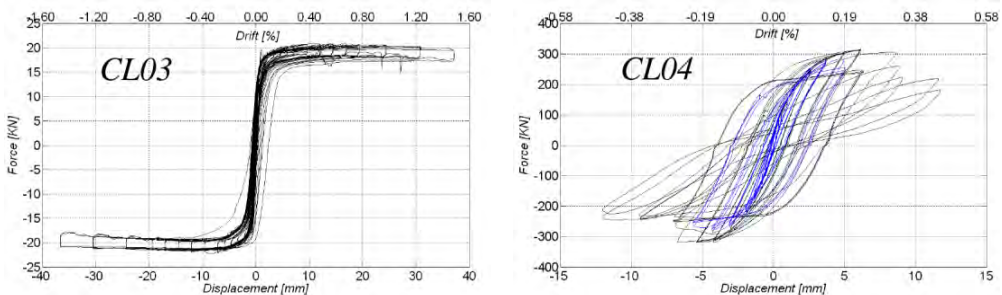


Figure 2.3.6 Flexural (left) and shear (right) response of clay-block masonry piers subject to in-plane cyclic shear-compression tests (after Magenes et al., 2008).

If for example a 3 m x 2.6 m x 0.3 m ($l$ x $h$ x $t$) wall is considered, the obtained interaction diagrams, which were calculated using the two hypotheses $f_v = f_{vmo} + \mu \frac{N}{l't} \; or \; f_v = 0.065 f_b$, are reported in Figure 2.3.7. It can be noted that the second hypothesis (second criterion) provides the lower value of strength, consistently with the typical observation of shear cracks crossing the blocks.
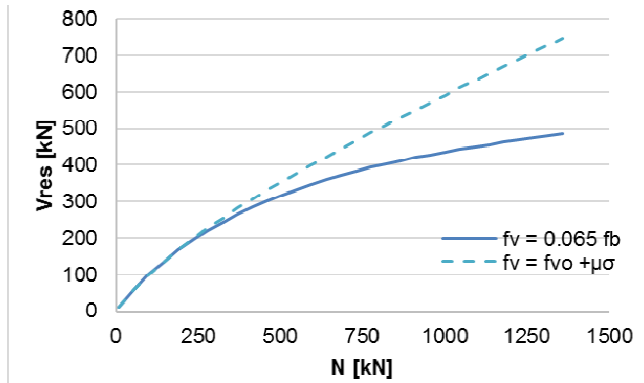


Figure 2.3.7 Interaction diagrams for shear failure according to the criteria of EC6, for a double-fixed 3m x 2.6m x 0.3m wall.

The values of shear strength obtained using the second criterion, for double-fixed walls characterized by the height of 2.6 m, the thickness of 0.3 m, with the applied compression level of 0.5 MPa and different values of length, are reported in Table 2.3.4.

Table 2.3.4 Values of shear strength obtained with the second criterion.

| $l$ [m] | 1.25 | 2.0 | 2.5 | 3.0 | 3.5 |
|---|---|---|---|---|---|
| $V_{res}$ [kN] | 70.1 | 157.0 | 226.3 | 302.4 | 384.0 |

The strength parameters of the macroelement shear model, $c_{eff}$ and $\mu_{eff}$, were thus calibrated by minimizing the difference between the strength exhibited according to the selected criterion and the shear strength of the macroelement. The following set of two parameters provides a good approximation of the strength for walls of length between 2.5 and 3.5 m (maximum error around 10%), whereas for slender walls, the approximation is larger, with an overestimation of the shear strength, which however is not significantly affecting the wall strength, as it is governed by flexural failure modes.

- $c_{eff}$ = 0.375 MPa
- $\mu_{eff}$ = 0.125

The other parameters of the shear model (nonlinear deformation before the peak $Gc_t$ and slope of the softening branch $\beta$) were calibrated to derive a cyclic behavior as close as possible to that observed during experimental tests on modern clay block masonry:

- $Gc_t$ = 5
- $\beta$ = 0.6

An example of the cyclic shear behavior of a 3 m x 2.6 m x 0.3 m wall is shown in Figure 2.3.8.
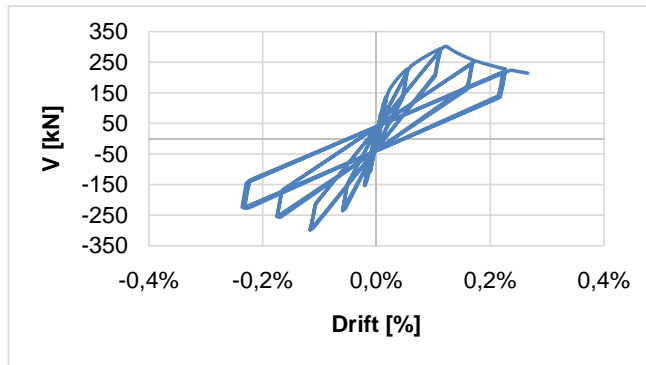
Figure 2.3.8 Base-shear-drift cycles for a 3m long wall.

The combined effect of flexural and shear failure modes in the building piers generally provides realistic global hysteretic curves for the building models subjected to time history analyses (Figure 2.3.9).
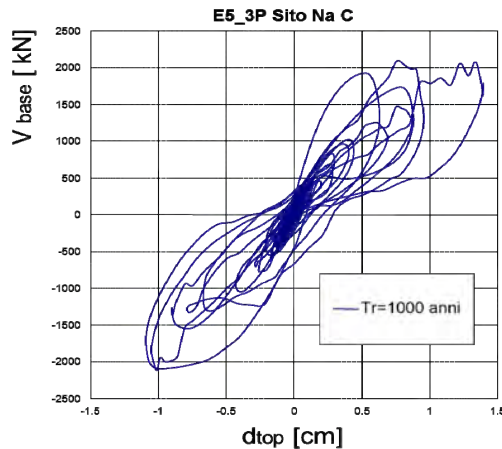


Figure 2.3.9 Example of hysteretic base-shear-top displacement curve for building E5 (3 stories).

*Improved macroelement mechanical model*

An improved version of the macroelement model described in the previous section was also used. With respect to the macroelement proposed by Penna et al. (2014), the improved macroelement is characterized by:

1) a different constitutive law governing the axial behavior of the springs located at the top and bottom interfaces of the macroelement: in particular, the unloading branch is assumed parallel to the elastic branch and it does not correspond anymore to the secant branch;
2) the possibility of automatically reproducing the flexural stiffness of each element with the variation of boundary conditions;
3) the possibility of considering more than one shear failure mechanism at each step of the analysis;
4) the automatic calibration of the shear strength equivalent parameters $c_{eff}$ and $\mu_{eff}$ to be used in the shear damage model;

5) the possibility of calibrating the shear deformability parameter $G'c_t$ in order to insure that, for each element, the peak shear strength is attained at a fixed level of drift.

In order to guarantee the consistency of the results with the ones obtained by the University of Genoa, the shear strength criteria for sliding along the whole cross section and for tensile failure of the bricks were adopted (Mann and Muller, 1982). However, the reduction of the strength by means of the factor $(1 + α_v)$, proposed by Magenes and Calvi (1997), was not applied.

The shear deformability parameter $G'c_t$ was calculated at each step of the analysis and for each element, in order to guarantee that the peak shear strength is reached at a drift equal to the mid-point of the constant shear branch of the tri-linear element used by the University of Genoa.

The automatic calibration of $G'c_t$ was checked by means of cyclic analyses performed on four panels, characterized by different slenderness ratios and failure mechanisms. In particular, all the panels had the same material, with $E$ = 4660 MPa, $G$ = 1854 MPa, $ρ$ = 900 kg/m$^3$, $f_m$ = 6.66MPa, $c$ = 0.29 MPa, $μ$ = 0.4, $f_{bt}$ = 1.143 MPa, $tanθ$ = 0 (i.e., no correction of Mann and Muller, 1982) and were characterized by double-fixed boundary conditions. The parameters varying from panel to panel are reported in Table 2.3.5. Panels named (a), (b) and (c) are squat walls, whereas panel (d) is a slender wall. The geometric parameters and axial loads ($N_0$ in Table 2.3.5) were selected in order to have pure shear failure in panel (a), hybrid mechanism in panel (b) and flexural failure in panels (c) and (d).

Table 2.3.5 Parameters of the four considered panels.

| Panel | l [m] | h [m] | t [m] | $N_0$ [kN] |
|---|---|---|---|---|
| (a) Squat - Shear | 3.55 | 2.726 | 0.25 | 571.0 |
| (b) Squat - Hybrid | 3.55 | 2.726 | 0.25 | 380.6 |
| (c) Squat - Flexure | 3.55 | 2.726 | 0.25 | 285.4 |
| (d) Slender - Flexure | 1.40 | 1.750 | 0.30 | 180.1 |

The calibration of $G'ct$ was performed automatically, whereas the values of $β$ were assumed equal to 0.9 in all the cases, in order to match the softening branch of the tri-linear model. In particular, this value of $β$ allows the softening branch of the macroelement model to pass from the 80% of the peak shear strength at a value of drift where the first strength decay of the tri-linear model is present. Incremental static analyses in displacement control were performed and the results in terms of base-shear vs. drift are shown in Figure 2.3.10. The fact that the strength decay of the new macroelement is overestimated in the case of panel (b) is related to the necessity of selecting a single value of $β$ for all the panels: in particular, it was decided to use a value leading to the best representation of the strength decay in the case of a pure shear failure, instead of a hybrid mechanism. The improved macroelement is implemented in TREMURI and it was applied only for the piers, whereas for the spandrels the tri-linear element proposed by the University of Genoa was used.

(a)                                                                         (b)



(c)                                                                         (d)
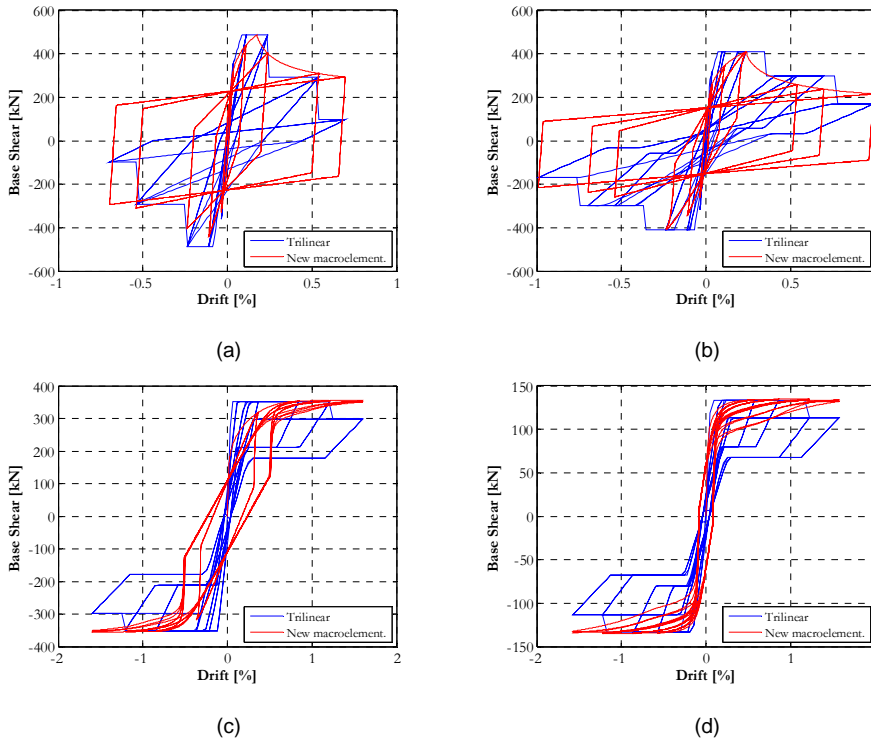
Figure 2.3.10 Base-shear vs. drift curves of the four considered panels: squat panel with shear failure (a), squat panel with hybrid failure (b), squat panel with flexural failure (c) and slender panel with flexural failure (d).

## 2.4   Assessment, results, and discussion

### 2.4.1   Definition of the collapse condition

The collapse prevention limit state was primarily defined through checks on the attainment of given thresholds of a selected Engineering Demand Parameter (EDP). The latter was chosen as the maximum inter-story drift ($\theta_{max}$) assessed at single-wall scale, that is as $\theta_{max}=max(\theta_{w,l})$ where *w* and *l* refer to the wall number and level number, respectively. It was computed by accounting for the contribution of both horizontal displacement and rotation, even though the latter had a limited role in the examined structures. Considering the different behavior of the buildings in the two directions, the maximum inter-story drift was evaluated separately for each direction ($\theta_{max,X}$ and $\theta_{max,Y}$).

The selection of such EDP is motivated by the following main reasons:

- the presence of reinforced concrete ring beams leads to a seismic behavior dominated by the concentration of nonlinearity in the piers, with very limited damage to the spandrels. Moreover, ring beams ensure good coupling among piers, that usually work together;
- the presence of rigid diaphragms – in addition to RC ring beams -  promotes a box behavior in which a soft story failure mode is expected.

Both these conditions render checks performed on single structural elements (piers) less significant for the identification of global failure modes. On the contrary, global failure modes may be identified in a robust manner with direct reference to the inter-story drift. Considering the

maximum value among all the walls – instead of an average value at the floor level – also allows to identify local concentration of damage induced, for example, by torsional effects.

The reference thresholds of $\theta_{max}$ was defined as follows:

- since the analyzed buildings present a different behavior in the X and Y directions, two different thresholds - one for each direction - have to be defined ($\theta_{C,X}$ and $\theta_{C,Y}$);
- for each one, a first reference range was established through the execution of NLSA by considering, for X and Y directions, two load patterns (namely proportional to masses and inverted triangular) and both positive and negative directions. In particular, for each one, the value of maximum inter-story drift corresponding to a 50% overall base-shear degradation was identified. By varying the load pattern and the configuration examined (e.g., as a function of the number of stories) such a value may differ significantly, due to the activation of different failure modes (e.g., with a prevailing shear or flexural response).
- within this range, the final reference threshold in each direction was defined as the minimum value between those obtained from the four analyses (that is uniform or triangular distribution, positive or negative directions), also making comparisons with the results of NLDA. Such comparisons are, in fact, essential for several reasons: (i) in order to check if the load pattern associated to the selected threshold is reliable in defining the ultimate displacement capacity consistently with the actual dynamic behavior; (ii) in order to assess possible reduction of such displacement capacity due to torsional effects, which are more pronounced in the NLDA, or due the cyclic degradation.
- in the cases where the displacement capacity obtained from the NLDA was lower than that obtained from the NLSA, in order to take into account this effect it has been decided to choose as the reference threshold the value of maximum inter-story drift corresponding to an overall base-shear degradation equal to 35% instead of 50% and then follow the same rationale as before (already used for defining the specific values of the thresholds in each direction).

The aforementioned procedure led to the definition of the two specific thresholds ($\theta_{C,X}$ and $\theta_{C,Y}$) for each one of the examined structures. Then, the collapse limit state function $Y_C=\max(\theta_{max,X}/\theta_{C,X}\;;\;\theta_{max,Y}/\theta_{C,Y})$ is evaluated, being equal to 1 at the attainment of collapse.

In addition to the checks of the EDP thresholds, the adopted constitutive laws – which are quite efficient and robust in converging, even for very high levels of nonlinearity - allow to identify the condition associated with dynamic instability. The latter was identified to correspond to a strongly pronounced overall base-shear degradation, conventionally assumed equal to 90% of the maximum shear. Such a condition corresponds to the so-called "certain collapse".

Figure 2.4.1 shows an example of comparison between time history analysis results and pushover analyses performed with different load patterns.
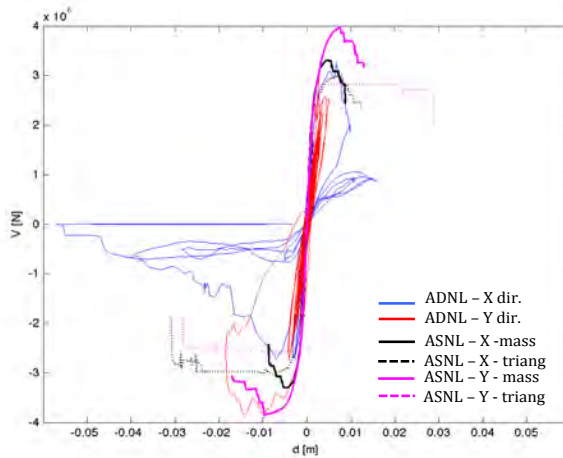
Figure 2.4.1 Comparison between NLSA and NLDA to identify the EDP threshold.

### 2.4.2    Definition of the Damage Limit State

The attainment of the damage limit state (DLS) was carried out according to the multi-criteria approach described in Appendix A proposed by the working group consisting of the various RUs involved in the RINTC project.

In particular, it was defined by monitoring the attainment of given thresholds of the selected EDP, which is, as mentioned previously, the maximum inter-story drift ($\theta_{max}$) assessed at single-wall scale. As for the collapse, the reference thresholds of $\theta_{max}$ for the damage limit state was defined separately for the X and the Y directions ($\theta_{D,X}$ and $\theta_{D,Y}$), for each configuration.

In order to define these thresholds, NSA was performed by considering, for X and Y directions, only the inverted triangular load pattern and both positive and negative directions. Then, the attainment of the first among the three criteria listed below was identified on the obtained pushover curves (Figure 2.4.2):

A. The 50% of the masonry piers (in terms of resistant area) has reached the condition of light/moderate damage;
B. A masonry pier has reached a severe damage condition (drift threshold corresponding to the DL3, as indicated in Table 2.3.3, in the case of the phenomenological nonlinear beam or attainment of the toe-crushing condition in the case of the macroelement mechanical model);
C. The base-shear has reached the 95% of the peak resistance.

In any case the final threshold should be associated to a value of the base-shear not lower than the 85% of the peak resistance. This lower bound is in particular justified by the fact that URM buildings may show slight but widespread damage even for values of the base-shear far from the peak value.

Regarding the criterion A, in the case of the phenomenological nonlinear beam the condition of light/moderate damage corresponds to the DL2 (peak strength). In the case of the macroelement mechanical model the definition is different, depending on the failure mode:

- for shear failure, the local light/moderate damage is identified by the drift level corresponding to the attainment of the maximum lateral strength of the pier;

- for flexural failure, the local light/moderate damage condition is associated with the attainment of the partialization at one of the end sections of the pier.

For each examined building, this procedure led to the definition of two specific thresholds ($\theta_{D,X}$ and $\theta_{D,Y}$), as the minimum between the positive and negative direction. Then, the damage limit state function $Y_D = \max(\theta_{max,X}/\theta_{D,X};\ \theta_{max,Y}/\theta_{D,Y})$ is evaluated, being equal to 1 at the attainment of the damage limit state.
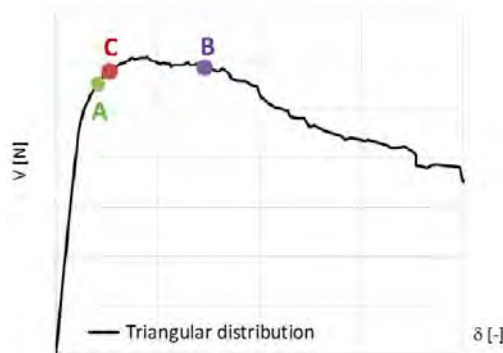


Figure 2.4.2 Shear base-maximum drift curve (black) and identification of the three criteria for the definition of the damage limit state.

### 2.4.3    Results of the "C" and "I" type configurations

The final values of the EDP thresholds used for each configuration to determine the attainment of damage and collapse limit states are provided in Table 2.4.1.

Table 2.4.1. Values of EDP thresholds for each "C" and "I" configuration.

| Configuration | Regularity | Stories | EDP threshold [%] | | | |
|:---:|:---:|:---:|:---:|:---:|:---:|:---:|
| | | | $\theta_{D,X}$ | $\theta_{D,Y}$ | $\theta_{C,X}$ | $\theta_{C,Y}$ |
| C1 | REG. | 3 | 0.0411 | 0.0299 | 0.78 | 1.22 |
| C2 | REG. | 3 | 0.0373 | 0.0273 | 0.77 | 1.19 |
| C3 | REG. | 3 | 0.0338 | 0.0223 | 0.63 | 1.03 |
| C4 | REG. | 3 | 0.0344 | 0.0214 | 0.63 | 0.98 |
| C5 | REG. | 3 | 0.0295 | 0.0196 | 0.63 | 1.16 |
| C6 | REG. | 3 | 0.0298 | 0.0189 | 0.68 | 0.91 |
| C1 | REG. | 2 | 0.0313 | 0.0187 | 0.88 | 1.16 |
| C2 | REG. | 2 | 0.0301 | 0.0176 | 0.78 | 1.16 |
| C3 | REG. | 2 | 0.0179 | 0.0141 | 0.71 | 1.15 |
| C4 | REG. | 2 | 0.0179 | 0.0141 | 1.08 | 1.15 |
| C7 | REG. | 2 | 0.0154 | 0.0136 | 0.95 | 1.15 |
| I1 | IRREG. | 2 | 0.0265 | 0.0179 | 1.08 | 0.38 |
| I2 | IRREG. | 3 | 0.0247 | 0.0193 | 1.28 | 0.92 |

In almost cases the lower bound associated to the attainment of the 85% of the peak base-shear was the prevailing condition. Indeed, the attainment of criterion A in general corresponded to a rate of the base-shear varying from 65% to 75% of the peak of the pushover curve; in some

cases it occurred very close to the global criterion (criterion C), as for C4 two-story configuration in correspondence of the base-shear ratio equal to 93% of the peak (see Figure 2.4.3).

Figure 2.4.3 shows the attainment of the Damage Limit State and of the Collapse Limit State on the global pushover curves for some selected building configurations. Although in Figure 2.4.3 only the pushover curves resulting for the triangular distribution are illustrated, it is worth highlighting that, as specified in §2.4.1, in the case of the CLS the final interstory drift threshold ($\theta_C$) is computed for each direction considering the worst case between the two load patterns considered.
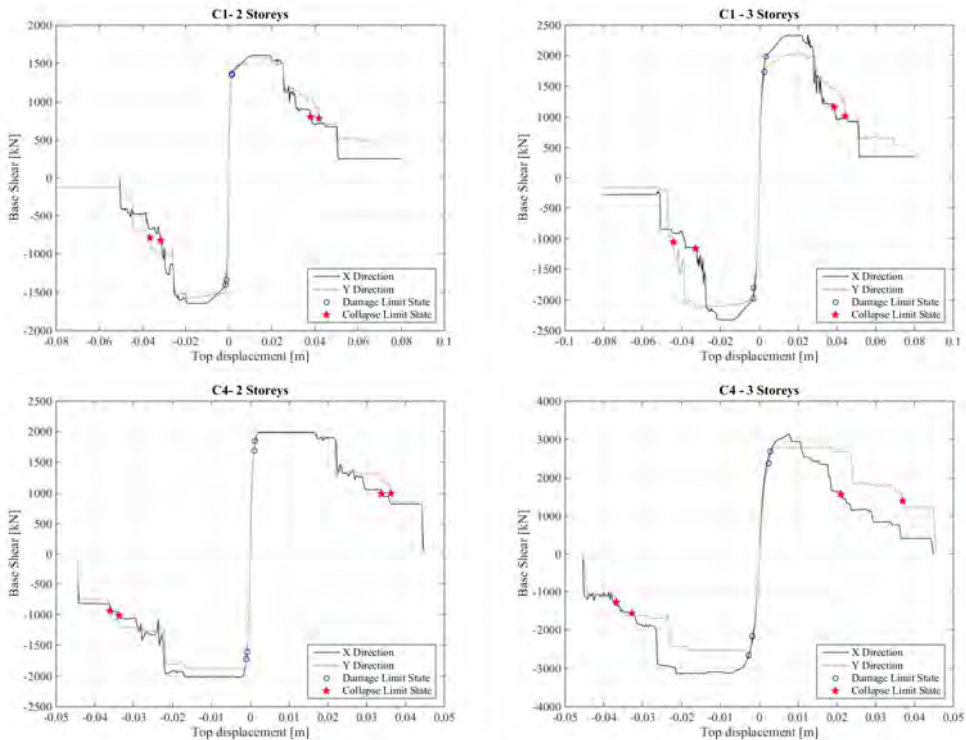


Figure 2.4.3 Pushover curves (triangular distribution) in the two directions of analysis, for 4 selected building configurations, with the identification of the thresholds of DLS (in blue) and CLS (in red).

The dynamic analyses were performed for all the defined configurations by using the MSA. By processing the obtained results, it was possible to represent the overall base-shear-average top displacement curves for each configuration and for each stripe (20 different cycles per stripe for a fixed configuration), both in the X and in the Y directions. In Figure 2.4.4 some of these curves are shown: each graph represents, for a given configuration in a fixed site and for a given direction, the hysteretic curves produced by the time histories of a given stripe, together with the associated pushover curve. For simplicity, only two hysteretic cycles for a fixed stripe was represented: one is the cycle associated to the time history of the fixed stripe that produced the maximum top displacement, while the other is the cycle associated to the time history of the fixed stripe that produced the minimum top displacement.
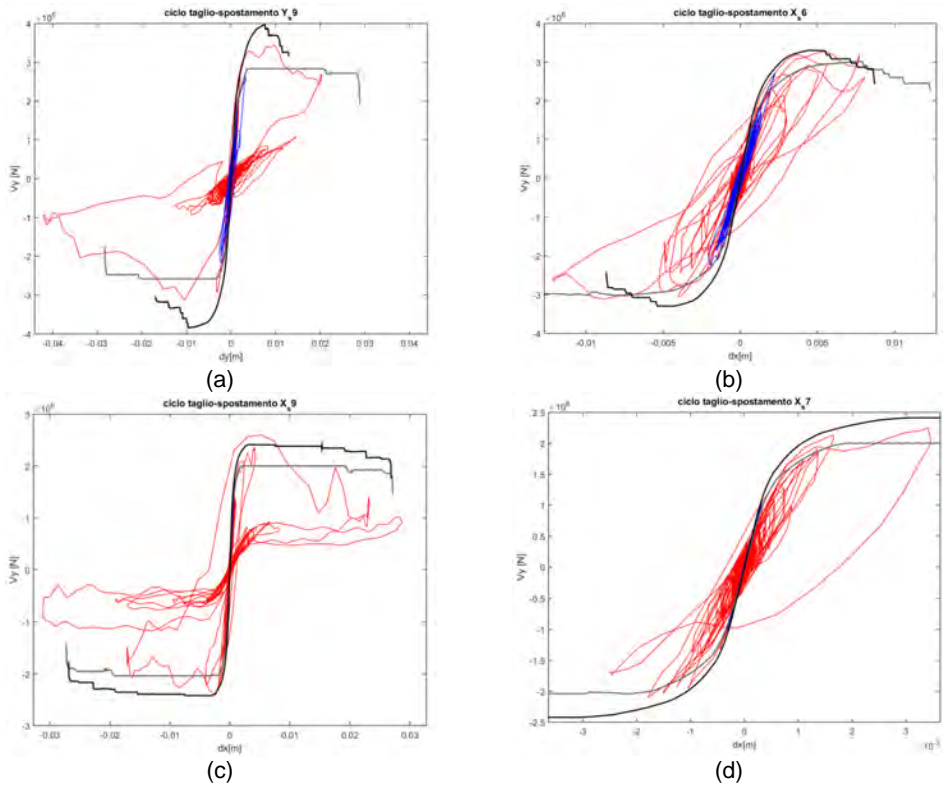
Figure 2.4.4 Hysteretic cycles and related pushover curves for: (a) C3, 3-story, Naples soil type C, Y direction, stripe 9; (b) C3, 3-story, Naples soil C, X direction, stripe 6; (c) C4, 2-story, Naples soil C, X direction, stripe 9; (d) C4, 2-story, Naples soil C, X direction, stripe 7; Red refers to the time history of the stripe producing the maximum top displacement while blue refers to the time history giving the minimum top displacement.

The activation of a dominant soft story mechanism is confirmed by the observation of the damage in the structural elements, as shown in Figure 2.4.5 and Figure 2.4.6, where the damage produced by different time histories of a given stripe in a fixed wall of a given configuration is represented. From these figures it can be seen that, even if the effects of each time history on the building can be different (due to record-to-record variability), in general the damage level in the piers is higher than the damage level reached in the spandrels; furthermore, it can be observed that the soft story collapse mechanism generally occurs at the ground level.
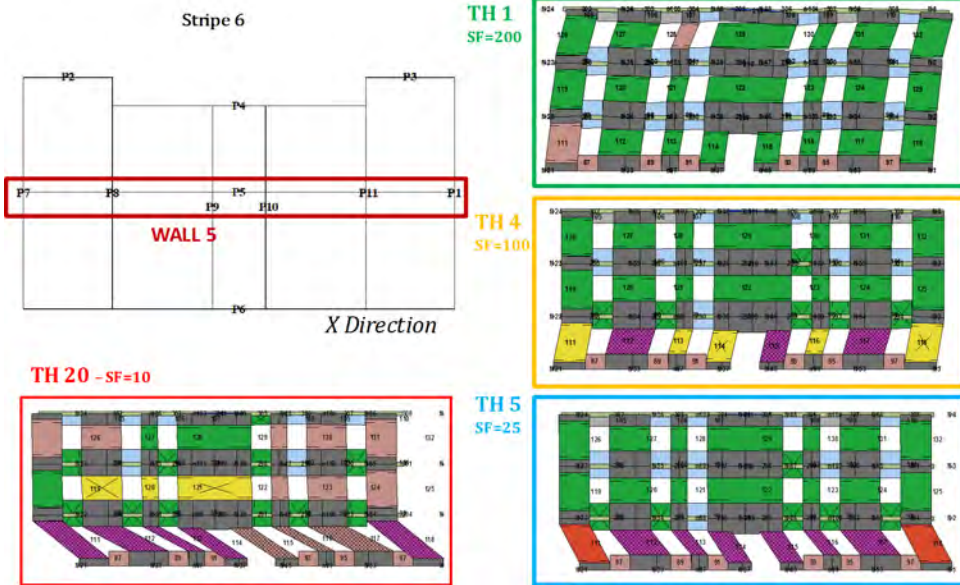
Figure 2.4.5 Damage occurred in a fixed wall (wall 5, X direction) of C1, three-story, located in L'Aquila, soil type A as a consequence of different time histories of the stripe 6. SF = Scaling factor (see Figure 2.3.1a for the damage legend).
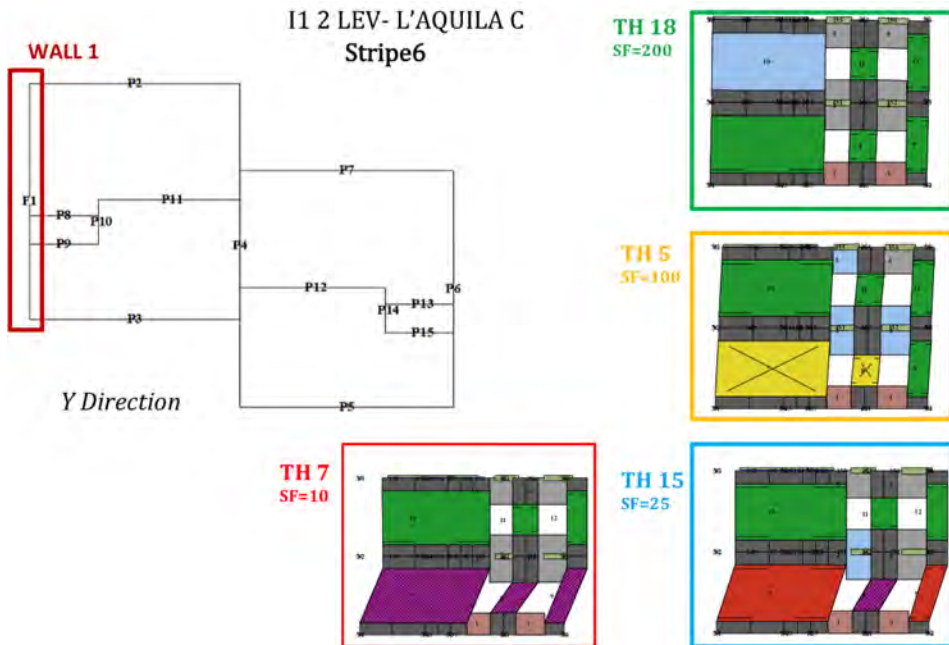


Figure 2.4.6 Damage occurred in a fixed wall (wall 1, Y direction) of I1, two-story, located in L'Aquila, soil type C as a consequence of different time histories related to the stripe 6. SF = Scaling factor (see Figure 2.3.1a for the damage legend).

For each dynamic analysis performed, the maximum inter-story drifts in the X direction ($\theta_{max,X}$) and in the Y direction ($\theta_{max,Y}$) were evaluated, since they were chosen as the EDP representing the structural response. These values were divided for the correspondent threshold related to the collapse condition ($\theta_{C,X}$ $\theta_{C,Y}$) and the damage limit state condition ($\theta_{D,X}$ $\theta_{D,Y}$), respectively, in order to obtain the limit state functions $Y_C$ (collapse limit state) and $Y_D$ (for the damage limit state). In this way it was possible to represent for each "building – site" combination a graph with the values of Y (for both the limit states) obtained from each dynamic analysis. According to the rationale behind the MSA, the results obtained from the analyses in terms of Y, when represented in a IM-Y graph, are aligned in correspondence to the considered IM values, thus forming given stripes.

A lognormal distribution has been assumed for the Y values associated with each stripe, in order to evaluate the median value and also the 16% and 84% percentiles; then, by assuming a linear interpolation between the different stripes, the corresponding "IDA curves" – even if not obtained by scaling time histories - were obtained. In Figure 2.4.7 some "IDA curves" related to different building-site combinations and referring to the collapse limit state are provided, together with the vertical line $Y_C$=1, corresponding to the attainment of the collapse state.  By observing the obtained results it may be said that in the sites where the seismic hazard is high (i.e., L'Aquila and Naples) the collapse limit state is always reached (the "IDA curves" always cross the vertical line of the EDP threshold), while in the sites where the seismic hazard is lower the collapse is reached only for a few time histories belonging to the last stripe (Rome) or, in the case of Milan and Caltanissetta, the collapse is never reached (the "IDA curves" do not cross the vertical line of the EDP threshold).
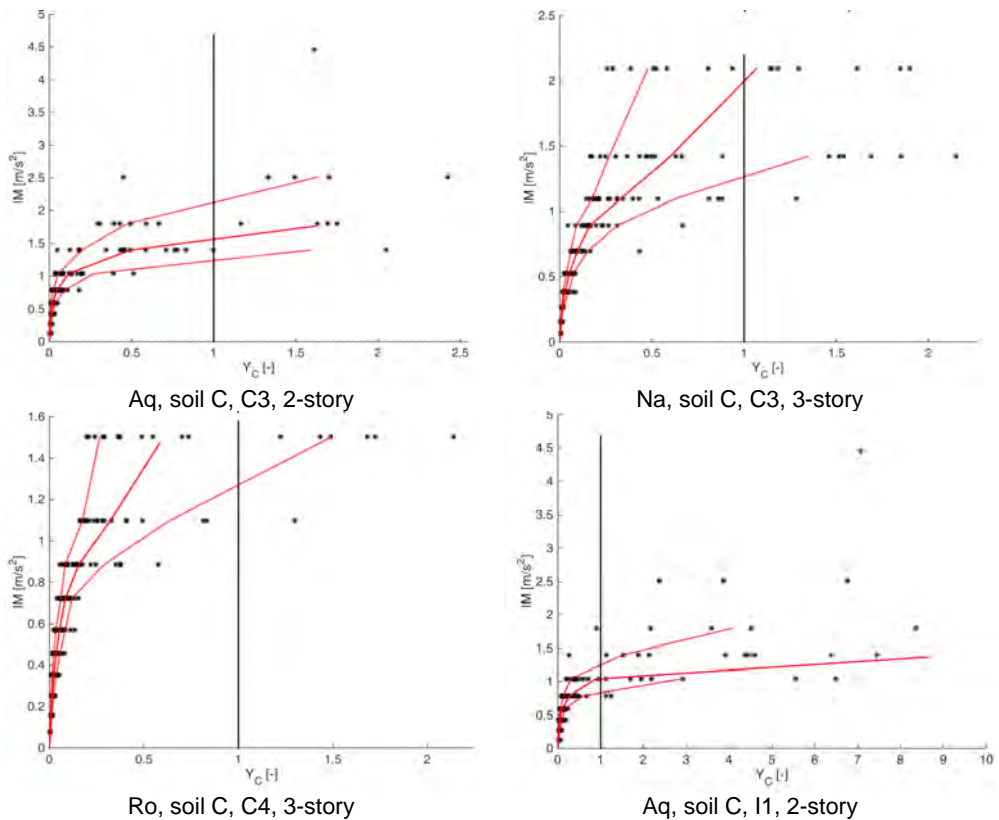


Figure 2.4.7 "IDA curves" (median, 16% and 84%) for the collapse limit state and for different building – site combinations; the vertical line indicates collapse (limit state function $Y = 1$).

### 2.4.4    Results of the "E" type configurations

Numerical analyses were performed on the models of the eight building configurations designed to barely comply with the code requirements (partially reported in Table 2.2.13) with the objective of assessing the seismic vulnerability in terms of frequency of exceedance of two considered limit states: damage and collapse. Thirty site-structure combinations were investigated in total, as summarized in Table 2.4.2.

Table 2.4.2 Building-site combinations analyzed with the updated models.

| Configuration | Stories | Regularity | Site |
|---------------|---------|------------|------|
| E2 | 2 | REG. | MI-A, MI-C, CL-A, AQ-A, AQ-C |
| | 3 | REG. | MI-A, MI-C, CL-A, AQ-A, NA-C |
| E5 | 2 | IRREG. | MI-A, AQ-C |
| | 3 | IRREG. | MI-A, NA-A |
| E8 | 2 | REG. | CL-C, RM-A, RM-C, NA-A, AQ-C |
| | 3 | REG. | MI-C, CL-A, CL-C, RM-A, NA-C, AQ-A |
| E9 | 2 | REG. | CL-C, RM-A, AQ-C |
| | 3 | REG. | MI-C, CL-A |

The structural models were accurately defined in order to get more stable and meaningful results: a particular attention was dedicated to the definition of the mesh of the floors, the convergence parameters of the analyses and other modelling assumptions related to the equivalent width of the ring beams (in order to simulate properly the flexural stiffness of the horizontal diaphragms). The improved version of the macroelement model, developed by Bracchi et al. (2017) and briefly described in section 2.3.1.2 was used. All these analyses were carried out considering only the uncertainty related to the seismic action, in terms of a seismic hazard curve and ground-motion record-to-record variability.

Two different limit states were considered: damage and collapse as defined at §2.4.1 and §2.4.2, respectively.

Figure 2.4.8 shows the pushover curves in the two directions of analysis (black and grey curves for X and Y directions, respectively) for 4 selected building configurations (E2 – two-story, E5 – 3-story, E8 – three-story, and E9 – two-story), with the identification of the thresholds of the limit states considered: DLS in blue and Collapse Limit State (CLS) in red. The values of EDP thresholds obtained (minimum among those resulting from the different verse of analyses) are summarized in Table 2.4.3.
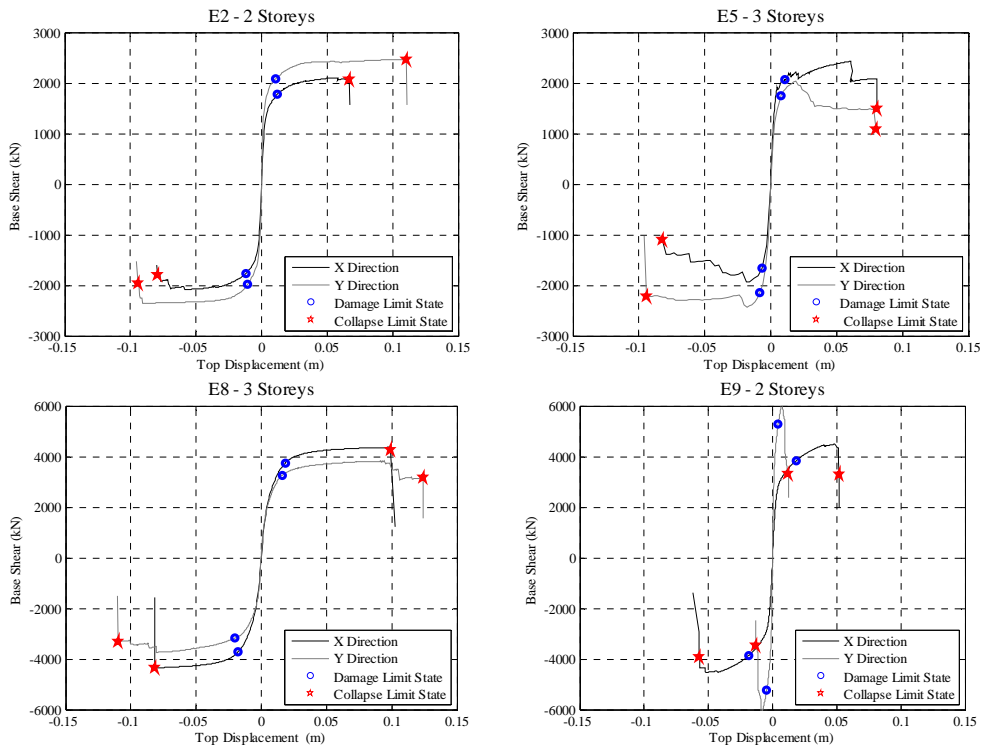
Figure 2.4.8 Pushover curves in the two directions of analysis, for 4 selected building configurations, with the identification of the thresholds of DLS (in blue) and CLS (in red).

Table 2.4.3. Values of EDP threshold corresponding to DLS and CLS limit states.

| Configuration | Regularity | Stories | EDP DLS threshold [%] | | CLS threshold [%] | |
|---|---|---|---|---|---|---|
| | | | X direction | Y direction | X direction | Y direction |
| E2 | REG. | 2 | 0.182 | 0.177 | 1.236 | 1.502 |
| | | 3 | 0.269 | 0.240 | 1.485 | 1.472 |
| E5 | IRREG. | 2 | 0.099 | 0.132 | 0.716 | 1.204 |
| | | 3 | 0.059 | 0.080 | 0.743 | 0.622 |
| E8 | REG. | 2 | 0.096 | 0.156 | 1.647 | 0.916 |
| | | 3 | 0.243 | 0.172 | 1.109 | 0.657 |
| E9 | REG. | 2 | 0.372 | 0.086 | 1.026 | 0.514 |
| | | 3 | 0.351 | 0.083 | 0.861 | 0.265 |

For all the models analyzed, the limit condition determining the definition of the SLD was that associated with the attainment of the lower bound fixed in the 85% of the peak resistance. That corresponds to a condition in which the structure is still fully capable of withstanding horizontal forces, as confirmed by the observation of damage in the structural elements reported in Figure 2.4.9 for the selected building (E8, 2-story, analyzed in the transversal direction). In the figure, it is possible to notice that the ultimate collapse condition is governed by a concentration of shear damage at the ground level.
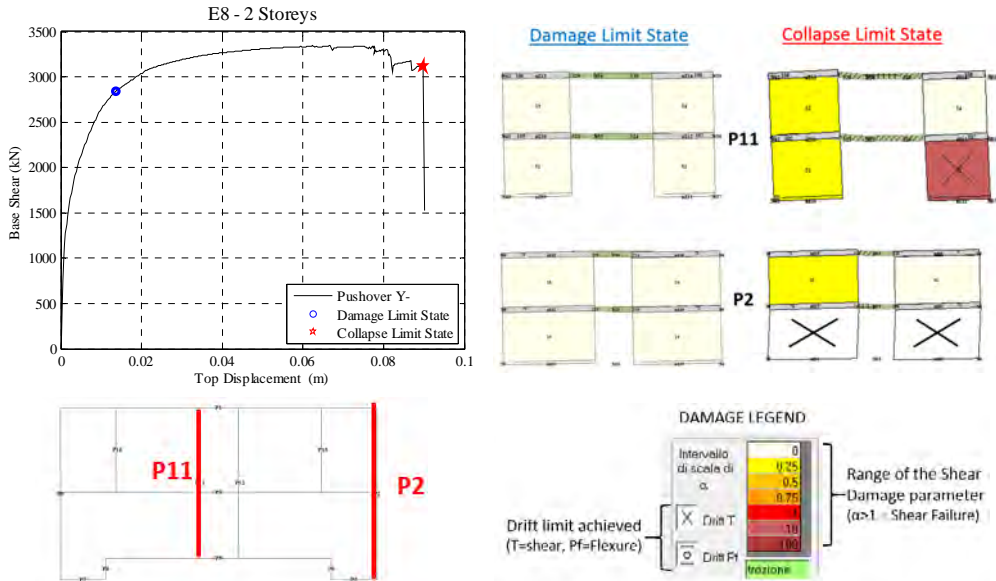
Figure 2.4.9 Damage observed in two significant walls (wall 11 and 2) of building E8 - 2-story,
at the end of a pushover analysis in the Y direction.

For each combination of site and soil type, it was hence possible to calculate the percentage of exceedance of the two considered limit states, for increasing values of the return period, by means of nonlinear dynamic analyses. Figure 2.4.10 reports the results for some significant selected cases.

It is possible to observe that, for all the cases analyzed, the first collapse never occurs for the return periods less than 1000 years, while the first occurrence of damage is observed for a return period of 250 years.

As expected, for a fixed combination of site and soil typology, the analyses carried out with a three-story building lead, in general, to more vulnerable results in comparison to the corresponding two-story configuration, both in terms of damages and collapses (see in particular the results of E2 building – in L'Aquila – soil A, reported at the top of Figure 2.4.10).
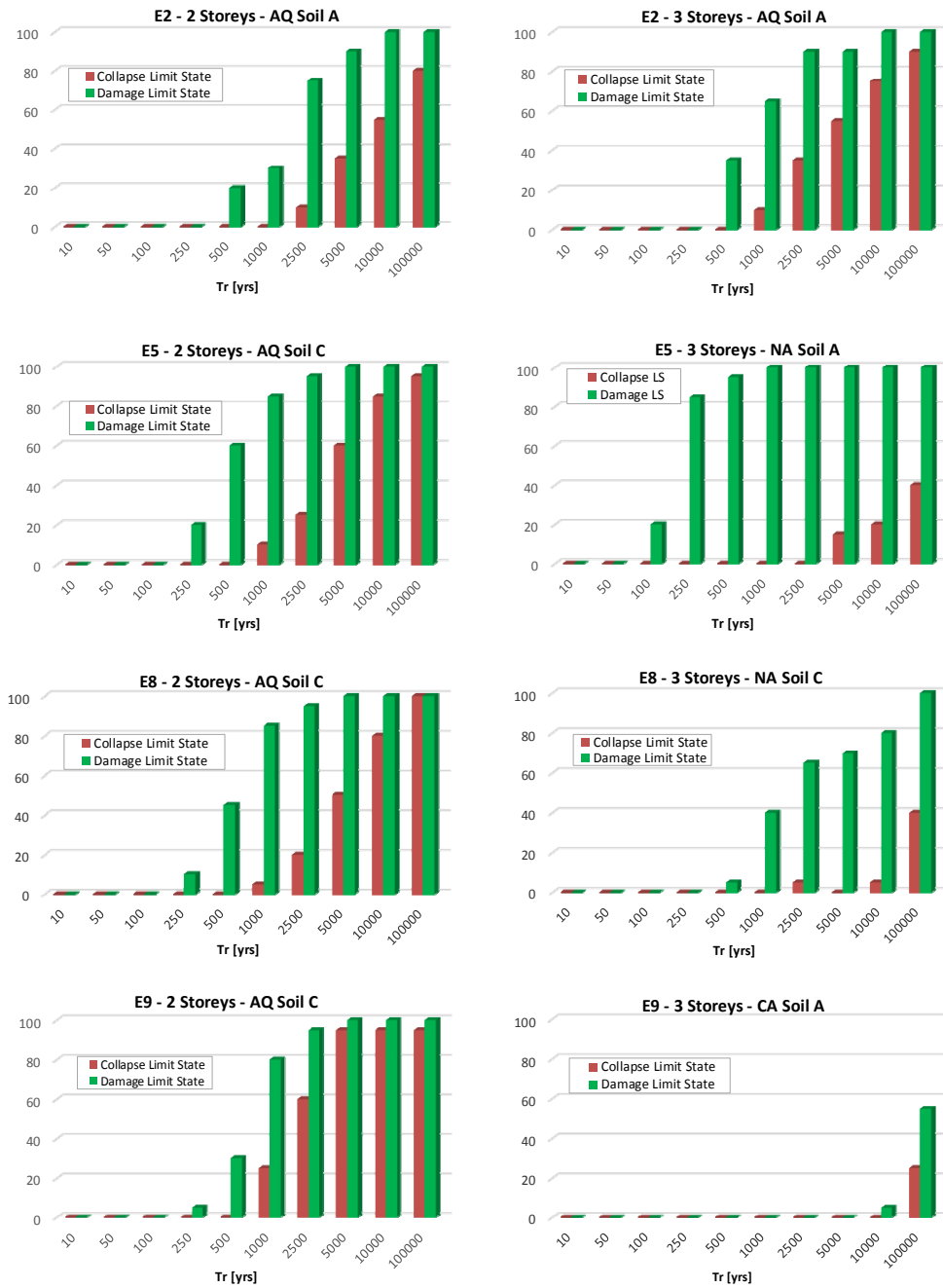
Figure 2.4.10. Frequency of occurrence (%) of damage (green bars) and collapse (red bars) limit states, as a function of return period, for some significant building-site combinations.

### 2.4.5    Results of the "F" and "G" type configurations

The defined EDP thresholds (minima among those resulting from the different pushover analyses) used for each defined configuration to determine the collapse occurrence are provided in Table 2.4.4.

Table 2.4.4. Values of EDP threshold used for "F" and "G" configurations to determine collapse.

| Configuration | Regularity | Stories | EDP threshold [%] | |
|:---:|:---:|:---:|:---:|:---:|
| | | | $\theta_{C,X}$ | $\theta_{C,Y}$ |
| F1 | IRREG. | 2 | 0.35 | 0.43 |
| F2 | IRREG. | 2 | 0.28 | 0.36 |
| F3 | IRREG. | 2 | 0.31 | 0.24 |
| F4 | IRREG. | 2 | 0.44 | 0.38 |
| G5 | IRREG. | 3 | 0.27 | 0.47 |
| G6 | IRREG. | 3 | 0.25 | 0.55 |
| G7 | IRREG. | 3 | 0.25 | 0.47 |

The dynamic analyses were performed for all the defined configurations by using the MSA. For each analysis, the maximum inter-story drift in the X direction ($\theta_{max,X}$) and in the Y direction ($\theta_{max,Y}$) were evaluated.

## 2.5    Uncertainty propagation: design, modelling and aleatory variables

The analyses described in the previous sections were carried out considering only the uncertainty related to the seismic action (i.e., the record-to-record variability). Then in order to quantify the effects on the results of structure-related uncertainty as well, new analyses were performed with this specific purpose. They are described in this section.

These analyses were limited to the sites of L'Aquila soil type A and Rome soil type A and to the regular "C" type configurations, both two- and three-story buildings. These two sites were chosen since L'Aquila soil type A is interesting to be investigated due to its high seismic hazard, while Rome soil type A is the last site where it is still possible to have configurations designed according to LSA. In fact, it is useful recall that in L'Aquila, Naples and Rome soil type C, due to the higher seismic hazard, it was impossible to design the considered configurations with LSA.

The choice of the "C" type configurations depends on the fact that they are characterized (as explained in Section 2.2) by a progressive increase of the resistant area (from C1 to C7).

In particular, the structure-related uncertainties investigated in these analyses can be grouped into the following three categories:

1) *Uncertainties due to the adopted design procedure*, which are related to the design phase and depend on the choice of the adopted design method (according to the rules proposed in NTC 2008);

2) *Modelling uncertainties,* which influence both the design and the analysis phase and concern the possible modelling choices that can be selected by the designer/analyst and the different constitutive laws that can be adopted;

3) *Aleatory uncertainties,* which are related to the assessment phase and depend on the variability of the mechanical properties of the structural materials (stiffness and strength)

and on the variability of the ultimate displacement capacity of the masonry panels (as consequence of the uncertainty on the drift thresholds).

The following sections describe in detail each one of these categories of uncertainty and explain how they were treated and accounted for in the performed analyses.

### 2.5.1    Uncertainty due to the adopted design procedure

Regarding structure-related uncertainty, one of the first sources of uncertainty is represented by the choice of the design method. As seen in Section 2.2, indeed, different methods are allowed by NTC 2008 for the design of masonry structures, so that a professional engineer can freely choose among them.

However, the results of the design change depending on the adpbted method.

In this study, five different design methods were considered:

- Rules for the so-called 'simple masonry building';
- Linear Static Analysis (LSA):
  - Cantilever model with force-redistribution;
  - Cantilever model without force-redistribution;
  - Frame model without force-redistribution;
- Non Linear Static Analysis (NLSA).

The frequency with which professional engineers choose the method reflects the popularity of some modelling techniques over others (i.e., frame models are in general more used than cantilever models) and also the opportunity given by their implementation in the commercial software currently used in professional practice (i.e., nonlinear static analysis is more commonly used in the engineering-practice for masonry buildings than in case of other typologies, such as reinforced concrete).

Moreover, as seen in Section 2.2, with LSA it is very difficult to obtain configurations complying with the code requirements for the high seismic hazard sites, so it may happen that in these cases a professional engineer would design with another, more successful, method.

By combining all these observations, a proper weight has been assigned to each design method, to represent its probability to be used (Table 2.5.1).

Table 2.5.1 Probability attributed to the selection of each design method for the two sites.

| Site | Simple masonry building | LSA | NLSA |
|------|-------------------------|-----|------|
| AQ   | 40%                     | 5%  | 55%  |
| RO   | 60%                     | 15% | 25%  |

It can be noted that the probability was differentiated depending on the site under consideration, because, as explained above, the seismic hazard characterizing the site of interest can influence the choice of the method.

*- Additional issues on the design of the "C" configuration according to the LSA with force redistribution*

The set of preliminary analyses carried out on the clay masonry structural configurations was completed, to identify the most suitable configurations for the design according to the different criteria to be adopted for the evaluation of the effect of uncertainties. As already recalled, using the LSA, both with the cantilever and the equivalent frame models, none of these configurations complied with the requirements, apart from the lowest seismicity sites. The reason was typically identified in the early inelastic behavior of a limited number of wall elements, even for low values

of the horizontal force. This condition was worsened by the assumptions of the Genoa RU regarding the spanning direction of the diaphragms and the subdivision of the dead loads into the different walls, which resulted in a reduced level of compression in some wall panels, with a consequent reduced strength to horizontal actions.

Considering the obtained results, the Pavia RU decided to try and improve the risk index of the C7 configuration (the one with the largest percentage of masonry among those proposed), both for the two-story and the three-story cases, using LSA with force redistribution, assuming a cantilever model approach.

The following tables show a comparison of the design results for the C7 structural configuration originally proposed by the Genoa RU, using LSA, without (Table 2.5.2 and Table 2.5.3) and with (Table 2.5.4 and Table 2.5.5) the application of the force redistribution.

Red cells in Table 2.5.2 and Table 2.5.3 indicate buildings whose design does not comply with the requirements, in yellow buildings largely complying with them and in green buildings that are considered as meaningful for each reference site. Empty cells correspond to cases in which a specific building does not even comply for the return period $T_R$ = 30 years.

Table 2.5.2 Results of the design of the two-story C7 configuration originally proposed by the Genoa RU, by means of linear static analysis without force redistribution.

| Site | AQ_C | AQ_A | NA_C | RM_C | NA_A | RM_A | CL_C | MI_C | CL_A | MI_A |
|---|---|---|---|---|---|---|---|---|---|---|
| $PGA^d$ | 0.347 | 0.261 | 0.245 | 0.182 | 0.168 | 0.121 | 0.109 | 0.074 | 0.073 | 0.049 |
| $S_d(T)^d$ | 0.228 | 0.171 | 0.162 | 0.133 | 0.111 | 0.089 | 0.080 | 0.055 | 0.052 | 0.036 |
| $T_R^C$ | | | | | 54 | 60 | 72 | 175 | 212 | 681 |
| $PGA^c$ | | | | | 0.062 | 0.058 | 0.057 | 0.055 | 0.056 | 0.054 |
| $\alpha_{PGA}$ | | | | | 0.370 | 0.477 | 0.524 | 0.747 | 0.771 | 1.096 |
| $\alpha_{Sd(T)}$ | | | | | 0.364 | 0.453 | 0.506 | 0.736 | 0.766 | 1.104 |

Table 2.5.3 Results of the design of the three-story C7 configuration originally proposed by the Genoa RU, by means of linear static analysis without force redistribution.

| Site | AQ_C | AQ_A | NA_C | RM_C | NA_A | RM_A | CL_C | MI_C | CL_A | MI_A |
|---|---|---|---|---|---|---|---|---|---|---|
| $PGA^d$ | 0.347 | 0.261 | 0.245 | 0.182 | 0.168 | 0.121 | 0.109 | 0.074 | 0.073 | 0.049 |
| $S_d(T)^d$ | 0.228 | 0.171 | 0.162 | 0.133 | 0.111 | 0.089 | 0.080 | 0.055 | 0.052 | 0.036 |
| $T_R^C$ | | | | | 54 | 60 | 72 | 175 | 212 | 681 |
| $PGA^c$ | | | | | 0.062 | 0.058 | 0.057 | 0.055 | 0.056 | 0.054 |
| $\alpha_{PGA}$ | | | | | 0.331 | 0.428 | 0.472 | 0.676 | 0.700 | 0.992 |
| $\alpha_{Sd(T)}$ | | | | | 0.326 | 0.408 | 0.458 | 0.660 | 0.687 | 0.992 |

Table 2.5.4 Results of the design of the two-story C7 configuration originally proposed by the Genoa RU, by means of LSA with force redistribution.

| Site | AQ_C | AQ_A | NA_C | RM_C | NA_A | RM_A | CL_C | MI_C | CL_A | MI_A |
|---|---|---|---|---|---|---|---|---|---|---|
| $V_{Rd,X}$ | KO | KO | KO | OK | OK | OK | OK | OK | OK | OK |
| $V_{Rd,Y}$ | KO | KO | KO | KO | OK | OK | OK | OK | OK | OK |
| $dV_{Ed}$ | OK | OK | OK | OK | OK | OK | OK | - | - | - |
| | KO | KO | KO | KO | KO | KO | KO | OK | OK | - |

| | |
|---|---|
| KO | Force redistribution not applicable/ineffective |
| OK | Force redistribution applicable/effective |
| - | Force redistribution not necessary |

It can be noted that both the original two-story and three-story configurations, if designed without force redistribution, could comply with the requirements for the site of MI-A only. By applying force redistribution, they could comply up to MI-C.

Based on these results, it was decided to further increase the risk index, to allow designing this configuration in the sites selected for the evaluation of the effect of uncertainties. To this end, a set of analyses was carried out on a number of numerical models obtained by fixing the structural configuration (spatial distribution and dimensions of structural elements) and assuming different hypotheses regarding the direction of spanning of the floors, the subdivision of the dead loads of the floors among the walls (100-0% or 80-20%, respectively in the directions perpendicular and parallel to the floor's direction of spanning) and the masonry typology. In particular, two different masonry typologies were considered:

- C7: clay blocks with a characteristic strength $f_{bk}$ = 8 MPa and M10 mortar
- C7+: clay blocks with a characteristic strength $f_{bk}$ = 15.1 MPa and M10 mortar

Table 2.5.5 Results of the design of the three-story C7 configuration originally proposed by the Genoa RU, by means of linear static analysis with force redistribution.

| site | AQ_C | AQ_A | NA_C | RM_C | NA_A | RM_A | CL_C | MI_C | CL_A | MI_A |
|---|---|---|---|---|---|---|---|---|---|---|
| $V_{Rd,X}$ | KO | KO | KO | OK | OK | OK | OK | OK | OK | OK |
| $V_{Rd,Y}$ | KO | KO | KO | KO | OK | OK | OK | OK | OK | OK |
| $dV_{Ed}$ | OK | OK | OK | OK | OK | OK | OK | - | - | - |
| | KO | KO | KO | KO | KO | KO | KO | OK | OK | OK |

| | |
|---|---|
| KO | Force redistribution not applicable/ineffective |
| OK | Force redistribution applicable/effective |
| - | Force redistribution not necessary |

Nevertheless, none of the considered configurations could comply with the requirements for the site with the highest seismicity if designed with LSA, not even applying the redistribution of forces.

Therefore, the two-story and three-story configurations, complying at least up to RM-A, to which the lowest values of global safety factor obtained from the design without any force redistribution were associated, were redesigned. These configurations were considered those for which the design was better calibrated for the reference site and were hence adopted for the evaluation of the effect of uncertainties presented in a following section. The obtained results are summarized in Table 2.5.6, Table 2.5.7, Table 2.5.8, and Table 2.5.9. In particular, the simple adoption of the 80-20% option regarding the subdivision of the floors' dead loads on the walls (instead of 100-

0%) allows to design the two-story building with LSA with force redistribution up to RM-A, whereas without force redistribution it could not be designed for a seismicity higher than MI-C.

In order to design the three-story building, with LSA and with force redistribution, at RM-A, it was necessary to adopt a more resistant masonry (C7+) and a different direction of spanning for some of the floors. Instead, the assumption of subdividing the floors' loads only among the walls orthogonal to the direction of spanning, as selected by the Genoa RU, was maintained. In this case, the design with LSA without any force redistribution was not able to comply with the requirements for any of the sites.

Table 2.5.6 Results of the re-design of the two-story C7 configuration with LSA without any force redistribution.

| site | AQ_C | AQ_A | NA_C | RM_C | NA_A | RM_A | CL_C | MI_C | CL_A | MI_A |
|------|------|------|------|------|------|------|------|------|------|------|
| $PGA^d$ | 0.347 | 0.261 | 0.245 | 0.182 | 0.168 | 0.121 | 0.109 | 0.074 | 0.073 | 0.049 |
| $S_d(T)^d$ | 0.228 | 0.171 | 0.162 | 0.133 | 0.111 | 0.089 | 0.080 | 0.055 | 0.052 | 0.036 |
| $T_R^C$ | | 55 | 72 | 85 | 163 | 240 | 325 | 1157 | 1137 | 2475 |
| $PGA^c$ | | 0.108 | 0.108 | 0.100 | 0.108 | 0.097 | 0.097 | 0.093 | 0.094 | 0.075 |
| $\alpha_{PGA}$ | | 0.415 | 0.442 | 0.552 | 0.647 | 0.803 | 0.885 | 1.253 | 1.291 | 1.514 |
| $\alpha_{Sd(T)}$ | | 0.408 | 0.433 | 0.525 | 0.632 | 0.788 | 0.873 | 1.279 | 1.332 | 1.586 |

Table 2.5.7 Results of the re-design of the two-story C7 configuration with LSA with force redistribution.

| site | AQ_C | AQ_A | NA_C | RM_C | NA_A | RM_A | CL_C | MI_C | CL_A | MI_A |
|------|------|------|------|------|------|------|------|------|------|------|
| $V_{Rd,X}$ | KO | KO | KO | OK | OK | OK | OK | OK | OK | OK |
| $V_{Rd,Y}$ | KO | KO | KO | KO | OK | OK | OK | OK | OK | OK |
| $dV_{Ed}$ | OK | OK | OK | OK | OK | OK | OK | - | - | - |
| | KO | KO | KO | KO | KO | OK | OK | - | - | - |

| | |
|---|---|
| KO | Force redistribution not applicable/ineffective |
| OK | Force redistribution applicable/effective |
| - | Force redistribution not necessary |

Table 2.5.8 Results of the re-design of the three-story C7 configuration with LSA without any force redistribution.

| site | AQ_C | AQ_A | NA_C | RM_C | NA_A | RM_A | CL_C | MI_C | CL_A | MI_A |
|------|------|------|------|------|------|------|------|------|------|------|
| $PGA^d$ | 0.347 | 0.261 | 0.245 | 0.182 | 0.168 | 0.121 | 0.109 | 0.074 | 0.073 | 0.049 |
| $S_d(T)^d$ | 0.228 | 0.171 | 0.162 | 0.133 | 0.111 | 0.089 | 0.079 | 0.055 | 0.052 | 0.036 |
| $T_R^C$ | | | | | 35 | 37 | 39 | 85 | 112 | 323 |
| $PGA^c$ | | | | | 0.049 | 0.046 | 0.045 | 0.044 | 0.045 | 0.044 |
| $\alpha_{PGA}$ | | | | | 0.290 | 0.378 | 0.416 | 0.596 | 0.619 | 0.893 |
| $\alpha_{Sd(T)}$ | | | | | 0.285 | 0.358 | 0.401 | 0.577 | 0.601 | 0.889 |

Table 2.5.9 Results of the re-design of the three-story C7 configuration with LSA with force redistribution.

| site | AQ_C | AQ_A | NA_C | RM_C | NA_A | RM_A | CL_C | MI_C | CL_A | MI_A |
|------|------|------|------|------|------|------|------|------|------|------|
| $V_{Rd,X}$ | KO | KO | KO | OK | OK | OK | OK | OK | OK | OK |
| $V_{Rd,Y}$ | KO | KO | KO | KO | OK | OK | OK | OK | OK | OK |
| $dV_{Ed}$ | OK | OK | OK | OK | OK | OK | OK | - | - | - |
| | KO | KO | KO | KO | KO | OK | OK | OK | OK | OK |

| KO | Force redistribution not applicable/ineffective |
|----|--------------------------------------------------|
| OK | Force redistribution applicable/effective |
| - | Force redistribution not necessary |

### 2.5.2    Modelling uncertainty

2.5.2.1 Uncertainty due to modelling choices

Another source of uncertainty is represented by the so-called "epistemic uncertainties", which are related to the different possible modelling choices that a professional engineer can do in order to pass from the architectural configuration of a given building to the corresponding structural model. This is possible because the NTC 2008 provides only general recommendations regarding the definition of the structural models. Furthermore, there are no specific indications about how to model all the possible structural details. Therefore, since not all the modelling aspects are standardized by the code, engineers can make arbitrary choices about how to model the building itself, thus obtaining different results for the design.

In the present study, the most common epistemic uncertainties and the related possible modelling options were identified and analyzed. They are summarized as follows:

1) definition of the unloading direction of the diaphragms;
2) definition of the effective length of the RC ring beams;
3) definition of the quality of the connection between orthogonal walls.

Referring to point 1), the RC rigid diaphragms used in the new masonry buildings usually have a prevalent unidirectional behavior. In reality, a partial slab-like behavior can be generated and hence modelling of either unidirectional or partially bidirectional behavior is not trivial. For this reason, two modelling options have been considered (consistently with those already introduced in §2.5.1 for the additional design carried out in case of C configuration through LSA method):

- *OPTION A - unidirectional behavior*: 100% of load transferred in the principal direction of the diaphragm;
- *OPTION B – partial bidirectional behavior*: 80% of load transferred in the principal direction and 20% in the orthogonal one.

Referring to the point 2), the choice of the effective length of the ring beams is again arbitrary. Although ring beams actually have a length equal to the length of the corresponding wall, the coupling between masonry panels can be more or less effective and this can be taken into account by varying their effective length. The modelling options considered in this case are:

- *OPTION A* - effective length equal to the total length of the wall (long ring beams – named in the following as "CL");
- *OPTION B* - effective length equal to the width of the corresponding opening (short ring beams – named in the following as "CC").

Finally, referring to point 3), two extreme modelling options were considered:

- *OPTION A* - Perfect connection between orthogonal walls;
- *OPTION B* - Reduced connection between orthogonal walls.

The modelling uncertainties discussed above affect the definition of the structural model and so they influence both the design phase and the analysis phase.

Regarding the design phase, it is worth noting that, depending on the adopted design method, only the uncertainties (and the related modelling choices) that may affect the structural response were considered. In particular, regarding the design with LSA, for the cantilever models only the two different hypotheses about the behavior of the diaphragms were considered. In this kind of models, indeed, both the effective length of the ring beams and the quality of the connection between walls do not affect significantly the structural response. On the contrary, in the case of frame models (used for NLSA and LSA without force redistribution) all the introduced epistemic uncertainties and the related modelling options were considered.

Regarding the analysis phase, the designed buildings (deriving from the different possible combinations of the alternative modelling options) were modelled with the most reliable approaches with respect to the effective structural behavior. For this reason, once defining building-to-site combinations, as a result of the design phase previously described, some choices about the modelling strategies were carried out. In particular, the following options were selected:

- Unidirectional behavior of the diaphragms (option A);
- Perfect quality of the connection between orthogonal walls (option A)
- Effective length of the RC ring beams: both options A and B were considered.

The choice regarding the behavior of the diaphragms is motivated by the results of some preliminary analyses which showed that the unidirectional or partial bidirectional behavior of the diaphragms does not significantly affect the structural response. The connection between orthogonal walls was assumed perfect because this study concerns new masonry buildings, for which the code prescribes the presence of specific structural details in order to guarantee a box-like behavior, hence ensuring a perfect coupling between orthogonal walls. Finally, regarding the effective length of the RC ring beams, it was decided to consider the both options because, as seen in the preliminary analyses, this choice affects significantly the structural response.

2.5.2.2  Uncertainty due to the constitutive models

As mentioned before, the considered model uncertainties include also the adoption of possible alternative constitutive laws aimed to describe the response of masonry panels. To this aim, the two different constitutive laws implemented in TREMURI Program (the piecewise-linear force-deformation relationship and the macroelement mechanical model) were adopted for nonlinear dynamic analyses. The equivalence between the mechanical parameters of the two models was guaranteed according to the criteria illustrated in § 2.3.1.2.

**2.5.3  Aleatory uncertainty**

For both models, a common sampling procedure was defined for buildings realized with the different structural materials, as discussed in Appendix B.

This procedure allows sampling values of the mechanical properties of the different structural elements, taking into account the assumed marginal probability distributions of the intra- and inter- element correlations of the structure and of the intra-building correlation, i.e., to reflect the possibility of having a lower dispersion of mechanical properties (and partially also of the displacement capacity associated with the different failure mechanisms) within the same building than for different buildings. This is due to, for example, a more homogeneous workmanship, the origin of materials from the same suppliers, homogeneous climate conditions during the construction of a single building.

Differently from other structural typologies, such as reinforced concrete buildings, a significantly higher correlation among structural elements belonging to the same story was not considered, as in this case the construction of structural elements at the same story is not typically simultaneous.

The following sections clarify how the covariance and correlation matrices introduced in Appendix B were defined for the case of masonry buildings.

2.5.3.1  Definition of the intra-element correlation among parameters from experimental data

To account for uncertainties in the definition of mechanical parameters and their variability within the structures, several random variables were introduced. Their marginal probability density functions were defined starting from experimental results available in the literature. In particular, vertical compression tests on vertically perforated clay block masonry walls with filled head- and bed-joints provided the values of elastic modulus $E$ and masonry compressive strength $f_m$ reported in Figure 2.5.1.
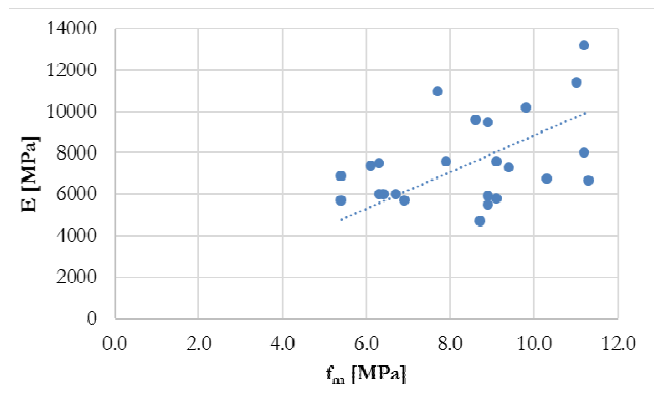


Figure 2.5.1 Values of elastic modulus ($E$) and masonry compressive strength ($f_m$) obtained from vertical compression tests on vertically perforated clay block masonry walls with filled head- and bed-joints.

Similarly, the marginal probability density functions of the ultimate drift values were defined starting from the results of cyclic shear-compression tests on clay block masonry piers (Morandi et al., 2015; Morandi et al., 2016). The values considered are reported in Figure 2.5.2.
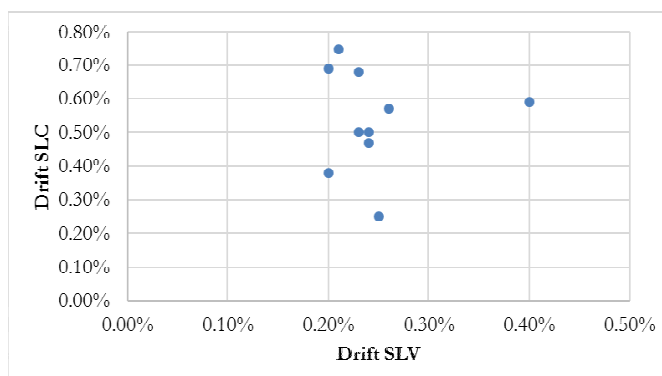


Figure 2.5.2 Values of the ultimate drift at the ultimate limit state (SLV) and near collapse limit state (SLC), derived from cyclic shear-compression tests on clay block masonry piers.

Considering the parameters governing the stiffness of the masonry panel, the elastic modulus ($E$) was described by a lognormal random variable, whose parameters (median 2823 MPa and $\beta$ = 0.25, where $\beta$ is the standard deviation of the normal distribution associated to the lognormal) were derived starting from the experimental data reported in Figure 2.5.1.

The relationship between the Young's modulus in compression, $E$, and the shear modulus $G$ was assumed to be deterministic: $G = 0.4E$.

Considering instead the parameters governing the strength of the masonry panel, the masonry compressive strength, $f_m$, was defined by a lognormal random variable, with a median of 6.46 MPa and $\beta$ = 0.25. Similarly, the initial shear strength of masonry in the absence of compression, $f_{v0}$, was described by a lognormal variable with the median of 0.27 MPa and $\beta$ = 0.3, estimated based on expert judgement.

The unit compressive strength and the unit shear strength ($f_b$ and $f_{bt}$, respectively) were assumed to be deterministically related to the masonry compressive strength $f_m$:

- $f_b$ = 11.43 MPa (mean value, obtained from the unit characteristic strength),
- $f_{vlt}$ (mean value) = 0.065 $f_b$ / 0.7 (0.7 accounts for the ratio between the mean value of $f_{vlt}$ and its characteristic value,
- $f_{bt}$ = 0.1 $f_b$.

The friction coefficient was assumed as deterministic: $\mu$ = 0.4.

The correlation between the different random variables described so far were defined based on the available experimental data and using expert judgement. The following assumptions were adopted:

- a correlation coefficient between $E$ and $f_m$ equal to 0.5,
- a correlation coefficient between $E$ and $f_{v0}$ equal to 0.35,
- a correlation coefficient between $f_m$ and $f_{v0}$ equal to 0.35.

The ultimate displacement capacity of the panel is governed by the following parameters:

- shear drift threshold corresponding to a 20% strength decay (SLV), $\theta_{3,T}$ = 0.001 + $\alpha_{3,T}$, in which $\alpha_{3,T}$ is a lognormal random variable, with median 0.0014 and $\beta$ = 0.3,
- shear drift threshold corresponding to a 50% strength decay (SLC), $\theta_{4,T}$ = $\theta_{3,T}$ + $\alpha_{4,T}$, in which $\alpha_{4,T}$ is a lognormal random variable, with median 0.003 and $\beta$ = 0.25. From this, $\theta_{4,T}$ has a median value of 0.0052,
- flexural drift threshold corresponding to a null lateral strength, $\theta_{5,PF}$ = 0.002 + $\alpha_{5,PF}$, in which $\alpha_{5,PF}$ is a lognormal random variable, with median 0. 0165 and $\beta$ = 0.4. From this, $\theta_{5,PF}$ has a median value of 0. 0186.

The other ultimate displacement capacity parameters were assumed as perfectly correlated to these three random variables:

- shear drift threshold corresponding to a null lateral strength, $\theta_{5,T}$ modelled as perfectly correlated to $\theta_{4,T}$: $\theta_{5,T}$ = $\theta_{4,T}$ + 0.0016,
- flexural drift threshold corresponding to a 20% strength decay: $\theta_{4,PF}$ - modelled as perfectly correlated to $\theta_{5,PF}$: $\theta_{4,PF}$ = $\theta_{5,PF}$ - 0.006.

Table 2.5.10 summarizes, on the diagonal, the values of median and dispersion of the mechanical parameters considered as aleatory variables. The off-diagonal terms report instead the assumed correlation coefficients between the different parameters.

Table 2.5.10 Matrix of the median values and dispersions (on the diagonal) and of the correlation coefficients between the different parameters (off-diagonal).

| | E | $f_m$ | $f_{v0}$ | $\alpha_{3,T}$ | $\alpha_{4,T}$ | $\alpha_{5,PF}$ |
|---|---|---|---|---|---|---|
| E | $\mu = 2823$ MPa $\beta = 0.25$ | 0.5 | 0.35 | 0 | 0 | 0 |
| $f_m$ | 0.5 | $\mu\ 6.46$ MPa $\beta = 0.25$ | 0.35 | 0 | 0 | 0 |
| $f_{v0}$ | 0.35 | 0.35 | $\mu = 0.27$ MPa $\beta = 0.3$ | 0 | 0 | 0 |
| $\alpha_{3,T}$ | 0 | 0 | 0 | $\mu = 0.0014$ $\beta = 0.3$ | 0 | 0 |
| $\alpha_{4,T}$ | 0 | 0 | 0 | 0 | $\mu = 0.003$ $\beta = 0.25$ | 0 |
| $\alpha_{5,PF}$ | 0 | 0 | 0 | 0 | 0 | $\mu = 0.0165$ $\beta = 0.4$ |

### 2.5.3.2 Definition of the intra-building correlation among parameters from experimental data

To define a correlation structure among mechanical properties of the structural elements belonging to a single building, experimental results were collected. Due to the lack of correlation data on modern masonry typologies, it was necessary to resort to other sources of information.

In particular, data from an in-situ experimental campaign on several masonry existing buildings in the area of Groningen (Tondelli et al., 2015) were used, as multiple tests on structural elements belonging to the same building were available, for different buildings. These mechanical characterization tests, realized in situ or on masonry samples taken in situ and tested in the laboratory, concern the main mechanical properties that are used in a structural model, i.e., Young modulus, masonry compression strength, initial shear strength, for clay masonry with cement mortar (or bastard mortar). Figure 2.5.3 reports some results of this experimental campaign of in-situ tests. A comparison of the distribution of parameters for the different buildings and the data sampled within a single building highlights a lower dispersion of values within the same building, as well as a substantial independency of the variability of the mean value of the parameters among the different buildings and the variability of the parameters within a single building. This allowed deriving the ratio of the average coefficients of variation of the mechanical parameters within a single building and the coefficients of variation of the entire experimental set, which result to be similar among the different considered mechanical properties.

Based on this, an inter-building correlation coefficient matrix was defined, to be used for sampling the different variables, as summarized in the following table. The post-processing of available data allowed to provide an estimate only for the parameters E, $f_m$ and $f_{v,0}$ while in the case of drift thresholds data are not available. As a consequence, the correlation coefficients proposed for the $\alpha_{3,T}, \alpha_{4,T}$ and $\alpha_{5,PF}$ variables have been defined on expert judgment basis.
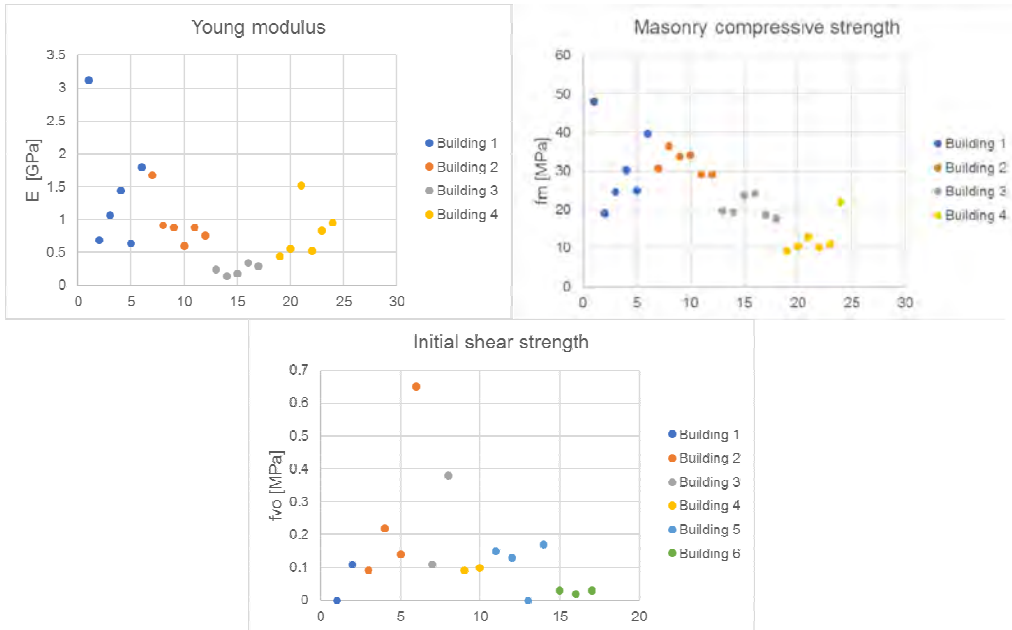
Figure 2.5.3 Mechanical properties derived from an in-situ experimental campaign on buildings belonging to the same clay masonry typology considered in the project (from Tondelli et al., 2015)

Table 2.5.11 Intra-building correlation coefficients assumed for each aleatory variable

| E | $f_m$ | $f_{v0}$ | $\alpha_{3,T}$ | $\alpha_{4,T}$ | $\alpha_{5,PF}$ |
|------|------|------|------|------|------|
| 0.65 | 0.65 | 0.65 | 0.2 | 0.2 | 0.2 |

## 2.5.4    Results and discussion

### 2.5.4.1  Results of the design phase

By combining the uncertainties due to the design method adopted described in Section 2.5.1 and the modelling uncertainties described in Section 2.5.2, the logic tree represented in Figure 2.5.4 was obtained.

Each branch of this logic tree represents, for a fixed site and a fixed number of stories of the building, a possible outcome of the design. It comes out that, considering all the possible combinations, for a fixed site and a fixed number of stories, twenty-one possible choices have to be considered, each of them can theoretically leads to a different structural configuration that can be designed at that site.

The procedure described in Figure 2.5.4 was repeated in order to identify which structural configuration among those considered (C1, C2,..,C7, C7+) barely complies with the code requirements for each site. The results are represented in Table 2.5.12.

The main outcome confirms what to be expected, i.e., that, for a fixed site and for a fixed number of stories, the use of different design methods combined with the different possible modelling hypotheses actually leads to different structural configurations. For example, in the case of L'Aquila soil A – 2-story, it can be seen that the rules for simple buildings lead to the configuration C5, while NLSA leads to configuration C1.
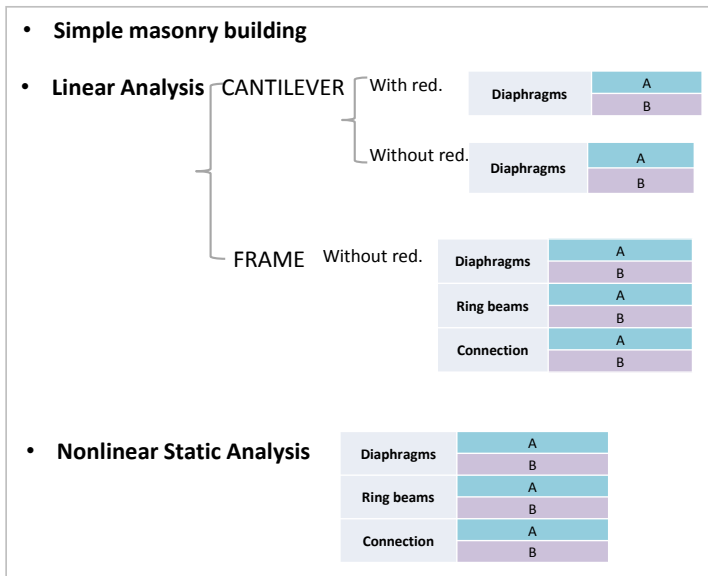
Figure 2.5.4 Logic tree obtained by combining the uncertainties due to the selected design
method and the considered modelling uncertainties.

Moreover, in case of LSA, the different modelling hypotheses used to account for the epistemic uncertainties do not influence the obtained structural configuration for a fixed site and a fixed number of stories, while they do in the case of NLSA. In particular, in the case of L'Aquila soil A-three-story, if ring beams are more effective and the connection between walls is perfect, the C1 configuration is obtained, otherwise the C3 has to be used.

Another important aspect is that for L'Aquila soil A none of the available configurations (either two- and three-story) is verified with LSA.

A summary of the results of the design phase are represented in Table 2.5.13, together with the probability associated to each design method (as introduced in Section 2.5.1). However, since the modelling uncertainties influence the outcomes of the design in the case of NLSA (as seen before in Table 2.5.12), it is necessary to integrate the probability attributed to each design method introduced in Section 2.5.1 with the consideration of the epistemic uncertainties. In particular this has been done by splitting the probability attributed to the NLSA into two parts: one related to the case of ring beams or wall connection more effective (hypothesis 1) and the other related to ring beams and wall connection less effective (hypothesis 2). In fact, depending on which one of these two hypotheses is used, the resulting configuration changes. In particular, both in L'Aquila and in Rome, a higher probability was attributed to hypothesis 1, that is considered the most used in practice by professional engineers.

In this way, for a fixed site and a fixed number of stories, it is possible to associate to each configuration the correspondent probability. In particular, for the cases in which with a specific design method no configurations were found (it is the case of LSA in L'Aquila), the probability associated to that method were subdivided among the other more successful methods.

Table 2.5.12 Results of the design phase when both the uncertainties due to the design method adopted and the modelling uncertainties are considered.

| Mod | Design method | | | Diaphragm | Ring beams | Connection | | | | |
|---|---|---|---|---|---|---|---|---|---|---|
| 1 | SIMPLE MASONRY BUILDING | | | - | - | - | C5 | C6 | C2 | C3 |
| 2 | LSA | CANTIL. | With red. | A | - | - | - | - | C7 | C7+ |
| 3 | | | | B | - | - | - | - | C7 | C7+ |
| 4 | | | No red. | A | - | - | - | - | C7 | C7+ |
| 5 | | | | B | - | - | - | - | C7 | C7+ |
| 6 | | FRAME | No red. | A | A | A | - | - | C7 | C7+ |
| 7 | | | | B | A | A | - | - | C7 | C7+ |
| 8 | | | | A | B | A | - | - | C7 | C7+ |
| 9 | | | | A | A | B | - | - | C7 | C7+ |
| 10 | | | | B | B | A | - | - | C7 | C7+ |
| 11 | | | | B | A | B | - | - | C7 | C7+ |
| 12 | | | | A | B | B | - | - | C7 | C7+ |
| 13 | | | | B | B | B | - | - | C7 | C7+ |
| 14 | NLSA | | | A | A | A | C1 | C1 | C1 | C1 |
| 15 | | | | B | A | A | C1 | C1 | C1 | C1 |
| 16 | | | | A | B | A | C1 | C1 | C1 | C1 |
| 17 | | | | A | A | B | C1 | C3 | C1 | C1 |
| 18 | | | | B | B | A | C1 | C1 | C1 | C1 |
| 19 | | | | B | A | B | C1 | C3 | C1 | C1 |
| 20 | | | | A | B | B | C1 | C1 | C1 | C1 |
| 21 | | | | B | B | B | C1 | C1 | C1 | C1 |

| LEGEND | | | | | |
|---|---|---|---|---|---|
| **Diaphragm** | | **Ring beams** | | **Connection** | |
| A | Unidirectional (100%) | A | Long ring beams | A | Perfect |
| B | Bidirectional (80%-20%) | B | Short ring beams | B | Reduced |

Table 2.5.13 Summary of the results of the design phase and related frequencies considering the different design methods and the epistemic uncertainties.

| | Design method | Simple masonry building | LSA | NLSA (Hp 1: ring beams or wall connection more effective) | NLSA (Hp 2: ring beams and wall connection less effective) |
|---|---|---|---|---|---|
| | **Frequency– AQ** | **40%** | **5%** | **40%** | **15%** |
| **Aq_A– 2 lev** | **Configuration P(%)** | C5 42.1% | - | C1 57.9% | |
| **Aq_A–3 lev** | **Configuration P(%)** | C6 42.1% | - | C1 42.1% | C3 15.8% |
| | **Frequency– RO** | **60%** | **15%** | **20%** | **5%** |
| **Ro_A–2 lev** | **Configuration P(%)** | C2 60% | C7 15% | C1 25% | |
| **Ro_A–3 lev** | **Configuration P(%)** | C2 60% | C7+ 15% | C1 25% | |

2.5.4.2    Results of the analyses

Dynamic analyses were performed for all the individuated building-site combinations by using the MSA.

Regarding the epistemic uncertainties, the modelling hypotheses adopted are those described in section 2.5.2.1, and in particular: perfect connection between orthogonal walls and unidirectional behavior for the diaphragms. Since it was decided to treat the effective length of the ring beams as an epistemic uncertainty (at the actual knowledge state it is not possible to make a choice based on the more reliable option), for each building-site combination both the modelling hypothesis of long ring beams (CL) and of short ring beams (CC) were explored.

Table 2.5.14 shows the final building-site combinations that were analyzed (in total 22), together with the probability associated with the selected design method. It has to be noted that, for a fixed building-site combination, an equal probability was assigned to the configuration with short ring beams and to the one with long ring beams.

Table 2.5.14 Analyzed building-site combinations and related abbreviation.

| Site | Story | Configuration | P [%] | Site | Story | Configuration | P [%] |
|---|---|---|---|---|---|---|---|
| Aq_A | 2 | C1, 2 stories, CC | 28.95 | Ro_A | 2 | C1, 2 stories, CC | 12.5 |
| | | C1, 2 stories, CL | 28.95 | | | C1, 2 stories, CL | 12.5 |
| | | C5, 2 stories, CC | 21.05 | | | C2, 2 stories, CC | 30 |
| | | C5, 2 stories, CL | 21.05 | | | C2, 2 stories, CL | 30 |
| | 3 | C1, 3 stories, CC | 21.05 | | | C7, 2 stories, CC | 7.5 |
| | | C1, 3 stories, CL | 21.05 | | | C7, 2 stories, CL | 7.5 |
| | | C3, 3 stories, CC | 7.9 | | 3 | C1, 3 stories, CC | 12.5 |
| | | C3, 3 stories, CL | 7.9 | | | C1, 3 stories, CL | 12.5 |
| | | C6, 3 stories, CC | 21.05 | | | C3, 3 stories, CC | 30 |
| | | C6, 3 stories, CL | 21.05 | | | C3, 3 stories, CL | 30 |
| | | | | | | C7+, 3 stories, CC | 7.5 |
| | | | | | | C7+, 3 stories, CL | 7.5 |

For each one of the two models (long and short ring beams) associated to a given building–site combination, twenty models were generated through the sampling of the aleatory variables, described in Appendix C and in Section 2.5.3.1.

Then, for each stripe, an one-to-one association between these twenty models and the twenty records of the stripe was done. As discussed in Section 2.4, in order to define the attainment of the collapse and of the damage limit states, specific thresholds (different for the X and the Y directions) have to be defined. In this case, for a given configuration, twenty different thresholds were defined, each one corresponding to one of the twenty models generated by sampling values from the aleatory variables. Therefore, it was necessary to define the pushover curves associated to each one of the twenty models deriving from the sampling for a given building configuration.

Then, the two different constitutive laws described in 2.3.1 were adopted. The results obtained with the adoption of the piecewise-linear force-deformation relationship are presented first. Figure 2.5.5 presents the pushover curves associated to two selected building configurations. For each configuration the curves associated to the twenty models generated through the sampling of the aleatory variables are shown together with the curve of the correspondent model characterized by the median values of the aleatory variables.
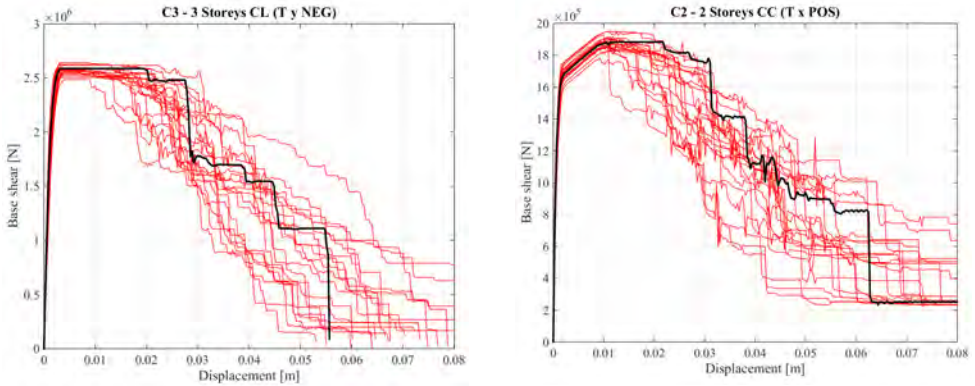
Figure 2.5.5 Pushover curves of two selected configurations: curves of the twenty models generated through the sampling of the aleatory variables (in red) and curve of the correspondent model characterized by the median values of the aleatory variables (in black).

By processing the results of the dynamic analyses, it was possible to obtain, as in the case of the previous analyses, the IM-Y graphs and the "IDA curves" associated to each building-site combination, for both the collapse and the damage limit state. Figure 2.5.6 shows some ''IDA curves'' related to different building-site combinations, together with the vertical line Y=1, corresponding to the attainment of the considered limit state.



*(a1) - Damage limit state*            *(a2) - Collapse limit state*

Aq, soil A, C1, 2 stories, CL



*(b1) - Damage limit state*            *(b2) - Collapse limit state*

Ro, soil A, C2, 2 stories, CL
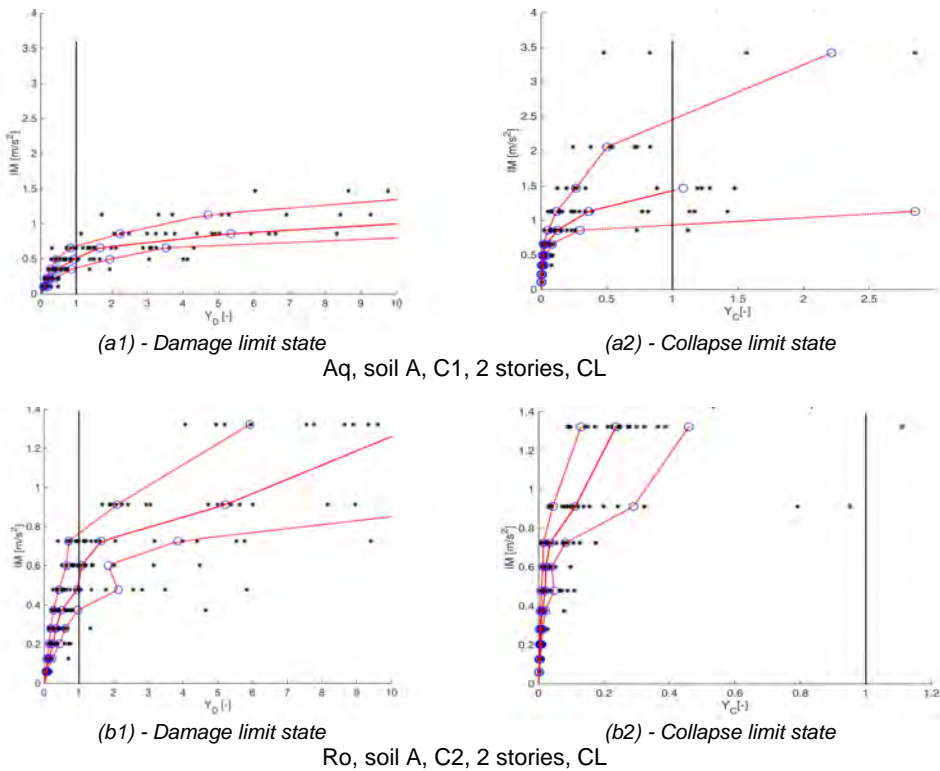
Figure 2.5.6 ''IDA curves'' (median, 16% and 84%) for both the damage (a1, b1) and the collapse limit state (a2, b2) for different building–site combinations; the vertical black line indicates the attainment of the limit state (limit state function $Y = 1$).

In general, the obtained results confirm what was observed in the previous analyses. In particular, it may be said that, regardless of the configuration considered, the damage limit state is reached both in Rome (starting from the second-third stripe) and in L'Aquila (already for a few time histories belonging to the first stripe). On the other hand, the collapse limit state is always reached in L'Aquila, while in Rome only a few time histories belonging to the last stripes lead to the exceedance of the defined threshold.

Moreover, for each one of the analyzed building-site combinations, the corresponding numerical fragility curves for the collapse and the damage limit states were defined. In particular, for each stripe of a fixed building-site combination, it was possible to calculate a point of the corresponding fragility curve; this point represents, in fact, the probability of exceedance of the defined threshold. Therefore, it can be calculated as the area included between the vertical line corresponding to Y=1 and the curve representing the lognormal distribution assumed for the Y values associated to each stripe. Of course, if some "certain collapses" (as defined in section 2.4.1) are present, the associated probability must be added.

Finally, Figure 2.5.7 shows a comparison between the median "IDA curves" associated to the collapse and the damage limit states for a specific building-site combination, together with the ratio of the median intensity measure associated to the collapse limit state (SLC) to that associated to the damage limit state (SLD), $IM_{50\_SLC}/IM_{50\_SLD}$, for some fixed building-site combinations. It can be seen that, on average, the value of this ratio, that can be defined as a sort of "behavior factor", is close to 3.2.



| Site | Configuration | IM50_SLC/ IM50_SLD |
|------|---------------|--------------------|
| Aq_A | C1_LEV2_CC | 2.59 |
| Aq_A | C1_LEV2_CL | 2.82 |
| Aq_A | C5_LEV2_CC | 3.45 |
| Aq_A | C5_LEV2_CL | 3.35 |
| Aq_A | C1_LEV3_CC | 3.59 |
| Aq_A | C1_LEV3_CL | 3.02 |
| Aq_A | C3_LEV3_CC | 3.32 |
| Aq_A | C3_LEV3_CL | 3.35 |
| Aq_A | C6_LEV3_CC | 3.43 |
| Aq_A | C6_LEV3_CL | 3.28 |
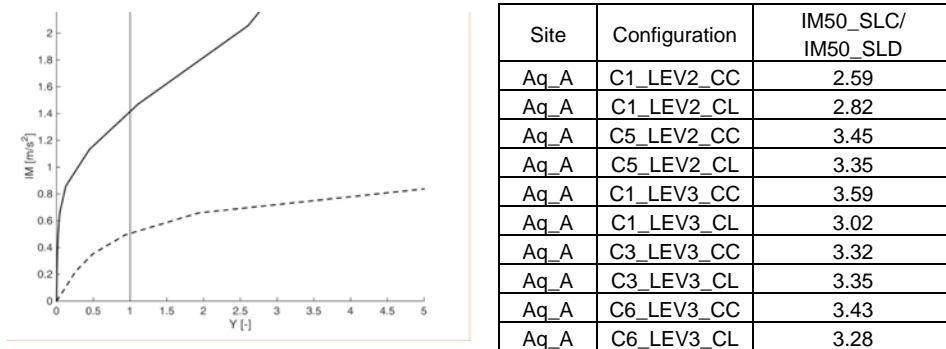
Figure 2.5.7 Left: median "IDA curves" associated to the collapse and the damage limit state for Aq, soil A, C1, 2 stories, CL. Right: values of the ratio between $IM_{50}$ associated to collapse limit state (SLC) and the value of $IM_{50}$ associated to damage limit state (SLD) for some fixed building-site combinations.

2.5.4.3  Results of the analyses with the refined macroelement model (Bracchi et al., 2017)

All the 22 building-site combinations (considering both the modelling hypotheses of long ring beams and short ring beams, to evaluate the effect of the epistemic uncertainty in the definition of the model) reported in Table 2.5.13 were re-analyzed adopting the improved version of the macroelement model (developed by Bracchi et al., 2017 and briefly described in Section 2.3.1.2), and defining mechanical properties according to the procedure reported in Appendix B. Different values of each parameter were sampled for each masonry pier of a given configuration, according to the procedure explained in Section 2.5.3.1.

As already discussed, to define the attainment of the collapse and damage limit states, specific thresholds (different for the X and the Y directions) have to be defined. For a given configuration, twenty different thresholds were defined, each one corresponding to one of the twenty models generated by sampling values from the probability distributions of the different aleatory variables. Therefore, for each configuration, pushover curves were derived for each one of the twenty models deriving from sampling, for a total of 1280 pushover analyses carried out.

The frequency of occurrence of the EDP threshold values (minima among those resulting from the different directions of analysis) obtained for a selected building configuration (Building C3, 3-story, long ring beams) are summarized in Figure 2.5.8, for the two limit states and both directions of analysis.

Figure 2.5.9 shows the pushover curves in the two directions of analysis (X in Figure 2.5.9a and Y in Figure 2.5.9b) for two selected building configurations (building C3 – three-story – short ring beam and building C5 – two-story – long ring beam), with the identification of the thresholds of the considered limit states. It can be noticed that the variability of the mechanical parameters determines a limited variability of the pushover curves, whereas it has a significant effect on the displacement thresholds corresponding to the ultimate limit state. For all the analyzed models, the limit condition determining the definition of the DLS was that associated with the lower bound fixed in the attainment of the 85% of the peak base-shear.
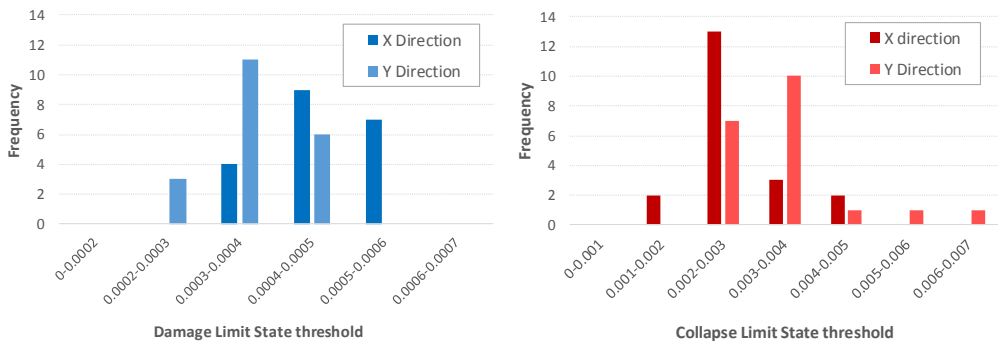


Figure 2.5.8 Frequency of occurrence of the EDP threshold values corresponding to DLS and CLS of Building C3, three-story (with the long ring beam assumption), for the two directions of analysis.
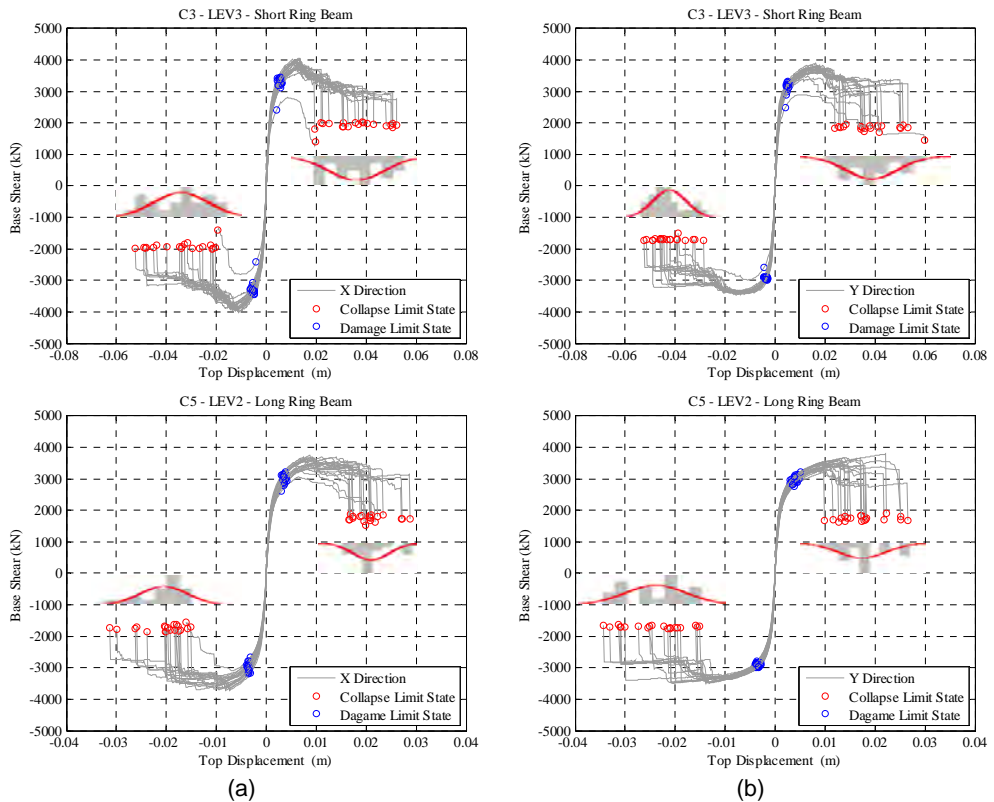
Figure 2.5.9 Pushover curves in the two directions, X in (a) and Y in (b), of analysis for 2 selected building configurations, with the identification of limit state thresholds: DLS in blue and CLS in red.

In the second step, an one-to-one association between these models and the twenty records of each stripe (corresponding to a value of the return period used for the definition of seismic input) was done, for a total of 4400 nonlinear dynamic analyses carried out. For each combination of site and soil type, it was possible to calculate the percentage of exceedance of the two considered limit states, for increasing values of the return period. For all the analyzed cases, the first exceedance never occurred for the return periods less than 500 years, both for damage and collapse limit states.

Figure 2.5.10 reports the frequency of occurrence of the two considered limit states, for some significant cases. From the shown comparisons, it is noticed that, fixing all the other conditions, the adoption of an effective length of the ring beams equal to the clear dimension of the openings ("short ring beam") results in a generally higher estimate of the building vulnerability, for both damage and collapse limit states (see in particular Building C6, three-story, located in L'Aquila soil type A).

As expected, the presence of an additional story (see for example the first comparison reported in Figure 2.5.10 for Building C1 located in L'Aquila soil type A) leads, in general, to a higher vulnerability compared to the corresponding two-story configuration, both with respect to damage and collapse limit states. Similar considerations could be extended also for the very last comparison reported in the figure, in which the influence of higher wall thickness (present in Building C7) in reducing the building vulnerability is clearly highlighted.
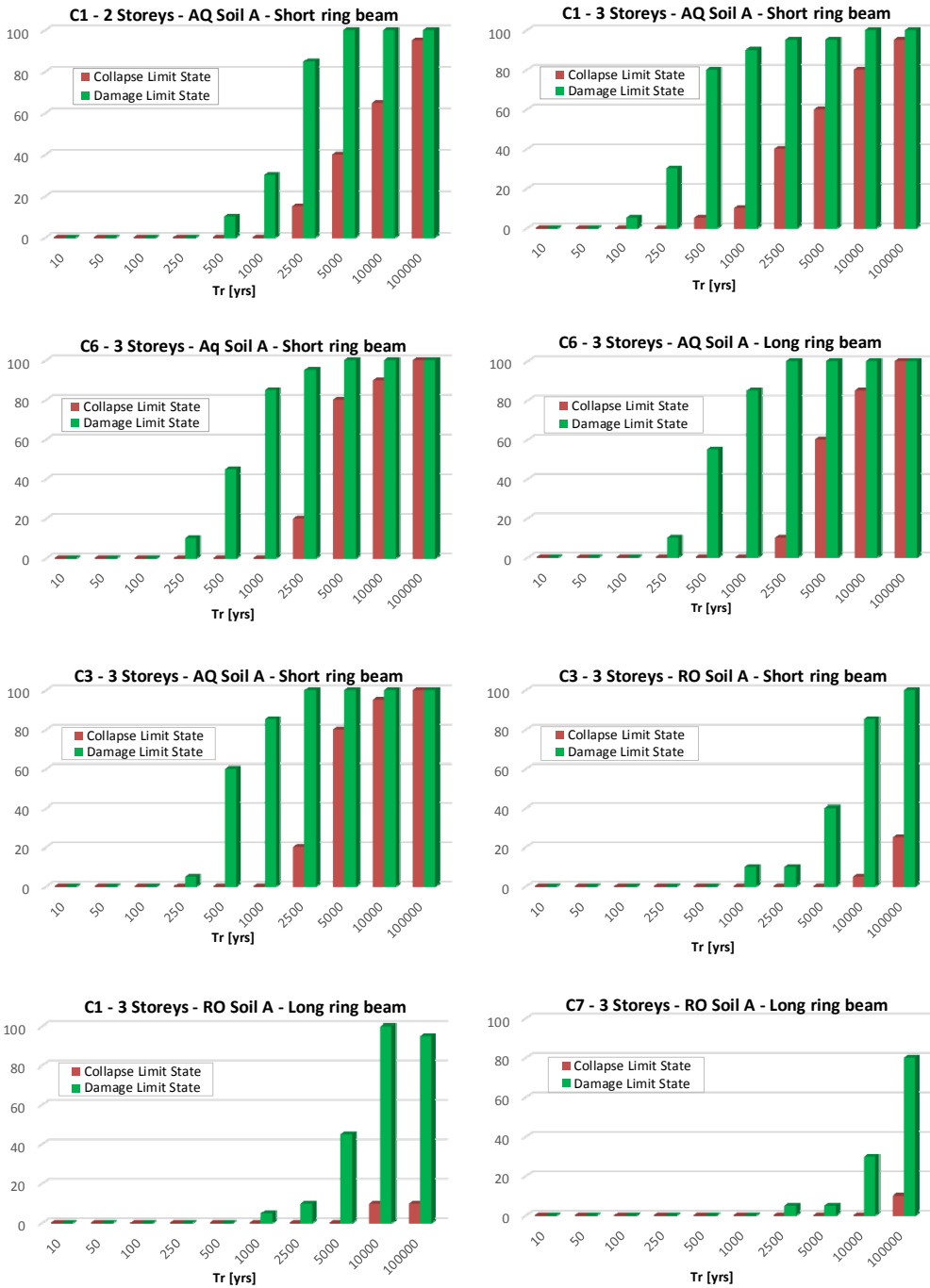
Figure 2.5.10. Frequency of occurrence (%) of damage (green bars) and collapse (red bars) limit states, as a function of return period, for some significant building-site combinations.

## 2.6 Final remarks

One of the distinctive features of masonry buildings is that different methods of analysis are usually adopted for the design. Therefore, for a given site, different structural configurations could be obtained for the same architectural layout, which leads to the attainment of different safety levels. Even though this result was expected, the differences among analysis methods turned out to be particularly significant.

The use of linear analysis without force redistribution among structural elements resulted into largely conservative designs, confirming the fact that this type of analysis cannot be used to design unreinforced masonry buildings in moderate-to-high seismicity regions, as already pointed out by Magenes (2006). The adoption of linear analysis with force redistribution in the case of type "C" configuration with the cantilever models allowed to design for seismicity levels up to (and including) the Rome site with soil A, thus with some additional margin not yet sufficient to reach the high seismicity levels.

On the other hand, unreinforced masonry buildings designed by means of nonlinear analysis turned out to be characterized by high values of probability of collapse. Possible causes could be the use of design parameters (shear drift limits) that are not safe enough with respect to experimentally derived values, which have been used for the assessment by nonlinear dynamic analyses. This could be possibly solved by properly defining drift limits identified from the distribution of the available experimental results for the near collapse limit state. An indication in this direction is already included in the draft of the updated version of the Italian building code.

The results, which were obtained to preliminarily quantify the effect of uncertainty propagation (design, modeling and aleatory uncertainty), highlighted that, even if the dispersion of the obtained fragility curves slightly increased, the role of record-to-record variability is predominant.

As a general conclusion, the work showed that the level of safety reached in the design is not homogeneous across the different sites, and that, in the high seismicity sites, the failure rate is even higher than the occurrence rate of the design earthquake considered for ultimate limit state. This is probably due to the use of nonlinear static analysis for masonry building design, which represents quite closely the actual nonlinear behavior (indeed, for other building types, it is used more for the assessment of existing buildings rather than for the design of new ones).

However, it is worth noting that the observed response of modern masonry buildings after the last earthquakes in Italy was fully satisfactory, even in the cases in which the shock was higher than the design one (L'Aquila 2009, Emilia 2012). This is probably due to some conservative assumptions adopted during design, such as: (a) the contribution of out-of-plane behavior of masonry wall is neglected; (b) material properties of masonry are probably higher than the nominal values indicated by the brick producers; (c) flexural criterion neglects the tensile strength of mortar joints that is not zero; (d) the equivalent frame model (piers and spandrels) localizes the deformation in structural elements and concentrates masses in rigid nodes: this increases the generalized forces and deformations (drift).

## 2.7   References

Bracchi S., Galasco A., Penna A. (2017) "An improved macroelement model accounting for energy dissipation in in-plane flexural behavior of masonry walls." Proceedings of the 16th World Conference on Earthquake Engineering, Santiago, Chile.

Cattari S., Lagomarsino S. (2013) Masonry structures, pp.151-200, in: Developments in the field of displacement based seismic assessment, Edited by T. Sullivan and G.M.Calvi, Ed. IUSS Press and EUCENTRE, pp.524, ISBN:978-88-6198-090-7.

Gambarotta L., Lagomarsino S. (1997) "Damage models for the seismic response of brick masonry shear walls. Part II: the continuum model and its applications." Earthquake Engineering & Structural Dynamics, 26:441–462.

Lagomarsino S, Penna A, Galasco A, Cattari S. (2013) TREMURI program: an equivalent frame model for the nonlinear seismic analysis of masonry buildings, Engineering Structures, 56: 1787-1799.

Magenes G. (2006) "Masonry building design in seismic areas: recent experiences and prospects from a European standpoint", Keynote 9, 1st European Conference on Earthquake Engineering and Engineering Seismology, 3-8 September 2006, Geneva, Switzerland, CD-ROM.

Magenes G., Morandi P., Penna A. (2008) "Experimental in-plane cyclic response of masonry walls with clay units" Proceedings of the 14th WCEE, Beijing, China, Paper No. 95, 8 p.

Manzini C.F., Morandi P., Magenes G., Calliari R. (2013) "ANDILWall (versione 3.0) Software di calcolo e verifica di edifici in muratura ordinaria, armata o mista – Manuale d'uso" (in Italian).

Morandi P., Albanesi L., Magenes G. (2015) "Prestazioni sismiche di pannelli murari in blocchi di laterizio a setti sottili soggetti a test ciclici nel piano", Atti del XVI Convegno ANIDIS - L'ingegneria Sismica in Italia, L'Aquila, Italy.

Morandi P., Albanesi L., Magenes G. (2016) "In-plane test campaign on different load-bearing URM typologies with thin shell and web clay units," 16th International Brick and Block Masonry Conference, Padua, Italy.

Penna A., Lagomarsino S., Galasco A. (2014) "A nonlinear macroelement model for the seismic analysis of masonry buildings," Earthquake Engineering & Structural Dynamics, 43(2): 159-179.

Petry S., Beyer K. (2014) Influence of boundary conditions and size effect on the drift capacity of URM walls, Engineering Structures, 65, 76-88.

S.T.A.Data 2015, 3Muri Program, Release 10.1 (www.3muri.com).

Tondelli M., Graziotti, F., Rossi, A., Magenes, G. (2015) "Characterization of masonry materials in the Groningen area by means of in-situ and laboratory testing", Technical Report, Eucentre, Pavia, Italy, www.eucentre.it/nam.

# CHAPTER III – PRECAST INDUSTRIAL STRUCTURES

## 3.1  Introduction

In the following, industrial, single-story precast RC buildings are investigated. The structural elements are designed and verified according to the Italian building code D. M. 14/01/2008 2008 and Circolare 02/02/2009 n. 617 2009. For further structural verifications, missing from or not well specified in the Italian building code, Eurocodes (CEN 2004; CEN 2005) and CNR (CNR 10018 1999; CNR 10025/98 2000) provisions are taken into account.

The structural non-linear behavior is modeled using a lumped plasticity approach and the seismic response of the modeled buildings is investigated by means of static and dynamic analyses. Failure criteria are defined, considering the global and local structural response, and the safety factors with respect to the collapse condition are evaluated in order to describe the structural reliability.

## 3.2  Case study structures

The reference structure consists of precast columns fixed at the base with isolated socket foundations: the sockets are connected in both directions by a concrete gridwork. The columns are connected, by means of dowel connections, to the main precast prestressed beams in the transversal direction, and by means of bolted connections to the girders, in the longitudinal direction (Figure 3.2.1). The main precast beams have variable cross-section width and height, with the top sloping at 10%. The longitudinal girder beams are assumed to have a rectangular cross section. They are also connected to the main beams by bolted steel angles. The roof consists of precast adjacent $\pi$-shaped elements. A rigid diaphragm is considered, obtained through a cast in situ concrete slab, 5 cm deep, which connects the ribs.

The cladding system consists of vertical precast panels (specific weight of 4 kN/m$^2$), connected to the horizontal roof beams (i.e. to the main beams, along the transversal direction, and to the girders, along the longitudinal direction). Assuming industrial use for the building, the presence of a crane is considered: precast corbels in the internal side of the columns support crane runway beams to which the crane is connected. The crane runway beams are considered to be the same for all the case studies, i.e., HEA400 steel beam, assuming that they do not reach the maximum deflection level according to CNR provisions ($f_{max}$=L/800, where $f_{max}$ is the maximum deflection displacement and L is the beam span).
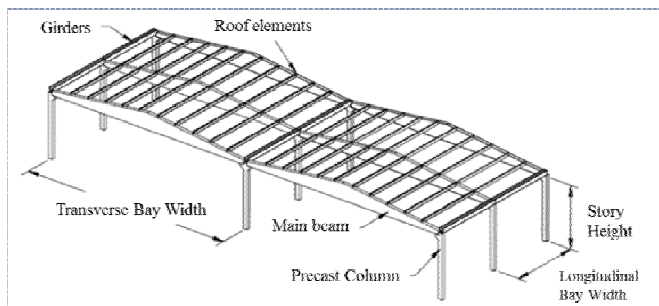


Figure 3.2.1 Structural layout for industrial precast buildings.

### 3.2.1  Geometry and materials

The geometrical features of the structural and non structural elements, as well as the span lengths and the building height, reflect the structural typology frequently used for Italian industrial buildings according to the available national databases. Figure 3.2.2a shows the schematic plan view of the considered structures, with one bay in the transversal direction (i.e. the x direction) and four bays in the longitudinal direction (i.e., the z direction). Figure 3.2.2b shows the transversal frame with the position of the column corbel.

The span length along x ($L_1$) and y direction ($L_2$), the corbel position ($L_3$) and the column height ($H_{tot}=L_3+L_4$) are assumed as variables so that four different geometries can be defined. Table 3.2.1 shows the span lengths in the transversal and longitudinal direction, the column height and the runway crane beam position in the four cases. In the following, geometries with $L_1$=15m, $L_2$=6m are defined as "short span" (SS), while geometries with $L_1$=20m, $L_2$=8m are defined as "long span" (LS).
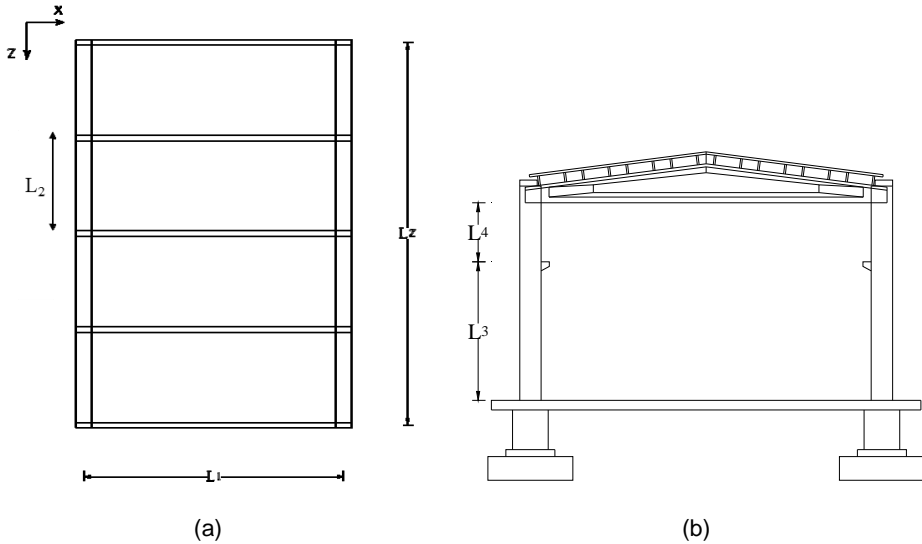


(a)                                                              (b)

Figure 3.2.2 Schematic plan view (a) and transversal frame (b).

Table 3.2.1 Geometry parameters for the considered case studies.

| Geometry | L1 | L2 | Lz | L3 | L4 | Htot |
|---|---|---|---|---|---|---|
| | [m] | [m] | [m] | [m] | [m] | [m] |
| 1 | 15.00 | 6.00 | 24.00 | 4.50 | 1.50 | 6.00 |
| 2 | 20.00 | 8.00 | 32.00 | 4.50 | 1.50 | 6.00 |
| 3 | 15.00 | 6.00 | 24.00 | 7.50 | 1.50 | 9.00 |
| 4 | 20.00 | 8.00 | 32.00 | 7.50 | 1.50 | 9.00 |

Table 3.2.2 shows the adopted materials and the corresponding nominal values of their mechanical properties. In the following, Table 3.2.2 to Table 3.2.5 show the mechanical properties of the precast concrete C45/55 [11.2.10 NTC], of the reinforcement steel B450C [11.3.2.1 NTC] and of the prestressing steel [11.3.3.2 NTC], evaluated according to the Italian building code. In particular, Table 3.2.3 refers to the concrete properties showing in the order of: the characteristic compressive strength ($f_{ck}$), the average and characteristic tensile strengths ($f_{ctm}$ and $f_{ctk}$, respectively), the average Young modulus, the design compressive strength, and the ultimate strain value. Table 3.2.4 refers to the reinforcement steel properties showing in the order of: the characteristic yielding strength ($f_{yk}$), the design yielding strength ($f_{yd}$), the Young modulus ($E_s$), and the ultimate strain value ($\varepsilon_{su}$). Table 3.2.5 refers to the prestressing steel properties and shows in the order of: the characteristic ultimate tensile strength ($f_{ptk}$), the characteristic tensile strength for 1% of residual strain ($f_{p(1)k}$), the Young modulus ($E_s$) and the ultimate strain values ($\varepsilon_{su}$).

Table 3.2.2 Adopted materials for structural elements.

| Element | Concrete | Mild steel | Prestressing steel |
|---|---|---|---|
| Concrete slab | C25/30 | B450C | - |
| Roof element | C45/55 | B450C | Seven-wire strands |
| Precast main beam | C45/55 | B450C | Seven-wire strands |
| Column | C45/55 | B450C | - |

Table 3.2.3 Mechanical properties for C45/55 precast concrete.

| $f_{ck}$ | $f_{ctm}$ | $f_{ctk}$ | $E_{cm}$ | $f_{cd}$ | $\varepsilon_{cu}$ |
|---|---|---|---|---|---|
| [N/mm$^2$] | [N/mm$^2$] | [N/mm$^2$] | [N/mm$^2$] | [N/mm$^2$] | [-] |
| 45.0 | 3.80 | 2.66 | 36283 | 25.5 | 0.35% |

Table 3.2.4 Mechanical properties for B450C reinforcement steel.

| $f_{yk}$ | $f_{yd}$ | $E_s$ | $\varepsilon_{su}$ |
|---|---|---|---|
| [N/mm$^2$] | [N/mm$^2$] | [N/mm$^2$] | [-] |
| 450.0 | 391.3 | 200000 | 7.50% |

Table 3.2.5 Mechanical properties for prestressing steel.

| $f_{ptk}$ | $f_{p(1)k}$ | $E_s$ | $\varepsilon_{su}$ |
|---|---|---|---|
| [N/mm$^2$] | [N/mm$^2$] | [N/mm$^2$] | [-] |
| 1870 | 1670 | 190000 | 1.00% |

## 3.3   Design of precast buildings

### 3.3.1   Load combinations

The load combinations considered for the structural design according to D.M. 14/01/2008 are reported in the following [2.5.3 - NTC]:

a) Fundamental combination, applied for the ultimate limit states:

$$\gamma_{G1} \cdot G_1 + \gamma_{G2} \cdot G_2 + \gamma_P \cdot P + \gamma_{Q1} \cdot Q_{k1} + \gamma_{Q2} \cdot \Psi_{02} \cdot Q_{k2} + \gamma_{Q3} \cdot \Psi_{03} \cdot Q_{k3} + \cdots \qquad 3.1$$

b) Characteristic combination, applied for irreversible service limit states:

$$G_1 + G_2 + P + Q_{k1} + \Psi_{02} \cdot Q_{k2} + \Psi_{03} \cdot Q_{k3} + \cdots \qquad 3.2$$

c) Frequent combination, applied for reversible service limit states:

$$G_1 + G_2 + P + \Psi_{11} \cdot Q_{k1} + \Psi_{22} \cdot Q_{k2} + \Psi_{23} \cdot Q_{k3} + \cdots \qquad 3.3$$

d) Quasi permanent combination, applied for long term effects:

$$G_1 + G_2 + P + \Psi_{21} \cdot Q_{k1} + \Psi_{22} \cdot Q_{k2} + \Psi_{23} \cdot Q_{k3} + \cdots \qquad 3.4$$

e) Seismic combination, applied for service and ultimate limit states related to the seismic action E:

$$E + G_1 + G_2 + P + \Psi_{21} \cdot Q_{k1} + \Psi_{22} \cdot Q_{k2} + \Psi_{23} \cdot Q_{k3} + \cdots \qquad 3.5$$

In the above equations:

- $G_1$ is the dead load of the structural elements;
- $G_2$ is the dead load of the non-structural elements;
- P is the prestressing load;
- E is the seismic load;
- $Q_{k1}$ is the characteristic value of the predominant variable load;
- $Q_{k,i}$ is the characteristic value of the non-predominant variable load;
- $\gamma_{G,j}$ is the partial coefficient for the dead load [Tab. 2.6.I – NTC];
- $\gamma_P$ is the partial coefficient for prestressing load;
- $\gamma_{Q,i}$ is the partial coefficient for the variable load [Tab. 2.6.I – NTC];
- $\psi_{ij}$ is the combination coefficient for the variable load [Tab. 2.5.I – NTC].

### 3.3.2  Seismic loads

The seismic design of the precast buildings is performed by means of modal response spectrum analysis. According to the Italian building code D.M. 14/01/2008, the seismic action can be evaluated using response spectra, related to the site hazard and the reference limit state. The site hazard is defined by the seismic hazard parameters ($a_g$, $F_0$, $T_c^*$), for damage limit state DLS and life safety limit state (LLS), reported in the Annex B of the Italian building code, depending on the geographical position and on the return periods. Table 3.3.1 shows the seismic hazard parameters for the reference sites and for the considered limit states in the design process.

Table 3.3.1 Hazard parameters.

| Site | Longitude | Latitude | Limit state | $a_g$ [g] | $F_o$ [-] | $T_c^*$ [s] |
|---|---|---|---|---|---|---|
| L'Aquila | 13.399 | 42.349 | DLS | 0.104 | 2.332 | 0.281 |
|  |  |  | LLS | 0.261 | 2.364 | 0.347 |
| Naples | 14.268 | 40.854 | DLS | 0.060 | 2.335 | 0.312 |
|  |  |  | LLS | 0.168 | 2.374 | 0.338 |
| Rome | 12.479 | 41.872 | DLS | 0.055 | 2.502 | 0.268 |
|  |  |  | LLS | 0.123 | 2.633 | 0.288 |
| Caltanissetta | 14.060 | 37.480 | DLS | 0.034 | 2.509 | 0.262 |
|  |  |  | LLS | 0.073 | 2.587 | 0.436 |
| Milan | 9.186 | 45.465 | DLS | 0.024 | 2.554 | 0.191 |
|  |  |  | LLS | 0.050 | 2.656 | 0.280 |

3.3.2.1  Soil and topographic category

The response spectrum depends on the soil and topographic category. The soil category can be defined considering the stratigraphic profiles and the average shear wave velocity $V_{s,30}$. For the reference case studies, referring to Tab. 3.2.II – NTC, soil type A and type C are considered. Flat ground level is assumed for the case studies (topographic category $T_1$, according to Tab. 3.2.IV – NTC).

3.3.2.2  Elastic response spectrum for the horizontal acceleration component

The elastic response spectrum is defined by Eq. 3.2.4 (horizontal acceleration component) and Eq. 3.2.10 (vertical acceleration component) of the Italian building code. Table 3.3.2 to Table 3.3.4 show the seismic parameters for the horizontal (soil type A and soil type C) and vertical

spectrum definition: the stratigraphic ($S_S$) and topographic ($S_T$) soil factor ($S=S_S \cdot S_T$), the characteristic period values ($T_B$, $T_C$, $T_D$) and the damping factor ($\xi$). According to the Italian building code, design seicmic vertical component is only taken into account for medium-high seismicity zones.

In the following, Figure 3.3.1 to Figure 3.3.5 show the horizontal and vertical elastic response spectra for soil type A and C, for life safety and damage limit state and for each considered site.

Table 3.3.2 Horizontal elastic acceleration spectrum parameters for soil type C.

| Site | Limit state | $S_S$ | $S_T$ | $S$ | $C_c$ | $T_C$ | $T_B$ | $T_D$ | $\xi$ |
|------|-------------|-------|-------|-----|-------|-------|-------|-------|-------|
| | | [-] | [-] | [-] | [-] | [sec] | [sec] | [sec] | [%] |
| L'Aquila | DLS | 1.50 | | 1.50 | 1.60 | 0.449 | 0.150 | 2.016 | |
| | LLS | 1.33 | | 1.33 | 1.49 | 0.517 | 0.172 | 2.644 | |
| Naples | DLS | 1.50 | | 1.50 | 1.54 | 0.481 | 0.160 | 1.840 | |
| | LLS | 1.46 | | 1.46 | 1.50 | 0.508 | 0.169 | 2.272 | |
| Rome | DLS | 1.50 | 1.00 | 1.50 | 1.622 | 0.435 | 0.145 | 1.820 | 5% |
| | LLS | 1.50 | | 1.50 | 1.583 | 0.456 | 0.152 | 2.092 | |
| Caltanissetta | DLS | 1.50 | | 1.50 | 1.634 | 0.428 | 0.143 | 1.736 | |
| | LLS | 1.50 | | 1.50 | 1.381 | 0.602 | 0.201 | 1.892 | |
| Milan | DLS | 1.50 | | 1.50 | 1.813 | 0.346 | 0.115 | 1.696 | |
| | LLS | 1.50 | | 1.50 | 1.598 | 0.448 | 0.149 | 1.800 | |

Table 3.3.3 Horizontal elastic acceleration spectrum parameters for soil type A.

| Site | Limit state | $S_S$ | $S_T$ | $S$ | $C_c$ | $T_C$ | $T_B$ | $T_D$ | $\xi$ |
|------|-------------|-------|-------|-----|-------|-------|-------|-------|-------|
| | | [-] | [-] | [-] | [-] | [sec] | [sec] | [sec] | [%] |
| L'Aquila | DLS | | | | | 0.281 | 0.094 | 2.016 | |
| | LLS | | | | | 0.347 | 0.116 | 2.644 | |
| Naples | DLS | | | | | 0.312 | 0.104 | 1.840 | |
| | LLS | | | | | 0.338 | 0.113 | 2.272 | |
| Rome | DLS | 1.00 | 1.00 | 1.00 | 1.00 | 0.268 | 0.089 | 1.820 | 5% |
| | LLS | | | | | 0.288 | 0.096 | 2.092 | |
| Caltanissetta | DLS | | | | | 0.262 | 0.087 | 1.736 | |
| | LLS | | | | | 0.436 | 0.145 | 1.892 | |
| Milan | DLS | | | | | 0.191 | 0.064 | 1.696 | |
| | LLS | | | | | 0.280 | 0.093 | 1.800 | |

Table 3.3.4 Vertical elastic acceleration spectrum parameters.

| Site | Limit state | $S_S$ | $S_T$ | S | $F_V$ | $T_C$ | $T_B$ | $T_D$ | ξ |
|------|-------------|-------|-------|---|-------|-------|-------|-------|---|
|      |             | [-] | [-] | [-] | [-] | [sec] | [sec] | [sec] | [%] |
| L'Aquila | LLS | 1.00 | 1.00 | 1.00 | 1.63 | 0.05 | 0.15 | 1.00 | 5% |
| Naples |  |  |  |  | 1.31 |  |  |  |  |
| Rome | - | - | - | - | - | - | - | - | - |
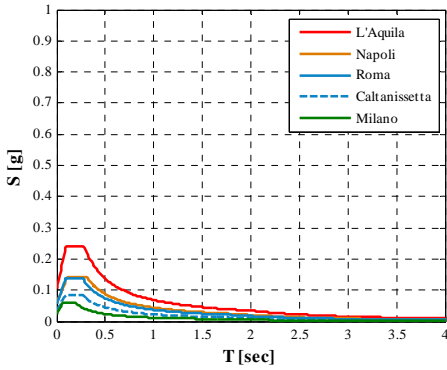


Figure 3.3.1 Elastic response spectrum for horizontal acceleration component (DLS, soil type A).
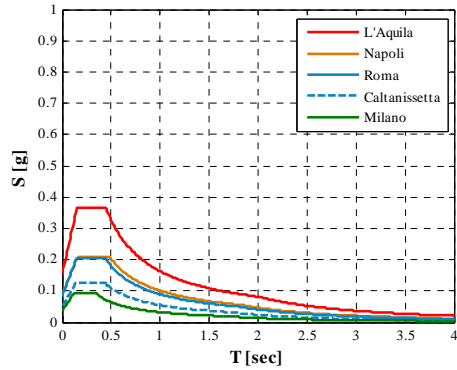


Figure 3.3.2 Elastic response spectrum for horizontal acceleration component (DLS, soil type C).
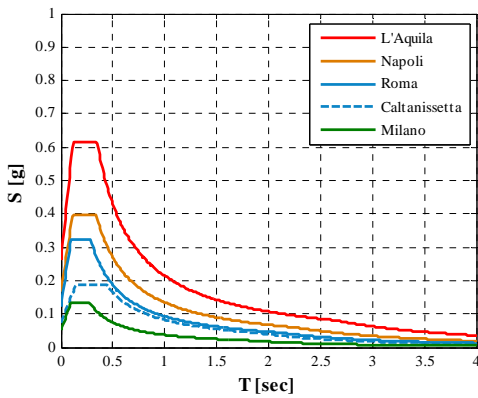


Figure 3.3.3 Elastic response spectrum for horizontal acceleration component (LLS, soil type A).
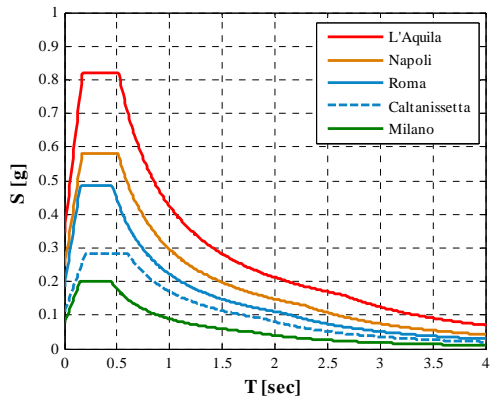


Figure 3.3.4 Elastic response spectrum for horizontal acceleration component (LLS, soil type C).
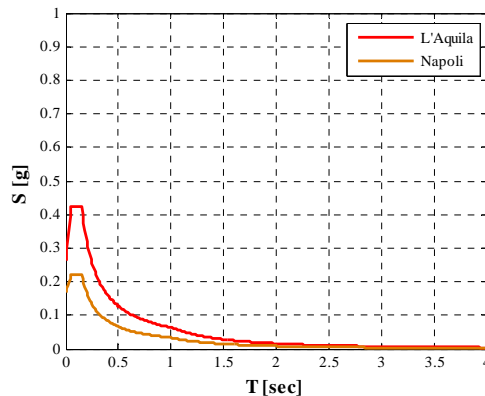
Figure 3.3.5 Elastic response spectrum for vertical acceleration component (LLS).

### 3.3.2.3 Design response spectrum for life safety limit state

The design response spectrum can be obtained from the elastic one, changing $\eta$ with $1/q$, i.e., the behavior factor for precast structures with isostatic columns equal to:

$$q = q_0 \cdot K_R \qquad\qquad 3.6$$

For the considered structural typology, $q_0$ is equal to 3.5 for high ductility class and equal to 2.5 for low ductility class[2].

$K_R$ is the regularity coefficient equal to one for regular structures (in plan and elevation). For the case studies (low ductility class[2] and regular plan and elevation), the behavior factor which should be applied to the seismic horizontal component is equal to 2.5. The behavior factor for the seismic vertical component is equal to 1.5.

Figure 3.3.6 and Figure 3.3.7 show the design response spectra of horizontal acceleration component, for the life limit state, corresponding to soil A and C, respectively. Figure 3.3.8 shows the design response spectrum of vertical acceleration component.

---

[2] EC08 adopts three ductlility classes for building structures: Ductility Class Low (DC L), Ductility Class Medium (DC M), Ductility Hight (DC H). EC08 suggests using DCL is only for sites with low seismicity (i.e., in areas with maximum ground design acceleration less than 0.10g) and normally the buildings are designed for DC M or DC H, which correspond to "CD B" (Classe di duttilità bassa, q>1.5) and "CD A" (Classe di duttilità alta, q>4.0) in NTC08, respectively.
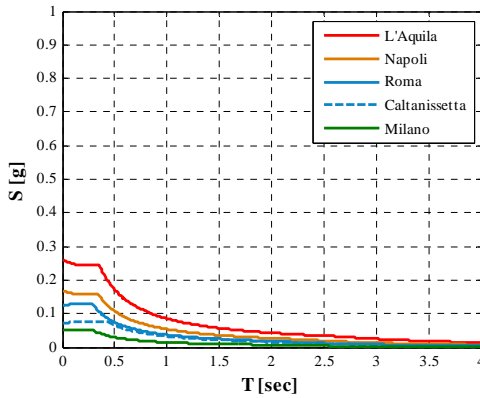
Figure 3.3.6 Design response spectrum for horizontal acceleration (LLS, soil type A).
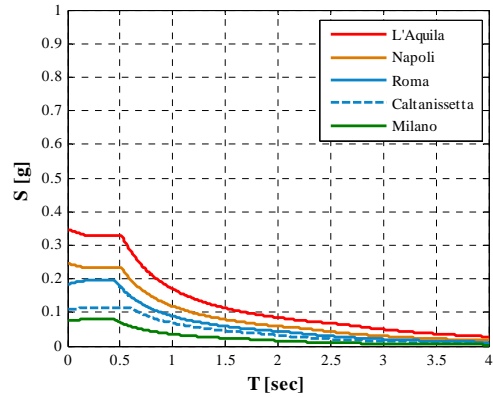
Figure 3.3.7 Design response spectrum for horizontal acceleration (LLS, soil type C).
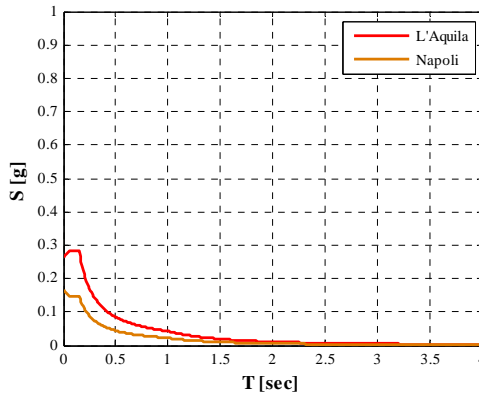


Figure 3.3.8 Design response spectrum for vertical acceleration (LLS).

### 3.3.3    Non-seismic loads

For the structural design of the constitutive elements of the reference buildings, also non seismic loads are considered. In particular, dead loads can be evaluated considering the structural self-weight of the elements. Figure 3.3.9 shows the considered dead loads in the model, in which:

- $p_{beam}$ is the distributed dead load of the main beam
- $q_{roof}$ is the distributed dead load due to the roof structural and non-structural elements. For the rigid diaphragm the $q_{roof}$ takes into account the dead loads of the cast in situ slab components;
- $N_{column}$ is the axial force on the column due to its self-weight dead load $p_{col}$;
- $N_{girder}$ is the axial force on the column due to self-weight of the girders;
- $N_{crane}$ and $N_{c.beam}$ are the self-weight of the crane (50kN) and of the crane runway beam ($N_{c.beam}=p_{c.beam}\cdot L_2/2$, considering $p_{c.beam}=1.55kN/m$).
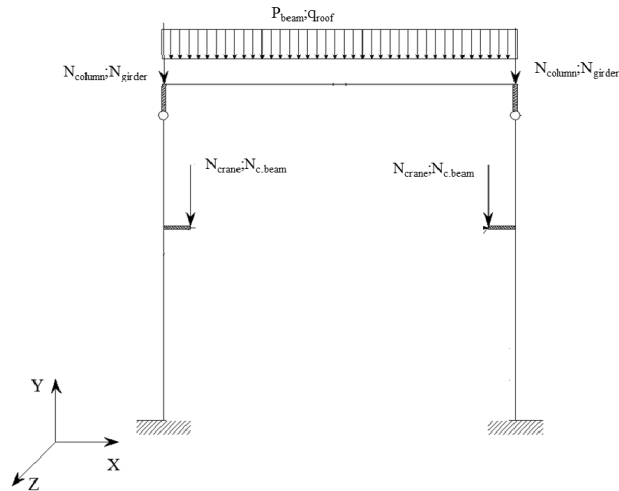
Figure 3.3.9 Dead loads configuration.

In the following, variable loads are described in detail. Accidental loads can be defined considering accessible roof for maintenance ($q_{acc}$=0.5kN/m). Moreover, it should be considered as variable load the axial force on the column top end due to the water flowing in the girder beams $N_{water}$=$p_{water} \cdot L_2$, assuming $p_{water}$=1.50kN/m.

3.3.3.1  Snow load

The static load due to the snow weight can be evaluated as:

$$q_s = \mu_i \cdot q_{sk} \cdot C_E \cdot C_t \qquad\qquad 3.7$$

where:

- $q_s$ is the snow weight on the roof;
- $\mu_i$ is the roof shape coefficient [3.4.5 – NTC], assumed equal to 0.8;
- $q_{sk}$ is the characteristic value of the ground snow weight, with a return period of 50 years at the site of interest [3.4.2 – NTC]. It depends on elevation ($a_s$) and on the local climatic and exposition conditions, considering the variability in the snow precipitation.
- $C_E$ is the exposition coefficient [3.4.3 – NTC], assumed equal to 1;
- $C_t$ is the thermal coefficient [3.4.4 – NTC], assumed equal to 1.

Table 3.3.5 shows load values for the five considered sites.

Table 3.3.5 Snow load parameters.

| Site | Snow zone | $a_s$ | $q_{sk}$ | $\mu_i$ | $C_E$ | $C_t$ | $q_s$ |
|------|-----------|-------|----------|---------|-------|-------|-------|
| [-] | [-] | [m] | [kN/m²] | [-] | [-] | [-] | [kN/m²] |
| L'Aquila | III | 716 | 1.64 | | | | 1.31 |
| Naples | III | 6 | 0.60 | | | | 0.48 |
| Rome | III | 60 | 0.60 | 0.80 | 1.00 | 1.00 | 0.48 |
| Caltanissetta | III | 585 | 1.26 | | | | 1.01 |
| Milan | I - Mediterranea | 110 | 1.50 | | | | 1.20 |

3.3.3.2 Wind load

The wind action is generally considered as a horizontal load acting along the principal directions of the building. It consists of a dynamic load which can be modeled as equivalent static loads represented by normal forces (on the orthogonal surfaces with respect to the wind direction) and tangential forces (on the parallel surfaces with respect to the wind direction).

The equivalent static loads can be evaluated according to the Italian building code [3.3 - NTC], considering the parameters in Table 3.3.6, which depend on the specific site. In particular, the reference velocity $v_b$ and the reference kinetic pressure $q_b$ can be evaluated according to Equations 3.3.1 and 3.3.4, respectively, of the Italian building code.

Table 3.3.6 Wind load parameters

| Site | Wind zone | Roughness | Exposition category | $a_s$ | $a_0$ | $k_a$ | $v_{b,0}$ | $v_b$ | $q_b$ |
|---|---|---|---|---|---|---|---|---|---|
| [-] | [-] | [-] | [-] | [m] | [m] | [1/s] | [m/s] | [m/s] | [kN/m$^2$] |
| L'Aquila | 3 | | IV | 716 | 500 | 0.02 | 27.00 | 31.32 | 0.61 |
| Naples | 3 | | III | 6 | 500 | 0.02 | 27.00 | 27.00 | 0.46 |
| Rome | 3 | B | III | 60 | 500 | 0.02 | 27.00 | 27.00 | 0.46 |
| Caltanissetta | 4 | | IV | 585 | 500 | 0.02 | 28.00 | 29.70 | 0.55 |
| Milan | 1 | | IV | 110 | 1000 | 0.01 | 25.00 | 25.00 | 0.39 |

The normal wind pressure can be evaluated as:

$$p = q_b \cdot c_e \cdot c_p \cdot c_d$$                                            3.8

where:

- $q_b$ is the reference kinetic pressure [3.3.6 – NTC];
- $c_e$ is the exposure coefficient [3.3.7 – NTC]. The exposure coefficient depends on the distance from foundation z, on the topography ($c_t = 1$) and on the exposure category. For the case studies, it is assumed to be constant along the building height and equal to the maximum possible value. The exposure category can be defined depending on the site geographical position and on the site's ground roughness;
- $c_p$ is the shape coefficient, which depends on the structural typology and geometry and on the building orientation with respect to the wind direction [C3.3.10 – Circ. N.617]. It is assumed to be equal to 0.8 for the external windward surfaces, equal to 0.4 for the external leeward surfaces and equal to ±0.2 for the internal surfaces (3.12);
- $c_d$ is the dynamic coefficient, assumed equal to 1, which accounts for the non-contemporary maximum effects related to the static pressures and the dynamic structural response [3.3.8 – NTC].

The tangential pressure can be evaluated as:

$$p_f = q_b \cdot c_e \cdot c_f$$                                            3.9

where $c_f$ is the friction coefficient, assumed equal to 0.02 [C3.3.11 – Circ. n.617], depending on the surface roughness.

The normal and tangential wind loads are applied in both directions and the maximum effects in terms of horizontal force at the column top end is finally considered ($F_v$, Figure 3.3.11).
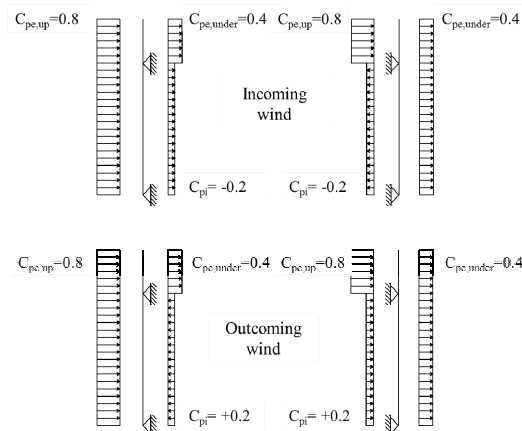
Figure 3.3.10 Shape coefficient values for wind load.
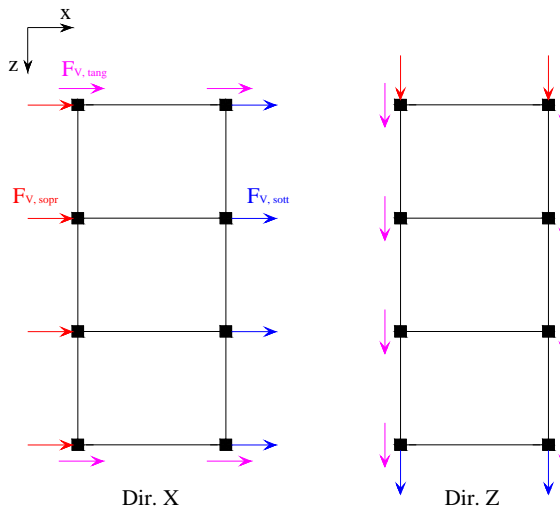


Figure 3.3.11 Considered directions for normal and tangential wind loads.

### 3.3.3.3 Crane load

The presence of the crane induces, on the structure, static and dynamic actions, which can be assumed as equivalent static actions. In particular, the following forces should be considered:

- $F_1$ that is the hanged weight;
- $F_t$ is the horizontal force due to the crane twist movements, according to CNR 10021:

$$F_t = \frac{1}{7} \left( N_{car} + F_1 \right) \qquad 3.10$$

- $F_b$ is the horizontal braking force during the crane movements:

$$F_b = \frac{1}{10}\,(N_{car} + F_1)$$

3.11

The position of the crane loads considers variability in the crane position (along the longitudinal direction of the building, Figure 3.3.12a and of the hook (along the transversal direction of the building, Figure 3.3.12b).



(a)                                                                                (b)
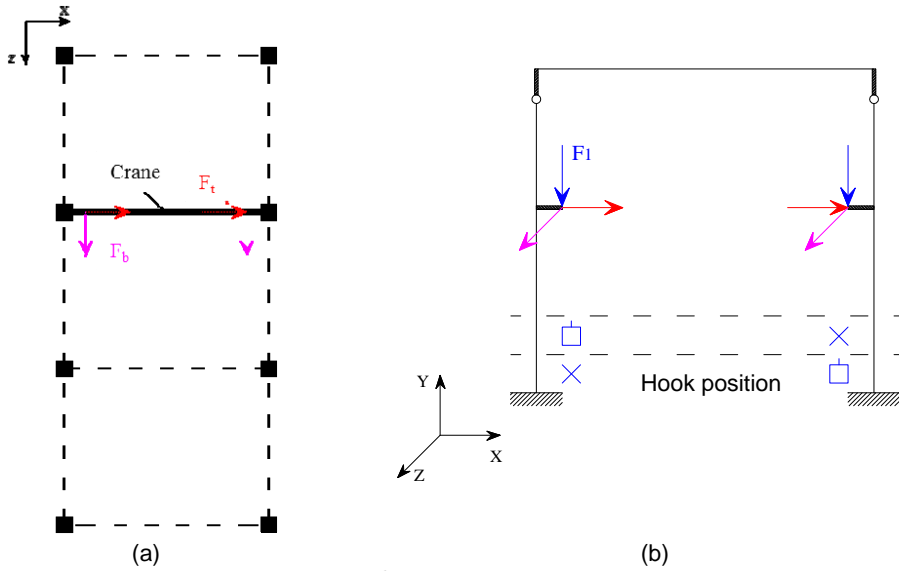
Figure 3.3.12 Crane position variability.

### 3.3.3.4 Geometrical imperfections

For industrial precast structures characterized by very high columns, geometrical imperfections due to wrong positioning of the column can be taken into account using global equivalent static forces according to the Italian building code [C4.2.3.5 – Circ. N.617] and Eurocodes [5.2 – EC2].

In particular, considering the total height of the column h, the total imperfection is assumed equal to:

$$\phi = \alpha_h \cdot \alpha_m \cdot \phi_0$$

3.12

where:

- $\phi_0$ = h/200 is the reference value of the geometrical imperfection for the single column;
- h is the building height;
- $\alpha_h$ is the reduction factor $\alpha_h = \dfrac{2}{\sqrt{h}}$ with $2/3 \leq \alpha_h \leq 1$;
- $\alpha_m$ is the reduction factor $\alpha_m = \sqrt{0.5 \cdot \left(1 + \dfrac{1}{m}\right)}$ which accounts for the number of elements (m) along the considered direction.

The global equivalent static force at the column top end can be evaluated as:

$$H_i = \phi \cdot N_a \qquad\qquad 3.13$$

In which $N_a$ is the column axial force evaluated for ultimate limit state combination and for the seismic one. The equivalent static force is calculated for the lateral and corner columns.

### 3.3.3.5 Thermal variations

It is assumed that thermal effects do not induce critical effects for the reference buildings so that it is possible to consider only the constant thermal action obtained from Tab. 3.5.II – NTC:

$$\Delta T_U = T - T_0 = \pm 15° \qquad\qquad 3.14$$

The thermal load is applied to the roof elements introduced in the numerical model, i.e. the girder beams and the main variable beams.

### 3.3.4 Ultimate limit state load combinations

Considering the load combinations defined in the previous section, with reference to the ultimate limit state combination, each of the variable actions described above should be considered alternatively as predominant or not. For this reason, the following combinations could be recognized:

a) Snow and geometrical imperfections considered as predominant actions:

$$E_d = \gamma_G \cdot \left(N_{pil} + p_{beam} + q_{roof} + N_{girder} + N_{crane} + N_{c.beam}\right) + \gamma_Q$$
$$\cdot (q_{snow} + H_i) + \gamma_Q \cdot \psi_0$$
$$\cdot (F_1 + F_t + F_b + F_V + \Delta T_U + N_{water} + q_{acc}) \qquad 3.15$$

b) Wind and geometrical imperfections considered as predominant actions:

$$E_d = \gamma_G \cdot \left(N_{pil} + p_{beam} + q_{roof} + N_{girder} + N_{crane} + N_{c.beam}\right) + \gamma_Q \cdot \left(F_V + H_i\right)$$
$$+ \gamma_Q \cdot \psi_0 \cdot (F_1 + F_t + F_b + q_{snow} + \Delta T_U + N_{water} + q_{acc}) \qquad 3.16$$

c) Thermal variations and geometrical imperfections considered as predominant actions:

$$E_d = \gamma_G \cdot \left(N_{pil} + p_{beam} + q_{roof} + N_{girder} + N_{crane} + N_{c.beam}\right) + \gamma_Q$$
$$\cdot (\Delta T_U + H_i) + \gamma_Q \cdot \psi_0$$
$$\cdot (F_1 + F_t + F_b + F_V + q_{snow} + N_{water} + q_{acc}) \qquad 3.17$$

d) Crane loads and geometrical imperfections considered as predominant actions:

$$E_d = \gamma_G \cdot \left(N_{pil} + p_{beam} + q_{roof} + N_{girder} + N_{crane} + N_{c.beam}\right) + \gamma_Q$$
$$\cdot (F_1 + F_t + F_b + H_i) + \gamma_Q \cdot \psi_0$$
$$\cdot (q_{snow} + F_V + \Delta T_U + N_{water} + q_{acc}) \qquad 3.18$$

e) Wind and geometrical imperfections considered as predominant actions, snow neglected:

$$E_d = \gamma_G \cdot \left(N_{pil} + p_{beam} + q_{roof} + N_{girder} + N_{crane} + N_{c.beam}\right) + \gamma_Q$$
$$\cdot (F_V + H_i) + \gamma_Q \cdot \psi_0$$
$$\cdot (F_1 + F_t + F_b + \Delta T_U + N_{water} + q_{acc}) \qquad 3.19$$

Concerning the seismic combination, only the crane load of the suspended loads should be considered as variable action.

$$E_d = \left(N_{pil} + p_{beam} + q_{roof} + N_{girder} + N_{crane} + N_{c.beam}\right) + \psi_{2j} \cdot (F_1 + H_i) + E(32 \text{ combinations})$$  3.20

in which E represent the effect of the seismic action, computed by means of a dynamic linear analysis. The 32 combinations (Figure 3.3.13) are due to the fact that the seismic action is considered applied in both horizontal directions and verses (±$E_x$ and ±$E_z$, combined with the 30% of the orthogonal direction) and accounting for an accidental eccentricity of the mass center in both of the principal directions of the buildings ($e_X = 0.05 \cdot L_X$, $e_Z = 0.05 \cdot L_Z$).

In the following, Table 3.3.7 shows the combination coefficients for the considered combinations.



$$1° : + E_x + 30\% \, E_z \; ; \qquad 2° : + E_x - 30\% \, E_z$$
$$3° : - E_x + 30\% \, E_z \qquad\quad 4° : - E_x - 30\% \, E_z$$
$$5° : + 30\% \, E_x + E_z \; ; \qquad 6° : + 30\% \, E_x - E_z$$
$$7° : - 30\% \, E_x + E_z \; ; \qquad 8° : - 30\% \, E_x - E_z$$
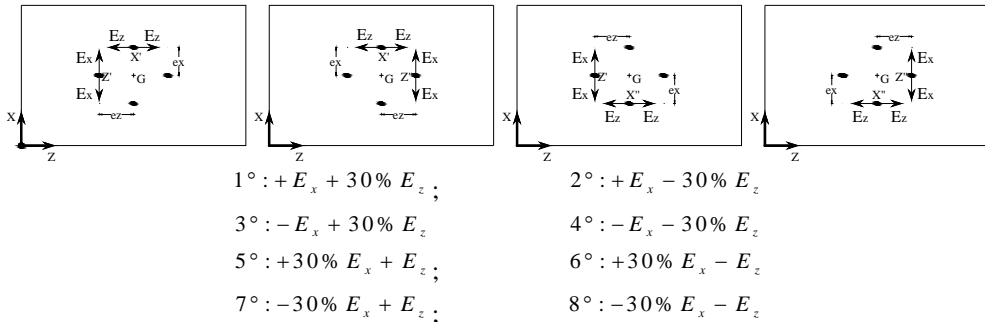
Figure 3.3.13 Seismic load combinations.

Table 3.3.7 Combination load coefficients.

| Combo | Gk | Qk | Snow | Imp, ULS | Imp, E | ΔT | wind | $N_{c.beam}$ | $F_b$ | $F_t$ | $F_1$ | $N_{crane}$ |
|---|---|---|---|---|---|---|---|---|---|---|---|---|
| ULS, snow | 1.3 | 0.0 | 1.5 | 1.5 | - | 0.9 | 0.9 | 1.3 | 1.5 | 1.5 | 1.5 | 1.3 |
| ULS, wind | 1.3 | 0.0 | 0.75 | 1.5 | - | 0.9 | 1.5 | 1.3 | 1.5 | 1.5 | 1.5 | 1.3 |
| ULS, thermal | 1.3 | 0.0 | 0.75 | 1.5 | - | 1.5 | 0.9 | 1.3 | 1.5 | 1.5 | 1.5 | 1.3 |
| ULS, crane | 1.3 | 0.0 | 0.75 | 1.5 | - | 0.9 | 0.9 | 1.3 | 1.5 | 1.5 | 1.5 | 1.3 |
| ULS, wind- no snow | 1.3 | 0.0 | 0.0 | 1.5 | - | 0.9 | 1.5 | 1.3 | 1.5 | 1.5 | 1.5 | 1.3 |
| Seismic | 1.0 | 0.0 | 0.0 | - | 1.0 | 0.0 | 0.0 | 0.0 | 0.0 | 0.0 | 0.8 | 1.0 |

The combined vertical loads are applied as uniformly distributed at the roof level, the horizontal loads (e.g., wind loads, imperfections) are applied at each column top end, other horizontal loads (e.g., crane loads) are applied at the corresponding application points and the seismic loads are applied in the center of mass, considering the accidental eccentricity.

### 3.3.5    Design procedure

In the following, the horizontal elements (main beams and roof elements) are designed for vertical loads whereas the vertical elements (columns) are designed for horizontal loads.

To account for the concrete cracking in precast RC elements (columns), concrete Young modulus is considered halved; for pre-stressed elements (roof elements, main beams) the entire concrete Young modulus is considered, to take into account the reduced concrete cracking.

### 3.3.5.1 Pre-stressed roof element design

Roof elements' width is defined considering the available span length, i.e., $L_1$ minus the minimum space for the positioning of the girders on both sides of the transversal span length, equal to 15 cm on each side of the transversal beam. The roof element height is defined considering the maximum distributed load that the roof element should carry, considering the maximum roof span length ($L_2$). For all the considered case studies the roof elements height is equal to 40cm. Figure 3.3.14 shows the final geometry for the roof elements cross section, of all the reference buildings, so that the transversal area and the self-weight can be evaluated.
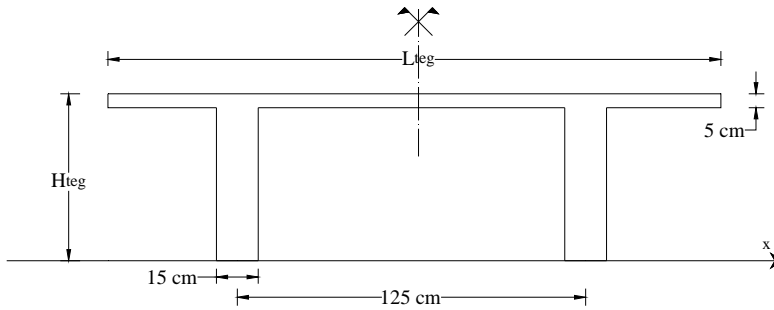


Figure 3.3.14 Roof elements cross section parameters.

$$A_{teg} = L_{teg} \cdot 0.05 + 2 \cdot (H_{teg} - 0.05) \cdot 0.15 \qquad \text{3.21}$$

$$G_{teg} = (A_{teg} \cdot \gamma_{cls})/L_{teg} \qquad \text{3.22}$$

### 3.3.5.2 Precast pre-stressed variable beam design

Dimensions for the beam cross section can be obtained from manufacturer's catalogues, considering the beam span length and the maximum characteristic value of the total distributed load acting on the element. These geometrical features can be modified so that all the structural verifications are fulfilled.

For the main beams it is assumed that:

- section depth is variable along the longitudinal axis of the element in order to improve the flexural strength at mid span, where the flexural moment reaches the maximum value (Figure 3.3.15);
- the cross section has variable width along the longitudinal axis: in particular, the maximum width is encountered at the end-supports where the shear force reaches its maximum value (Figure 3.3.16).

The cross section width ($b_w$) represents the design parameter and it should satisfy the compressive shear strength:

$$V_{Rcd} = 0.9 \cdot d \cdot b_w \cdot \alpha_c \cdot f'_{cd}(ctg\alpha + ctg\theta)/(1 + ctg^2\theta) \qquad \text{3.23}$$

where:

- $f'_{cd}$ is the concrete compressive strength without considering the web concrete ( $f'_{cd} = 0.5 \cdot f_{cd}$ );
- $b_w$ is the minimum cross-section width;
- d is the effective cross section depth (in mm);
- $\alpha_c$ accounts for normal stresses and it is assumed to be equal to one, neglecting the prestressing effect;
- $\theta$ and $\alpha$ represent the concrete strut and tie inclination, respectively; ctg $\theta$ is assumed equal to one.

The shear force acting on the element is evaluated considering the most unfavorable combination among the combinations for ultimate limit state and seismic conditions.

For the defined cross section, the average area for the cross section can be calculated and the beam dead load, distributed along the beam span length, can be estimated ($pp_{TSV} = A_{average} \cdot \gamma_{cls}$).
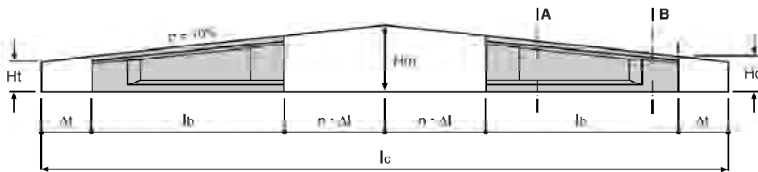

Figure 3.3.15 Variable main beam longitudinal layout.
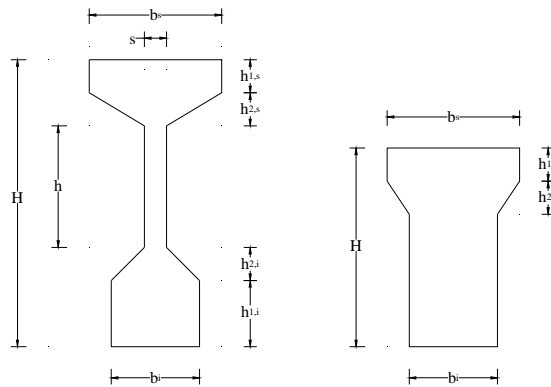

Figure 3.3.16 Variable main beam cross section parameters.

3.3.5.3  Precast column design

For the definition of the cross-section dimensions, structural verifications at the damage limit state are performed for the columns, according to the Italian building code [7.3.7.2 – NTC], in order to avoid non-structural damage which could compromise the serviceability of the building.

The total seismic force applied at the center of mass at the roof level is assumed equal to:

$$F_h = S_d(T_1) \cdot \frac{W}{g} \cdot \lambda \qquad\qquad 3.24$$

where:

- $S_d (T_1)$ is the spectral acceleration value corresponding to the fundamental period $T_1$ on the design spectrum. Considering the building height and the structural coefficient $C_1=0.16$, according to Magliulo et al. (2014), with reference to the building code formulation, $T_1$ is equal to:

$$T_1 = C_1 \cdot H^{3/4} = 0.16 \cdot (L_4 + L_5)^{3/4}$$

3.25

- W is the total seimic weigth considering a tentative value of $w=10kN/m^2$;
- g is the gravity acceleration
- $\lambda$ is a coefficient which takes into account the number of floors ($\lambda=1$ for single floor structures)

The total seismic force is equally distributed to each column, considering the presence of a rigid diaphragm and equal cross sections for all the columns.

The control parameter is the lateral drift of each column, $d_{rp}$, considering a cantilever static scheme:

$$d_{rp} \leq 0.01 \cdot h$$

3.26

$$d_{rp} = \frac{\delta \cdot F_{h,pil}(L_4 + L_5)^3}{3 \cdot EI_{cr}}$$

3.27

where:

- d is an amplification coefficient equal to 1.3 to take into account torsional effects;
- $F_{h,pil}$ is the seismic force acting on the single column;
- E is the concrete Young modulus;
- $I_{cr}$ is the moment of inertia of the cracked cross section.

Considering suitable column cross section dimensions, the structural linear model is set up and a modal response spectrum analysis is performed in order to obtain the seismic demand and check all the structural verifications, according to the Italian building code. In the following, Table 3.3.8 to Table 3.3.11 show the final column cross section geometry (square cross section with dimension $B_{col}$), longitudinal reinforcement ($\rho$ [%]) and the transversal reinforcement for structural models.

Table 3.3.8 Design details for columns – geometry 1.

| Geometry 1 | | | | |
|---|---|---|---|---|
| | Site | $B_{col}$ [m] | $\rho$[%] | Transversal reinforcement |
| Soil type A | L'Aquila | 0.55 | 1.20% | $\phi$10/10cm |
| | Naples | 0.55 | 1.20% | $\phi$ 10/10cm |
| | Rome | 0.55 | 1.06% | $\phi$ 10/10cm |
| | Caltanissetta | 0.55 | 1.06% | $\phi$ 10/10cm |
| | Milan | 0.55 | 1.06% | $\phi$ 10/10cm |
| Soil type C | L'Aquila | 0.60 | 2.51% | $\phi$10/9cm |
| | Naples | 0.55 | 1.66% | $\phi$ 10/10cm |
| | Rome | 0.55 | 1.20% | $\phi$ 10/10cm |
| | Caltanissetta | 0.55 | 1.06% | $\phi$ 10/10cm |
| | Milan | 0.55 | 1.06% | $\phi$10/10cm |

Table 3.3.9 Design details for columns – geometry 2.

| Geometry 2 | | | | |
|---|---|---|---|---|
| | Site | $B_{col}$ [m] | $\rho$[%] | Transversal reinforcement |
| Soil type A | L'Aquila | 0.70 | 1.48% | $\phi$10/8cm |
| | Naples | 0.70 | 1.03% | $\phi$10/8cm |
| | Rome | 0.65 | 1.19% | $\phi$ 0/9cm |
| | Caltanissetta | 0.65 | 1.19% | $\phi$10/9cm |
| | Milan | 0.65 | 1.19% | $\phi$10/9cm |
| Soil type C | L'Aquila | 0.70 | 2.89% | $\phi$ 0/8cm |
| | Naples | 0.70 | 1.73% | $\phi$ 10/8cm |
| | Rome | 0.70 | 1.48% | $\phi$10/8cm |
| | Caltanissetta | 0.65 | 1.19% | $\phi$10/9cm |
| | Milan | 0.65 | 1.19% | $\phi$10/9cm |

Table 3.3.10 Design details for columns – geometry 3.

| Geometry 3 | | | | |
|---|---|---|---|---|
| | Site | $B_{col}$ [m] | $\rho$[%] | Transversal reinforcement |
| Soil type A | L'Aquila | 0.75 | 1.29 | $\phi$10/6.5cm |
| | Naples | 0.75 | 1.29 | $\phi$10/6.5cm |
| | Rome | 0.75 | 1.29 | $\phi$10/6.5cm |
| | Caltanissetta | 0.75 | 1.29 | $\phi$10/6.5cm |
| | Milan | 0.75 | 1.00 | $\phi$10/11cm |
| Soil type C | L'Aquila | 0.90 | 1.34 | $\phi$10/7cm |
| | Naples | 0.75 | 1.29 | $\phi$10/6.5cm |
| | Rome | 0.75 | 1.29 | $\phi$10/6.5cm |
| | Caltanissetta | 0.75 | 1.29 | $\phi$10/6.5cm |
| | Milan | 0.75 | 1.00 | $\phi$10/11cm |

Table 3.3.11 Design details for columns – geometry 4.

| Geometry 4 | | | | |
|---|---|---|---|---|
| | Site | $B_{col}$ [m] | $\rho$[%] | Transversal reinforcement |
| Soil type A | L'Aquila | 0.85 | 1.25 | $\phi$10/7.5cm |
| | Naples | 0.85 | 1.25 | $\phi$10/7.5cm |
| | Rome | 0.85 | 1.25 | $\phi$10/7.5cm |
| | Caltanissetta | 0.85 | 1.25 | $\phi$10/7.5cm |
| | Milan | 0.85 | 1.00 | $\phi$10/7.5cm |
| Soil type C | L'Aquila | 0.90 | 1.71 | $\phi$8/8cm |
| | Naples | 0.90 | 1.08 | $\phi$10/9cm |
| | Rome | 0.85 | 1.25 | $\phi$10/7.5cm |
| | Caltanissetta | 0.85 | 1.25 | $\phi$10/7.5cm |
| | Milan | 0.85 | 1.00 | $\phi$10/5.5cm |

## 3.4   Modelling issues and strategy

In order to perform non-linear dynamic analyses, a numerical structural model is created in OpenSees software.

Considering the geometrical description of section 3.2, the structural model features are:

- columns fixed at the base, due to the effective restraint provided by the socket foundation and by the rigid industrial floor;
- elastic elements to represent the main beam and the girders; the main beams are assigned a constant cross section characterized by the mean value of the variable height and width obtained from the mean value of the cross-sectional area: b=$A_{mean}$/$h_{mean}$;
- roof elements are not inserted in the model and a rigid diaphragm constraint is applied at the roof level, thanks to the presence of the cast in situ concrete slab (5cm deep);
- rigid elements represent geometrical eccentricities of the structural elements;
- perfect hinge constraints between main beams and columns, due to the presence of dowel connections;
- perfect hinge constraints between girder beams and columns due to dowel connections;
- the cladding panels are not considered in the model in terms of lateral stiffness: they are considered only in terms of masses and loads applied to the main structure; this reflects the hypothesis that they are connected to the structures with isostatic hinge connections which absorb high shear force during the seismic event but, due to their low shear strength, they collapse, even for low seismic intensity, in the early steps of the analysis, so that the presence of the cladding panels does not influence the global failure condition.
- the non-linear behavior of the building is modeled considering a lumped plasticity approach with plastic hinges at the column bases including elastic and plastic deformation and rigid column elements (Figure 3.4.1);
- the curvature and the yielding moment are obtained from fiber analysis of the column cross-section (Figure 3.4.2).
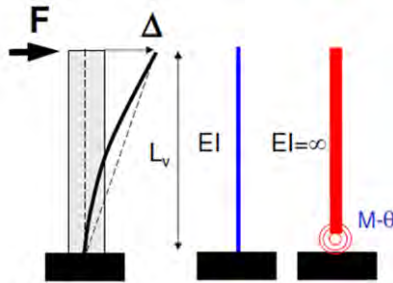
Figure 3.4.1 Non-linear model for structural members.
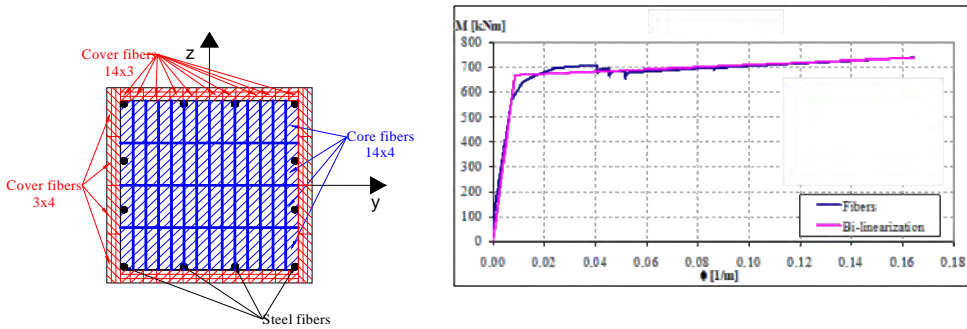


Figure 3.4.2 Fiber analysis of the column cross section.

In the OpenSees software, the plastic hinge is modeled using the Modified Ibarra-Medina-Krawinkler deterioration model (Figure 3.4.3) which accounts for cyclic deterioration by means of a moment-rotation envelope defined by the following mechanical parameters:

- effective yield strength and rotation ($M_y$ and $\theta_y$)
- effective stiffness $K_e = M_y/\theta_y$
- capping strength and associated rotation for monotonic loading ($M_c$ and $\theta_c$)
- pre-capping rotation capacity for monotonic loading $\theta_p$
- post-capping rotation capacity $\theta_{pc}$
- residual strength $M_r = k\, M_y$
- ultimate rotation capacity $\theta_u$
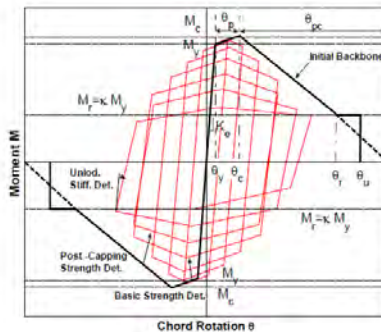


Figure 3.4.3 Modified Ibarra-Medina-Krawinkler deterioration model.

The above cited mechanical parameters can be evaluated according to Fischinger et al. (2008). In particular:

- the yielding rotation:

$$\theta_y = \phi_y \frac{L_s}{3} + 0.00275 + a_{sl} \frac{\varepsilon_y}{(d-d')} \cdot \frac{0.2 d_b f_y}{\sqrt{f_c'}}$$

3.28

- the capping rotation:

$$\theta_{cap} = 0.12 \cdot (1 + 0.4 a_{sl}) \cdot 0.2^{\nu} \cdot (0.02 + 40\rho_{sh})^{0.52} \cdot 0.56^{0.01 f_c'} \cdot 2.37^{10\rho_l}$$

3.29

- the post-capping rotation:

$$\theta_{pc} = 0.76 \cdot 0.031^{\nu} \cdot (0.02 + 40\rho_{sh})^{0.52} \leq 0.1$$

3.30

- the degradation parameter:

$$\lambda = 127.2 \cdot 0.19^{\nu} \cdot 0.24^{s/d} \cdot 0.595^{V_p/V_n} \cdot 4.25^{\rho_{sh,\text{eff}}}$$

3.31

Figure 3.4.4 shows the moment-rotation envelope which results from the plastic hinge definition for L'Aquila, geometry 1 and soil type A, as an example.



(a)                                                                     (b)
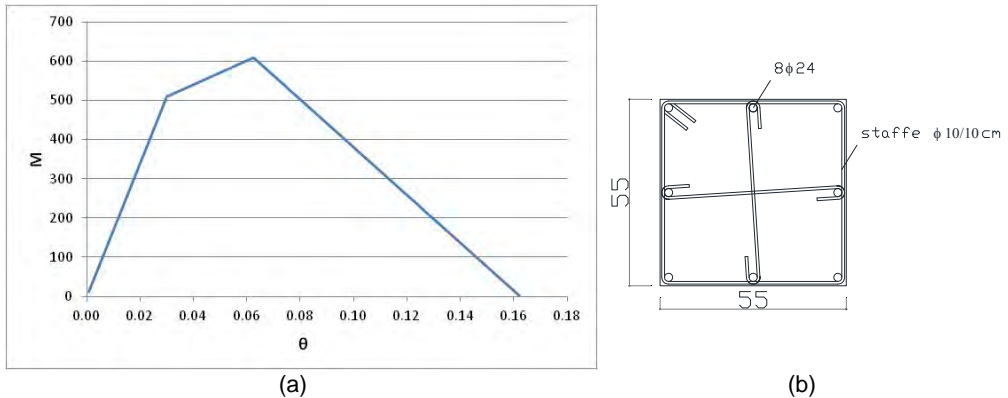
Figure 3.4.4 Moment-rotation envelope (a) and cross section details (b) for the definition of the plastic hinge, L'Aquila, geometry 1 – soil type A.

## 3.5   Collapse Limit State: analyses' results and discussion

Nonlinear static and dynamic analyses were performed in both the horizontal directions (i.e., x and z directions), for all the considered case studies, i.e. for the four considered geometries, the four sites (L'Aquila, Naples, Rome, and Milan) and the two soil types (type A and C).

Two collapse conditions are considered in the following: one is a global collapse condition referring to the attainment of the maximum roof displacement, and the other is a local collapse condition referring to the attainment of the shear strength in the roof connections.

The pushover curves, obtained from nonlinear static analyses, lead to the definition of the global collapse condition which corresponds to 50% degradation of the maximum base-shear. The corresponding inter-story drift value on the pushover curve (for each horizontal direction)

represents the collapse EDP threshold (displacement capacity). Displacement capacity for buildings with geometry 3 (SS) and 4 (LS) and the sites L'Aquila, Naples, Rome and Milan are reported in Table 3.5.1.

Table 3.5.1 Dispacement capacity for buildings with geometry 3 (SS) and 4 (LS).

| Site | Soil type | Lateral displacement [m] | | | | Soil type | | | | |
| --- | --- | --- | --- | --- | --- | --- | --- | --- | --- | --- |
| | | SS | | LS | | | SS | | LS | |
| | | X | Z | X | Z | | X | Z | X | Z |
| AQ | A | 0.871 | 0.926 | 0.861 | 0.928 | C | 0.923 | 0.981 | 0.920 | 0.991 |
| NA | | 0.871 | 0.926 | 0.861 | 0.928 | | 0.871 | 0.927 | 0.853 | 0.920 |
| RM | | 0.870 | 0.926 | 0.861 | 0.928 | | 0.871 | 0.927 | 0.861 | 0.928 |
| MI | | 0.831 | 0.884 | 0.834 | 0.899 | | 0.832 | 0.884 | 0.834 | 0.899 |

The local collapse condition is defined as the attainment of the maximum shear strength of the dowel beam-to-column connection, designed according to the CNR 10025/98 (vertical dowels diameters and stirrups details are provided in Table 3.5.2), considering a ductile behavior of the connection at the collapse, due to vertical dowel yielding and crushing of the surrounding concrete).

Table 3.5.2 Dowel diameters and connection stirrups (D=nominal diameter, R.D.=resistant diameter, $S_t$=total number of stirrups in the connection region and space).

| Site | Soil type | SS | | LS | |
| --- | --- | --- | --- | --- | --- |
| | | D (R.D [mm]) | St | D (R.D [mm]) | St |
| AQ | A | M22 (19.6) | 3 ϕ10/5 cm | M27 (24.2) | 4 ϕ10/5 cm |
| NA | | M20 (17.7) | 3 ϕ10/5 cm | M27 (24.2) | 3 ϕ10/5 cm |
| RM | | M20 (17.7) | 3 ϕ10/5 cm | M22 (19.6) | 3 ϕ10/5 cm |
| MI | | M18(W) (15.6) | 3 ϕ10/5 cm | M20(W) (17.7) | 3 ϕ10/5 cm |
| AQ | C | M30 (26.7) | 5 ϕ10/5 cm | M33 (29.7) | 9 ϕ8/3 cm |
| NA | | M22 (19.6) | 3 ϕ10/5 cm | M27 (24.2) | 4 ϕ10/5 cm |
| RM | | M22 (19.6) | 3 ϕ10/5 cm | M27 (24.2) | 4 ϕ10/5 cm |
| MI | | M18 (15.6) | 3 ϕ10/5 cm | M22 (19.6) | 3 ϕ10/5 cm |

The connection shear strength is estimated as the minimum value between the following code and literature formulations, in which $n$ represents the number of vertical dowels ($n$=2), $d_b$ represents the dowel resistant diameter, $f_y$ and $f_u$ represent the mean values of yielding and ultimate strength of the steel dowels, $f_c$ represents the concrete mean compression strength, $\alpha_{gap}$=1.0 in case of no hole clearance between anchor and fixture and $\alpha_{seism}$=0.85 is the reduction factor to take into account the influence of large cracks in case of anchor group, $\alpha = \sigma / f_y$, where $\sigma$ is the normal tensile stress acting on dowels.

$$V_{Rd}^{CNR} = n \cdot 1.6 \cdot d_b^2 \sqrt{f_y \cdot f_c}$$

$$V_{R,mono}^{V\&T} = n \cdot 1.3 \cdot d_b^2 \cdot \sqrt{f_y \cdot f_c}$$

$$V_{R,mono}^{EOTA} = n \cdot 0.5 \cdot A_s \cdot f_u$$

$$V_{R,cycl}^{EOTA} = \alpha_{gap} \cdot \alpha_{seism} \cdot V_{R,mono}^{EOTA}$$

$$V_{R}^{Safecast} = n \cdot 0.9 \cdot d_b^2 \cdot \sqrt{f_y \cdot f_c \cdot \left(1 - \alpha^2\right)}$$

Table 3.5.3 Beam-to-column dowel connection shear strength capacity.

| Site | Soil type | Connection shear strength [kN] | | Soil type | | |
|------|-----------|------|------|-----------|------|------|
|      |           | SS | LS | | SS | LS |
| AQ | A | 153.38 | 232.34 | C | 283.97 | 351.30 |
| NA | A | 124.02 | 232.34 | C | 153.38 | 232.34 |
| RM | A | 124.02 | 153.38 | C | 153.38 | 232.34 |
| MI | A | 97.19 | 124.02 | C | 97.19 | 153.38 |

Nonlinear dynamic analyses were performed, using the input records selected according to Section 1.3 of this report, with the conditioning period of 2.0 s. In particular, twenty records are provided for each intensity level and ten different intensity levels were considered, each corresponding to a return period.

During each dynamic analysis a collapse matrix for each selected EDP was filled, where the demand to capacity (D/C) ratios were collected. The "demand" corresponds to the maximum value of the selected EDP (i.e. the top displacement or the shear force in the beam-to-column connections) during each record (ordered on the rows of the matrix), for all the intensity levels (ordered on the columns of the matrix, for each return period). The "capacity" corresponds to the two different conditions described above.

In the following, the demand/capacity ratios obtained from the non-linear dynamic analyses for each site and for each soil, in the case of geometries 3 (SS) and 4 (LS) are presented in Figures 3.5.1-8. Square markers (columns) represent the D/C ratios related to the roof displacement, while circle markers (connection) represent the D/C ratios related to the connection strength.
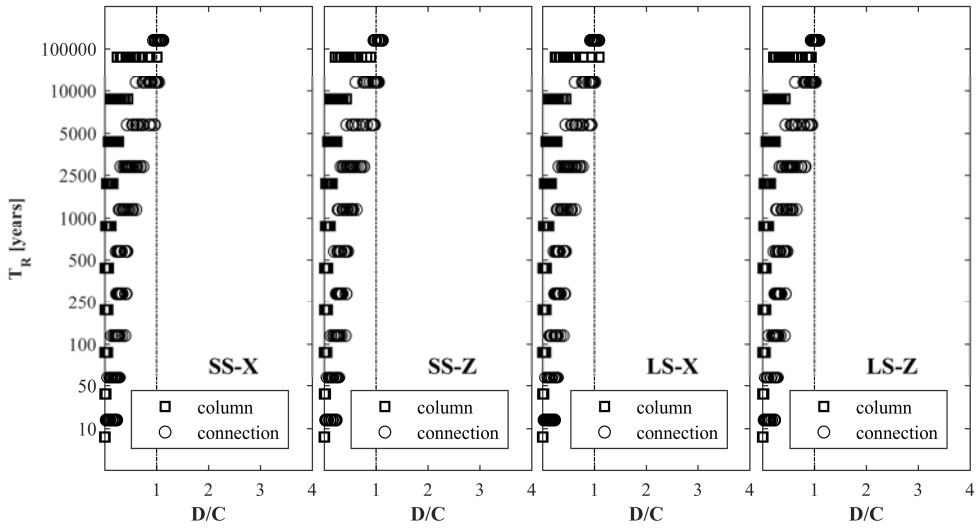
Figure 3.5.1 D/C ratios at CLS for L'Aquila, soil A.
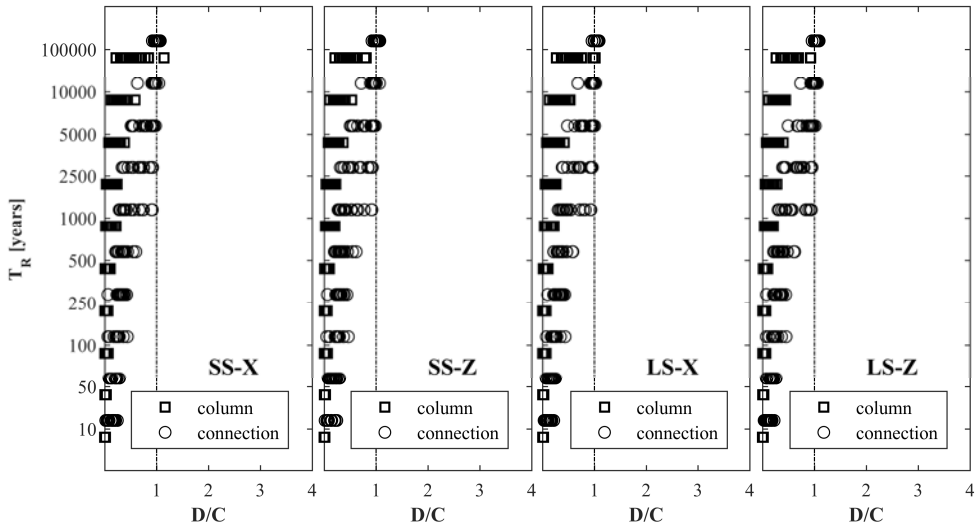


Figure 3.5.2 D/C ratios at CLS for L'Aquila, soil C.
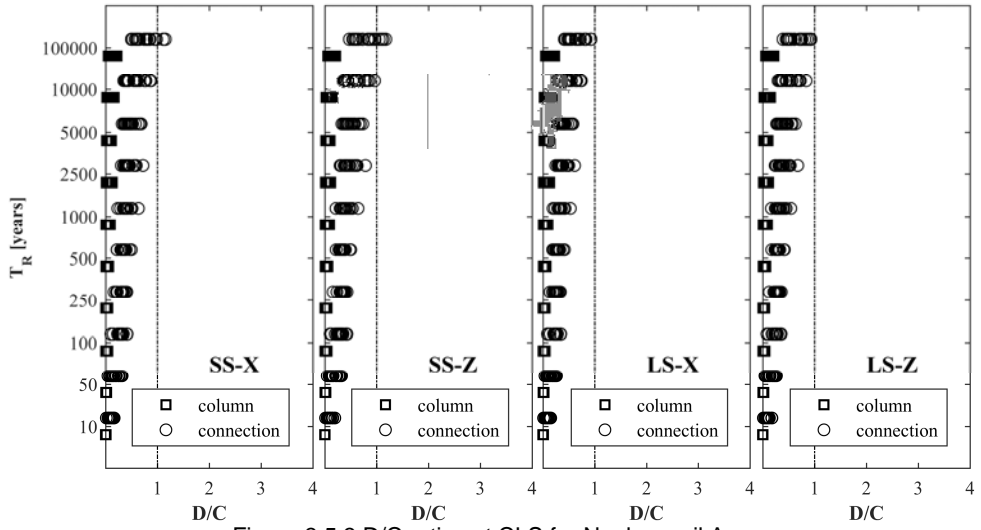
Figure 3.5.3 D/C ratios at CLS for Naples, soil A.
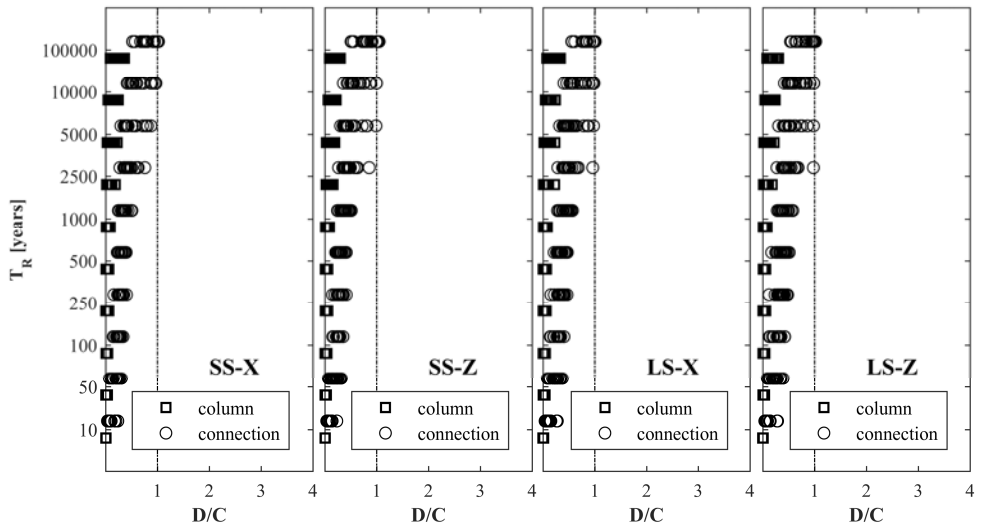


Figure 3.5.4 D/C ratios at CLS for Naples, soil C.
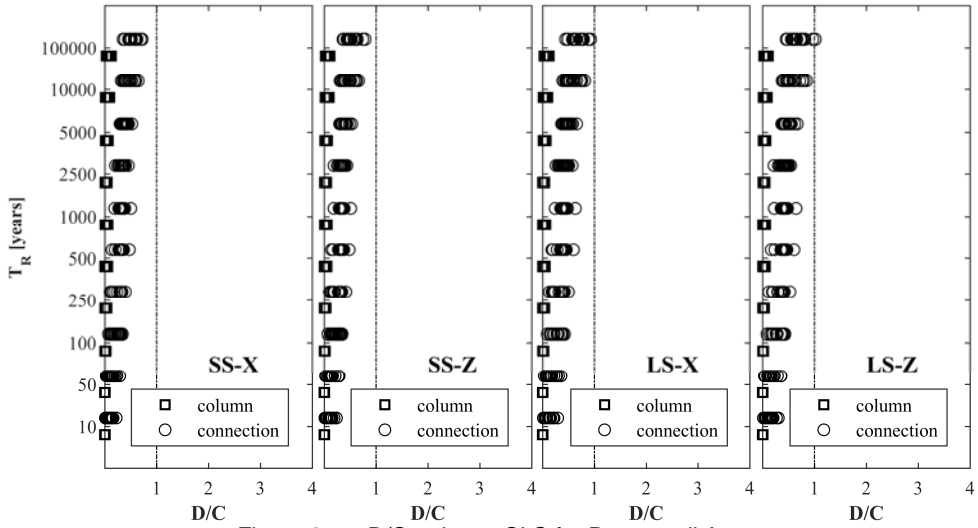
Figure 3.5.5 D/C ratios at CLS for Rome, soil A.
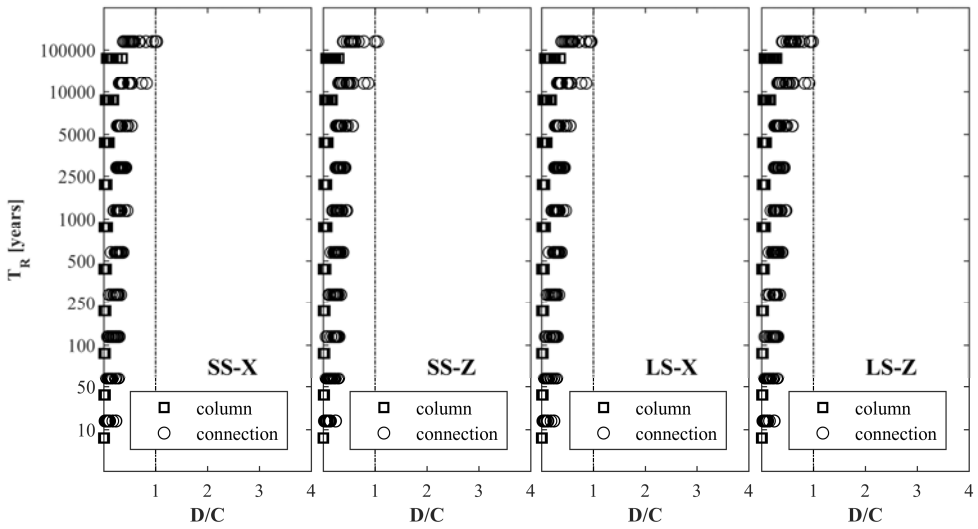


Figure 3.5.6 D/C ratios at CLS for Rome, soil C.
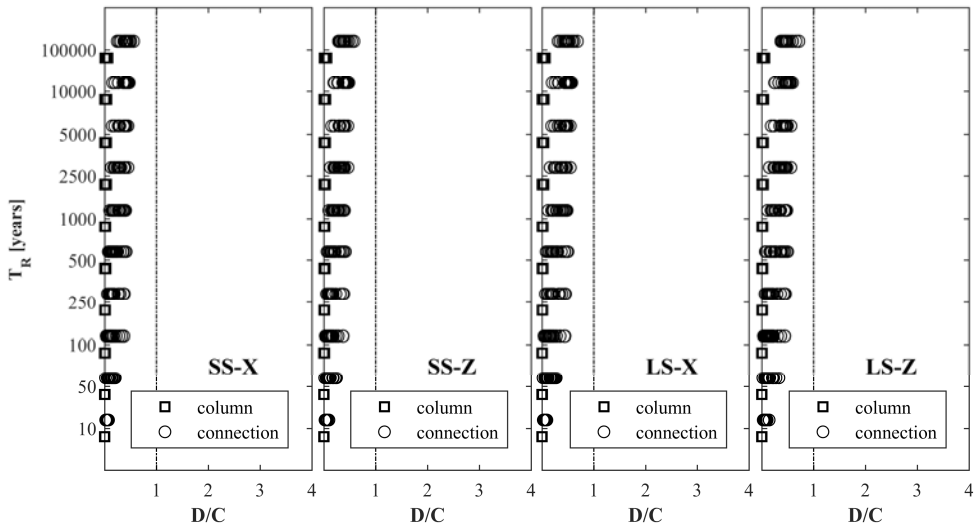
Figure 3.5.7 D/C ratios at CLS for Milan, soil A.
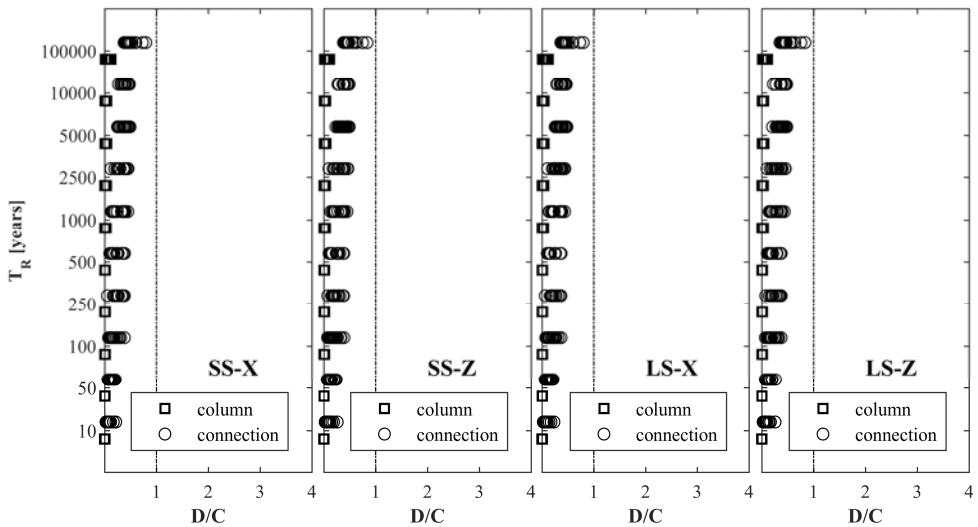


Figure 3.5.8 D/C ratios at CLS for Milan, soil C.

## 3.6   Damage Limit State: analyses' results and discussion

In the following, the results in terms of D/C ratio for interstory drift referring to the damage limit state are presented. In particular, for the damage limit state the capacity was evaluated according to NTC 2008 as the interstory drift value (1%) which corresponds to the damage prevention of non-structural components fixed in a way so as not to interfere with structural deformations. Furthemore, analysis on the same structures modelled with cladding panels and panel-to-structure connections, which are not reported herein for the sake of brevity, show that 1% drift corresponds to the attainment of the damage of at least the 50% of the panel-to-structure connections.
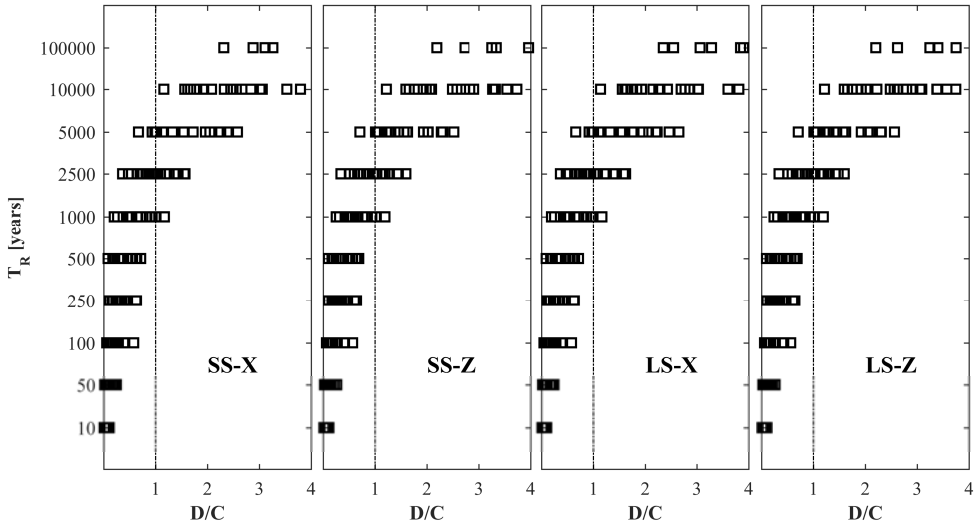
Figure 3.6.1 D/C ratios at DLS for L'Aquila, soil A.
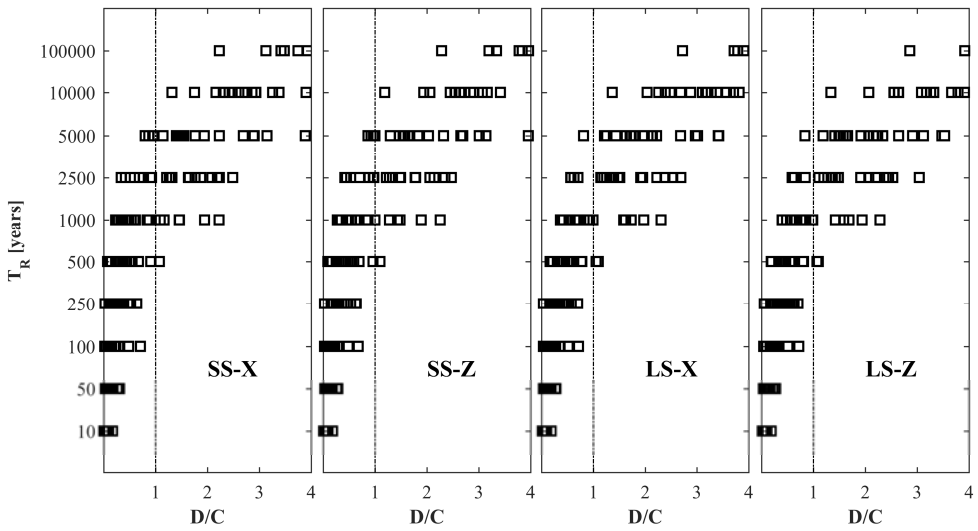


Figure 3.6.2  D/C ratios at DLS for L'Aquila, soil C.
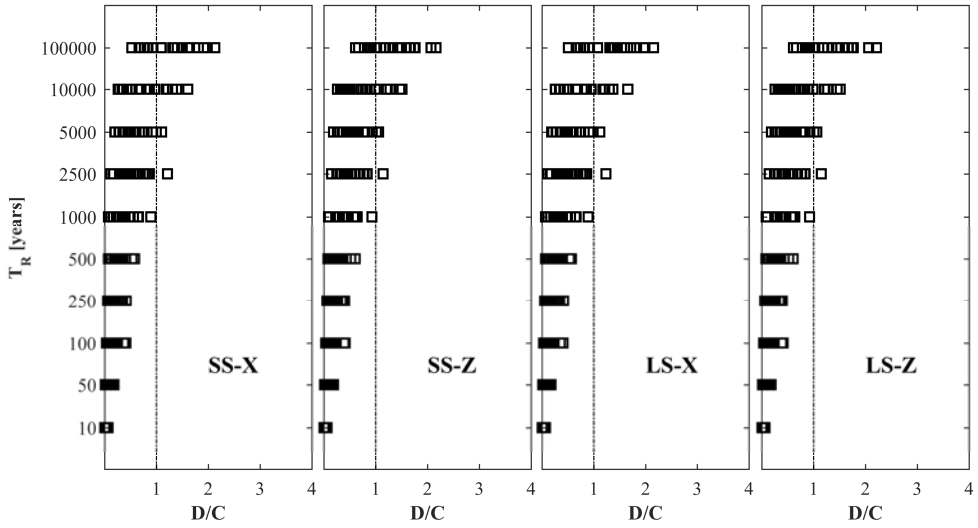
Figure 3.6.3 D/C ratios at DLS for Naples, soil A.
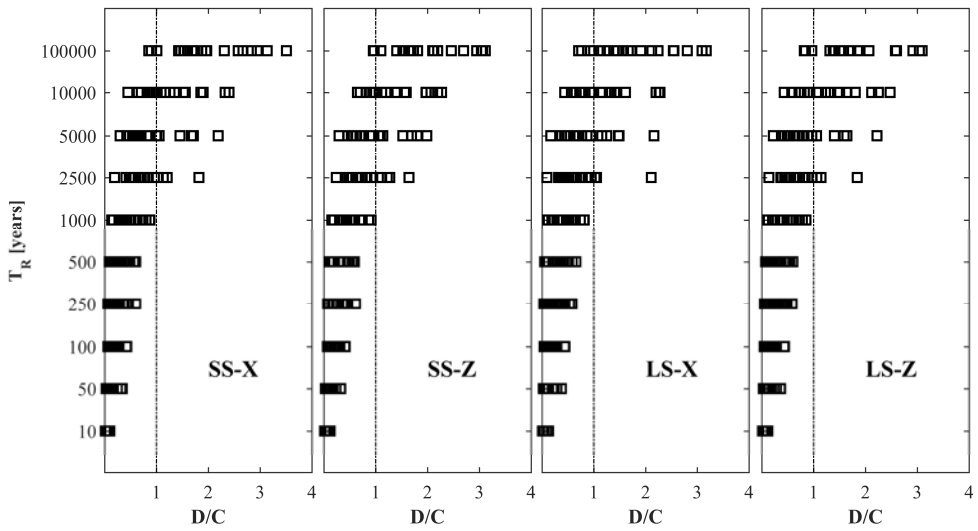


Figure 3.6.4 D/C ratios at DLS for Naples, soil C.
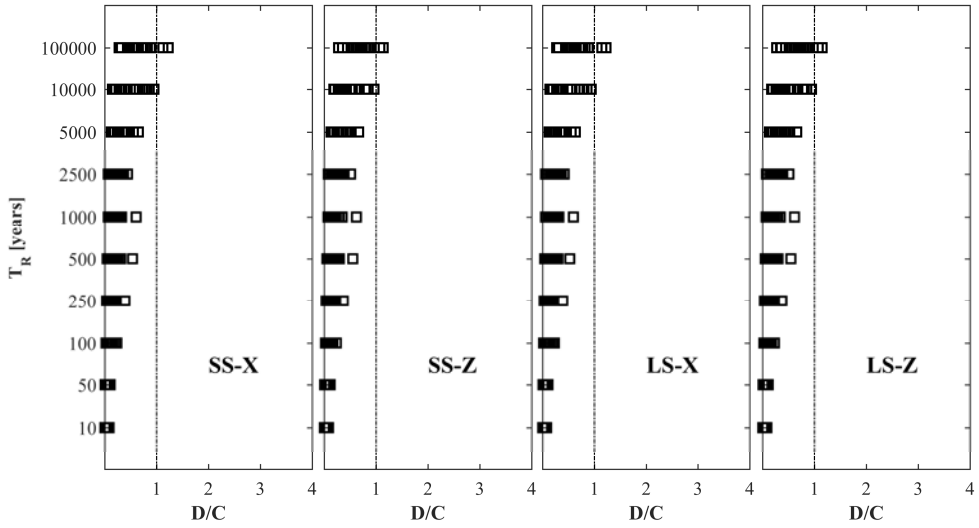
Figure 3.6.5 D/C ratios at DLS for Rome, soil A.
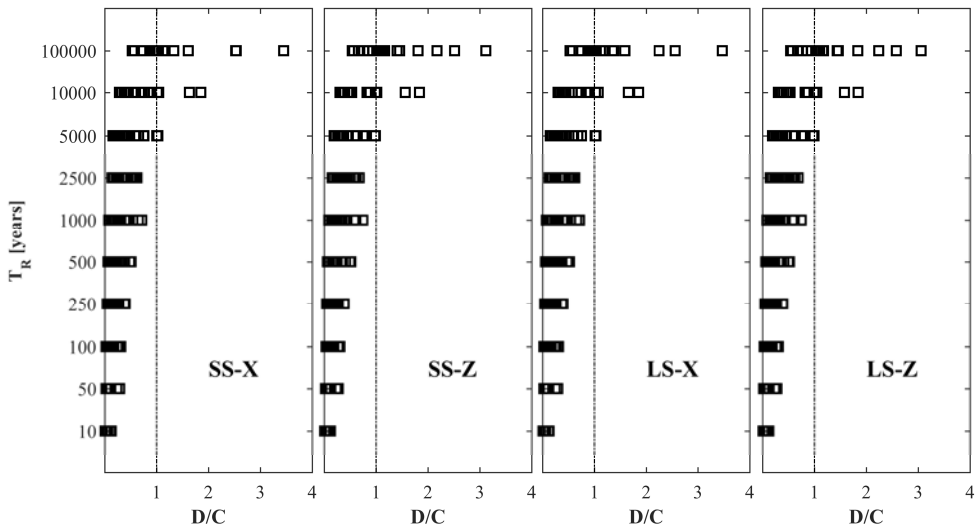


Figure 3.6.6 D/C ratios at DLS for Rome, soil C.
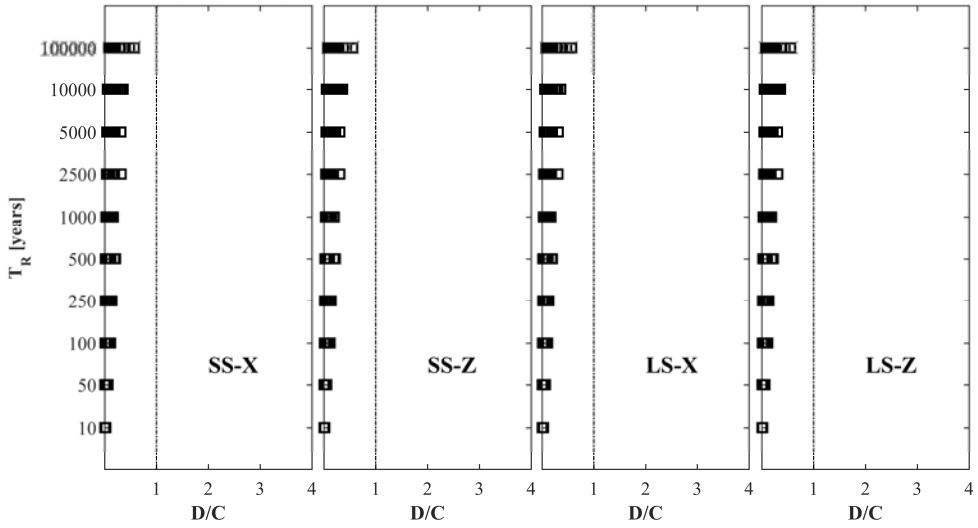
Figure 3.6.7 D/C ratios at DLS for Milan, soil A.
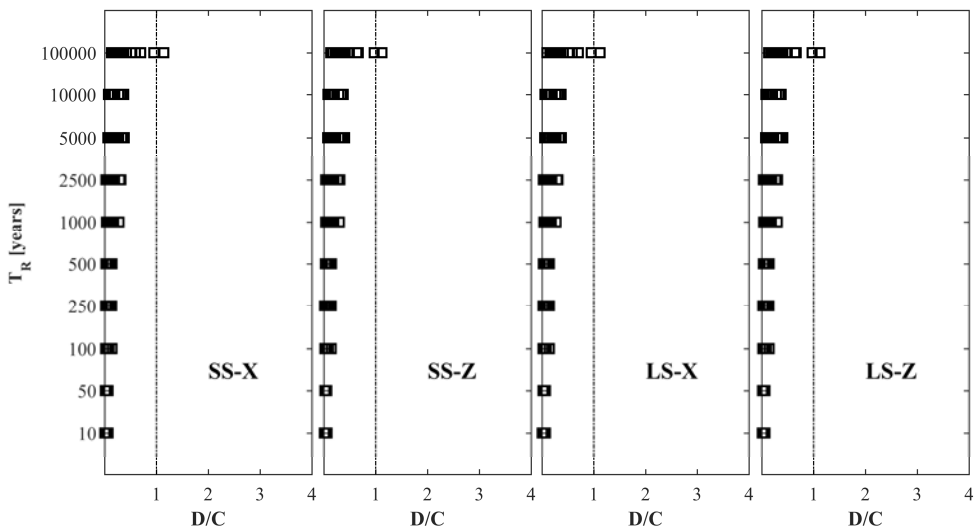


Figure 3.6.8 D/C ratios at DLS for Milan, soil C.

## 3.7   References

CEN (2004). "Eurocode 2: design of concrete structures - Part 1-1: General rules and rules for buildings."Brussels, Belgium.

CEN (2005). "Eurocode 3: design of steel structures - Part 1-8: Design of joints. EN 1993-1-8."Brussels, Belgium.

Circolare 02/02/2009 n. 617 (2009). "Istruzioni per l'applicazione delle "Nuove norme tecniche per le costruzioni" di cui al D.M. 14 gennaio 2008." M. d. I. e. d. Trasporti, ed.Gazzetta Ufficiale n. 47 del 26 febbraio 2009.

CNR 10018 (1999). "Apparecchi di appoggio per le costruzioni (in Italian)." Bollettino Ufficiale del CNR.

CNR 10025/98 (2000). "Istruzioni per il progetto, l'esecuzione ed il controllo delle strutture prefabbricate in calcestruzzo (in Italian)." Bollettino Ufficiale del CNR.

D. M. 14/01/2008 (2008). "NormeTecniche per le Costruzioni (in Italian) ", G.U. n. 29 4 febbraio 2008.

Fischinger, M., Kramar, M., and Isaković, T. (2008). "Cyclic response of slender RC columns typical of precast industrial buildings." Bulletin of Earthquake Engineering, 6(3), 519-534.

Zoubek, Blaž, Matej Fischinger, and Tatjana Isakovic. "Estimation of the cyclic capacity of beam-to-column dowel connections in precast industrial buildings. Bulletin of Earthquake Engineering2015; 13(8): 2145-2168.

Magliulo G., Ercolino M., Cimmino M., Capozzi V., Manfredi G.. "Cyclic shear test on a dowel beam-to-column connection of precast buildings". Earthquake and Structures 2015; 9(3): 541-562.

Magliulo G., Ercolino M., Manfredi G.. "Influence Of Cladding Panels On The First Period Of One-Story Precast Buildings". Bulletin of Earthquake Engineering 2015; 13: 1531-1555.

Magliulo G., Ercolino M., Cimmino M., Capozzi V., Manfredi G.. "FEM analysis of the strength of RC beam-to-column dowel connections under monotonic actions". Construction and Building Materials 2014; 69: 271-284.

Magliulo G., Ercolino M., Petrone C., Coppola O., Manfredi G.. "Emilia Earthquake: the Seismic Performance of Precast RC Buildings". Earthquake Spectra 2014; 30(2): 891-912.

Magliulo G., Capozzi V., Fabbrocino G., Manfredi G.. "Neoprene-concrete friction relationships for seismic assessment of existing precast buildings". Engineering Structures 2011; 33(2): 532–538.

Faggiano B., Iervolino, I., Magliulo, G., Manfredi G., Vanzi I.. "Il comportamento delle strutture industriali nell'evento de L'Aquila". Progettazione Sismica 2009; 3:207-213.

Magliulo G., Fabbrocino G., Manfredi G.. "Seismic assessment of existing precast industrial buildings using static and dynamic nonlinear analyses". Engineering Structures 2008; 30(9): 2580-2588.

# CHAPTER IV – REINFORCED CONCRETE STRUCTURES

## 4.1 Case study structures

Five different cities are selected from five different seismicity zones according to the Italian national hazard map. The sites are listed in Table 4.1.1, together with the relevant PGAs for soil type A and type C. Figure 4.1.1 shows the locations of the five cities.

Table 4.1.1 Seismic parameters of selected sites.

| Site | Longitude | Latitude | PGA ($T_R$=475) [g] (Soil type A) | PGA ($T_R$=475) [g] (Soil type C) | Seismic zone |
|---|---|---|---|---|---|
| Milan | 9.186 | 45.465 | 0.049 | 0.075 | IV |
| Caltanisetta | 14.060 | 37.480 | 0.073 | 0.110 | III-b |
| Rome | 12.479 | 41.872 | 0.120 | 0.183 | III-a |
| Naples | 14.268 | 40.854 | 0.168 | 0.245 | II |
| L'Aquila | 13.399 | 42.349 | 0.261 | 0.347 | I |
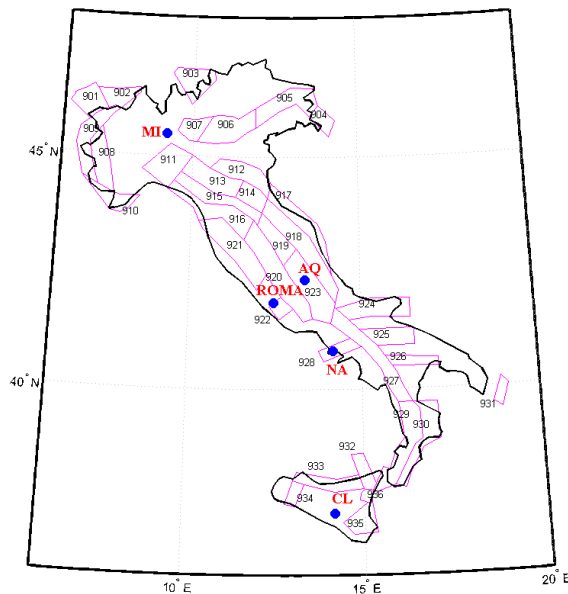


Figure 4.1.1 Locations of the five sites.

### 4.1.1 Prototype buildings

Three sets of 3-, 6- and 9-story Moment-Resisting Frame (MRF) buildings and a set of 9-story Shear Wall (SW) buildings were designed. The buildings are all intended for residential use (except for the ground level that can have a commercial use) and are characterized by regularity in plan and elevation. The ground level is 3.4m high, all other stories being 3.05m high (Figure 4.1.3). The building structure includes the staircase, designed with knee beams. The typical floor plan of Figure 4.1.2 shows two independent structures with an expansion joint. All buildings have identical floor plans (floor beams and floor slabs), the only differences lie in the column dimensions and reinforcement.
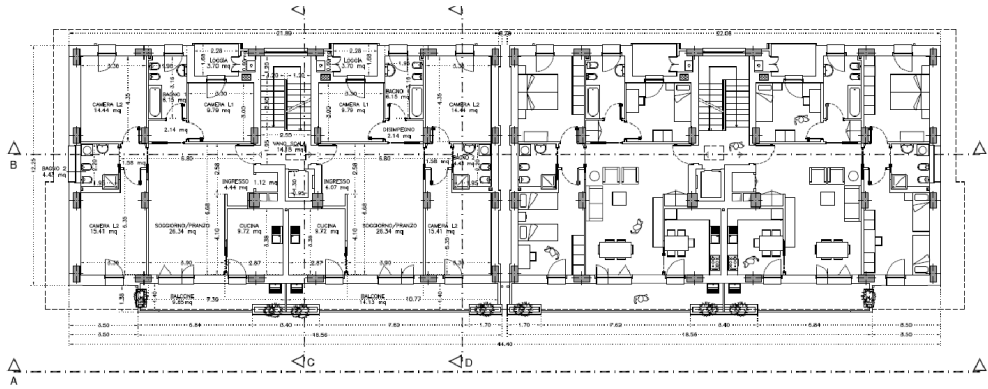
Figure 4.1.2 Prototype building plan.





Figure 4.1.3 Vertical section and view of the prototype building.

## 4.2 Design of reinforced concrete buildings

Design of the RC buildings followed the Italian NTC 2008 (§7.4) design code. The reference design limit state is Life Safety. All buildings were designed in low ductility class (the Italian code considers only high and low ductility classes[2]) using Response Spectrum Analysis, following the design practice for new buildings. The buildings are on soil type A and type C. The buildings are all classified as ordinary, thus the importance factor is $c_u=1$.

### 4.2.1 General design criteria

The structures were designed as MRFs and SWs , following the Italian practice for the type of building under consideration. Similarly, the staircase is part of the building structure and is designed with knee beams. The structures are assumed fixed at the base, without any modeling of the foundation. The beam-column joints are modeled (in both linear and nonlinear analyses) without rigid end zones.

#### 4.2.1.1 Geometry and materials

Due to architectural requirements, the minimum column dimension is 35 cm. Figure 4.2.1 and Figure 4.2.2 show the typical structural plan, where the fixed reference grid is highlighted. The arrows indicate that the slabs are all one way. The outer beams are all deep, while all internal beams are flat (for this reason the building automatically falls into the low ductility category of NTC 2008). The slab thickness is 25cm. Figure 4.2.3 shows the beam details.
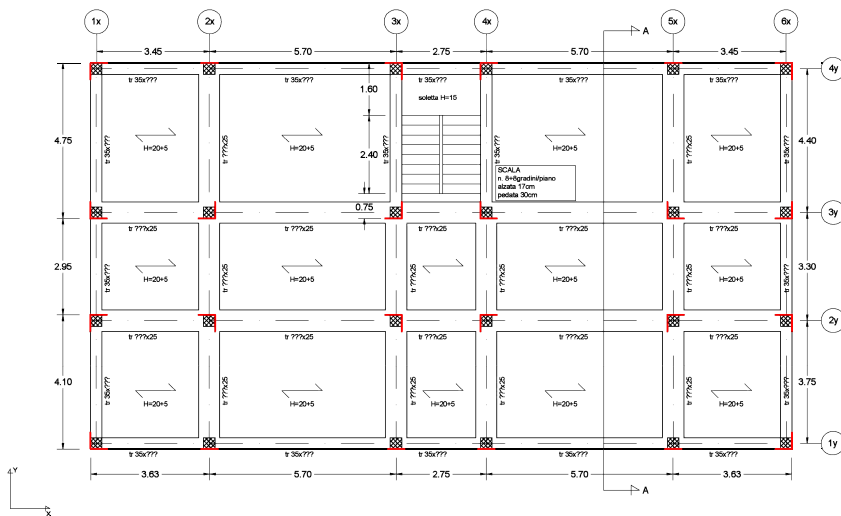


Figure 4.2.1 Floor plan with fixed reference grid and one way slab orientation in MRF.
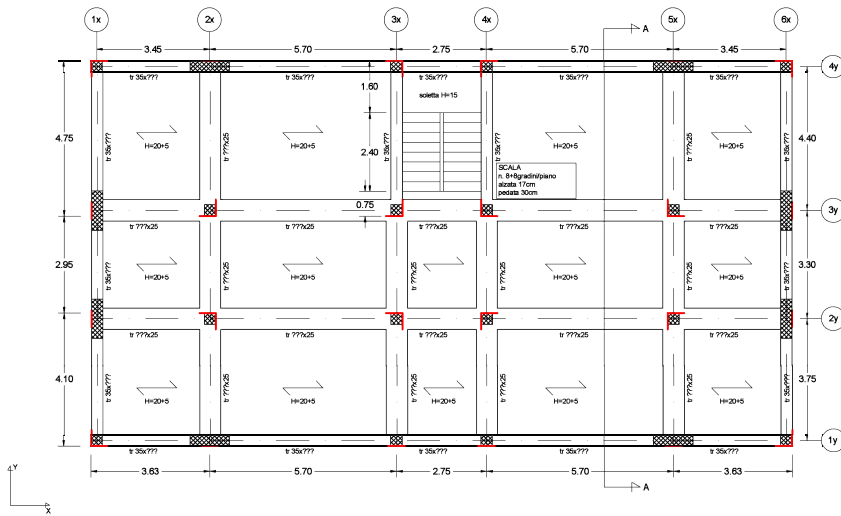
Figure 4.2.2 Floor plan with fixed reference grid and one way slab orientation in SW.

It is commonplace in Italy to use masonry infills in the building outer walls. Infills may be interrupted at the ground level to allow large openings (for garage and/or commercial use). For the above reasons, three different infill configurations are considered in this study, as summarized in Figure 4.2.4:

- Bare Frame (BF), i.e., buildings in which the infills only contribute to the dead load and are neglected in terms of stiffness and strength (these are considered the reference structures);
- Infill Frame (IF), i.e., buildings with infills regularly distributed in plan and in elevation (both infill stiffness and strength are considered);
- Pilotis Frame (PF), i.e., buildings with open ground floor(both infill stiffness and strength are considered).
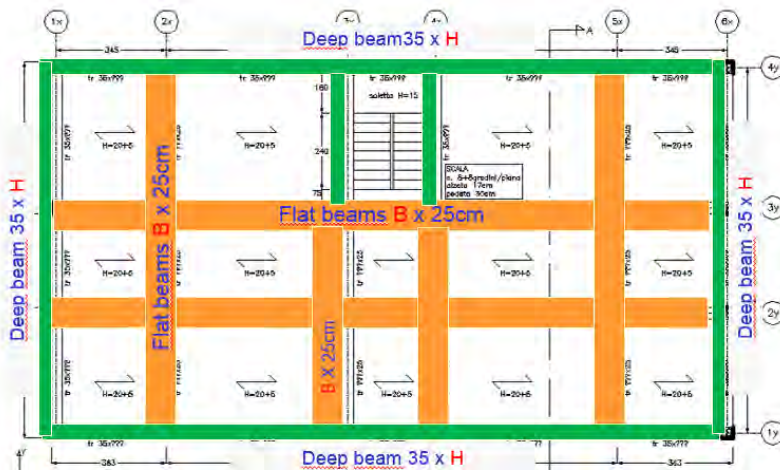


Figure 4.2.3 Beam types and minimum column size.

(a)                                                  (b)                                                  (c)
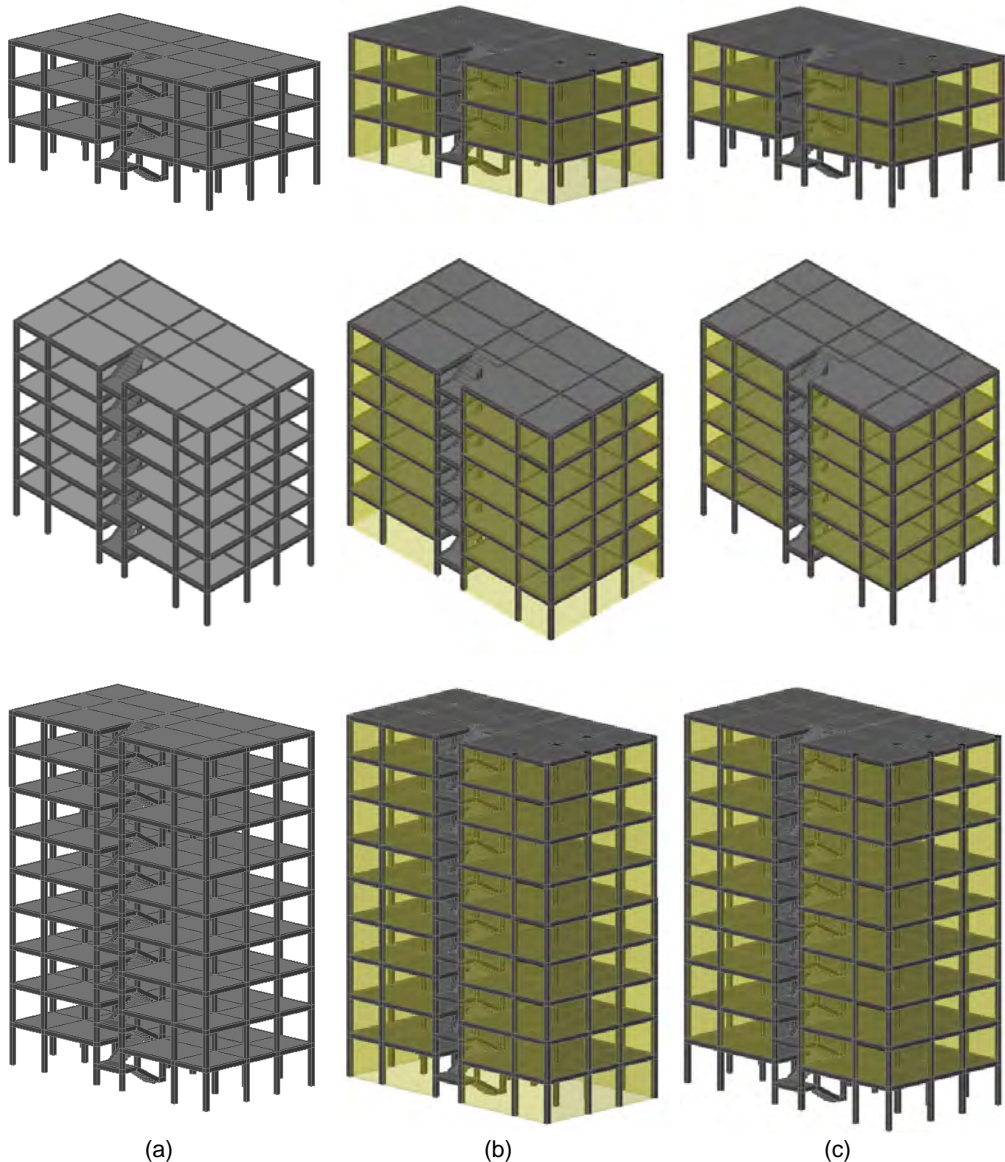
Figure 4.2.4 Different structural types: bare frame BF (a); infill frame IF (b); pilotis frame PF (c).

From a design viewpoint, BF and IF are identical, because during design the infills are not included as structural elements in the building model but are only considered as dead loads. The Italian building code NTC2008§7.2.3 considers that in buildings with an infill distribution irregular in elevation  (such as the case of PF buildings) damage may concentrate in a single story. For this reason, the code prescribes that all actions must be increased by 40% for the vertical elements in stories with an infill reduction (the ground level in the PF building of Figure 4.2.4).

Table 4.2.1 summarizes all the buildings designed and analyzed in the study. The initial analyses – carried out on the six-story buildings, involved five cities. The results, later presented in this report, show that there is no major difference among the sites with low seismicity. For the remaining analyses, carried out on the three- and nine-story buildings, only three sites were considered: Milan (low seismicity), Naples (medium seismicity) and L'Aquila (high seismicity).

Most buildings were designed for Soil Type C, the nine-story building in L'Aquila was designed for both Soil Type A and C. For each site and soil type, three configurations are considered in the study: BF, IF and PF.

Table 4.2.1 Summary of buildings.

| | City | Milan | | Caltanissetta | | Rome | | Naples | | L'Aquila | |
|---|---|---|---|---|---|---|---|---|---|---|---|
| | Soil | Type A | Type C | Type A | Type C | Type A | Type C | Type A | Type C | Type A | Type C |
| MRF | 3-Story | | X | | | | | | X | | X |
| MRF | 6-Story | | X | | X | | X | | X | | X |
| MRF | 9-Story | | X | | | | | | X | X | X |
| SW | 9-Story | | X | | | | | | X | | X |

The following structural materials are used:

- concrete C28/35 [11.2.10 NTC2008] (its mechanical properties are reported in Table 4.2.2;
- B450C steel [11.3.2.1 NTC2008] (its mechanical properties are reported in Table 4.2.3).

Table 4.2.2 reports all concrete properties. It shows that in order to account for element cracking in linear analyses, reduced concrete elastic moduli are used for the beam ($E_{cm-bm}$), for the column and wall ($E_{cm-cl}$).

Table 4.2.2 Mechanical properties for C28/35 concrete.

| $f_{ck}$ | $f_{ctm}$ | $E_{cm}$ | $E_{cm-cl}$ [0.75 $E_{cm}$] | $E_{cm-bm}$ [0.5 $E_{cm}$] | $f_{cd}$ | $\varepsilon_{cu}$ |
|---|---|---|---|---|---|---|
| [MPa] | [MPa] | [MPa] | [MPa] | [MPa] | [MPa] | [-] |
| 28.0 | 2.77 | 32300 | 24225 | 16150 | 15.87 | 0.35% |

Table 4.2.3 Mechanical properties for B450C reinforcing steel.

| $f_{yk}$ | $f_{yd}$ | $E_s$ | $\varepsilon_{su}$ |
|---|---|---|---|
| [N/mm$^2$] | [N/mm$^2$] | [N/mm$^2$] | [-] |
| 450.0 | 391.3 | 200000 | 7.50% |

### 4.2.1.2  Non-seismic loads

Table 4.2.4 reports all permanent and variable loads used for the buildings' design.

Table 4.2.4 Permanent (G) and Variable (Q) loads.

| Description | Units | Value |
|---|---|---|
| G1_RC elements | kN/m$^3$ | 25.00 |
| G1_slabs (floor and roof) | kN/m$^2$ | 3.20 |
| G2_slabs (floor) | kN/m$^2$ | 3.10 |
| G2_roof | kN/m$^2$ | 1.60 |
| G2_staircase | kN/m$^2$ | 0.80 |
| Q_slabs (floor) | kN/m$^2$ | 2.00 |
| Q_roof (snow) | kN/m$^2$ | Site dependent |
| Q_staircase | kN/m$^2$ | 4.00 |
| G2_infills | kN/m$^2$ | 3.50(*) |

*(\*) The assumed value accounts for the presence of openings through a correction coefficient estimated at 0.85.*

### 4.2.1.3  Seismic action

The seismic design of the RC buildings is performed by means of modal response spectrum analysis. According to the Italian building code NTC 2008, the seismic action can be evaluated using response spectra, related to the site hazard and the reference limit state. The site hazard is defined by the seismic hazard parameters ($a_g$, $F_0$, $T_c^*$), for life safety limit state (LS), reported in the Annex B of the Italian building code NTC2008, depending on the geographical position and on the return periods.

Soil and topographic category

The response spectrum depends on the soil and topographic category of the construction site. The soil category can be defined considering the stratigraphic profiles and the average shear wave velocity, $V_{s,30}$. For the reference case studies, referring to Tab. 3.2.II – NTC 2008, Soil Type C was selected (for one case, Soil Type A was considered too, see Table 4.2.1). Flat topographic conditions were assumed for the case studies (topography category $T_1$, according to Tab. 3.2.IV – NTC 2008).

Design response spectrum for life safety limit state

The elastic response spectrum is defined by Eq. 3.2.4 (horizontal acceleration component) of the Italian building code NTC 2008 (Figure 4.2.5 and Figure 4.2.8). The design response spectrum can be obtained from the elastic one using the behavior factor q, defined as:

$$q = q_0 \cdot K_R \qquad\qquad 4.1$$

For MRF frames, $q_0$ is equal to 3.9 for low ductility class[2] (NTC2008 § Tab7.4.I).

For SWs, $q_0$ is equal to 3.0 for low ductility class[2] (NTC2008 § Tab7.4.I).

$K_R$ is the regularity coefficient equal to one for regular structures (in plan and elevation). Thus, in the horizontal direction for MRF frames q=3.9 is assumed (Figure 4.2.7, Figure 4.2.10), for SWs q=3.0 is assumed (Figure 4.2.6, Figure 4.2.9). The earthquake vertical component was neglected in all analyses (linear and nonlinear).
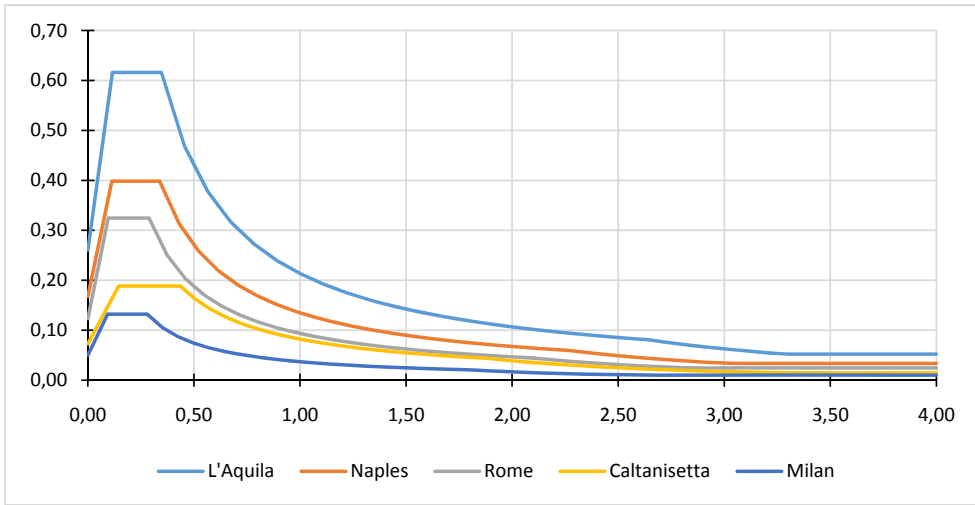
Figure 4.2.5 Horizontal elastic response spectra for 475 years return period design earthquake at five building sites (Soil Type A).
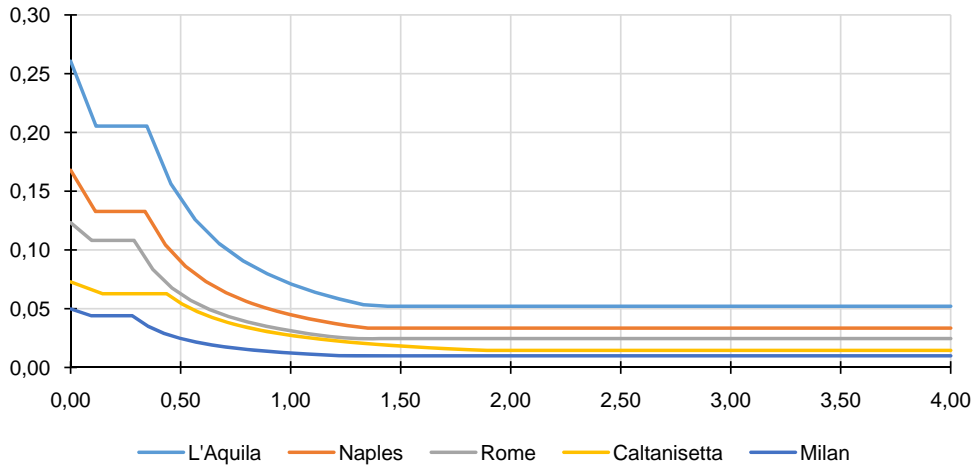


Figure 4.2.6 Horizontal design response spectra for 475 years return period design earthquake at five building sites (Soil Type A) – q = 3.00.
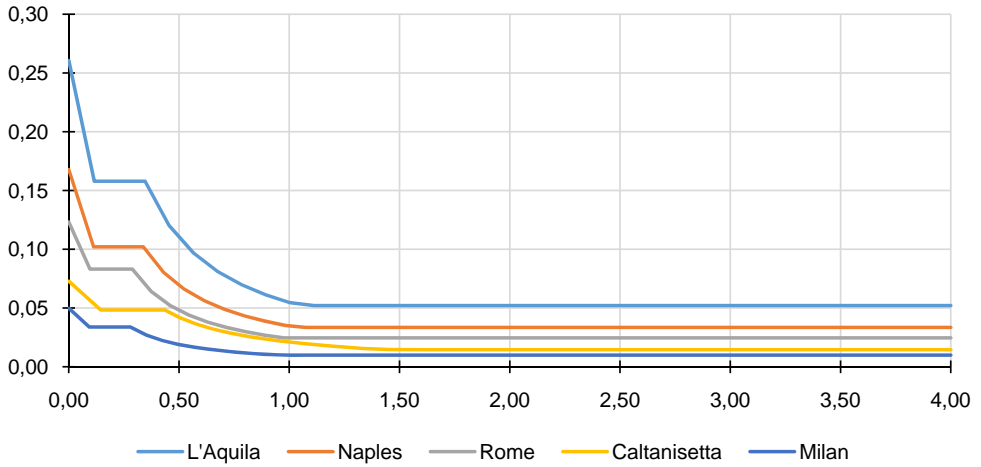
Figure 4.2.7 Horizontal design response spectra for 475 years return period design earthquake at five building sites (Soil Type A) – q = 3.90.
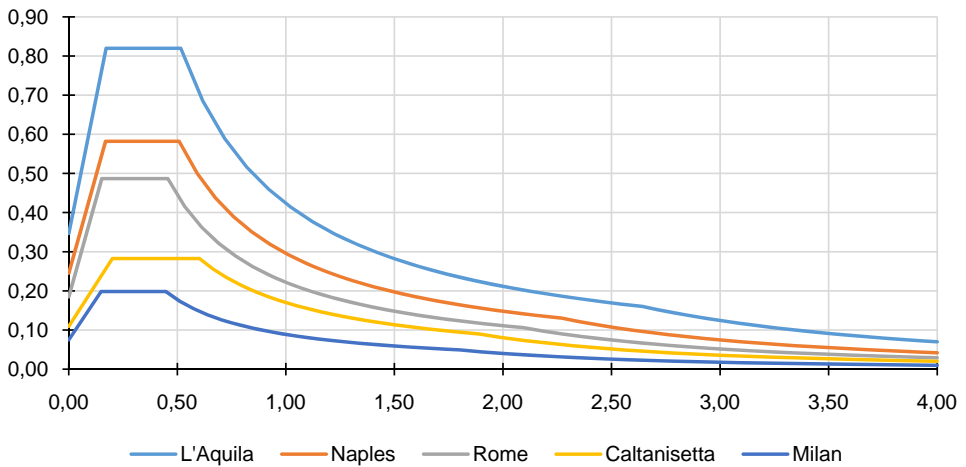


Figure 4.2.8 Horizontal elastic response spectra for 475 years return period design earthquake at five building sites (Soil Type C).
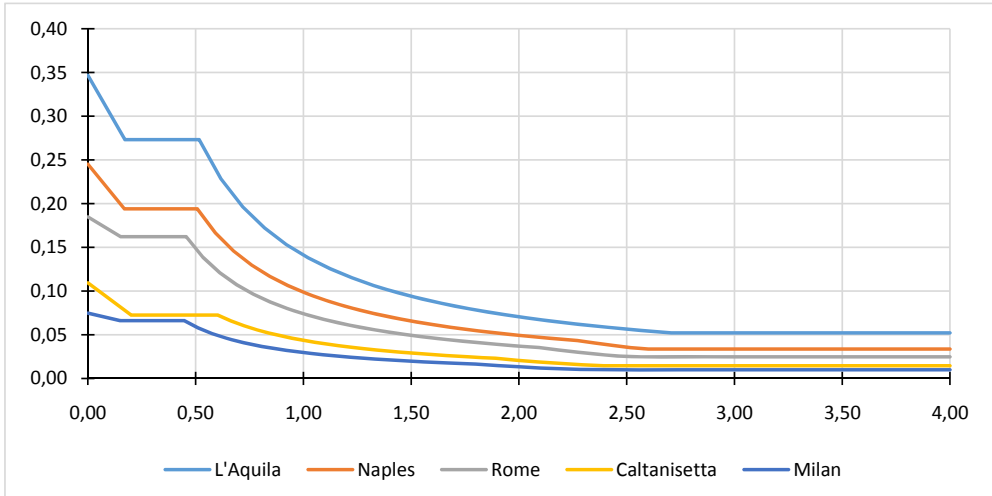
Figure 4.2.9 Horizontal design response spectra for 475 years return period design earthquake at five building sites (Soil Type C) – q = 3.00.
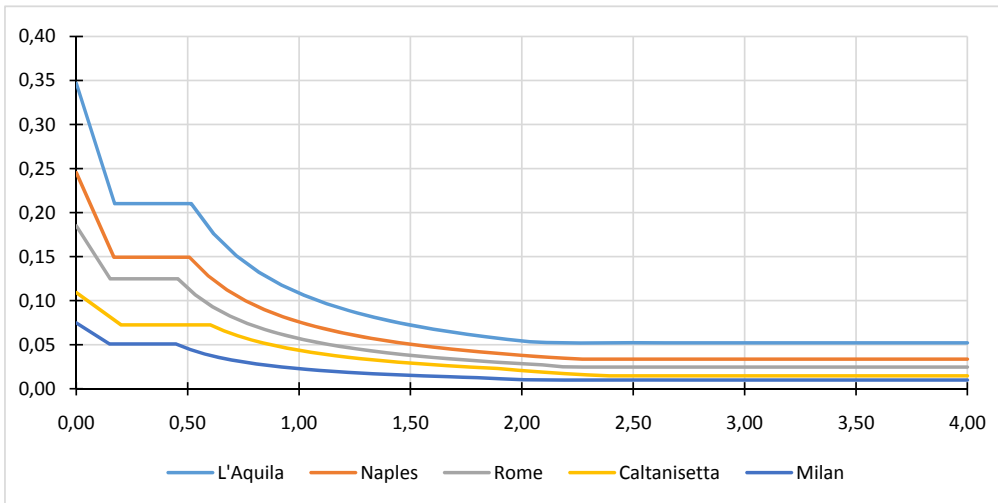


Figure 4.2.10 Horizontal design response spectra for 475 years return period design earthquake at five building sites (Soil Type C) – q = 3.90.

### 4.2.2    Design summary for MRF three-story RC buildings

The following tables summarize the main design data for the three buildings considered. The following symbols are used:

$T_x$, $M_x$ = fundamental period in the x direction and corresponding mass participation factor;

$T_y$, $M_y$ = fundamental period in the y direction and corresponding mass participation factor;

ΣA_col/A_floor = total column area at the ground floor/total floor area;

$\rho_{b\_deep,1,m}$ = average deep beams' longitudinal steel ratio;

$\rho_{b\_flat,1,m}$ = average flat beams' longitudinal steel ratio;

$\rho_{c,1,m}$ = average base floor columns' steel ratio.

Table 4.2.5 Summary of modal parameters for all buildings.

| City / Soil | $T_x$ [s] | $M_x$ [%] | $T_y$ [s] | $M_y$ [%] |
|---|---|---|---|---|
| Milan/C | 0.86 | 89 | 0.74 | 60 |
| Naples /C | 0.62 | 79 | 0.63 | 84 |
| L'Aquila /C | 0.44 | 76 | 0.46 | 80 |

Table 4.2.6 Summary of design data for all buildings.

| City / Soil | Types | ΣA_col/A_floor [%] | $\rho_{b\ deep,1,m}$ [%] | $\rho_{b\ flat,1,m}$ [%] | $\rho_{c,1,m}$ [%] |
|---|---|---|---|---|---|
| Milan/C | BF - IF | 0.90 | 0.8 ÷ 1.0 | 0.6 ÷ 2.2 | 1.1 ÷ 2.3 |
| | PF | 0.90 | 0.8 ÷ 1.0 | 0.6 ÷ 2.2 | 1.1 ÷ 2.3 |
| Naples/C | BF - IF | 1.29 | 0.8 ÷ 1.7 | 1.0 ÷ 1.9 | 1.3 ÷ 2.1 |
| | PF | 1.29 | 0.8 ÷ 1.7 | 1.0 ÷ 1.9 | 1.5 ÷ 2.6 |
| L'Aquila/C | BF - IF | 2.26 | 0.7 ÷ 1.4 | 1.0 ÷ 2.0 | 1.5 ÷ 2.1 |
| | PF | 2.26 | 0.7 ÷ 1.4 | 1.0 ÷ 2.0 | 1.5 ÷ 2.8 |

### 4.2.3   Design summary for MRF 6-story RC buildings

The following tables summarize the main design data for the five buildings under consideration.

Table 4.2.7 Summary of modal parameters for all buildings.

| City / Soil | $T_x$ [s] | $M_x$ [%] | $T_y$ [s] | $M_y$ [%] |
|---|---|---|---|---|
| Milan/C | 1.66 | 75 | 1.42 | 83 |
| Caltanissetta/C | 1.09 | 83 | 0.90 | 83 |
| Rome/C | 1.04 | 81 | 0.97 | 82 |
| Naples/C | 0.88 | 82 | 0.80 | 83 |
| L'Aquila/C | 0.90 | 78 | 0.79 | 77 |

Table 4.2.8 Summary of design data for all buildings.

| City / Soil | Types | ΣA_col/A_floor [%] | $\rho_{b\ deep.1.m}$ [%] | $\rho_{b\ flat.1.m}$ [%] | $\rho_{c.1.m}$ [%] |
|---|---|---|---|---|---|
| Milan/C | BF - IF | 1.16 | 0.43 | 0.34 | 1.37 |
| | PF | 1.16 | 0.43 | 0.34 | 1.37 |
| Caltanissetta/C | BF - IF | 1.57 | 0.89 | 1.10 | 1.53 |
| | PF | 1.57 | 0.89 | 1.10 | 1.53 |
| Rome/C | BF - IF | 1.60 | 0.96 | 0.93 | 1.29 |
| | PF | 1.60 | 0.96 | 0.93 | 1.29 |
| Naples/C | BF - IF | 2.17 | 0.72 | 0.84 | 1.46 |
| | PF | 2.17 | 0.72 | 0.84 | 1.46 |
| L'Aquila/C | BF - IF | 3.10 | 1.51 | 1.23 | 1.08 ÷ 1.41 |
| | PF | 3.10 | 1.51 | 1.23 | 1.08 ÷ 1.41 |

## 4.2.4   Design summary for MRF 9-story RC buildings

The following tables summarize the main design data for the four buildings considered.

Table 4.2.9 Summary of modal parameters for all buildings.

| City / Soil | $T_x$ [s] | $M_x$ [%] | $T_y$ [s] | $M_y$ [%] |
|---|---|---|---|---|
| Milan/C | 1.57 | 79 | 1.40 | 79 |
| Naples/C | 1.62 | 78 | 1.47 | 78 |
| L'Aquila/A | 1.51 | 77 | 1.34 | 76 |
| L'Aquila/C | 1.47 | 79 | 1.24 | 77 |

Table 4.2.10 Summary of design data for all buildings.

| City / Soil | Types | ΣA_col/A_floor [%] | $\rho_{b\ deep.1.m}$ [%] | $\rho_{b\ flat.1.m}$ [%] | $\rho_{c.1.m}$ [%] |
|---|---|---|---|---|---|
| Milan/C | BF - IF | 2.0 | 0.34÷ 0.37 | 0.7 ÷ 1.0 | 1.25 ÷ 1.6 |
| | PF | 2.0 | 0.34÷ 0.37 | 0.7 ÷ 1.0 | 1.25 ÷ 1.6 |
| Naples/C | BF - IF | 2.36 | 0.90÷ 1.37 | 0.80 ÷ 1.47 | 1.15 ÷ 1.72 |
| | PF | 2.36 | 0.90 ÷ 1.37 | 0.80 ÷ 1.47 | 1.15 ÷ 1.72 |
| L'Aquila/A | BF - IF | 2.55 | 0.92 ÷ 1.26 | 1.07 ÷ 1.49 | 1.01 ÷ 1.15 |
| | PF | 2.55 | 0.92 ÷ 1.26 | 1.07 ÷ 1.49 | 1.01 ÷ 1.27 |
| L'Aquila/C | BF - IF | 3.01 | 0.75 ÷ 1.80 | 0.9 ÷ 1.26 | 1.45 ÷ 2.08 |
| | PF | 3.01 | 0.75 ÷ 1.60 | 0.9 ÷ 1.26 | 1.45 ÷ 3.19 |

## 4.2.5   Design summary for SW 9-story RC buildings

The following tables summarize the main design data for the three buildings under consideration. The following symbols are used:

ΣA_wall/A_floor = total wall area at the ground floor/total floor area;

$\rho_{w,1,m}$ = average base floor walls' steel ratio.

Table 4.2.11 Summary of modal parameters for all buildings.

| City / Soil | $T_x$ [s] | $M_x$ [%] | $T_y$ [s] | $M_y$ [%] |
|---|---|---|---|---|
| Milan/C | 1.32 | 77 | 1.15 | 78 |
| Naples/C | 1.25 | 77 | 1.07 | 77 |
| L'Aquila/C | 1.15 | 76 | 0.97 | 76 |

Table 4.2.12 Summary of design data for all buildings.

| City / Soil | Types | ΣA_wall/ A_floor [%] | ΣA_col/ A_floor [%] | $\rho_{b\ deep,1,m}$ [%] | $\rho_{b\ flat,1,m}$ [%] | $\rho_{c.1.m}$ [%] | $\rho_{w.1.m}$ [%] |
|---|---|---|---|---|---|---|---|
| Milan/C | BF - IF | 1.15 | 1.08 | 0.68 ÷0.77 | 0.68 ÷1.02 | 1.01÷1.1 | 1.03 |
|  | PF | 1.15 | 1.08 | 0.68 ÷0.77 | 0.68 ÷1.02 | 1.01÷1.1 | 1.03 |
| Naples/C | BF - IF | 1.34 | 1.15 | 0.85 ÷2.53 | 0.68 ÷1.02 | 1.54÷3.05 | 1.13÷1.7 |
|  | PF | 1.34 | 1.15 | 0.85 ÷2.53 | 0.68 ÷1.02 | 1.54÷3.05 | 2.09÷2.62 |
| L'Aquila/C | BF - IF | 1.63 | 1.22 | 0.85 ÷3.04 | 0.68 ÷1.02 | 1.41÷3.8 | 2.53 |
|  | PF | 1.63 | 1.22 | 0.85 ÷3.04 | 0.68 ÷1.02 | 1.41÷3.8 | 3.02÷3.77 |

### 4.2.6   Design considerations

The following preliminary considerations can be drawn from the above data:

- The column dimensions mainly derive from pre-dimensioning based on the assumed maximum normalized axial load;
- Following design practice, all buildings were designed to be regular in elevation;
- In most cases the amount of reinforcement is given by the minimum reinforcement requirements of NTC 2008, thus reducing the differences between IF/BF and PF buildings to a minimum (they are, in some cases, identical);
- The staircase knee beams experience high tension/compression excursions, pointing to possible numerical issues in the nonlinear analyses;
- The column area increases with the site seismic intensity, while the reinforcement ratio stays almost constant, due to the minimum reinforcement requirements in the NTC2008 design code;
- For the MRF buildings, the design data reflects the inherent building-to-building variability due to different design approaches. Each building was in fact designed by a different research group (except for the three-story buildings), thus different approaches were followed within the leeway allowed by the code. It was decided, for example, to keep the column sizes in all six-story buildings to a minimum of 35 cm x 35 cm. In Milan, smaller columns could have been easily used. As mentioned in the previous sections, in some cases the BF building was so over-designed that the corresponding PF building did not require any section or reinforcement increase;
- For the SW buildings, similarly to the MRF buildings, the wall design of the Milan building was based on the minimum size requirements by NTC2008. In other words, smaller sizes could have been used, but the building would not have fallen into the shear building category.

## 4.3   Modelling issues and strategies

Each of the buildings designed and analyzed has a standard three-dimensional frame structure, following Italian common practice even in high seismicity areas. For the purpose of probabilistic seismic risk assessment based on inelastic time history response analysis, cyclic constitutive laws are potentially required for the following components of the building:

- reinforced concrete beam and column members, including inclined members of the staircase structure
- reinforced concrete walls (modeled as line elements)
- reinforced concrete joints
- reinforced concrete floor slabs
- masonry infill panels
- foundations

The following two sections describe and discuss the choices made for RC components and infill panels, respectively.

### 4.3.1   Reinforced concrete members

The constraints imposed by the size of the buildings (example: six floors, 38 beams and 26 column members per floor, plus the staircase members, for more than 400 frame elements in the models) and the type of analysis carried out (multiple stripe analysis at 10 intensity levels using 20 motions per stripe, repeated for three configurations - BF, IF, and PF - for a total of 600 time history response analyses per site) called for pragmatic choices in the modeling. Furthermore, any selected model would have to be among those implemented in the chosen analysis platform (OpenSees), even though this was not really a limitation.

4.3.1.1  Beam, column and wall members

For beam and column members, the available options can be reduced to:

- a 'mechanical' model, like a fiber section-discretization, coupled with either a concentrated or a distributed inelasticity frame element formulation, generally referred to as 'fiber- model' (Spacone, Fillippou, and Taucer 1996a,b);
- a 'phenomenological' model, like a piece-wise linear moment-curvature or -rotation law at the section level, usually combined with a concentrated inelasticity frame element formulation, generally referred to as 'plastic-hinge model'.

The respective advantages and disadvantages of the two modeling strategies are well known.

The former describes the cyclic response of frame members with flexural behavior in a more accurate manner and, in particular, allows for biaxial moment and axial force interaction to be properly taken into account. The basic versions of this section model are based on the plane-section constraint and require simple uniaxial constitutive laws at the fiber level. For RC members this is required for a concrete cyclic law and a steel cyclic law. Within the OpenSees package usually the Kent-Scott-Park model (Concrete01) and the Menegotto-Pinto model (Steel01) are selected.

On the other hand, as already stated, if member response is not predominantly flexural, as it happens for instance with older non-conforming members, where shear comes into play, the plain 'fiber-model' is not capable of describing correctly the response, especially at larger excursions in the inelastic range. A relatively recent overview of possible solutions for the case where shear-flexure interaction is relevant is given in (Ceresa et al., 2007). Enhanced 'fiber-models' have been proposed, e.g., Petrangeli et al (1999), Bairan and Mari(2007), Mohr et al.(2010). Also, several approximate hybrid modeling strategies have been proposed and used,

employing phenomenological models to describe the shear component of response, e.g., Ranzo and Petrangeli (1998), Elwood (2004), Marini and Spacone (2006), Franchin and Pinto (2009). The 'Elwood' model, in particular, is very attractive, and has been used in the context of probabilistic seismic risk assessment, to perform IDA on a twelve-story (plane) frame (Baradaran-Shoraka et al., 2012). Nonetheless, independent tests have shown that the model lacks the necessary computational robustness. More generally, even when shear is not necessarily critical, at larger response levels (closer to collapse) the fiber-model based on the plane-section assumption fails to capture correctly the negative stiffness branch of response. It should be noted that there are many instances (e.g., in Goulet et al., 2007) where a 'fiber-model' is employed for the lower intensity and response levels and a 'plastic-hinge model' is used for the higher ones.

The buildings considered in this project are all designed up to modern code provisions both for global and local ductility, thus ductile flexural failure is expected. Nevertheless, given that the interest is in the collapse limit state, the reliability of the 'fiber-model' was questioned.

Also in terms of computational burden, this modeling strategy is not very attractive. Even though, depending on the response quantity of interest, very refined section discretization may not be required, still 16 (4x4) to 25 (5x5) concrete integration points plus one point per rebar are needed to have a decent response at section stress resultant and member displacement levels (Kostic and Filippou, 2011) in three-dimensional analysis. Even considering a concentrated inelasticity element formulation for the six-story building, like the one by Scott and Fenves (2006), implemented in the 'BeamWithHinges' element in OpenSees, the total number of inelastic integration points, not including masonry infills, would be in the order of 400 elements x 2 sections x ~30 points = 24,000. Each of these 24,000 integration points would require a state determination (an evaluation of the constitutive law) in each of the equilibrium iterations (more than one on average) within each time step of the response history analysis (say, 2000 with an average 20 seconds time series duration and 0.01 time step). A feasibility study was carried out to appraise the total analysis time and storage requirements which showed that the 'fiber-model' strategy was not a viable option for the task at hand, requiring tens of terabyte of output storage and more time than available within the project term (see below with reference to the phenomenological model). Similar conclusions, albeit with reference to existing non-conforming buildings have been drawn also in the recent Italian CNR guidelines for probabilistic seismic assessment of existing RC and masonry buildings.

For the reasons described above, it was chosen to adopt a simple phenomenological model.

The chosen model is the well-tested model by Ibarra, Medina and Krawinkler (2005), in its most recent OpenSees implementation (modIMKmodel). The model has already been used in a similar setting, i.e., for the probabilistic seismic performance assessment of both existing and code-conforming (plane) frame structures (Haselton et al., 2010, Liel et al., 2010).

The model is defined through seven parameters, five for the monotonic envelope and two for the degradation mechanism (actually more in the modified implementation in OpenSees, where for instance non-symmetric backbones, e.g., for beams, are considered, thus doubling all backbone definition parameters):

- elastic stiffness
- effective yield strength
- strain hardening ratio
- pre-capping rotation or plastic rotation capacity
- post-capping rotation
- cyclic deterioration parameters

This model can be used to describe the moment-rotation relationship, independently of axial load and in a single plane of flexure. As a result, the coupled NM2M3 section response is replaced by two independent flexural responses for a constant axial load, and an independent axial force-displacement uniaxial law. Technically this is done via the section aggregator feature

of OpenSees, where the section response is obtained by assembling independent uniaxial (or coupled multi-axial) laws on each degree of freedom.

Thus the main disadvantage of this modeling strategy lies in neglecting the coupling, which is otherwise captured automatically by the 'fiber-model'. Also, the model describes the pre-yield response with a single linear branch. The stiffness of this branch must thus be chosen as an intermediate value between the uncracked and the secant-to-yield values. A smart work-around is possible within OpenSees, as proposed by the UniNA-V research unit, making use of the Parallel and Series features to aggregate uniaxial laws, but it was not implemented after all given that the increase in precision at the lower response intensity is counter-balanced by the decrease in computational robustness.

Advantages of the model, on the other hand, are:

- computational efficiency: 3 integration points (the uniaxial laws on the three dof's) versus ~30 of the 'fiber-model', i.e., a reduction by one order of magnitude.
- computational robustness: the IMK model, coupled with the element assembly strategy described below, is extremely robust, as opposed to the 'fiber model' which was shown to have problems, for instance, when the magnitude of axial force variations is too large within a single integration step.
- the capability of describing, albeit in an aggregate manner, the degrading response arising from a set of interacting phenomena like conventional flexural response, bar-slippage or buckling, shear sliding, etc. In particular, the model allows both in-cycle and cyclic degradation (Haselton et al., 2009).
- the availability of predictive equations for the IMK model parameters, obtained by statistical regression on actual test results for several hundreds of specimens, and in particular 255 RC members (predictive equations by Haselton et al., 2009) and >300 steel specimens (Lignos and Krawinkler, 2012). The importance of these equations cannot be understated, since they allow easy determination of the model parameters from basic geometric and mechanical input data, without the need for prior moment-curvature section analysis. Most importantly, these equations provide a median and an associated logarithmic standard deviation which allows accounting for the model error.

As already stated, the chosen modeling strategy has been the same as that already adopted in Haselton et al., (2010), Liel et al., (2010) and the Italian DT212 guidelines. Instead of employing an inelastic beam element formulation like the BeamWithHinges element in OpenSees, an assembly of simpler elements was used, as shown in Figure 4.3.1. A Tcl/Tk procedure is used to generate internal nodes coincident with the i and j nodes of each member, and *zerolength* elements are used to describe inelastic response confined in these end sections. The internal portion is modelled with an elastic frame element. The advantage of this modelling approach, which requires a larger number of nodes and elements like the *BeamWithHinges* one, is that more refined element formulations employ the flexibility formulation (i.e., forces and moments are interpolated along the element, rather than the deformation field), which is the best theoretical choice and certainly more accurate in the nonlinear range than displacement-based formulations (which requires to increase the number of elements per member in order to reach the same degree of accuracy). The downside of the flexibility formulation is that it requires internal iteration on the equilibrium. All implementations in OpenSees seem to be too inflexible in terms of the degrees of freedom left to the user in the way that those parameters can be used in order to increase the convergence rate. There is therefore no option more robust than leaving complete control over the iterations to the global algorithm, by employing nodes with global degrees of freedom (called 'internal' in the figure) also for the plastic hinges.
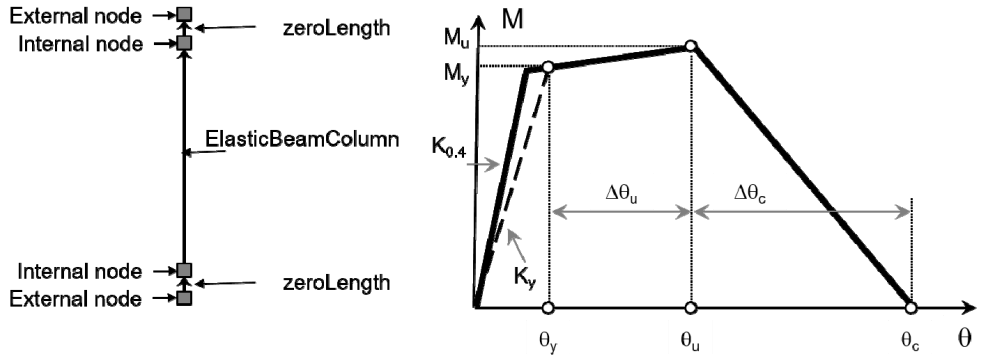
Figure 4.3.1 Adopted frame model: assembly of zeroLength inelastic elements and elasticBeamColumn element (left), moment-rotation law (backbone) according to the Ibarra et al. (2005) model (right).

To sum-up, for each plane of flexure, the following parameters have been determined for the member-level moment-rotation properties:

$$\Delta\theta_u = 0.13(1+0.55a_{sl})(0.13)^{\nu}(0.02+40\rho_{sh})^{0.65}(0.57)^{0.01f_c} \tag{4.2}$$

$$\Delta\theta_c = 0.76(0.31)^{\nu}(0.02+40\rho_{sh})^{1.02} \leq 0.10 \tag{4.3}$$

$$k_{0.4} = 0.17+1.61\nu\begin{cases}\geq 0.35 \\ \leq 0.80\end{cases}, \quad K_{0.4} = k_{0.4}\frac{3EI_0}{L_V} \tag{4.4}$$

$$k_y = 0.065+1.05\nu\begin{cases}\geq 0.20 \\ \leq 0.60\end{cases}, \quad K_y = k_y\frac{3EI_0}{L_V} \tag{4.5}$$

$$\alpha_y = \frac{M_u}{M_y} = 1.25(0.89)^{\nu}(0.91)^{0.01f_c} \tag{4.6}$$

$$\gamma = \frac{E_t}{M_y\theta_y} = 170.7(0.27)^{\nu}(0.10)^{s/d} \tag{4.7}$$

The above was distributed among *zeroLength* sections and the central elastic beam/column element in order to preserve the total flexibility (flexibility in series), as shown in the examples in the following Figure 4.3.2.
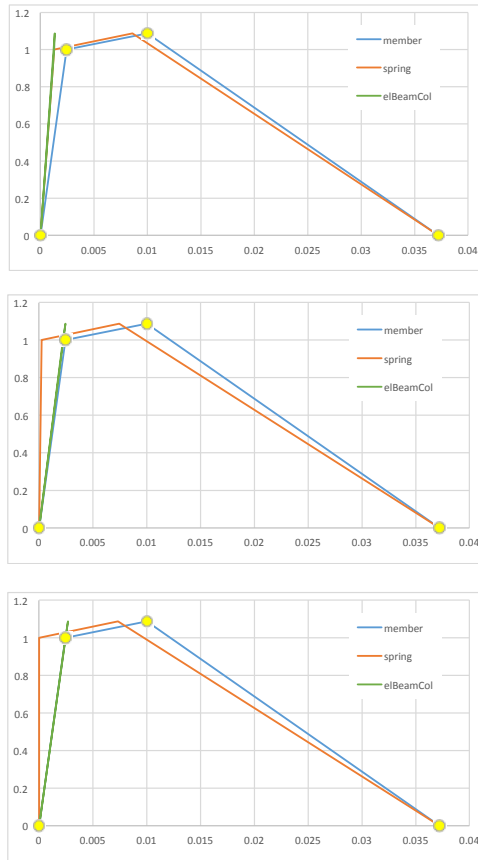
Figure 4.3.2 Distribution of stiffness among the zeroLength and the elasticBeamColumn elements, as a function of the initial stiffness ratio n=$k_s$/$k_e$ between section and internal elastic element: n = 1, 10 and 100, respectively, from top to bottom.

Since the elements are in series, the moment thresholds of the inelastic sections are the same as those of the member, while deformation thresholds are a function of the stiffness ratio $n = k_s/k_e$, where the "s" and "e" subscripts denote the section and the elastic element, respectively (Ibarra and Krawinkler, 2005 – Appendix B).

It is given as:

$$\frac{1}{k_m} = \frac{1}{k_s} + \frac{1}{k_e} = \frac{1}{nk_e} + \frac{1}{k_e} \rightarrow k_e = \frac{n+1}{n}k_m \rightarrow k_s = (n+1)k_m$$

4.8

and also:

$$\frac{1}{k_m} = \frac{1}{k_s} + \frac{1}{k_e} \rightarrow \theta_m = \theta_s + \theta_e \rightarrow \Delta\theta_m = \Delta\theta_s + \Delta\theta_e$$

4.9

from which follows:

$$\Delta\theta_s = \Delta\theta_m - \Delta\theta_e = \Delta\theta_m - \frac{\Delta M}{k_e} = \Delta\theta_m - \frac{\Delta M}{k_m}\frac{n}{n+1} = \Delta\theta_m\left(1 - \frac{n}{n+1}\right)$$
$$= \Delta\theta_m\frac{1}{n+1}$$

4.10

### 4.3.1.2 Staircases

The stairwell structure comprises inclined beams and cantilever steps. The inclined beams are subjected to large magnitude axial force variations. These forces have a projection on the horizontal axis that introduces large shear forces into the adjoining members. In order to limit these forces to values compatible with the inclined beam strength, the modelling adopted for the beam and column members needs to be modified.

Given the relatively small numbers of such elements, the alternatives include the use of the 'fiber-model' limited to these inclined beams. Numerical tests, however, have shown that the introduction of these elements severely limits the overall computational robustness of the building model. For this reason, the phenomenological IMK model was maintained, yet modified. In particular, the stiffness of the axial degree of freedom of the internal *elasticBeamColumn* element was reduced to zero, while putting an inelastic truss element in parallel to it. The truss element adopts a non-symmetric elastic-plastic constitutive law with limits proportional to $A_s f_y$ ($A_s$ being the total section reinforcement) in tension and $A_c f_c$ in compression, respectively.

### 4.3.1.3 Joints

Joints were not modelled, as these components are prevented from failing based on capacity design prescriptions. In any case, internal joints are always confined on all six faces and are generally not modelled even in existing non-conforming buildings. Thus the choice of not modelling joints amounted to not describing the (likely minor) flexibility contribution of perimeter joints due to cracking in the elastic range. This is deemed to be compensated by the choice of not employing end-offsets for beam and column members.

### **4.3.2   Masonry Infills**

The contribution of the masonry infill panels to the response of the reinforced concrete frame is modeled by replacing the panel with an equivalent strut acting only in compression (Figure 4.3.3). The equivalent diagonal strut is a consolidated engineering model for infilled frames that is also proposed for the design of infilled frames by several codes.



$\omega$ = strut width for solid infill
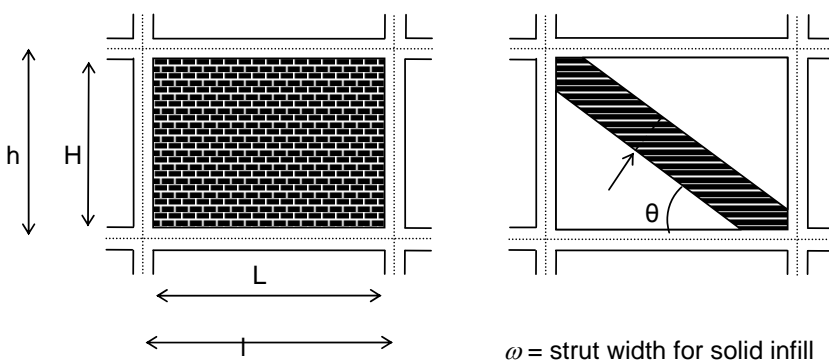
Figure 4.3.3 Diagonal strut model.

Between a wide range of different relationships that describe the parameters governing the monotonic and cyclic behavior of the diagonal strut, as a function of the mechanical and geometrical characteristics of masonry infill, we chose the Decanini et al. model (Decanini and Fantin ,1986; Bertoldi et al., 1993; Liberatore, 2001; Decanini et al., 2004; Decanini et al., 2014)

The resistance of the infill panel was simulated by a fictitious failure compressive stress $\sigma_{br}$, taking into account the different failure modes occurring both laboratory tests and real structures subjected to seismic action. Four basic failure modes are considered, with the corresponding equivalent failure compressive stresses: (a) diagonal tension, $\sigma_{br(1)}$; (b) sliding shear along horizontal joints, $\sigma_{br(2)}$; (c) crushing in the corners in contact with the frame, $\sigma_{br(3)}$; (d) diagonal compression, $\sigma_{br(4)}$.

$$\sigma_{br_{(1)}} = \frac{0.6\tau_{m0} + 0.3\sigma_o}{\omega/d} \tag{4.11}$$

$$\sigma_{br_{(2)}} = \frac{(1.2\sin\theta + 0.45\cos\theta)u + 0.3\sigma_o}{\omega/d} \tag{4.12}$$

$$\sigma_{br_{(3)}} = \frac{(1.12\sin\theta \cdot \cos\theta)}{K_1(\lambda h)^{-0.12} + K_2(\lambda h)^{-0.88}}\sigma_{m0} \tag{4.13}$$

$$\sigma_{br_{(4)}} = \frac{1.16\sigma_{mo}\tan\theta}{K_1 + K_2\lambda h} \tag{4.14}$$

where $\sigma_{m0}$ is the vertical compression strength measured on masonry specimens, $\tau_{m0}$, is the shear strength measured with the diagonal compression test, u is the sliding resistance in the joints measured form the triplet test, and $\sigma_0$ is the vertical stress due to working loads.

The ultimate lateral strength, $H_{mfc}$, of the equivalent strut was selected as the minimum value among the capacities associated with the four in-plane failure modes: diagonal tension, diagonal compression, shear failure at the horizontal wall-to-frame interface, and crushing of the wall corners in contact with the frame.

$$H_{mfc} = (\sigma)_{min}e\,\omega\,cos\theta \tag{4.15}$$

Based on the available experimental data, the ultimate lateral strength $H_{mfc}$ was incremented by a factor estimated at 1.18 to obtain the median value of the available database.

The width of the strut, $\omega$, is introduced by means of the relative stiffness parameter $\lambda h$ proposed by Stafford-Smith (1963) and by two constants $K_1$ and $K_2$ calibrated on the basis of experimental tests:

$$\omega = \left(\frac{K_1}{\lambda h} + K_2\right)d \tag{4.16}$$

where $\lambda h$ is a non-dimensional parameter depending on the geometric and mechanical characteristics of the frame-infill system, $K_1$ and $K_2$ are coefficients that change according to $\lambda h$, and $d$ is the length of the equivalent strut (Table 4.3.1).

Table 4.3.1 Coefficients $K_1$ and $K_2$.

|  | $K_1$ | $K_2$ |
|---|---|---|
| $\lambda h \leq 3.14$ | 1.3 | -0.178 |
| $3.14 \leq \lambda h \leq 7.85$ | 0.707 | 0.01 |
| $\lambda h \geq 7.85$ | 0.47 | 0.04 |

It is well known that the parameter $\lambda h$, is defined by the following expression:

$$\lambda h = \sqrt[4]{\frac{E_m e \ \sin(2\theta)}{4 E_c I \ h_m}} h \qquad 4.17$$

where $E_m$ is the elastic equivalent modulus corresponding to the complete cracking stage of the infill, $E_c$ is the elastic modulus of concrete, $t$ is the slope of the strut to the respect of the horizontal axis, $e$ is the thickness of the masonry panel, $h$ is the story height, $h_m$ is the height of the masonry panel, and $I$ is momentum of inertia of the columns.

The stiffness of the equivalent strut $K_{mfc}$ at complete cracking stage is given by the following relation:

$$K_{mfc} = \frac{E_m e \omega}{d} \cos^2 \theta \qquad 4.18$$

The skeleton curve of the lateral force-displacement ($H_m$-u) relationship considers four branches (Figure 4.3.4). The first linear elastic ascending branch corresponds to the un-cracked stage, the second branch refers to the post-cracking phase up to the development of the maximum strength ($H_{mfc}$). The point FC corresponds to the complete cracking stage of the infill panel. The descending third branch of the curve describes the post-peak strength deterioration of the infill up to the residual strength and displacement $H_{mr}$ and $u_r$, respectively; after that the curve continues horizontally. The model essentially needs the definition of the width of the equivalent strut $\omega$, the stiffness at complete cracking stage $K_{mfc}$, and the strength $H_{mfc}$, as a function of the geometric and mechanical characteristics of the frame.
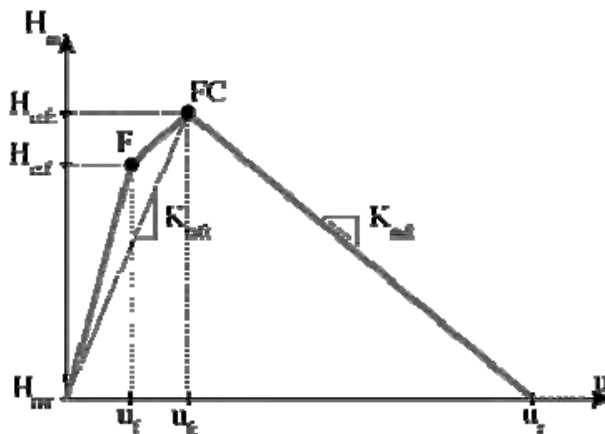


Figure 4.3.4 Backbone curve for the equivalent strut model.

The openings in the infill walls lead to significant uncertainty in the assessment of the seismic behavior of the structure due to the variability of their size and location. In general, the presence of openings results in reductions of stiffness and ultimate strength of the panel. The presence of

openings in the infills was taken into account by means of a simple model based on the use of reduction factors to be employed in the diagonal no-tension strut modelling approach (Decanini et al., 2014).

The original model by Decanini et al. was updated based on the works by Cardone and Perrone (2015) and by Sassun et al. (2016), where the masonry infill drift limits are revisited based on experimental evidence (the strength values are not affected by these more recent studies). The above works found that the drift limits computed based on the estimated elastic stiffness and the strength values are not in agreement with the corresponding experimentally observed drifts.

The force and drift values of the main points of the infills' backbone curves are reported in Figure 4.3.5. In the table, the forces are normalized with respect to the panel strength, which depends on the panel geometry and on the percentage of openings.



| | force | Drift θ | |
|---|---|---|---|
| | | openings | |
| | H / Hmfc | w/o | w/ |
| | 0 | 0 | 0 |
| cracking | 0.8 | 0.00209 | 0.00095 |
| peak | 1.0 | 0.00487 | 0.00334 |
| residual | 0 | 0.02599 | 0.02543 |
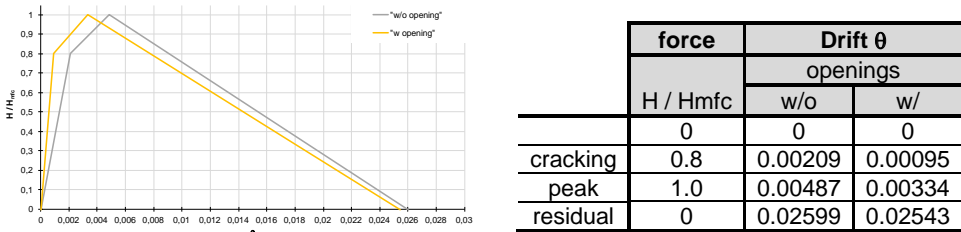
Figure 4.3.5 – Example infills w-w/o openings.

The cyclic behavior is fully described in Liberatore (2001). In this case, the infills were modeled in Opensees with the Concrete01 model (Figure 4.3.6).
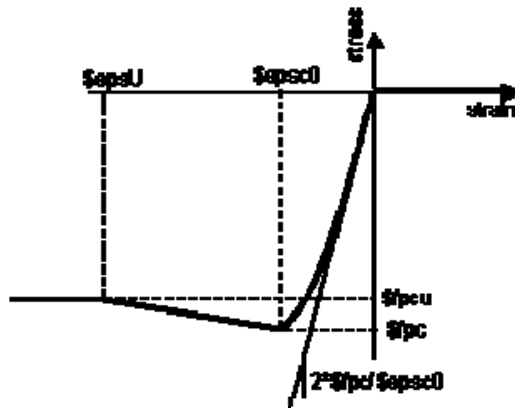


Figure 4.3.6 Adopted uniaxial constitutive law to approximate the strut backbone.

The mechanical characteristics of the infills are:

- Vertical stress          $\sigma_o$ = 0 MPa
- Compression strength      $\sigma_{mo}$ = 6.0 MPa
- Shear strength           $\tau_{mo}$ = 0.775 MPa
- Slide resistance          u = 0.542 MPa
- Young's modulus          E = 4312 MPa

$\tau_{mo}$ was derived from the correlation relation $\tau_{mo} = \gamma \sqrt{\sigma_{mo}}$ (where $\gamma$, that usually varies between 0.6-1.5, was considered equal to 1; $\sigma_{mo}$ is expressed in kg/cm$^2$), while $u$ was obtained from the empirical relation u = 0.7 $\tau_{mo}$.

With Concrete01 material, it is not possible to change the elastic stiffness in the origin with respect to the secant one, therefore the half value of the actual peak deformation was hypothetically adopted in order to obtain the correct elastic stiffness at the origin.

Table 4.3.2 reports the adopted values of the strength parameters, as well as the percentage residual strength of the equivalent struts as a function of openings size on each panel of the facades. Figure 4.3.7 shows the percentage of openings of the infill panels adopted in six-story buildings at the L'Aquila sites; the percentages of openings of the infill panels along the vertical planes at longitudinal (X) and transversal (Y) coordinates are provided for each span, which is labeled from left to right and from bottom to top, respectively, correspondingly to Table 4.3.2. The infills along the vertical plane at the transverse distance from the lower left corner Y = 0m, for example, have 40% of openings (brown color) for span 1 and 5, 22% of openings (orange color) at for span 2 and 4, and 0% (red color) for span 3.

Table 4.3.2 Masonry infill panels: strength values and percent residual strength as a function of openings adopted for six story building and the five sites.

|  | Masonry | | | Infill panels //X @ Y = 0 | | | | | Infill panels //X @ Y = 0 | | | | | Infill panels //Y | | |
|---|---|---|---|---|---|---|---|---|---|---|---|---|---|---|---|---|
|  | $\sigma_m$ (kPa) | $\tau_m$ (kPa) | $\tau_g$ (kPa) | 1 | 2 | 3 | 4 | 5 | 1 | 2 | 3 | 4 | 5 | 1 | 2 | 3 |
| Milano | 6000 | 775 | 542 | 47.2 | 27.1 | 100.0 | 27.1 | 47.2 | 47.2 | 27.1 | 0.0 | 27.1 | 47.2 | 100.0 | 100.0 | 100.0 |
| Caltanissetta | 6000 | 775 | 542 | 41.0 | 60.6 | 100.0 | 60.6 | 41.0 | 41.0 | 60.6 | 100.0 | 60.6 | 41.0 | 100.0 | 100.0 | 100.0 |
| Roma | 6000 | 775 | 542 | 44.8 | 60.4 | 100.0 | 60.4 | 44.8 | 44.8 | 60.4 | 100.0 | 60.4 | 44.8 | 100.0 | 100.0 | 100.0 |
| Napoli | 6000 | 775 | 542 | 47.2 | 27.1 | 100.0 | 27.1 | 47.2 | 47.2 | 27.1 | 0.0 | 27.1 | 47.2 | 100.0 | 100.0 | 100.0 |
| L'Aquila | 6000 | 775 | 542 | 40.0 | 22.0 | 0.0 | 22.0 | 40.0 | 40.0 | 22.0 | 0.0 | 22.0 | 40.0 | 100.0 | 100.0 | 100.0 |
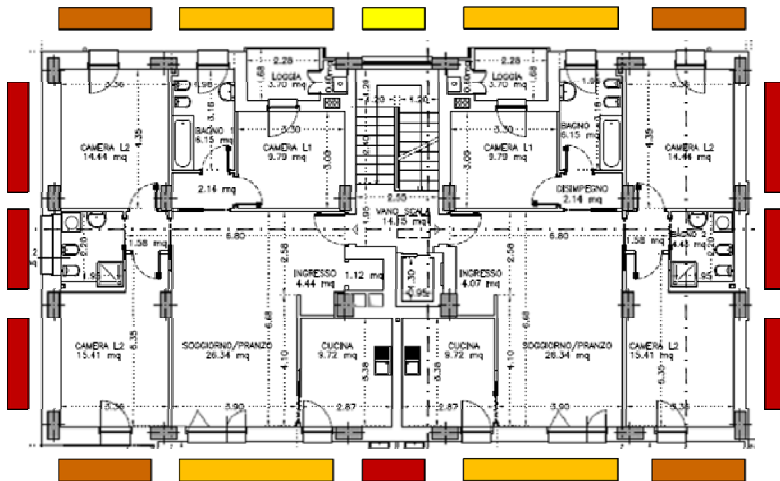


Figure 4.3.7 Masonry infill panels: percentage of openings (from 100% yellow to 0% red).

### 4.3.3   Foundations

The foundations were modelled as simple external restraints, owing to the capacity design that requires them to remain elastic and the traditional conservative design of foundation in Italy.

## 4.4   Analyses' results and discussion

### 4.4.1   Summary of modal analysis

Modal analysis was performed on all models to determine the conditioning IM to be used in the inelastic response history analyses. The following tables report the first vibration periods in each plan direction for all sites, buildings and the three infill configurations (BF, IF, and PF), together with the associated conditioning IM. The reported periods, obtained with models that account for the infills and use more refined stiffness evaluations, are different from those of the models used in design and reported in the previous sections. For the BF configuration of 6-story buildings in Naples and L'Aquila the conditioning IM was set to 1.50 s for the sake of comparison of results with other sites.

Table 4.4.1 Summary of modal parameters for 3-story buildings.

| City / Soil | Model | $T_x$ [s] | $T_y$ [s] | IM |
|---|---|---|---|---|
| L'Aquila/C | BF | 0.66 | 0.67 | 1.00 |
| | IF | 0.23 | 0.25 | 0.15 |
| | PF | 0.43 | 0.45 | 0.50 |
| Milan/C | BF | 1.04 | 0.90 | 1.00 |
| | IF | 0.21 | 0.24 | 0.15 |
| | PF | 0.71 | 0.67 | 0.50 |
| Naples/C | BF | 0.89 | 0.83 | 1.00 |
| | IF | 0.22 | 0.24 | 0.15 |
| | PF | 0.45 | 0.59 | 0.50 |

Table 4.4.2 Summary of modal parameters for 6-story buildings.

| City / Soil | Model | $T_x$ [s] | $T_y$ [s] | IM |
|---|---|---|---|---|
| Caltanissetta/C | BF | 1.37 | 1.10 | 1.50 |
| | IF | 0.55 | 0.57 | 0.50 |
| | PF | 0.76 | 0.72 | 0.50 |
| L'Aquila/C | BF | 1.13 | 0.88 | 1.50 |
| | IF | 0.51 | 0.50 | 0.50 |
| | PF | 0.60 | 0.54 | 0.50 |
| Milan/C | BF | 1.70 | 1.50 | 1.50 |
| | IF | 0.53 | 0.58 | 0.50 |
| | PF | 0.92 | 0.88 | 0.50 |
| Naples/C | BF | 1.25 | 1.11 | 1.50 |
| | IF | 0.52 | 0.56 | 0.50 |
| | PF | 0.69 | 0.73 | 0.50 |
| Roma/C | BF | 1.53 | 1.38 | 1.50 |
| | IF | 0.45 | 0.49 | 0.50 |
| | PF | 0.71 | 0.75 | 0.50 |

Table 4.4.3 Summary of modal parameters for 9-story moment-resisting frame buildings.

| City / Soil | Model | $T_x$ [s] | $T_y$ [s] | IM |
|---|---|---|---|---|
| L'Aquila/A | BF | 1.87 | 1.57 | 2.00 |
| | IF | 0.79 | 0.84 | 1.00 |
| | PF | 0.92 | 0.88 | 1.00 |
| L'Aquila/C | BF | 1.86 | 1.67 | 2.00 |
| | IF | 0.76 | 0.84 | 1.00 |
| | PF | 0.92 | 0.89 | 1.00 |
| Milan/C | BF | 2.12 | 1.93 | 2.00 |
| | IF | 0.77 | 0.84 | 1.00 |
| | PF | 0.97 | 1.01 | 1.00 |
| Naples/C | BF | 1.88 | 1.55 | 2.00 |
| | IF | 0.89 | 0.87 | 1.00 |
| | PF | 0.99 | 0.94 | 1.00 |

Table 4.4.4 Summary of modal parameters for 9-story wall-frame buildings.

| City / Soil | Model | $T_x$ [s] | $T_y$ [s] | IM |
|---|---|---|---|---|
| L'Aquila/C | BF | 1.57 | 1.25 | 1.50 |
| | IF | 0.97 | 0.85 | 1.00 |
| | PF | 1.00 | 0.88 | 1.00 |
| Milan/C | BF | 1.84 | 1.59 | 2.00 |
| | IF | 0.89 | 0.85 | 1.00 |
| | PF | 0.97 | 0.92 | 1.00 |
| Naples/C | BF | 1.67 | 1.43 | 1.50 |
| | IF | 0.85 | 0.83 | 1.00 |
| | PF | 0.91 | 0.89 | 1.00 |

### 4.4.2 Collapse Criterion

The identification of global collapse through a numerical response analysis is not a trivial task and the topic of relatively intense research in the last decade. In purely theoretical terms, one can adopt the definition of collapse given in Villaverde (2007), which states that "a global collapse is assumed to occur whenever the base-shear-lateral displacement curve attains a negative slope (due to P-delta effects) and afterwards reaches a point of zero base-shear. Such a point implies no lateral resistance and the inability of the structure to resist gravity loads". This definition is basically equivalent to that based on the incremental dynamic analysis curve (so-called IDA curve; Vamvatsikos and Cornell, 2002), since the attainment of a zero base-shear on the negative slope branch of the base-shear-lateral displacement curve corresponds to the flat-lining of the IDA curve, or global dynamic instability condition. The former definition, however, has the important advantage of being detectable within the single inelastic response analysis, rather than as a tangent to a curve that requires analyses at multiple intensity levels to be drawn (the IDA curve). For this reason, it is the preferred choice in the case at hand where multiple-stripe analysis is employed to characterize the intensity-response relation, rather than IDA. This approach requires the inspection of the cyclic base-shear-lateral displacement curve and is also

named 'state-evolution approach' (Mehanny and Deierlein, 2000), see Figure 4.4.1, as opposed to the 'supply-demand approach', which is based on local, member-level demand to capacity or capacity to demand ratios. The latter is the typical 'design-verification' approach, whereby, in simpler conventional terms, the structural system is treated as a system in series, and the weakest link governs the verification of design. Some approaches exist (Jalayer et al., 2007) to combine local D/C ratios in order to arrive at a global ratio and provide a less conservative estimate of the global structural system state. In general, a hybrid approach is used, with a global definition supplemented by local D/C ratios on the so-called non-simulated collapse modes, in recognition of the fact that only an ideal numerical model could account for all possible collapse modes. Typically, when a 'flexural' model is adopted, shear checks are performed *a posteriori*, through post-processing. Even when more refined models are adopted, like the 'Elwood' one in Baradaran-Shoraka et al., (2013), a posteriori checks are needed for axial collapse (loss of vertical load-bearing capacity by shear-damaged columns).



*Global dynamic criterion: analysis of force-deformation loop (state evolution approach)*



*Global equivalent static criterion (approximate):*
*Deformation capacity obtained from a pushover curve*
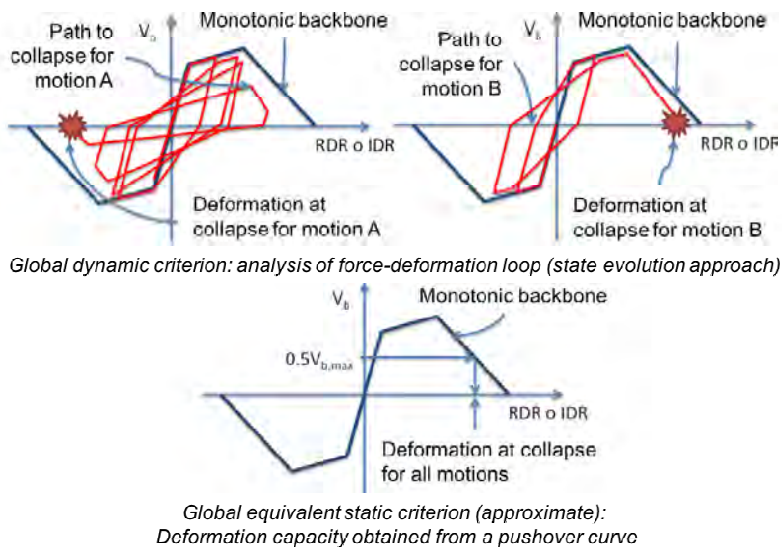
Figure 4.4.1 Collapse criteria: state evolution approach, with collapse determined based on dynamic hysteresis cycle, different for each motion  (top) and approximate approach based on displacement threshold from pushover analysis (bottom).

The buildings analyzed in this project are code-conforming, therefore no defective collapse modes should be activated. This implies that a purely global, state-evolutionary approach could be more reliably adopted. Inspection of the cyclic base-shear- lateral displacement curves, however, has revealed the difficulty, in the case of these buildings and partly due to three-dimensional nature of the analysis, insetting up an automatic procedure to check collapse. For this reason, it has been pragmatically chosen to employ a still global, but simplified collapse criterion based on a global capacity obtained from pushover analysis. Criticisms of this choice are known (Villaverde, 2007) (Goulet et al., 2007), since a single capacity value, related to the collapse mechanism occurring in the pushover analysis, is adopted, rather than motion-specific values. As shown at the top of Figure 4.4.1, each motion induces a different hysteretic loop, leading to different cyclic degradation and collapse drift (larger, and closer to the monotonic values for pulse-like motions like that on the right, lower for motions with a larger number of similar amplitude cycle, like that on the left).

The adopted criterion is therefore an approximate one and capacity is defined as the value of drift (inter-story-drift or roof-drift-ratio, IDR or RDR, respectively, can be used indifferently for these buildings) at 50% decrease in base-shear on the negative slope. This value is preferred since it is easier to identify on the pushover curves and because it is lower than the monotonic

value of displacement at zero base-shear, and thus ideally closer to a generic 'cyclic' value of displacement at zero base-shear.

Two values are determined, one in the X and the other in the Y direction (maximum absolute value), and the D/C ratio is reported independently in both directions.

### 4.4.3 Summary of results of nonlinear time history response analyses for all building and all sites

Results of the analyses are summarized in this section in terms of D/C ratios (larger absolute values of the top displacement demand-to-capacity in X and Y directions). Ratios are presented for each site and building type and each run, and a comparison of median values against mean annual frequency (MAF) of exceedance of the associated intensity is also provided. Before showing the results of response-history analysis, the following figures present results of the nonlinear static analysis, used to establish roof displacement thresholds at collapse. Differences mainly arise from design, where in addition to different seismicity, each research unit entrusted with designing the buildings at a single site, made slightly different (but reasonable) design decision.

Figure 4.4.2 to Figure 4.4.9 show the results of the pushover curves by number of story-building, building type, and direction, comparing directly the results of each site. It appears quite clearly that the curves for the three lower seismicity sites tend to lump in one group, and this is especially true for the BF configuration. This configuration is also the one where differences can only be tracked to RC members and initial design. For these sites the minimum values in design play an important role and this reduces differences between the buildings. At the other end of the spectrum, it is interesting to note how the buildings in Naples and L'Aquila are compared. While in the Y direction the curves reflect the expected order based on site seismicity and design seismic action, in the X direction the two buildings are closer and actually very close in the BF configuration. The similarity needs further investigation.

Finally, Figure 4.4.10, Figure 4.4.11, Figure 4.4.12, and Figure 4.4.13 report the D/C ratios (in terms of top floor displacement) for all buildings and all sites computed through nonlinear time history response analyses at the ten selected intensity levels. It is recalled that the intensity levels are characterized in terms of a fixed mean annual frequency or mean return period for the conditioning IM, which varies from building to building, thus, each level corresponds in each site to a different intensity. For each non-linear time history analysis (NLTHA) run, the reported D/C ratio is the largest between the X and Y directions.
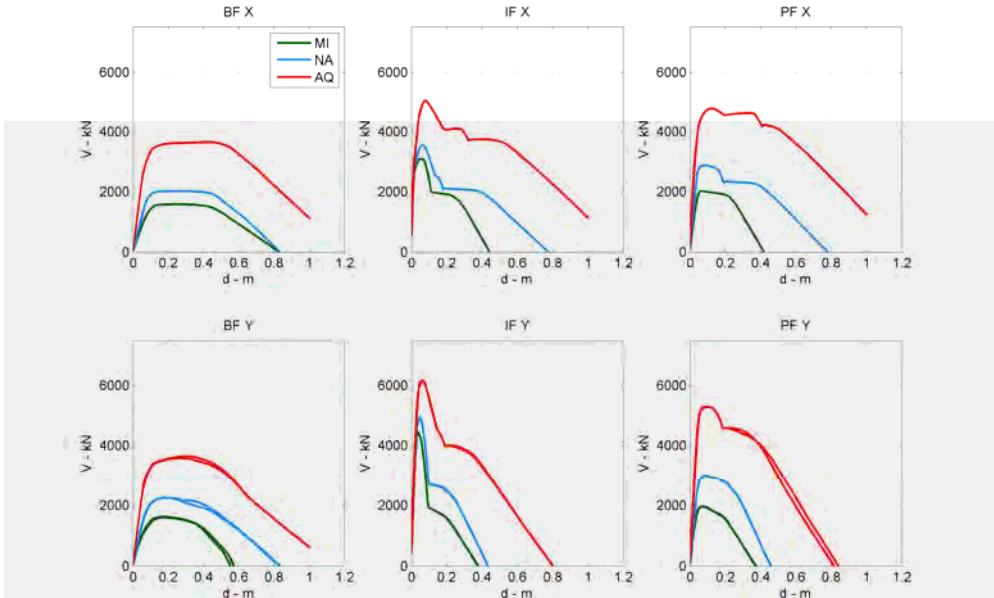
Figure 4.4.2 Pushover curves MRF 3-story buildings (Modal distrubution) in the X (top row) and Y (bottom row) directions, for the three configurations (BF, IF and PF from left to right).
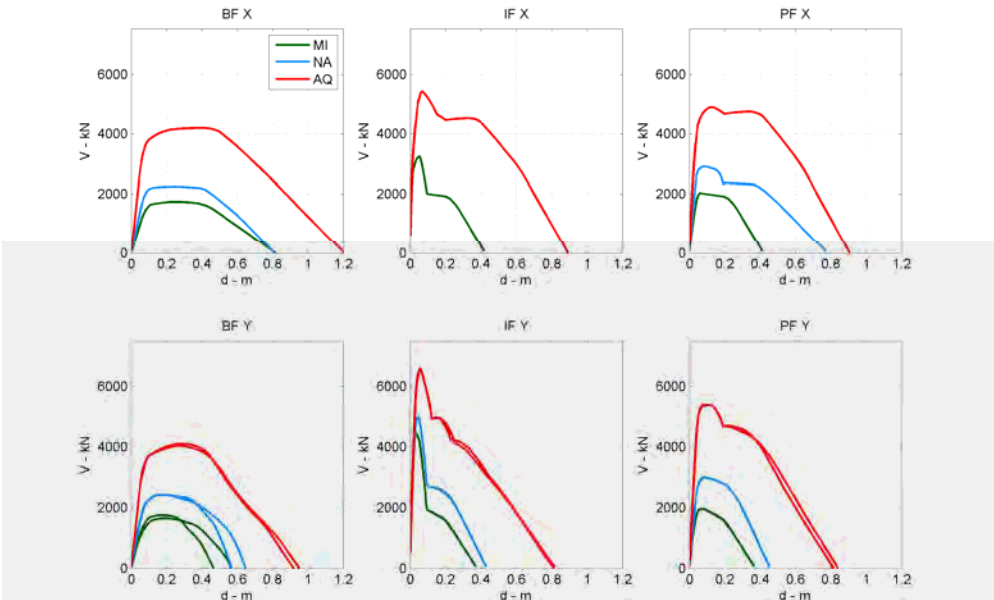


Figure 4.4.3 Pushover curves MRF 3-story buildings (Uniform distrubution) in the X (top row) and Y (bottom row) directions, for the three configurations (BF, IF and PF from left to right).
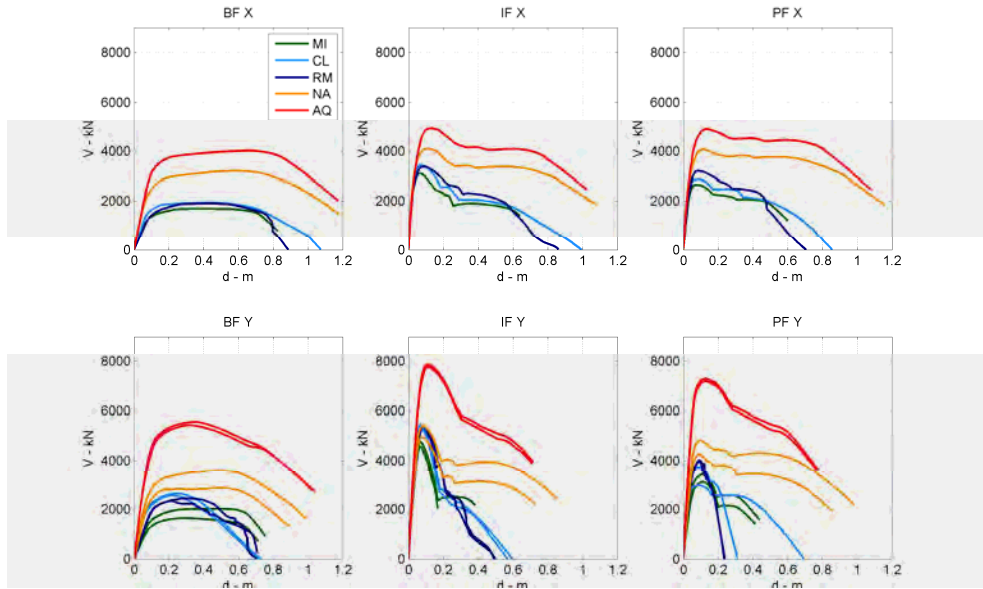
Figure 4.4.4 Pushover curves MRF 6-story buildings (Modal distrubution) in the X (top row) and Y (bottom row) directions, for the three configurations (BF, IF and PF from left to right).
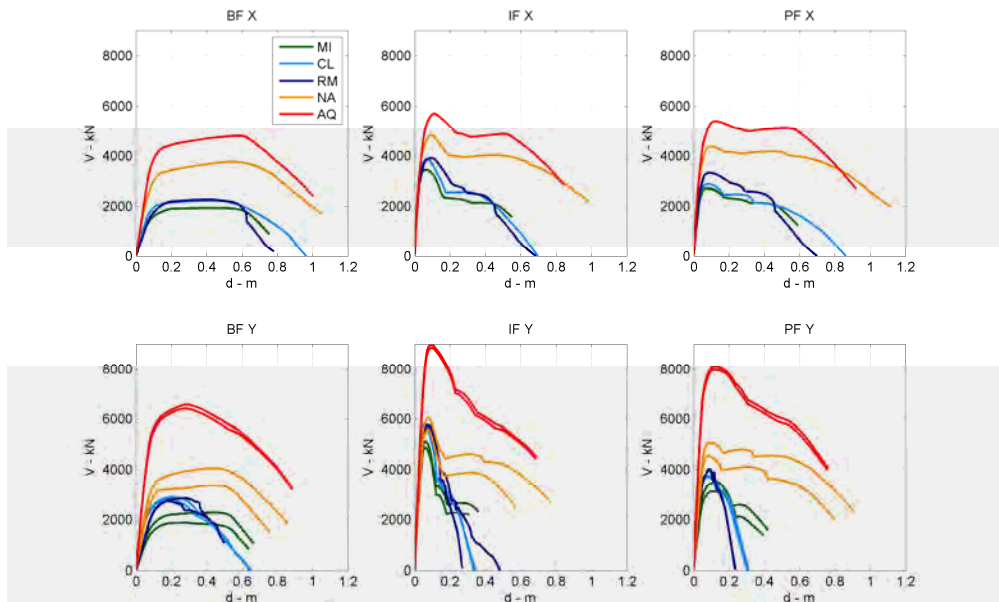


Figure 4.4.5 Pushover curves MRF 6-story buildings (Uniform distrubution) in the X (top row) and Y (bottom row) directions, for the three configurations (BF, IF and PF from left to right).
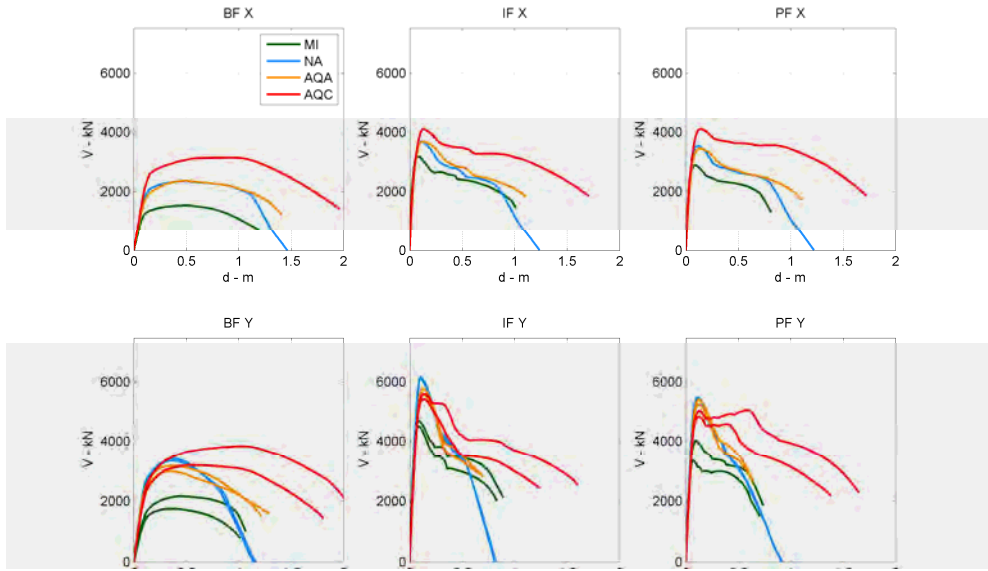
Figure 4.4.6 Pushover curves MRF 9-story buildings (Modal distrubution) in the X (top row) and Y (bottom row) directions, for the three configurations (BF, IF and PF from left to right).
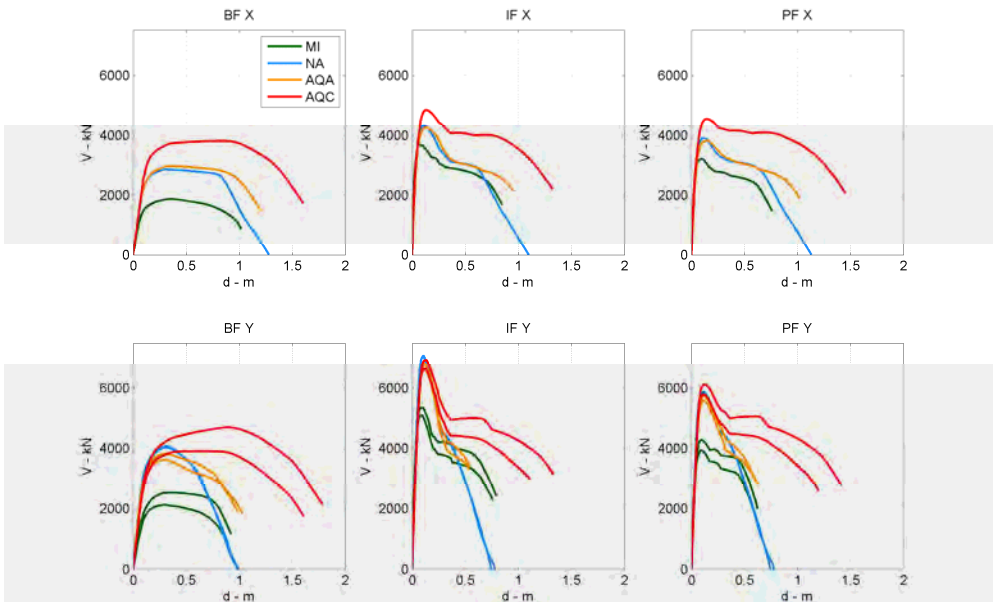


Figure 4.4.7 Pushover curves MRF 9-story buildings (Uniform distrubution) in the X (top row) and Y (bottom row) directions, for the three configurations (BF, IF and PF from left to right).
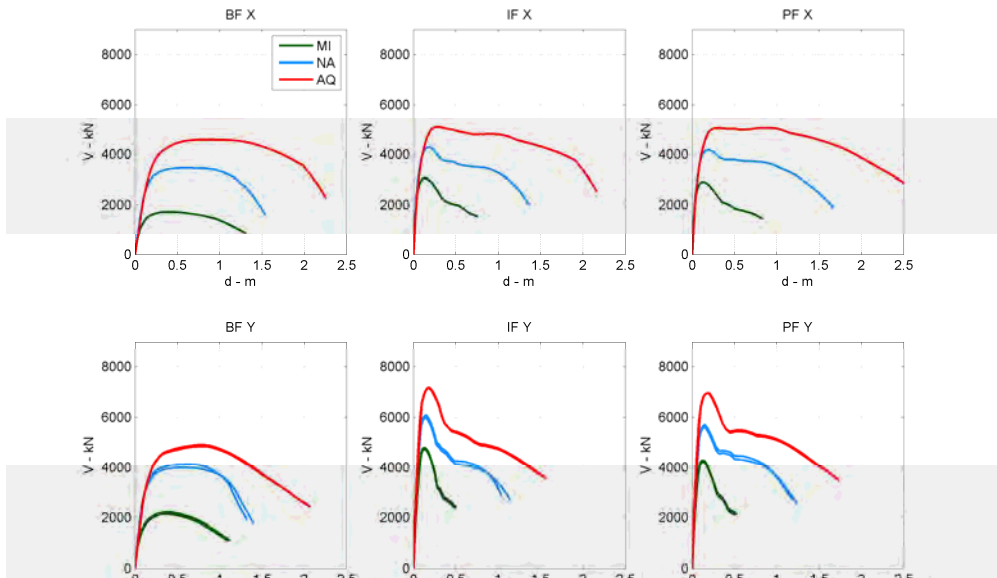
Figure 4.4.8 Pushover curves SW 9-story buildings (Modal distrubution) in the X (top row) and Y (bottom row) directions, for the three configurations (BF, IF and PF from left to right).
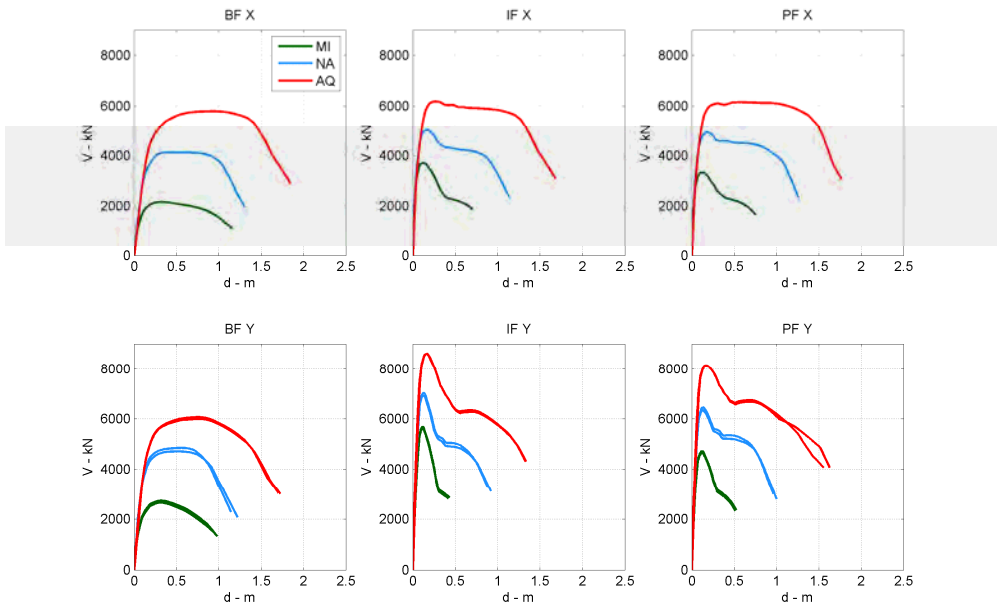


Figure 4.4.9 Pushover curves SW 9-story buildings (Uniform distrubution) in the X (top row) and Y (bottom row) directions, for the three configurations (BF, IF and PF from left to right).
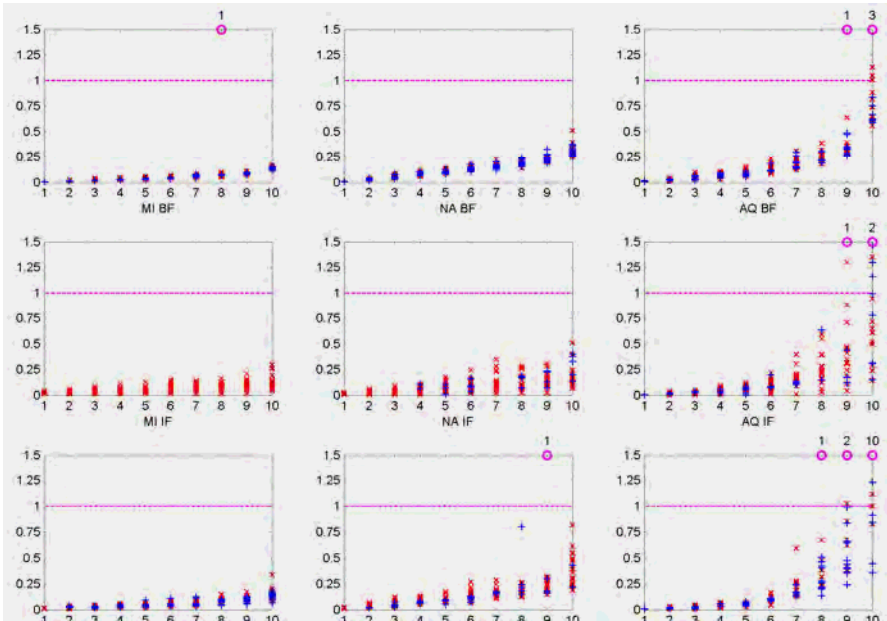
Figure 4.4.10 D/C ratios for MRF 3-story buildings and sites: BF, IF and PF on the top, middle and bottom row, respectively. The figure reports on each intensity levels the number of collapses (below red dots).
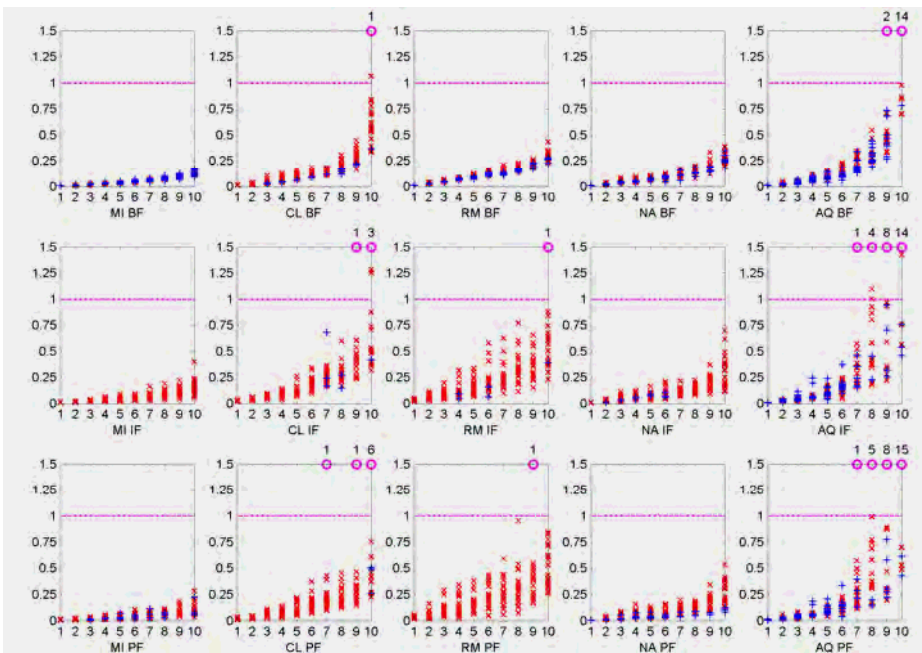


Figure 4.4.11 D/C ratios for MRF 6-story buildings and sites: BF, IF and PF on the top, middle and bottom row, respectively. The figure reports on each intensity levels the number of collapses (below red dots).
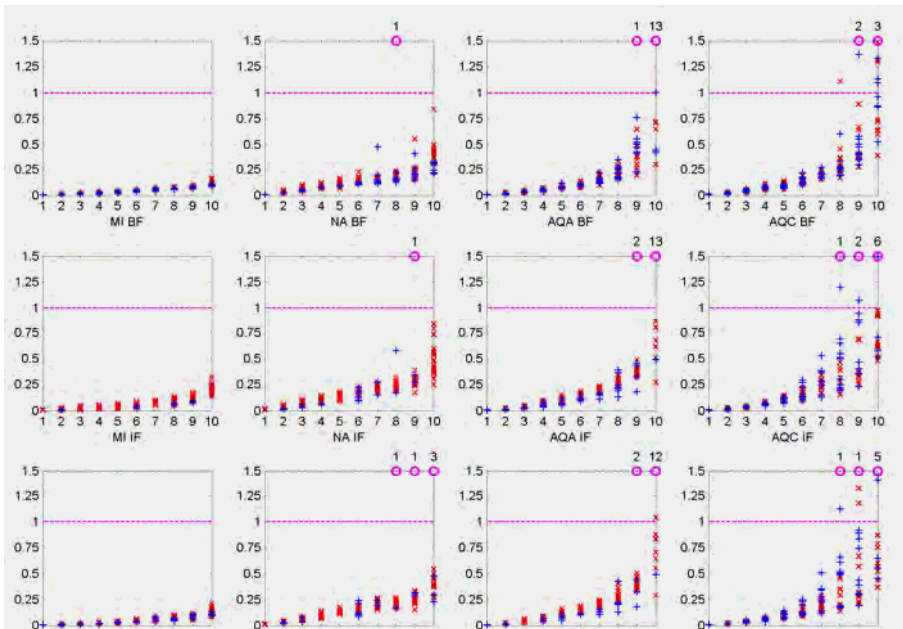
Figure 4.4.12 D/C ratios for MRF 9-story buildings and sites: BF, IF and PF on the top, middle and bottom row, respectively. The figure reports on each intensity levels the number of collapses (below red dots).
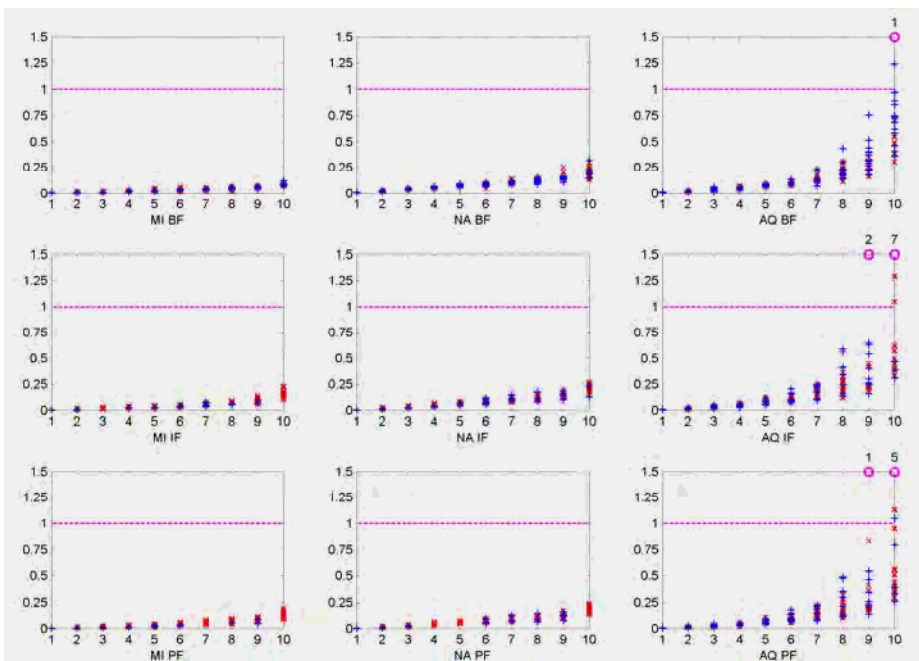


Figure 4.4.13 D/C ratios for SW 9-story buildings and sites: BF, IF and PF on the top, middle and bottom row, respectively. The figure reports on each intensity levels the number of collapses (below red dots).

Figure 4.4.14, Figure 4.4.15, Figure 4.4.16, and Figure 4.4.17 show the median D/C ratio for all buildings and all sites. The y axis values correspond to the exceedance rate of each stripe. It

should be noted how in these figures medians are computed on all 20 data points for each stripe, including the collapse cases indicated in Figure 4.4.10, to which a conventional value of 1.0 is assigned.
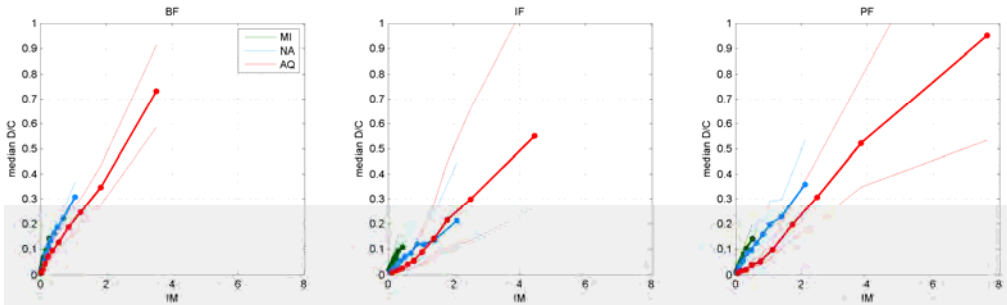


Figure 4.4.14 Median values of the D/C ratio for MRF 3-Story Building, all configuration types.
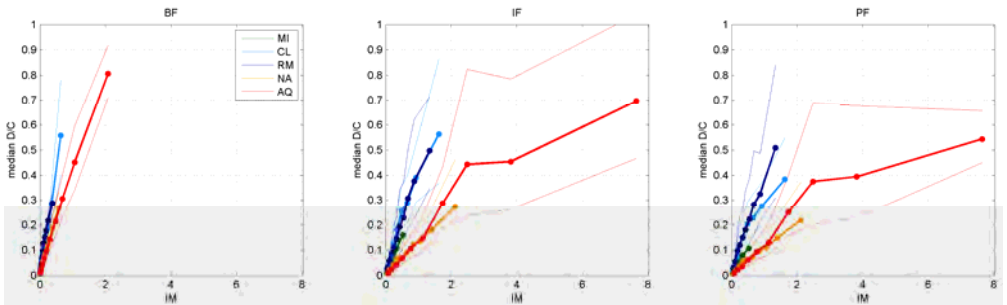


Figure 4.4.15 Median values of the D/C ratio for MRF 6-Story Building, all configuration types.
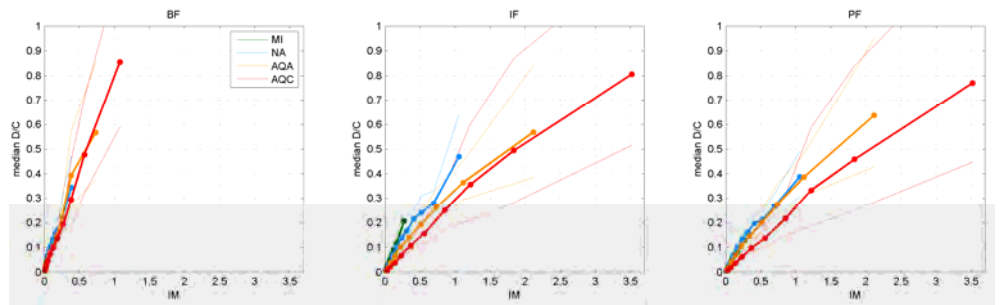


Figure 4.4.16 Median values of the D/C ratio for MRF 9-Story Building, all configuration types.
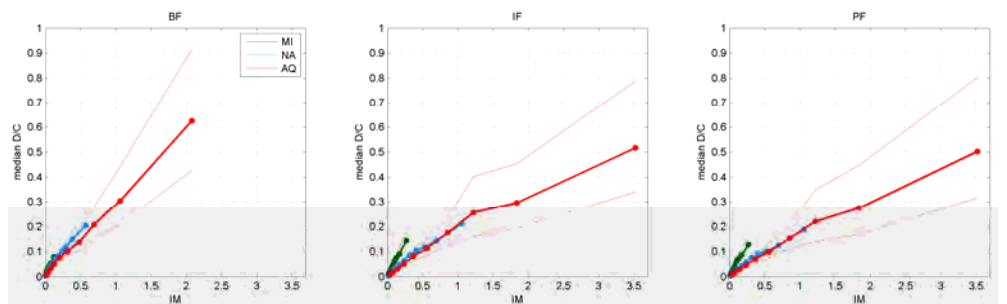


Figure 4.4.17 Median values of the D/C ratio for SW 9-Story Building, all configuration types.

### 4.4.4   Discussion of of Collapse Prevention Results

The results indicate that in general the D/C ratios are much lower than 1.0, except the NLTHA runs for the L'Aquila buildings at the IMLs corresponding to the $10^5$ years return period. Also, the higher seismic intensity at the site is, the larger is the observed D/C ratio. The median responses of Figure 4.4.14, Figure 4.4.15, and Figure 4.4.16 indicate a clear trend for the two sites with the lowest and highest seismicity (Milan and L'Aquila). For the other sites, differences in the hazard calculations at different return periods and in the design assumptions may justify the fact that not all median points follow the site hazard intensity. In interpreting the plot, however, it should be kept in mind that they report at the same ordinate (same MAF) the median D/C ratios of structures with different fundamental periods of vibration and, hence, conditioning IM, and also different top displacement capacities. On the other hand, producing plots in terms of intensity versus median D/C ratios is made difficult because different conditioning IM have been used at each site, depending on the fundamental period. Converting the plots to the same IM would require the conditional spectra for each stripe and it has not been done at this stage. Further analysis is required to gain the necessary insight, given that no clear trend is visible among the three 'intermediate' sites of Naples, Rome and Caltanissetta. In summary, input differences justifying the observed output should be traceable to:

- seismic design intensity
- fundamental period and conditioning IM
- prevalent direction of strong bending axis in rectangular cross-sections
- reinforcement ratios and columns' concrete cross-section area
- effect of percent reduction in masonry infill strength as a function of openings in each direction

### 4.4.5  Damage Limit State

The Damage Limit State is defined in NTC2008 as the limit state where "the structure, including structural and nonstructural elements, and machinery relevant to its functions, exhibit damage that does not expose its occupants to any risks, and that does not compromise the strength and stiffness of the structure with respect to the vertical and horizontal loads. The structure is immediately usable even if some machineries are not fully operational." Based on the above definitions, NTC 2008 defines Inter-story Drift Ratio (IDR) limits: if the model includes the infills, IDR ≤ 0.003 (IF and PF cases), in the BF case IDR ≤ 0.005.

For the BF, the above IDR limit of 0.005 was used to define the Damage Limit State, in accordance with NTC2008. For the IF and PF frames, it was assumed that the building capacity at the Damage Limit State is defined by the smallest of the top floor displacements corresponding to the following three conditions in the PO curves:

- Attainment of a light-widespread damage condition, corresponding to the attainment of a maximum lateral force around the peak strength in the relevant skeleton curve with no more than 50% of masonry infills in each PO direction (Figure 4.4.18-a);
- Attainment of a severe damage condition, corresponding to the attainment of 50% strength drop from the peak strength in the relevant skeleton curve for the first masonry infill (Figure 4.4.18-b);
- Attainment of a limit value of base-shear (corresponding to 95% of the peak strength from PO curve), corresponding to a condition where the structure still retains its original strength and most of its original stiffness (no need for structural repair). (Figure 4.4.18-c).
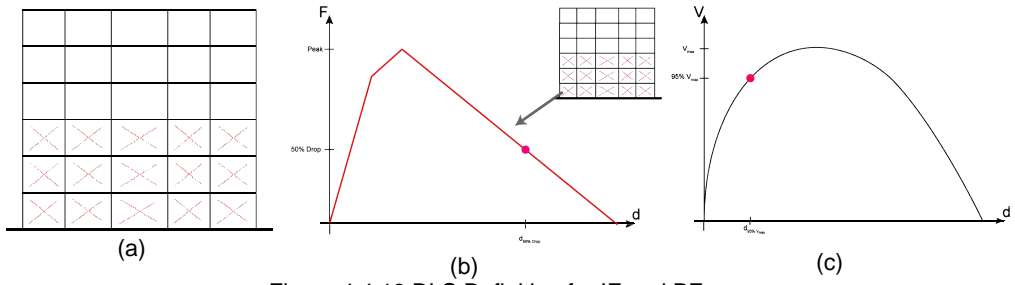
Figure 4.4.18 DLS Definition for IF and PF.

The following figures report the D/C ratios for all buildings considered in this study.
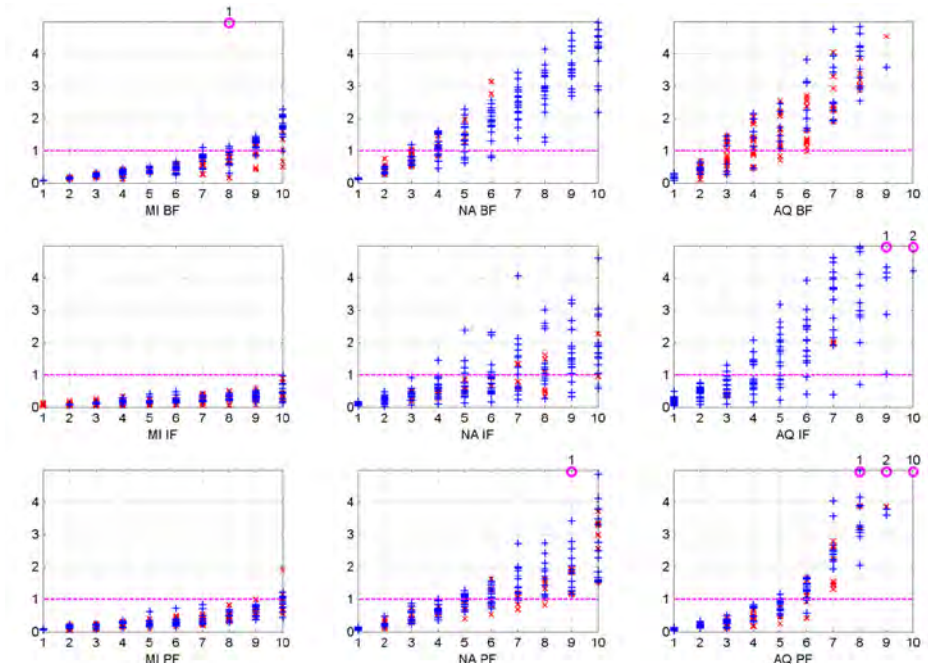


Figure 4.4.19 D/C ratios for MRF 3-story buildings.
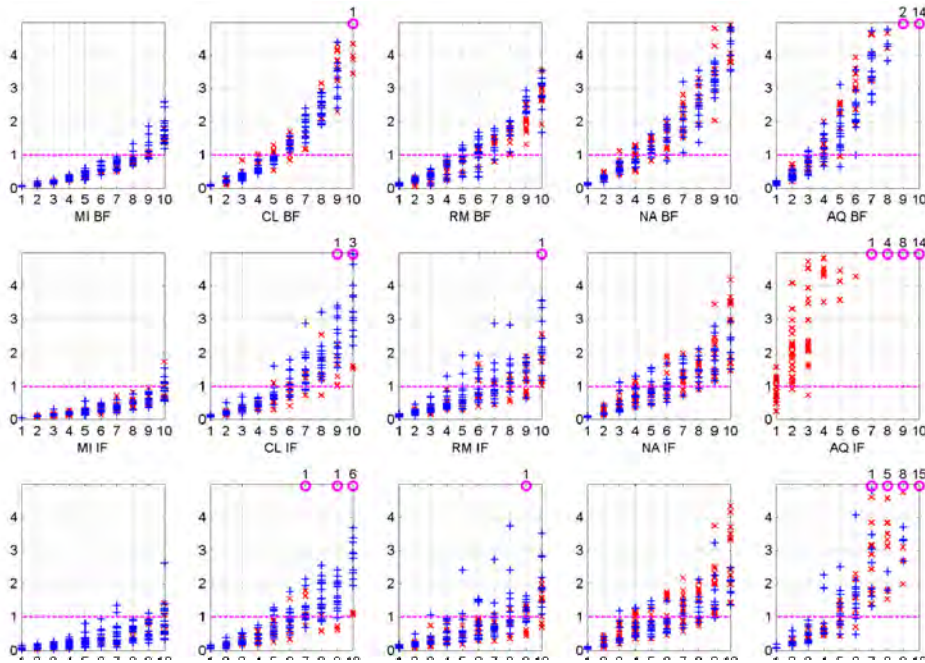
Figure 4.4.20 D/C ratios for MRF 6-story buildings.
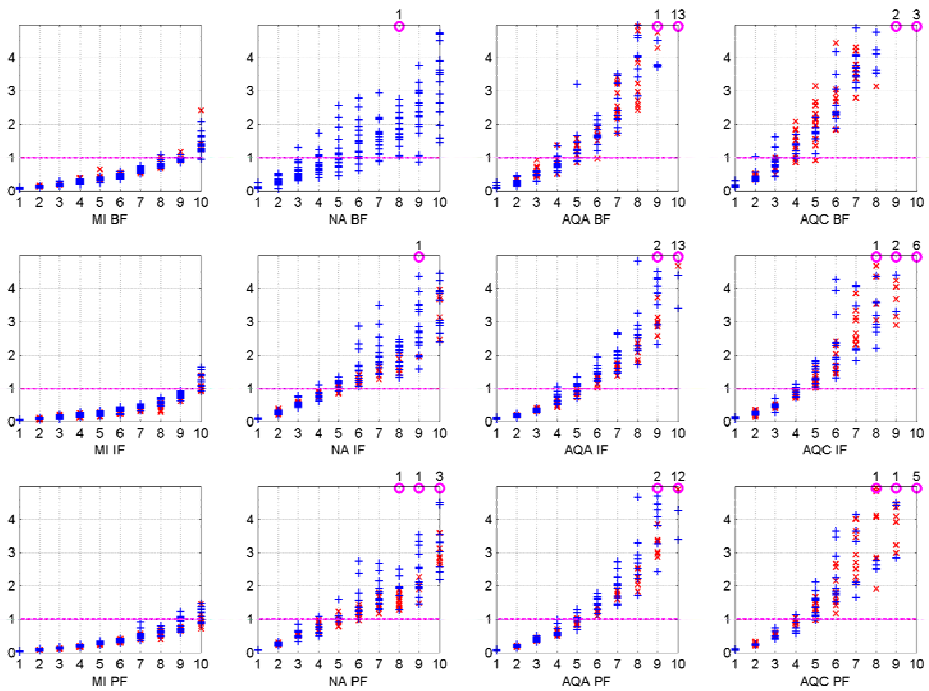


Figure 4.4.21 D/C ratios for MRF 9-story buildings.
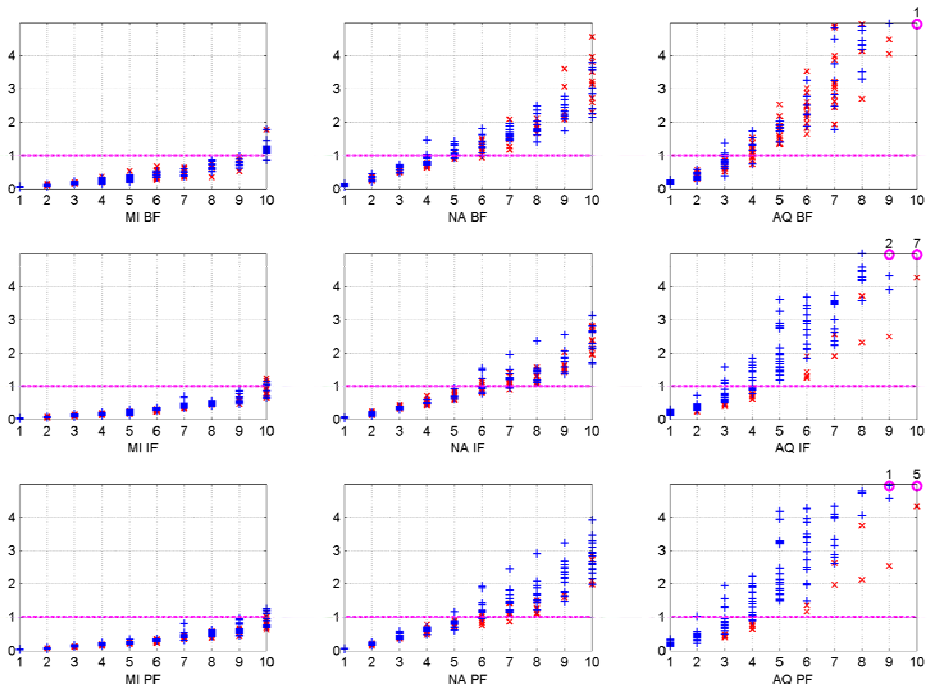
Figure 4.4.22 D/C ratios for SW 9-story buildings.

The above figures show that the DLS is reached after the first few stripes. This is in line with the design procedure: the DLS is checked for an earthquake intensity roughly corresponding to the second stripe.

The following figures show the median D/C ratios for all buildings and all sites.
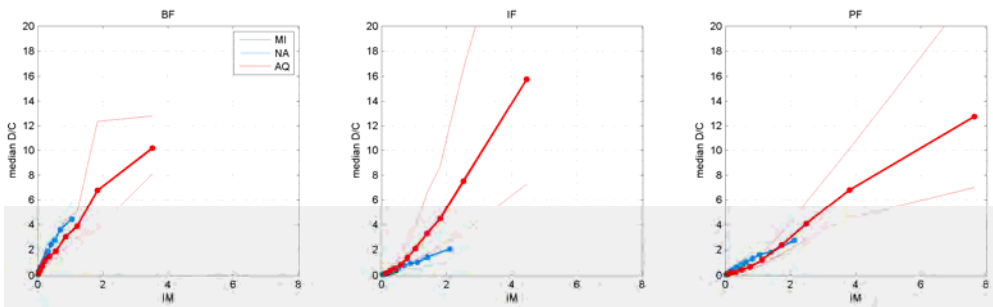


Figure 4.4.23 Median values of the D/C ratio for MRF 3-story Building, all configuration types.
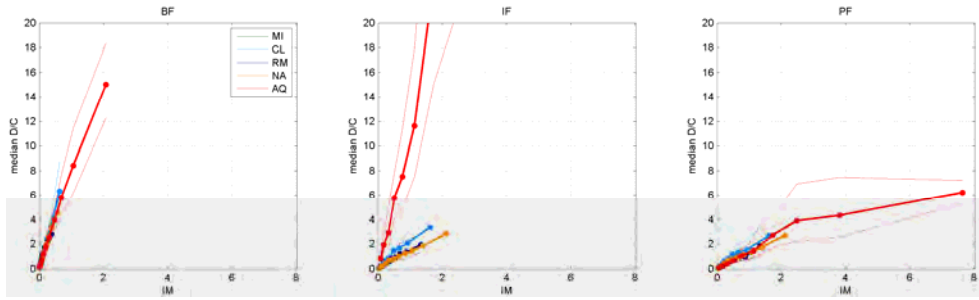
Figure 4.4.24 Median values of the D/C ratio for MRF 6-story Building, all configuration types.
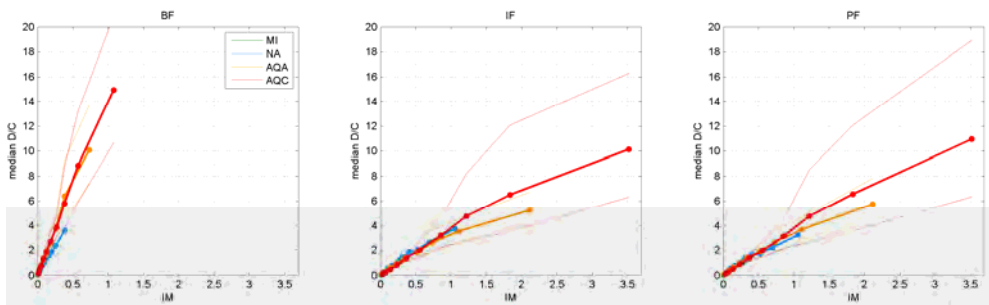


Figure 4.4.25 Median values of the D/C ratio for MRF 9-story Building, all configuration types.
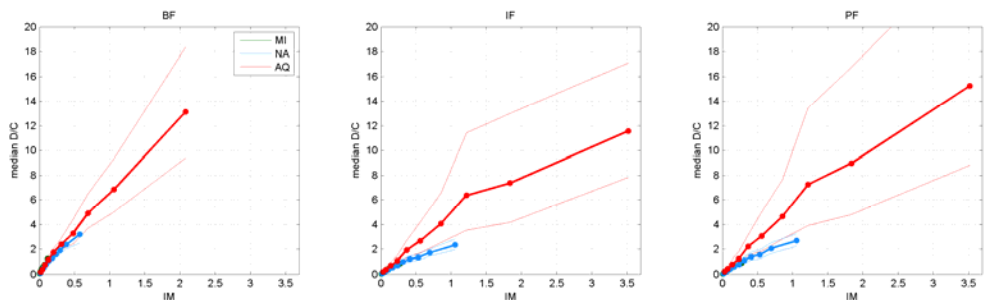


Figure 4.4.26 Median values of the D/C ratio for SW 9-story Building, all configuration types.

## 4.5   References

Bairan, J. M., & Mari, A. R. (2007). Multiaxial-coupled analysis of RC cross-sections subjected to combined forces. Engineering structures, 29(8), 1722-1738.

Baradaran Shoraka, M., Yang, T. Y., & Elwood, K. J. (2013). Seismic loss estimation of non-ductile reinforced concrete buildings. Earthquake Engineering & Structural Dynamics,42(2), 297-310.

Bertoldi, S.H., Decanini, L.D., Gavarini, C. (1993). Telai tamponati soggetti ad azioni sismiche, un modello semplificato, confronto sperimentale e numerico, 6° Convegno Nazionale L'ingegneria Sismica in Italia, Perugia.

Cardone, D., Perrone,  G. (2015). Developing fragility curves and loss functions  for masonry infill walls. Earthquakes and Structures, 9(1), 257-279.

Ceresa, P., Petrini, L., & Pinho, R. (2007). Flexure-shear fiber beam-column elements for modeling frame structures under seismic loading—state of the art. Journal of Earthquake Engineering, 11(S1), 46-88.

Decanini L.D., Fantin G.E., (1986). Modelos simplificados de la mamposteria incluida en porticos. Caracteristicas de rigidez y resistencia lateral en estado limite, Jornadas Argentinas de Ingenieria Estructural, Buenos Aires, Argentina, 2, 817-836 (in Spanish).

Decanini, L., Mollaioli, F., Mura, A., Saragoni R., (2004). Seismic performance of masonry infilled R/C frames, Proc. 13th WCEE, Paper 165, Vancouver, B.C., Canada, August 1-6.

Decanini L., Liberatore L., Mollaioli F. (2014) "Strength and stiffness reduction factors for infilled frames with openings", Earthquake Engineering and Engineering Vibration, 13(3): 437-454.

Elwood, K. J. (2004). Modelling failures in existing reinforced concrete columns. Canadian Journal of Civil Engineering, 31(5), 846-859.

Franchin, P., & Pinto, P. E. (2009). Allowing traffic over mainshock-damaged bridges. Journal of Earthquake Engineering, 13(5), 585-599.

Goulet, C. A., Haselton, C. B., Mitrani-Reiser, J., Beck, J. L., Deierlein, G. G., Porter, K. A., & Stewart, J. P. (2007). Evaluation of the seismic performance of a code-conforming reinforced-concrete frame building—from seismic hazard to collapse safety and economic losses. Earthquake Engineering & Structural Dynamics, 36(13).

Haselton, C.B., Liel, A.B., Taylor Lange, S. & Deierlein, G.G. (2008) Beam-Column Element Model Calibrated for Predicting Flexural Response Leading to Global Collapse of RC Frame Buildings, PEER report 2007/03.

Haselton, C. B., Liel, A. B., & Deierlein, G. G. (2009). Simulating structural collapse due to earthquakes: model idealization, model calibration, and numerical solution algorithms. Computational Methods in Structural Dynamics and Earthquake Engineering (COMPDYN).

Haselton, C. B., Liel, A. B., Deierlein, G. G., Dean, B. S., & Chou, J. H. (2010). Seismic collapse safety of reinforced concrete buildings. I: Assessment of ductile moment frames. Journal of Structural Engineering, 137(4), 481-491.

Ibarra, L. F., & Krawinkler, H. (2005). Global collapse of frame structures under seismic excitations. Rep. No. TB 152, The John A. Blume Earthquake Engineering Center.

.Ibarra, L. F., Medina, R. A., & Krawinkler, H. (2005). Hysteretic models that incorporate strength and stiffness deterioration. Earthquake engineering & structural dynamics, 34(12), 1489-1511.

Kostic, S. M., & Filippou, F. C. (2011). Section discretization of fiber beam-column elements for cyclic inelastic response. Journal of Structural Engineering, 138(5), 592-601.

Liberatore L (2001), Approcci innovativi in termini di energia e di spostamento per la valutazione della risposta sismica di strutture a più gradi di libertà, PhD Dissertation, "Sapienza" University of Rome, Italy. (In Italian).

Liel, A. B., Haselton, C. B., & Deierlein, G. G. (2010). Seismic collapse safety of reinforced concrete buildings. II: Comparative assessment of nonductile and ductile moment frames. Journal of Structural Engineering, 137(4), 492-502.

Lignos, D.G. and Krawinkler, H. (2012). "Sidesway collapse of deteriorating structural systems under seismic excitations," Rep.No.TB 177, The John A. Blume Earthquake Engineering Research Center, Stanford University, Stanford, CA. [electronic version: https://blume.stanford.edu/tech_reports].

Marini, A., & Spacone, E. (2006). Analysis of reinforced concrete elements including shear effects.ACI Structural Journal, 103(5), 645.Spacone, E., Filippou, F. C., & Taucer, F. F. (1996). Fiber beam-column model for non-linear analysis of R/C frames: Part I. Formulation. Earthquake engineering and structural dynamics, 25(7), 711-726.

Mehanny, S. S. F., & Deierlein, G. G. (1999).Modeling and assessment of seismic performance of composite frames with reinforced concrete columns and steel beams (Doctoral dissertation, Stanford University).

Mohr, S., Bairán, J. M., & Marí, A. R. (2010). A frame element model for the analysis of reinforced concrete structures under shear and bending. Engineering Structures, 32(12), 3936-3954.

Petrangeli, M., Pinto, P. E., & Ciampi, V. (1999). Fiber element for cyclic bending and shear of RC structures. I: Theory. Journal of Engineering Mechanics, 125(9), 994-1001.

Ranzo, G., & Petrangeli, M. (1998). A fiber finite beam element with section shear modelling for seismic analysis of RC structures. Journal of earthquake engineering, 2(03), 443-473.

Sassun, K., Sullivan, T. J., Morandi, P., Cardone, D., (2016). Characterising the in-plane seismic performance of infill masonry. Bulletin of the New Zealand Society for Earthquake Engineering, 49(1),100-117.

Spacone, E., Filippou, F. C., & Taucer, F. F. (1996). Fiber beam-column model for non-linear analysis of R/C frames: Part II. Applications.Earthquake Engineering and Structural Dynamics,25(7), 727-742.

Stafford Smith, B., 1963. Lateral stiffness of infilled frames, Journal of Structural Division, ASCE, 88(ST 6),183-199.

Vamvatsikos, D., & Cornell, C. A. (2002). Incremental dynamic analysis. Earthquake Engineering & Structural Dynamics, 31(3), 491-514.

Villaverde, R. (2007). Methods to assess the seismic collapse capacity of building structures: State of the art. Journal of Structural Engineering, 133(1), 57-66.

# CHAPTER V – SINGLE STORY STEEL BUILDINGS

## 5.1   Introduction

Industrial single-story steel buildings equipped with a travelling overhead crane are considered in this chapter. In line with the goal of the project, some geometrical configurations were selected as to represent typical European applications. The case studies were designed assuming three different site locations corresponding to three levels of seismic hazard, according to the criteria of the current Italian code D.M. 14/01/2008 (NTC08).

## 5.2   Case study structures

### 5.2.1   Description of the structural system

The building structure is composed of five single span duo-pitch portal frames repeated in the longitudinal direction at a constant distance between them. The frames are connected in the longitudinal direction by hot-rolled beams at the apex, at the eaves and at the crane-supporting bracket level. The 3D view of the structural system is presented in Figure 5.2.1. According to the reference grid shown in this figure, the X-direction is represented by the dash-and-dot lines labelled with numbers, while the Y-direction is given by those labelled with letters. The vertical Z-direction is consequently defined. Unlike gravity loads, which are supported by all members, horizontal forces are withstood by two different seismic-resistant structure typologies acting along two orthogonal directions. In the X-direction the resistance to lateral forces is mainly due to continuous and rigid frame action. In the Y-direction the resistance to horizontal forces is provided by vertical bracings placed in the outer spans of the building. Secondary structural elements were also considered. Purlins used to support the roof cladding and positioned every 2.5 m, transfer the forces from the roof cladding to the rafters. Roof bracings are arranged in the outer bays to transfer horizontal forces to the vertical bracings.
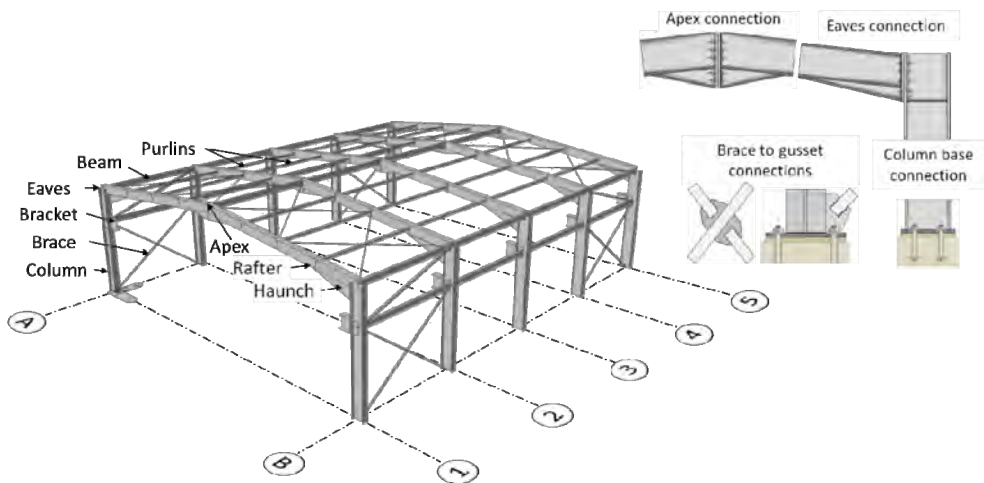


Figure 5.2.1 Description of the structural system.

The structural efficiency of portal frames is due to moment resisting connections between beams and columns. The case study structures assumed the adoption of full-strength bolted end-plate connections at eaves and apex. As typical for this structural type, the rafter connection to the column comprises a haunch used to improve the performance of the rafter and facilitate a bolted connection to the column. In this study, the length of the eaves' haunch was assumed as equal to 10% of the span. To facilitate the bolted connection, small haunches were considered at the apex too. The roof purlins were connected to the rafters by pinned connections and assumed as simple spanned between two consecutive frames. All the columns were assumed as hinged at their base. Hot-rolled I or H sections were used for beams, columns and purlins. Cold-formed

steel square hollow sections were chosen for vertical braces, while hot-rolled L-shaped profiles were used for roof bracings. The selected steel grade is S275.

## 5.2.2    Design configurations and material

The transverse bay width (Lx), the longitudinal bay width (Ly), the height at the eaves (H) and the height of the crane-supporting bracket (measured at top surface of the bracket) were assumed as design parameters (Figure 5.2.2a). Four geometrical configurations were selected, as shown by the parameter values provided in Table 5.2.1. In all cases, the roof pitch was set equal to 6°.



**(a)**                                                                      **(b)**
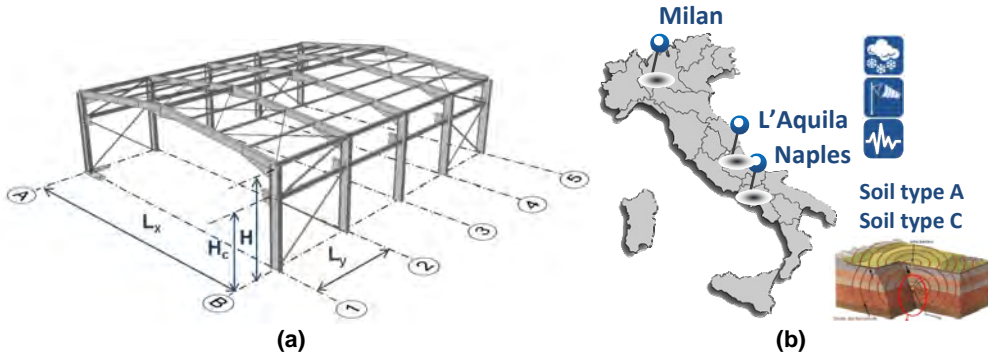
Figure 5.2.2 Geometrical parameters (a) and building site locations (b).

To characterize variable loads and seismic actions, these structural systems were assumed to be located in three different sites in Italy: Milan, Naples, and L'Aquila. For the seismic input two soil types were considered: type A and type C (NTC 2008).

Combining the geometrical properties with the features of location sites, twenty-four design configurations were derived. Details of such combinations are shown in Figure 5.2.3.

Table 5.2.1 Geometry parameters for the considered case studies.

| Structural system | $L_x$, H, $H_c$, (m, m,m) | $L_y$ (m) |
|---|---|---|
| 1 | 20, 6, 4.5 | 6.00 |
| 2 | 20, 6, 4.5 | 8.00 |
| 3 | 30, 9, 7.5 | 6.00 |
| 4 | 30, 9, 7.5 | 8.00 |

To identify each design configuration, they were labelled with an alphanumerical string containing the main geometrical parameters characterizing the case study, in the following order: transverse bay width (Lx20 or Lx30), longitudinal bay length (Ly6 or Ly8), site location (MI, AQ, NA) and soil type (A or C).
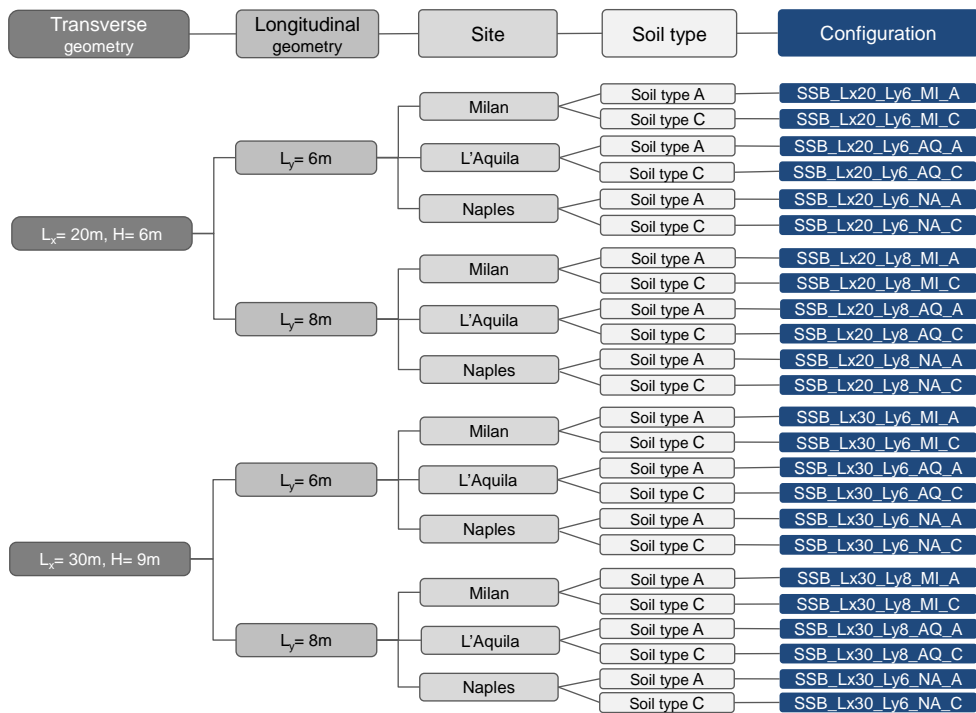
Figure 5.2.3 Design configurations.

Figure 5.5.2 provides the main design properties of the assumed steel grade. In the table, $f_{yk}$ is the characteristic value of the yield strength, $f_{tk}$ is the characteristic tensile strength of the material; E is the Young's modulus.

Table 5.2.2 Mechanical properties of S275 steel grade.

| $f_{yk}$ (N/mm$^2$) | $f_{tk}$ (N/mm$^2$) | E (N/mm$^2$) |
|---|---|---|
| 275 | 430 | 210000 |

## 5.3 Design of the case study structures

### 5.3.1 Finite element models

The global behavior of the case study structures was analyzed by the structural analysis program Midas Gen (Midas GEN, 2016). The 3D model is shown in Figure 5.3.1. The beams and the columns were represented by two-node three-dimensional beam elements, taking into account the stiffness effects of tension/compression, shear, bending and torsional deformations. Two-node truss elements were used to model longitudinal and roof braces, representing uniaxial tension-only members. Pinned end connections were introduced by the Beam End Release option available in Midas. Column-base connections were represented by pinned restraints.
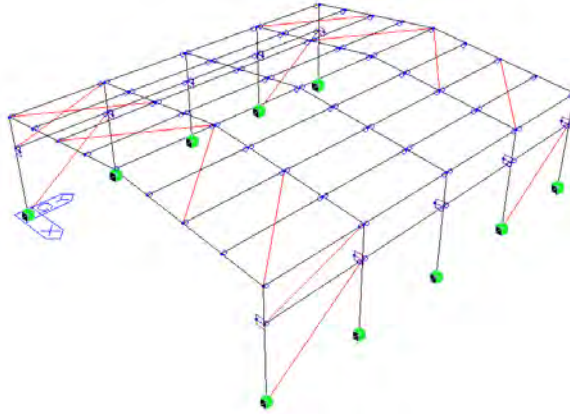
Figure 5.3.1 Three-dimensional FEM model of the building in Midas Gen.

The vertical (dead and imposed) loads from the roof are transferred to the secondary elements (purlins) and from there to the primary beams, columns and finally to the ground. Horizontal forces are mainly resisted by the continuity of the frame structure in the transverse direction (X) and by members subjected to axial forces in the longitudinal direction (Y). Following the current European and Italian seismic codes (D.M., 2008, CEN, 2005), the design model assumed that horizontal forces can be resisted by tension-only diagonal braces, i.e., the contribution of the compression diagonals to the lateral force resistance was neglected at the design stage. As stated before, in this study a travelling overhead crane was considered. The crane runway beams were assumed to be the same for all cases and made of a HEA400 steel beam. The crane runway beam was explicitly included in the global analysis model. Their presence was taken into account by equivalent static actions on the column brackets.

### 5.3.2    Load combinations

According to the Italian code, loads expected to act on the structure should be combined so as not to exceed the limit state for the relevant design situations. Structures are deemed to satisfy the ultimate limit state (ULS) and the serviceability limit state (SLS), to ensure a safe and functional structure, respectively. NTC08 recommends the following load combination for ULS checks (§ 2.5.3, NTC08):

$$F_{d,ULS} = \gamma_{G1} G_1 + \gamma_{G2} G_2 + \gamma_{Q1} Q_{k1} + \sum_i \gamma_{Qi} \Psi_{0i} Q_{ki} \qquad 5.3.1$$

Structure functionality should be verified by three different load combinations. Equation 5.3.2 is the characteristic load combination normally used for irreversible limit states. Equation 5.3.3 is the frequent load combination used for reversible limit states. The quasi-permanent load combination, represented by Equation 5.3.4 is normally used for long-term effects.

$$F_{d,SLS,characteristic} = G_1 + G_2 + Q_{k1} + \sum_i \Psi_{0i} Q_{ki} \qquad 5.3.2$$

$$F_{d,SLS,frequent} = G_1 + G_2 + \Psi_{11} Q_{k1} + \sum_i \Psi_{1i} Q_{ki} \qquad 5.3.3$$

$$F_{d,SLS,quasi-permanent} = G_1 + G_2 + \Psi_{21} Q_{k1} + \sum_i \Psi_{2i} Q_{ki} \qquad 5.3.4$$

If the seismic action is included, the following additional load combination should be considered:

$$F_{d,seismic} = E + G_1 + G_2 + \Psi_{21}Q_{k1} + \sum_i \Psi_{2i}Q_{ki} \qquad 5.3.5$$

In all the above equations, $G_1$ is the permanent load due to the self-weight of structures, $G_2$ is the permanent load due to self-weight of non-structural elements and internal equipment; $Q_{k1}$ is the characteristic value of the leading variable action; $Q_{k,i}$ is the characteristic value of the accompanying variable actions; $\gamma_{G,j}$ is the partial factor for the permanent load; $\gamma_{Q,i}$ is the partial factor for the variable load; $\psi_{ij}$ is the combination coefficient for the variable load accounting for the reduced probability of simultaneous occurrence of their characteristic values. Recommended values of $\psi_{ij}$ are given in Table 5.3.1 for all variable loads expected to act on the buildings, whose detailed description is provided in the following section.

Table 5.3.1 Combination coefficients for variable loads.

| Actions | $\Psi_{0,j}$ | $\Psi_{1,jk}$ | $\Psi_{2,j}$ |
|---------|------|------|------|
| Snow    | 0.5  | 0.2  | 0    |
| Wind    | 0.6  | 0.2  | 0    |
| Thermal | 0.6  | 0.5  | 0    |
| Crane   | 1    | 0.9  | 0.8  |

### 5.3.3 Actions

#### 5.3.3.1 Permanent loads

Self-weights of structural elements are the main permanent loads. Such values are automatically computed by the calculation software on the basis of the geometry of the structural elements and the weight per unit volume of the structural steel.



Figure 5.3.2 Roof and wall cladding.

Self-weight of non-structural elements, such as the roof and wall claddings, are also classified as permanent loads. There are a number of types of claddings that may be used in single-story buildings. A very common solution, for both roofing and walls in industrial buildings, is represented by composite or sandwich panels. A sandwich panel consists of a rigid insulation layer between two metal sheets. In this study profiled composite panels were used for roofs while flat panels were chosen for the side walls. In both cases an inner polyurethane foam insulating layer was considered. Self-weight of these panels was derived from some product catalogues arbitrarily selected among the many available on the market. Figure 5.3.2 contains the details of the metal claddings, together with their self-weight. These permanent loads,

provided here as a force per unit area, were then modelled as uniformly distributed loads on the roof purlins and columns. Figure 5.3.3 shows the permanent load modelling.

The travelling crane self-weight ($G_c$), as well as the weight of the runway beams ($G_{b,c}$), were modelled as concentrated forces acting on the top of the column bracket which is supposed to be welded to the column flange (Figure 5.3.3).
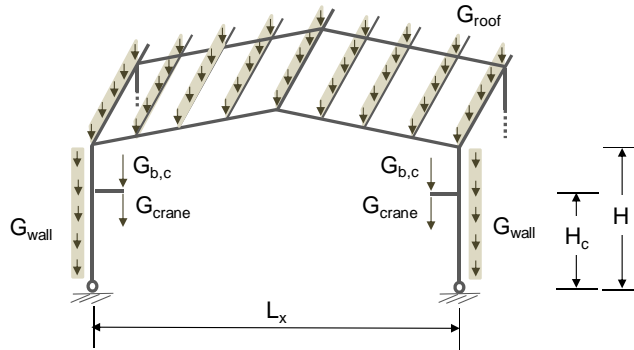


Figure 5.3.3 Permanent loads modelling.

5.3.3.2  Wind loads

Wind actions were represented by a set of pressures both normal and parallel to surfaces. The magnitude of normal pressures was calculated with Equation 5.3.6 (NTC08):

$$p = q_b \cdot c_e \cdot c_p \cdot c_d \qquad\qquad 5.3.6$$

where $q_b$ is the basic velocity pressure, $c_e$ is the exposure coefficient, $c_p$ is the shape coefficient, and $c_d$ is the dynamic coefficient. The wind climate effect is described by $q_b$, that is the kinetic energy per unit volume of the air, calculated as half of the product of the air density ($\rho$) and square basic wind velocity, $v_b$. The latter is the characteristic 10 minutes mean wind velocity, at 10 m above ground of terrain category II (Table 3.3.II of NTC08). It depends on the site climate and altitude. A formula permits its definition by $v_{b,0}$, that is the basic wind velocity, which is reported in tables for the nine wind climatic zones identified in Italy. According to the Italian wind climate map, Milan is classified as zone 1, while L'Aquila and Naples belong to wind zone 3. The values of the wind velocity and the corresponding velocity pressure calculated for the three sites are shown in Table 5.3.2. To introduce different exposure conditions and heights from the ground, the $c_e$ coefficient is introduced by NTC08. Assuming the roughness class of terrain type B, Milan and L'Aquila belong to exposure class IV, while Naples belongs to exposure class III. NTC08 provides a formula to evaluate the exposure factor as a function of height, with the recommended value of the topography factor ($c_t = 1$). In this study, the value of $c_e$ was assumed constant along the building height and equal to that calculated at the eaves height (H). For a given site, two different values of $c_e$ were calculated, corresponding to H = 6 m and H = 9 m, respectively. These values are shown in the second last column of Table 5.3.2. As far as the dynamic coefficient $c_d$ is concerned, accounting for the reduced probability of simultaneous occurrence of maximum effects due to static pressures and the dynamic structural response, it was assumed as equal to 1.

Table 5.3.2 Wind load parameters

| Site | Wind zone | $a_s$ (m) | $v_b$ (m/s) | $q_b$ (kN/m$^2$) | Terrain roughness | Exposure class | $c_e$ | $c_d$ |
|---|---|---|---|---|---|---|---|---|
| Milan | 1 | 110 | 25.00 | 0.39 | | IV | 1.63 1.84 | |
| L'Aquila | 3 | 714 | 31.32 | 0.61 | B | IV | 1.63 1.84 | 1 |
| Naples | 3 | 6 | 27.00 | 0.46 | | III | 1.85 2.09 | |

The external pressure coefficients $c_{pe}$ for buildings depend on the wind direction and the slope of the walls. External pressure coefficients for rectangular plan buildings and pitched roofs are shown in Figure 5.3.4, according to the Italian code. The inner pressure coefficients consider a percentage of wall opening surface lower than 33%.
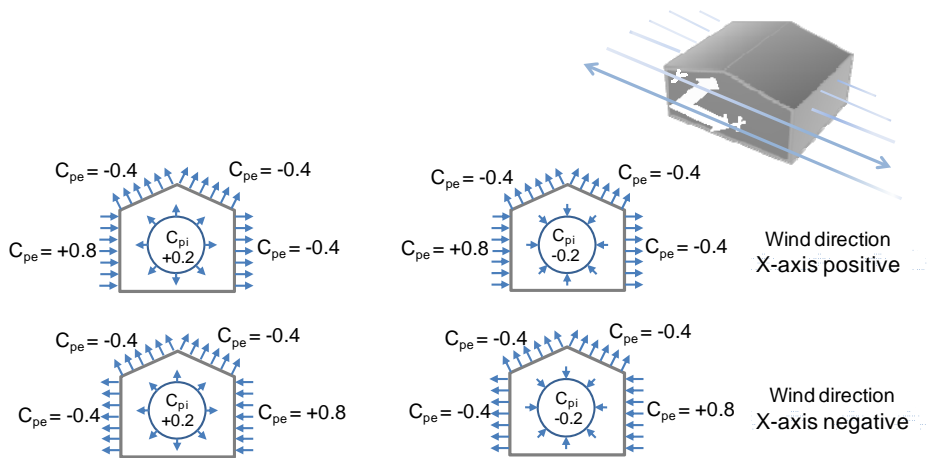


Figure 5.3.4 External and internal pressure coefficient for buildings.

As displayed, internal and external pressures are considered to act at the same time. The internal pressure is supposed to act in equal and opposite directions on the leeward and windward elements. Finally, the normal wind load on element surfaces, determined by the product of the wind pressure and the exposed area, was modelled as a uniform force per unit length (in kN/m) acting on columns, whose value was calculated assuming the panels simply supported by the columns.

The wind friction pressure was evaluated as follows (3.3.5 NTC08):

$$p_f = q_b \cdot c_e \cdot c_f$$

5.3.7

where $c_f$ is the friction factor and it is assumed equal to 0.02 that is the suggested value corresponding to "Roogh" surface, according to the Italian code.

5.3.3.3  Snow loads

Local meteorological climate conditions as well as roof geometry, its thermal properties and exposure conditions, influence the value of snow load on the roof. Snow layers can have many different patterns depending on the roof shape. Some geometries are such as to produce a reduction of the reference value of the snow load because of the snow sliding off the roof. Snow

accumulation on the roof could be reduced because heat loss by roof causes snow melting. The presence of nearby buildings and the characteristics of the surrounding terrain can increase or decrease the actual value of the snow load, because it influences the wind effect. NTC08 provides a guidance for the determination of the snow load for structural design of buildings for sites at altitudes under 1500 m, accounting for all these aspects by the following formula:

$$q_s = \mu_i \cdot q_{sk} \cdot C_E \cdot C_t$$

<div align="right">5.3.8</div>

where $q_s$ in the snow load on the roof, $\mu_i$ is the snow load shape coefficient, $q_{sk}$ is the characteristic value of the snow load on the ground, $C_E$ is the exposure coefficient, and $C_t$ is the thermal coefficient. The snow load on the roof is practically derived multiplying the reference value of snow load on the ground, due to local climate conditions, by three different factors accounting for the aspects that actually influence the value of the snow load on the roof.

The characteristic value of the snow load on the ground with a return period of 50 years depends on the geographical position and the altitude of the building above the sea level. It can be derived by the Italian ground snow load map, a subdivision of the Italian territory into four homogeneous climatic snow zones. Each climatic zone is characterized by different values of the ground snow load. Within each zone the characteristic value is defined by altitude functions. Milan, Naples, and L'Aquila belong to two different climatic zones, as shown in Table 5.3.3. The characteristic value of the snow load on the ground calculated for each site, at the given altitude, is given in the fourth column of the same table.

In this study the three adjustment coefficients were the same for all cases. The shape coefficient, $\mu_i$, is determined on the basis of the roof inclination, which is fixed and equal to 6 for all the configurations. Concerning the exposure coefficient $C_E$, in this study a reference exposure condition was assumed for all cases, corresponding to areas where there is no significant removal of snow by wind, because of terrain, other construction works or trees. About the coefficient $C_t$, the Italian code provides a reference value corresponding to the absence of specific studies on the thermal properties of the roof cladding. The values of all coefficients are provided in the following table. The value of the snow load on the roof for each site is given in the last column of Table 5.3.3.

<div align="center">Table 5.3.3 Snow load on roof for different location sites.</div>

| Site | Climatic zone | $a_s$ (m) | $q_{sk}$ (kN/m²) | $\mu_i$ | $C_E$ | $C_t$ | $q_s$ (kN/m²) |
|---|---|---|---|---|---|---|---|
| Milan | I - Mediterranean | 110 | 1.50 | | | | 1.20 |
| L'Aquila | III | 716 | 1.64 | 0.80 | 1.00 | 1.00 | 1.31 |
| Naples | III | 6 | 0.6 | | | | 0.48 |

### 5.3.3.4 Thermal loads

In this study, the thermal effects were assumed to be not critical for the structure functionality, as well as its safety. In this case the code requires that the structural elements are subjected to a uniform temperature component ΔTu, given by the difference between the mean temperature $T$ acting on the element and its conventional initial temperature $T_0$. The magnitude of such thermal actions is provided in Table 3.5.II of the code, according to the exposure of the building and the structural typology. For steel protected buildings, the recommended value of ±15° was assumed.

### 5.3.3.5 Crane loads

Case study structures were supposed to be equipped with overhead cranes. The machinery induces vertical and horizontal actions on the structure, with static and dynamic components. In addition to the self-weight, the structure is subjected to the vertical variable hoist load, horizontal variable forces caused by acceleration and deceleration of the crane due to its movement along

the runway beams, and horizontal forces caused by skewing of the crane also due to its movement along the runway beam. Each of those forces was modelled as a static equivalent action and evaluated according to the Italian code, as follows:

$$F_L = \frac{1}{7}(G_c + F_h)$$

5.3.9

$$F_T = \frac{1}{10}(G_c + F_h)$$

5.3.10

where $G_c$ is the self-weight of the crane, $F_h$ is the crane working load, $F_L$ is the horizontal longitudinal action caused by acceleration and deceleration of the crane, $F_T$ is the horizontal transversal action due to crane skewing.

Two positions of the crane, along the longitudinal direction of the building, were considered in order to obtain the worst load arrangements for ULS and SLS conditions, respectively. They are displayed in Figure 5.3.5. The variable crane load was located at the minimum allowable distance from the runway beam in the transverse direction.



(a)

(b)
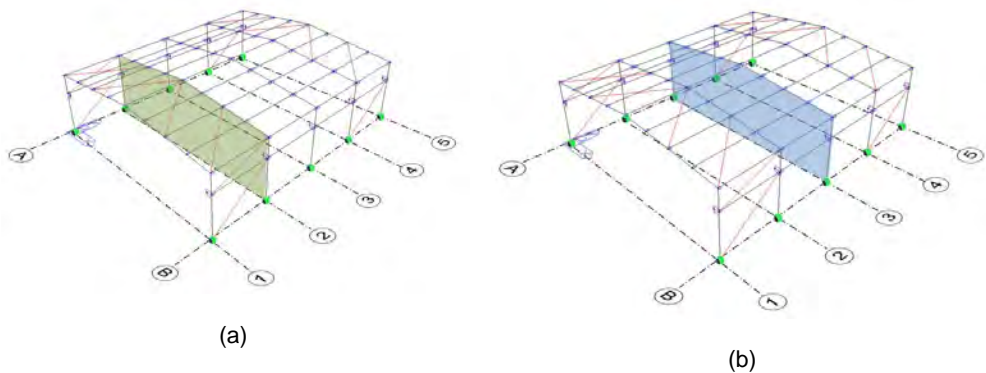
Figure 5.3.5 Crane positions for SLS (a) and ULS (b) verifications.

5.3.3.6  Frame imperfections

Frame imperfections, including residual stresses and geometrical imperfections such as lack of verticality, lack of straightness, lack of flatness, lack of fit and eccentricities greater than acceptable tolerances, were modelled by the simplified approach suggested by the Italian code. The global imperfections were described by means of a global equivalent initial sway imperfection $\phi$, given by the following formula:

$$\phi = \alpha_h \cdot \alpha_m \cdot \phi_0$$

5.3.11

where $\phi_0$ is the basic value of the equivalent geometrical imperfection for a single column equal to 1/200, $\alpha_h$ and $\alpha_m$ are factors accounting for the column height and the number of load-carrying columns in a row, respectively. The effects of the global initial sway imperfection were replaced by systems of equivalent horizontal forces, obtained by the product of the maximum design value of the axial force ($N_{Ed}$) and the global initial sway imperfection $\phi$:

$$F_h = \phi \cdot N_{Ed}$$

5.3.12

These equivalent horizontal forces were applied in the same direction at the top of each column.

5.3.3.7  Seismic loads

Earthquake motion at a point on the ground surface was represented by an elastic ground acceleration response spectrum, $S_e(T)$. The horizontal seismic action was described by two orthogonal components represented by the same response spectrum. The vertical component of the seismic action was also considered in the design, because of the large transverse span.

The NTC08 formulation takes into account a series of parameters that allow to define local spectra. The soil factor, S, allows to consider ground type C. Different levels of seismic hazard are described by the seismic hazard parameters ($a_g$, $F_0$, $T_c^*$) and reported in the Italian building code as a function of the geographical position and the reference return period. Such parameters corresponding to Milan, Naples, and L'Aquila are shown in the following Table 5.3.4 for both the Damage Limit State (DLS) and the Life safety Limit State (LLS). The response spectra were derived assuming the topography condition $T_1$ (table 3.2.IV of NTC08).

Table 5.3.4 Hazard parameters.

| Site | Latitude | Longitude | Limit state | $a_g$ (g) | $F_o$ | $T_c^*$ (sec) |
|------|----------|-----------|-------------|-----------|-------|---------------|
| L'Aquila | 13.396 | 42.356 | DLS | 0.104 | 2.330 | 0.280 |
|          |        |        | LLS | 0.261 | 2.360 | 0.350 |
| Naples | 14.2600 | 40.850 | DLS | 0.059 | 2.330 | 0.310 |
|        |         |        | LLS | 0.168 | 2.370 | 0.340 |
| Milan | 9.1900 | 45.4640 | DLS | 0.024 | 2.550 | 0.190 |
|       |        |         | LLS | 0.050 | 2.660 | 0.280 |

In the following, Figure 5.3.6 and Figure 5.3.7 show the horizontal and vertical elastic response spectra for soil type A and C, for both life safety and damage limit state.
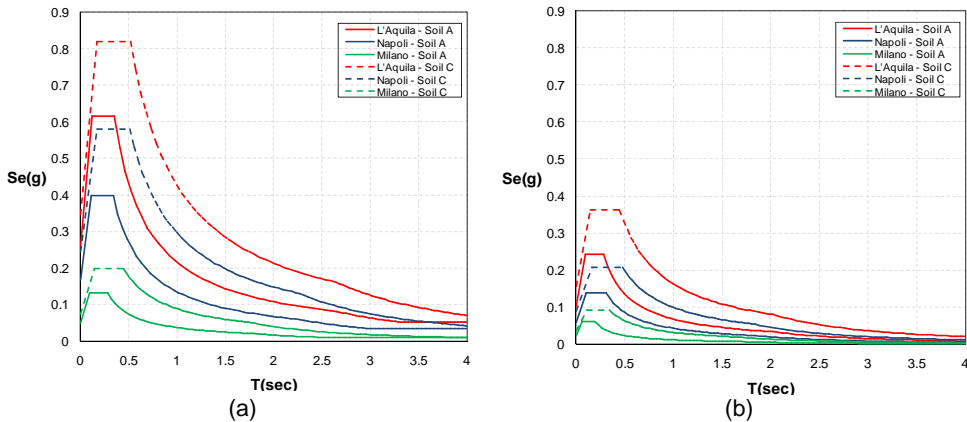


Figure 5.3.6 Horizontal elastic response spectra at LLS (a) and DLS (b).
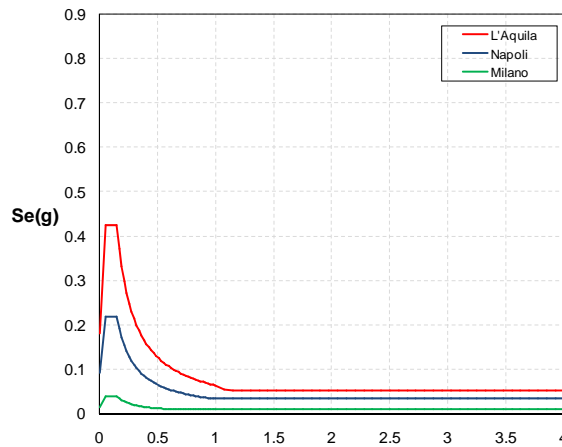
Figure 5.3.7 Vertical elastic response spectra at LLS.

The case study structures were designed by assuming a low-dissipative structural behavior. Under this assumption, for both moment-resisting frames and frames with concentric bracings, NTC08 prescribes q-factor equal to 4, i.e., factor used to reduce the elastic response spectra to obtain the design response spectra. The corresponding design response spectra obtained for Milan, Naples, and L'Aquila, assuming soil types A and C, are shown in the following figures.
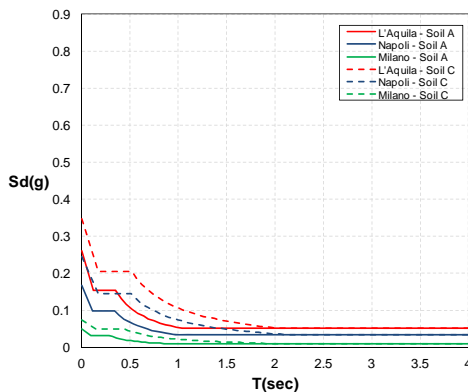


Figure 5.3.8 Horizontal design response spectra at LLS.
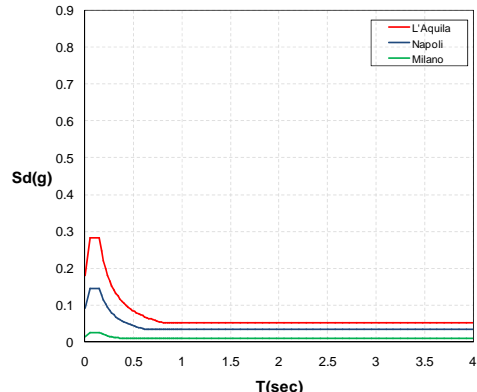


Figure 5.3.9 Vertical design response spectra at LLS.

### 5.3.4   Main results of global analysis

Maximum values of member forces and displacements were calculated by an elastic global analysis. Modal response spectrum analysis was performed to evaluate bending moments, axial forces and shear forces due to seismic actions. As recommended by NTC08, seismic action effects were evaluated considering a number of vibration modes, such that the sum of the effective modal masses amounts to at least 85% of the total seismic mass. To satisfy this requirement, about 100 modes of vibration were taken into account in the modal response spectrum analysis. Although the first ten modes were sufficient to meet this requirement both in X and Y directions, a higher number of vibration modes was required in Z direction. The Complete Quadratic Combination (CQC) rule for the combination of different modes was used. Four mode shapes and the corresponding vibration periods for case study structures are shown in the following figures (Figure 5.3.10 to Figure 5.3.18). It is worth pointing out that the results

presented in this section are referred to models for linear global analysis, according to the European and Italian seismic codes (D.M., 2008, CEN, 2005), that do not take into account the structural contribution of the compressed members, considered buckled and unable to provide resistance to lateral loads. The dynamic properties of the structural models developed in OpenSees and accounting for both tension and compression diagonals can be found in Section 5.4.6.



Mode=1; T=0.60 sec    Mode=2; T=0.50 sec    Mode=3; T=0.414 sec    Mode=4; T=0.412 sec
Figure 5.3.10 First four modal shapes and natural vibration periods for SSB_Lx20_Ly6_AQ.



Mode=1; T=0.97 sec      Mode=2; T=0.83 sec      Mode=3; T=0.72 sec    Mode=4; T=0.556 sec
Figure 5.3.11 First four modal shapes and natural vibration periods for SSB_Lx30_Ly6_AQ
and SSB_Lx30_Ly6_MI.
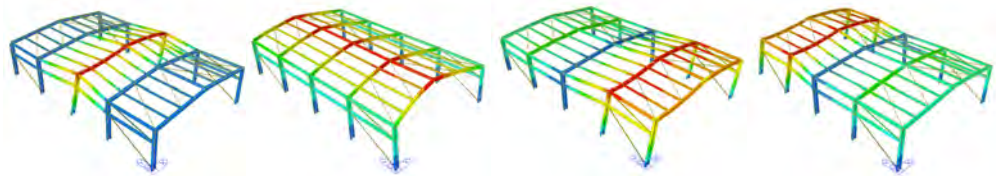


Mode=1; T=0.67 sec    Mode=2; T=0.506 sec    Mode=3; T=0.484 sec    Mode=4; T=0.483 sec
Figure 5.3.12 First four modal shapes and natural vibration periods for SSB_Lx20_Ly8_AQ
and SSB_Lx20_Ly8_MI.

Mode=1; T=0.964 sec   Mode=2; T=0.887 sec   Mode=3; T=0.726 sec   Mode=4; T=0.626 sec
Figure 5.3.13 First four modal shapes and natural vibration periods for SSB_Lx30_Ly8_AQ
and SSB_Lx30_Ly8_MI.
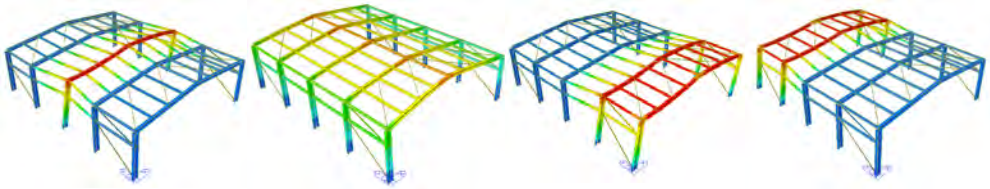


Mode=1; T=0.678 sec   Mode=2; T=0.481 sec   Mode=3; T=0.460 sec   Mode=4; T=0.459 sec
Figure 5.3.14 First four modal shapes and natural vibration periods for SSB_Lx20_Ly6_MI.



Mode=1; T=0.657 sec   Mode=2; T=0.467 sec   Mode=3; T=0.437 sec   Mode=4; T=0.436 sec
Figure 5.3.15 First four modal shapes and natural vibration periods for SSB_Lx20_Ly6_NA.
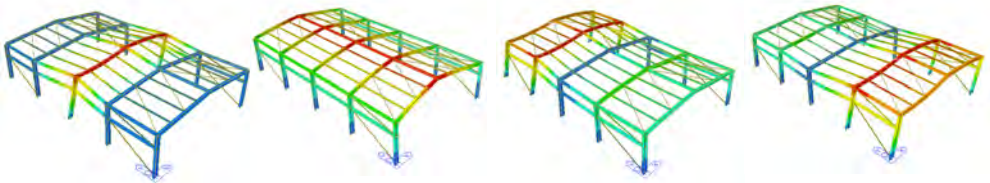


Mode=1; T=0.654 sec   Mode=2; T=0.489 sec   Mode=3; T=0.468 sec   Mode=4; T=0.467 sec
Figure 5.3.16 First four modal shapes and natural vibration periods for SSB_Lx20_Ly8_NA.

Mode=1; T=0.964 sec   Mode=2; T=0.805 sec   Mode=3; T=0.722 sec   Mode=4; T=0.531 sec
Figure 5.3.17 First four modal shapes and natural vibration periods for SSB_Lx30_Ly6_NA.



Mode=1; T=0.964 sec   Mode=2; T=0.869 sec   Mode=3; T=0.725 sec   Mode=4; T=0.607 sec
Figure 5.3.18 First four modal shapes and natural vibration periods for SSB_Lx30_Ly8_NA.

### 5.3.5    Design criteria

Concerning ultimate limit state design, axial, bending and shear resistance and combined bending and axial force resistance of structural steel members were verified according to NTC08. When checking the rafter stability, the roof purlins were assumed to provide only lateral restraints, i.e., no additional torsional restraint was assumed at intermediate rafter locations. The column stability was checked assuming torsional restraints at the column bracket level.

According to seismic design recommendations, the diagonal members of X-braced frames were designed in such way that their non-dimensional slenderness was in the range (1.3, 2). For single-bay diagonal braces the non-dimensional slenderness was limited to 2.0.

Serviceability limit state verifications were performed to ensure that the deflections are acceptable at 'working loads'. Horizontal deflection of the portal frame for the characteristic combination of loads was limited to $\Delta_i/H=1/300$, according to NTC08. For the damage preventing limit state (SLD), the horizontal drift was limited to 1/200. The difference of horizontal deflection between two consecutive portal frames, $\Delta_{ij}/L_y$, was also checked not to exceed 1/200 (ArcelorMittal, 2008). NTC08 provides vertical deflection limits for horizontal members. Such displacements, evaluated for the characteristic combination of loads, were limited to $\Delta_{max}/L_x =1/200$ and $\Delta_2/L_x=1/250$. NTC08 does not provide vertical deflection limits for portal frame apex. Typical limiting values were used as reference values (ArcelorMittal, 2008): $\Delta_{max}/L_x =1/200$ and $\Delta_2/L_x=1/250$ accordingly.

### 5.3.6    Design results

Table 5.3.5 contains, for each case study, a list of cross-sections of all structural members. As shown, the 24 case studies resulted into only 9 different structural configurations. In the X-direction, the design of frame structures was governed by SLS deflection limits, in terms of

horizontal deflection or difference of deflection between two consecutive portal frames. In the Y-direction, the cross section of the beams and diagonals was affected by the slenderness limits. Three different frames were derived: the beam-to-column combinations H 600 M - HE 500 A and H 600 M - HE 450 A satisfy deflection limits for SS_Lx20 configurations, whereas the combination of H 900 M - HE 800 A is suitable for all SSB_Lx30 geometries. Each transversal frame structure is connected in the Y-direction by two different longitudinal beams, depending on the Y-bay length: IPE 270 for Ly= 6 m and HEB 300 for Ly= 8 m. Four types of both X-braced diagonals and single diagonals were selected for the same number of diagonal lengths.

Table 5.3.5 Case study sections.

| Case Study | Column | Rafter | Vertical bracing X-braced – One braced | | Long. beam | Purlins | Roof bracing |
|---|---|---|---|---|---|---|---|
| SSB_Lx20_Ly6_AQ_A SSB_Lx20_Ly6_AQ_C | HE 600 M | HE 500 A | RHS-CF-60x60x2 | RHS-CF-90x90x2.6 | IPE 270 | HE 220 A | L20x3 |
| SSB_Lx20_Ly8_AQ_A SSB_Lx20_Ly8_AQ_C | HE 600 M | HE 500 A | RHS-CF-70x70x2.6 | RHS-CF-100x100x2.6 | HE 300 B | HE 220 A | L20x3 |
| SSB_Lx30_Ly6_AQ_A SSB_Lx30_Ly6_AQ_C | HE 900 M | HE 800 A | RHS-CF-80x80x2.6 | RHS-CF-100x100x2.6 | IPE 270 | HE 220 A | L50x4 |
| SSB_Lx30_Ly8_AQ_A SSB_Lx30_Ly8_AQ_C | HE 900 M | HE 800 A | RHS-CF-90x90x2.6 | RHS-CF-120x120x3.2 | HE 300 B | HE 220 A | L50x4 |
| SSB_Lx20_Ly6_MI_A SSB_Lx20_Ly6_MI_C | HE 600 M | HE 450 A | RHS-CF-60x60x2 | RHS-CF-90x90x2.6 | IPE 270 | HE 220 A | L20x3 |
| SSB_Lx20_Ly8_MI_A SSB_Lx20_Ly8_MI_C | HE 600 M | HE 500 A | RHS-CF-70x70x2.6 | RHS-CF-100x100x2.6 | HE 300 B | HE 220 A | L20x3 |
| SSB_Lx30_Ly6_MI_A SSB_Lx30_Ly6_MI_C | HE 900 M | HE 800 A | RHS-CF-80x80x2.6 | RHS-CF-100x100x2.6 | IPE 270 | HE 220 A | L50x4 |
| SSB_Lx30_Ly8_MI_A SSB_Lx30_Ly8_MI_C | HE 900 M | HE 800 A | RHS-CF-90x90x2.6 | RHS-CF-120x120x3.2 | HE 300 B | HE 220 A | L50x4 |
| SSB_Lx20_Ly6_NA_A SSB_Lx20_Ly6_NA_C | HE 600 M | HE 450 A | RHS-CF-60x60x2 | RHS-CF-90x90x2.6 | IPE 270 | HE 160 A | L20x3 |
| SSB_Lx20_Ly8_NA_A SSB_Lx20_Ly8_NA_C | HE 600 M | HE 500 A | RHS-CF-70x70x2.6 | RHS-CF-100x100x2.6 | HE 300 B | HE 160 A | L20x3 |
| SSB_Lx30_Ly6_NA_A SSB_Lx30_Ly6_NA_C | HE 900 M | HE 800 A | RHS-CF-80x80x2.6 | RHS-CF-100x100x2.6 | IPE 270 | HE 160 A | L50x4 |
| SSB_Lx30_Ly8_NA_A SSB_Lx30_Ly8_NA_C | HE 900 M | HE 800 A | RHS-CF-90x90x2.6 | RHS-CF-120x120x3.2 | HE 300 B | HE 160 A | L50x4 |

Design details are given from Table 5.3.6 to Table 5.3.17. In such tables, for each relevant load combination, the demand (D) to capacity (C) ratio is given for the following structural elements: column, rafter and bracings. In each table, the ratios at SLS in the first row are referred to the horizontal deflection of the column in the X-direction and Y-direction, respectively. In the second row the vertical deflection of the frame apex (in Z-direction) is given. The subsequent D/C ratios are those measured for DLS combinations for both orthogonal directions. The values associated with the ULS and LLS verifications of the column and the rafter are those measured for the resistance of the cross section to combined bending and axial compression, tagged with (R), and buckling resistance of member under combined bending and axial compression, tagged with (ST). As expected, for the vertical bracings and roof bracings the D/C ratio corresponding to the cross-section resistance to tension is provided.

The design of portal frames was governed by serviceability limit state criteria. However, the D/C ratios evaluated for horizontal deflections at SLS appeared always greater than those measured for DLS load combinations. For the structural configurations having a frame span equal to 20 m, in case of high seismicity, the effects of SLS and DLS load combinations are comparable. Analysing D/C ratios corresponding to the ultimate limit states, those referred to ULS are always grater than D/C ratios related to the LLS. The D/C ratios at LLS vary from 0.188 to 0.617 for

rafters, from 0.090 to 0.283 for columns. In the longitudinal direction, the highest D/C ratios are measured at ULS. The D/C ratios at LLS vary from 0.063 to 0.54 for the diagonals.

Table 5.3.6 Design details for SSB_Lx20_Ly6_AQ.

| Load combination | Limit state | D/C | |
|---|---|---|---|
| | | Column HE 600 M | Rafter HE 500 A |
| $F_d = G_1 + 0.5Q_{snow} + Q_c + Q_{wind} + I$ | SLS (dir-x) SLS (dir-y) | 0.760 0.380 | |
| $F_d = G_1 + Q_{snow} + Q_c + 0.6Q_{wind} + I$ | SLS (dir-z) | | 0.280 |
| $F_d = G_1 + 0.5Q_{snow} + Q_c + Q_{wind} + I$ (Deflection between two consecutive portal frames) | SLS (dir-x) | 0.670 | |
| $F_d = E + G_1 + 0.8Q_c + I$ | DLS (dir-x) | 0.840 | |
| $F_d = E + G_1 + 0.8Q_c + I$ | DLS (dir-y) | 0.350 | |
| $F_d = 1.3G_1 + 1.5Q_{snow} + 1.5Q_c + 1.5I$ | ULS | 0.309 (R) 0.329 (ST) | 0.689 (R) 0.677 (ST) |
| $F_d = 1.3G_1 + 1.5Q_{snow} + 1.5Q_c + 1.5I + 0.9Q_{wind}$ | ULS (dir-x) | 0.322 (R) 0.343 (ST) | 0.719 (R) 0.708 (ST) |
| $F_d = 1.3G_1 + 1.5Q_{wind} + 1.5Q_c + 1.5I + 0.75Q_{snow}$ | ULS (dir-x) | 0.25 (R) 0.265 (ST) | 0.567 (R) 0.556 (ST) |
| $F_d = E + G_1 + 0.8Q_c + I$ | LLS (dir-x) | 0.153 (R) 0.162 (ST) | 0.35 (R) 0.34 (ST) |
| | | Vertical braces RHS-CF-60x60x2 | Roof braces L20x3 |
| $F_d = 1.3G_1 + 1.5Q_{wind} + 1.5Q_c + 1.5I + 0.75Q_{snow}$ | ULS (dir-y) | 0.658 | 0.906 |
| $F_d = E + G_1 + 0.8Q_c + I$ | LLS (dir-y) | 0.542 | 0.605 |

Table 5.3.7 Design details for SSB_Lx30_Ly6_AQ.

| Load combination | Limit state | D/C | |
|---|---|---|---|
| | | Column HE 900 M | Rafter HE 800 A |
| $F_d = G_1 + 0.5Q_{snow} + Q_c + Q_{wind} + I$ | SLS (dir-x) SLS (dir-y) | 0.970 0.480 | |
| $F_d = G_1 + Q_{snow} + Q_c + 0.6Q_{wind} + I$ | SLS (dir-z) | | 0.300 |
| $F_d = G_1 + 0.5Q_{snow} + Q_c + Q_{wind} + I$ (Deflection between two consecutive portal frames) | SLS (dir-x) | 0.970 | |
| $F_d = E + G_1 + 0.8Q_c + I$ | DLS (dir-x) | 0.900 | |
| $F_d = E + G_1 + 0.8Q_c + I$ | DLS (dir-y) | 0.257 | |
| $F_d = 1.3G_1 + 1.5Q_{snow} + 1.5Q_c + 1.5I$ | ULS | 0.420 (R) 0.609 (ST) | 0.736 (R) 0.506 (ST) |
| $F_d = 1.3G_1 + 1.5Q_{snow} + 1.5Q_c + 1.5I + 0.9Q_{wind}$ | ULS (dir-x) | 0.440 (R) 0.637 (ST) | 0.770 (R) 0.538 (ST) |
| $F_d = 1.3G_1 + 1.5Q_{wind} + 1.5Q_c + 1.5I + 0.75Q_{snow}$ | ULS (dir-x) | 0.345 (R) 0.493 (ST) | 0.620 (R) 0.444 (ST) |
| $F_d = E + G_1 + 0.8Q_c + I$ | LLS (dir-x) | 0.197 (R) 0.283 (ST) | 0.370 (R) 0.268 (ST) |
| | | Vertical braces RHS-CF-80x80x2.6 | Roof braces L50x4 |
| $F_d = 1.3G_1 + 1.5Q_{wind} + 1.5Q_c + 1.5I + 0.75Q_{snow}$ | ULS (dir-y) | 0.900 | 0.802 |
| $F_d = E + G_1 + 0.8Q_c + I$ | LLS (dir-y) | 0.347 | 0.331 |

Table 5.3.8 Design details for SSB_Lx20_Ly6_MI.

| Load combination | Limit state | D/C | |
|---|---|---|---|
| | | Column<br>HE 600 M | Rafter<br>HE 500 A |
| $F_d = G_1 + 0.5Q_{snow} + Q_c + Q_{wind} + I$ | SLS (dir-x)<br>SLS (dir-y) | 0.67<br>0.019 | |
| $F_d = G_1 + Q_{snow} + Q_c + 0.6Q_{wind} + I$ | SLS (dir-z) | | 0.270 |
| $F_d = G_1 + 0.5Q_{snow} + Q_c + Q_{wind} + I$<br>(Deflection between two consecutive portal frames) | SLS (dir-x) | 0.670 | |
| $F_d = E + G_1 + 0.8Q_c + I$ | DLS (dir-x) | 0.35 | |
| $F_d = E + G_1 + 0.8Q_c + I$ | DLS (dir-y) | 0.095 | |
| $F_d = 1.3G_1 + 1.5Q_{snow} + 1.5Q_c + 1.5I$ | ULS | 0.294 (R)<br>0.312 (ST) | 0.656 (R)<br>0.643 (ST) |
| $F_d = 1.3G_1 + 1.5Q_{snow} + 1.5Q_c + 1.5I + 0.9Q_{wind}$ | ULS (dir-x) | 0.302 (R)<br>0.321 (ST) | 0.674 (R)<br>0.663 (ST) |
| $F_d = 1.3G_1 + 1.5Q_{wind} + 1.5Q_c + 1.5I + 0.75Q_{snow}$ | ULS (dir-x) | 0.233 (R)<br>0.247 (ST) | 0.530 (R)<br>0.519 (ST) |
| $F_d = E + G_1 + 0.8Q_c + I$ | LLS (dir-x) | 0.105 (R)<br>0.110 (ST) | 0.241 (R)<br>0.230 (ST) |
| | | Vertical braces<br>RHS-CF-60x60x2 | Roof braces<br>L20x3 |
| $F_d = 1.3G_1 + 1.5Q_{wind} + 1.5Q_c + 1.5I + 0.75Q_{snow}$ | ULS (dir-y) | 0.467 | 0.613 |
| $F_d = E + G_1 + 0.8Q_c + I$ | LLS (dir-y) | 0.189 | 0.157 |

Table 5.3.9 Design details for SSB_Lx30_Ly6_MI.

| Load combination | Limit state | D/C | |
|---|---|---|---|
| | | Column<br>HE 900 M | Rafter<br>HE 800 A |
| $F_d = G_1 + 0.5Q_{snow} + Q_c + Q_{wind} + I$ | SLS (dir-x)<br>SLS (dir-y) | 0.806<br>0.355 | |
| $F_d = G_1 + Q_{snow} + Q_c + 0.6Q_{wind} + I$ | SLS (dir-z) | | 0.300 |
| $F_d = G_1 + 0.5Q_{snow} + Q_c + Q_{wind} + I$<br>(Deflection between two consecutive portal frames) | SLS (dir-x) | 0.930 | |
| $F_d = E + G_1 + 0.8Q_c + I$ | DLS (dir-x) | 0.385 | |
| $F_d = E + G_1 + 0.8Q_c + I$ | DLS (dir-y) | 0.064 | |
| $F_d = 1.3G_1 + 1.5Q_{snow} + 1.5Q_c + 1.5I$ | ULS | 0.402 (R)<br>0.582 (ST) | 0.707 (R)<br>0.487 (ST) |
| $F_d = 1.3G_1 + 1.5Q_{snow} + 1.5Q_c + 1.5I + 0.9Q_{wind}$ | ULS (dir-x) | 0.414 (R)<br>0.600 (ST) | 0.728 (R)<br>0.507 (ST) |
| $F_d = 1.3G_1 + 1.5Q_{wind} + 1.5Q_c + 1.5I + 0.75Q_{snow}$ | ULS (dir-x) | 0.324 (R)<br>0.463 (ST) | 0.585 (R)<br>0.415 (ST) |
| $F_d = E + G_1 + 0.8Q_c + I$ | LLS (dir-x) | 0.150 (R)<br>0.217 (ST) | 0.270 (R)<br>0.191 (ST) |
| | | Vertical braces<br>RHS-CF-80x80x2.6 | Roof braces<br>L50x4 |
| $F_d = 1.3G_1 + 1.5Q_{wind} + 1.5Q_c + 1.5I + 0.75Q_{snow}$ | ULS (dir-y) | 0.622 | 0.553 |
| $F_d = E + G_1 + 0.8Q_c + I$ | LLS (dir-y) | 0.130 | 0.005 |

Table 5.3.10 Design details for SSB_Lx20_Ly6_NA.

| Load combination | Limit state | D/C | |
|---|---|---|---|
| | | Column HE 600 M | Rafter HE 450 A |
| $F_d = G_1 + 0.5Q_{snow} + Q_c + Q_{wind} + I$ | SLS (dir-x) SLS (dir-y) | 0.95 0.330 | |
| $F_d = G_1 + Q_{snow} + Q_c + 0.6Q_{wind} + I$ | SLS (dir-z) | | 0.190 |
| $F_d = G_1 + 0.5Q_{snow} + Q_c + Q_{wind} + I$ (Deflection between two consecutive portal frames) | SLS (dir-x) | 0.870 | |
| $F_d = E + G_1 + 0.8Q_c + I$ | DLS (dir-x) | 0.600 | |
| $F_d = E + G_1 + 0.8Q_c + E + I$ | DLS (dir-y) | 0.350 | |
| $F_d = 1.3G_1 + 1.5Q_{snow} + 1.5Q_c + 1.5I$ | ULS | 0.190 (R) 0.207 (ST) | 0.545 (R) 0.533 (ST) |
| $F_d = 1.3G_1 + 1.5Q_{snow} + 1.5Q_c + 1.5I + 0.9Q_{wind}$ | ULS (dir-x) | 0.207 (R) 0.219 (ST) | 0.575 (R) 0.564 (ST) |
| $F_d = 1.3G_1 + 1.5Q_{wind} + 1.5Q_c + 1.5I + 0.75Q_{snow}$ | ULS (dir-x) | 0.184 (R) 0.194 (ST) | 0.517 (R) 0.507 (ST) |
| $F_d = E + G_1 + 0.8Q_c + I$ | LLS (dir-x) | 0.086 (R) 0.090 (ST) | 0.231 (R) 0.230 (ST) |
| | | Vertical braces RHS-CF-60x60x2 | Roof braces L20x3 |
| $F_d = 1.3G_1 + 1.5Q_{wind} + 1.5Q_c + 1.5I + 0.75Q_{snow}$ | ULS (dir-y) | 0.556 | 0.763 |
| $F_d = E + G_1 + 0.8Q_c + I$ | LLS (dir-y) | 0.298 | 0.302 |

Table 5.3.11 Design details for SSB_Lx30_Ly6_NA.

| Load combination | Limit state | D/C | |
|---|---|---|---|
| | | Column HE 900 M | Rafter HE 800 A |
| $F_d = G_1 + 0.5Q_{snow} + Q_c + Q_{wind} + I$ | SLS (dir-x) SLS (dir-y) | 0.870 0.450 | |
| $F_d = G_1 + Q_{snow} + Q_c + 0.6Q_{wind} + I$ | SLS (dir-z) | | 0.190 |
| $F_d = G_1 + 0.5Q_{snow} + Q_c + Q_{wind} + I$ (Deflection between two consecutive portal frames) | SLS (dir-x) | 0.970 | |
| $F_d = E + G_1 + 0.8Q_c + I$ | DLS (dir-x) | 0.490 | |
| $F_d = E + G_1 + 0.8Q_c + I$ | DLS (dir-y) | 0.260 | |
| $F_d = 1.3G_1 + 1.5Q_{snow} + 1.5Q_c + 1.5I$ | ULS | 0.283 (R) 0.404 (ST) | 0.517 (R) 0.360 (ST) |
| $F_d = 1.3G_1 + 1.5Q_{snow} + 1.5Q_c + 1.5I + 0.9Q_{wind}$ | ULS (dir-x) | 0.300 (R) 0.428 (ST) | 0.546 (R) 0.387 (ST) |
| $F_d = 1.3G_1 + 1.5Q_{wind} + 1.5Q_c + 1.5I + 0.75Q_{snow}$ | ULS (dir-x) | 0.272 (R) 0.385 (ST) | 0.503 (R) 0.363 (ST) |
| $F_d = E + G_1 + 0.8Q_c + I$ | LLS (dir-x) | 0.136 (R) 0.201 (ST) | 0.223 (R) 0.164 (ST) |
| | | Vertical braces RHS-CF-80x80x2.6 | Roof braces L50x4 |
| $F_d = 1.3G_1 + 1.5Q_{wind} + 1.5Q_c + 1.5I + 0.75Q_{snow}$ | ULS (dir-y) | 0.787 | 0.664 |
| $F_d = E + G_1 + 0.8Q_c + I$ | LLS (dir-y) | 0.209 | 0.228 |

Table 5.3.12 Design details for SSB_Lx20_Ly8_AQ.

| Load combination | Limit state | D/C | |
|---|---|---|---|
| | | Column HE 600 M | Rafter HE 500 A |
| $F_d = G_1+0.5Q_{snow}+Q_c+Q_{wind}+I$ | SLS (dir-x) | 0.860 | |
| | SLS (dir-y) | 0.380 | |
| $F_d = G_1+Q_{snow}+Q_c+0.6Q_{wind}+I$ | SLS (dir-z) | | 0.360 |
| $F_d = G_1+0.5Q_{snow}+Q_c+Q_{wind}+I$ (Deflection between two consecutive portal frames) | SLS (dir-x) | 0.700 | |
| $F_d = E+G_1+0.8Q_c+I$ | DLS (dir-x) | 0.790 | |
| $F_d = E+G_1+0.8Q_c+E+I$ | DLS (dir-y) | 0.320 | |
| $F_d = 1.3G_1+1.5Q_{snow}+1.5Q_c+1.5I$ | ULS | 0.382 (R) 0.407 (ST) | 0.841 (R) 0.821 (ST) |
| $F_d = 1.3G_1+1.5Q_{snow}+1.5Q_c+1.5I +0.9Q_{wind}$ | ULS (dir-x) | 0.400 (R) 0.427 (ST) | 0.884 (R) 0.866 (ST) |
| $F_d = 1.3G_1+1.5Q_{wind}+1.5Q_c+1.5I+0.75Q_{snow}$ | ULS (dir-x) | 0.304 (R) 0.323 (ST) | 0.682 (R) 0.667 (ST) |
| $F_d = E+G_1+0.8Q_c+I$ | LLS (dir-x) | 0.140 (R) 0.149 (ST) | 0.308 (R) 0.305 (ST) |
| | | Vertical braces RHS-CF-70x70x2.6 | Roof braces L20x3 |
| $F_d = 1.3G_1+1.5Q_{wind}+1.5Q_c+1.5I+0.75Q_{snow}$ | ULS (dir-y) | 0.391 | 0.844 |
| $F_d = E+G_1+0.8Q_c+I$ | LLS (dir-y) | 0.319 | 0.746 |

Table 5.3.13 Design details for SSB_Lx30_Ly8_AQ.

| Load combination | Limit state | D/C | |
|---|---|---|---|
| | | Column HE 900 M | Rafter HE 800 A |
| $F_d = G_1+0.5Q_{snow}+Q_c+Q_{wind}+I$ | SLS (dir-x) | 1.00 | |
| | SLS (dir-y) | 0.39 | |
| $F_d = G_1+Q_{snow}+Q_c+0.6Q_{wind}+I$ | SLS (dir-z) | | 0.400 |
| $F_d = G_1+0.5Q_{snow}+Q_c+Q_{wind}+I$ (Deflection between two consecutive portal frames) | SLS (dir-x) | 1.00 | |
| $F_d = E+G_1+0.8Q_c+I$ | DLS (dir-x) | 0.770 | |
| $F_d = E+G_1+0.8Q_c+I$ | DLS (dir-y) | 0.235 | |
| $F_d = 1.3G_1+1.5Q_{snow}+1.5Q_c+1.5I$ | ULS | 0.515 (R) 0.755 (ST) | 0.886 (R) 0.605 (ST) |
| $F_d = 1.3G_1+1.5Q_{snow}+1.5Q_c+1.5I +0.9Q_{wind}$ | ULS (dir-x) | 0.541 (R) 0.792 (ST) | 0.931 (R) 0.647 (ST) |
| $F_d = 1.3G_1+1.5Q_{wind}+1.5Q_c+1.5I+0.75Q_{snow}$ | ULS (dir-x) | 0.414 (R) 0.597 (ST) | 0.732 (R) 0.523 (ST) |
| $F_d = E+G_1+0.8Q_c+I$ | LLS (dir-x) | 0.256(R) 0.340 (ST) | 0.617 (R) 0.449 (ST) |
| | | Vertical braces RHS-CF-90x90x2.6 | Roof braces L50x4 |
| $F_d = 1.3G_1+1.5Q_{wind}+1.5Q_c+1.5I+0.75Q_{snow}$ | ULS (dir-y) | 0.678 | 0.755 |
| $F_d = E+G_1+0.8Q_c+I$ | LLS (dir-y) | 0.268 | 0.361 |

Table 5.3.14 Design details for SSB_Lx20_Ly8_NA.

| Load combination | Limit state | D/C | |
|---|---|---|---|
| | | Column<br>HE 600 M | Rafter<br>HE 500 A |
| $F_d = G_1+0.5Q_{snow}+Q_c+Q_{wind}+I$ | SLS (dir-x)<br>SLS (dir-y) | 0.810<br>0.240 | |
| $F_d = G_1+Q_{snow}+Q_c+0.6Q_{wind}+I$ | SLS (dir-z) | | 0.190 |
| $F_d = G_1+0.5Q_{snow}+Q_c+Q_{wind}+I$<br>(Deflection between two consecutive portal frames) | SLS (dir-x) | 0.500 | |
| $F_d = E+G_1+0.8\,Q_c+I$ | DLS (dir-x) | 0.510 | |
| $F_d = E+G_1+0.8\,Q_c+E+I$ | DLS (dir-y) | 0.190 | |
| $F_d = 1.3G_1+1.5Q_{snow}+1.5Q_c+1.5I$ | ULS | 0.233 (R)<br>0.247 (ST) | 0.525 (R)<br>0.512 (ST) |
| $F_d = 1.3G_1+1.5Q_{snow}+1.5Q_c+1.5I +0.9Q_{wind}$ | ULS (dir-x) | 0.248 (R)<br>0.263 (ST) | 0.559 (R)<br>0.548 (ST) |
| $F_d = 1.3G_1+1.5Q_{wind}+1.5Q_c+1.5I+0.75Q_{snow}$ | ULS (dir-x) | 0.218 (R)<br>0.231 (ST) | 0.498 (R)<br>0.487 (ST) |
| $F_d = E+G_1+0.8\,Q_c+I$ | LLS (dir-x) | 0.108(R)<br>0.115 (ST) | 0.237 (R)<br>0.235 (ST) |
| | | Vertical braces<br>RHS-CF-70x70x2.6 | Roof braces<br>L20x3 |
| $F_d = 1.3G_1+1.5Q_{wind}+1.5Q_c+1.5I+0.75Q_{snow}$ | ULS (dir-y) | 0.359 | 0.719 |
| $F_d = E+G_1+0.8\,Q_c+I$ | LLS (dir-y) | 0.228 | 0.434 |

Table 5.3.15 Design details for SSB_Lx30_Ly8_NA.

| Load combination | Limit state | D/C | |
|---|---|---|---|
| | | Column<br>HE 900 M | Rafter<br>HE 800 A |
| $F_d = G_1+0.5Q_{snow}+Q_c+Q_{wind}+I$ | SLS (dir-x)<br>SLS (dir-y) | 1.000<br>0.320 | |
| $F_d = G_1+Q_{snow}+Q_c+0.6Q_{wind}+I$ | SLS (dir-z) | | 0.220 |
| $F_d = G_1+0.5Q_{snow}+Q_c+Q_{wind}+I$<br>(Deflection between two consecutive portal frames) | SLS (dir-x) | 0.750 | |
| $F_d = E+G_1+0.8\,Q_c+I$ | DLS (dir-x) | 0.510 | |
| $F_d = E+G_1+0.8\,Q_c+I$ | DLS (dir-y) | 0.150 | |
| $F_d = 1.3G_1+1.5Q_{snow}+1.5Q_c+1.5I$ | ULS | 0.319 (R)<br>0.458 (ST) | 0.574 (R)<br>0.396 (ST) |
| $F_d = 1.3G_1+1.5Q_{snow}+1.5Q_c+1.5I +0.9Q_{wind}$ | ULS (dir-x) | 0.342 (R)<br>0.490 (ST) | 0.613 (R)<br>0.433 (ST) |
| $F_d = 1.3G_1+1.5Q_{wind}+1.5Q_c+1.5I+0.75Q_{snow}$ | ULS (dir-x) | 0.304 (R)<br>0.432 (ST) | 0.503 (R)<br>0.363 (ST) |
| $F_d = E+G_1+0.8\,Q_c+I$ | LLS (dir-x) | 0.145(R)<br>0.215 (ST) | 0.238 (R)<br>0.173 (ST) |
| | | Vertical braces<br>RHS-CF-90x90x2.6 | Roof braces<br>L50x4 |
| $F_d = 1.3G_1+1.5Q_{wind}+1.5Q_c+1.5I+0.75Q_{snow}$ | ULS (dir-y) | 0.598 | 0.617 |
| $F_d = E+G_1+0.8\,Q_c+I$ | LLS (dir-y) | 0.183 | 0.238 |

Table 5.3.16 Design details for SSB_Lx20_Ly8_MI.

| Load combination | Limit state | D/C | |
|---|---|---|---|
| | | Column<br>HE 600 M | Rafter<br>HE 500 A |
| $F_d = G_1+0.5Q_{snow}+Q_c+Q_{wind}+I$ | SLS (dir-x)<br>SLS (dir-y) | 0.710<br>0.190 | |
| $F_d = G_1+Q_{snow}+Q_c+0.6Q_{wind}+I$ | SLS (dir-z) | | 0.350 |
| $F_d = G_1+0.5Q_{snow}+Q_c+Q_{wind}+I$<br>(Deflection between two consecutive portal frames) | SLS (dir-x) | 0.670 | |
| $F_d = E+G_1+0.8\,Q_c+I$ | DLS (dir-x) | 0.190 | |
| $F_d = E+G_1+0.8\,Q_c+I$ | DLS (dir-y) | 0.095 | |
| $F_d = 1.3G_1+1.5Q_{snow}+1.5Q_c+1.5I$ | ULS | 0.363 (R)<br>0.387 (ST) | 0.802 (R)<br>0.791 (ST) |
| $F_d = 1.3G_1+1.5Q_{snow}+1.5Q_c+1.5I +0.9Q_{wind}$ | ULS (dir-x) | 0.347 (R)<br>0.399 (ST) | 0.827 (R)<br>0.818 (ST) |
| $F_d = 1.3G_1+1.5Q_{wind}+1.5Q_c+1.5I+0.75Q_{snow}$ | ULS (dir-x) | 0.283 (R)<br>0.300 (ST) | 0.643 (R)<br>0.624 (ST) |
| $F_d = E+G_1+0.8\,Q_c+I$ | LLS (dir-x) | 0.087(R)<br>0.092 (ST) | 0.188 (R)<br>0.186 (ST) |
| | | Vertical braces<br>RHS-CF-<br>70x70x2.6 | Roof braces<br>L20x3 |
| $F_d = 1.3G_1+1.5Q_{wind}+1.5Q_c+1.5I+0.75Q_{snow}$ | ULS (dir-y) | 0.275 | 0.563 |
| $F_d = E+G_1+0.8\,Q_c+I$ | LLS (dir-y) | 0.082 | 0.172 |

Table 5.3.17 Design details for SSB_Lx30_Ly8_MI.

| Load combination | Limit state | D/C | |
|---|---|---|---|
| | | Column<br>HE 900 M | Rafter<br>HE 800 A |
| $F_d = G_1+0.5Q_{snow}+Q_c+Q_{wind}+I$ | SLS (dir-x)<br>SLS (dir-y) | 0.903<br>0.258 | |
| $F_d = G_1+Q_{snow}+Q_c+0.6Q_{wind}+I$ | SLS (dir-z) | | 0.387 |
| $F_d = G_1+0.5Q_{snow}+Q_c+Q_{wind}+I$<br>(Deflection between two consecutive portal frames) | SLS (dir-x) | 0.930 | |
| $F_d = E+G_1+0.8\,Q_c+I$ | DLS (dir-x) | 0.235 | |
| $F_d = E+G_1+0.8\,Q_c+I$ | DLS (dir-y) | 0.064 | |
| $F_d = 1.3G_1+1.5Q_{snow}+1.5Q_c+1.5I$ | ULS | 0.491 (R)<br>0.718 (ST) | 0.848 (R)<br>0.579 (ST) |
| $F_d = 1.3G_1+1.5Q_{snow}+1.5Q_c+1.5I +0.9Q_{wind}$ | ULS (dir-x) | 0.507 (R)<br>0.741 (ST) | 0.876 (R)<br>0.606 (ST) |
| $F_d = 1.3G_1+1.5Q_{wind}+1.5Q_c+1.5I+0.75Q_{snow}$ | ULS (dir-x) | 0.387 (R)<br>0.556 (ST) | 0.685 (R)<br>0.484 (ST) |
| $F_d = E+G_1+0.8\,Q_c+I$ | LLS (dir-x) | 0.123 (R)<br>0.185 (ST) | 0.192 (R)<br>0.135 (ST) |
| | | Vertical braces<br>RHS-CF-<br>90x90x2.6 | Roof braces<br>L50x4 |
| $F_d = 1.3G_1+1.5Q_{wind}+1.5Q_c+1.5I+0.75Q_{snow}$ | ULS (dir-y) | 0.459 | 0.617 |
| $F_d = E+G_1+0.8\,Q_c+I$ | LLS (dir-y) | 0.063 | 0.004 |

## 5.4   Modelling issues and strategies

The nonlinear response of the structural systems designed in the previous section was investigated using the open source software OpenSees. The structural models, developed through the OpenSees software, account for both geometric and material nonlinearities. In

particular, as it will be described below, all the structural elements were modelled using nonlinear fiber sections with steel cyclic constitutive law. The corotational approach is adopted in order to take into account the nonlinear geometric effects due to both the large displacements and the local imperfections of the vertical bracing systems. Multi-stripe analysis at 10 Intensity Measure (IM) levels (with IM chosen to be the spectral pseudo-acceleration at the fundamental period of the system) were carried out, by using a set of 20 X-Y-pairs of ground motions for each IM level in order to simulate the seismic record-to-record variability. Pushover (PO) analyses were also carried out for comparison and preliminary investigation purposes. Figure 5.4.1 shows a qualitative scheme of the finite element model. An in-depth description of all the modelling details is reported below.



*X direction*                                                            *Y direction*
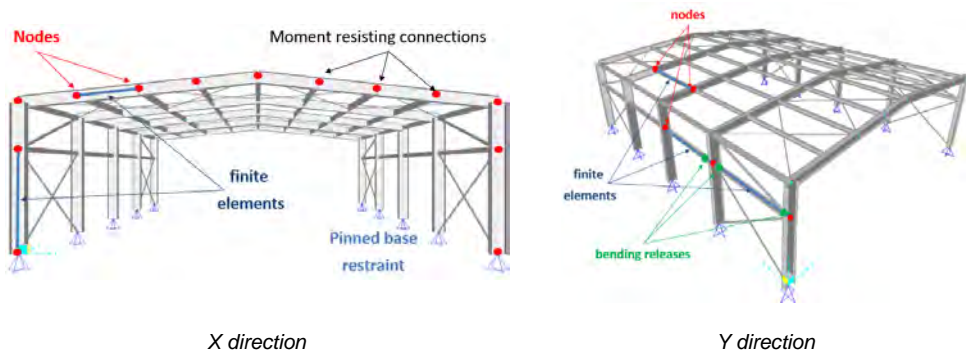
Figure 5.4.1 The structural model of the building.

### 5.4.1    Materials and constitutive laws

The elastic properties of each structural element were taken as follow:

- Elastic Modulus (Young's modulus) $E_s = 2.1 \cdot 10^8$ kN/m$^2$
- Transversal Deformability Modulus (Poisson's ratio) $\nu = 0.3$
- Shear Stiffness Modulus $G_s = E_s / 2(1+ \nu) = 0.808$ kN/m$^2$
- Specific Weight $\gamma_s = 76.98$ kN/m$^3$

The nonlinear behavior was modelled by assigning to each section's fiber the uniaxialMaterial Steel02 constitutive law (Giuffre-Menegotto-Pinto steel material object with isotropic strain hardening, Figure 5.4.2a) available within the OpenSees library. The constitutive properties assumed for the stress-strain relationship are listed below:

- Nominal Yielding Tension $f_y = 316200$ kN/m$^2$ (Da Silva et al. 2009)
- Post-elastic isotropic hardening ratio $E_p = 0.01 E_s$

Other constitutive law parameters governing the transition from the elastic to the inelastic branches assumed equal to default values as suggested in the OpenSees user manual R0 = 19.000, R1 = 0.925, R2 = 0.150.

Figure 5.4.2b shows an example of the cyclic flexural behavior (i.e., Moment-Rotation relationship) for a general beamColumn element.

(a)                                                                    (b)
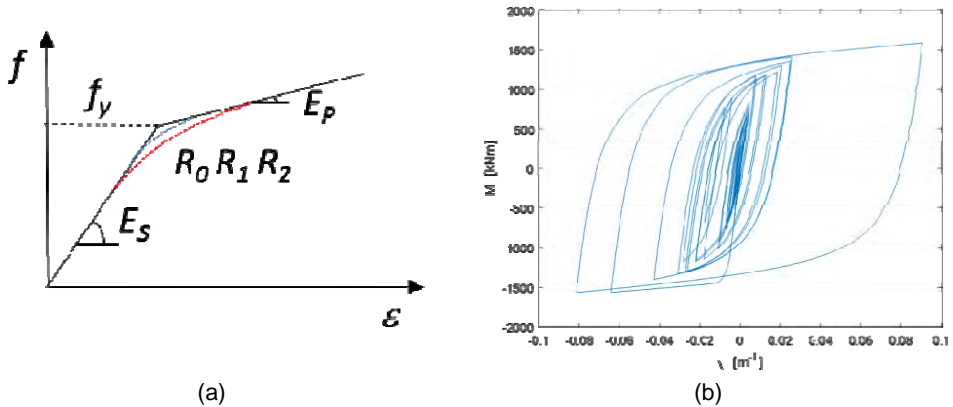
Figure 5.4.2 Giuffre-Menegotto-Pinto stress-strain law (a) and Force-Axial Strain (b).

The system' damping was accounted trough the Rayleigh damping ratio $\xi$=5% for the first and third eigenvalues.

### 5.4.2    Boundary conditions and releases

All columns are hinged at their bases. The pinned-end connections in longitudinal direction were modelled by generating a pair of nodes (one master and one slave) having the same spatial coordinates and by linking them with a proper equalDOF constraint available in the OpenSees library (see Figure 5.4.3). In particular, the properties of the equalDOF constraint are such that the slave node inherits all the degrees of freedom of the master node except for the rotational ones around the global X and Z directions (i.e., the rotations $\varphi_1$ and $\varphi_3$ respectively).
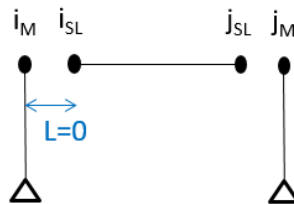


Figure 5.4.3 Scheme of the rotational GdL release.

### 5.4.3    Loads and masses

Loads were assigned as either point or distributed forces while the masses were lumped at the structural nodes according to their real spatial distribution and influence area.

### 5.4.4    Elements modelling

All the elements were modelled as Force-Based nonlinear BeamColumn elements (force-based approach relies on the availability of an exact equilibrium solution within the basic system of the element, that still holds in the range of constitutive nonlinearity) and a variable Number of Integration Points (NIPs) was adopted depending on the length of the elements themselves: the longer the element, the larger NIPs in order to improve the accuracy of the solution. A NIPs between 5 and 8 was always ensured and the Gauss-Lobatto integration method was adopted.

A distributed plasticity approach allows an accurate description of the yielding processes occurring along the element; the number of sections' fibers was defined with the aim of providing a trade-off between the convergence improvement and a not excessive rise of the computational burden during the analysis.

These are the sections employed in the model with the relevant number of fibers adopted:

- hollow squared RHS-CF sections used for the vertical braces are discretized by 10x10 fibers in both the flanges and the webs;
- L-shaped sections used for the roof braces are discretized by 10x10 fibers;
- IPE/HE-shaped sections (used for all the other elements) are discretized by 14x14 fibers in both the flanges and the web.

The torsional stiffness ($J_tG_s$) was introduced by adding this contribution (in series) to that of the fiber section, by means of the OpenSees *section Aggregator.*

### 5.4.5 Vertical braces modelling

For what concerns the vertical braces there are two main modelling aspects requiring a particular care: accounting for the buckling phenomenon in compression and a proper modelling of the gusset plate connections, that in real structures are neither pinned nor fixed joints. The adopted method for modelling the bracing systems is the one proposed by Hsiao (2012, 2013) and consists in simulating the nonlinear out-of-plane rotational behavior of the gusset plate connections by means of a rotational nonlinear spring located at the physical end of the brace; this nonlinear spring elastic stiffness $k_{col}$ is calibrated properly upon the actual geometry of the connection through the following expression (5.4.1)

$$k_{col} = \frac{Es}{L_a}\left(\frac{W_W t^3}{12}\right)$$

5.4.1

in which, $E_s$ is Young's modulus, $W_W$ is the Whitmore width defined by a 45° projection angle, $L_a$ is the average of L1, L2 and L3 as shown in Figure 5.4.4, and t is the thickness of the gusset plate. The post elastic stiffness was assumed to be the 1.0% of the elastic one $k_{col}$.
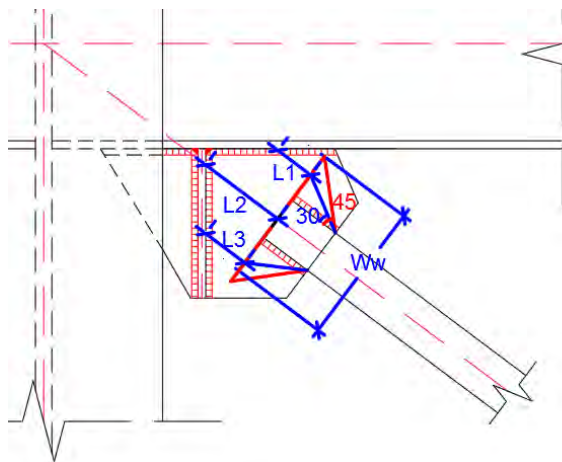


Figure 5.4.4 Geometrical quantities involved into the Gusset modelling.

The nonlinear spring was modelled in OpenSees through a zero-length element having the out-of-plane rotational degree of freedom represented by a Steel02 material with the properties obtained as explained above. In order to simulate the buckling of the vertical braces during the

compression phases, each brace was discretized into a proper number of nonlinear (with distributed plasticity) sub-elements and a sinusoidal curvature was assigned by modifying parametrically the coordinates of the nodes of the intermediate sub-elements (see Figure 5.4.9 and Figure 5.4.10). This initial curvature, representing the local imperfection of the diagonal brace, has got the role of triggering the buckling by furnishing a preferential buckling shape to the element. The value of the initial imperfection was chosen in such a way to furnish a buckling axial force consistent with the ultimate value $N_{b,Rd}$ provided by the equation 5.4.2.

$$N_{b,Rd} = \frac{\chi \cdot A \cdot f_y}{\gamma_{M1}}$$

$\qquad\qquad\qquad\qquad\qquad\qquad\qquad\qquad\qquad\qquad\qquad\qquad\qquad\qquad\qquad$ 5.4.2

with $\gamma_M$ = 1, a cross section area, nominal yielding stress $f_y$, and the buckling reduction factor $\chi$, depending by the profile type and the slenderness of the element.

For this purpose, each single brace was modelled separately, according to its actual section and configuration (i.e., length and gusset connections), and then it was subjected to several nonlinear static analyses (controlled by displacements) repeated with different values of the initial imperfection. This procedure was stopped once the maximum axial force reached during the analysis matched the $N_{b,Rd}$ provided by the code's formula. Figure 5.4.5 shows, as example, the curve axial force – lateral displacement N-$\delta$ ($\delta$ observed in the middle of the element) obtained by assigning an imperfection equal to $L_{eff}$/1000 to the single brace and by performing a nonlinear static analysis controlled by displacements (the sign of the displacements in the chart is positive even if representing a brace's shortening). The value of $N_{b,Rd}$ provided by the code for this element with its geometry and slenderness is $N_{b,Rd}$ = 85 kN, and the maximum value reached by the axial force during the analysis is exactly 85 kN, meaning that the imperfection $L_{eff}$/1000 is correct and consistent with the code's provisions.
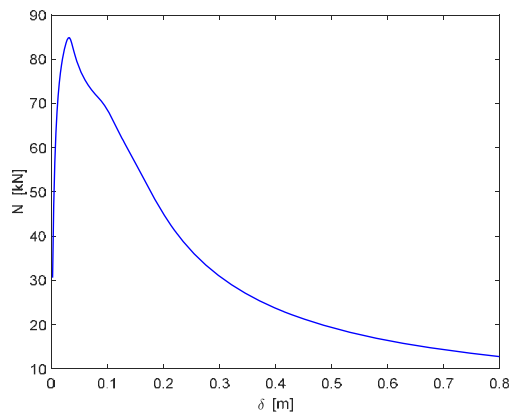


Figure 5.4.5 N-$\delta$ curve for single braces ($N_{b,Rd}$ = 85 kN).

The N-$\delta$ curves for other brace's configurations are reported below (Figure 5.4.6).

$N_{b,Rd}$ = 16.00 kN                          $N_{b,Rd}$ = 62.00 kN

(a)                                          (b)
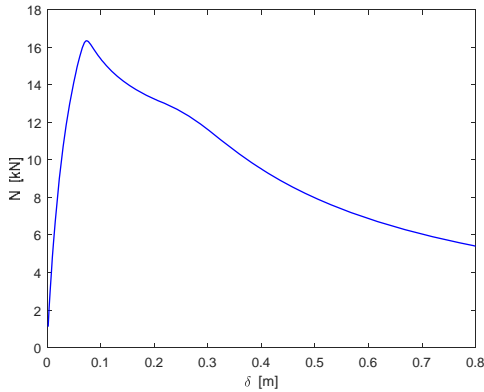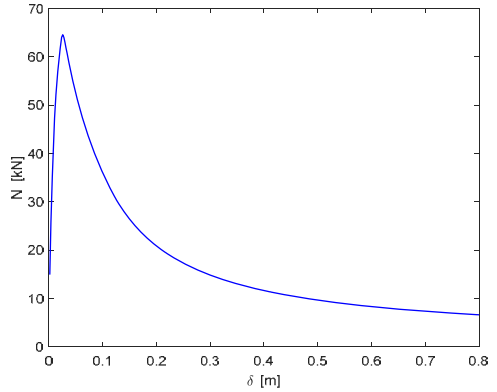
Figure 5.4.6 N-δ curve for continuous X braces (a) and for cut X braces.

The modelling technique presented so far allows to account for the complex cyclic (tension-compression) behavior of the vertical braces; the Force-Displacement cyclic response of a vertical brace under a displacement-controlled test and the Moment-Rotation cyclic response of the gusset plate, are shown in Figure 5.4.7a and b, respectively.



(a)                                          (b)
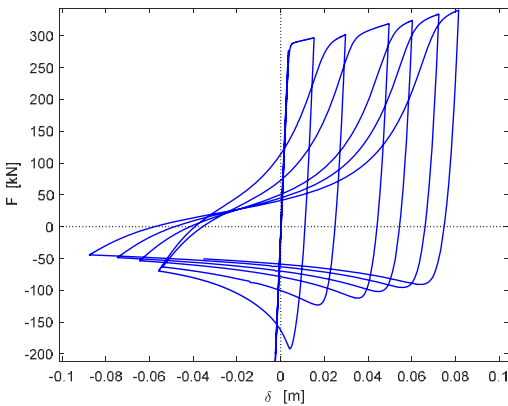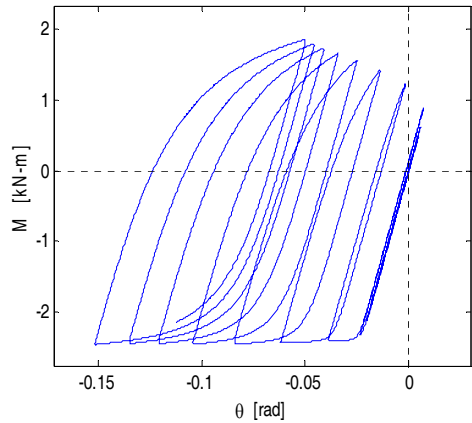
Figure 5.4.7 F-δ cyclic response of a single brace (a) and M-θ cyclic response of the gusset plate (b).

As stated in the previous section, there are two different configurations of vertical braces: a single brace configuration and a X-configuration. The latter is made by two braces intersecting each other through a properly designed gusset plate connection; this connection needs one of the two braces to be cut (Figure 5.4.8).
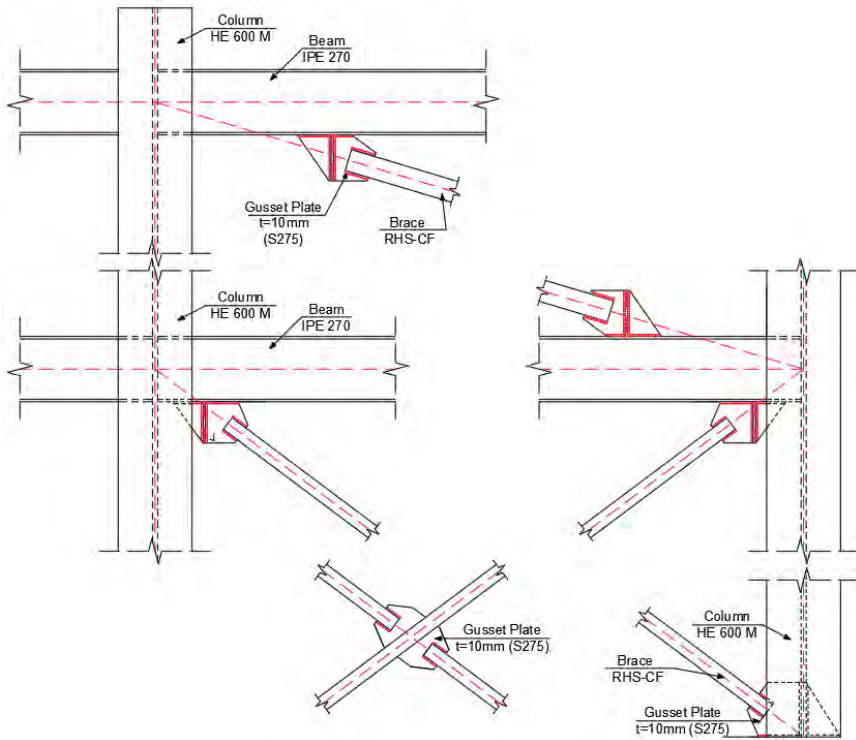
Figure 5.4.8 Vertical bracing systems.

A schematic representation of the modelling criteria adopted for the different braces configuration is given in the next Figure 5.4.9 and Figure 5.4.10, in which the local imperfections δ are also highlighted.



(a)                                          (b)
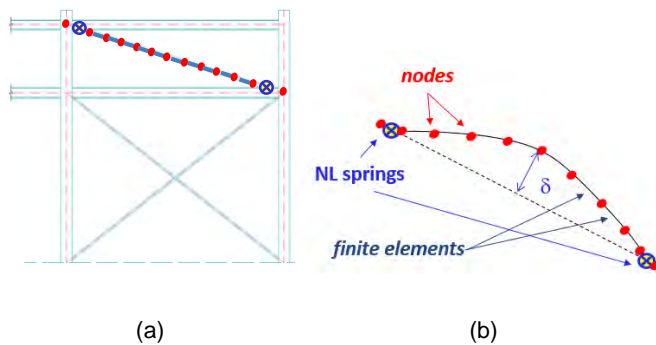
Figure 5.4.9 NL springs and subelements (a) and the initial imperfection (b) for the single brace.

(a)                                                           (b)
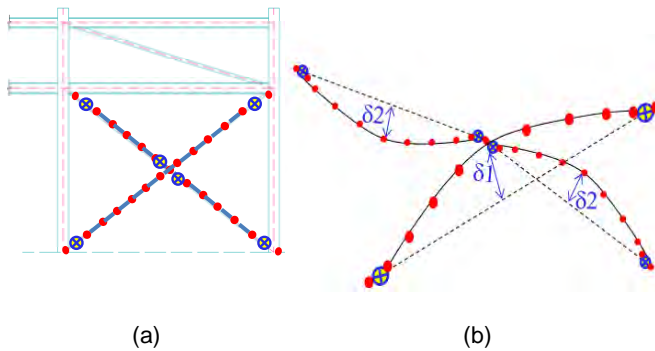
Figure 5.4.10 NL springs and sub-elements (a) and initial imperfections (b) the X-braces.

Figure 5.4.11 shows, in top- and front- schematic views, the local imperfections (significantly amplified) assigned to the vertical braces.



(a)                                                                       (b)
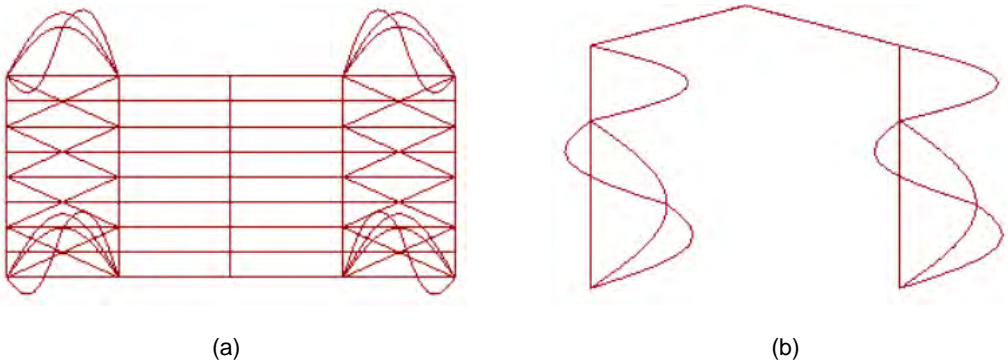
Figure 5.4.11 Out-of-plan imperfections: top (a) and front side (b) views.

### 5.4.6   Modal properties of the OpenSees models

The first four vibration periods for all of the structural models developed in OpenSees are summarized from Table 5.4.1 to Table 5.4.3, while a schematic representation of the modal shapes, which are common for all the buildings, is illustrated in Figure 5.4.12. The first mode is a local translational mode in X direction, at which the central portal frame dominantely vibrates; also at the second and third modes the portal frames dominantely deform along X, and their vibration periods are very close to each other; the fourth mode is a global longitudinal (along Y) mode. It is worth to note that both the periods and modes slightly change with respect to the cases presented in Section 5.3.4, in which the finite element models were developed (in Midas Gen) by considering that only the tension diagonals are active. In fact, the X-mode of the central portal frame is the same in both the OpenSees and Midas models, while all the modes directly affected by the concentric braces (both vertical and roof braces) are now shifted towards higher frequencies or even changed because of the symmetric bracing configuration.

Table 5.4.1 First four vibration periods for L'Aquila case studies.

| Case L'Aquila | T1 (Tx) (s) | T2 (s) | T3 (s) | T4 (Ty) (s) |
|---|---|---|---|---|
| Lx20_Ly8_AQ | 0.67 | 0.4796 | 0.4795 | 0.35 |
| Lx20_Ly6_AQ | 0.60 | 0.4107 | 0.4106 | 0.32 |
| Lx30_Ly8_AQ | 0.86 | 0.6151 | 0.6150 | 0.38 |
| Lx30_Ly6_AQ | 0.80 | 0.56 | 0.56 | 0.39 |

Table 5.4.2 First four vibration periods for Naples case studies.

| Case Naples | T1 (Tx) (s) | T2 (s) | T3 (s) | T4 (Ty) (s) |
|---|---|---|---|---|
| Lx20_Ly8_NA | 0.65 | 0.4646 | 0.4644 | 0.34 |
| Lx20_Ly6_NA | 0.67 | 0.4443 | 0.4442 | 0.30 |
| Lx30_Ly8_NA | 0.84 | 0.594 | 0.594 | 0.37 |
| Lx30_Ly6_NA | 0.79 | 0.54 | 0.54 | 0.37 |

Table 5.4.3 First four vibration periods for Milan case studies.

| Case Milan | T1 (Tx) (s) | T2 (s) | T3 (s) | T4 (Ty) (s) |
|---|---|---|---|---|
| Lx20_Ly8_MI | 0.67 | 0.48 | 0.48 | 0.35 |
| Lx20_Ly6_MI | 0.68 | 0.4595 | 0.4594 | 0.32 |
| Lx30_Ly8_MI | 0.86 | 0.62 | 0.62 | 0.38 |
| Lx30_Ly6_MI | 0.80 | 0.56 | 0.56 | 0.39 |
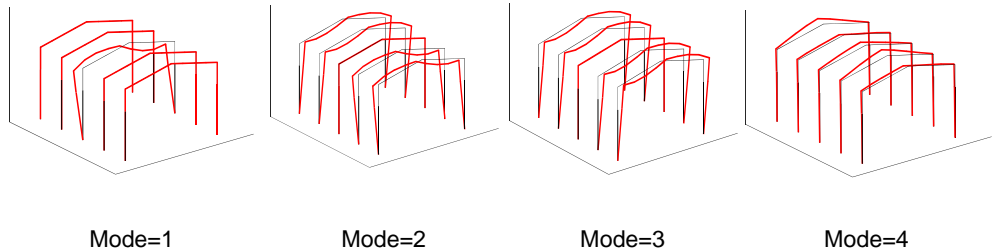


Mode=1            Mode=2            Mode=3            Mode=4
Figure 5.4.12 First four modal shapes for all of the case studies.

### 5.4.7    Roof and wall cladding modelling

This section focuses on the modelling issues concerning the non-structural elements, such as roof and wall claddings. To the aim of assessing the contribution provided by such elements, both at the serviceability limit state (SLD) as well as at failure conditions. The panel typology assumed in this work, corresponding to type A in the work of De Matteis and Landolfo (2000), consists of sandwich panels made of external embossed steel sheets (with slight stiffening ribs), with a thickness of 0.6 mm, and insulating polyurethane core. Each panel has the dimension of 1000 mm x 2500mm x 40 mm, and the number of panels employed in each structural case study varies based on the specific geometric configuration. A schematic representation of cladding

arrangement is given in Figure 5.4.13 for case SSB_Lx20_Ly8, in which the opening locations on the cladding walls are also depicted. It is noted that the cladding panels in the longitudinal direction (Y) do not cover the entire façade of the building, as they extend up to the crane support level, leaving the whole upper field free for ribbon windows.
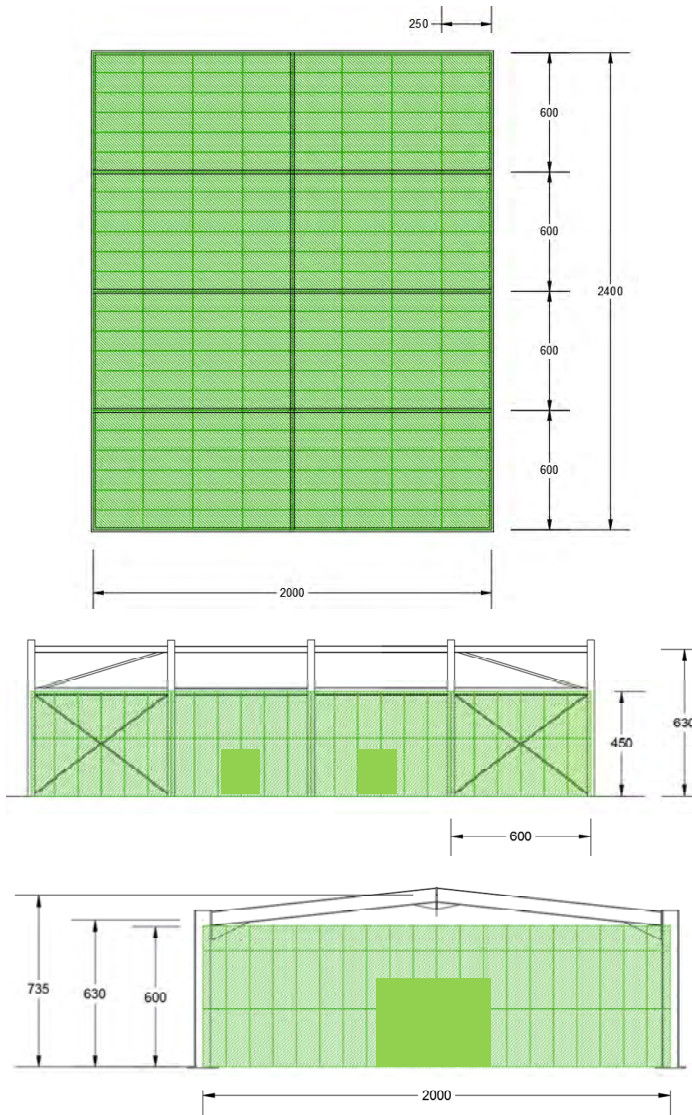


Figure 5.4.13 Arrangement of wall and roof claddings.

For what concerns the panels modelling in OpenSees, couples of nonlinear truss elements were adopted to reproduce the contribution of groups of assembled panels belonging to different structural fields, as shown in Figure 5.4.14 (truss elements are depicted for the facade view only, but are inserted in the shadow sides as well).
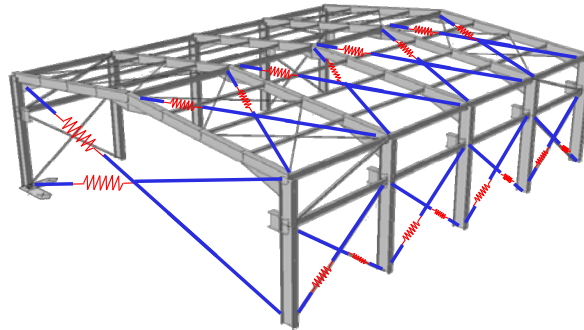
Figure 5.4.14 Equivalent truss elements within the structural model.

For each truss element, the *Pinching4* uniaxial material available in the OpenSees library was adopted to simulate the nonlinear cyclic behavior of the panel assembly, and the experimental results provided in De Matteis and Landolfo (1999) (2000) were used to calibrate the parameters required. Specifically, the backbone curve of the uniaxial material was calibrated in order to fit the experimental envelope curve (Figure 5.4.15) described by the cyclic response of a single panel (1000 mm x 2500 mm x40 mm). The resulting backbone (Figure 5.4.16) exhibits a trilinear curve characterized by a yielding point at 12 kN (d=20 mm), a hardening behavior until the maximum shear 17 kN (d=80 mm), and a gradual softening branch with the force dropping to zero at d=320 mm. It is important to clarify that the latter part of the curve (softening) was extrapolated from the experimental results trying to realistically describe the complex degrading behavior (panels buckling, connections failure, etc.), although the available test results do not characterize the response beyond the 80 mm displacement threshold (Figure 5.4.15b).



(a)                                                              (b)
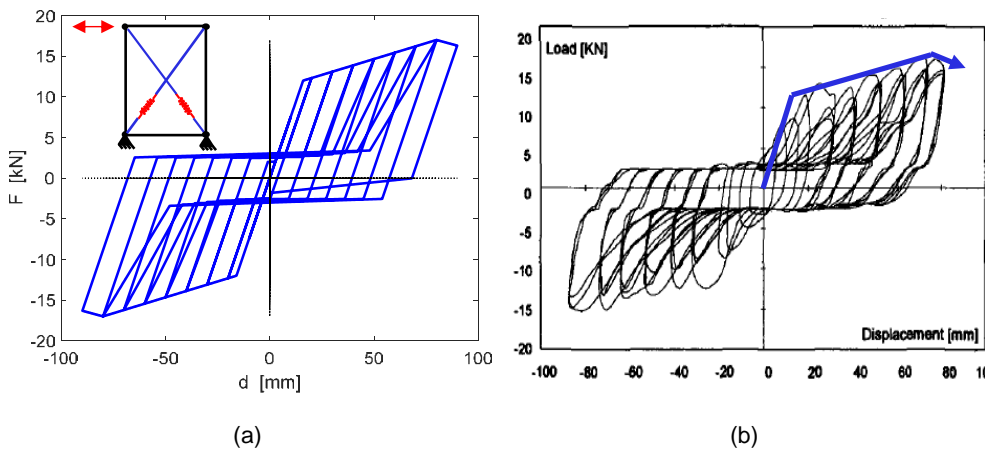
Figure 5.4.15 Simulated (a) and experimental cyclic response (b) of one-panel system (1000 mm x 2500 mm x 40 mm) under shear dynamic loads.
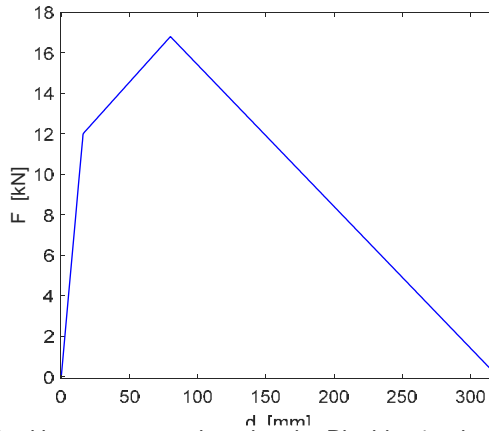
Figure 5.4.16 Backbone curve assigned to the Pinching4 uniaxial material.

According to the modelling strategy described, each couple of truss elements is equivalent, in terms of cyclic response, to a single panel. In order to account for the real number of panels present within the different structural fields (see Figure 5.4.13 for what concerns the SSB_Lx20_Ly8 geometric configuration), the following hypotheses were made:

- the presence of several adjacent panels was accounted by increasing the strength and the stiffness of each pair of truss elements by a factor equal to the number of single panels (i.e., the actual number of panels, which can also be a fractional number); it is worth to note that the aforementioned modelling strategy is consistent with the assumption of panels working in parallel;

- conversely, the presence of multiple rows of panels along the height was accounted by following the analogy of a system working in series, according to which the displacements of Ns rows of panels are Ns times larger than those of a single row, while the stiffness of the whole system is reduced by a factor equal to 1/Ns.

The effect of the connections between adjacent panels was not explicitly accounted for in this modelling approach. The presence of concentrated openings was accounted by a reduction factor equal to 0.5 to both the stiffness and the strength of the truss elements.

### 5.4.8    Alternative approaches for plasticity modelling

A distributed plasticity approach (force-based nonlinear elements with fiber sections) was used for the purposes of the present study, in order to explicitly account for the interaction between axial forces and (in-plane and out-of-plane) bending moments of the elements. This feature is particularly useful along the system's longitudinal direction (Y) for simulating properly the buckling phenomenon and hence describing the cyclic behavior of the concentric vertical braces in a realistic manner. A concentrated plasticity modelling was instead adopted to account for the out-of-plane deformability of the gusset plate connections at the ends of the brace elements, as thoroughly described in the relevant section.

For what concerns the moment-resisting portal frames (in the X direction), unlike the case of concentric braces in which the distributed plasticity approach was strongly advisable, several alternative strategies were possible. However, because of the non-negligible axial forces experienced even by the beams of the portals (because of the interaction with both the roof braces and the roof panels, which work as strut-and-tie systems), the distributed plasticity approach was adopted for the whole structural system, at the expense of a higher computational effort.

No cyclic deterioration models were adopted for structural elements until this stage of the work. However, degradation was indirectly considered when selecting ultimate values of the portal frame horizontal drift (FEMA 350). The beam-column connections were assumed as rigid and this is consistent with the capacity design criteria followed, according to which proper over-strength factors were used with respect to the beam elements.

For the sake of completeness, the alternative strategies, which haven't been investigated though, are presented and discussed by highlighting the main advantages and drawbacks.

5.4.8.1  Concentrated plastic hinge (CPH) model

According to this approach, the moment-resisting frame is modelled with elastic beam-column elements connected by rotational springs (zeroLength elements in OpenSees) accounting for the system's nonlinear behavior. The main advantage of such method, beside the reduced computational burden, is the possibility to directly assign moment-rotation relationships to the zero-length springs. On the other hand, the main drawbacks are as follows.

- Axial force–bending moment interaction neglected.
- The need to overcome the additional flexibility of the element by introducing a specific parameter (Ibarra and Krawinkler 2005) (in order to increase the elastic stiffness of the springs, change the post-yielding ratios and modify the stiffness of the interior element) whose value is not trivial to determine and which could affect the numerical stability.
- Larger numbers of nodes, elements and constraints required.

5.4.8.2  Finite-length plastic hinge (FLPH) model

According to this formulation, plastic hinge regions are assigned to the ends of the elements (the plasticity is distributed over a defined length), where either nonlinear moment-curvature relationships or explicit fiber-section integrations can be adopted to characterize the cross sections. The axial and flexural responses of each plastic hinge region are defined as separate sections.

The main advantages of such approach are listed below (Ribeiro et al. 2014).

- Avoid localization issues (possible with distributed plasticity approach), in particular by exploiting the Modified Gauss-Radau integration scheme proposed by Scott and Fenves (2006).
- Lower modelling effort compared to the CPH formulation.
- Lower computational effort.

The main disadvantages are:

- plastic hinge lengths need to be assigned, whose sizes notably affect the analysis results;
- it is not possible to directly use the empirically calibrated moment-rotation relationships, but a preliminary conversion into moment-curvature laws is required.

5.4.8.3  Cyclic deterioration models

The use of moment-rotations models that account for strength and stiffness deterioration of structural members can be very important in evaluating the actual structural response, particularly around the collapse conditions. The Modified Ibarra-Medina-Krawinkler model proposed by Lignos and Krawinkler (2010) is a general moment-rotation model based on a backbone curve representing the response under monotonic loads, which accounts for six different deterioration mechanisms. The deterioration model parameters can be determined through the predictive equations developed by Lignos and Krawinkler (2009, 2011) with multi-variate regression analysis of a steel component database of more than 300 steel specimens.

As said before, the empirically calibrated moment-rotation models can be directly assigned to the zero-length springs when a CPH formulation is adopted, or they can be used in a FLPH approach after converting all the moment-rotation relationships into moment curvature laws.

Bosco and Tirca (2017) recently proposed a fiber-based hinge damage accumulation model that is able to simulate the cyclic response deterioration of wide-flange beams in steel moment-resisting frames. The study also provides empirical equations to determine the deterioration model parameters. Such relationships were calibrated for wide-flange beams typically used in North America. Therefore, applicability to the European shapes and influence of the axial forces in the rafters of the portal frames should be investigated prior to implementing this model.


## 5.5   Analysis results and discussion

### 5.5.1   Elastic model calibration

A preliminary calibration was carried out in order to validate the model developed in OpenSees (loads, masses, releases, modal properties, etc.) compared to the elastic one built within Midas Gen and used for design purposes. To this aim, a linear elastic OpenSees model with elastic BeamColumn elements was adopted, with only half bracing elements modelled (as in the Midas model). The comparison was carried out in terms of:

- eigenvectors and eigenvalues,
- base reactions, stresses and deformation under vertical static loads combination.

The case study with Lx = 20 m, Ly = 6 m located in L'Aquila is considered. In Figure 5.5.1, a comparison between the first four vibration modes (shapes and periods) for both the OpenSees (left pictures, with a graphical post-processing performed within MATLAB) and Midas models are shown.

The comparison in terms of vertical base reactions under the seismic combination of gravity loads is shown in Table 5.5.1, while Table 5.5.2 and Table 5.5.3 show some node displacements and some element internal forces, respectively (see Figure 5.5.2 for the nodes and elements numbering).

The results arising from the comparison highlight a good match between the models. Some slight differences are due to the self-weight of the longitudinal beams and vertical braces assigned as lumped nodal force in OpenSees instead of distributed ones such as in Midas. Despite this, such small differences are negligible when the seismic input is taken into account.

T = 0.60 s



T = 0.60 s



T = 0.48 s



T = 0.49 s



T = 0.409 s



T = 0.413 s



T = 0.408 s



T = 0.412 s
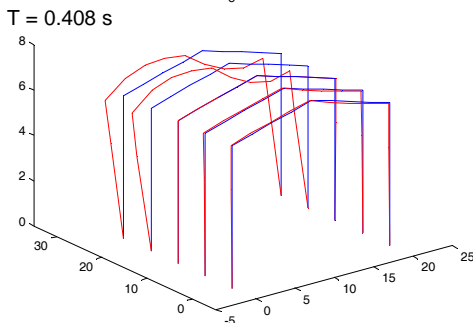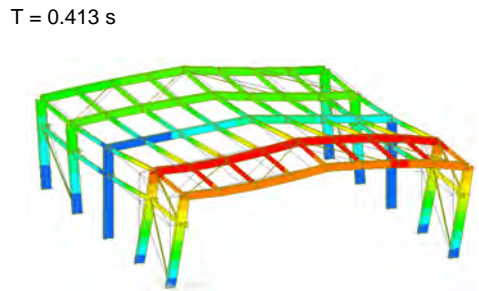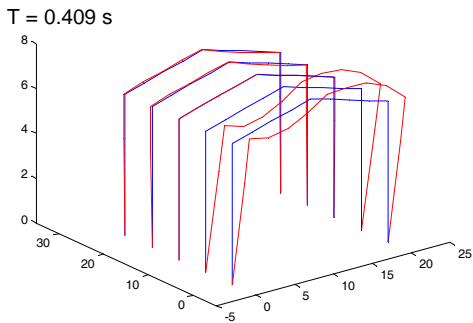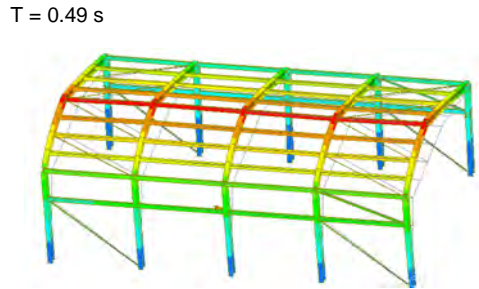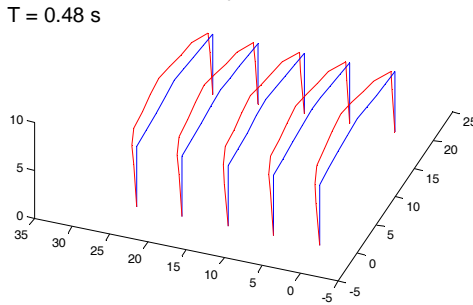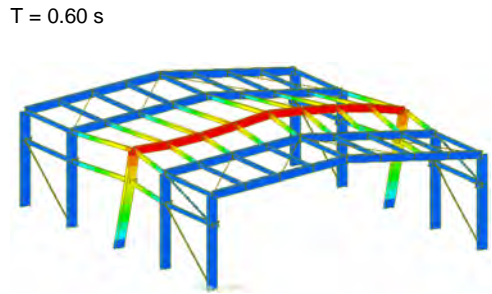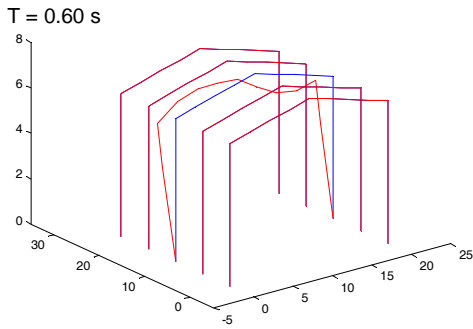


a - OpenSees                                                     b - Midas Gen

Figure 5.5.1 Comparison between OpenSees results and Midas Gen results.

Table 5.5.1 Comparison between OpenSees and Midas Gen results in term of vertical reactions.

| Portal frames | Vertical Reactions (kN) | |
|---|---|---|
| | OpenSees | Midas Gen |
| 1 and 5 (left) | 57.01 | 57.02 |
| 1 and 5 (right) | 57.01 | 57.02 |
| 2 and 4 (left) | 67.53 | 67.48 |
| 2 and 4 (right) | 67.53 | 67.48 |
| 3 (left) | 196 | 195.13 |
| 3 (right) | 118 | 119.13 |

Table 5.5.2 Comparison between OpenSees and Midas Gen results in term of displacements.

| Node | Dir. | Displacements (m) | |
|---|---|---|---|
| | | OpenSees | Midas Gen |
| 7 | X | $6.67 \cdot 10^{-8}$ | $8.8 \cdot 10^{-8}$ |
| | Y | $8.7 \cdot 10^{-5}$ | $6.8 \cdot 10^{-5}$ |
| | Z | -0.0060 | -0.0064 |
| 37 | X | 0.0010 | 0.0036 |
| | Y | $3.0 \cdot 10^{-5}$ | $3.0 \cdot 10^{-5}$ |
| | Z | $-7.3 \cdot 10^{-5}$ | $-7.4 \cdot 10^{-5}$ |
| 55 | X | $-7.5 \cdot 10^{-4}$ | $-6.4 \cdot 10^{-4}$ |
| | Y | $3.2 \cdot 10^{-5}$ | $3.2 \cdot 10^{-5}$ |
| | Z | $-3.5 \cdot 10^{-5}$ | $-3.5 \cdot 10^{-5}$ |

Table 5.5.3 Comparison between OpenSees and Midas Gen results in term of internal forces.

| Element | Internal forces | OpenSees | | Midas Gen | |
|---|---|---|---|---|---|
| - | (kN or kNm) | end 1 | end 2 | end 1 | end 2 |
| 24 | N | -11.65 | -11.25 | -11.63 | -11.22 |
| | $V_y$ | 3.60 | 0.00 | 3.20 | 0.00 |
| | $M_{z,i}$ | 33.50 | 38.00 | 34.70 | 39.00 |
| 110 | N | 0.017 | 0.017 | 0.09 | 0.06 |
| | $V_y$ | - | - | - | - |
| | $M_{z,i}$ | - | - | - | - |
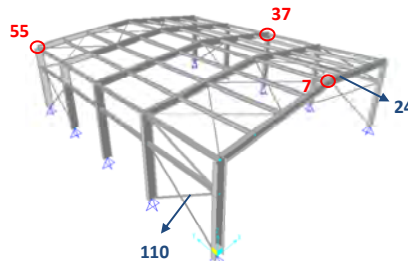


Figure 5.5.2 Nodes and Elements numbering.

### 5.5.2    Pushover analysis

5.5.2.1  Case without panels

A preliminary investigation of the nonlinear lateral behavior of the structure was carried out by means of nonlinear static analysis (pushover) for the case in which the cladding and roof panels were not explicitly modelled but their contribution was only accounted in terms of mass and weight. A set of forces with unit values was applied to the structural nodes at the top of the columns head in both X and Y directions separately; the analysis was performed with displacement control in order to catch any softening effects due to both the geometrical and mechanical nonlinearities. Figure 5.5.3 shows the X and Y control nodes monitored during the analysis.
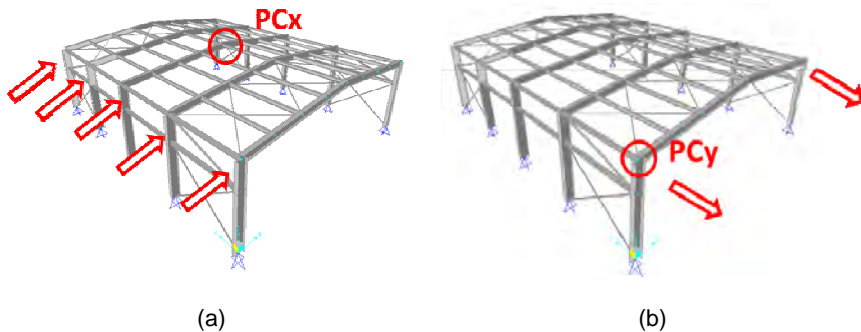


(a)                                                                 (b)
Figure 5.5.3 Control nodes for the pushover analysis in the X (a) and Y direction (b).

Pushover analysis was carried out after a preliminary analysis for gravity loads and the lateral loads analysis from the last step of this previous analysis. Gravity loads analysis was performed with a load-control integrator using the Newton algorithm (tangent stiffness updates at each iteration) in such a way that the gravity was applied with 10 steps of 0.1g. The lateral loads analysis was carried out using a displacement-control integrator and the Secant Newton Line Search algorithm was adopted. The step amplitude was equal to 0.001 m while the target maximum displacement was generally assumed large enough for describing the post-elastic behavior.

The capacity curves are shown in Figure 5.5.4, only for the case study SSB_Lx20_Ly8. However, the following discussion of results applies to the other case studies as well.
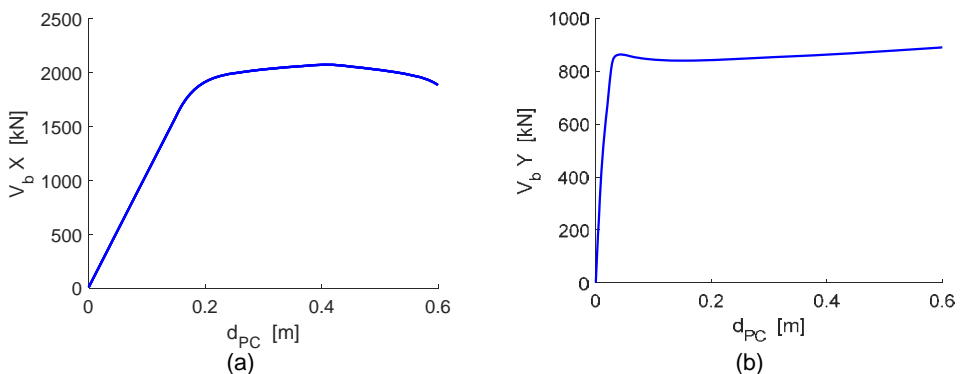


(a)                                                                 (b)
Figure 5.5.4 Pushover curve in X (a) and Y direction (b).

The structure shows different responses in X and Y directions. As illustrated by the pushover curves in Figure 5.5.4, the ductility along the transversal direction (portal frames direction, X) is around 2.2 while the ductility along the longitudinal direction (braced direction, Y) is almost three times that value; on the other hand, the maximum base-shear reached in X direction is almost four times higher than the maximum base-shear observed in Y direction. The maximum displacement reached at the control point is 0.5 m in X and no softening is observed in that direction. Quite different is the longitudinal response in which both the second order effects and the compressed brace buckling lead to a post-elastic behavior characterized by an initial branch with a negative stiffness (softening) followed by a gradual stiffness recover due to the steel strain-hardening, whose contribution is large enough to compensate and even overtake the second order effects.

Figure 5.5.5 reports the lateral deformation of the system at an intermediate step of the analysis in order to show qualitatively the buckling phenomenon experienced by the compressed braces. Figure 5.5.6 contains the plots of the axial force versus the axial displacement monitored during the analysis on the braces highlighted by numbers in Figure 5.5.5. It is observable how both the strength and stiffness of the compressed braces drop down once the axial force reached the maximum allowable value $N_{b,Rd}$ consistent with the element features (i.e., gusset geometry, section and slenderness of the element). This behavior explains the loss of stiffness shown by the Y capacity curve following the peak resistance. On the other hand, the post-elastic stiffness, originating from strain hardening in the tensioned braces, leads to new gradual and slow rise in stiffness in the following part of the Y capacity curve.



(a)                                                                                         (b)
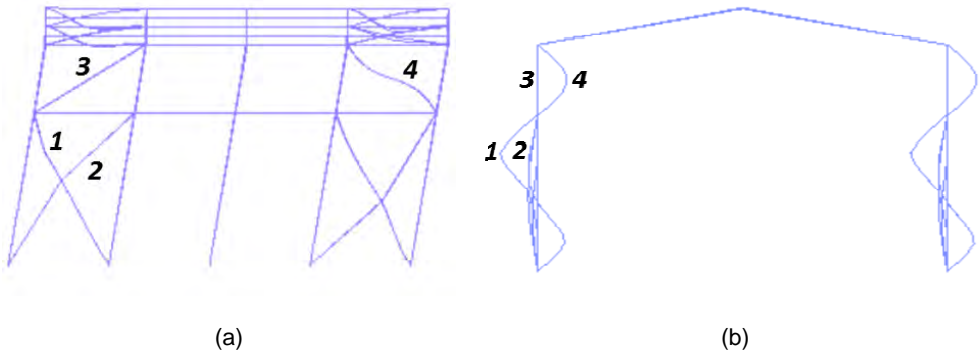
Figure 5.5.5 Y-lateral deformation during PO analysis and braces numbering (a) and frontal view during PO analysis and braces numbering (b).

Regarding the lateral response along the X direction, the nonlinear behavior was mainly governed by the mechanical nonlinearities (i.e., yielding and hardening of the elements composing the moment resisting frames). The most pronounced second order effect was observable on the central portal frame, which, around the last steps of the analysis, showed larger displacements than the other portal frames despite the entity of the lateral loads was the same as for the others. This phenomenon finds an explanation into the lacking of a roof-bracing system around that portal, and the longitudinal (pinned) beams do not contribute to retain the portal.

In Figure 5.5.7, the transversal deformation is shown by both front and top views. Instead, Figure 5.5.8a shows the stress-strain, $\sigma-\varepsilon$, diagrams recorded at three different section fibers for the beam element 1 (Figure 5.5.7); in particular, fibers at the top and bottom flanges, as well as at the centroid of the cross section, were considered. Figure 5.5.8b reports an example of the in-plane Moment-Rotation, $M-\theta$, curve for the same element (beam 1).

Based on the results obtained from this study on the lateral response, it is possible to state that the model developed in OpenSees is able to account for all the sources of nonlinear behavior of

the structure, from the mechanical nonlinearity to the geometrical one (i.e., elements buckling and global post-elastic stiffness reduction).



Compression of the X-cut-brace (1)

Tension of the X-continuos-brace (2)

Tension of the single-brace (3)

Compression of the single-brace (4)
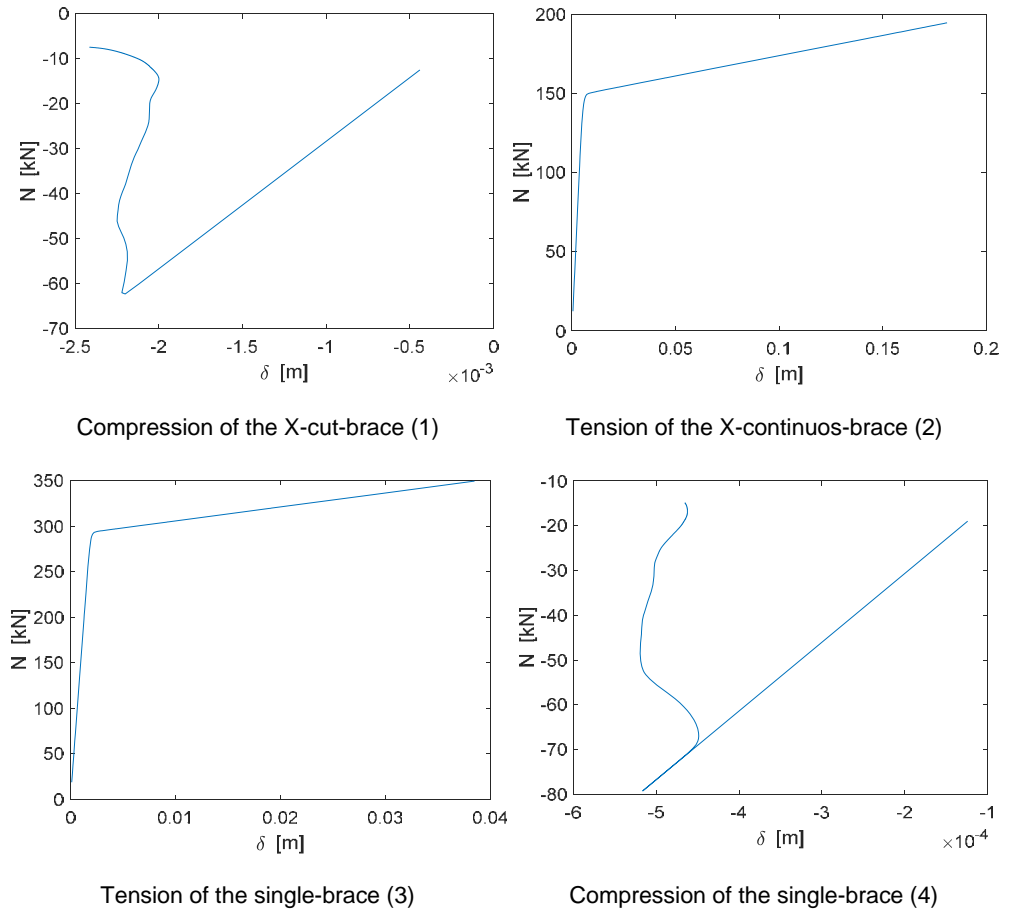
Figure 5.5.6 Axial force versus axial displacement for braces numbered in Figure 5.5.5.



(a)

(a)
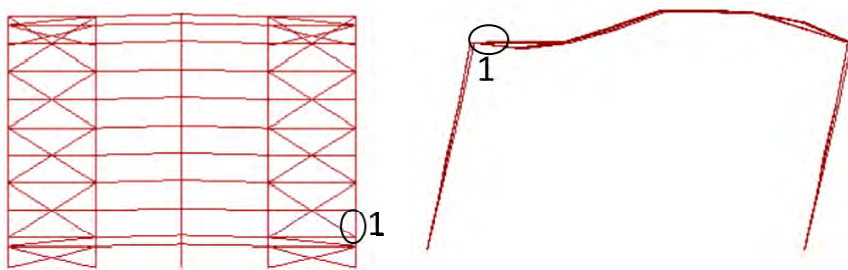
Figure 5.5.7 X-lateral deformation from a top view (a) and a front view (b) during PO analysis.
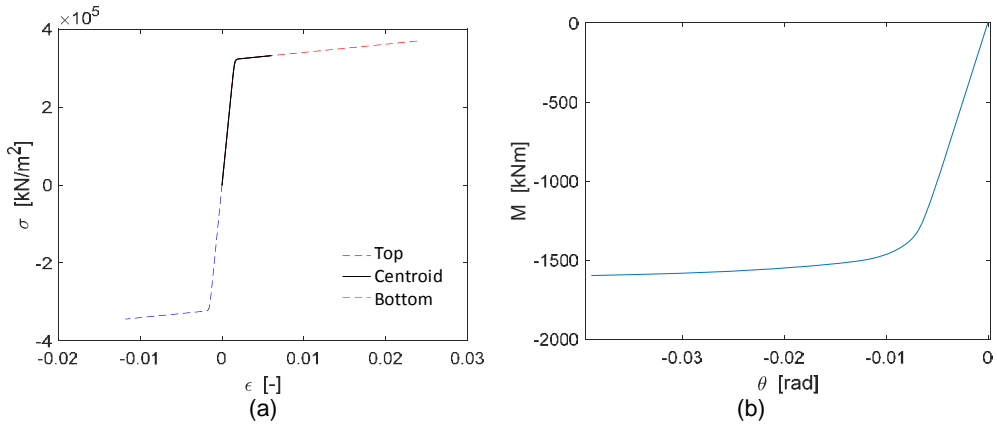
Figure 5.5.8 σ−ε curves for the top, bottom and barycentre fibers of the 1-beam section (a)
and M−θ relationship for the beam 1(b).

## 5.5.2.2  Case with panels

In this section the influence of the cladding and roof panels on the lateral response is evaluated. As shown in Figure 5.5.9, the two nodes controlled during the push over analyses both belong to one of the two perimeter portal frames. However, the nodes were chosen at different heights for the two orthogonal directions: the top of the column in X direction, and the crane level in Y direction.

The capacity curves (case SSB_Lx20_Ly8) are shown in Figure 5.5.10 in both directions. Each chart reports a comparison between the bare system (black curve) and the system with panels (red dashed curve). The contribution provided by the panels consists of a slight elastic stiffness increment and a rise of the maximum shear capacity in both the X and Y directions. However, the rise in resistance is particularly significant in the longitudinal direction (Y), mainly because of the higher number of panels contributing to withstand the lateral loads.
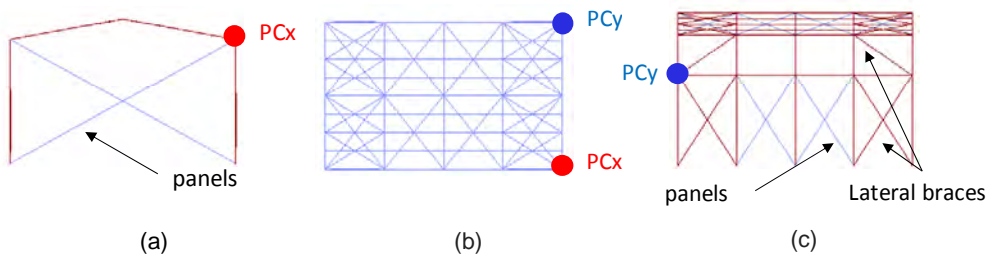


Figure 5.5.9 Locations of the X and Y pushover control nodes: front (portal frame) view (a);
view from the top (b); lateral (concentrically-braced frame) view (c).

(a)                                                    (b)
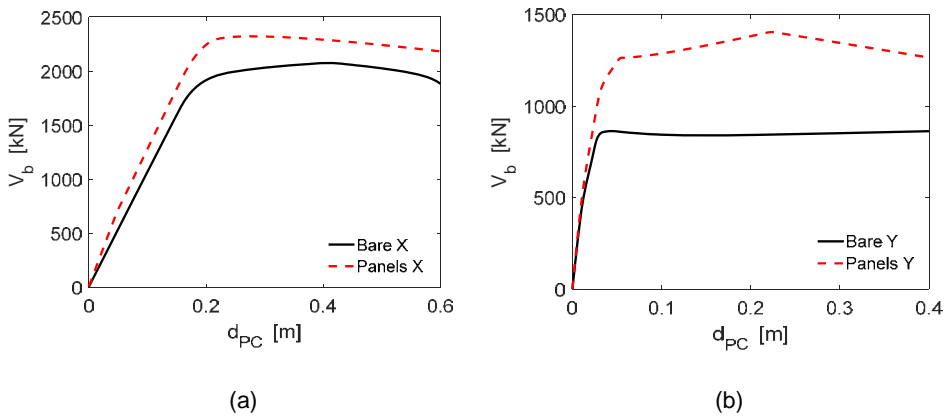
Figure 5.5.10 Capacity curves with and without (bare system) panels contribution: response dir. X (a) and response dir. Y (b).

Moreover, it is worth noting that, despite the symmetrical location of the panels in both the plan directions, only the panels in the X direction modify the resistance mechanism. Indeed, they change the load paths, activating the structural elements in a different way with respect to the case without panels. This is shown in Figure 5.5.11, which reports the internal stresses for the beams of the perimeter portal frames.

The aforementioned phenomenon is not observed in the response along the Y direction, as shown in Figure 5.5.12 which reports axial forces in the vertical braces.

Such behavioral difference between the two directions can be explained as the combined effect of the following two causes:

- as already discussed in the previous section (5.5.2.1), the resistance mechanism in X direction is quite complex and sensitive to the second order effects because of the higher lateral deformability of the central portal frame (not restrained by the roof braces), and the presence of the cladding panels only at the perimeter portals further amplify the aforesaid imbalance;
- the roof panels behave like a roof bracing system involving also the middle portal frames.



(a)                                    (b)                                    (c)
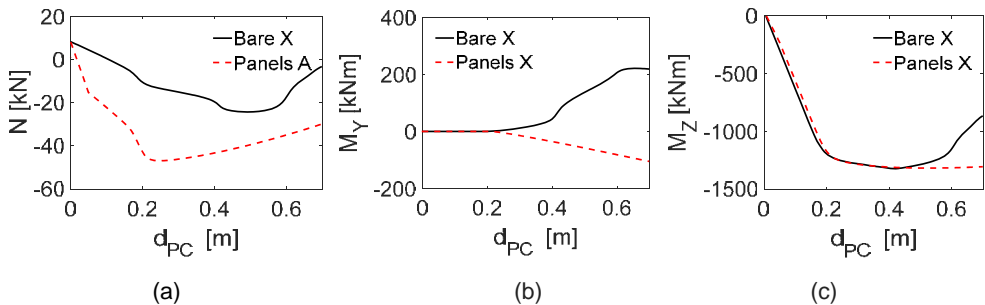
Figure 5.5.11 Eaves beam (perimeter portal frame) internal stresses evolution during pushover X analyses: axial force (a); out-of-plane bending moment (b); in-plane bending moment (c).

(a)                                                              (b)
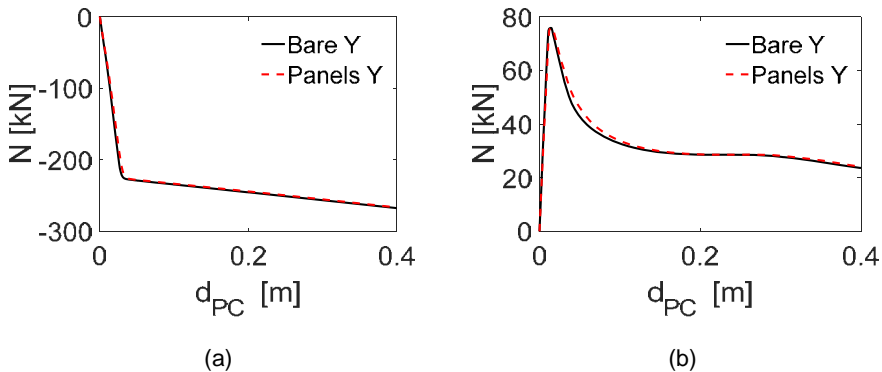
Figure 5.5.12 Concentric vertical braces (longitudinal direction) axial force evolution during pushover Y analyses: tension brace (a); compression brace (b).

### 5.5.3    Multiple Stripe Analysis

This section describes the nonlinear dynamic analysis of the structures to a set of ground motions (GMs). The technique called Multiple Stripe Analysis (MSA) was adopted, following the procedure in Chapter 1. The analysis was carried out using 10 values of the ground motion Intensity Measure, IM, which was assumed to be represented by the spectral pseudo-acceleration at the fundamental period of the system. For each IM value, 20 pairs of GMs with two components (X and Y) were assumed to act at the ground level. The description of seismic hazard at the building sites was provided in Chapter 1: the GMs were selected as to be consistent with the site-hazard and scaled to desired levels of IM with respect to the conditioning periods, 0.5 s and 1.0 s, which were considered to be sufficiently close to the fundamental vibration periods of the buildings with the main portal frame spans equal to 20 m and 30 m respectively. The convergence solver consisted of a standard Newmark integration with a Secant Newton Line Search algorithm controlling the iterations for the convergence of the solution. Analysis time-steps were chosen adaptively by the OpenSees solver within a range between 0.0005 s and the time-step used for sampling the seismic records. The response parameters monitored and saved during the analysis are listed below:

- Inter-story drifts monitored at both the bridge-crane and eaves levels of each portal frame;
- Displacements at the ridge nodes of each portal frame;
- Internal forces (axial, shear and bending moments) for the main beam and column elements;
- Deformations (axial deformation, rotation and curvatures) for the main beam and column elements;
- Stress-strain responses at the fiber level of some column/beam elements;
- Axial forces and deformations for the vertical braces;
- Out-of-plane moment-rotation responses of the gusset plates.

It is worth pointing out that the maximum section strain was obtained by adding the contribution from the section curvature to the mean (centroid) axial strain.

Some of the most interesting findings from the MSA analysis are discussed hereafter. The objective here is to give a summarized description of the structural response under earthquakes with different intensities. One of the following sections will provide more information, as well as a statistic/probabilistic interpretation of the results.

Hereafter, the results for the following case studies are shown: L'Aquila, Soil C, Lx = 30 m and Ly = 8 m. Figure 5.5.13 provides information about variation of the peak story drifts recorded with the IM parameter. The plotted drifts refer to the same nodes as described for the pushover analysis, i.e., at the level of the crane runway beam and at the top of columns. With reference to the column top, Figure 5.5.13a shows the results for the X (portal frame) response, while Figure 5.5.13b provides the results for the Y (concentrically braced frame) response. Similarly, Figure 5.5.14 shows peak horizontal displacement demand at the column node corresponding to the crane level. Comparing Figure 5.5.13 to Figure 5.5.14, it can be seen that the drift demand has similar values at the levels of the crane and top of the column, hence no local mechanisms are activated.



(a)                                                              (b)
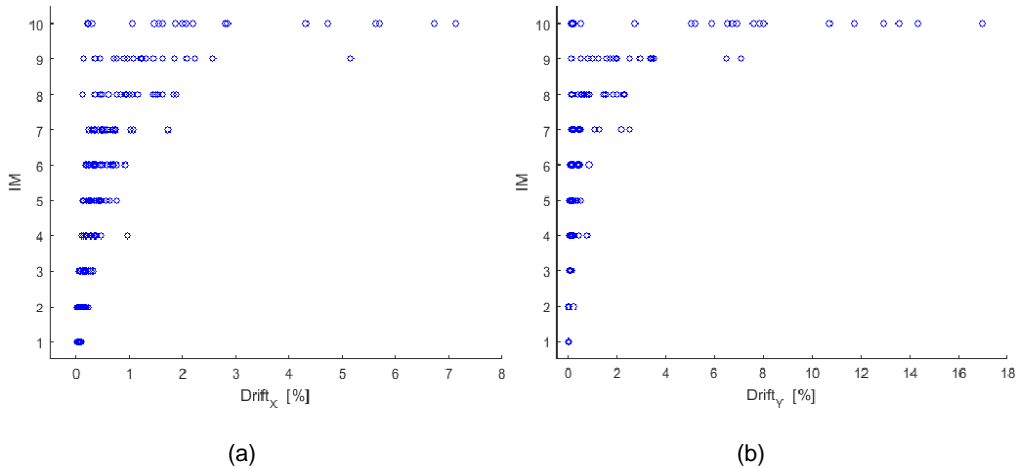
Figure 5.5.13 Drift X (a) and Drift Y (b) for Node 3 - L'Aquila Lx 30 Ly 8 soil C case study.



(a)                                                              (b)
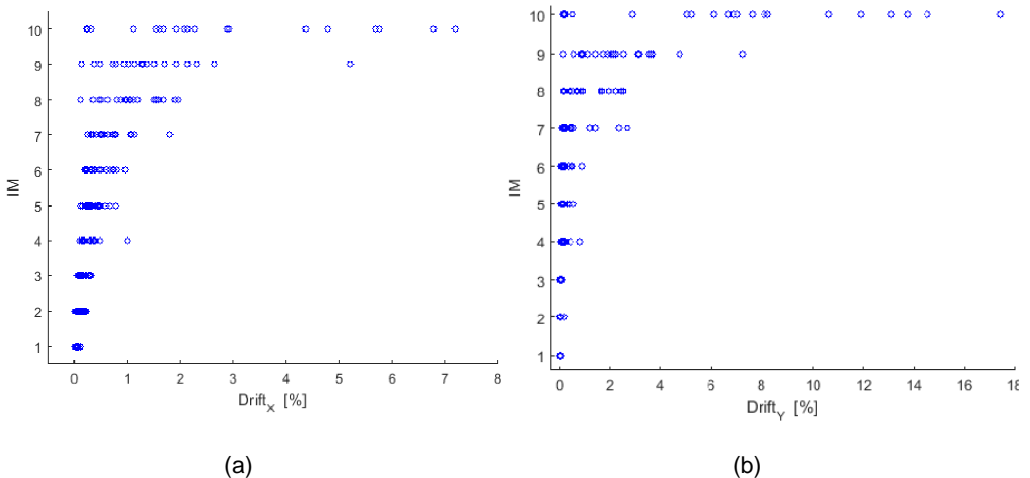
Figure 5.5.14 Drift X (a) and Drift Y (b) for Node 2 - L'Aquila Lx 30 Ly 8 soil C case study.

The structure responses subjected to two selected pairs of GMs (Figure 5.5.15), one pair conditional to IM = 4 and the other conditional to IM = 8, are described hereafter. This comparison allows to recognize the difference in responses at different values of IM. The following engineering demand parameters, EDPs, are adopted for this comparison: displacements (node 7 for Y direction and node 37 for X direction, as shown in Figure 5.5.2), portal beam moment-rotation response, axial force-displacement response of vertical braces, and moment-rotation responses of the brace gusset plates. Figure 5.5.16 shows the displacement time-histories for both the X-Y directions and for both GMs time-histories (with a

red line the response in Y and with a blue line the response in X). It is worth to note that, seismic events at IM = 8 lead to permanent deformations of the bracing system, as shown by the baseline trend in Figure 5.5.16d, which is almost 0.02 m lower than the reference zero value (i.e., the original configuration). It has to be pointed out how  rare seismic events with intensity levels above IM = 8 or higher are.
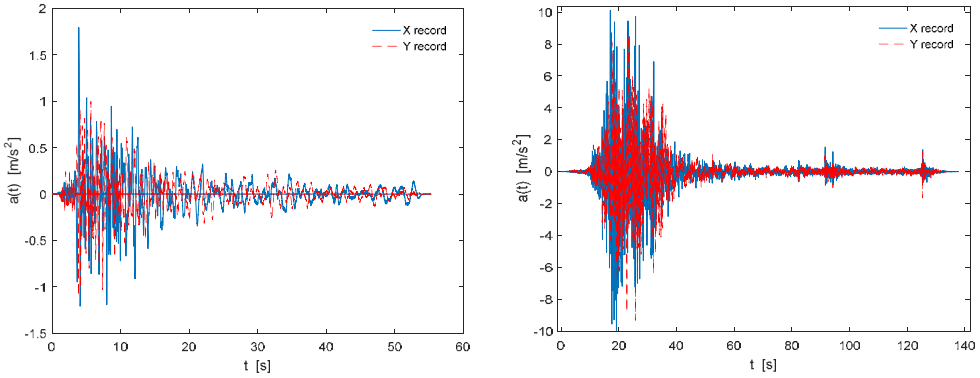


IM = 4  Acc 8                                IM = 8  Acc 17
Figure 5.5.15 Seismic records in X and Y directions.
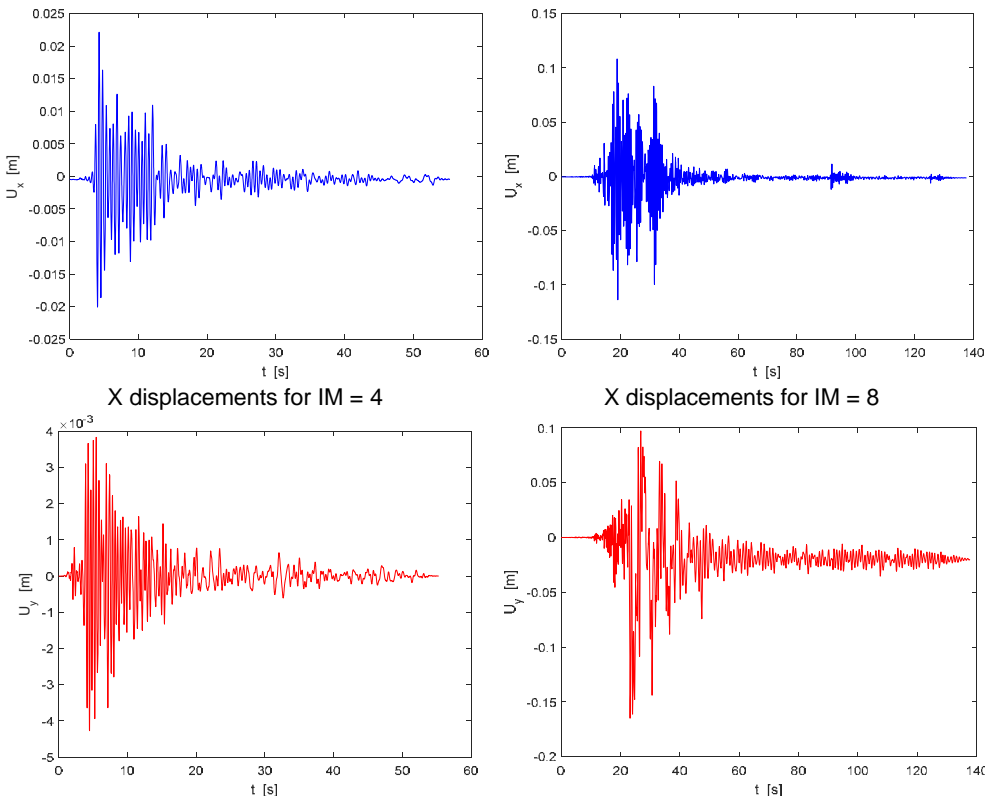


(c) Y displacements for IM = 4              (d) Y displacements for IM = 8
Figure 5.5.16 Displacement time-histories for X and Y directions.

Concerning the vertical brace responses, the IM = 4 ground motion does not produce any remarkable nonlinear effects (slight yielding and buckling) and hence no plots are reported here. Instead, Figure 5.5.17, 18 show the brace response to the selected GM with IM = 8. Figure 5.5.17 reports the axial force-displacement (N $-\delta$) cyclic responses for the cut brace 1 (see Figure 5.5.2 for element identification) composing the X-bracing system: the left plot for the left side of the structure and the right plot for the right side. Figure 5.5.18 shows N $-\delta$ cyclic responses for the single brace 3 and the continuous brace 2 from the X-bracing system. The non-symmetric cyclic response in tension and compression and the buckling phenomenon are clearly observed. Also, the accumulation of plastic deformations in all of the vertical braces can be noticeably observed, and this is consistent with the Uy time-history shown in Figure 5.5.16.

The out-of-plane moment-rotation, M$-\theta$, cyclic responses of the gusset plates located at the two ends of the single brace 3 are illustrated in Figure 5.5.19. The fact that the springs simulating this physical phenomenon are activated (i.e., they undergo plastic deformations) testify the usefulness of the adopted modelling strategy, in order to properly account for both buckling and second order effects.
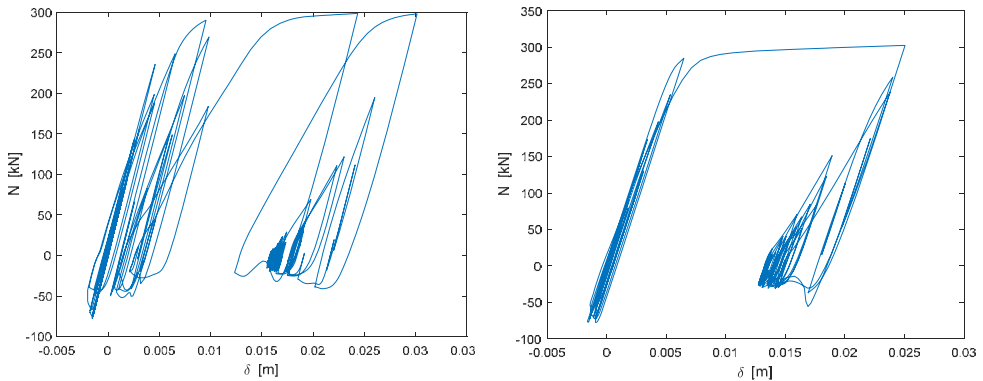


N$-\delta$ cut X-brace 1 – left side of the structure     N$-\delta$ cut X-brace 1 – right side of the structure
Figure 5.5.17 N - $\delta$ cyclic responses of braces.
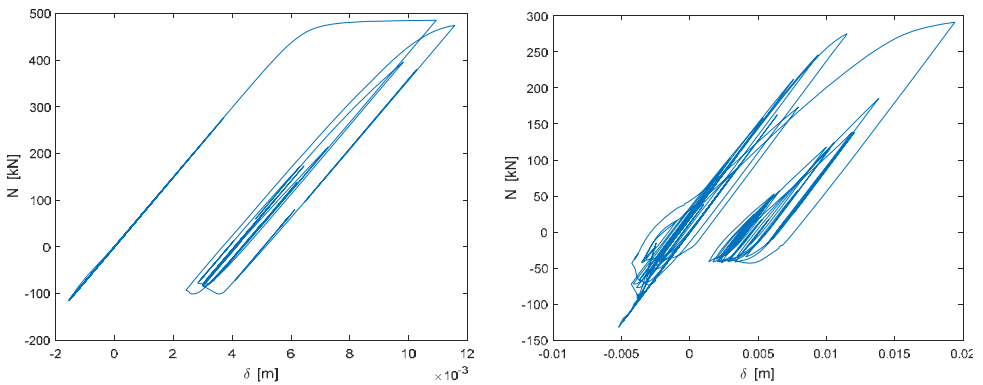


N$-\delta$ single brace 3 – left side of the structure     N$-\delta$ contin. X-brace 2 – left side of the structure
Figure 5.5.18 N - $\delta$ cyclic responses of braces.
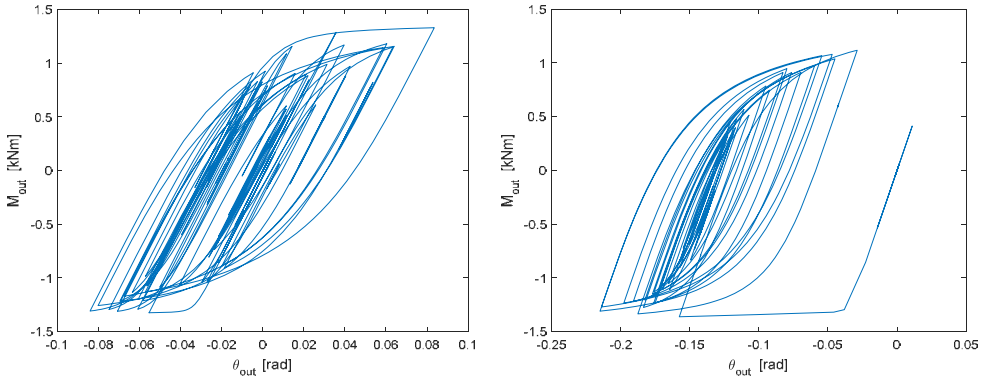
top end of single brace                              bottom end of single brace

Figure 5.5.19 Out-of-plane cyclic M$-\theta$ responses of the gusset plates at the two ends of the single brace 3.

### 5.5.4   Collapse criteria

The adopted collapse criteria were based on the post-processing of the response results. Specifically, different criteria were used for the two directions, i.e., transversal moment-resisting frames and longitudinal concentrically braced frames. For the moment-resisting mechanism, the collapse criterion was based on a limit value of the inter-story drift ratio (IDR). Following FEMA-350, the limiting value was assumed equal to 0.10 (Table 5.5.4). For comparative purposes, a second and more stringent local criterion was considered, again according to FEMA-350 (Table 5.5.5). Such a criterion considers the following behavioral characteristics: 1) onset of local flange buckling, 2) degradation of moment capacity, 3) initiation of fracture resulting in significant strength degradation, 4) complete failure of the connection (inability to sustain gravity loads). However, this second criterion was not subsequently considered in failure rate calculations, which were instead based on the IDR limit value.

Table 5.5.4 Global interstory drift angle capacity and resistance factor for regular SMF and OMF buildings according to FEMA-350.

| Building Height | Performance Level | | | |
|---|---|---|---|---|
| | Immediate Occupancy | | Collapse Prevention | |
| | Interstory Drift Angle Capacity C | Resistance Factor $\phi$ | Interstory Drift Angle Capacity C | Resistance Factor $\phi$ |
| Special Moment Frames (SMF) | | | | |
| Low Rise (3 stories or less) | 0.02 | 1.0 | 0.10 | 0.90 |
| Mid Rise ( 4 – 12 stories) | 0.02 | 1.0 | 0.10 | 0.85 |
| High Rise (> 12 stories) | 0.02 | 1.0 | 0.085 | 0.75 |
| Ordinary Moment Frames (OMF) | | | | |
| Low Rise (3 stories or less) | 0.01 | 1.0 | 0.10 | 0.85 |
| Mid Rise ( 4 – 12 stories) | 0.01 | 0.9 | 0.08 | 0.70 |
| High Rise (> 12 stories) | 0.01 | 0.85 | 0.06 | 0.60 |

Table 5.5.5 Drift angle capacity for prequalified connections as limited by local connection response according to FEMA-350.

| Connection Type | Strength Degradation Limit Drift Angle (radians) | Immediate Occupancy | | Collapse Prevention | |
|---|---|---|---|---|---|
| | $\theta_{SD}$ | Limit Drift Angle (radians) | Capacity Reduction Factor | Limit Drift Angle (radians) | Capacity Reduction Factor |
| | | $\theta_{IO}$ | $\phi$ | $\theta_C$ | $\phi$ |
| WUF-B | 0.031-0.0003$d_b$ | 0.015 | 0.9 | 0.060-0.006$d_b$ | 0.9 |
| WUF-W | 0.051 | 0.020 | 0.9 | 0.064 | 0.9 |
| FF | 0.061-0.00064$d_b$ | 0.020 | 0.9 | 0.080-0.00064$d_b$ | 0.9 |
| RBS | 0.060-0.0003 $d_b$ | 0.020 | 0.9 | 0.080-0.0003 $d_b$ | 0.9 |
| WFP | 0.04 | 0.020 | 0.9 | 0.07 | 0.9 |
| BUEP | 0.071-0.0013 $d_b$ | .015 | 0.9 | 0.081-0.0013 $d_b$ | 0.9 |
| BSEP | 0.071-0.0013 $d_b$ | .015 | 0.9 | 0.081-0.0013 $d_b$ | 0.9 |
| BFP | 0.12-0.002 $d_b$ | .015 | 0.9 | 0.10-0.001 $d_b$ | 0.9 |
| DST | 0.12-0.0032 $d_b$ | .015 | 0.9 | 0.14-0.0032 $d_b$ | 0.9 |

Regarding the collapse criterion for the concentrically braced frames, the limit was assigned to the maximum strain range in the braces, according to the indications by Hsiao et al. (2013) and Tirca et al. (2015), having assumed a limit value of 0.049 = 4.9% reported in Table 1 of Hsiao et al. (2013) and referenced to the experimental tests by Tremblay et al. (2003).
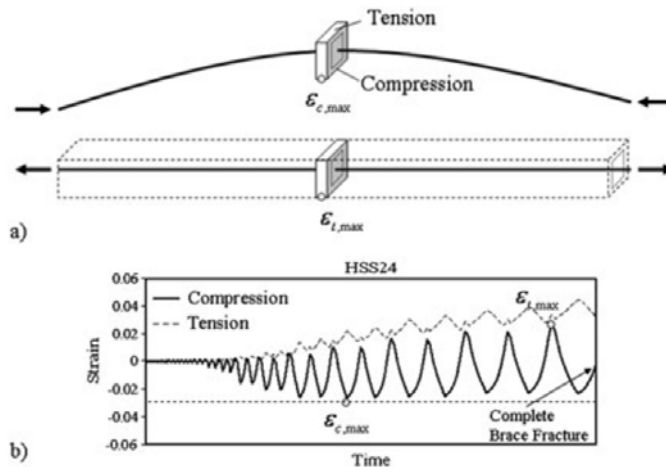


Figure 5.5.20 Collapse criterion for concentric braces.

## 5.5.5   Serviceability limit state

A multi-criteria approach was followed for identifying the attainment of the serviceability limit state (SLD). The approach was developed by consensus agreement within the RINTC research project. The approach was articulated as follows:

- Pushover analyses were performed separately in X and Y directions by using the model including explicitly the non-structural (cladding and roofing) panels.
- Identification of the displacements $d_{PO,X}$ and $d_{PO,Y}$ (for X and Y directions separately) corresponding to the attainment of the first among the following conditions:

      o   Light damage state reached by 50% of the panels. The panel light damage state was defined as the attainment of the panel elastic resistance (point A of the panel backbone curve as shown in Figure 5.5.21);

      o   Severe damage state reached by at least 1 panel. The severe damage state was defined as the attainment of the maximum shear strength (point B of the panel backbone curve as shown in Figure 5.5.21);

      o   Attainment of 95% of maximum base-shear force resistance of the complete structure. This third criterion was introduced to consider cases where the structure could be damaged while the panels do reach none of the above two damage states.

- Nonlinear time-history analyses were performed, and for each ground motion peak values of the displacements $d_{TH,X}$ and $d_{TH,Y}$ of the nodes considered in the PO analyses were obtained.
- The DLS was reached if $d_{TH,X} \geq d_{PO,X}$ or $d_{TH,Y} \geq d_{PO,Y}$.

In Figure 5.5.22, the resulting performance points corresponding to the three conditions discussed above are superimposed to the capacity curves (for the case SSB_Lx20_Ly8). It can be observed that, for both the directions, the DLS activation is governed by the light-damage criteria (i.e., 50% of the panels beyond the elastic field), and hence the corresponding displacements of the control nodes are assumed as reference values for predicting the DLS condition via nonlinear dynamic structural analyses.
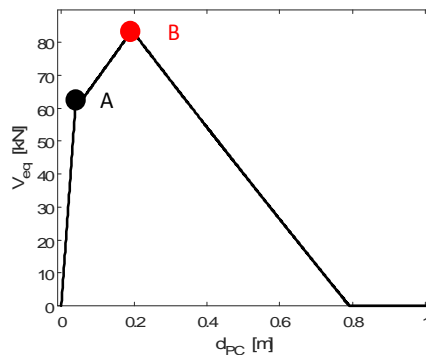


Figure 5.5.21 Panels backbone curve with the identification of the low damage condition (A) and strong damage condition (B).
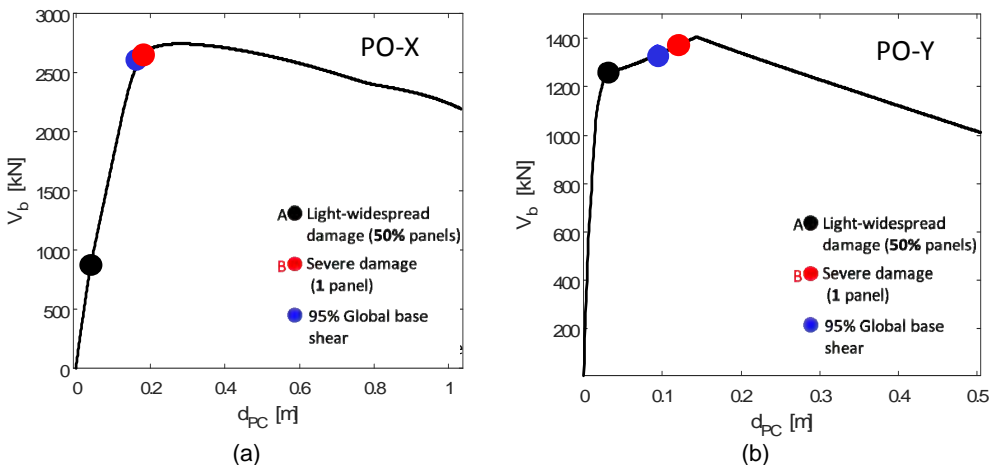


Figure 5.5.22 Capacity curves in a) X and b) Y directions. The performance points corresponding to the multicriteria for the DLS evaluation are superimposed.

Table 5.5.6 summarizes the limit values for the DLS activation obtained from the PO analyses by following the procedure described above.

Table 5.5.6. Drift values at DLS activation from pushover analysis.

|  | SSB_Lx20_Ly6 | SSB_Lx20_Ly8 | SSB_Lx30_Ly6 | SSB_Lx30_Ly8 |
|---|---|---|---|---|
| $d_{PO,X}$ (m) | 0.0406 | 0.0400 | 0.0602 | 0.0594 |
| $d_{PO,Y}$ (m) | 0.0283 | 0.0280 | 0.0469 | 0.0473 |

The results concerning the time-history analysis are presented in Section 5.5.7.3. It should be observed that because the sandwich panels of the horizontal roofs never exceed the point A, the DLS assessment was carried out by excluding such elements from the computation: the percentages of non-structural elements attaining the aforesaid damage conditions were evaluated with respect to the total number of vertical panels only, by distinguishing between the panels along the X and Y directions.

### 5.5.6    Model uncertainties

In order to consider the model uncertainties, the following parameters were assumed as random variables: the yielding strength of the steel elements, the amplitudes of the local imperfections of the vertical braces. Specifically, the following assumptions were made for the variability of the steel yield strength:

- lognormal distribution with median $\mu_{fy}$ = 1.15*$f_{y,nom}$ = 316.2 MPa (previous analysis were carried out by assuming this value as deterministic) and a coefficient of variation (COV) equal to $\text{COV(fy)}$ = 0.09, the latter according to the values suggested in Da Silva et al. (2009);
- coefficient of correlation equal to $\rho_{fy}$ = 0.65 within the cold-formed elements (vertical braces), according to Idota et al. (2009);
- coefficient of correlation equal to $\rho_{fy}$ = 0.65 within the hot-rolled elements, according to Idota et al. (2009);
- no correlation between cold-formed and hot-rolled elements.

Regarding the variability of the brace local imperfections, a bonded uniform distribution was assumed having the following properties:

- upper bound of the distribution set equal to the imperfection which produces a maximum axial force equal to the $N_{b,Rd}$ value provided by the design code (NTC 2008) (but with unit values of the partial safety factors and assuming the nominal value of the steel yield strength);
- lower bound of the distribution set equal to the imperfection which produces a maximum axial force consistent with the Eulerian buckling force;
- no correlation among braces.

The extreme values of the uniform distribution ($\delta_{low}$ and $\delta_{up}$) for the local imperfections are summarized in Table 5.5.7 to Table 5.5.10 for the different case studies.

Table 5.5.7 Uniform distribution extreme values for SSB_Lx20_Ly6.

| Braces | $\delta_{low}(N_{Cr})$ | $\delta_{up}(N_{b,Rd})$ |
|---|---|---|
| Single | 1/1500 | 1/240 |
| Cross-continuous | 1/1200 | 1/290 |
| Cross-cut | 1/1500 | 1/190 |

Table 5.5.8 Uniform distribution extreme values for SSB_Lx20_Ly8.

| Braces | $\delta_{low}(N_{Cr})$ | $\delta_{up}(N_{b,Rd})$ |
|---|---|---|
| Single | 1/2300 | 1/240 |
| Cross-continuous | 1/5000 | 1/270 |
| Cross-cut | 1/5000 | 1/180 |

Table 5.5.9 Uniform distribution extreme values for SSB_Lx30_Ly8.

| Braces | $\delta_{low}(N_{Cr})$ | $\delta_{up}(N_{b,Rd})$ |
|---|---|---|
| Single | 1/8000 | 1/230 |
| Cross-continuous | 1/1000 | 1/190 |
| Cross-cut | 1/2000 | 1/180 |

Table 5.5.10 Uniform distribution extreme values for SSB_Lx30_Ly6.

| Braces | $\delta_{low}(N_{Cr})$ | $\delta_{up}(N_{b,Rd})$ |
|---|---|---|
| Single | 1/20000 | 1/275 |
| Cross-continuous | 1/1000 | 1/200 |
| Cross-cut | 1/2000 | 1/200 |

The propagation of the above considered model uncertainties to the structural seismic response was achieved by following the approach proposed by Franchin et al (2017), in which a one-to-one association of sets of structural parameter realizations and ground motions is made, rather than analyzing all the possible combinations of ground motions and structure-related random samples (e.g., Dolsek 2011). Such approach notably reduces the computational effort, by preserving the total number of nonlinear dynamic (time-history) analyses carried out in case of a deterministic structural model.

A direct sampling approach was used for generating a set of random model parameters: two independent multi-variate lognormal samplings were performed on the yielding strength values of the two element categories (cold-formed and hot-rolled); an independent single uniform sampling was performed on the local imperfections.

### 5.5.7   Summary of results and discussion

5.5.7.1  Results for the deterministic model without non-structural elements

A selection of the results obtained though the adoption of the above collapse criteria provided the results summarized in the following figures. Each plot in the figures shows, in form of histograms, the 20 EDP values corresponding to the (20) ground motion records selected for each IM value. The assumed EDP limits are also superimposed with red solid lines in the figures. It is worth to recall that the monitored EDPs are as follows: maximum inter-storey drift ($IDR_{max}$) in the direction X, and maximum brace strain range ($\Delta\varepsilon_{max}$) in the direction Y. It is observed that:

- The EDP-IM trends are different for the moment-resisting frame (direction X) and the concentric brace mechanism (direction Y). The story drift shows more gradual increases with the IM than the brace strain, as expected given the effect of the braces' buckling.
- Collapse is attained only at the L'Aquila site for IM values larger than those assumed in the limit states considered in the design.
- Safety margin against collapse decreases with the increase of the site hazard, i.e., in the following order of the sites: Milan, Naples, and L'Aquila.
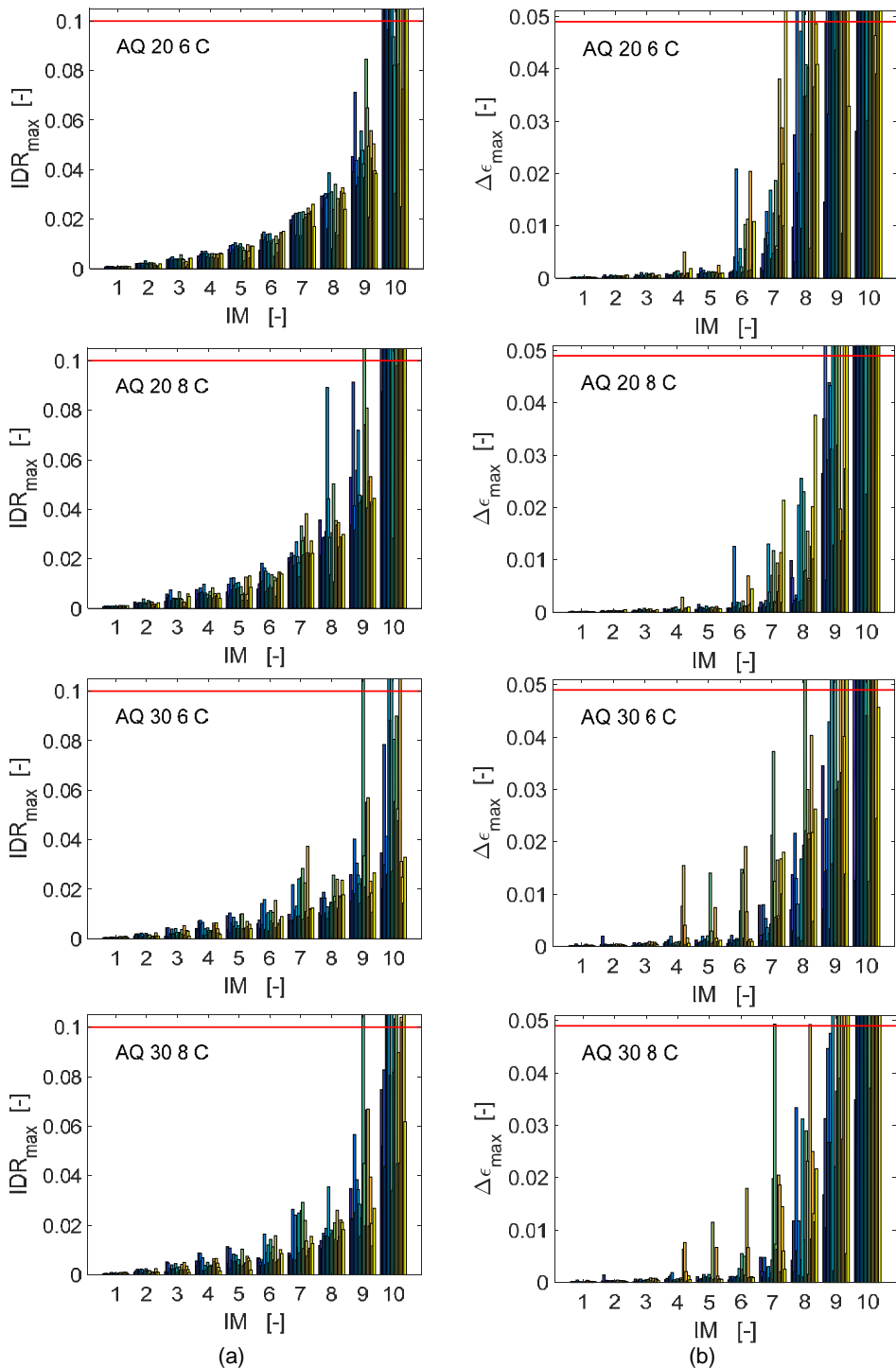
Figure 5.5.23 MSA results for the deterministic model without non-structural elements. Comparison with the limits from the collapse criteria. Case L'Aquila soil C: (a) maximum interstory drift ($IDR_{max}$) along X, and (b) maximum brace strain range ($\Delta\epsilon_{max}$) along Y.
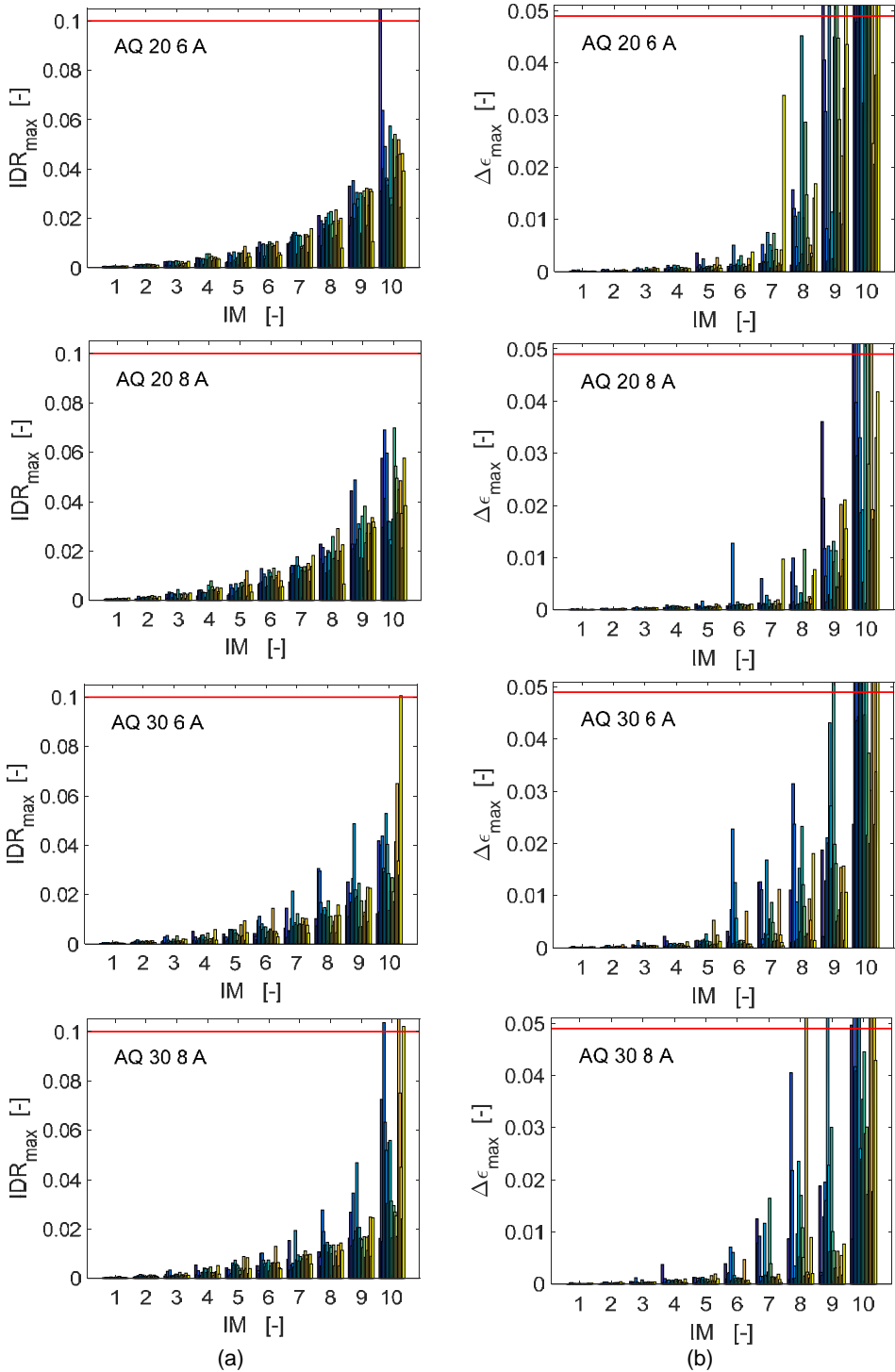
Figure 5.5.24 MSA results for the deterministic model without non-structural elements. Comparison with the limits from the collapse criteria. Case L'Aquila soil A: (a) maximum interstory drift (IDR$_{max}$) along X, and (b) maximum brace strain range ($\Delta\varepsilon_{max}$) along Y.

(a)                                                                    (b)
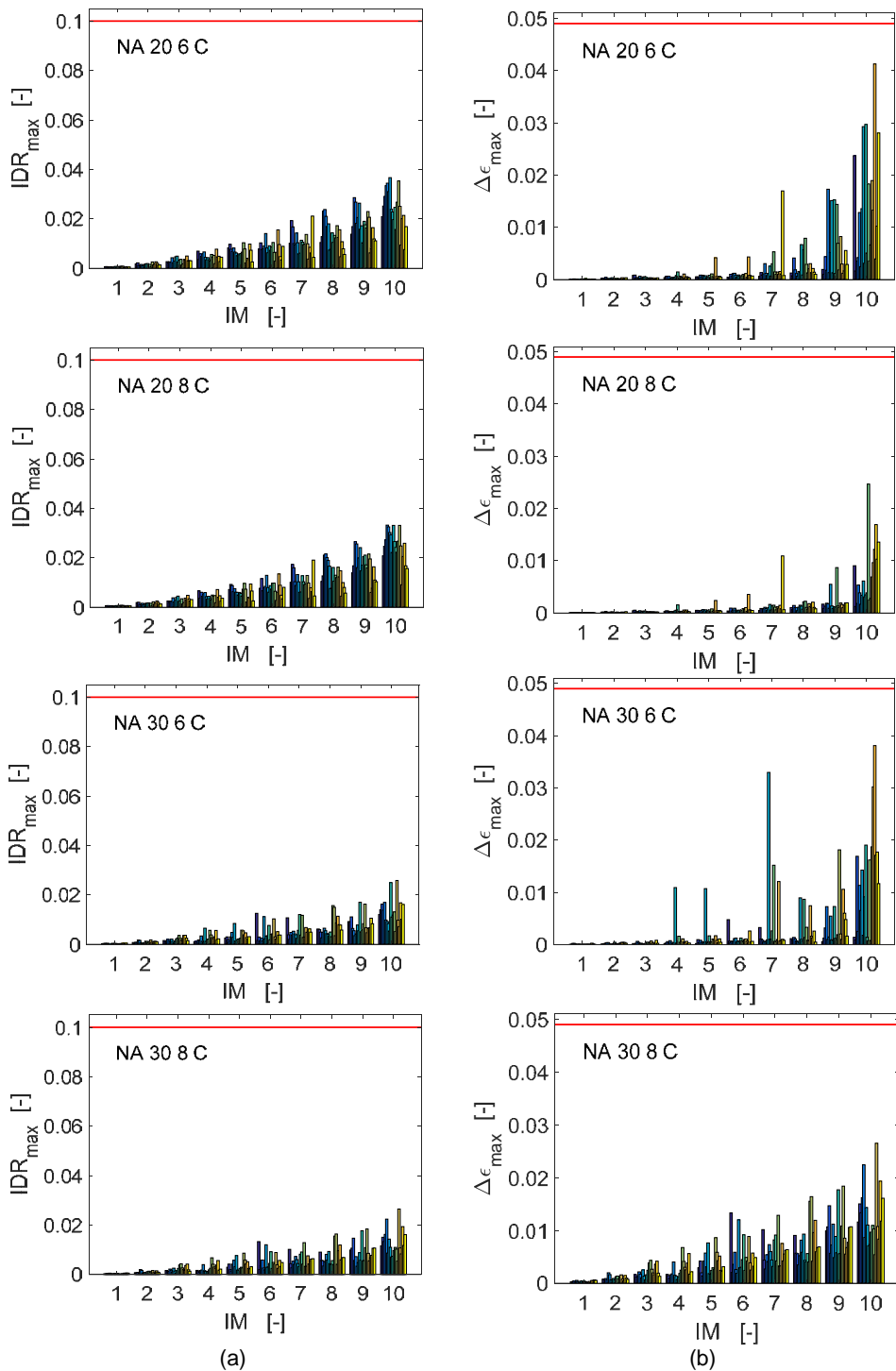
Figure 5.5.25 MSA results for the deterministic model without non-structural elements. Comparison with the limits from the collapse criteria. Case Naples soil C: (a) maximum interstory drift ($IDR_{max}$) along X, and (b) maximum brace strain range ($\Delta\epsilon_{max}$) along Y.

(a)                                                              (b)
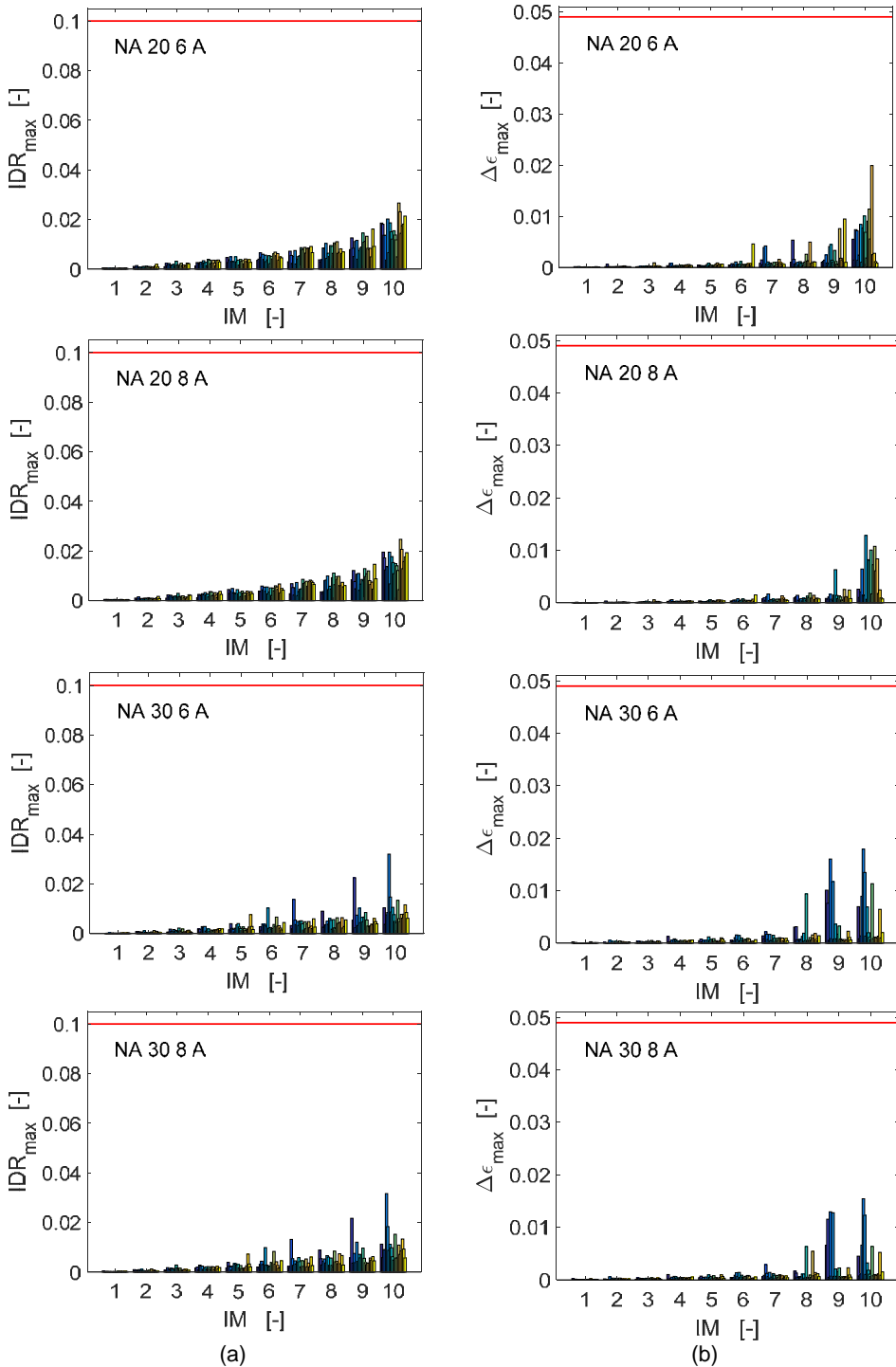
Figure 5.5.26 MSA results for the deterministic model without non-structural elements. Comparison with the limits from the collapse criteria. Case Naples soil A: (a) maximum interstory drift (IDR$_{max}$) along X, and (b) maximum brace strain range ($\Delta\epsilon_{max}$) along Y.
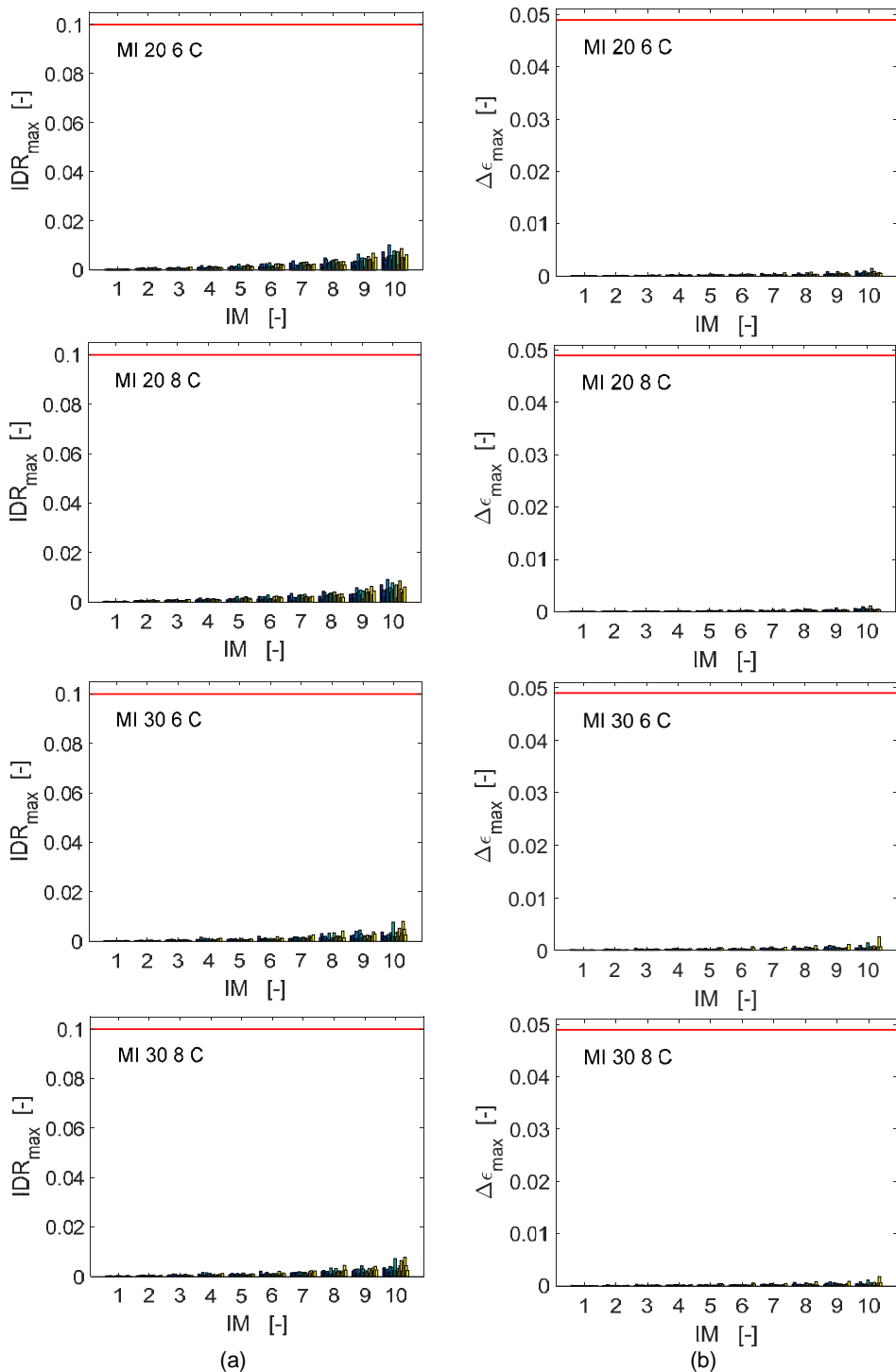
Figure 5.5.27 MSA results for the deterministic model without non-structural elements. Comparison with the limits from the collapse criteria. Case Milan soil C: (a) maximum interstory drift (IDR$_{max}$) along X, and (b) maximum brace strain range ($\Delta\epsilon_{max}$) along Y.

(a)                                                              (b)
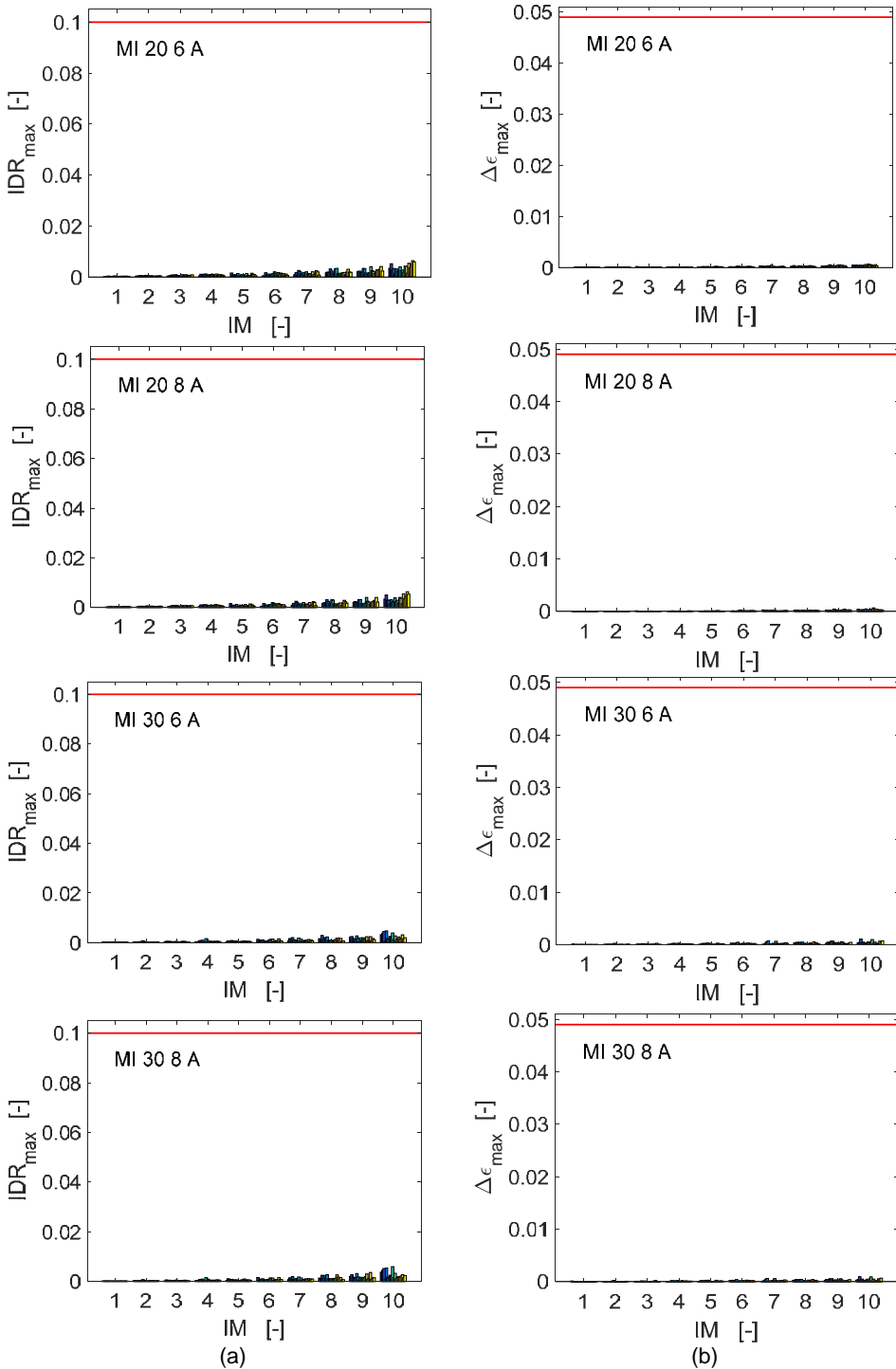
Figure 5.5.28 MSA results for the deterministic model without non-structural elements. Comparison with the limits from the collapse criteria. Case Milan soil A: (a) maximum interstory drift (IDR$_{max}$) along X, and (b) maximum brace strain range ($\Delta\epsilon_{max}$) along Y.

5.5.7.2  Influence of the seismic vertical component

Given the span lengths of the considered case studies, attention should be paid to the possible effect of the vertical component of the seismic accelerations. To this end, the dynamic analyses with the bare structure models were run for the second time by adding the relevant vertical accelerograms (only available for ten out of twenty stripes). It was observed that the vertical component of the seismic acceleration produces non-negligible effects on the structures (Figure 5.5.31, Figure.5.5.32). However, the vertical seismic accelerations have a very small influence on the horizontal displacements (Figure 5.5.29); thus, the near collapse limit state for the moment-resisting mechanism and the damage limit state are basically not affected. Similarly, the vertical seismic accelerations have very small influence on the deformation of the braces (Figure 5.5.30). Thus, it was concluded that the vertical components of the accelerograms could be neglected for the purpose of the evaluation of the considered limit states.
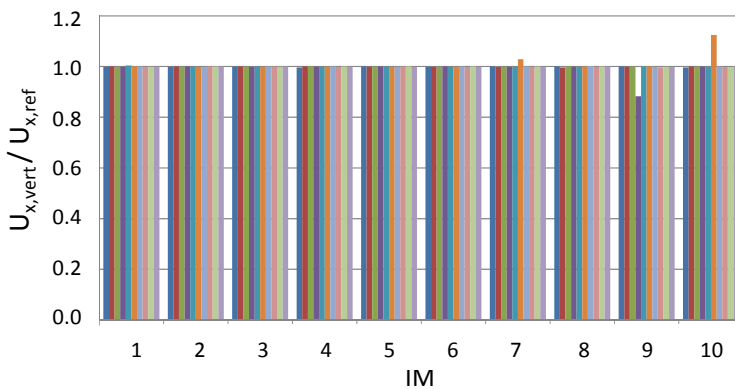


Figure 5.5.29 Influence of the seismic vertical component on the transverse top displacements.
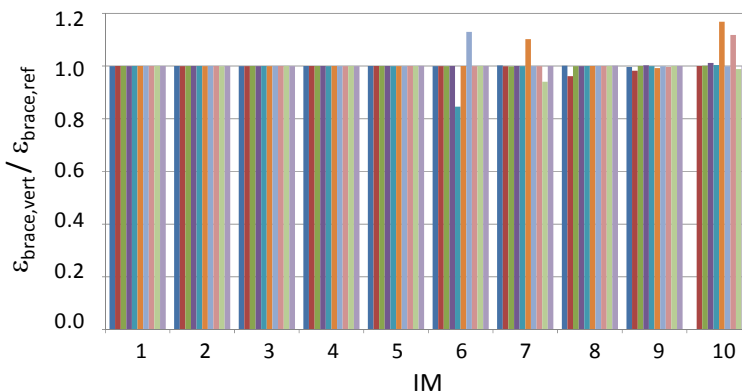


Figure 5.5.30 Influence of the seismic vertical component on the total strain of vertical braces.
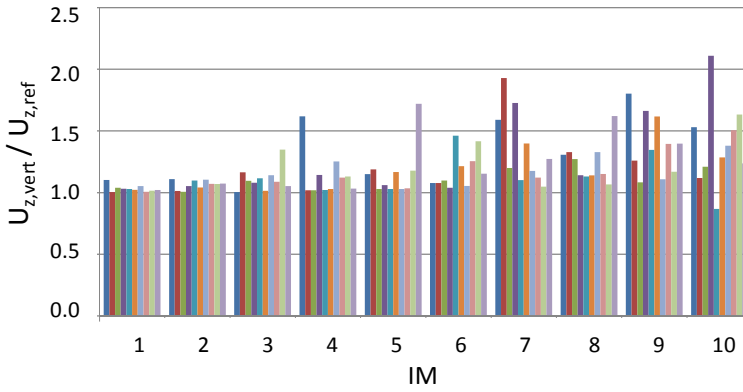
Figure 5.5.31 Influence of the seismic vertical component on the vertical displacement at the portal frame ridge.
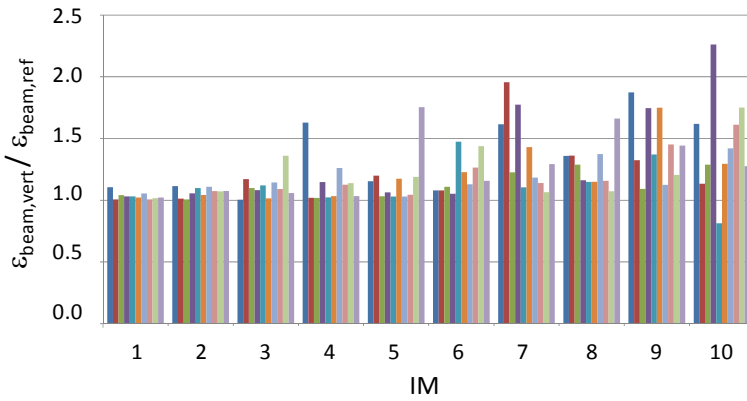


Figure.5.5.32 Influence of the seismic vertical component on the strain of the transverse beams.

5.5.7.3  Results for the deterministic model with non-structural elements (SLD evaluation)

In this section, the probabilities of exceeding the DLS conditional to a given IM level, *P[SLD|IM]*, are presented, in form of histograms, for the L'Aquila case studies (soil A in Figure 5.5.33, and soil C in Figure 5.5.34). The main conclusions can be summarized as follows:

- The serviceability limit state is generally attained for seismic intensities larger or equal to the ones characterizing the ultimate limit state, that is for IM = 5, corresponding to events with return period of 500 years.
- A small probability, lower than 10%, is observed at IM = 4 (return period of 250 years) for the case studies with Lx 30m and soil category C.
- For IM > 6 (return period >1000 years) the probabilities *P[SLD|IM]* increase gradually with the seismic intensity, reaching values very close to 100% at the IM =9/10 (return period >10000 years).
- The probabilities grow rapidly from IM = 7 to IM = 10 when the soil category is C.
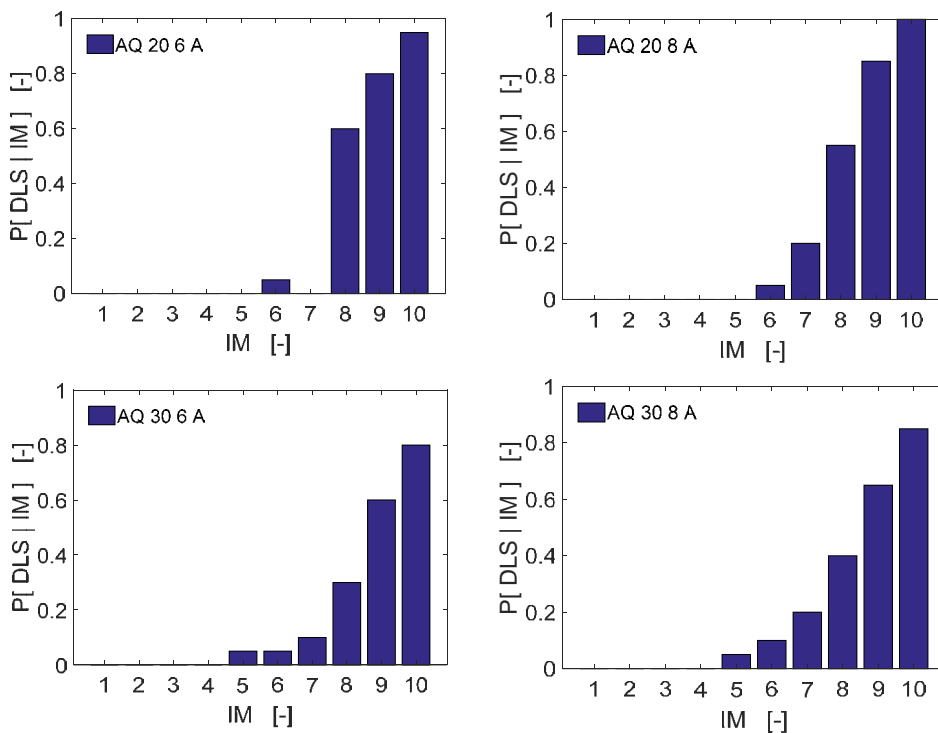


Figure 5.5.33 DLS probabilities conditional to different IM levels (L'Aquila soil A).
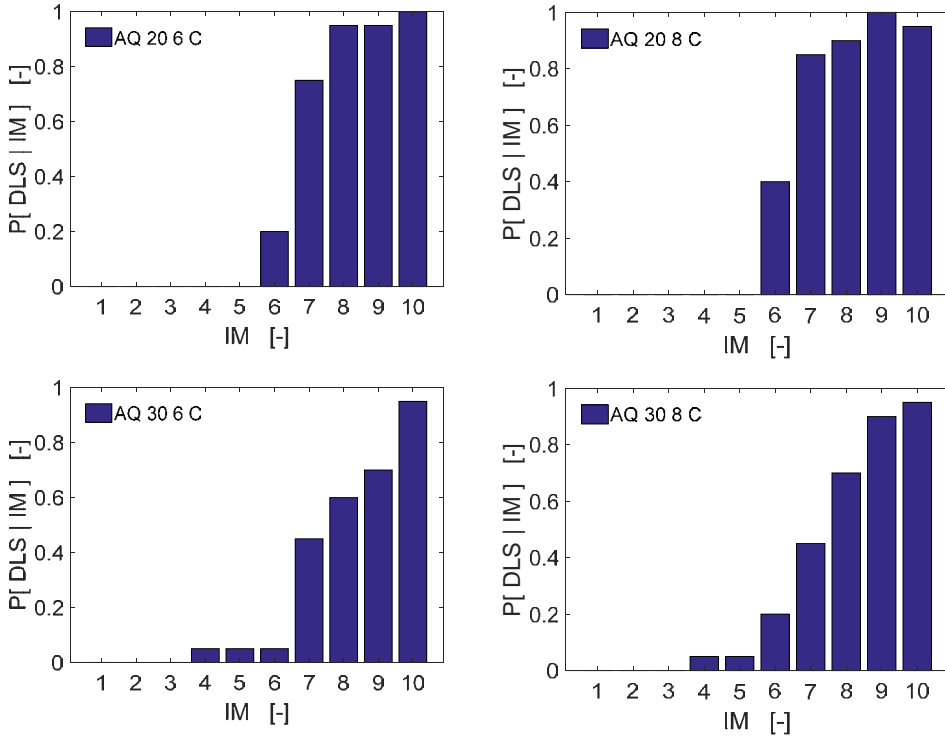
Figure 5.5.34 DLS probabilities conditional to different IM levels (L'Aquila soil C).

The influence of the explicit modelling of the panels contribution on the calculated seismic risk is presented in the Section 7.5 of this report. Instead, in the following part of this section, the vulnerability of the buildings located in L'Aquila is examined by observing the trend of the seismic response in both X and Y directions. Different EDPs are monitored (as already introduced above): the story drift is assumed as a descriptor of the response of the portal frames (X direction), while the maximum strain range experienced by the vertical braces is assumed to describe the seismic performance in the longitudinal (Y) direction.

Despite similarities in qualitative response trends as observed for the case studies without the panels (section 5.5.7.1), the measured maximum responses computed from the model with the panels (Figure 5.5.35 and Figure 5.5.36) are notably lower than the model without panels. Hence, the results prove the beneficial contribution of the non-structural components even on very rare IM values, i.e., beyond the serviceability limit state. In this case, indeed, the collapse cases are reduced in both X and Y directions, with the most demanding conditions represented by the case study with soil C (Figure 5.5.36), in which the collapse limits are attained for the highest IM levels.

(a)                                                              (b)
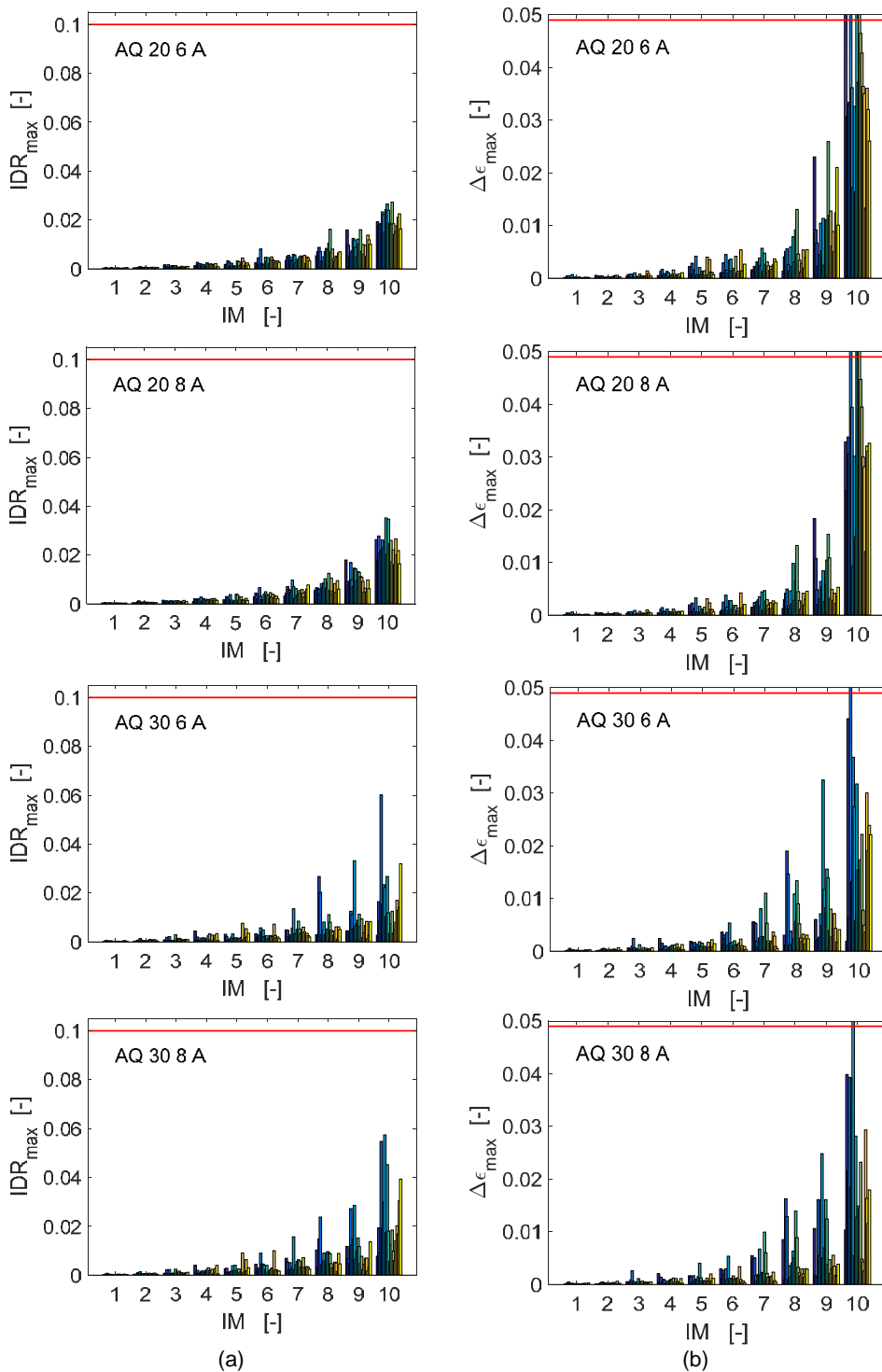
Figure 5.5.35 MSA results for the deterministic model with non-structural elements. Comparison with the limits from the collapse criteria. Case L'Aquila soil A: (a) maximum interstory drift ($IDR_{max}$) along X, and (b) maximum brace strain range ($\Delta\epsilon_{max}$) along Y.
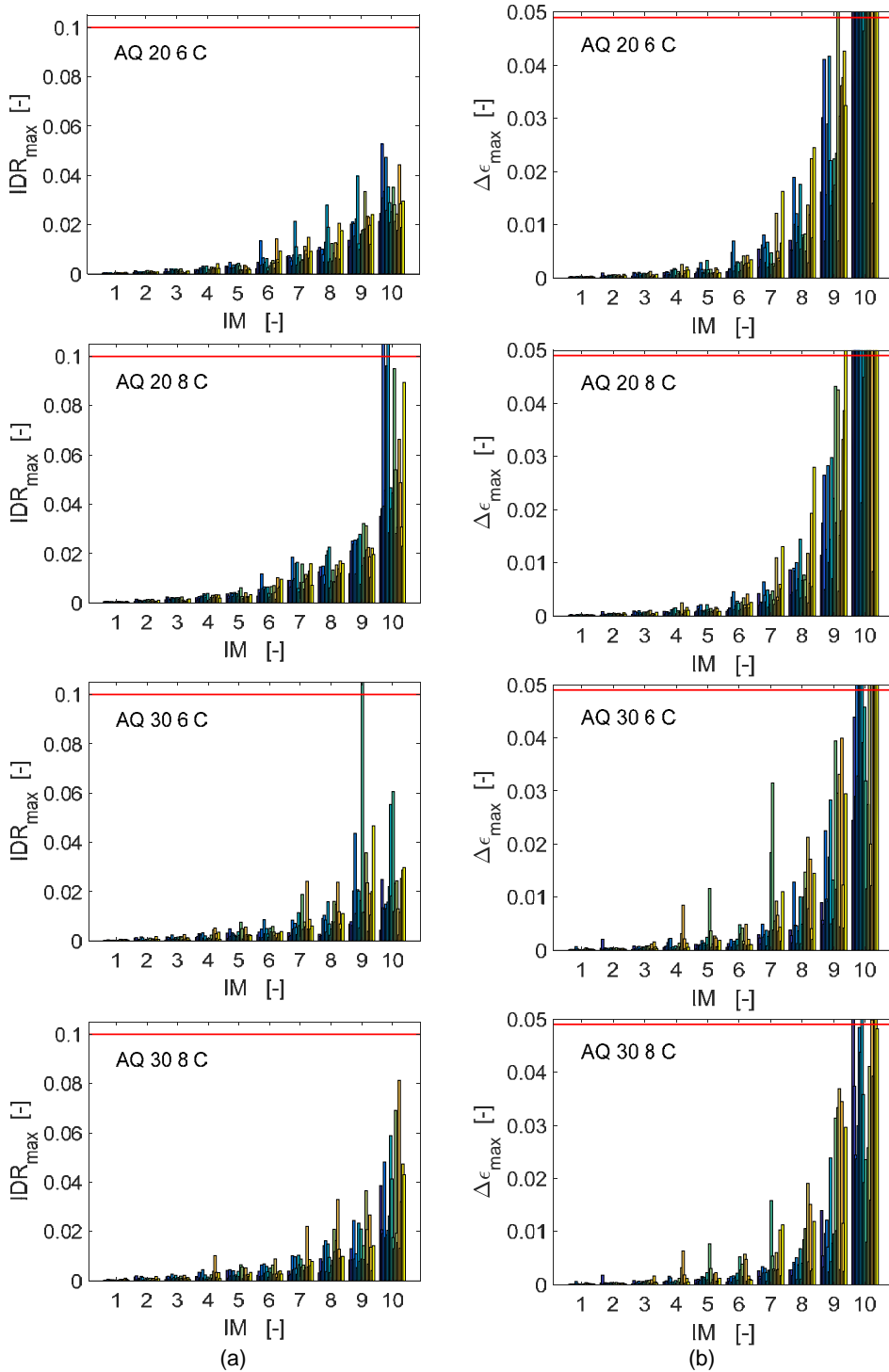
Figure 5.5.36 MSA results for the deterministic model with non-structural elements. Comparison with the limits from the collapse criteria. Case L'Aquila soil C: (a) maximum interstory drift ($IDR_{max}$) along X, and (b) maximum brace strain range ($\Delta\varepsilon_{max}$) along Y.

5.5.7.4  Results of the model with uncertain parameters and non-structural elements

The influence of the uncertain model parameters on the seismic risk is presented in Section 7.5 of this report. In the next part of this section, instead, the vulnerability of the buildings located in L'Aquila is examined by observing the trend of the seismic response in both X and Y directions. Different EDPs are monitored (as already introduced above): the story drift is assumed as EDP to describe the response in the portal frame (X) direction, while the maximum strain range experienced by the vertical brace section fibers is assumed as EDP for the longitudinal (Y) direction.

The major effect of the model uncertainties on the seismic vulnerability (Figure 5.5.37 and Figure 5.5.38) consists of an increment of the response dispersion, which in some cases leads to the attainment of the collapse condition at IM intensities lower than the ones observed for the case with deterministic model parameters. The most affected direction is the Y direction (concentrically braced frames), in which both the material (steel yielding strength) and the geometrical (local imperfection) uncertainties play a role in influencing the response.
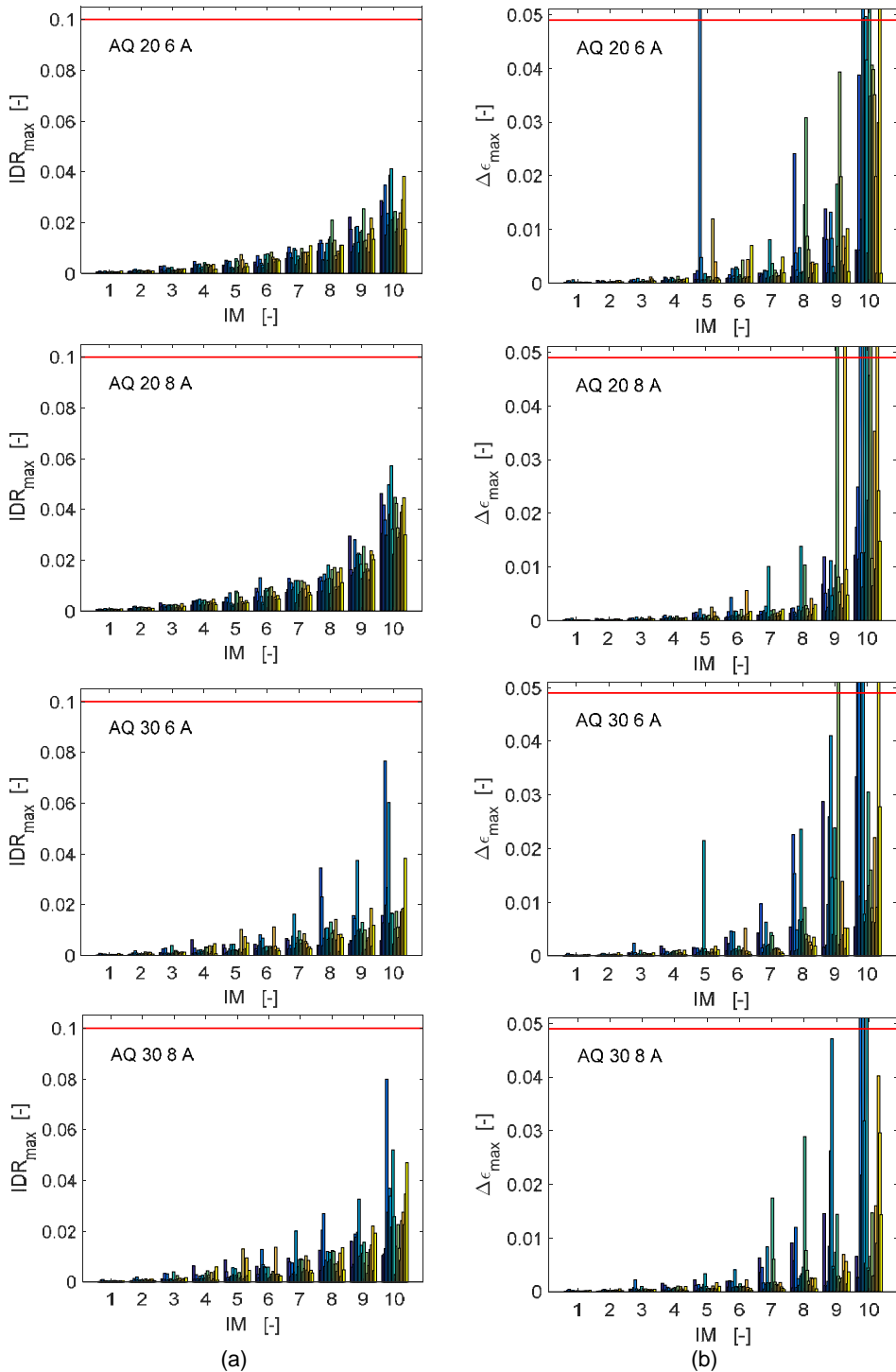
Figure 5.5.37 MSA results for the uncertain model with non-structural elements. Comparison with the limits from the collapse criteria. Case L'Aquila soil A: (a) maximum interstory drift (IDR$_{max}$) along X, and (b) maximum brace strain range ($\Delta\epsilon_{max}$) along Y.
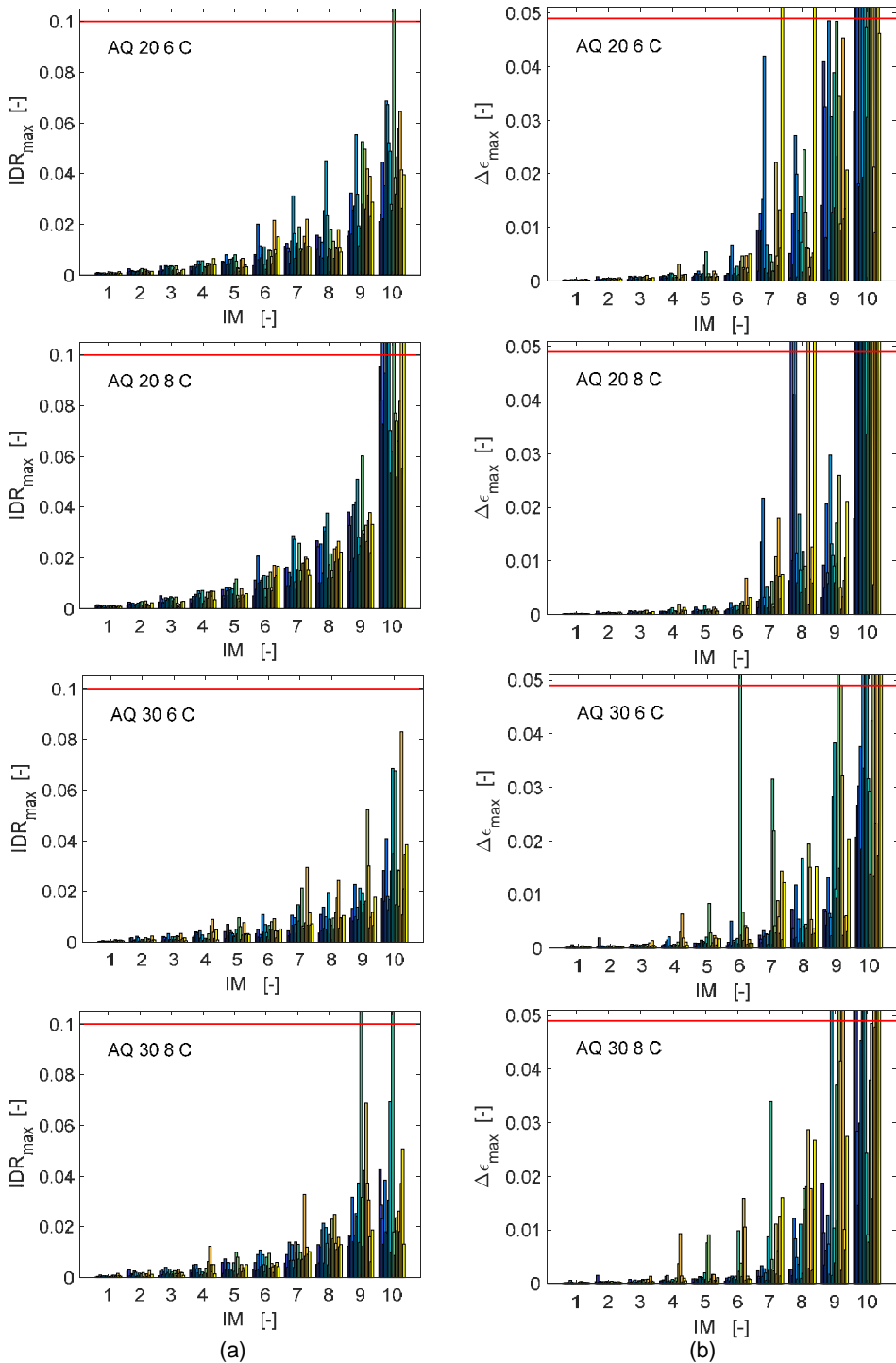
Figure 5.5.38 MSA results for the uncertain model with non-structural elements. Comparison with the limits from the collapse criteria. Case L'Aquila soil C: (a) maximum interstory drift ($IDR_{max}$) along X, and (b) maximum brace strain range ($\Delta\varepsilon_{max}$) along Y.

## 5.6   References

ArcelorMittal (2008). Design Manuals "Steel Buildings in Europe" - Single storey buildings. Part 4: Detailed design of portal frames. http://sections.arcelormittal.com/fileadmin/redaction/4-Library/4-SBE/EN/SSB04_Detailed_design_of_portal_frames.pdf.

Bosco, M., & Tirca, L. (2017). Numerical simulation of steel I-shaped beams using a fiber-based damage accumulation model. Journal of Constructional Steel Research, 133, 241-255.

European Committee for Standardization. Eurocode 3: Design of steel structures - Part 1-1: General rules and rules for buildings. EN1993-1-1, August 2005.

Circolare 02/02/2009 n. 617 (2009). Istruzioni per l'applicazione delle "Nuove norme tecniche per le costruzioni" di cui al D.M. 14 gennaio 2008. M. d. I. e. d. Trasporti, ed. Gazzetta Ufficiale n. 47 del 26 febbraio 2009.

D.M. 14/01/2008 (2008). Norme Tecniche per le Costruzioni (in Italian), G.U. n. 29 4 febbraio 2008.

Da Silva, L. S., Rebelo, C., Nethercot, D., Marques, L., Simões, R., & Real, P. V. (2009). Statistical evaluation of the lateral–torsional buckling resistance of steel I-beams, Part 2: Variability of steel properties. Journal of Constructional Steel Research, 65(4), 832-849.

Dolsek, M. (2011). Estimation of seismic response parameters through extended incremental dynamic analysis. Computational methods in earthquake engineering, Springer Netherlands. 285-304.

Franchin, P., Mollaioli, F., & Noto, F. (2017). RINTC project: Influence of structure-related uncertainties on the risk of collapse of Italian code-conforming reinforced concrete buildings. COMPDYN 2017-6th ECCOMAS Thematic Conference on Computational Methods in Structural Dynamics and Earthquake Engineering (pp. 15-17). Rhodes Island, Greece.

Hsiao, P. C., Lehman, D. E., & Roeder, C. W. (2012). Improved analytical model for special concentrically braced frames. Journal of Constructional Steel Research, 73, 80-94.

Hsiao, P. C., Lehman, D. E., & Roeder, C. W. (2013). Evaluation of the response modification coefficient and collapse potential of special concentrically braced frames. Earthquake Engineering & Structural Dynamics, 42(10), 1547-1564.

Ibarra L.F., & Krawinkler, H. (2005). Global collapse of frame structures under seismic excitations. Report No. TB 152, The John A. Blume Earthquake Engineering Center, Stanford University, Stanford, CA.

Idota H, Guan L, & Yamazaki K. Statistical correlation of steel members for system reliability analysis. Proceedings of the 9th international conference on structural safety and reliability (ICOSSAR), Osaka, Japan; 2009

Lignos, D. G., & Krawinkler, H. (2010). Deterioration modeling of steel components in support of collapse prediction of steel moment frames under earthquake loading. Journal of Structural Engineering, 137(11), 1291-1302.

Lignos, D.G., & Krawinkler, H. (2009). Sidesway collapse of deteriorating structural systems under seismic excitations. Report No.TB 172, The John A. Blume Earthquake Engineering Research Center, Stanford University, Stanford, CA.

Scott, M. H., & Fenves, G. L. (2006). Plastic hinge integration methods for force-based beam–column elements. Journal of Structural Engineering, 132(2), 244-252.

Midas GEN v2.1 (2016). Integrated Solution System for Building and General Structures. Midas Information Technology Co. Ltd.

Ribeiro, F. L., Barbosa, A. R., Scott, M. H., & Neves, L. C. (2014). Deterioration modeling of steel moment resisting frames using finite-length plastic hinge force-based beam-column elements. Journal of Structural Engineering, 141(2), 04014112.

Tirca, L., Chen, L., & Tremblay, R. (2015). Assessing collapse safety of CBF buildings subjected to crustal and subduction earthquakes. Journal of Constructional Steel Research, 115(1), 47-61.

Tremblay R, Archambault M-H, & Filiatrault A. (2003). Seismic response of concentrically braced steel frames made with rectangular hollow bracing members. Journal of Structural Engineering. 129(12), 1626-1636.

# CHAPTER VI – BASE-ISOLATED REINFORCED CONCRETE STRUCTURE

## 6.1   Case study structures

For case studies of base-isolated buildings, the sites with the first two highest seismicity of the five considered in the project, L'Aquila and Naples (soil type C), were selected. The site characteristics are listed in Table 6.1.1 with PGA values corresponding to 475 years return period earthquake at the sites while Figure 6.1.1 shows the location of the sites. Each of case study buildins is equipped with one of the following three isolation systems: a system composed of High Damping Rubber bearings (HDRBs), a hybrid isolation system composed of both HDRBs and Flat Sliding Bearings (FSBs), and a Friction Pendulum System (FPS). For both of the two sites, the buildings differ only in the dimensions and mechanical properties of elastomeric, friction pendulum and steel-PTFE devices while featuring the same prototype building (Figure 6.1.2) with similar dimensions and reinforcements of structural elements.

Table 6.1.1 Seismic parameters of selected sites.

| Site | Lat. | Long. | PGA ($T_R$=475 yrs) [g] (Soil Type C) | Seismic zone |
|---|---|---|---|---|
| L'Aquila | 13.399 | 42.349 | 0.345 | I |
| Naples | 14.268 | 40.854 | 0.24338 | II |



Figure 6.1.1 Site Location.
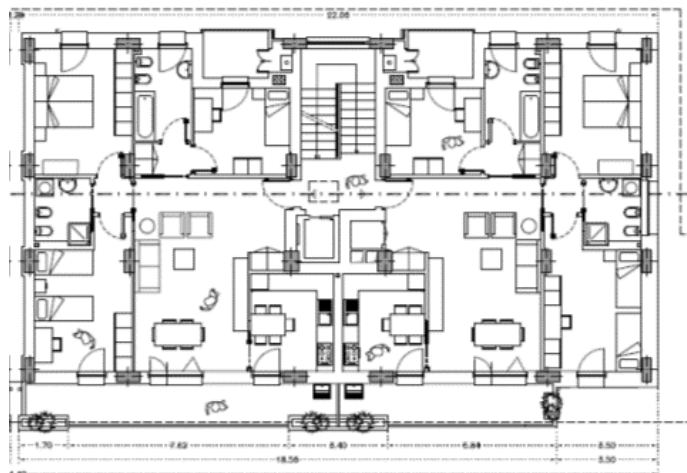


Figure 6.1.2 Prototype building plan.

### 6.1.1    The six-story building prototype

The superstructures of the isolated prototype buildings analyzed in the present study were designed in a similar manner as for the six-story fixed-base RC infilled frame buildings examined in Chapter 4: following the same design philosophy, the superstructures were designed considering the load transfer from the isolation system. As a matter of fact, the architectural characteristics and the material properties of the buildings examined were derived by the aforementioned legacy.

In particular, the six-story RC infilled frame building is intended for residential use and it is characterized by a regular plan of approximately 240 square meters. The height of the ground level is 3.4m while that of all the other stories is equal to 3.05m. The building structure includes the staircase, designed with knee beams. All floor plans are identical except beam-column dimensions and reinforcement.

## 6.2   Structural design of the base-isolated buildings

Different typologies of base-isolated buildings were considered by each Research Group (RG) during the design phase (Table 6.2.1).

Table 6.2.1 Isolation System typologies for each RG.

| RG | Isolation system typology |
|---|---|
| HDRB | elastomeric |
| HDRB-FSB | hybrid (elastomeric + steel/PTFE sliders) |
| FPS | friction pendulum |

### 6.2.1    Isolation system

6.2.1.1    HDRB general design criteria

The HDRB research group considered an elastomeric isolation system. In this case, due to the large number of elastomeric bearings (one under each columns), it was not possible to obtain isolation periods larger than 2.5 sec. Consequently, isolation period ranging from 2.0 to 2.5 sec was considered and the damping ratio, $\xi$, was set to 15% in order to minimize the base-shear transferred to the superstructure. In the 2016 RINTC project, two case studies were designed at L'Aquila site, the first (case 1-A) characterized by the isolation period of about 2 sec and the second (case 2-A) characterized by the isolation period of about 2.5 sec. Among those, the second one, that minimizes the base-shear transferred to the superstructure, was also considered in the present project for further analyses. In addition, in the 2017 RINTC project other two case studies were designed at the Naples site. Similarly to L'Aquila, the first (case 1-N) was characterized by the isolation period of about 2 sec and the second (case 2-N) was characterized by the isolation period of about 2.5 sec, both with the damping ratio equal to 15%. In all the cases, the isolation ratio, defined as the ratio between the period of the base-isolated building and the period of the same building in its fixed-base configuration, $T_{is}/T_{fb}$, is greater than 2 and the isolation system was designed by performing response spectrum analysis and by considering the following limitations, suggested in §7.10.4.2 and C11.9.7 of NTC2008 on the Collapse Limit State (SLC).

1) the shear deformation value satisfies:

$$\gamma_s \leq \gamma* /1.5 \leq 2 \tag{6.3}$$

where:

$\gamma_s$ is the shear deformation of rubber layers due to the total seismic displacement, included torsional effects

$\gamma*$ is maximum shear deformation obtained from qualification tests aimed to assess the effective rubber-steel adhesion

2) the total shear deformation satisfies:

$$\gamma_t \leq 5 \qquad\qquad (6.2)$$

where:

$\gamma_t = \gamma_c + \gamma_s + \gamma_\alpha$ : the total deformation

$\gamma_c$ : shear deformation of rubber layers due to axial load

$\gamma_\alpha$ : shear deformation of rubber layers due to angular rotation

3) the maximum tensile stress of the critical device should be lower than the minimum between $2G_{din}$ and 1 MPa as required in §7.10.4.2 of NTC2008;

4) the maximum compression force should be lower than $V_{max,c}/2$, where $V_{max,c}$ is buckling load evaluated as reported in C11.9.7:

$$V_{max,c} = \frac{G_{din}A_r S_1 D}{t_e} \qquad\qquad (6.3)$$

Table 6.2.2 shows the characteristics of the case study building of L'Aquila (case 1-A and case 2-A), whereas Table 6.2.3 shows the characteristics of the case study buildings at Naples (case 1-N and case 2-N). In these tables $T_{is}$ is the isolation period of the base-isolated building, $T_{is}/T_{fb}$ is the isolation ratio, i.e. the ratio between the period of the base-isolated building and the period of the same building in its fixed-base configuration. The displacement of HDRBs corresponding to the design strain $\gamma_d$=200% is also indicated ($d_{max,HDRB}$) as well as the maximum shear strain ($\gamma_{max}$) obtained by the analyses at the CLS and accounting for rotational effects. In the same tables, D/C represent the demand/capacity ratios, expressed in terms of shear strain (D/C shear), vertical compression load (D/C comp.) and vertical tensile stress (D/C tens.) In particular, the HDRB are identified by a two number code representing a set of two parameters, defining the diameter and the total rubber layer thickness, respectively. Figure 6.2.1 shows the devices configuration for the case study buildings at the L'Aquila site, while in Figure 6.2.2 the configuration for the two case study buildings of Naples are illustrated. For both the sites, when necessary, bigger devices were placed under the columns with larger axial loads.

Table 6.2.2 Geometric characteristics and design outcomes for HDRB isolation system (L'Aquila).

| CASE | HDRB $\Phi/T_r$ | $\xi$ (%) | $d_{max,HDRB}$ (mm) | $T_{is}$ (s) | $\gamma_{max}$ | D/C shear | D/C compr. | D/C tens. | $T_{is}/T_{bf}$ | D/C drift SLD |
|---|---|---|---|---|---|---|---|---|---|---|
| case 1-A | 600/128 700/130 | 15 | 250 | 2.04 | 1.63 | 0.82 | 0.82 | 0.99 | 2.60 | 0.31 |
| case 2-A | 550/154 600/150 | 15 | 300 | 2.46 | 1.71 | 0.86 | 0.97 | 0.33 | 3.46 | 0.21 |

Table 6.2.3 Geometric characteristics and design outcomes for HDRB isolation system.
(Naples)

| CASE | HDRB Φ/$T_r$ | ξ (%) | $d_{max,HDRB}$ (mm) | $T_{is}$ (s) | $γ_{max}$ | D/C shear | D/C compr. | D/C tens. | $T_{is}/T_{bf}$ | D/C drift SLD |
|------|------|------|------|------|------|------|------|------|------|------|
| case 1-N | 550/105 | 15 | 200 | 2.17 | 1.50 | 0.75 | 0.83 | 0.38 | 2.27 | 0.22 |
| case 2-N | 500/126 550/126 | 15 | 250 | 2.51 | 1.48 | 0.75 | 0.88 | 0 | 2.64 | 0.16 |



SI-S 600/128   SI-S 700/130          SI-S 550/154   SI-S 600/150
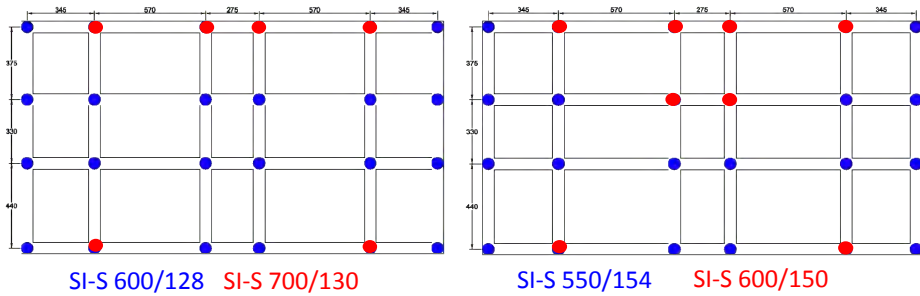
Case 1-A                              Case 2-A
Figure 6.2.1 Isolation system configuration of HDRB typology (L'Aquila)
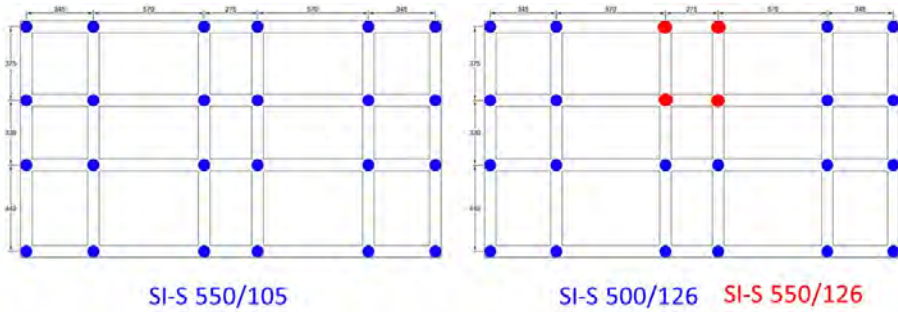


SI-S 550/105                    SI-S 500/126   SI-S 550/126
Case 1-N                              Case 2-N
Figure 6.2.2 Isolation system configuration of HDRB typology (Naples).

6.2.1.2    HDRB-FSB general design criteria

The HDRB-FSB research group considered an hybrid (elastomeric & steel/PTFE sliders) isolation system. Figure 6.2.3 shows the device configuration examined by the HDRB-FSB research group. It is worth noting that the number of sliders was assumed equal to one third of the total number of isolation devices, in order to ensure an appropriate horizontal rigidity.
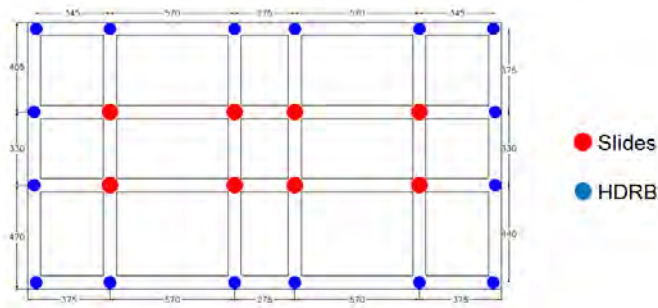
Figure 6.2.3 Isolation system configuration of HDRB-FSB typologies.

In the 2016 RINTC project, four case study buildings were designed at the L'Aquila site, characterized by damping ratio equal to 10 or 15% and by an isolation period ranging from 2.66 sec to 3.04 sec. Among those, the two cases, 2-A and 3-A, characterized by periods equal to 2.84 s and 3.04 s respectively, were also considered in the 2017 RINTC project for further analysis. In addition, in the 2017 RINTC project other two case studies were designed at the Naples site. The first (case 1-N) is characterized by an isolation period of about 2.8 sec with a damping ratio equal to 15% and the second (case 2-N) is characterized by an isolation period of about 2.4 sec with a damping ratio equal to 10%. Among those, for each site, the one that maximizes the base-shear transferred to the superstructure was used for the structural design of the building.

In all the cases, the isolation ratio $T_{is}/T_{fb}$ is greater than 2 and the isolation sistem was designed by performing a response spectrum analysis and by considering the same limitations as for the case of HDRB (§7.10.4.2 of NTC2008 and C11.9.7) at the Collapse Limit State (SLC).

Table 6.2.4 shows the characteristics of the case study building of L'Aquila under consideration, whereas Table 6.2.5 shows the characteristics of the case of studies of Naples. In particular, the HDRB are identified by a two number code representing a set of two parameters, defining the first the diameter of the rubber and the second one the total rubber layer thickness.

Table 6.2.4 Geometric characteristics and design outcomes for HDRB-FSB isolation systems of cases site in L'Aquila.

| CASE | HDRB $\Phi/T_r$ | SLIDES $V/d_{max,Slides}$ | $\xi$ (%) | $d_{max,HDRB}$ (mm) | $d_{max,Slides}$ (mm) | $T_{is}$ (s) | $\gamma_{max}$ | D/C shear | D/C compr. | D/C tens. | $T_{is}/T_{bf}$ |
|---|---|---|---|---|---|---|---|---|---|---|---|
| case 1-A | 650/180 | 350/700 | 10 | 350 | 350 | 2.84 | 1.83 | 0.94 | 0.89 | 0.83 | 3.05 |
| case 2-A | 600/152 | 350/600 | 15 | 300 | 300 | 2.84 | 1.88 | 0.95 | 0.82 | 0.54 | 3.05 |
| case 3-A | 600/176 | 350/700 | 15 | 350 | 350 | 3.04 | 1.7 | 0.85 | 0.98 | 0.19 | 3.27 |
| case 4-A | 700/180 | 350/700 | 10 | 350 | 350 | 2.66 | 1.69 | 0.87 | 0.65 | 0.94 | 2.86 |

Table 6.2.5 Geometric characteristics and design outcomes for HDRB-FSB isolation systems of cases site in Naples.

| CASE | HDRB $\Phi/T_r$ | SLIDES $V/d_{max,Slides}$ | $\xi$ (%) | $d_{max,HDRB}$ (mm) | $d_{max, Slides}$ (mm) | $T_{is}$ (s) | $\gamma_{max}$ | D/C shear | D/C compr. | D/C tens. | $T_{is}/T_{bf}$ |
|---|---|---|---|---|---|---|---|---|---|---|---|
| case 1-N | 500/102 | 350/200 | 15 | 200 | 200 | 2.79 | 1.73 | 0.88 | 0.79 | 0 | 3 |
| case 2-N | 600/104 | 350/200 | 10 | 200 | 200 | 2.39 | 1.82 | 0.95 | 0.41 | 0.65 | 2.57 |

### 6.2.1.3 FPS general design criteria

The design of the isolation system with FPS was performed to reach high isolation periods and to obtain the same target value of base acceleration of the superstructure at Life-safety Limit State (LLS), for both construction sites (Naples and L'Aquila). With this strategy, the design of superstructure can be made in the same way, independently from the hazard of the site, thanks to the adaptation of the isolation system. The target value of base acceleration was fixed at 0.10g.

The isolation system consists in 24 Double Curved Sliding Surface (DCSS) devices which are selected from a commercial catalog. For linear analysis, the effective design parameters are calculated with the following relations:

$$K_{eff} = N_{Sd} \cdot \left( \frac{1}{R} + \frac{\mu}{d_{bd}} \right) \tag{6.4}$$

$$\zeta_{eff} = \frac{2}{\pi} \cdot \frac{1}{\dfrac{d_{bd}}{\mu \cdot R} + 1} \tag{6.5}$$

$$T_{eff} = 2\pi \sqrt{\frac{1}{g \cdot \left( \dfrac{1}{R} + \dfrac{\mu}{d_{bd}} \right)}} \tag{6.6}$$

All of these design parameters depend on the design displacement $d_{bd}$ and is calculated with an iterative procedure, as described in §7.10.5.2 - NTC2008. The design displacement value also accounts for the accidental torsion effects as provided in §7.10.5.3.1 – NTC2008.

The effective radius and the overall lateral displacement capacity $d_m$ of the DCSS were selected on the basis of the different seismic demand of the construction sites at Collapse Limit State (CLS), as prescribed in in §7.10.6.2 – NTC2008. The nominal value of the friction coefficient $\mu_{nom}$ is the same for both cases and refers to a Low Friction material with $\mu_{nom} = 2.5\%$.

From static gravity analysis, the total weight of the structure corresponding to the service condition is $W \approx 22,000$kN, and the medium vertical load on each isolators is $N_{Sd} \approx 900$ kN. In function of the vertical load, the design coefficient of friction $\mu_d$ is calculated through the relationship given by the manufacturer [FIP, 2014]:

$$\mu_d = 2.5 \cdot \left( \frac{N_{Sd}}{N_{Ed}} \right)^{-0.834}$$

(6.7)

where

- $N_{Sd}$ is the vertical load in service (non-seismic) condition;
- $N_{Ed}$ is the maximum vertical load capacity of the device in seismic condition.

The results of these calculations are summarized in Table 6.2.6, where the effective radius $R_e$ = 2500mm for the site of Naples and $R_e$ = 3700mm for the site of L'Aquila was selected. In order to account for the vertical load variation in seismic conditions, a DCSS with vertical load capacity $N_{Ed}$ = 1500kN was considered. From nominal properties, the diameter of the rigid slider is 280mm with a maximum value of contact pressure about 24 MPa.

The same procedure was repeated for Life-safety Limit State (LLS) in order to evaluate the base acceleration of the superstructure. In Table 6.2.7, the design values obtained with the selected DCSS isolators are listed. As can be seen also in Figure 6.2.4, the values of the design base accelerations, $a_g$, are about the same for both sites.

Table 6.2.6 Design properties of the isolation system at CLS.

|  | $R_e$ | $N_{Ed}$ | $N_{Sd}$ | $\mu_{nom}$ | $\mu_d$ | $d_{bd}$ | $K_{eff}$ | $\xi_{eff}$ | $T_{eff}$ | $d_{bd}^*$ | $d_m$ | $d_m/d_{bd}^*$ |
|---|---|---|---|---|---|---|---|---|---|---|---|---|
| *Site* | *[mm]* | *[kN]* | *[kN]* | *[%]* | *[%]* | *[mm]* | *[kN/m]* | *[%]* | *[sec]* | *[mm]* | *[mm]* | *[-]* |
| **Naples** | 2500 | 1500 | 900 | 2.5 | 3.8 | 120 | 648.4 | 28% | 2.36 | 143 | ±150 | 1.05 |
| **L'Aquila** | 3700 | 1500 | 900 | 2.5 | 3.8 | 220 | 399.9 | 25% | 3.01 | 263 | ±300 | 1.14 |

*\*Accounted for accidental torsional effects*

Table 6.2.7 Design properties at LLS.

|  | $R_e$ | $\mu_d$ | $d_{bd}$ | $K_{eff}$ | $\xi_{eff}$ | $T_{eff}$ | $a_g$ |
|---|---|---|---|---|---|---|---|
| *Site* | *[mm]* | *[%]* | *[mm]* | *[kN/m]* | *[%]* | *[sec]* | *[g]* |
| **Naples** | 2500 | 3.8 | 90 | 748.9 | 33.1 | 2.20 | 0.074 |
| **L'Aquila** | 3700 | 3.8 | 146 | 478.8 | 31.3 | 2.75 | 0.078 |
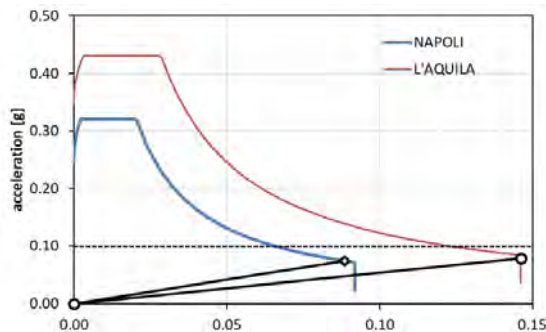


Figure 6.2.4 Design spectrum at Life-safety Limit State.

### 6.2.2   Superstructure

According to NTC 2008, the Life Safety limit state was taken as reference for the structural design. All buildings were designed by means of Response Spectrum Analysis, neglecting capacity design while considering low ductility class[2] for structural details. The superstructure is classified as ordinary, thus the importance factor is cu=1.

The staircase is a part of the building structure and was designed using knee beams. An additional floor slab was added to connect the bases of the first story columns, also equipped with a grid of RC beams.

### 6.2.2.1    Geometry and materials

Due to architectural requirements, the minimum column dimension is set to 35 cm. Figure 6.2.5 shows the structural plan of the typical floor. The arrows indicate that the slabs are all one-way. The outer beam webs are all deeper than the slab, while all internal beams are flat. Slab thickness is 25cm. Beam details are shown in Figure 6.2.6.
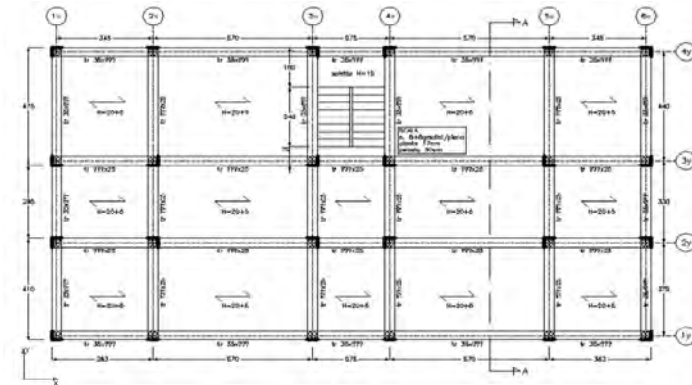


Figure 6.2.5 Floor plan with fixed reference grid and one way slab orientation.
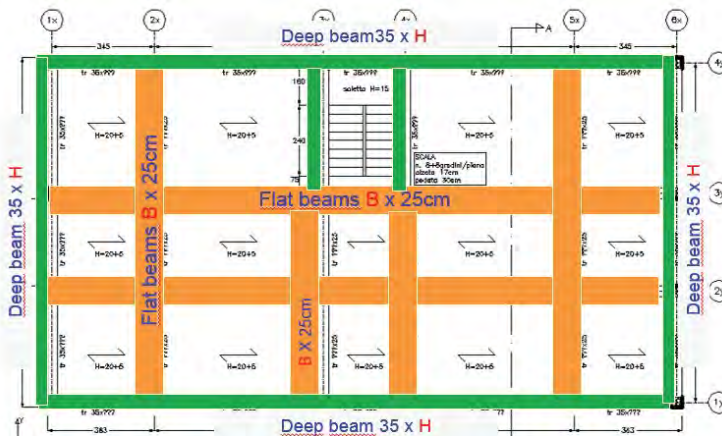


Figure 6.2.6 Beam types and minimum column size.

It is commonplace in Italy to use masonry infills for the outer walls of a building. Consequently, infill panels distributed regularly, in plan and elevation, were considered. In the design process, infills are not included in the building model as structural elements, but are only considered as dead load, and the following structural materials were used:

- Concrete C28/35 [11.2.10 NTC2008];
- B450C steel [11.3.2.1 NTC2008].

The mechanical properties of the aforementioned materials are reported in Table 6.2.8 and in Table 6.2.9. It is worth noting that, in order to account for element cracking in linear analyses, reduced concrete elastic moduli are used for beams ($E_{cm-bm}$) and columns ($E_{cm-cl}$).

Table 6.2.8 Mechanical properties for C28/35 concrete.

| $f_{ck}$ | $f_{ctm}$ | $E_{cm}$ | $E_{cm-cl}$ [0.75 $E_{cm}$] | $E_{cm-bm}$ [0.5 $E_{cm}$] | $f_{cd}$ | $\varepsilon_{cu}$ |
|------|------|------|------|------|------|------|
| [MPa] | [MPa] | [MPa] | [MPa] | [MPa] | [MPa] | [-] |
| 28.0 | 2.77 | 32300 | 24225 | 16150 | 15.87 | 0.35% |

Table 6.2.9 Mechanical properties for B450C reinforcing steel.

| $f_{yk}$ | $f_{yd}$ | $E_s$ | $\varepsilon_{su}$ |
|------|------|------|------|
| [N/mm$^2$] | [N/mm$^2$] | [N/mm$^2$] | [-] |
| 450.0 | 391.3 | 200000 | 7.50% |

#### 6.2.2.2    Non-seismic loads

Permanent and variable loads used for the buildings design are listed in Table 6.2.10.

Table 6.2.10 Permanent (G) and Variable (Q) loads

| Description | Units | Value |
|------|------|------|
| G1_RC elements | kN/m$^3$ | 25.00 |
| G1_slabs (floor and roof) | kN/m$^2$ | 3.20 |
| G2_slabs (floor) | kN/m$^2$ | 3.10 |
| G2_roof | kN/m$^2$ | 1.60 |
| G2_staircase | kN/m$^2$ | 0.80 |
| Q_slabs (floor) | kN/m$^2$ | 2.00 |
| Q_roof (snow) | kN/m$^2$ | 1.64 |
| Q_staircase | kN/m$^2$ | 4.00 |
| G2_infills | kN/m$^2$ | 3.50(*) |

*(\*) The assumed value accounts for the presence of openings through a correction coefficient estimated at 0.85.*

### 6.2.3    Seismic action

As mentioned before, the seismic design of the RC buildings was performed by means of modal response spectrum analysis (RSA). According to the Italian building code NTC 2008, the seismic action can be evaluated using design response spectra, related to the site hazard and the reference limit state. Site hazard is defined by the seismic hazard parameters ($a_g$, $F_0$, $T_{c^*}$), for life safety limit state (LS), reported in the Annex B of the Italian building code NTC2008, depending on the geographical position and on the return periods.

The design response spectrum depends on the soil and topographic category of the construction site. The soil category can be defined considering the stratigraphic profiles and the average shear wave velocity $V_{s,30}$. For the reference case studies (L'Aquila and Naples), referring to Tab. 3.2.II – NTC 2008, Soil Type C was selected. Flat topographic conditions were assumed for both case studies (topography category T1, according to Tab. 3.2.IV – NTC 2008).

The elastic response spectrum is defined by Eq. 3.2.4 (horizontal acceleration component) of the Italian building code NTC 2008. The design response spectrum can be obtained from the elastic one using the behavior factor q assumed equal to 1.5 (§ 7.10.6.2.1 NTC 2008). The earthquake vertical component was neglected in all analyses (linear and nonlinear).

In the second part of the present study, the seismic response of the base-isolated buildings designed as described above was assessed by means of Nonlinear Time-History response Analyses (NTHAs). Such analyses have been performed using different sets of records selected based on the site-specific seismic hazard of the designed structures.

*HDRB:* The NTHAs were performed using the set of ground motions characterized by the conditioning period equal to 2.00 s for case 1-A and 1-N. For the case 2-A and the case 2-N, considering that a specific set for 2.50 s is not available, the set of ground motions characterized by the conditioning period equal to 3.00 s was used.

*HDRB & FSB:* The NTHAs were performed using the set of ground motions characterized by conditioning period equal to 3.00 s for all the cases at the L'Aquila site and for case 1-N sites in Naples. While, for case 2-N, a set of ground motions characterized by the conditioning period equal to 2.00 seconds was used.

*FPS*: The examined case studies are characterized by fundamental periods of 2.20 s (Naples) and 2.75 s (L'Aquila) at Collapse Limit State (CLS). The NTHAs were performed using the set of ground motions characterized by the conditioning period equal to 3.00 s for both case studies.

### 6.2.4   HDRB buildings

Table 6.2.11 and Table 6.2.12 report the structural elements dimensions of the two prototype buildings located at L'Aquila and Naples, respectively. Differences concern only the beam dimensions that are larger in the superstructure located at L'Aquila to avoid traction states on external bearings in the case of smaller isolation period (case 1-A).

Table 6.2.13 summarizes the design data of the selected prototypes (average floor seismic weight, total column area of the ground level divided by the floor area, average reinforcement ratio for the deep beams of the first floor, average reinforcement ratio for the flat beams of the first floor, and average reinforcement ratio for the columns of the ground floor). Finally, the modal parameters of each case study are summarized in Table 6.2.14.

Table 6.2.11 Beam and coloumn dimensions for L'Aquila case studies.

| L'Aquila | | | | | |
|---|---|---|---|---|---|
| Floor | Coloumn Dimension[cm] | | Deep Beam Dimension[cm] | | Flat Beam Dimension [cm] |
| 0 | - | - | - | | 60x40 |
| 1 | 35x50 | 50x50(staircase) | 35x60 | 35x40 (staircase) | 60x25 |
| 2 | 35x50 | 50x50(staircase) | 35x60 | 35x40 (staircase) | 60x25 |
| 3 | 35x40 | 40x40(staircase) | 35x50 | 35x40 (staircase) | 60x25 |
| 4 | 35x40 | 40x40(staircase) | 35x50 | 35x40 (staircase) | 60x25 |
| 5 | 35x35 | 35x35(staircase) | 35x40 | 35x40 (staircase) | 60x25 |
| 6 | 35x35 | 35x35(staircase) | 35x40 | 35x40 (staircase) | 60x25 |

Table 6.2.12 Beam and coloumn dimensions for Naples case studies.

| Naples | | | | |
|---|---|---|---|---|
| Floor | Coloumn Dimension[cm] | | Deep Beam Dimension [cm] | Flat Beam Dimension [cm] |
| 0 | - | - | - | 60x40 |
| 1 | 35x50 | 50x50(staircase) | 35x40 | 60x25 |
| 2 | 35x50 | 50x50(staircase) | 35x40 | 60x25 |
| 3 | 35x40 | 40x40(staircase) | 35x40 | 60x25 |
| 4 | 35x40 | 40x40(staircase) | 35x40 | 60x25 |
| 5 | 35x35 | 35x35(staircase) | 35x40 | 60x25 |
| 6 | 35x35 | 35x35(staircase) | 35x40 | 60x25 |

Table 6.2.13 HDRB - Summary of design data.

| RU | Average floor Seismic weight [kN/m$^2$] | ΣA_col/A_floor [%] | $\rho_{b\_deep,1,m}$ [%] | $\rho_{b\_flat,1,m}$ [%] | $\rho_{c,1,m}$ [%] |
|---|---|---|---|---|---|
| HDRB-L'Aquila | 13.1 | 1.80 | 1.0 | 1.1 | 1.19 |
| HDRB-Naples | 13.1 | 1.80 | 1.1 | 1.06 | 1.17 |

Table 6.2.14 HDRB - Modal parameters

| Case | $T_x$[s] | $M_x$[%] | $T_y$[s] | $M_y$[%] |
|---|---|---|---|---|
| HDRB-case 1A | 2.05 | 99 | 2.03 | 99 |
| HDRB-case 2A | 2.47 | 99 | 2.45 | 99 |
| HDRB-case 1N | 2.17 | 99 | 2.13 | 99 |
| HDRB-case 2N | 2.52 | 99 | 2.48 | 99 |

## 6.2.5   HDRB-FSB buildings

The dimensions of the structural elements of the two building prototypes located in L'Aquila and Naples are the same as those shown in Table 6.2.11 and Table 6.2.12 in case of HDRB. The modal parameters of each case study building are summarized in Table 6.2.15.

Table 6.2.16 summarizes the design data of the selected prototypes (average floor seismic weight, total column area of the ground level divided by the floor area, average reinforcement ratio for the deep beams of the first floor, average reinforcement ratio for the flat beams of the first floor, and average reinforcement ratio for the columns of the ground floor).

Table 6.2.15 HDRB & FSB - Modal parameters for each case study.

| Case | $T_x$ [s] | $M_x$ [%] | $T_y$ [s] | $M_y$ [%] |
|---|---|---|---|---|
| HDRB-FSB - Case 1-A | 2.84 | 99 | 2.84 | 99 |
| HDRB-FSB - Case 2-A | 2.84 | 99 | 2.84 | 99 |
| HDRB-FSB - Case 3-A | 3.04 | 99 | 3.04 | 99 |
| HDRB-FSB - Case 4-A | 2.66 | 99 | 2.66 | 99 |
| HDRB-FSB - Case 1-N | 2.79 | 99 | 2.79 | 99 |
| HDRB-FSB - Case 2-N | 2.39 | 99 | 2.39 | 99 |

Table 6.2.16 HDRB-FSB - Summary of design data.

| RU | Average floor Seismic weight [kN/m$^2$] | ΣA_col/A_floor [%] | $\rho_{b\_deep,1,m}$ [%] | $\rho_{b\_flat,1,m}$ [%] | $\rho_{c,1,m}$ [%] |
|---|---|---|---|---|---|
| HDRB-FSB L'Aquila | 13.1 | 1.80 | 1.0 | 1.1 | 1.19 |
| HDRB-FSB Naples | 13.1 | 1.80 | 1.1 | 1.06 | 1.17 |

### 6.2.6    FPS building

The seismic design of the superstructure was performed through modal response spectrum analysis in SAP2000 program [CSI, 2014], following the current design practice for new buildings.

As provided in §7.10.2-NTC2008, the superstructure shall remain in the elastic range and the design can be performed following the provisions of §4.1-NTC2008 for non-seismic conditions, without seismic reinforcement details requirement. However, some energy dissipation of the superstructure can be considered by reducing seismic actions through the behavior factor $q$ = 1.5 (§7.10.6.2.1).

The dimensions of the structural elements are:

- *Columns*: 35x50cm at 1$^{st}$ and 2$^{nd}$ level, 35x40cm at 3$^{rd}$ and 4$^{th}$ level, 35x35cm at 5$^{th}$ and 6$^{th}$ level;
- *Deep beams*: 35x50cm at all levels;
- *Flat beams*: 60x25cm at all levels.

The column dimensions are mainly attributed to the preliminary size selection based on the maximum axial load. The design of reinforcement was conducted in order to obtain minimum values of over-resistance and, in most cases, the amount of reinforcement is imposed by the minimum requirement of NTC 2008.

The results of modal analysis were reported in Table 6.2.17 and the summary of reinforcement design is reported in Table 6.2.18. The symbols used in the following tables are:

- $T_X$, $M_X$ = fundamental period in the x direction and corresponding mass participation factor;
- $T_Y$, $M_Y$ = fundamental period in the y direction and corresponding mass participation factor;
- $\Sigma A_{col}/A_{floor}$ = total column area at the ground floor divided by the total floor area;
- $\rho_{b\_deep,1,m}$ = average deep beam longitudinal steel ratio;
- $\rho_{b\_flat,1,m}$ = average flat longitudinal steel ratio;
- $\rho_{c,1,m}$ = average base floor column steel ratio.

Table 6.2.17 Modal parameters for each site.

|  | $T_X$ | $M_X$ | $T_Y$ | $M_Y$ |
|---|---|---|---|---|
| **Site** | [s] | [%] | [s] | [%] |
| **Naples** | 2.29 | 98.9 | 2.28 | 99.5 |
| **L'Aquila** | 2.80 | 98.6 | 2.79 | 99.6 |

Table 6.2.18 Summary of design data.

| Average floor weight | $\Sigma A_{col}/A_{floor}$ | $\rho_{b\_deep,1,m}$ | $\rho_{b\_flat,1,m}$ | $\rho_{c,1,m}$ |
|---|---|---|---|---|
| [kN/m$^2$] | [%] | [%] | [%] | [%] |
| 14.7 | 1.77 | 0.8 | 0.8 | 0.9 |

### 6.2.7    Summary of design

The following tables summarize the main design data of the examined prototype buildings.

Table 6.2.19 Prototype buildings' modal parameters.

| Case | $T_x$ [s] | $M_x$ [%] | $T_y$ [s] | $M_y$ [%] |
|---|---|---|---|---|
| HDRB - Case 1A | 2.05 | 99 | 2.03 | 99 |
| HDRB - Case 2A | 2.47 | 99 | 2.45 | 99 |
| HDRB - Case 1N | 2.17 | 99 | 2.13 | 99 |
| HDRB - Case 2N | 2.52 | 99 | 2.48 | 99 |
| HDRB-FSB - Case 1-A | 2.84 | 99 | 2.84 | 99 |
| HDRB-FSB - Case 2-A | 2.85 | 99 | 2.84 | 99 |
| HDRB-FSB - Case 3-A | 3.04 | 99 | 3.04 | 99 |
| HDRB-FSB - Case 4-A | 2.66 | 99 | 2.66 | 99 |
| HDRB-FSB - Case 1-N | 2.79 | 99 | 2.79 | 99 |
| HDRB-FSB - Case 2-N | 2.39 | 99 | 2.39 | 99 |
| FPS - Naples | 2.29 | 99 | 2.28 | 99 |
| FPS - L'Aquila | 2.80 | 99 | 2.79 | 99 |

Table 6.2.20 Summary of design data for all buildings.

| RU | Average floor Seismic weight [kN/m$^2$] | $\Sigma A\_col/A\_floor$ [%] | $\rho_{b\_deep,1,m}$ [%] | $\rho_{b\_flat,1,m}$ [%] | $\rho_{c,1,m}$ [%] |
|---|---|---|---|---|---|
| HDRB-L'Aquila | 13.1 | 1.80 | 1.0 | 1.1 | 1.19 |
| HDRB-Naples | 13.1 | 1.80 | 1.1 | 1.06 | 1.17 |
| HDRB-FSB L'Aquila | 13.1 | 1.80 | 1.0 | 1.1 | 1.19 |
| HDRB-FSB Naples | 13.1 | 1.80 | 1.1 | 1.06 | 1.17 |
| FPS | 14.7 | 1.77 | 0.8 | 0.8 | 0.9 |

The following considerations can be drawn from the above data:

- The column dimensions mainly are attributed to the preliminary size selection based on the assumed maximum normalized axial load.
- In most cases the amount of reinforcement is dictated by the minimum reinforcement requirements of NTC 2008.
- The staircase knee beams experience high tension/compression excursions, hinting at possible numerical issues in the nonlinear analyses.
- The above design data also reflects some inherent variability in design from one building to another, due to variations in design approach. In fact, distinct building groups was designed by different research groups, thus different approaches were followed within the range permitted by the code. In this context, it was decided, to maintain a common minimum column size of 35 cm x 35 cm across all designs.

## 6.3   Modelling issues and strategies

The examined base-isolated buildings feature a standard three-dimensional frame structure. For the purpose of probabilistic seismic risk assessment based on nonlinear time history response analysis, cyclic constitutive laws are potentially required for the following components of the building:

- reinforced concrete beam and column members, including inclined members of the staircase structure;
- reinforced concrete joints;
- reinforced concrete floor slabs;
- masonry infill panels;
- foundations;
- isolation system;
- seismic gap.

### 6.3.1   Reinforced concrete members

The constraints imposed by the size of the buildings (six floors, 38 beams and 26 column members per floor, plus the staircase members, for more than 400 frame elements in the models) and the type of analysis carried out (multiple stripe analysis with 10 intensity levels and 20 ground motion records per stripe, that means, in total, 200 time history response analyses per case) called for pragmatic choices during modeling. Furthermore, all models had to be selected among those already implemented in the chosen analysis platforms (OpenSees and SAP2000), even though this was not a really serious limitation.

#### 6.3.1.1   Beam and column members

A lumped plasticity model was chosen for beam and column members. Considering that modeling choices concerning the structural (and non-structural) elements of the superstructure were derived from those previously adopted by WP4 (see Chapter 4 for all modeling details). Obviously, a beam grid was added to the aforementioned WP4 model, to simulate the real configuration of the base floor required for installing the isolation system.

#### 6.3.1.2   Staircases

The staircase structure comprises inclined beams and cantilever steps. The inclined beams are subjected to large-magnitude axial force variations. These forces have a projection on the horizontal axis that introduces large shear forces into the adjoining members. In order to limit these forces to values compatible with the inclined beam strength, the modelling adopted for the beam and column members needs to be modified.

An alternative approach, given the relatively small numbers of such elements, could be the use of the 'fiber-model', limited to these inclined beams. Numerical tests, however, showed that the introduction of these elements severely limits the overall computational robustness of the building model. For this reason, the phenomenological IMK model was kept but modified. In particular, the stiffness of the axial degree of freedom of the internal elastic BeamColumn element was reduced to zero, while putting an inelastic truss element in parallel. To the latter a non-symmetric elastic plastic constitutive law is assigned with limits proportional to $A_s f_y$ ($A_s$ being the total section reinforcement) in tension and $A_c f_c$ in compression, respectively.

#### 6.3.1.3   Joints

Joints were not modeled, as these components are prevented from failing based on capacity design prescriptions. In any case, internal joints are always confined on all six faces and are generally not modelled even in existing non-conforming buildings. Thus the choice of modelling without joints amounted to neglecting the (likely minor) flexibility contribution of perimeter joints

due to cracking in the elastic range. It is assumed that this is compensated by the choice of neglecting end-offsets for beam and column members.

## 6.3.2    Masonry infills

The contribution of the masonry infill panels to the response of the reinforced concrete frame is modeled by replacing the panel with an equivalent strut acting only in compression (Figure 6.3.1). The equivalent diagonal strut is a well-established engineering model for infilled frames and is described in Section 4.3.2 by WP4.



$\omega$ = strut width for solid infill
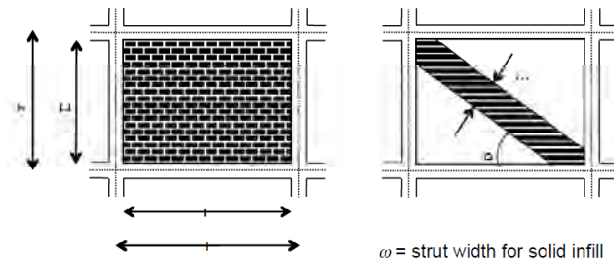
Figure 6.3.1 Diagonal strut model.

Among a wide range of different relationships that describe the parameters governing the monotonic and cyclic behavior of the diagonal strut, as a function of the mechanical and geometrical characteristics of masonry infill, the Decanini et al. model (Decanini et al. 2014) was adopted for the definition of the forces.

On the other hand, as suggested by Sassun et al. (2016), the median values of the fragility curves associated with different limit states were considered to define the displacement thresholds. It is worth noting that the third branch of the curve describes the post-peak strength deterioration of the infill that extends until reaching zero (Figure 6.3.2).
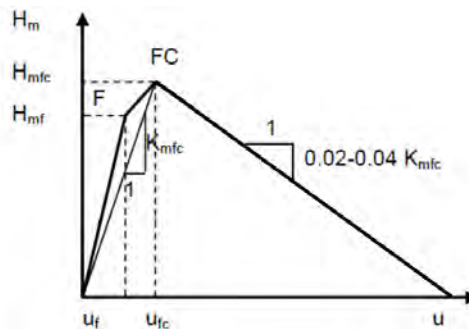


Figure 6.3.2 Backbone curve for the equivalent strut model.

The openings in the infill walls lead to significant uncertainty in the assessment of the seismic behavior of the structure due to the variability of their size and location. In general, the presence of openings results in a reduction of stiffness and ultimate strength of the panel. The presence of openings in the infills was taken into account by means of a simple model based on the use of reduction factors to be employed in the diagonal no-tension strut modelling approach (Decanini et al., 2014); Figure 6.3.4 shows the percentage of openings of the infill panels along the vertical planes at longitudinal (X) and transversal (Y) coordinates for each span, which is numbered from left to right and from bottom to top, respectively; correspondingly to Table 6.3.1, the infills along the vertical plane at the transverse distance from the lower left corner Y = 0m, for example, have 40% of openings (brown color) for span 1 and 5, 22% of openings (orange color) at for span 2

and 4, and 0% (red color) for span 3. The cyclic behavior is fully described in Liberatore 2001. The infills were modeled in Opensees using the Concrete01 uniaxial material (Figure 6.3.3).

Table 6.3.1 Masonry infill panels: strength values and percentage of openings adopted for the WP6 buildings in L'Aquila.

| Masonry | | | Infill panels IIX @ Y = 0m span # | | | | | Infill panels IIX @ Y=11.45m span # | | | | | Infill panels IIY: span # | | |
|---|---|---|---|---|---|---|---|---|---|---|---|---|---|---|---|
| $\sigma_m$ (kPa) | $\tau_m$ (kPa) | $\tau_g$ (kPa) | 1 | 2 | 3 | 4 | 5 | 1 | 2 | 3 | 4 | 5 | 1 | 2 | 3 |
| 6000 | 775 | 542 | 40.0 | 22.0 | 0.0 | 22.0 | 40.0 | 40.0 | 22.0 | 100.0 | 22.0 | 40.0 | 0.0 | 0.0 | 0.0 |
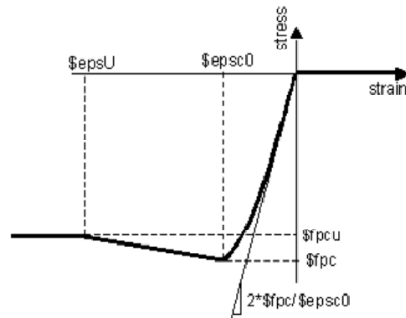


Figure 6.3.3 Adopted uniaxial constitutive law to approximate the strut backbone.
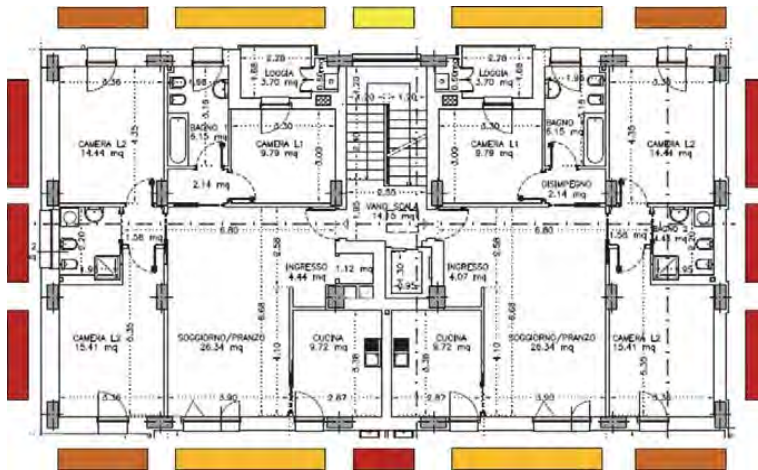


Figure 6.3.4 Masonry infill panels: percentage of openings (from 100% yellow to 0% red)

### 6.3.3    Foundations

The foundations were modeled as simple external restraints, owing to the capacity design that requires them to remain elastic and the traditional conservative design of foundations in Italy.

### 6.3.4    Isolation system

#### *HDRB devices*

In order to accurately predict the response of the isolated buildings, an accurate model was selected to describe the cyclic behavior of the HDRBs. The selected model is the one recently developed by Kumar et al. (2014) and implemented in Opensees as HDR Bearing Element. The physical model is considered as a two-node, twelve degrees-of-freedom discrete element. The two nodes are connected by six springs that represent the mechanical behavior in the six basic directions of a bearing. The degrees of freedom and discrete spring representation of an elastomeric bearing are shown in Figure 6.3.5.

The coupling of the two shear springs is considered directly by using a coupled bi-directional model. All other springs are uncoupled. The coupling of vertical and horizontal directions are considered indirectly by using expressions for mechanical properties in one direction that are dependent on the response parameters in the other direction. Linear uncoupled springs are considered in the torsion and the two rotational springs, as they are not expected to significantly affect the response of an elastomeric bearing.

The described discrete spring model has the advantages of easy implementation and being computationally efficient. The mechanical properties of the six springs are defined using analytical solutions available from the analysis of elastomeric bearings. The expression for mechanical properties, including stiffness and buckling load capacity, are derived using explicit consideration for geometric nonlinearity due to large displacement effects. The P-Delta effect, which is an approximate method to account for geometric nonlinearity in structural analysis problems, is therefore not considered. The material models in six directions are:

- Axial direction: a mathematical model that captures the behavior under cyclic tension proposed by Kumar et al. (2014)
- Two shear directions: a bidirectional model proposed by Grant et al. (2004)
- Torsion: a linear elastic model
- Two rotational directions: linear elastic models
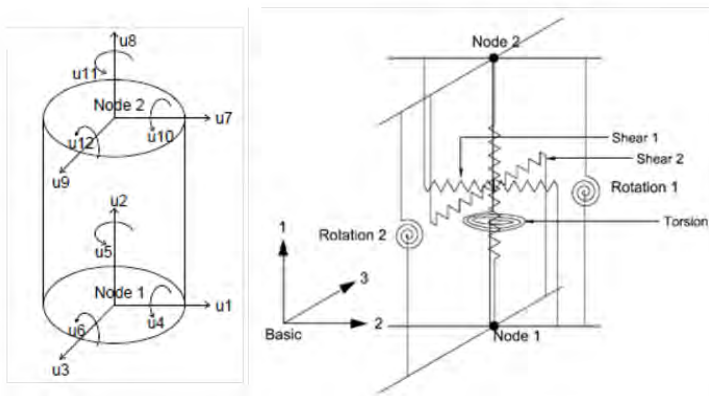


Figure 6.3.5 Degrees of freedom and discrete spring representation of an elastomeric bearing

In addition to the behavior captured by similar existing models implemented in Opensees, this element can capture the following:

- Degradation of bearing stiffness and damping due to scragging effects in shear
- Cavitation and post-cavitation behavior in tension
- Variation in critical buckling load capacity due to lateral displacement
- Variation in vertical axial stiffness with horizontal displacement

The limitation of the model, as implemented in Opensees, is that no variation in horizontal stiffness due to the axial load is taken into account.

*Cavitation phenomenon*: An elastomeric bearing under tensile loading is characterized by the occurrence of cavities in the volume of rubber.

The critical tensile strength, known as cavitation strength, mainly depends on the rubber composition. A significant decrease of the vertical stiffness is observed after the cavitation phenomenon.

Gent (1990) suggests that cavitation occurs at a negative pressure of about 3G, where G is the shear modulus. The cavitation force, $F_c$, is given by the following expression:

$$F_c = 3GA_0 \tag{6.8}$$

where:

- $A_0$ is the bonded rubber area;
- $G$ is the shear modulus of rubber obtained experimentally from the testing of elastomeric bearings at large shear deformation under nominal axial loads.

Most of the available mathematical models use a very small value of post-cavitation stiffness of an arbitrary magnitude. Constantinou et al. (2007) suggested a bilinear model and included cavitation strength and post-cavitation stiffness. The model ignores coupling of vertical stiffness and horizontal displacement in tensile loading. Tensile post-cavitation stiffness is given by:

$$k_{post-cavitation} = \frac{EA}{T_r} \tag{6.9}$$

where the modulus after cavitation takes the value of Young's modulus $E$ of rubber, as the state of stress in the rubber after cavitation reduces to that of uniaxial tension.

The load-deformation behavior of elastomeric bearings under cyclic tensile loading is illustrated in Figure 6.3.6.

It is worth noting that the cavitation strength of bearings decreases following the experience of large strains. Moreover, the history of loading plays an important role in the characteristics of the response. If the bearing experiences large tensile strains (and hence damage) early in the loading, the subsequent response of bearing will be primarily elastic. If the tensile strain increases incrementally during cyclic loading, damage and energy dissipation would be developed progressively.
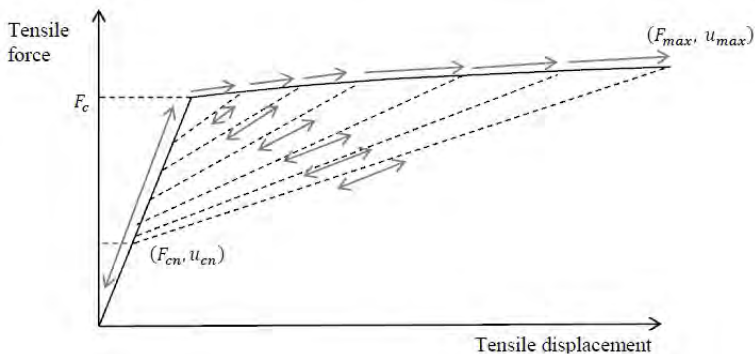


Figure 6.3.6 Deformation behavior of rubber bearings under tension

*Buckling phenomenon*: Buckling phenomenon can be described as an instability condition of the isolation device due to an axial load leading to a lateral deformed configuration until collapse.

The critical buckling load in compression is given by the following expression derived from the two-spring model approach (Koh and Kelly, 1987):

$$P_{cr} = \sqrt{P_s P_e} \tag{6.10}$$

where:

- $P_e = \frac{\pi^2 E I_s}{h^2}$;
- $P_s = G A_s$;
- $A_s = A\frac{h}{T_r}$, is the shear area of steel shims;
- $I_s = I\frac{h}{T_r}$, and moment of inertia of steel shims;
- $A$ is the bonded rubber area;
- $I$ is the area moment of inertia;
- $T_r$ is total rubber thickness;
- $h$ is the total height including the rubber and steel shims but excluding the end plates;
- $E = E_r$ the modulus of elasticity here is the rotation modulus. Rotation moduli and compression moduli of an incompressible material of circular and square bearings follow the relationship $E_r = \frac{E_c}{3}$, where $E_c$ is the compression modulus. For circular bearings rotation modulus is $E_r = 2GS^2$.

The critical buckling load varies with lateral displacement. The area reduction method was adopted to provide conservative results (Buckle and Liu, 1993; Buckle et al., 2002; Warn and Whittaker, 2006; Weisman and Warn, 2012). The reduced critical buckling load is given by:

$$P_{cr0} = P_{cr}\frac{A_r}{A} \tag{6.11}$$

where $A_r$ is the reduced area of a bearing with diameter D due to a lateral displacement $u_h$. For rectangular bearings of bonded area dimension $B_1 x B_2$, the reduced area is:

$$A_r = B_2(B_1 - \Delta) \tag{6.12}$$

For circular bearings of bonded area of diameter D, the reduced area is :

$$A_r = \frac{D^2}{4}(\delta - sin\delta) \tag{6.13}$$

where $\delta = 2cos^{-1}(\Delta/D)$ and $\Delta$ is the lateral displacement of the bearing (see Figure 6.3.7).
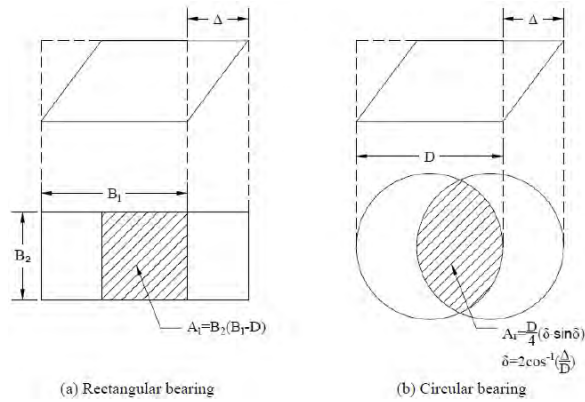
Figure 6.3.7 Reduced area of elastomeric bearings (adapted from Constantinou et al. (2007))

According to the area reduction method, a zero capacity is associated to an horizontal displacement equal to the bearing diameter (D). However, experimental tests showed a residual capacity of the bearing at displacement value equal to D. The model proposed by Warn and Whittaker (2006) was assumed in the present study. Such model is based on a linear approximation of the area reduction method and takes into account the finite buckling capacity of a bearing at zero overlap area. The piecewise linear approximation of the reduced area model is illustrated in Figure 6.3.8.



(a)                                                              (b)
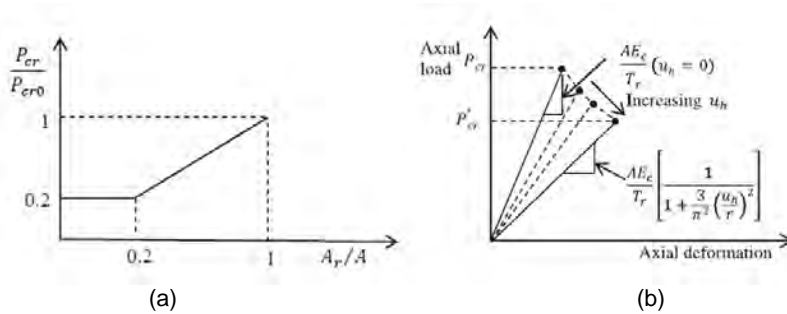
Figure 6.3.8 Bilinear variation of buckling load (a) and stress softening under compression (b)

At this point, once that the main axial failure modes was defined, the global mathematical model of an elastomeric bearing in the axial direction is constructed as presented in Figure 6.3.9. The model captures the following characteristics in the axial direction:

- Buckling in compression
- Coupling of vertical and horizontal motion
- Cavitation
- Post-cavitation variation
- Strength degradation due to cyclic loading

The model uses three unknown parameters:

1) a cavitation parameter, k;
2) a strength degradation parameter a;
3) a damage index, $\Phi_{max}$ .

Experimental tests are needed to determine the aforesaid parameters. As alternative, values referred to rubber bearings with similar properties could be adopted.
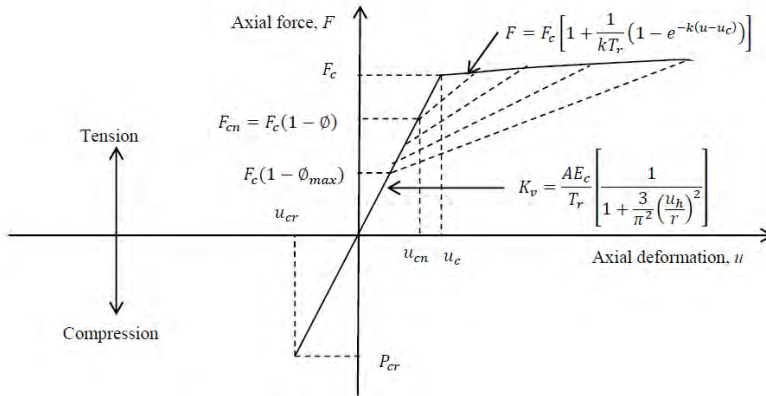
Figure 6.3.9 Global mathematical model of elastomeric bearings in axial direction

*Shear behavior*: The strain rate-independent bi-directional model proposed by Grant et al. (2004) was used to describe the behavior of HDR bearings in shear. This model is based on a simplified load-strain relationship and it can capture stiffness and damping degradation in HDR bearings due to short-term (Mullins') effect and long-term (scragging) effects (Figure 6.3.10) as well as the dependence of the hysteresis loops on the strain amplitude (Figure 6.3.11).

An iterative procedure was followed to calibrate the model parameters, based on the fitting of experimental tests carried out on real scale HDRBs (provided by UNIBAS) made by a soft rubber (G=0.4 MPa).The figures below show the comparison between the calibrated model (blue line) and the experimental data (red line) in terms of shear stress-strain relation. The first test was carried out up to a shear deformation equal to 1.5 on the virgin device (Figure 6.3.12-a), whereas the second is the repetition of the first test on the same devices (Figure 6.3.12-b) after a series of tests at larger strain (scragged device). Figure 6.3.13 reports three tests carried out up to large strains and their numerical simulation (blue line). The test result depicted with the yellow line was not considered for the calibration because the connection rupture occurred.
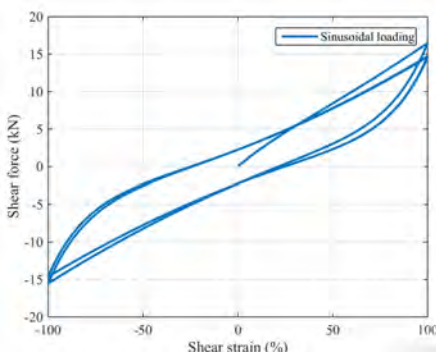


(a)
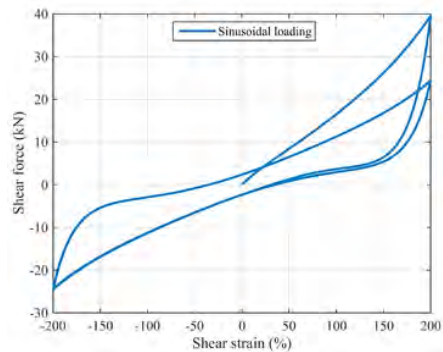
(b)

Figure 6.3.10 Global mathematical model of elastomeric bearings in shear accounting for the stress softening.
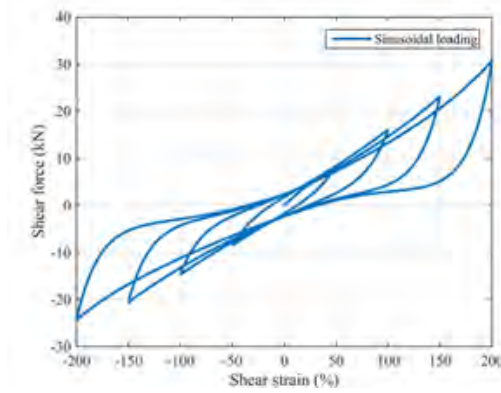
Figure 6.3.11 Dependence of the hysteresis loops on the strain amplitude



(a)                                                                                      (b)
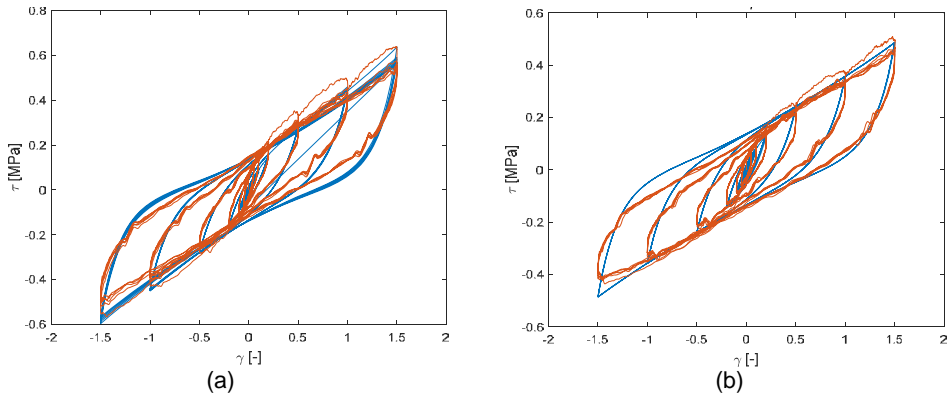
Figure 6.3.12 Cyclic shear test on the virgin (a) and scragged (b) device
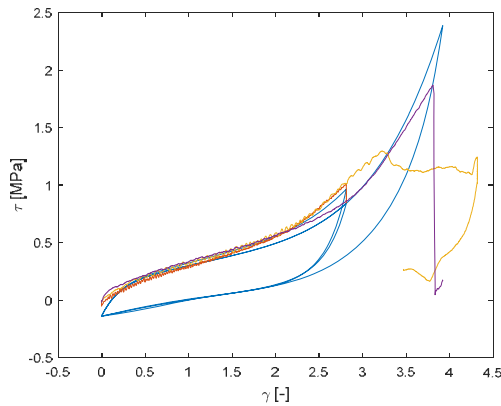


Figure 6.3.13 Shear tests up to large strains

The parameter obtained for the shear model are reported in Table 6.3.2 in terms of original rubber parameters used by Grant (first row) and modification factors. In particular, the second row of the table reports the parameters of the rubber of bearing used for the experimental tests, whose equivalent linear parameters at the third cycle are G=0.37 and ξ=0.137. In order to obtain the equivalent linear parameters used in the design (G=0.4 and ξ=0.15) the parameters was

modified as reported in the third row of the table. In the fourth row the parameters used in order to simulate the less dissipative rubber used in the design (G=0.4 and $\xi$=0.10) are reported. The differences between the two rubbers are illustrated by the cycles reported in Figure 6.3.14.

Table 6.3.2 Shear model parameters of the Grant model (first row and modification factors calibrated (first row) and adopted for the case with $\xi$=15% (second row) and the case with $\xi$=10% (third row)

| $\alpha_1$ | $\alpha_2$ | $\alpha_3$ | $\beta_1$ | $\beta_2$ | $\beta_3$ | $\xi_1$ | $\xi_2$ | $\xi_3$ | $\xi_4$ |
|---|---|---|---|---|---|---|---|---|---|
| 401.208 | 17.190 | 1.898 | 125.272 | 110.152 | 3.396 | 0.0099 | 0.0344 | 0.874 | 0.00005 |
| 0.65 | 1 | 1.9 | 1.1 | 0.7 | 1.5 | 1.3 | 2.5 | 0.95 | 1 |
| 0.688 | 1 | 1.9 | 1.36 | 0.7 | 1.5 | 1.3 | 2.5 | 0.95 | 1 |
| 0.785 | 1 | 1.9 | 0.8 | 0.7 | 1.5 | 1.3 | 2.5 | 0.95 | 1 |
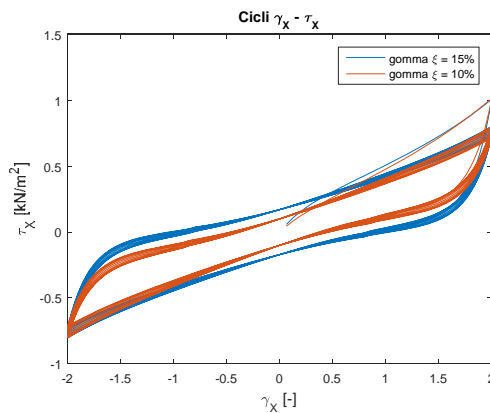


Figure 6.3.14 Shear behavior at the design shear strain of the two rubbers used in the design

Actually the Grant model has 10 parameters which define the behavior of the entire bearing ($a_1$, $a_2$, $a_3$ for the elastic component, $b_1$,$b_2$,$b_3$ for the inelastic component, $c_1$,$c_2$,$c_3$,$c_4$ for the damage). Thus, a procedure to converting rubber parameters to bearing parameters was developed, by implementing the following relations:

| a1 | a2 | a3 | b1 | b2 | b3 | c1 | c2 | c3 | c4 |
|---|---|---|---|---|---|---|---|---|---|
| $\alpha1*A/Tr$ | $\alpha2*A/Tr3$ | $\alpha3*A/Tr5$ | $\beta1*A$ | $\beta2*A/Tr2$ | $\beta 3/Tr$ | $\xi 1/Tr3$ | $\xi 2/Tr3$ | $\xi 3$ | $\xi 4/Tr3$ |

where A is the rubber area and $T_r$ is the total rubber thickness.

**Steel-PTFE sliders**

In order to reduce the computational and modeling effort, a simple truss element characterized by suitable axial stiffness values (depending on the coupled HDBR device) was used to model the Steel/PTFE sliders.

**FPS devices**

To describe the cyclic behavior of the DCSS, the selected model is the one implemented in OpenSees named *SingleFPBearing* element object (Figure 6.3.15).
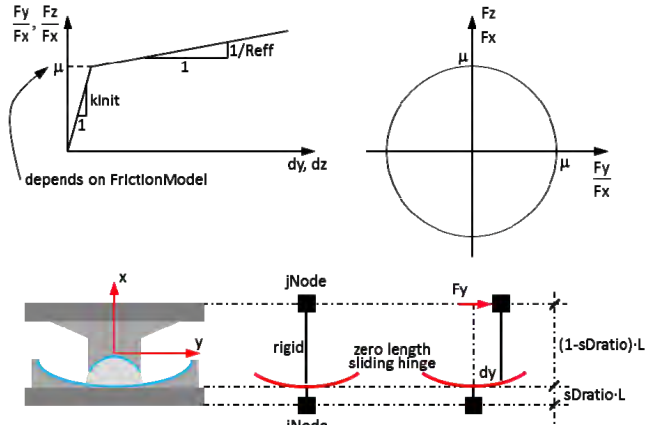
Figure 6.3.15 SingleFPBearing Element object as modelled in OpenSees.

This element is defined by two nodes with post-yield stiffening due to the concave sliding surface for the shear deformations. The adopted friction model defines the force-displacement behavior. In the axial direction, no-tension behavior is considered.

The coefficient of friction is modelled through the *Velocity and Normal Force Dependent Friction* command, which specifies the behavior of the coefficient of friction as a function of the absolute sliding velocity and the vertical load (Figure 6.3.16).

The vertical load, *N*; dependent value of the friction coefficient is evaluated through the model proposed by Bowden et al. (1964):

$$\mu = a \cdot N^{-b} \tag{6.14}$$

where *a*, and *b* are positive constants. The sliding velocity-dependent friction coefficient is evaluated through the model proposed by Constantinou et al. (1990):

$$\mu = \mu_{fast} - (\mu_{fast} - \mu_{slow}) \cdot e^{-r|v|} \tag{6.15}$$

where: *v* is the sliding velocity; $\mu_{fast}$ and $\mu_{slow}$ are the sliding coefficients of friction at fast and slow velocity; *r* is a constant value that controls the transition from $\mu_{slow}$ to $\mu_{fast}$.
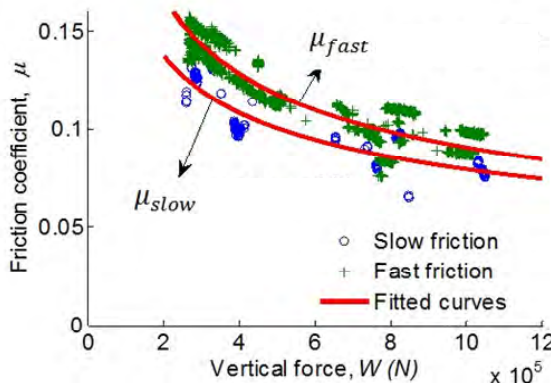


Figure 6.3.16 Velocity and Normal Force Dependent Friction model

The parameters of the friction model were defined on the basis of the following considerations:

- The vertical load dependent friction law is the same for both *slow* and *fast* velocity;
- The minimum value of the friction coefficient $\mu_{slow}$ is imposed equal to the nominal value declared by the manufacturer $\mu_{nom} = 2.5\%$ and referred to the maximum vertical seismic load $N_{Ed} = 1500kN$;
- The value of the friction coefficient at fast velocities is imposed as $\mu_{fast} = 2 \times \mu_{slow} = 5.0\%$

The values of the other parameters are listed in Table 6.3.3, which was obtained from several experimental tests performed at SisLab on full-size Double CSS and Single CSS, according to NTC2008 and EN15129 (CEN, 2009) provisions.

Table 6.3.3 Model parameters for SingleFPBearing element and friction model

| $R_e^*$ | $K_i$ | $\mu_{slow}$ | $\mu_{fast}$ | $a_{slow}$ | $a_{fast}$ | b | r |
|---|---|---|---|---|---|---|---|
| [mm] | [kN/m] | [-] | [-] | [-] | [-] | [-] | [s/m] |
| **Naples - 2500 L'Aquila - 3700** | 5000 | 0.025 | 0.050 | 62.34 | 124.68 | 0.45 | 5.0 |

### 6.3.5  Seismic gap

The "Elastic-Perfectly Plastic Gap Material" consisting of an initial gap and an elastic-perfectly plastic element is used to model the seismic gap in Opensees. This model is not dissipative during the impact and becomes dissipative only after the elastic limit (Fy) is exceeded (see Figure 6.3.17).
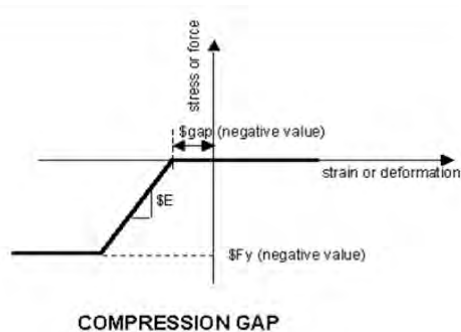


Figure 6.3.17 Opensees Modeling for seismic gap: "Elastic-Perfectly Plastic Gap Material"

In order to determine the gap model parameters some hypotheses were assumed. Firstly, it was assumed that the impact occurs between a rigid retain wall and a deformable base slab (see Figure 6.3.18); then, the presence of two Zero-Length gap elements (one in X direction and the other in Y direction) for each corner of the base slab was assumed. It is important to highlight that by this way, conservatively, the dissipation during the impact as well as the dissipation due to longitudinal friction were neglected.
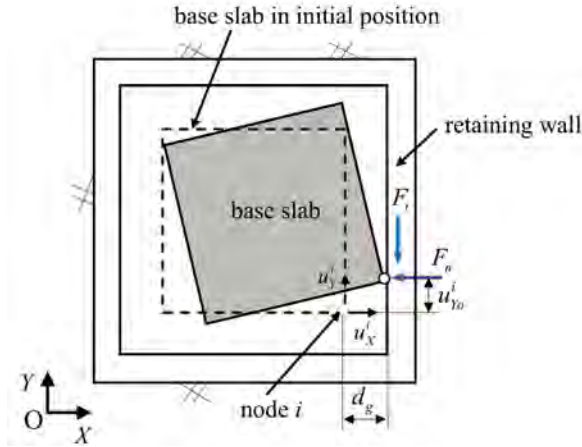
Figure 6.3.18 Representation of the main parameters and elements considered

Being in the building modeled in Opensees the base slab rigid (a rigid constrain was imposed) the elastic stiffness of the gap model has to be calculated as the axial stiffness of the slab portion involved in the impact. By assuming the most conservative case, where the impact occurs without rotation of the building (which only translate) half slab width was considered for each gap element. Similarly, the limit elastic force was assumed equal the axial strength of the half slab width. Thus, the following formulas were used to calculate the model stiffness ($E$) and elastic limit force ($F_y$) in the X and Y directions:

$$E_x = \frac{L_y}{2} E_c \frac{s}{L_x} \tag{6.16}$$

$$E_y = \frac{L_x}{2} E_c \frac{s}{L_y} \tag{6.17}$$

$$F_{y,x} = \frac{L_y}{2} f_{cm} s \tag{6.18}$$

$$F_{y,x} = \frac{L_x}{2} f_{cm} s \tag{6.19}$$

where $L_x$ and $L_y$ are the slab dimensions equal to 24.05 m and 11.45 m respectively; $s$ is the slab thickness equal to 0.20 m and $E_c$ and $f_{cm}$ are the concrete modulus and compression strength assumed equal to 32620 N/mm$^2$ and 37.17 N/mm$^2$ respectively. Results are reported in Table 6.3.4.

Table 6.3.4 Parameters of gap models in X and Y directions

| $E_x$ | $E_y$ | $F_{y,x}$ | $F_{y,y}$ |
|---|---|---|---|
| (kN/mm) | (kN/mm) | kN | kN |
| 1553 | 6852 | 42561 | 89397 |

Finally, despite the NTC2008 code imposes that gap dimension should be larger than the isolation system displacement evaluated at the Collapse Limit state, in this project the amplitude

of the gap was assumed equal to or larger than the isolation system displacement capacity, in accordance with the most common practice.

## 6.4   Model uncertainty

### 6.4.1   RC members and masonry infills uncertainty

The multi-variate statistical model of the structure-related uncertainty is developed with reference to reinforced concrete buildings, describing the variability of material properties as well as model error terms of the adopted response model for both RC member and masonry infills. See Chapter 4 for all details.

### 6.4.2   Isolation system uncertainty

A statistical model is developed to evaluate model uncertainties of isolation devices due to the factory production tolerance agreed from the code (EN15129 - NTC) on a set of laboratory tests. The chosen model is called ANOVA models II, in which the population is divided in several classes and each class has random means but the same variance. In this way there are a variability inside each stocks (intra-stocks variability or within-stocks variability) and variability between each different stock (inter-stock variability or between-stock variability). Starting from means and variances of each stocks parameters the statistical model is defined as shown hereafter.The total mean is the weighted mean of the stocks means:

$$\overline{y_.} = \sum_{i=1}^{k} \frac{n_i}{n} \overline{y_i}$$

where $\overline{y_i}$ is the mean of the $i$-stock , $n_i$ is the number of isolators of the $i$-stock, $n$ is the total number of isolators and $k$ is the number of stocks. This model is modified simulating the factory production control tests and then is used to generate the isolators stocks for the varied analysis models. Other sources of variability (such as temperature and aging) were not considered in this work.This model is then modified simulating the factory production control tests and then used to generate the isolators stocks for the varied analysis models. Other sources of variability (such as temperature and aging) were not considered in this work .

Table 6.4.1 summarizes the formulas to define the intra-stocks variance ($\sigma_W^2$) and the inter-stock variance ($\sigma_B^2$), in which $s_i^2$ is the variance of the sample of the single stock and $n'$ takes into account the unequal isolator sample size of the stocks as

$$n' = \frac{1}{n-1} \left[ \sum_{i=1}^{k} n_i - \sum_{i=1}^{k} n_i^2 \Big/ \sum_{i=1}^{k} n_i \right]$$

The total variance is the sum of the intra-stock variance and the inert-stock variance

$$\sigma_T^2 = \sigma_W^2 + \sigma_B^2$$

and the intra-class correlation (or intra-stock correlation) can be estimated using

$$IC = \frac{MS_B - MS_W}{MS_B + (n'-1)MS_W} \qquad \text{from} \qquad \left( IC = \frac{\sigma_B^2}{\sigma_W^2 + \sigma_B^2} = 1 - \frac{\sigma_W^2}{\sigma_T^2} \right)$$

This model is then modified simulating the factory production control tests and then used to generate the isolators stocks for the varied analysis models. Other sources of variability (such as temperature and aging) were not considered in this work .

Table 6.4.1 ANOVA table.

|  | Sum of Squares | Degrees of freedom | Mean Squares | E(MS) |
|---|---|---|---|---|
| Between class | $SS_B = \sum_{i=1}^{k} n_i \left( \overline{y}_i - \overline{y} \right)^2$ | $k-1$ | $MS_B = \dfrac{SS_B}{k-1}$ | $\sigma_W^2 + n' \sigma_B^2$ |
| Within class | $SS_W = \sum_{i=1}^{k} \sum_{j=1}^{n_i} n_i \left( y_{ij} - \overline{y}_i \right)^2$ | $\sum_{i=1}^{k} \left( n_i - 1 \right)$ | $MS_W = \dfrac{SS_W}{\sum_{i=1}^{k} \left( n_i - 1 \right)}$ | $\sigma_W^2$ |

### 6.4.2.1   HDBR devices

A sample of 113 specimens divided into 30 stocks with different number of isolator devices (from 2 to 8 devices per stock) of soft rubber with nominal values of G=0.4 N/mm$^2$ (shear stiffness) and ξ=15% (damping coefficient) at design deformation was used to evaluate the uncertainty affecting the HDBR isolator properties. In particular, the available data are mean values and standard deviations of G and ξ for each stock, related to tests made at 100% of deformation. The following elaborations were made:

1. The correlation index between mean values of G and ξ related to the same stock was calculated in order to evaluate the correlation between these two quantities. The correlation index calculated, is very small (equal to 0.27), thus in the sampling procedure a lack of correlation between G and ξ was assumed.

2. The mean value of G and ξ of each stock were corrected because nominal values given from the supplier refer to a design deformation ranging between 130% and 150% and so different from that one at which the tests were performed (equal to 100%). The mean values obtained are $\bar{G}$=0.41MPa and $\bar{\xi}$=15.6% and they are very close to nominal values given from the supplier. Consequently, in the sampling procedure mean values were directly assumed equal to the nominal values.

3. ANOVA model has been calculated and the sampling procedure for G and ξ was set up with the nominal parameters.

In Table 6.4.2 parameters of the statistical model adopted in the sampling procedure for G and ξ are reported. After the samples generation, due to the big number of specimens of G and ξ resulting not to be included in the allowed limits imposed by the Code (±20% of the nominal values), the procedure was modified simulating the factory production control test. In particular, the control test consists on extracting randomly 20% of the isolation devices for one stock (5 on 24 or 4 on 16) and on rejecting the stock generated from the procedure if one of the isolation device parameter is out of the limits given from the code. It is important to highlight that the total dispersion decreases after the check (see Figure 6.4.1) and that it is possible to have some stocks with isolation devices that have outranged parameters, due to a non-extraction.

Table 6.4.3, Table 6.4.4, Table 6.4.5 and Table 6.4.6 report the results of the sampling procedure for G and ξ  for the total rubber (24x20) and hybrid (16x20) isolation systems, respectively, and the orange color means that the parameter is out of the acceptance range.

Table 6.4.2 Calculated parameters.

| | $\mu_T$ [MPa] | $CV_T$ | $\sigma_T$ [MPa] | $\sigma_B$ [MPa] | $CV_W$ | $\sigma_W$ [MPa] | IC |
|---|---|---|---|---|---|---|---|
| G | 0.4 | 9% | 0.036 | 0.0332 | 3.49% | 0.0139 | 0.85 |
| $\xi$ | 0.15 | 7% | 0.0105 | 0.0097 | 2.71% | 0.0041 | 0.85 |
| | 0.10 | 7% | 0.007 | 0.065 | 2.71% | 0.0027 | 0.85 |

(a)  (b)
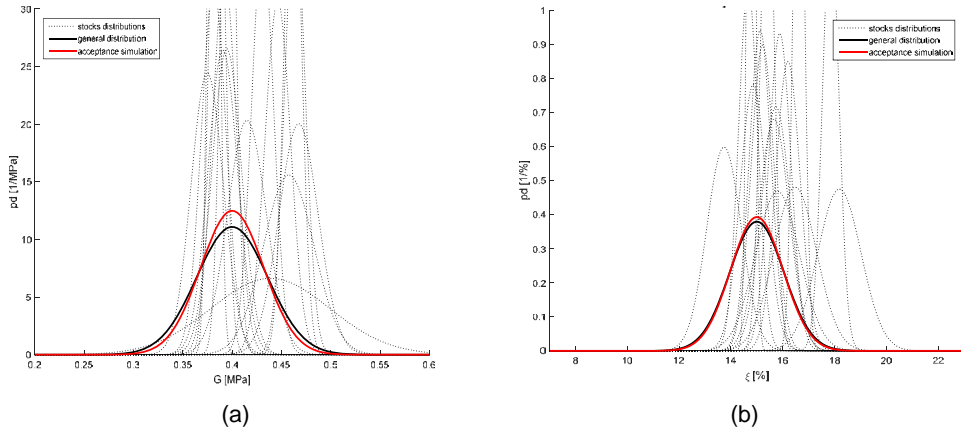
Figure 6.4.1 Distribution of the stocks (dot lines) and resulting distributio of the all speciments without (black curve) and with (red curve) the acceptance criteria, for (a) the parameter G and (b) the parameter ξ.

Table 6.4.3 Values for G for HDRB typology (24x20).

**G [MPa] — ISOLATION DEVICES**

| STOCKS | 1 | 2 | 3 | 4 | 5 | 6 | 7 | 8 | 9 | 10 | 11 | 12 | 13 | 14 | 15 | 16 | 17 | 18 | 19 | 20 | 21 | 22 | 23 | 24 |
|---|---|---|---|---|---|---|---|---|---|---|---|---|---|---|---|---|---|---|---|---|---|---|---|---|
| 1 | 0,400 | 0,384 | 0,397 | 0,401 | 0,408 | 0,415 | 0,412 | 0,398 | 0,409 | 0,389 | 0,403 | 0,400 | 0,422 | 0,405 | 0,415 | 0,406 | 0,389 | 0,389 | 0,391 | 0,381 | 0,398 | 0,388 | | |
| 2 | 0,431 | 0,438 | 0,432 | 0,417 | 0,422 | 0,416 | 0,428 | 0,429 | 0,429 | 0,427 | 0,407 | 0,438 | 0,419 | 0,447 | 0,414 | 0,445 | 0,396 | 0,415 | 0,432 | 0,416 | 0,424 | 0,422 | 0,427 | 0,436 |
| 3 | 0,385 | 0,394 | 0,403 | 0,391 | 0,420 | 0,370 | 0,429 | 0,398 | 0,423 | 0,385 | 0,404 | 0,387 | 0,422 | 0,423 | 0,420 | 0,396 | 0,376 | 0,384 | 0,396 | 0,401 | 0,409 | 0,404 | 0,414 | 0,405 |
| 4 | 0,403 | 0,403 | 0,410 | 0,392 | 0,381 | 0,404 | 0,394 | 0,396 | 0,426 | 0,388 | 0,401 | 0,386 | 0,392 | 0,405 | 0,400 | 0,384 | 0,417 | 0,385 | 0,431 | 0,411 | 0,384 | 0,408 | 0,421 | 0,422 |
| 5 | 0,409 | 0,427 | 0,412 | 0,418 | 0,398 | 0,408 | 0,422 | 0,426 | 0,432 | 0,414 | 0,434 | 0,391 | 0,434 | 0,432 | 0,411 | 0,407 | 0,410 | 0,421 | 0,416 | 0,424 | 0,412 | 0,418 | 0,398 | 0,419 |
| 6 | 0,437 | 0,464 | 0,450 | 0,430 | 0,451 | 0,405 | **0,484** | 0,439 | 0,416 | 0,431 | 0,413 | 0,438 | 0,427 | 0,444 | 0,434 | 0,418 | 0,421 | 0,435 | 0,465 | 0,412 | 0,431 | 0,424 | 0,419 | |
| 7 | 0,452 | 0,437 | 0,436 | 0,460 | 0,443 | 0,430 | 0,453 | 0,443 | 0,442 | 0,444 | 0,446 | 0,452 | 0,411 | 0,435 | 0,451 | 0,415 | 0,449 | 0,468 | 0,433 | 0,443 | 0,426 | 0,455 | 0,431 | 0,442 |
| 8 | 0,391 | 0,398 | 0,415 | 0,408 | 0,424 | 0,397 | 0,403 | 0,432 | 0,416 | 0,423 | 0,388 | 0,422 | 0,419 | 0,442 | 0,411 | 0,413 | 0,404 | 0,403 | 0,421 | 0,409 | 0,426 | 0,399 | 0,422 | 0,408 |
| 9 | 0,378 | 0,367 | 0,376 | 0,387 | 0,386 | 0,378 | 0,383 | 0,374 | 0,390 | 0,376 | 0,369 | 0,350 | 0,384 | 0,366 | 0,385 | 0,373 | 0,393 | 0,377 | 0,395 | 0,385 | 0,368 | 0,385 | 0,381 | 0,374 |
| 10 | 0,405 | 0,421 | 0,444 | 0,430 | 0,439 | 0,427 | 0,438 | 0,436 | 0,435 | 0,429 | 0,418 | 0,449 | 0,431 | 0,447 | 0,429 | 0,419 | 0,441 | 0,398 | 0,441 | 0,420 | 0,422 | 0,441 | 0,434 | 0,416 |
| 11 | 0,430 | 0,442 | 0,433 | 0,450 | 0,455 | 0,430 | 0,471 | 0,447 | 0,441 | 0,445 | 0,440 | 0,429 | 0,451 | 0,464 | 0,437 | 0,457 | 0,434 | 0,436 | 0,479 | 0,448 | 0,460 | 0,435 | 0,461 | 0,447 |
| 12 | 0,381 | 0,376 | 0,360 | 0,367 | 0,375 | 0,370 | 0,355 | 0,370 | 0,368 | 0,382 | 0,407 | 0,363 | 0,373 | 0,387 | 0,392 | 0,385 | 0,363 | 0,385 | 0,375 | 0,387 | 0,367 | 0,398 | 0,377 | 0,371 |
| 13 | 0,431 | 0,425 | 0,427 | 0,446 | 0,421 | 0,416 | 0,428 | 0,422 | 0,428 | 0,457 | 0,427 | 0,408 | 0,401 | 0,448 | 0,430 | 0,417 | 0,441 | 0,437 | 0,407 | 0,415 | 0,441 | 0,415 | 0,443 | 0,424 |
| 14 | 0,385 | 0,403 | 0,403 | 0,412 | 0,439 | 0,394 | 0,429 | 0,395 | 0,379 | 0,415 | 0,395 | 0,419 | 0,392 | 0,408 | 0,398 | 0,412 | 0,388 | 0,379 | 0,408 | 0,410 | 0,414 | 0,421 | 0,394 | |
| 15 | 0,355 | 0,344 | 0,355 | 0,344 | 0,341 | 0,345 | 0,335 | 0,363 | **0,319** | 0,350 | 0,357 | 0,345 | 0,359 | 0,336 | 0,330 | 0,342 | 0,330 | 0,347 | 0,347 | 0,344 | 0,364 | 0,361 | 0,374 | 0,341 |
| 16 | 0,422 | 0,404 | 0,423 | 0,411 | 0,429 | 0,404 | 0,428 | 0,436 | 0,419 | 0,441 | 0,403 | 0,406 | 0,420 | 0,419 | 0,394 | 0,427 | 0,439 | 0,390 | 0,405 | 0,421 | 0,423 | 0,432 | 0,395 | 0,425 |
| 17 | 0,413 | 0,394 | 0,398 | 0,402 | 0,391 | 0,408 | 0,400 | 0,385 | 0,418 | 0,421 | 0,414 | 0,410 | 0,394 | 0,402 | 0,427 | 0,425 | 0,397 | 0,407 | 0,397 | 0,408 | 0,376 | 0,391 | 0,407 | 0,400 |
| 18 | 0,390 | 0,402 | 0,416 | 0,399 | 0,413 | 0,400 | 0,424 | 0,396 | 0,391 | 0,410 | 0,408 | 0,409 | 0,426 | 0,409 | 0,403 | 0,419 | 0,392 | 0,403 | 0,409 | 0,420 | 0,402 | 0,433 | 0,410 | |
| 19 | 0,473 | 0,454 | 0,450 | 0,453 | 0,446 | 0,443 | 0,447 | 0,465 | **0,483** | 0,463 | **0,512** | 0,450 | **0,483** | 0,450 | 0,451 | 0,470 | 0,475 | 0,478 | 0,461 | 0,476 | 0,473 | 0,470 | **0,506** | 0,462 |
| 20 | 0,407 | 0,420 | 0,392 | 0,428 | 0,429 | 0,393 | 0,417 | 0,417 | 0,411 | 0,416 | 0,426 | 0,406 | 0,418 | 0,425 | 0,401 | 0,393 | 0,400 | 0,402 | 0,412 | 0,386 | 0,400 | 0,406 | 0,400 | 0,427 |

Table 6.4.4 Values for ξ for HDRBs typology (24x20).

**ξ [-] — ISOLATION DEVICES**

| STOCKS | 1 | 2 | 3 | 4 | 5 | 6 | 7 | 8 | 9 | 10 | 11 | 12 | 13 | 14 | 15 | 16 | 17 | 18 | 19 | 20 | 21 | 22 | 23 | 24 |
|---|---|---|---|---|---|---|---|---|---|---|---|---|---|---|---|---|---|---|---|---|---|---|---|---|
| 1 | 0,150 | 0,149 | 0,143 | 0,145 | 0,147 | 0,143 | 0,142 | 0,153 | 0,152 | 0,144 | 0,144 | 0,148 | 0,143 | 0,145 | 0,145 | 0,147 | 0,148 | 0,145 | 0,153 | 0,146 | 0,141 | 0,143 | 0,140 | 0,147 |
| 2 | 0,168 | 0,175 | 0,180 | 0,166 | 0,177 | 0,173 | 0,167 | 0,167 | 0,170 | 0,175 | 0,172 | 0,170 | 0,169 | 0,164 | 0,176 | 0,167 | 0,169 | 0,164 | 0,168 | 0,178 | 0,176 | 0,170 | **0,185** | 0,172 |
| 3 | 0,132 | 0,143 | 0,135 | 0,142 | 0,138 | 0,141 | 0,142 | 0,143 | 0,142 | 0,136 | 0,135 | 0,142 | 0,141 | 0,138 | 0,136 | 0,141 | 0,144 | 0,140 | 0,140 | 0,137 | 0,144 | 0,142 | 0,139 | 0,139 |
| 4 | 0,138 | 0,144 | 0,147 | 0,148 | 0,145 | 0,145 | 0,148 | 0,142 | 0,139 | 0,148 | 0,144 | 0,144 | 0,150 | 0,144 | 0,143 | 0,144 | 0,146 | 0,143 | 0,148 | 0,147 | 0,147 | 0,149 | 0,151 | 0,147 |
| 5 | 0,147 | 0,150 | 0,148 | 0,145 | 0,145 | 0,149 | 0,151 | 0,150 | 0,149 | 0,144 | 0,147 | 0,154 | 0,151 | 0,147 | 0,149 | 0,146 | 0,150 | 0,157 | 0,146 | 0,150 | 0,155 | 0,142 | 0,149 | 0,153 |
| 6 | 0,161 | 0,154 | 0,157 | 0,160 | 0,163 | 0,167 | 0,163 | 0,165 | 0,160 | 0,165 | 0,163 | 0,161 | 0,166 | 0,165 | 0,161 | 0,165 | 0,163 | 0,163 | 0,167 | 0,166 | 0,162 | 0,162 | 0,159 | 0,164 |
| 7 | 0,162 | 0,155 | 0,161 | 0,163 | 0,156 | 0,155 | 0,163 | 0,159 | 0,168 | 0,166 | 0,166 | 0,157 | 0,157 | 0,155 | 0,158 | 0,155 | 0,159 | 0,159 | 0,155 | 0,147 | 0,154 | 0,154 | 0,156 | 0,164 |
| 8 | 0,140 | 0,127 | 0,131 | 0,138 | 0,132 | 0,128 | 0,138 | 0,135 | 0,132 | 0,137 | 0,132 | 0,135 | 0,140 | 0,135 | 0,136 | 0,133 | 0,131 | 0,127 | 0,129 | 0,138 | 0,133 | 0,137 | 0,128 | 0,126 |
| 9 | 0,160 | 0,164 | 0,164 | 0,158 | 0,155 | 0,160 | 0,158 | 0,163 | 0,161 | 0,168 | 0,160 | 0,159 | 0,161 | 0,158 | 0,162 | 0,169 | 0,159 | 0,159 | 0,169 | 0,154 | 0,157 | 0,164 | 0,157 | 0,172 |
| 10 | 0,160 | 0,171 | 0,164 | 0,150 | 0,165 | 0,158 | 0,161 | 0,159 | 0,161 | 0,167 | 0,160 | 0,162 | 0,168 | 0,159 | 0,164 | 0,161 | 0,159 | 0,156 | 0,166 | 0,155 | 0,158 | 0,157 | 0,154 | 0,160 |
| 11 | 0,147 | 0,146 | 0,142 | 0,143 | 0,135 | 0,145 | 0,139 | 0,143 | 0,136 | 0,140 | 0,140 | 0,143 | 0,136 | 0,141 | 0,144 | 0,139 | 0,143 | 0,142 | 0,144 | 0,144 | 0,145 | 0,142 | 0,140 | 0,142 |
| 12 | 0,163 | 0,173 | 0,167 | 0,156 | 0,168 | 0,160 | 0,160 | 0,169 | 0,159 | 0,165 | 0,162 | 0,162 | 0,167 | 0,164 | 0,162 | 0,171 | 0,159 | 0,159 | 0,166 | 0,162 | 0,165 | 0,161 | 0,159 | 0,160 |
| 13 | 0,153 | 0,141 | 0,139 | 0,146 | 0,145 | 0,148 | 0,143 | 0,150 | 0,145 | 0,145 | 0,145 | 0,143 | 0,147 | 0,142 | 0,145 | 0,145 | 0,146 | 0,145 | 0,140 | 0,146 | 0,141 | 0,142 | 0,144 | 0,150 |
| 14 | 0,154 | 0,159 | 0,151 | 0,150 | 0,151 | 0,151 | 0,151 | 0,150 | 0,150 | 0,149 | 0,145 | 0,145 | 0,145 | 0,143 | 0,144 | 0,148 | 0,151 | 0,151 | 0,143 | 0,148 | 0,143 | 0,152 | | |
| 15 | 0,137 | 0,136 | 0,127 | 0,136 | 0,135 | 0,137 | 0,134 | 0,139 | 0,137 | 0,142 | 0,130 | 0,139 | 0,136 | 0,129 | 0,132 | 0,134 | 0,134 | 0,143 | 0,136 | 0,134 | 0,137 | 0,142 | 0,140 | 0,129 |
| 16 | 0,153 | 0,153 | 0,145 | 0,144 | 0,146 | 0,142 | 0,149 | 0,150 | 0,152 | 0,156 | 0,146 | 0,151 | 0,148 | 0,148 | 0,151 | 0,146 | 0,148 | 0,151 | 0,149 | 0,146 | 0,142 | 0,142 | 0,146 | 0,146 |
| 17 | 0,147 | 0,144 | 0,143 | 0,142 | 0,139 | 0,139 | 0,135 | 0,147 | 0,142 | 0,140 | 0,136 | 0,141 | 0,138 | 0,143 | 0,134 | 0,141 | 0,143 | 0,135 | 0,137 | 0,134 | 0,145 | 0,139 | 0,140 | 0,136 |
| 18 | 0,143 | 0,141 | 0,142 | 0,143 | 0,141 | 0,139 | 0,143 | 0,138 | 0,139 | 0,132 | 0,142 | 0,139 | 0,139 | 0,131 | 0,145 | 0,141 | 0,144 | 0,139 | 0,146 | 0,143 | 0,136 | 0,137 | 0,137 | 0,140 |
| 19 | 0,135 | 0,135 | 0,142 | 0,132 | 0,134 | 0,136 | 0,130 | 0,140 | 0,134 | 0,143 | 0,138 | 0,132 | 0,139 | 0,128 | 0,137 | 0,137 | 0,136 | 0,135 | 0,129 | 0,140 | 0,133 | 0,138 | 0,130 | 0,131 |
| 20 | 0,156 | 0,153 | 0,153 | 0,152 | 0,154 | 0,157 | 0,159 | 0,161 | 0,152 | 0,160 | 0,149 | 0,157 | 0,154 | 0,156 | 0,158 | 0,152 | 0,163 | 0,159 | 0,154 | 0,157 | 0,162 | 0,159 | 0,154 | 0,162 |

Table 6.4.5 Values for G for HDRBs+FSB typology (16x20).

| G [MPA] | | ISOLATION DEVICES | | | | | | | | | | | | | | |
|---|---|---|---|---|---|---|---|---|---|---|---|---|---|---|---|---|
| | | 1 | 2 | 3 | 4 | 5 | 6 | 7 | 8 | 9 | 10 | 11 | 12 | 13 | 14 | 15 | 16 |
| | 1 | 0,372 | 0,401 | 0,402 | 0,402 | 0,403 | 0,393 | 0,401 | 0,402 | 0,388 | 0,409 | 0,394 | 0,388 | 0,395 | 0,398 | 0,390 | 0,397 |
| | 2 | 0,373 | 0,394 | 0,389 | 0,385 | 0,367 | 0,368 | 0,400 | 0,389 | 0,369 | 0,391 | 0,380 | 0,363 | 0,397 | 0,365 | 0,373 | 0,393 |
| | 3 | 0,376 | 0,374 | 0,372 | 0,369 | 0,392 | 0,378 | 0,355 | 0,412 | 0,382 | 0,364 | 0,400 | 0,373 | 0,353 | 0,371 | 0,371 | 0,361 |
| | 4 | 0,414 | 0,414 | 0,415 | 0,400 | 0,407 | 0,412 | 0,406 | 0,377 | 0,385 | 0,411 | 0,431 | 0,402 | 0,413 | 0,418 | 0,415 | 0,397 |
| | 5 | 0,375 | 0,393 | 0,385 | 0,443 | 0,375 | 0,403 | 0,436 | 0,405 | 0,386 | 0,393 | 0,408 | 0,426 | 0,404 | 0,419 | 0,413 | 0,398 |
| | 6 | 0,384 | 0,379 | 0,344 | 0,398 | 0,390 | 0,382 | 0,381 | 0,375 | 0,373 | 0,415 | 0,384 | 0,401 | 0,361 | 0,367 | 0,396 | 0,415 |
| S | 7 | 0,372 | 0,377 | 0,365 | 0,391 | 0,384 | 0,391 | 0,387 | 0,369 | 0,381 | 0,384 | 0,386 | 0,385 | 0,371 | 0,400 | 0,409 | 0,380 |
| T | 8 | 0,418 | 0,442 | 0,424 | 0,438 | 0,413 | 0,424 | 0,410 | 0,436 | 0,451 | 0,407 | 0,425 | 0,446 | 0,401 | 0,444 | 0,407 | 0,401 |
| O | 9 | 0,388 | 0,407 | 0,420 | 0,398 | 0,427 | 0,415 | 0,420 | 0,419 | 0,429 | 0,423 | 0,401 | 0,437 | 0,410 | 0,410 | 0,412 | 0,421 |
| C | 10 | 0,407 | 0,382 | 0,405 | 0,404 | 0,392 | 0,388 | 0,433 | 0,411 | 0,423 | 0,407 | 0,412 | 0,405 | 0,396 | 0,446 | 0,416 | 0,423 |
| K | 11 | 0,427 | 0,437 | 0,429 | 0,416 | 0,426 | 0,412 | 0,422 | 0,443 | 0,434 | 0,412 | 0,420 | 0,446 | 0,440 | 0,432 | 0,444 | 0,443 |
| S | 12 | 0,364 | 0,378 | 0,370 | 0,380 | 0,390 | 0,373 | 0,383 | 0,385 | 0,371 | 0,386 | 0,386 | 0,385 | 0,376 | 0,367 | 0,368 | 0,379 |
| | 13 | 0,447 | 0,433 | 0,432 | 0,396 | 0,422 | 0,413 | 0,413 | 0,431 | 0,462 | 0,428 | 0,424 | 0,400 | 0,436 | 0,433 | 0,443 | 0,394 |
| | 14 | 0,441 | 0,419 | 0,423 | 0,433 | 0,430 | 0,429 | 0,406 | 0,440 | 0,452 | 0,423 | 0,425 | 0,441 | 0,437 | 0,445 | 0,419 | 0,434 |
| | 15 | 0,480 | 0,477 | 0,457 | 0,452 | 0,464 | 0,423 | 0,477 | 0,460 | 0,436 | 0,442 | 0,449 | 0,424 | 0,461 | 0,477 | 0,439 | 0,454 |
| | 16 | 0,372 | 0,380 | 0,409 | 0,386 | 0,388 | 0,394 | 0,377 | 0,415 | 0,376 | 0,381 | 0,394 | 0,380 | 0,369 | 0,367 | 0,370 | 0,380 |
| | 17 | 0,345 | 0,329 | 0,323 | 0,326 | 0,308 | 0,354 | 0,326 | 0,326 | 0,320 | 0,329 | 0,307 | 0,325 | 0,342 | 0,333 | 0,330 | 0,323 |
| | 18 | 0,385 | 0,394 | 0,406 | 0,385 | 0,392 | 0,372 | 0,409 | 0,383 | 0,387 | 0,392 | 0,392 | 0,385 | 0,386 | 0,441 | 0,405 | 0,386 |
| | 19 | 0,402 | 0,384 | 0,413 | 0,403 | 0,410 | 0,402 | 0,373 | 0,393 | 0,394 | 0,384 | 0,397 | 0,413 | 0,392 | 0,411 | 0,397 | 0,405 |
| | 20 | 0,325 | 0,355 | 0,349 | 0,334 | 0,336 | 0,339 | 0,322 | 0,336 | 0,335 | 0,345 | 0,340 | 0,328 | 0,341 | 0,338 | 0,327 | 0,351 |

Table 6.4.6 Values for ξ for HDRBs+FSB typology (16x20).

| ξ [–] | | ISOLATION DEVICES | | | | | | | | | | | | | | |
|---|---|---|---|---|---|---|---|---|---|---|---|---|---|---|---|---|---|
| | | 1 | 2 | 3 | 4 | 5 | 6 | 7 | 8 | 9 | 10 | 11 | 12 | 13 | 14 | 15 | 16 |
| | 1 | 0,153 | 0,155 | 0,146 | 0,161 | 0,146 | 0,150 | 0,154 | 0,150 | 0,149 | 0,144 | 0,152 | 0,153 | 0,147 | 0,150 | 0,148 | 0,143 |
| | 2 | 0,155 | 0,154 | 0,157 | 0,158 | 0,161 | 0,149 | 0,155 | 0,154 | 0,142 | 0,152 | 0,155 | 0,151 | 0,156 | 0,144 | 0,154 | 0,153 |
| | 3 | 0,137 | 0,135 | 0,135 | 0,134 | 0,138 | 0,131 | 0,128 | 0,138 | 0,131 | 0,136 | 0,128 | 0,134 | 0,137 | 0,142 | 0,136 | 0,132 |
| | 4 | 0,144 | 0,152 | 0,143 | 0,146 | 0,143 | 0,151 | 0,146 | 0,143 | 0,144 | 0,152 | 0,146 | 0,150 | 0,150 | 0,141 | 0,146 | 0,144 |
| | 5 | 0,163 | 0,162 | 0,163 | 0,161 | 0,171 | 0,161 | 0,166 | 0,160 | 0,155 | 0,157 | 0,160 | 0,169 | 0,161 | 0,157 | 0,159 | 0,158 |
| | 6 | 0,153 | 0,154 | 0,156 | 0,159 | 0,154 | 0,156 | 0,152 | 0,154 | 0,159 | 0,150 | 0,148 | 0,160 | 0,163 | 0,156 | 0,156 | 0,168 |
| S | 7 | 0,138 | 0,151 | 0,144 | 0,150 | 0,150 | 0,145 | 0,145 | 0,149 | 0,146 | 0,151 | 0,148 | 0,147 | 0,150 | 0,145 | 0,146 | 0,143 |
| T | 8 | 0,159 | 0,144 | 0,153 | 0,145 | 0,154 | 0,153 | 0,144 | 0,155 | 0,144 | 0,144 | 0,147 | 0,143 | 0,150 | 0,145 | 0,148 | 0,149 |
| O | 9 | 0,170 | 0,166 | 0,161 | 0,172 | 0,170 | 0,164 | 0,163 | 0,164 | 0,164 | 0,170 | 0,167 | 0,167 | 0,169 | 0,169 | 0,167 | 0,173 |
| C | 10 | 0,141 | 0,146 | 0,145 | 0,140 | 0,143 | 0,145 | 0,142 | 0,139 | 0,139 | 0,140 | 0,142 | 0,154 | 0,143 | 0,138 | 0,138 | 0,144 |
| K | 11 | 0,154 | 0,152 | 0,153 | 0,160 | 0,158 | 0,150 | 0,153 | 0,157 | 0,148 | 0,155 | 0,160 | 0,152 | 0,160 | 0,162 | 0,156 | 0,156 |
| S | 12 | 0,154 | 0,147 | 0,149 | 0,145 | 0,157 | 0,151 | 0,156 | 0,153 | 0,150 | 0,159 | 0,147 | 0,151 | 0,151 | 0,150 | 0,150 | 0,152 |
| | 13 | 0,156 | 0,159 | 0,148 | 0,146 | 0,149 | 0,152 | 0,149 | 0,155 | 0,153 | 0,149 | 0,151 | 0,150 | 0,149 | 0,155 | 0,155 | 0,149 |
| | 14 | 0,151 | 0,150 | 0,155 | 0,155 | 0,151 | 0,153 | 0,153 | 0,152 | 0,155 | 0,152 | 0,154 | 0,151 | 0,160 | 0,157 | 0,151 | 0,153 |
| | 15 | 0,128 | 0,131 | 0,133 | 0,135 | 0,126 | 0,130 | 0,132 | 0,134 | 0,137 | 0,132 | 0,133 | 0,138 | 0,140 | 0,133 | 0,127 | 0,134 |
| | 16 | 0,158 | 0,155 | 0,159 | 0,158 | 0,158 | 0,155 | 0,159 | 0,156 | 0,156 | 0,156 | 0,156 | 0,155 | 0,153 | 0,154 | 0,153 | 0,151 |
| | 17 | 0,146 | 0,144 | 0,143 | 0,139 | 0,146 | 0,153 | 0,145 | 0,146 | 0,137 | 0,139 | 0,154 | 0,146 | 0,138 | 0,146 | 0,145 | 0,147 |
| | 18 | 0,144 | 0,151 | 0,149 | 0,151 | 0,155 | 0,151 | 0,148 | 0,146 | 0,149 | 0,146 | 0,146 | 0,145 | 0,164 | 0,155 | 0,145 | 0,147 |
| | 19 | 0,146 | 0,147 | 0,149 | 0,150 | 0,141 | 0,145 | 0,141 | 0,149 | 0,147 | 0,137 | 0,141 | 0,152 | 0,150 | 0,140 | 0,146 | 0,148 |
| | 20 | 0,138 | 0,136 | 0,145 | 0,136 | 0,141 | 0,136 | 0,137 | 0,137 | 0,134 | 0,130 | 0,140 | 0,137 | 0,135 | 0,139 | 0,141 | 0,139 |

Once random values of G and ξ were generated, a nonlinear regression procedure was implemented,which automatically calculates the varied parameters ($a_1$ and $b_1$) of the isolator model constructed in Opensees (see Section 6.3.4 and Figure 6.4.2). The paramenters were calculated so that the model gives at the third cycle the target values of the equivalent parameters G and ξ. An example of the cyclic behavior of an isolator with nominal (blue) and varied (red and orange) properties is reported in Figure 6.4.3.



(a)                                                  (b)
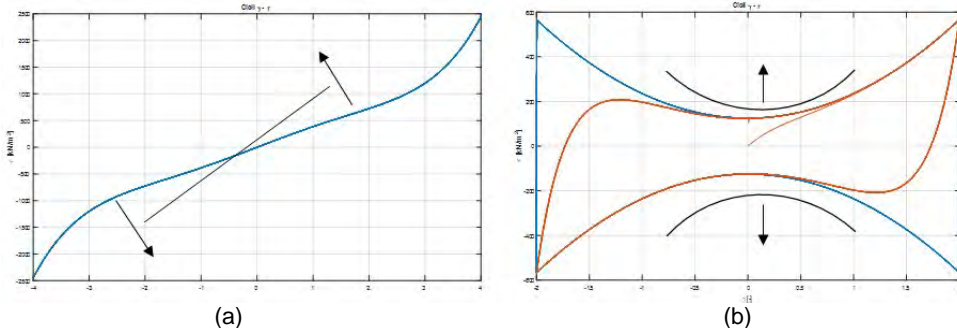
Figure 6.4.2 Identification of the parameter $a_1$ (a) $b_1$ (b).
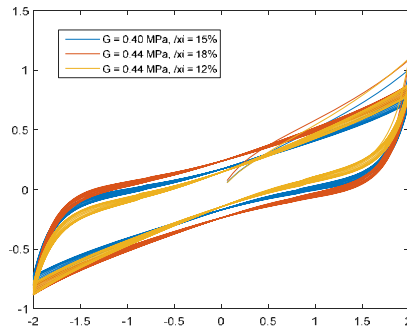
Figure 6.4.3 Cycles used in order to obtain stiffness and damping.

### 6.4.2.2    Sliders

Considering the low lateral (friction) resistance of the sliders, the uncertainties associated to their mechanical properties were not taken into account herein.

### 6.4.2.3    FP devices

For the friction coefficient (μ) of FP devices the same approach of HDRB was used, while a deterministic value is assumed for the curvature radius (R). In particular, a sample of 256 specimens was used, divided in 56 stocks with different number of isolator devices (from 2 to 17 devices per stock).  In this case, due to the different vertical loads used in tests of different stocks, mean values of the friction coefficient of each stock were divided from the nominal values corresponding to the vertical load used in the tests (normalized friction coefficients). After this correction, the mean value and the standard deviation of the normalized friction coefficient as well as the other parameters were calculated, according to the bullets 1, 2 and 3 illustrated for the HDBR devices (Section 6.4.2.1).The sampling procedure for the normalized friction coefficient was set up with the following parameters:

|  | $\mu_T$ | $CV_T$ | $\sigma_T$ | $\sigma_B$ | $\sigma_W$ | $IC$ |
|---|---|---|---|---|---|---|
| $\overline{\mu} / \mu_{nom}$ | 1 | 30% | 0.3 | 0.268 | 0.134 | 0.8 |

Also in this case the procedure was modified simulating the factory production control test. Similarly to HDRBs, the control test consists on extracting randomly 20% of the isolation devices for one stock (5 on 24) and on rejecting the stock generated from the procedure if one of the isolation device parameter is out of the limits given from the code. However, for FP devices the limit imposed by the code is on the maximum force (±15% of the maximum force corresponding to the maximum displacement). In the considered case, with the maximum displacement equal to 263mm (see Section 6.5.3) the corresponding limit on the friction coefficient is about ±43%. Also in this case the total dispersion decreases after the check (see Figure 6.4.4) and the differences about the two distributions are larger due to the large number of stock eliminated and re-generated after the check. Nevertheless, also in this case it is possible to have some stocks with isolation devices that have outranged parameters, due to a non-extraction (see Table 6.4.7 where the orange color means that the parameter is out of the acceptance range). Differently from the HDBR devices, this procedure gives directly the parameter used in Opensees, thus the nonlinear regression procedure is not necessary.
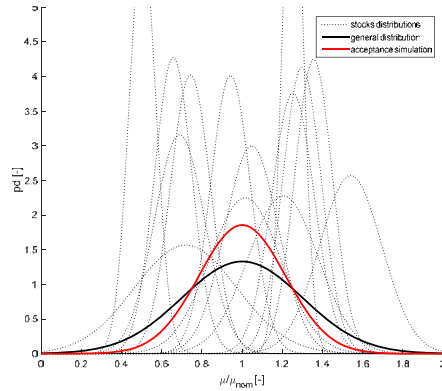
Figure 6.4.4 Distribution of the stocks(dot lines); mean value of the stocks (black curve) and acceptance simulation (red curve) for the parameter μ for FP.

Table 6.4.7 Values for μ for FP devices (24x20).

| μ | | 1 | 2 | 3 | 4 | 5 | 6 | 7 | 8 | 9 | 10 | 11 | 12 | 13 | 14 | 15 | 16 | 17 | 18 | 19 | 20 | 21 | 22 | 23 | 24 |
|---|---|---|---|---|---|---|---|---|---|---|----|----|----|----|----|----|----|----|----|----|----|----|----|----|----|
| | | | | | | | | | | | | | | | | *ISOLATION DEVICES* | | | | | | | | | |
| | 1 | 1,279 | 1,428 | 1,106 | 1,098 | 1,240 | 1,037 | 1,254 | 1,334 | 0,870 | 1,692 | 1,161 | 1,063 | 1,286 | 1,609 | 1,164 | 1,337 | 1,257 | 1,302 | 1,248 | 1,194 | 1,195 | 1,025 | 1,455 | 1,374 |
| | 2 | 0,622 | 0,765 | 0,726 | 0,660 | 0,669 | 0,665 | 0,721 | 0,665 | 0,647 | 0,705 | 0,684 | 0,837 | 0,483 | 0,643 | 0,678 | 0,678 | 0,616 | 0,690 | 0,660 | 0,687 | 0,777 | 0,722 | 0,610 | 0,734 |
| | 3 | 0,787 | 0,720 | 0,909 | 0,812 | 0,676 | 0,885 | 0,888 | 0,983 | 0,856 | 0,814 | 0,913 | 0,932 | 0,749 | 0,751 | 0,740 | 0,843 | 0,703 | 0,853 | 0,845 | 0,855 | 0,980 | 0,893 | 0,643 | 0,877 |
| | 4 | 0,724 | 0,981 | 0,874 | 0,961 | 0,887 | 1,051 | 0,855 | 0,962 | 1,126 | 0,783 | 0,782 | 1,176 | 0,833 | 0,715 | 0,972 | 0,744 | 1,041 | 0,979 | 0,924 | 1,089 | 1,195 | 0,888 | 0,921 | 1,044 |
| | 5 | 0,815 | 0,578 | 0,644 | 0,653 | 0,722 | 0,710 | 0,565 | 0,646 | 0,708 | 0,834 | 0,707 | 0,684 | 0,725 | 0,618 | 0,698 | 0,655 | 0,618 | 0,712 | 0,734 | 0,651 | 0,752 | 0,776 | 0,647 | 0,736 |
| S | 6 | 0,761 | 0,614 | 0,773 | 0,869 | 0,695 | 0,889 | 0,822 | 0,788 | 0,849 | 0,858 | 0,776 | 0,718 | 0,704 | 0,598 | 0,821 | 0,937 | 0,717 | 0,755 | 0,770 | 0,675 | 0,841 | 0,925 | 0,712 | 0,582 |
| T | 7 | 0,780 | 0,968 | 0,757 | 0,907 | 0,794 | 1,021 | 1,019 | 0,947 | 0,855 | 1,032 | 1,034 | 1,039 | 1,188 | 0,875 | 0,842 | 0,918 | 0,875 | 1,068 | 0,824 | 0,925 | 0,784 | 0,889 | 0,795 | 0,845 |
| O | 8 | 1,135 | 0,974 | 1,081 | 1,368 | 0,907 | 1,219 | 1,103 | 1,078 | 1,080 | 0,934 | 1,256 | 1,148 | 1,060 | 1,339 | 1,212 | 0,989 | 0,979 | 1,420 | 0,926 | 0,922 | 0,899 | 0,871 | 1,058 | 1,223 |
| C | 9 | 0,955 | 1,180 | 1,032 | 0,926 | 0,675 | 0,780 | 0,873 | 0,958 | 0,697 | 1,108 | 0,990 | 1,064 | 1,075 | 0,916 | 1,024 | 1,092 | 1,038 | 0,909 | 1,152 | 0,901 | 1,332 | 0,873 | 0,994 | 0,976 |
| K | 10 | 1,218 | 1,105 | 1,181 | 0,883 | 1,143 | 1,116 | 0,861 | 1,084 | 1,083 | 1,226 | 1,054 | 1,065 | 1,110 | 0,975 | 1,382 | 1,326 | 1,121 | 0,988 | 1,239 | 1,168 | 1,024 | 1,302 | 1,045 | 1,399 |
| S | 11 | 0,820 | 0,820 | 0,910 | 1,049 | 1,035 | 0,891 | 1,007 | 0,978 | 0,956 | 1,078 | 0,752 | 1,100 | 1,015 | 0,819 | 0,748 | 0,972 | 1,584 | 1,033 | 0,902 | 0,958 | 0,979 | 0,837 | 0,978 | 0,810 |
| | 12 | 1,186 | 1,309 | 1,024 | 1,251 | 1,087 | 1,089 | 1,292 | 1,271 | 1,354 | 1,287 | 0,983 | 1,217 | 1,214 | 1,390 | 1,326 | 1,232 | 1,199 | 1,176 | 1,209 | 1,384 | 1,087 | 1,351 | 1,059 | 1,385 |
| | 13 | 0,900 | 0,939 | 0,735 | 0,792 | 0,854 | 0,791 | 0,794 | 0,964 | 0,681 | 0,695 | 0,998 | 0,874 | 1,060 | 0,839 | 0,983 | 0,717 | 0,861 | 0,678 | 0,947 | 0,972 | 0,878 | 0,794 | 0,943 | 0,799 |
| | 14 | 0,915 | 0,763 | 0,715 | 0,611 | 0,813 | 0,735 | 0,795 | 0,888 | 0,717 | 0,866 | 0,746 | 0,987 | 0,769 | 0,944 | 0,791 | 0,820 | 0,958 | 0,733 | 0,764 | 0,786 | 0,859 | 0,800 | 0,763 | 0,823 |
| | 15 | 0,628 | 0,842 | 0,887 | 0,808 | 0,727 | 0,613 | 0,740 | 0,693 | 0,888 | 0,643 | 0,786 | 0,750 | 0,688 | 0,880 | 0,787 | 0,719 | 0,800 | 0,744 | 0,674 | 0,897 | 0,781 | 0,838 | 0,648 | 0,697 |
| | 16 | 0,863 | 0,936 | 0,883 | 0,734 | 0,624 | 0,862 | 0,621 | 0,822 | 0,871 | 0,852 | 0,604 | 0,700 | 0,731 | 0,895 | 0,798 | 0,740 | 0,749 | 0,801 | 1,061 | 0,600 | 0,872 | 0,804 | 0,697 | 0,879 |
| | 17 | 0,618 | 0,870 | 0,732 | 1,000 | 0,845 | 0,617 | 0,661 | 0,754 | 0,758 | 0,703 | 0,820 | 0,852 | 0,680 | 0,883 | 0,741 | 0,790 | 0,812 | 0,831 | 0,675 | 0,809 | 0,861 | 0,681 | 0,737 | 0,845 |
| | 18 | 0,828 | 0,712 | 0,654 | 0,690 | 0,820 | 0,902 | 0,653 | 0,745 | 0,880 | 0,768 | 0,784 | 0,948 | 0,786 | 0,798 | 0,744 | 0,818 | 0,867 | 0,621 | 0,782 | 0,749 | 0,827 | 0,770 | 0,905 | 0,585 |
| | 19 | 0,734 | 0,828 | 1,008 | 0,904 | 0,746 | 0,915 | 0,860 | 0,950 | 0,733 | 0,863 | 1,118 | 0,898 | 0,934 | 0,856 | 0,931 | 0,944 | 0,827 | 1,226 | 1,008 | 0,747 | 0,969 | 0,926 | 0,832 | 0,984 |
| | 20 | 1,036 | 1,337 | 1,235 | 0,911 | 0,877 | 1,298 | 0,994 | 1,114 | 1,108 | 1,240 | 1,294 | 1,204 | 1,266 | 1,048 | 1,123 | 1,337 | 1,298 | 1,268 | 1,184 | 1,125 | 1,010 | 0,932 | 1,054 | 1,032 |

## 6.5   Analyses results and discussion

### 6.5.1   Collapse Limit State

The identification of global collapse through a numerical response analysis represented the topic of relatively intense research in the last decade. For base-isolated buildings, the collapse condition could be related to the collapse of the superstructure or the collapse of the isolation system. The collapse conditions of both elements are described in the following sections.

6.5.1.1   Superstructure

The buildings analyzed in this project are code-conforming, therefore no defective collapse modes should be activated. Inspection of the cyclic base-shear-lateral displacement curves, however, revealed the difficulty in setting up an automatic procedure to check collapse, partly due to three-dimensional nature of the analysis. For this reason, it was pragmatically chosen to employ a still global, but simplified collapse criterion based on a global capacity obtained from pushover analysis. Criticism of this choice is known (e.g., Villaverde, 2007 and Goulet et al., 2007), since a single capacity value, related to the collapse mechanism occurring in the pushover analysis, is adopted, rather than motion-specific values.

The adopted criterion is therefore an approximate one and capacity is defined as the value of drift (inter-story-drift or roof-drift-ratio, IDR or RDR, respectively,can be used indifferently for these buildings) at 50% decrease in base-shear on the negative slope. This value is preferred since it is easier to identify on the pushover curves and because it is lower than the monotonic

value of displacement at zero base-shear, and thus ideally closer to a generic 'cyclic' value of displacement at zero base-shear. Obviously, the fixed base configuration was considered to perform the pushover analysis of the examined building. Two values of collapse are determined, one in the X and the other in the Y direction (single value, no significant difference was detected between '+' and '-'). Push over curves are reported in Figure 6.5.1 and Figure 6.5.2 for case studies with HDRBs, in Figure 6.5.3 and Figure 6.5.4 for case studies with HDRBs+FSBs and in Figure 6.5.5 for case studies with FPS.



(a)                                                                                                  (b)
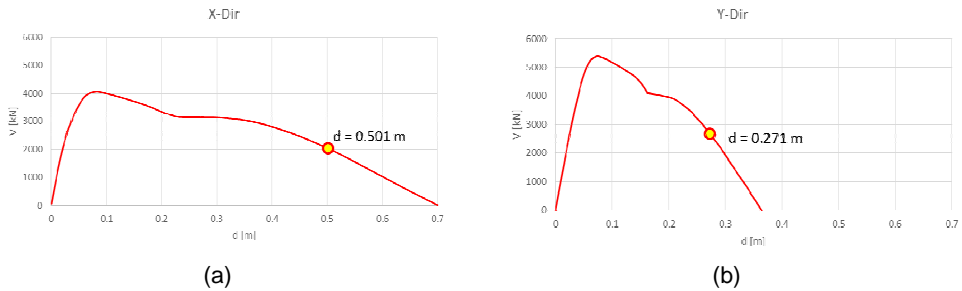
Figure 6.5.1 Pushover curves (case L'Aquila) and displacement thresholds in the X (a) and Y (b) directions for HDRB.



(a)                                                                                                  (b)
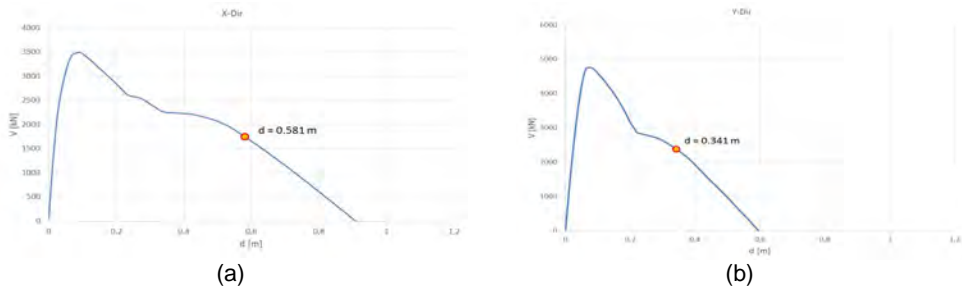
Figure 6.5.2 Pushover curves (case Naples) and displacement thresholds in the X (a) and Y (b) directions for HDRB.



(a)                                                                                                  (b)
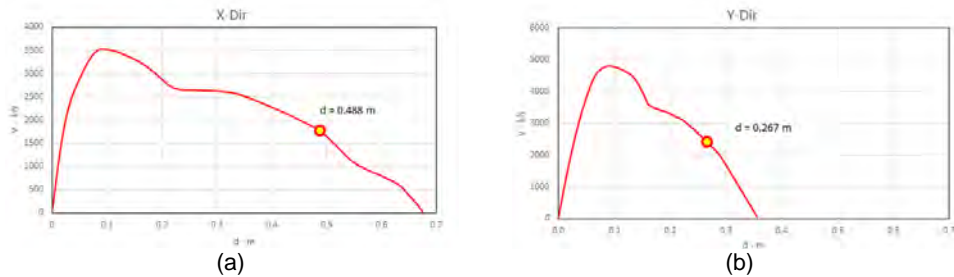
Figure 6.5.3 Pushover curves (case L'Aquila) and displacement thresholds in the X (a) and Y (b) directions for HDRB-FSB.

(a)                                                            (b)
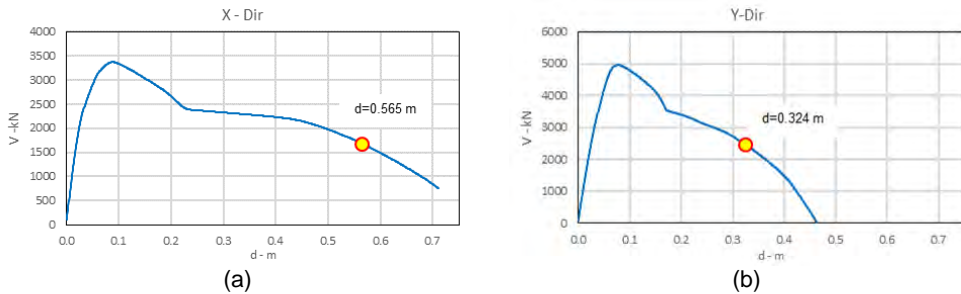
Figure 6.5.4 Pushover curves (case Naples) and displacement thresholds in the X (a) and Y (b) directions for HDRB-FSB.
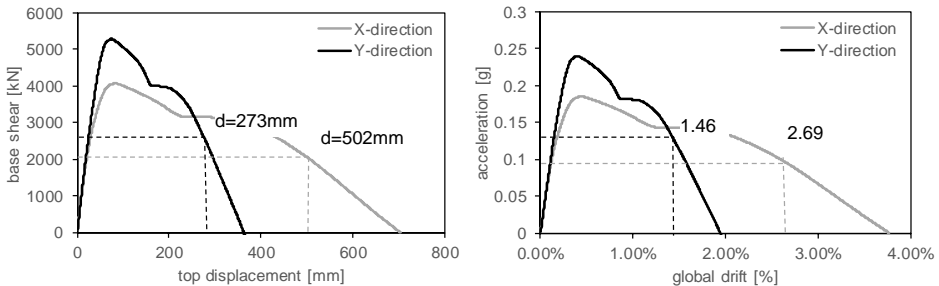


Figure 6.5.5 Pushover curves and displacement/drift thresholds in the X and Y directions for FPS (Naples and L'Aquila).

6.5.1.2    Isolation system

The global collapse condition of the isolation system depends on the typology and the associated failure modes of the specific devices composing the aforesaid system.

**Failure modes for elastomeric devices**

In the present study, the collapse of a singular elastomeric device was associated to the occurrence of one of the following failure modes:

a) Cavitation

b) Buckling

c) Shear

Each singular failure mode is described in details in the following sections.

*Cavitation*

Recent experimental tests have shown that elastomeric bearings can sustain large tensile strains up to 100% following cavitation, without rupture of the bearing (Iwabe et al., 2000).

In this work an assessment of the devices condition towards cavitation was performed in terms of deformations. The assumed thresholds were defined based on experimental tests conducted by Kumar (2015) on Low Damping Rubber Bearings (LDRB). In particular an axial tensile strain equal to 0.5 was prudently assumed as reference threshold.

*Buckling*

Using the above mentioned HDR Element, a value of the critical buckling load of each device can be obtained during the analyses in the Opensees environment, for each analysis step. As a consequence, the P/Pcr ratio between the current axial load and the critical buckling load can be evaluated in order to identify the collapsed devices i.e., when $P/P_{cr}=1$.

*Shear Failure*

Recent studies (Montuori et al. 2015) pointed out a lower bound limit for rubber failure in terms of shear deformation ($\gamma$) of about 260%, regardless the shape factor value and the applied pressure. (Figure 6.5.6).
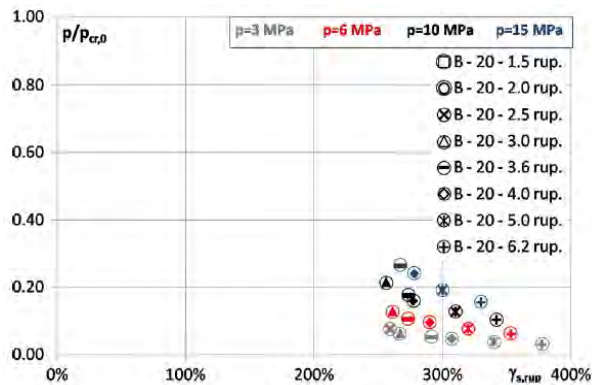


Figure 6.5.6 Rubber failure domain.

Such value seems to be excessively precautionary if compared to the experimental results obtained by Kawamata et al. (1992) and Muramatsu (2004), showing values of the order of 400-500%. All that considered, a limit value equal to 350% was assumed in the present study. This value also corresponds to the maximum shear strain of the experimental tests used to calibrate the horizontal shear behavior of the numerical model of HDBR bearings.

**Failure Modes for Steel/PTFE sliders**

The steel/PTFE sliders failure is associated to a horizontal displacement value equal to the device capacity increased by an extra displacement equal to the bearing radius. The current displacement of the base floor's centroid was assumed as displacement demand.

**Failure Modes for Friction Pendulum Bearings**

The failure of FP isolation system occurs when the actual horizontal displacement is greater than the overall displacement capacity $d_m$ of the devices. The current displacement at the external angle joint of the base floor was assumed as displacement demand.

In the scientific literature on the capability of CSS devices, lateral displacements greater than $d_m$ are still often considered as the limit state. As reported in Figure 6.5.7, in extreme conditions this is possible by exceeding the slider surface and reducing the contact area. As an example shown in Figure 6.5.8, the experimental loop of a CSS device shows an extra-displacement about the 50% of the design displacement value.
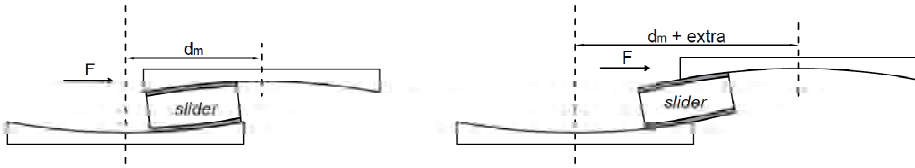
Figure 6.5.7 CSS device in extreme conditions with an increased displacement capability.

For the purpose of this study, the displacement of gravity center of the base floor was assumed as displacement demand. The failure condition was associated to a horizontal displacement value equal to the overall displacement capacity $d_m$ of the devices, increased by an extra-displacement capacity $\Delta_m$ calculated as 25% of the dimension of the rigid slider ($\Delta_m = 70mm$), as reported in Table 6.5.1.

Table 6.5.1 Failure condition values for isolation system.

|  | $d_m$ | $\Delta_m$ | failure disp. |
|---|---|---|---|
|  | [mm] | [mm] | [mm] |
| **Naples** | ±150 | 70 | 220 |
| **L'Aquila** | ±300 | 70 | 370 |
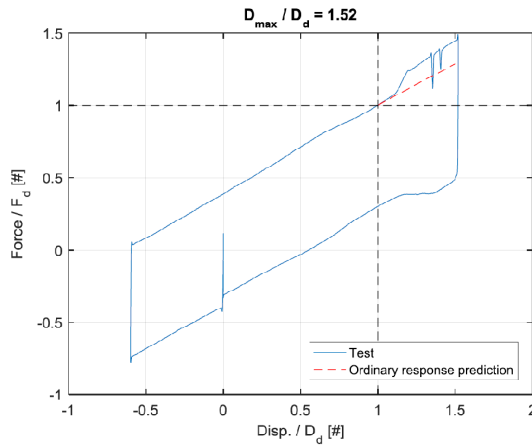


Figure 6.5.8 Experimental loop of CSS device in extreme conditions with an increased displacement capability of +50%.

6.5.1.3    Global collapse conditions

In this section, the collapse conditions for superstructure and isolation system are summarized for each UR (HDRB, HDRB+FSB, FPS). As mentioned before, for each UR, the collapse of the examined building is deemed attained when one of the collapse conditions presented in the corresponding Table (Table 6.5.2, Table 6.5.3, or Table 6.5.4) is reached.

Table 6.5.2 Collapse Conditions for HDRB typology.

| FAILURE MODE | COLLAPSE CONDITIONS | |
|---|---|---|
| Buckling | 50% of elastomeric devices (simultaneously) reaches a value of the axial compressive force equal to the critical buckling load; | P/Pcr=1 |
| Cavitation | 50% of elastomeric devices reaches an axial tensile strain ($\varepsilon_t$) greater or equal to 50%; | $\varepsilon_t \geq 50\%$ |
| Shear | 50% of elastomeric devices reaches a shear strain ($\gamma$) greater or equal to 3.5; | $\gamma \geq 3.5$ |
| Superstructure | The relative displacement of the center of gravity of the top floor with respect to that of the base floor is equal to the effective displacement corresponding to a 50% decrease in strength derived from pushover analysis performed in the X- or Y direction | L'Aquila limits 501 mm (dir x) 271 mm (dir y) Naples limits 581 mm (dir x) 342 mm (dir y) |

Table 6.5.3 Collapse conditions for HDRB+FSB typology.

| FAILURE MODE | COLLAPSE CONDITIONS | |
|---|---|---|
| Buckling | 50% of elastomeric devices (simultaneously) reaches a value of the axial compressive force equal to the critical buckling load; | P/Pcr=1 |
| Cavitation | 50% of elastomeric devices reaches an axial tensile strain ($\varepsilon t$) greater or equal to 50%; | $\varepsilon_t \geq 50\%$ |
| Shear | 50% of elastomeric devices reaches a shear strain ($\gamma$) greater or equal to 3.5; | $\gamma \geq 3.5$ |
| Sliders | The center of gravity of the base floor reaches an horizontal displacement equal to the device capacity increased by an extra-displacement. | $d_u = d_{max,slide} + \phi/2$ |
| Superstructure | The relative displacement of the center of gravity of the top floor with respect to that of the base floor is equal to the effective displacement corresponding to a 50% decrease in strength derived from pushover analysis performed in the X- or Y direction | L'Aquila limits 488 mm (dir x) 267 mm (dir y) Naples limits 565 mm (dir x) 324 mm (dir y) |

Table 6.5.4 Collapse conditions for FPS typology.

| FAILURE MODE | COLLAPSE CONDITIONS | |
|---|---|---|
| FPS disp. capacity | The external angle of the base floor reaches an horizontal displacement equal to the device capacity increased by an extra-displacement. | $d_u = d_m + \Delta_m$ |
| Superstructure | The relative displacement of the center of gravity of the top floor with respect to that of the base floor is equal to the effective displacement corresponding to a 50% decrease in strength derived from pushover analysis performed in the X- or Y direction | (Naples / L'Aquila) 502 mm (dir X) 273 mm (dir Y) |

### 6.5.2    Damage Limit State

In this present study, a multi-criteria approach was adopted to define the Damage Limit State. The latter combines concepts related to easy reparability of non-structural components and no service interruption with the requirement of protecting structural members from any damage under frequent earthquakes. The selected multi-criteria approach is described in detail in the Appendix A. The limit values for each building typology are summarized in the following Table 6.5.5.

Table 6.5.5 DLS limit value for the case studies of base-isolated reinforced concrete structures.

| | | Limit top displacement [mm] | |
|---|---|---|---|
| | | X dir | Y dir |
| **HDRB** | **Naples** | 60 | 56 |
| | **L'Aquila** | 59 | 57 |
| | **L'Aquila with uncertainty** (median values on the 20 varied buildings) | 53 | 54,5 |
| **HDRB-FSB** | **Naples** | 42 | 61 |
| | **L'Aquila** | 59 | 66 |
| | **L'Aquila with uncertainty** (median values on the 20 varied buildings) | 55 | 73 |
| **FP** | **Naples and L'Aquila** | 59 | 57 |
| | **L'Aquila with uncertainty** (median values on the 20 varied buildings) | 53 | 55 |

### 6.5.3    Results

The analyses results for the Collapse Limit State are summarized in this section in terms of number of failures. In other words, the total number of records determining a collapse condition for the base-isolated building is reported as a function of the seismic intensity, defined by intensity measure levels (IMLs) ranging from 1 to 10, as defined in Chapter I. Moreover, the failure mode that first caused the collapse are indicated for each record by using different colors, according to criteria defined in section 6.5.1.3. Also results at the Damage Limit State are reported in terms of D/C ratios, where D represents the largest IDR over X or Y directions of top displacement demand-absolute value, associated to each singular record and IML for each case study. The relevant capacity (C) is defined in section 6.5.2 for each isolation system.

6.5.3.1    HDBR isolation system

**Case study building in L'Aquila:** In Figure 6.5.9, the analyses results for the Collapse Limit State are summarized for the case study buildings located at L'Aquila. In particular, results point out that, for the intensity measure level corresponding to the return period equal to 1000 years (i.e., IML6), typically assumed as Collapse Limit State according to NTC2008, no failures are recorded. As a general trend, a significant number of failures is recorded above IML9. Such failures are mainly associated to the superstructure in the case 1-A, due to the lower value of the isolation ratio. Differently, in the case 2-A characterized by a lower margin with respect to the buckling load capacity, the failures are associated to both the superstructure and buckling of bearings. For the sake of completeness, a comparison between the results obtained for case 2-A using two different set of ground motions, with conditioning period 2.0 sec (case 2-A) and 3.0 sec (case 2-Ab) is presented in Figure 6.5.10a and b, respectively. The difference between the

obtained results can be ascribed to the characteristics of the ground motion set associated with a conditioning period T=2.0 s and T=3.0 s. Indeed, the first is characterized by a value of $S_a$ (T=2.0s) at IML6 equal to 0.184g, which is considerably lower than the corresponding value from the reference code spectrum (0.26g), while the second set is characterized by a value of $S_a$ (T=3.0s) at IML6 equal to 0.177g, which is similar to the corresponding value from the reference code spectrum (0.17g). Thus, a large number of failures is obtained by using this latter set of records, and they are associated mainly to buckling of bearings.
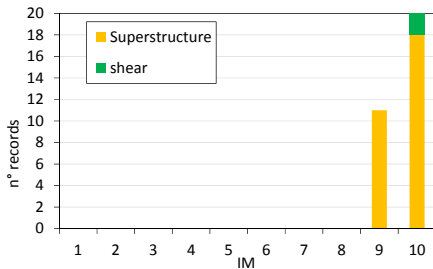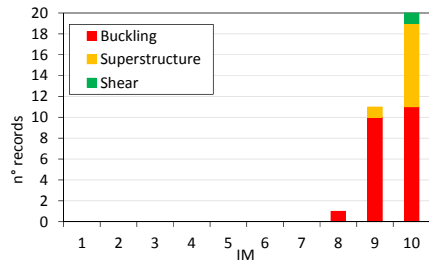


(a) case 1-A                    (b) case 2-A

Figure 6.5.9 Summary of NTHAs' results at CLS for (a) case 1-A, (b) case 2-A for HDRB.
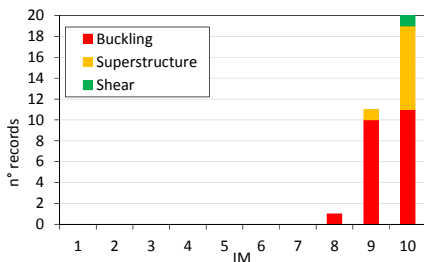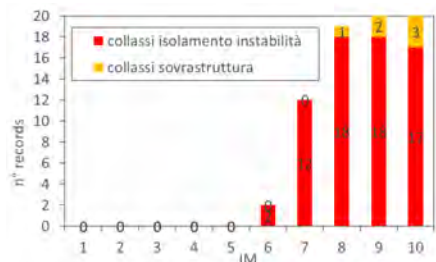


(a) case 2-A                    (b) case 2-Ab

Figure 6.5.10 NTHAs' results at CLS for HDRB case 2-A obtained using different sets of ground motions:(a) Conditioning period equal to 2.0s and (b) Conditioning period equal to 3.0s.

Among the two case studies, the second one that minimizes the base-shear transferred to the superstructure, was considered for further analyses by considering the set of ground motions with conditioning period 3.0 sec (case 2-Ab). In particular, the Damage Limit State is analyzed in this section, whereas the influence of the gap and of model uncertainties are analyzed in the following sections. The results of the Damage Limit State are summarized in Figure 6.5.11.
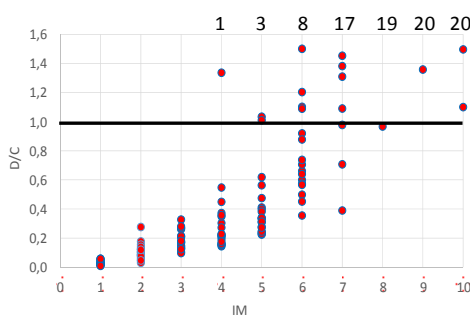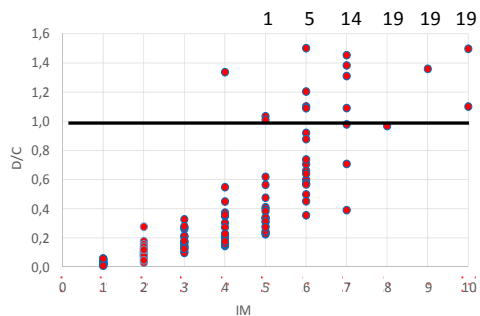


(a)                    (b)

Figure 6.5.11 D/C ratios for the reference case (Case 2-Ab) in the X (a) direction and the Y (b) direction

The results show that, for the intensity measure level corresponding to the return period equal to 50 years (i.e., IML2), typically assumed as Damage Limit State according to NTC2008, no failures are recorded and D/C ratios sensibly lower than 1 are obtained. The failure cases start to appear, (D/C≥1) only for seismic events characterized by IML4.

**Case study building in L'Aquila, with gap**: In Figure 6.5.12 the analyses results for the Collapse Limit State are summarized for the case study building located at L'Aquila with larger isolation period and with the set of ground motions with conditioning period 3.0 sec (case 2-Ab) by considering the presence of a seismic gap. In particular in Figure 6.5.12a the results of the case with gap amplitude equal to the isolation displacement capacity (300 mm) are reported, whereas in Figure 6.5.12b the results are relevant to a gap amplitude equal to 1.25 times as large as the isolation displacement capacity (375 mm).



(a)                                                          (b)
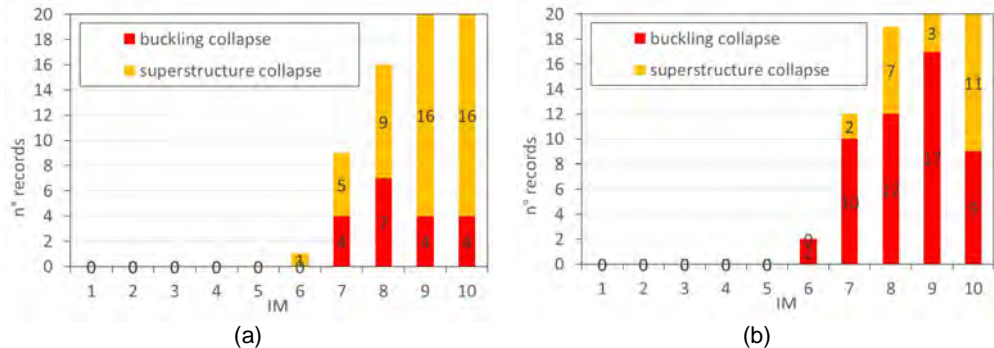
Figure 6.5.12 Collapse mechanisms for the case 2-Ab with gap 300mm (a) and with gap 375mm (b).

The comparison with Figure 6.5.9b highlights that the number of collapse is very similar in all the cases, but the type of the first collapse changes. More in detail, in the case without gap, there are mainly collapses due to the buckling of the isolation system, while in the cases with gap superstructure collapses appear. In particular, as expected, the number of superstructure collapses increase as the gap amplitude decreases. No analysis at the Damage Limit State was performed for these cases, since the presence of gap does not influence the isolated system behavior at low seismic intensities.

**Case study building in L'Aquila, with uncertainty**: In this section the analyses results for the Collapse Limit State followed by the results for the Damage Limit State, are summarized for the case study buiding located at L'Aquila with the largest isolation period and with conditioning period 3.0 sec (case 2-Ab) by considering model uncertainties. First, in Figure 6.5.13 the capacity curves of the 20 models with varied parameters (varied models) obtained by the push-over analyses are shown, for both the X and Y directions, together with the curves of the reference case without model uncertainties. The dots reported in Figure 6.5.13a, b represent the reduction from the peaks of the shear of 50%. It is shown that in Figure 6.5.13a the mean value of the collapse displacement is equal to 465mm with a dispersion of 208; while in case (b) the mean collapse displacement is 246mm with a dispersion of 119. Also, Figure 6.5.13c, d report the threshold for the Damage Limit State, indicated with dots, in accordance with the three criteria described in Section 6.5.2.
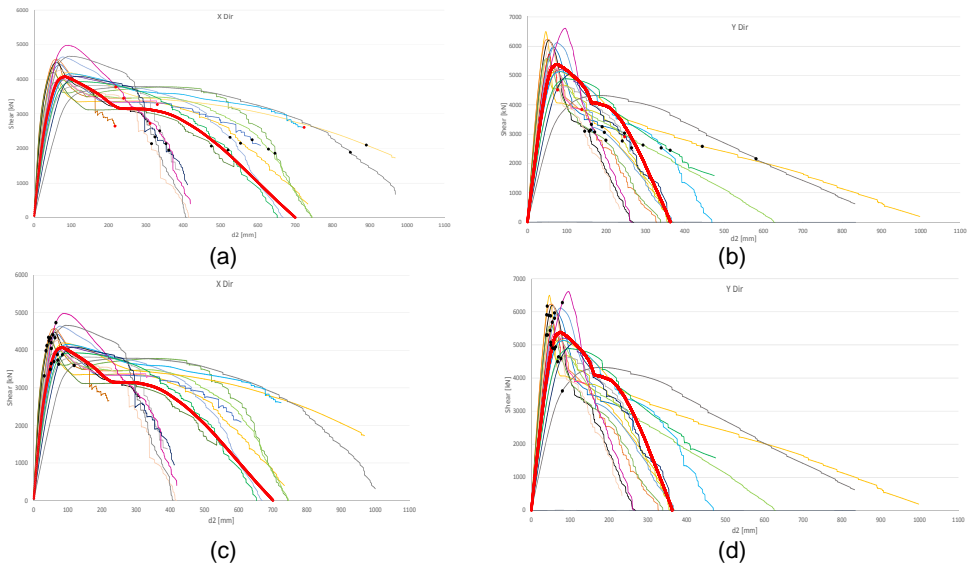
Figure 6.5.13 Pushover of the varied models and limit displacements for CLS in the X (a) and Y (b) directions and for DLS in the X (c) and Y (d) directions.

In Figure 6.5.14 results of the analyses for the Collapse Limit State are reported. In particular, in Figure 6.5.14a the results are related to the case where uncertainties of the isolation system are only introduced, i.e., for each IML the analyses were performing by associating one of the 20 ground motion records to one of the 20 model with varied isolation properties (one to one association). On the other hand, Figure 6.5.14b shows the results, in terms of number and mode of failures, and of the analyses carried out by introducing both the source of uncertainties (isolation system and superstructure). To this purpose, a random one-to-one association was done between a varied superstructure model and an isolation system with varied properties. Then, similarly to the previous case, one-to-one association was done between the records and the varied models.
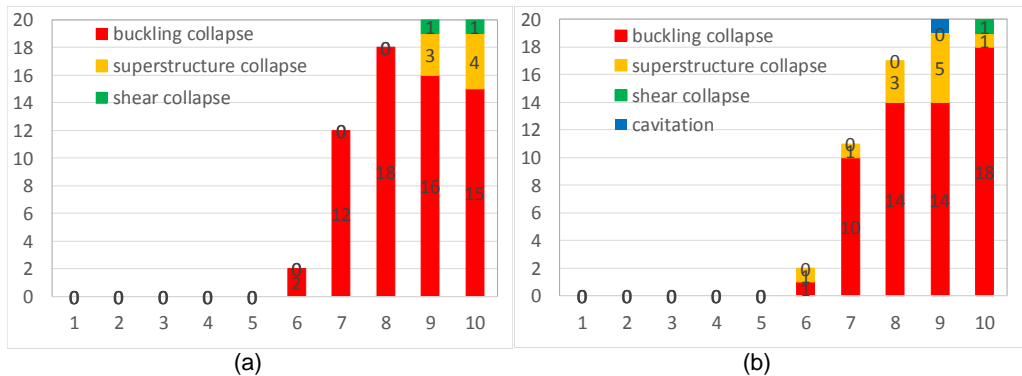


Figure 6.5.14 NTHAs' results at CLS for HDRB for L'Aquila case study without uncertainty (a) NTHAs' results at CLS for HDRB for L'Aquila case study with isolation system uncertainty (b)

By comparing Figure 6.5.14a and b with the reference case without uncertainties (Case 2-Ab) reported in Figure 6.5.9, it is noticeable that the variability of the isolation system, as well as the superstructure, does not modify significantly the number of collapse, but only the first collapse modality (more superstructure collapse and the other collapse types appear compared to the reference case).

Finally, the results for the Damage Limit State are summarized in terms of D/C ratios in Figure 6.5.15 for the models with isolation system and superstructure uncertainties. The comparison with the reference case without uncertainties (Figure 6.5.11) shows that no significant differences are evident between the two cases.



(a)                                                        (b)
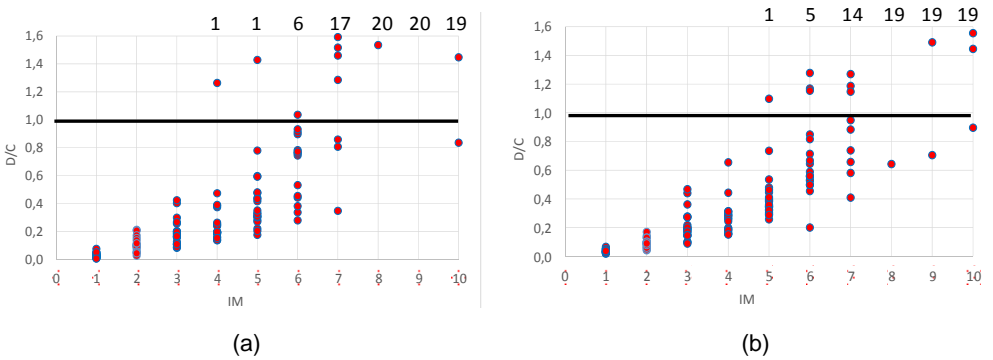
Figure 6.5.15 D/C ratios of the case with uncertainties in the X (a) direction and the Y (b) direction

**Case study building in Naples**: The analyses results for the Collapse Limit State followed by the results for the Damage Limit State, are summarized in this section, with reference to the case studies located at Naples. For the CLS, the results in terms of number of failures(presented in Figure 6.5.16) show that in the case 1-N (Figure 6.5.16a) no failures are recorded for all the intensity measure levels, whereas for the case 2-N (Figure 6.5.16b) very few failures occour only at IMLs larger than IML8. For the case 2-N two different sets of ground motions with conditioning period 2.0 and 3.0 seconds are used and the results are presented in Figure 6.5.17a and b, respectively. The difference between the obtained results can be ascribed to the characteristics of the ground motion set associated with a conditioning period T=2.0 s and T=3.0 s. Indeed, the first is characterized by a value of $S_a$ (T=2.0s) at IML6 equal to 0.119g, which is considerably lower than the corresponding value from the reference code spectrum (0.186g), while the second set is characterized by a value of $S_a$ (T=3.0s) at IML6 equal to 0.1g, which is similar to the corresponding value from the reference code spectrum (0.09g). Thus, a large number of failures is obtained by using this latter set of records, and they are associated mainly to buckling of bearings.
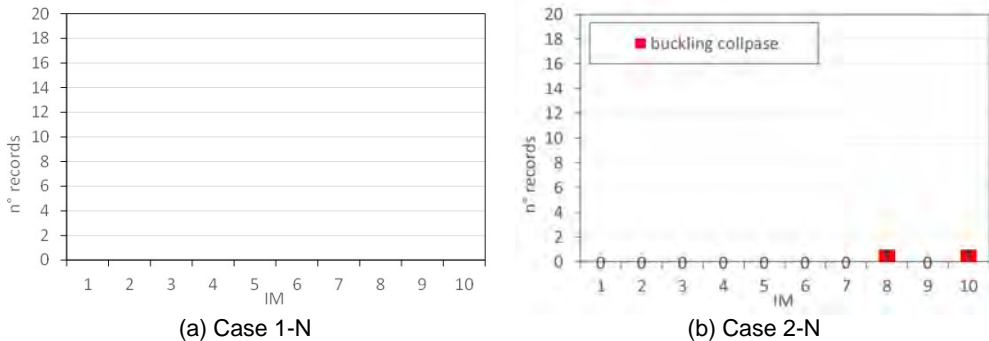


(a) Case 1-N                                      (b) Case 2-N

Figure 6.5.16 Summary of NTHAs' results at CLS for (a) case 1-N, (b) case 2-N for HDRB.
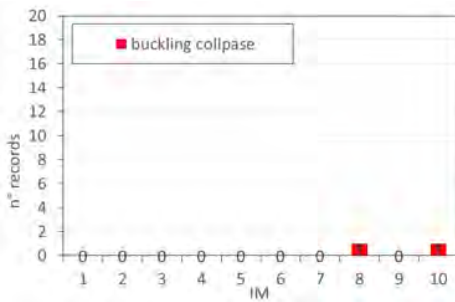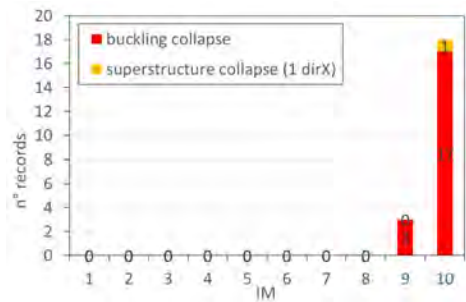
(a) Case 2-N                                                                (b) Case 2-Nb

Figure 6.5.17 NTHAs' results at CLS for HDRB case 2-N obtained using different sets of ground motions: (a) conditioning period equal to 2.0s and (b) conditioning period equal to 3.0 s.

The results for the Damage Limit State are reported in Figure 6.5.18, Figure 6.5.19, and Figure 6.5.20 in terms of D/C ratios associated to each singular record and IML. The results presented in Figure 6.5.18 refer to the case 1-N and show that, for the intensity measure level corresponding to the return period equal to 50 years (i.e., IML 2), typically assumed as Damage Limit State according to NTC2008, no failures are recorded and D/C ratios much lower than 1 are obtained. The failures start to be present, (D/C≥1) only for seismic events characterized by the return periods greater than 1000 years (i.e., IML 6), just in X direction. Only for the intensity measure level of 10 the number of failure cases is significant.
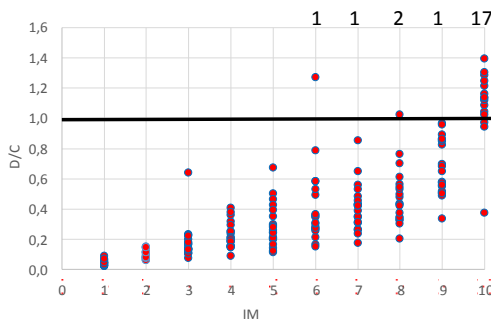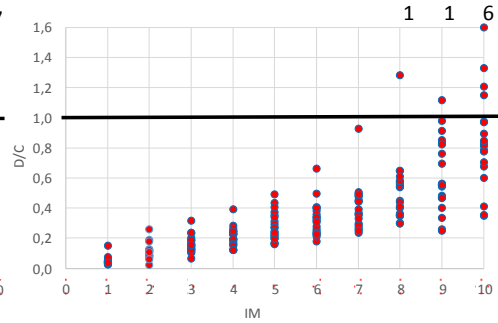


(a)                                                                               (b)

Figure 6.5.18 D/C ratios for (a) case 1-N direction X, (b) case 1-N direction Y for HDRB.
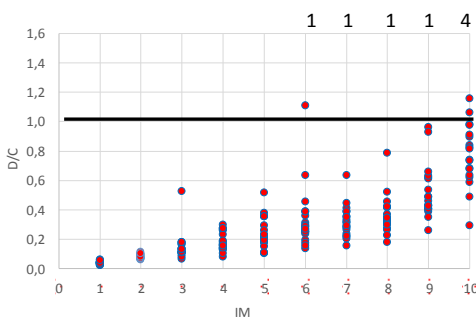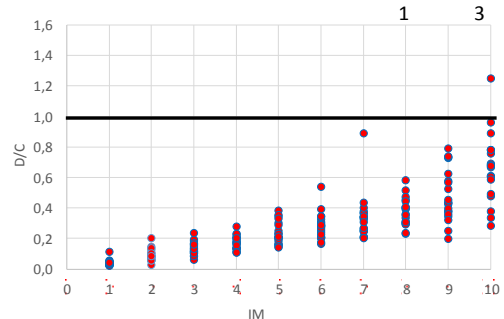


(a)                                                                               (b)

Figure 6.5.19 D/C ratios for (a) case 2-N direction X, (b) case 2-N direction Y for HDRB.
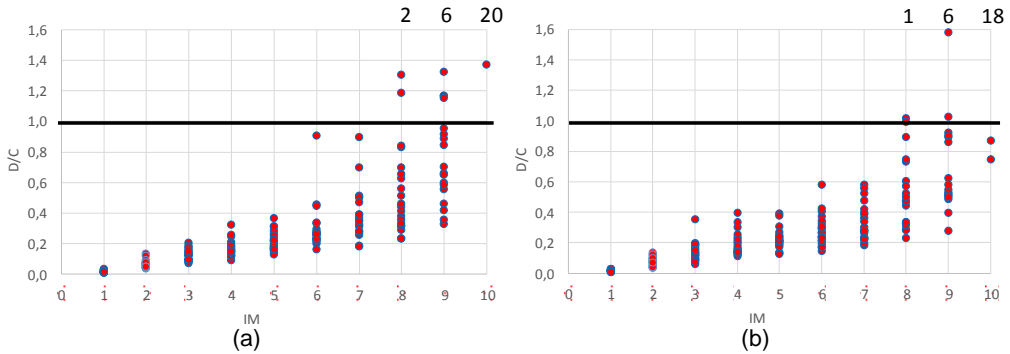
Figure 6.5.20 D/C ratios for (a) case 2-Nb direction X, (b) case 2-Nb direction Y for HDRB.

The results presented in Figure 6.5.19 and Figure 6.5.20 refer to the case 2-N and case 2-Nb and show the same trend: for an intensity measure level corresponding to the return period equal to 50 years (i.e., IML 2) no failures are recorded and D/C ratios are much lower than 1. Only for the case 2-Nb, for the intensity measure level of 10 the number of failure cases is significant.

### 6.5.3.2    HDRB-FSB isolation system

**Case study building of L'Aquila**: The analyses results of the case studies buildings located at L'Aquila for the Collapse Limit State are summarized in Figure 6.5.21.
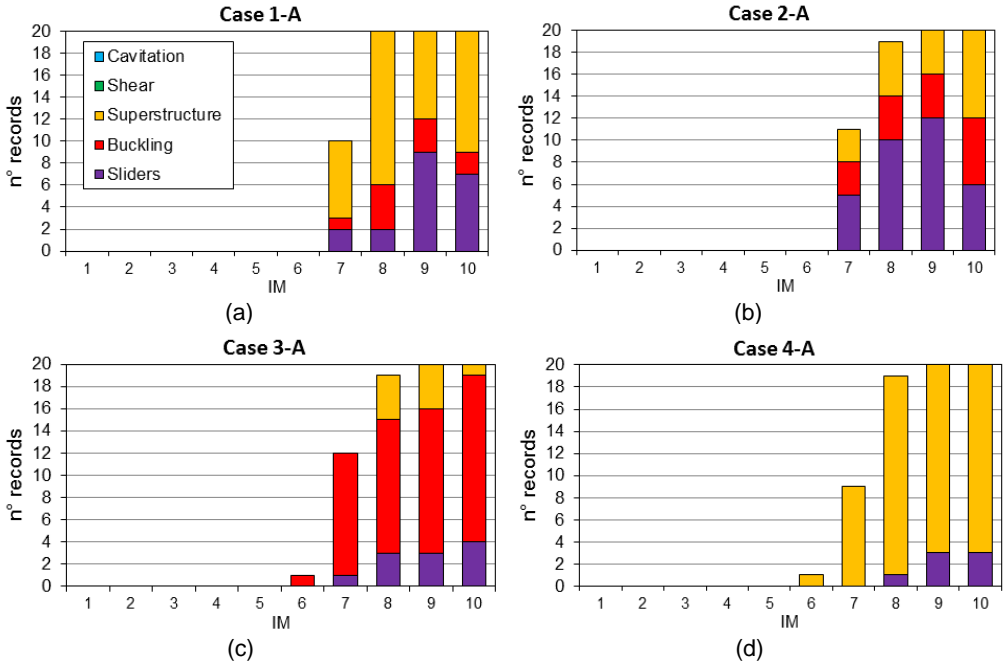


Figure 6.5.21 Summary of NTHAs' results at CLS for (a) case 1-A, (b) case 2-A, (c) case 3-A and (d) case 4-A for HDRB-FSB.

The obtained results show that, for the intensity measure level corresponding to the return period equal to 1000 years (i.e., IML 6), typically assumed as Collapse Limit State according to NTC2008, no failures are recorded. As a general trend, a significant number of failure cases is recorded above IML 7. For the case 4-A, as expected, the superstructure collapse is the prevalent failure mode due to a lower value of the isolation ratio.

The results of the Damage Limit State are summarized in Figure 6.5.22 in terms of D/C ratios) associated to each singular record and IML. Because of the similarities of the results, among the four case studies, the case 4-A, that maximizes the base-shear transferred to the superstructure, is shown.



(a)                                          (b)
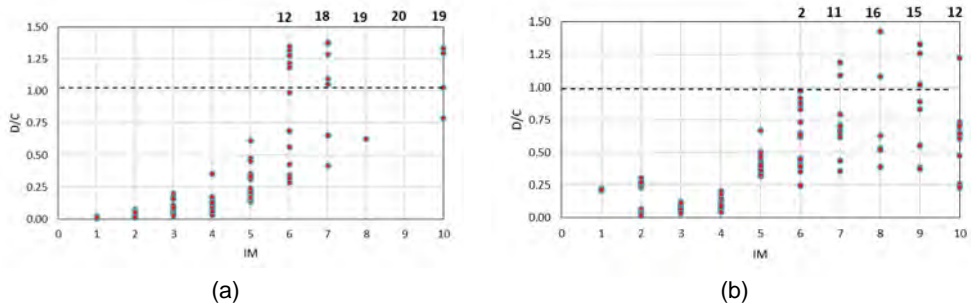
Figure 6.5.22 D/C ratios for the reference case (Case 4-A) in the X (a) direction and the Y (b) direction.

Similarly to the case studies buildings with HDRBs located at L'Aquila, failures start to be present, (D/C≥1) only for seismic events characterized by return periods greater than 1000 years (i.e. IML 6).

**Case study building with gap in L'Aquila**: In this section the analysis results for the Collapse Limit State are summarized for the case study building located at L'Aquila (case 2-A) with and without seismic gap. All the analyses were performed with the set of ground motions with the conditioning period of 3.0 second. Also in this case the results are presented in terms of number of failures and failure modes that first caused the collapse. In particular in Figure 6.5.23a, the results of the case study building with gap equal to the isolation displacement capacity (300 mm) are reported. In order to get a comprehensive overview, the analysis results of the same case study building without gap (case 2-A) are reported in Figure 6.5.23b.



(a)                                          (b)
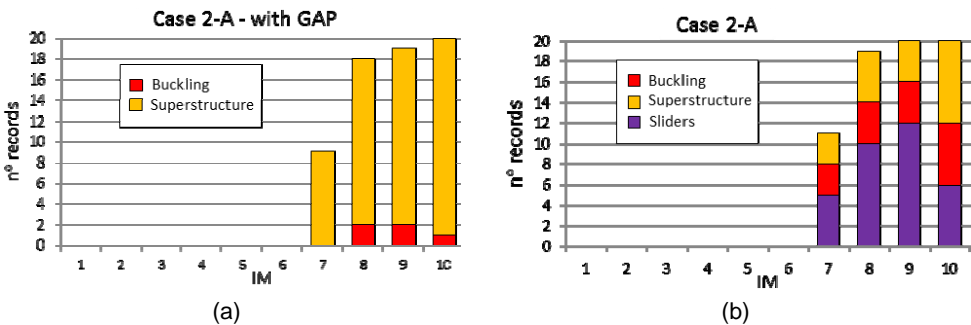
Figure 6.5.23 Collapse mechanisms for the case 2-A with Gap 300mm (a) without Gap (b).

The comparison highlights that the number of collapse are very similar in the two cases, but the collapse mode changes. More detailedly, in the case without gap, collapses are mainly due to the sliders, while in the case with gap, collapse can be mainly ascribed to the superstructure. No analysis at the Damage Limit State was performed for these cases, since the presence of gap does not influence the isolated system behavior at low seismic intensities.

**Case study building with uncertainty in L'Aquila**: In this section the analysis results for the case study building located at L'Aquila (case 3-A), with and without model uncertainties, are summarized. First, in Figure 6.5.24 the capacity curves of the 20 models with varied parameters (varied models) obtained from push-over analysis are shown, for both directions. The dots reported in Figure 6.5.24a, b correspond to 50% strength reduction from the maximum

resistance. It is shown that, in the X direction (Figure 6.5.24a), the mean value of the collapse displacement is equal to 488 mm with a dispersion of 117, while the mean collapse displacement is 318 mm with a dispersion of 126 in the Y direction (Figure 6.5.24b). The dots reported in Figure 6.5.24c, d refer to the Damage Limit State, according to the multi-criteria described in section 6.5.2.



(a)

(b)

(c)

(d)
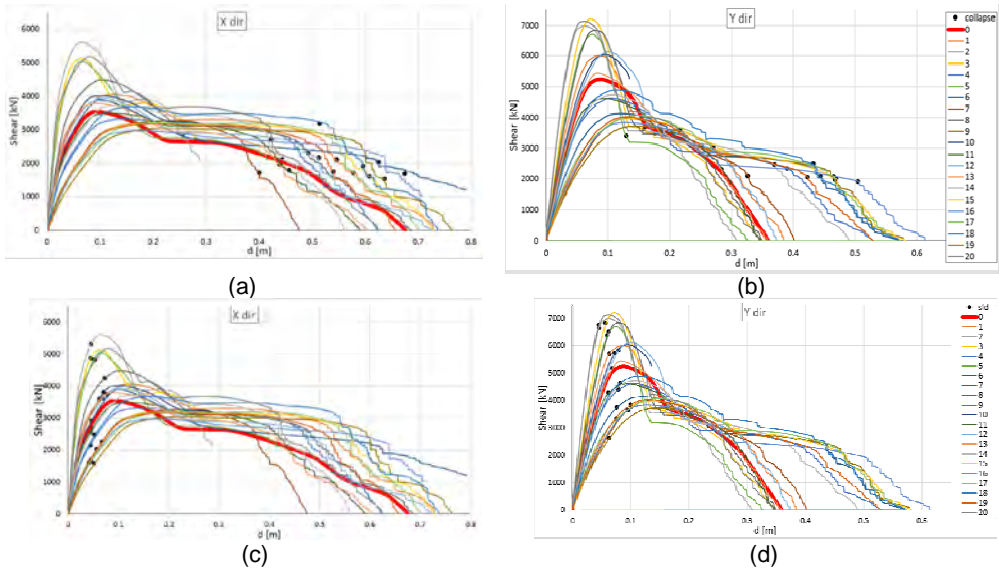
Figure 6.5.24 Pushover of the varied models and limit displacements for the CLS in the X (a) and Y (b) directions and for the DLS in the X (c) and Y (d) directions for HDRB-FSB.

In Figure 6.5.25 the results of the analysis for the Collapse Limit State are reported. In particular, Figure 6.5.25b refers to the case where uncertainties are taken into account. It is worth noting that the 20 varied models were generated randomly combining a varied model of the superstructure with an isolation system with varied properties. NTHAs were performed by randomly associating one of the 20 ground motion record pair to one of the 20 varied model.



(a)

(b)
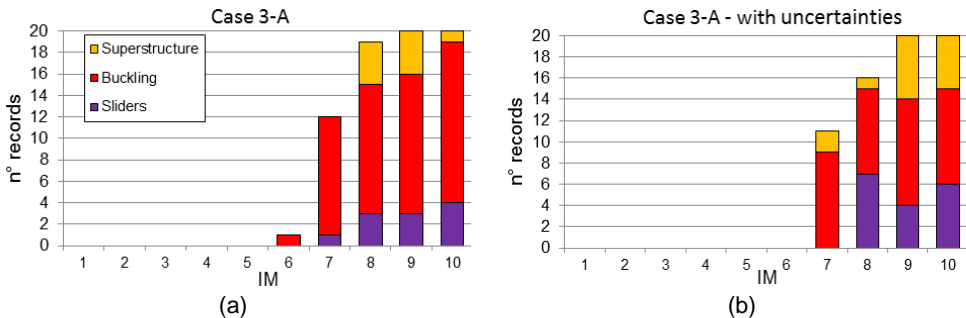
Figure 6.5.25 NTHAs' results at CLS for HDRB-FSB for L'Aquila case study 3-A without uncertainty (a) and with uncertainty (b).

By comparing Figure 6.5.25a, b it is noticeable that the variability does not modify significantly the number of collapse, but only the collapse mode (more superstructure collapse and sliders collapse are found with respect to the reference case).

Finally, the results for the Damage Limit State are summarized in terms of D/C ratios in Figure 6.5.26 for the models with isolation system and superstructure uncertainties and in Figure 6.5.27

for the reference case without uncertainties. The comparison shows that no significant differences are observed between the two cases.



(a)                                                                                (b)
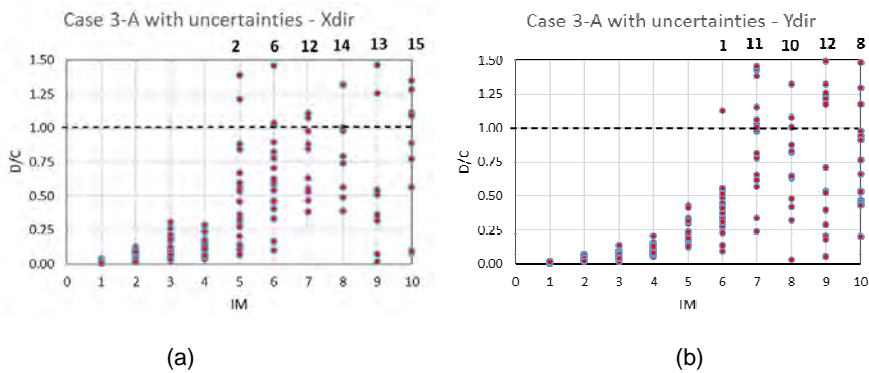
Figure 6.5.26 D/C ratios for the reference case with uncertainties in the X (a) direction and the Y (b) direction.



(a)                                                                                (b)
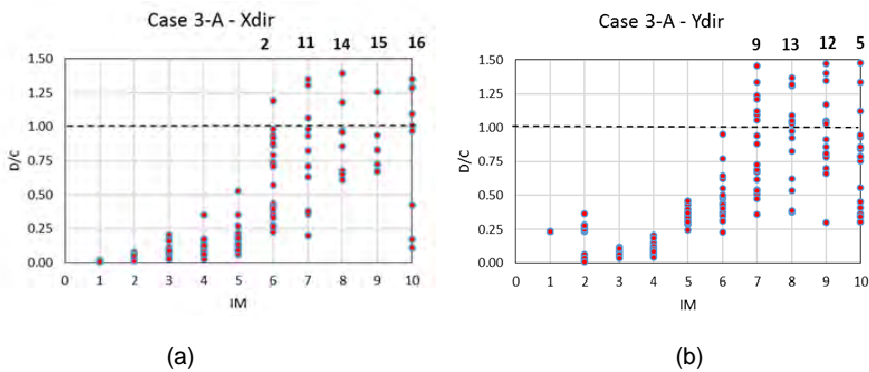
Figure 6.5.27 D/C ratios for the reference case (Case 3-A) without uncertainties in the X (a) direction and the Y (b) direction.

**Case study building of Naples:** The analysis results for the Collapse Limit State and Damage Limit State are summarized in this section, with reference to the case study buildings located at Naples.



(a)                                                                                (b)
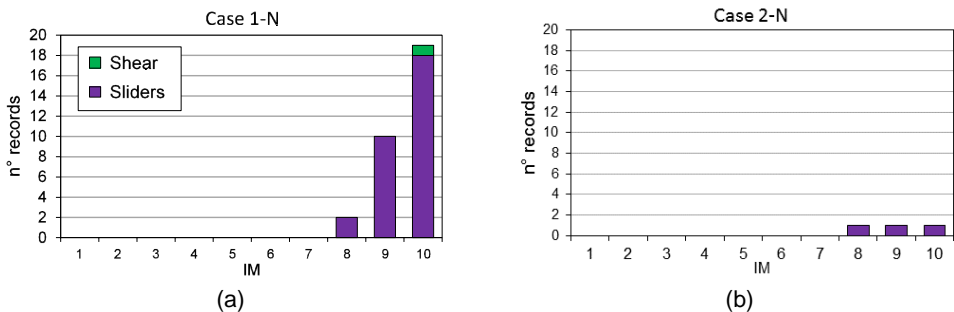
Figure 6.5.28 Summary of NTHAs results at CLS for (a) case 1-N, (b) case 2-N for HDRB-FSB.

In line with the results obtained for the case study 2-Nb with HDRBs (see Figure 6.5.17), the number of failure observed for the case study 2-N is very low (see Figure 6.5.28b). Once again, this can be ascribed to the characteristics of the ground motion set associated with the conditioning period T=2.0 s. Indeed, the latter is characterized by a value of $S_a$ (T=2.0s) at IML6

equal to 0.119g, which is considerably lower than the corresponding value from the reference code spectrum (0.186g).

The results for the Damage Limit State are summarized in terms of D/C ratios associated with each record and IML. Also in this case, results presented in Figure 6.5.29 and Figure 6.5.30 show that, for the intensity measure level corresponding to the return period equal to 50 years (i.e., IML 2), no failures are recorded and the computed D/C ratios are much lower than 1. Only for the intensity measure levels of 9 and 10 the number of failure cases is significant in the X-direction.



(a)                                                                (b)
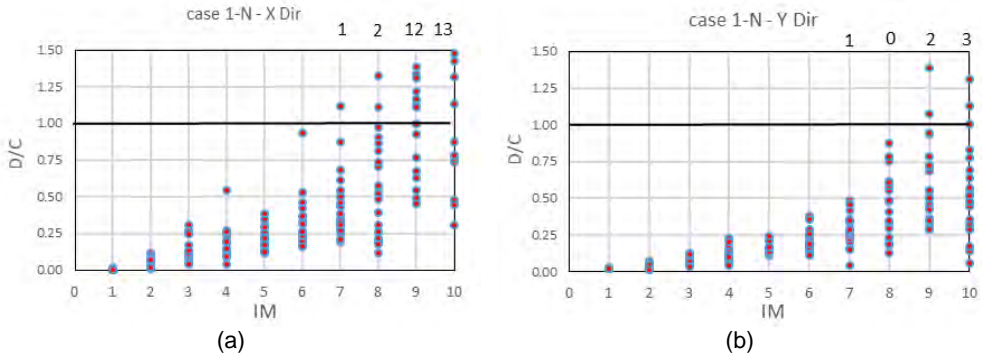
Figure 6.5.29 D/C ratios for (a) case 1-N in x direction, (b) case 1-N in y direction for HDRB-FSB.



(a)                                                                (b)
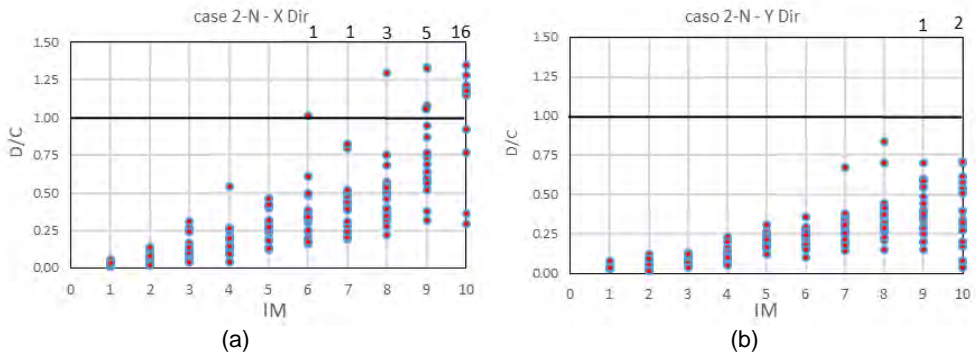
Figure 6.5.30 D/C ratios for (a) case 2-N in x direction, (b) case 2-N in y direction for HDRB-FSB.

6.5.3.3    FP isolation system

**Case study building in L'Aquila**: The analyses results for the Collapse Limit State are summarized in Figure 6.5.31. They show that, for the intensity measure level corresponding to the return period equal to 1000 years (i.e., IML 6), typically assumed as Collapse Limit State according to NTC2008, the number of collapse cases reached 20% of the total number of ground motion records. As a general trend, a significant number of failures associated with the isolation system is recorded above IML 6, while there is an increasing number of failures due to the superstructure collapse above IML 8.
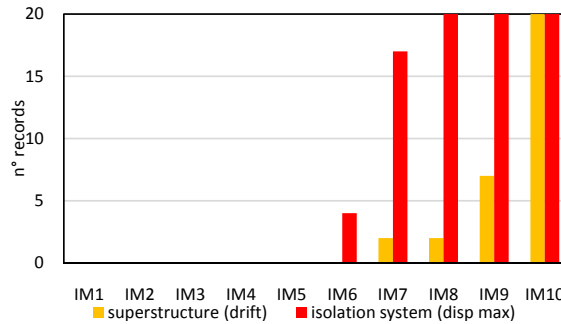
Figure 6.5.31 Summary of NTHAs' results for FPS case study (L'Aquila).

The results for the Damage Limit State are summarized in terms of D/C ratios associated to each singular record and IML in Figure 6.5.32.
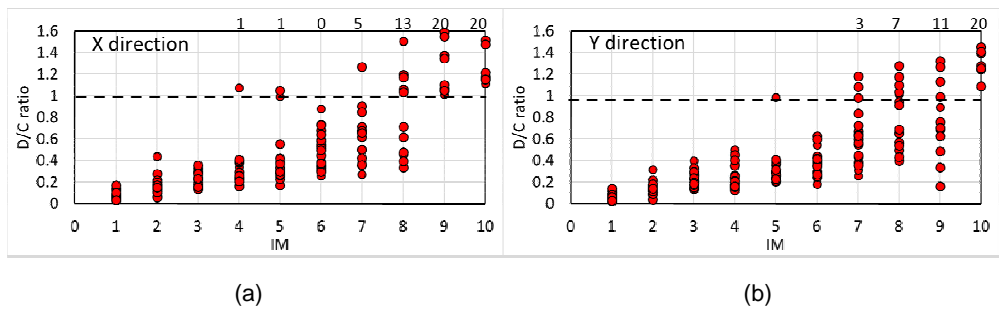


(a)(b)
Figure 6.5.32 D/C ratios in the X (a) direction and the Y (b) direction.

The results show that, for the intensity measure level corresponding to the return period equal to 50 years (i.e. IML 2), typically assumed as Damage Limit State according to NTC2008, no failures are recorded and D/C ratios lower than 1 are obtained. A significant number of failures starts to appear, (D/C≥1) only for seismic events characterized IML greter than IML 6.

**Case study building in L'Aquila, with gap**: In this section the analyses results for the Collapse Limit State are summarized for the case study located at L'Aquila with and without seismic gap. All the analyses are performed with the set of ground motions with the conditioning period of 3.0 second. In particular, in Figure 6.5.33a the results of the case with gap amplitude equal to the CLS design value (263 mm) are reported. Moreover, in order to get a comprehensive overview, the analyses results of the same case study without gap are reported Figure 6.5.33b.
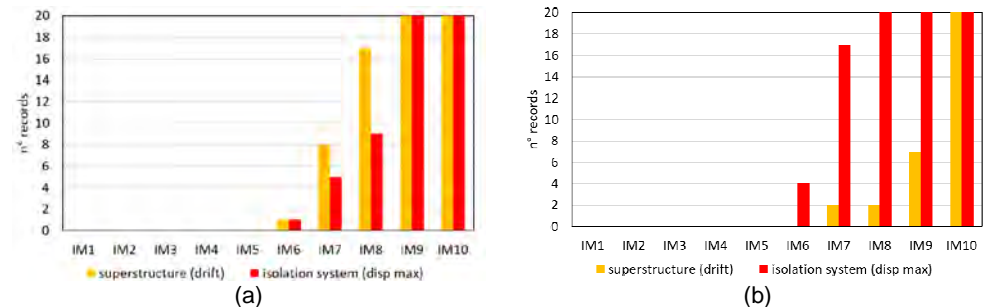


(a)(b)
Figure 6.5.33 Collapse mechanisms for the case of Gap 263mm (a) and without Gap (b).

The comparison highlights that the number of collapse are similar in all the cases, but the type of the first collapse changes. More in detail, in the case without gap, there are mainly collapses due to the isolation system, while in the cases with gap, superstructure collapses appear. No analysis at the Damage Limit State were performed for these cases, since the presence of gap does not influence the isolated system behavior at low seismic intensities.

**Case study building in L'Aquila, with uncertainty**: In this section the analyses results for the Collapse Limit State, followed by the results for the Damage Limit State, are summarized for the case study located at L'Aquila with and without model uncertainties. In Figure 6.5.34 the capacity curves of the 20 models with varied parameters (varied models) obtained by the pushover analyses are shown, for both the X and Y directions.
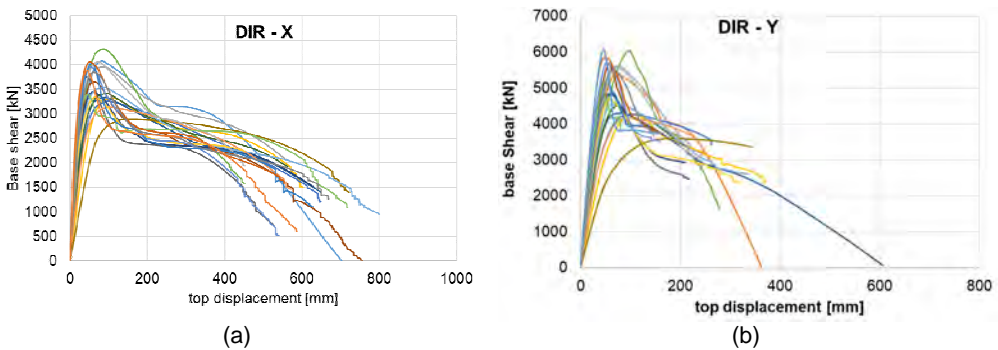


(a)                                                        (b)
Figure 6.5.34 Pushover of the varied models at CLS in the X and Y direction.

In Figure 6.5.35, the results of the analyses for the Collapse Limit State are reported. In particular, Figure 6.5.35a results are related to the case where uncertainties of the isolation system and superstructure are introduced, i.e., for each IML the analyses were performing by associating one of the 20 ground motion records to one of the 20 model with varying isolation properties (one to one association).
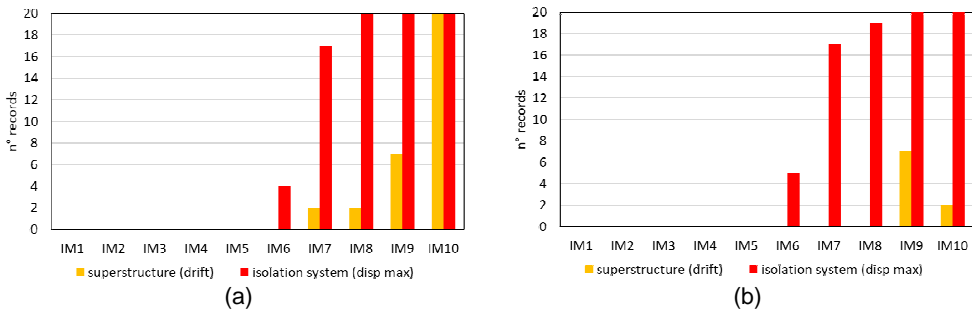


(a)                                                        (b)
Figure 6.5.35 NTHAs' results at CLS for FPS for L'Aquila case study without uncertainty(a) and with uncertainty (b).

By comparing Figure 6.5.35a with Figure 6.5.35b it is noticeable that the variability of the isolation system does not affect significantly the number of collapse. Also results for the Damage Limit State are not significantly affected by the model uncertenties introduction, as shown by in Figure 6.5.36.

(a)                                                                        (b)
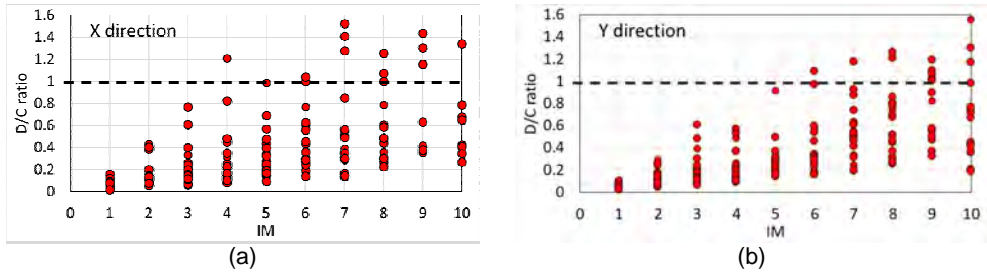
Figure 6.5.36 D/C ratios of the case with uncertainties in  the X (a) direction and the Y (b) direction.

**Case study building of Naples**: The analyses results for the Collapse Limit State of the case studies located at Naples are summarized in this section, followed by those for the Damage Limit State. For the CLS, the results in terms of number of failures and failure modalities are reported in Figure 6.5.37. They are in line with those of the other isolation systems and show that collapse cases are present only for IMLs larger than IML8.
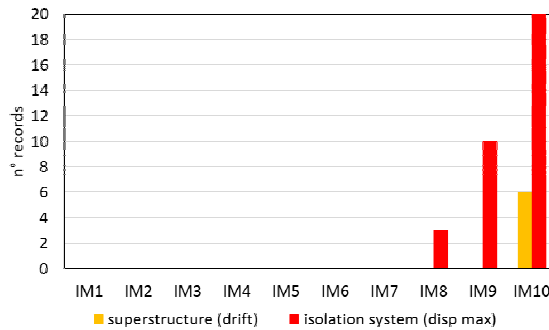


Figure 6.5.37 Summary of NTHAs' results at CLS for the Naples case building with FPS.

The results for the Damage Limit State are summarized in Figure 6.5.38. The obtained results show that, for the intensity measure level corresponding to the return period equal to 50 years (i.e., IML 2), typically assumed as Damage Limit State according to NTC2008, no failures are recorded and the computed D/C ratios are lower than 1. According to the other isolation systems, only for the intensity measure of 10 the number of failure cases is significant.



(a)                                                                        (b)
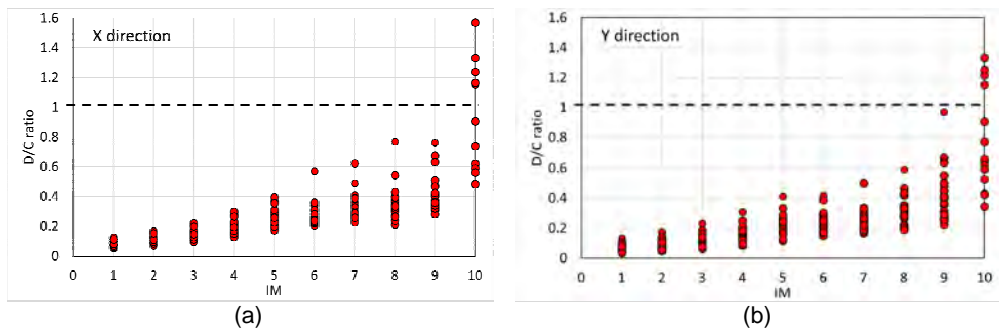
Figure 6.5.38 D/C ratios for the Naples case building in direction X and direction Y for FPS.

## 6.6   References

Bertoldi, S.H., Decanini, L.D., Gavarini, C., (1993). "Telai tamponati soggetti ad azioni sismiche, un modello semplificato, confronto sperimentale e numerico." 6° Convegno Nazionale L'ingegneria Sismica in Italia, Perugia, 13-15 Ottobre 1993, 2, 815-824.

Buckle, I. G., and Liu, H. (1993). "Stability of elastomeric seismic isolation systems." Proceedings: 1st Seminar on Seismic Isolation, Passive Energy Dissipation, and Control, Redwood City, CA, 293-305.

Buckle, I., Nagarajaiah, S., and Ferrell, K. (2002). "Stability of elastomeric isolation bearings: experimental study." Journal of Structural Engineering, 128(1), 3-11.

Constantinou, M. C., Whittaker, A. S., Kalpakidis, Y., Fenz, D. M., and Warn, G. P. (2007). "Performance of seismic isolation hardware under service and seismic loading." Report MCEER-07-0012, Multidisciplinary Center for Earthquake Engineering Research, State University of New York at Buffalo, NY.

Constantinou MC, Mokha A, Reinhorn A (1990). Teflon bearings in base isolation. II: modeling. Journal of Earthquake Engineering, 116(2), 455–474.

Decanini L., Liberatore L., Mollaioli F. (2014) "Strength and stiffness reduction factors for infilled frames with openings", Earthquake Engineering and Engineering Vibration, 13(3): 437-454, September, 2014.

Gent, A. (1990). "Cavitation in rubber: a cautionary tale." Rubber Chemistry and Technology, 63, 49.

Goulet, C. A., Haselton, C. B., Mitrani--□-Reiser, J., Beck, J. L., Deierlein, G. G., Porter, K. A., & Stewart, J. P. (2007). "Evaluation of the seismic performance of a code--□-conforming reinforced--□-concrete frame building from seismic hazard to collapse safety and economic losses." Earthquake Engineering & Structural Dynamics, 36(13), 1973-1997.

Grant, Fenves e Whittaker, (2004) "Bidirectional modeling of high-damping rubber bearings." Journal of Earthquake Engineering, 8(spec01), 161-185.

Haselton, C. B., Liel, A. B., Deierlein, G. G., Dean, B. S., & Chou, J. H. (2010). Seismic collapse safety of reinforced concrete buildings. I: Assessment of ductile moment frames." Journal of Structural Engineering, 137(4), 481-491.

Ibarra, L. F., & Krawinkler, H. (2005). "Global collapse of frame structures under seismic excitations." Rep. No. TB 152, Berkeley, CA: Pacific Earthquake Engineering Research Center.

Ibarra, L. F., Medina, R. A., & Krawinkler, H. (2005). "Hysteretic models that incorporate strength and stiffness deterioration." Earthquake engineering & structural dynamics, 34(12), 1489-1511.

Iwabe, N., Takayama, M., Kani, N., and Wada, A. (2000). "Experimental study on the effect of tension for rubber bearings." Proceedings: 12th World Conference on Earthquake Engineering, New Zealand.

Kawamata S, Nagai K (1992). "Ultimate deformation capacity of isolators. In: International workshop on recent developments in base-isolation techniques for buildings." Tokyo, 27–30 Apr,187–198.

Kumar M., Whittaker A., Constantinou M. C., (2015) "Experimental investigation of cavitation in elastomeric seismic isolation bearings." Engineering Structures, 101, 290-305.

Liel, A. B., Haselton, C. B., & Deierlein, G. G. (2010). "Seismic collapse safety of reinforced concrete buildings. II: Comparative assessment of nonductile and ductile moment frames." Journal of Structural Engineering, 137(4), 492-502.

Liberatore L (2001), Approcci innovativi in termini di energia e di spostamento per la valutazione della risposta sismica di strutture a più gradi di libertà, PhD Dissertation, "Sapienza" University of Rome, Italy. (In Italian).

Montuori G. M., Mele E., Marrazzo G., Brandonisio G., De Luca A. (2015), "Stability issues and pressure–shear interaction in elastomeric bearings: the primary role of the secondary shape factor." Bulletin of Earthquake Engineering, 14(2), 569-597.

Muramatsu Y., Inoue K., Kato R., Kamitani N., Sakaguchi T., Sasaki Y., Suzuki S., Sera S-. Miyazaki M., Kitamura H. (2004) "Test results of ultimate properties of rubber bearings for buildings." Journal of Architecture and Building Science, 20, 67-70 (in Japanese).

Sassun K., Cardone D., Sullivan T., Morandi P. (2016), "Characterising the seismic performance of infill masonry." Bulletin of New Zealand Society for Earthquake Engineering [ISSN: 11749857], 49(1), 100-117

Villaverde, R. (2007). Methods to assess the seismic collapse capacity of building structures: State of the art. Journal of Structural Engineering, 133(1), 57-66.

Warn, G. P., Whittaker, A. S. (2006). "A study of the coupled horizontal-vertical behavior of elastomeric and lead-rubber seismic isolation bearings." Report MCEER-06-0011, Multidisciplinary Center for Earthquake Engineering Research, State University of New York at Buffalo, NY.

Weisman, J., and Warn, G. P. (2012). "Stability of elastomeric and lead-rubber seismic isolation bearings." Journal of Structural Engineering, 138(2), 215-223.

CSI - Computers & Structures, Inc. (2014). "CSI Analysis Reference Manual", Berkeley, California, USA.

Bowden, F.P., Tabor, D. (1964) "The friction and lubrication of solids – part II" Oxford University Press, London, Great Britain.

CEN, European Committee for Standardization (2009) "EN 15129: Anti-Seismic Devices", Bruxelles, Belgium.

# CHAPTER VII – RESULTS

## 7.1 Computation of nominal failure rates and interpretation

In Chapter 1 it was discussed that the failure rates for the structure are computed according to:

$$\lambda_f = \lambda \cdot \int_0^{+\infty} P\left[ failure \middle| IM = x \right] \cdot f_{IM}(x) \cdot dx \tag{7.1}$$

Because the hazard analysis was computed only up to a 10,000 years return period of exceedance, the above integral cannot be fully computed. In fact, if the hazard curves are only available up to a certain return period, say $T_R^*$, to which corresponds a certain intensity value, $IM_{T_R^*}$, at each site, then the failure rate can only be approximated by $\lambda^*$, which is obtained as follows:

$$\lambda_f = \lambda \cdot \int_0^{IM_{T_R^*}} P\left[ failure \middle| IM = x \right] \cdot f_{IM}(x) \cdot dx + \lambda \cdot \int_{IM_{T_R^*}}^{+\infty} P\left[ failure \middle| IM = x \right] \cdot f_{IM}(x) \cdot dx \Rightarrow$$

$$\Rightarrow \lambda \cdot \int_0^{IM_{T_R^*}} P\left[ failure \middle| IM = x \right] \cdot f_{IM}(x) \cdot dx = \lambda^* \le \lambda_f \tag{7.2}$$

As the equation indicates, $\lambda^*$ certainly underestimates the sought $\lambda_f$. The largest difference between the approximated and 'true' rates is obtained assuming the structure would certainly fail for intensities larger than those where the hazard curve stops, $IM \ge IM_{T_R^*}$, that is:

$$P\left[ failure \middle| IM = x \right] = 1 \qquad \forall\ x \ge IM_{T_R^*} \tag{7.3}$$

In fact, in this case, it results that the maximum error is precisely the annual rate of exceedance of $IM_{T_R^*}$, that is the hazard for $IM_{T_R^*}$:

$$\left| \lambda^* - \lambda_f \right| = \lambda \cdot \int_{IM_{T_R^*}}^{+\infty} P\left[ failure \middle| IM = x \right] \cdot f_{IM}(x) \cdot dx = \lambda \cdot \int_{IM_{T_R^*}}^{+\infty} f_{IM}(x) \cdot dx = \lambda_{IM \ge IM_{T_R^*}} \tag{7.4}$$

For example, by not performing hazard analysis beyond intensity with a return period of 100,000 years, the maximum error in estimating the failure rate is $10^{-5}$. As a consequence, if the part of equation (7.1) that may be computed is especially low, then it is possible that the error in estimation of the rate is comparable or larger than the approximated rate $\lambda^*$.

In order to avoid underestimating the failure rates, the results presented in the rest of this chapter were computed as per in the following equation, which certainly overestimates the failure rate. In this calculation the part of the failure rate due to intensities for which hazard is not available was replaced by the rate of exceedance of the largest IM value for which hazard is available, which is tantamount to assuming failure for larger intensities. This certainly overestimates the failure rate and in some cases, illustrated in the following, when the first part of the integral is negligible with respect to $10^{-5}$, only allows to state that the annual failure rate is lower than $10^{-5}$. In the following sub-sections the failure rates are computed with the following expression and compared.

$$\lambda^* = \lambda \cdot \int_0^{IM_{T_R^*}} P\left[\,failure\,\middle|\,IM = x\right] \cdot f_{IM}\left(x\right) \cdot dx + \lambda \cdot \int_{IM_{T_R^*}}^{+\infty} 1 \cdot f_{IM}\left(x\right) \cdot dx =$$

$$= \lambda \cdot \int_0^{IM_{T_R^*}} P\left[\,failure\,\middle|\,IM = x\right] \cdot f_{IM}\left(x\right) \cdot dx + \lambda_{IM \geq IM_{T_R^*}} \qquad (7.5)$$

$$= \lambda \cdot \int_0^{IM_{T_R^*}} P\left[\,failure\,\middle|\,IM = x\right] \cdot f_{IM}\left(x\right) \cdot dx + 0.00001 > \lambda_f$$

## 7.2   Nominal failure and damage rates of masonry case studies

The rates of the analyzed masonry buildings in the considered cities and for both Soil Types A and C are summarized from Table 7.2.1 to Table 7.2.12. The Structure Name together with the Research Unit (UR) and the associated nominal rates are reported in the cited tables. The failure rates for the masonry case studies are provided in Figure 7.2.1 and Figure 7.2.2, while Figure 7.2.3 and Figure 7.2.4 show the rates associated to the onset of damage for both soil A and C. The results refer to regular (Reg) and irregular (Irreg) structures, together with some case studies designed according to the upcoming code (labelled as NTC18). Moreover, an additional limit state was considered, i.e., the onset of damage (later defined simply Damage). It may be observed that only at the site with lowest seismicity among those considered (Milan) the failure rates are given only as an upper bound to the real, as discussed at the beginning of this chapter.

Table 7.2.1 Collapse and Damage rates for masonry buildings in L'Aquila when local site condition is C according to Eurocode 8 classification.

| Soil Type C | | | |
|---|---|---|---|
| Regular 2-story structures | | | |
| UR | Structure ID | Collapse Rate | Damage Rate |
| *UniGe* | *Aq_C_2_C3* | 5.24E-04 | 8.00E-03 |
| *Eucentre* | *Aq_C_2_E2* | 4.32E-04 | 1.68E-03 |
| *Eucentre* | *Aq_C_2_E8* | 3.83E-04 | 2.77E-03 |
| *Eucentre* | *Aq_C_2_E9* | 9.27E-04 | 2.05E-03 |
| Irregular 2-story structures | | | |
| *UniGe* | *Aq_C_2_I1* | 2.24E-03 | 2.09E-02 |
| *Eucentre* | *Aq_C_2_E5* | 5.44E-04 | 3.97E-03 |

Table 7.2.2 Collapse and Damage rates for masonry buildings in L'Aquila when local site condition is A according to Eurocode 8 classification.

| Soil Type A | | | |
|---|---|---|---|
| Regular 2-story structures | | | |
| UR | Structure ID | Collapse Rate | Damage Rate |
| *UniGe* | *Aq_A_2_C1* | 4.87E-04 | 9.04E-03 |
| *UniGe* | *Aq_A_2_C3_NTC18* | 2.99E-04 | 8.30E-03 |
| *Eucentre* | *Aq_A_2_E2* | 2.54E-04 | 1.32E-03 |
| Irregular 2-story structures | | | |
| *UniGe* | *Aq_A_2_I1_NTC18* | 7.24E-04 | 3.30E-02 |
| Regular 3-story structures | | | |
| *UniGe* | *Aq_A_3_C1* | 8.41E-04 | 1.64E-02 |
| *Eucentre* | *Aq_A_3_E2* | 5.35E-04 | 2.53E-03 |
| *Eucentre* | *Aq_A_3_E8* | 4.37E-04 | 2.84E-03 |

Table 7.2.3 Collapse and Damage rates for masonry buildings in L'Aquila including modelling uncertainty when local site condition is A according to Eurocode 8 classification.

| Soil Type A | | | |
|---|---|---|---|
| 2-story structures | | | |
| UR | Structure ID | Collapse Rate | Damage Rate |
| *UniGe* | *Aq_StrUnc_2stCC[3]* | 4.07E-04 | 7.70E-03 |
| *UniGe* | *Aq_StrUnc_2stCL[3]* | 3.92E-04 | 7.01E-03 |
| *Eucentre* | *Aq_StrUnc_2stCC[3]* | 2.67E-04 | 1.23E-03 |
| *Eucentre* | *Aq_StrUnc_2stCL[3]* | 2.10E-04 | 9.46E-04 |
| 3-story structures | | | |
| *UniGe* | *Aq_StrUnc_3stCC[3]* | 7.74E-04 | 1.55E-02 |
| *UniGe* | *Aq_StrUnc_3stCL[3]* | 7.37E-04 | 1.46E-02 |
| *Eucentre* | *Aq_StrUnc_3stCC[3]* | 4.94E-04 | 3.95E-03 |
| *Eucentre* | *Aq_StrUnc_3stCL[3]* | 4.54E-04 | 3.13E-03 |

Table 7.2.4 Collapse and Damage rates for masonry buildings in Naples when local site condition is C according to Eurocode 8 classification.

| Soil Type C | | | |
|---|---|---|---|
| Regular 2-story structures | | | |
| UR | Structure ID | Collapse Rate | Damage Rate |
| *UniGe* | *Na_C_2_C1* | 4.61E-05 | 4.63E-03 |
| *UniGe* | *Na_C_2_C4* | 3.56E-05 | 3.04E-03 |
| *UniGe* | *Na_C_2_C2_NTC18* | 7.85E-05 | 4.14E-03 |
| Irregular 2-story structures | | | |
| *UniGe* | *Na_C_2_I1_NTC18* | 3.95E-04 | 7.02E-03 |
| Regular 3-story structures | | | |
| *UniGe* | *Na_C_3_C3* | 1.19E-04 | 6.66E-03 |
| *UniGe* | *Na_C_3_C5* | 8.36E-05 | 7.45E-03 |
| *UniGe* | *Na_C_3_C5_NTC18* | 8.36E-05 | 6.43E-03 |
| *Eucentre* | *Na_C_3_E2* | 4.62E-05 | 1.21E-03 |
| *Eucentre* | *Na_C_3_E8* | 8.59E-05 | 1.30E-03 |
| Irregular 3-story structures | | | |
| *UniGe* | *Na_C_3_I2_NTC18* | 1.72E-04 | 1.07E-02 |

Table 7.2.5 Collapse and Damage rates for masonry buildings in Naples when local site condition is A according to Eurocode 8 classification.

| Soil Type A | | | |
|---|---|---|---|
| Regular 2-story structures | | | |
| UR | Structure ID | Collapse Rate | Damage Rate |
| *UniGe* | *Na_A_2_C3* | 4.80E-05 | 2.06E-03 |
| *UniGe* | *Na_A_2_C1_NTC18* | 5.49E-05 | 3.19E-03 |
| *Eucentre* | *Na_A_2_E8* | 3.64E-05 | 4.90E-04 |
| Regular 3-story structures | | | |
| *UniGe* | *Na_A_3_C4* | 6.41E-05 | 6.02E-03 |
| *UniGe* | *Na_A_3_C1_NTC18* | 1.13E-04 | 6.24E-03 |
| Irregular 3-story structures | | | |
| *UniGe* | *Na_A_3_I2_NTC18* | 2.38E-04 | 1.19E-02 |
| *Eucentre* | *Na_A_3_E5* | 9.79E-05 | 1.25E-02 |

---

[3] The acronyms CC and CL stand respectively for "stiff tie-beams" and "flexible tie-beams" two divers modelling approach that have already been described in the masonry section.

Table 7.2.6 Collapse and Damage rates for masonry buildings in Rome when local site condition is C according to Eurocode 8 classification.

| Soil Type C | | | |
|---|---|---|---|
| Regular 2-story structures | | | |
| UR | Structure ID | Collapse Rate | Damage Rate |
| *UniGe* | *Ro_C_2_C3* | 1.65E-05 | 3.38E-03 |
| *UniGe* | *Ro_C_2_C1_NTC18* | 2.39E-05 | 4.65E-03 |
| *Eucentre* | *Ro_C_2_E8* | 1.26E-05 | 4.24E-04 |
| Regular 3-story structures | | | |
| *UniGe* | *Ro_C_3_C4* | 3.67E-05 | 5.12E-03 |
| *UniGe* | *Ro_C_3_C1_NTC18* | 3.03E-05 | 4.87E-03 |
| Irregular 3-story structures | | | |
| *UniGe* | *Ro_C_3_I2_NTC18* | 1.08E-04 | 1.27E-02 |

Table 7.2.7 Collapse and Damage rates for masonry buildings in Rome when local site condition is A according to Eurocode 8 classification.

| Soil Type A | | | |
|---|---|---|---|
| Regular 2-story structures | | | |
| UR | Structure ID | Collapse Rate | Damage Rate |
| *UniGe* | *Ro_A_2_C2* | 1.51E-05 | 2.00E-03 |
| *Eucentre* | *Ro_A_2_E8* | 1.04E-05 | 1.90E-04 |
| *Eucentre* | *Ro_A_2_E9* | 1.01E-05 | 3.29E-05 |
| Regular 3-story structures | | | |
| *UniGe* | *Ro_A_3_C3* | 1.72E-05 | 2.93E-03 |
| *Eucentre* | *Ro_A_3_E8* | 1.45E-05 | 5.25E-04 |

Table 7.2.8 Collapse and Damage rates for masonry buildings in Rome including modelling uncertainty when local site condition is A according to Eurocode 8 classification.

| Soil Type A | | | |
|---|---|---|---|
| 2-story structures | | | |
| UR | Structure ID | Collapse Rate | Damage Rate |
| *UniGe* | *Ro_StrUnc_2stCC* | 2.71E-05 | 1.40E-03 |
| *UniGe* | *Ro_StrUnc_2stCL* | 1.52E-05 | 1.47E-03 |
| *Eucentre* | *Ro_StrUnc_2stCC* | 1.14E-05 | 9.51E-05 |
| *Eucentre* | *Ro_StrUnc_2stCL* | 1.14E-05 | 8.21E-05 |
| 3-story structures | | | |
| *UniGe* | *Ro_StrUnc_3stCC* | 2.46E-05 | 4.01E-03 |
| *UniGe* | *Ro_StrUnc_3stCL* | 6.39E-05 | 3.12E-03 |
| *Eucentre* | *Ro_StrUnc_3stCC* | 2.56E-05 | 5.09E-04 |
| *Eucentre* | *Ro_StrUnc_3stCL* | 2.13E-05 | 3.52E-04 |

Table 7.2.9 Collapse and Damage rates for masonry buildings in Caltanissetta when local site condition is C according to Eurocode 8 classification.

| Soil Type C | | | |
|---|---|---|---|
| Regular 2-story structures | | | |
| UR | Structure ID | Collapse Rate | Damage Rate |
| *UniGe* | *Ca_C_2_C2* | 1.00E-05 | 1.18E-04 |
| *Eucentre* | *Ca_C_2_E8* | 1.11E-05 | 4.15E-05 |
| *Eucentre* | *Ca_C_2_E9* | 1.01E-05 | 3.29E-05 |
| Regular 3-story structures | | | |
| *UniGe* | *Ca_C_3_C3* | 1.01E-05 | 2.17E-04 |
| *Eucentre* | *Ca_C_3_E8* | 1.00E-05 | 4.76E-05 |

Table 7.2.10 Collapse and Damage rates for masonry buildings in Caltanissetta when local site condition is A according to Eurocode 8 classification.

| Soil Type A | | | |
|---|---|---|---|
| Regular 2-story structures | | | |
| UR | Structure ID | Collapse Rate | Damage Rate |
| *UniGe* | *Ca_A_2_C1* | 1.45E-05 | 1.09E-04 |
| *UniGe* | *Ca_A_2_C7* | 1.00E-05 | 3.92E-05 |
| *UniGe* | *Ca_A_2_E2* | 1.03E-05 | 2.99E-05 |
| Regular 3-story structures | | | |
| *UniGe* | *Ca_A_3_C2* | 1.90E-05 | 2.55E-04 |
| *Eucentre* | *Ca_A_3_E2* | 1.79E-05 | 6.34E-05 |
| *Eucentre* | *Ca_A_3_E8* | 1.13E-05 | 4.44E-05 |
| *Eucentre* | *Ca_A_3_E9* | 2.97E-05 | 6.03E-05 |

Table 7.2.11 Collapse and Damage rates for masonry buildings in Milan when local site condition is C according to Eurocode 8 classification.

| Soil Type C | | | |
|---|---|---|---|
| Regular 2-story structures | | | |
| UR | Structure ID | Collapse Rate | Damage Rate |
| *UniGe* | *Mi_C_2_C1* | 1.00E-05 | 1.99E-05 |
| *UniGe* | *Mi_C_2_C7* | 1.00E-05 | 1.13E-05 |
| *Eucentre* | *Mi_C_2_E2* | 1.00E-05 | 1.00E-05 |
| Regular 3-story structures | | | |
| *UniGe* | *Mi_C_3_C2* | 1.00E-05 | 1.03E-04 |
| *Eucentre* | *Mi_C_3_E2* | 1.00E-05 | 1.22E-05 |
| *Eucentre* | *Mi_C_3_E8* | 1.00E-05 | 2.28E-05 |
| *Eucentre* | *Mi_C_3_E9* | 1.13E-05 | 3.21E-05 |

Table 7.2.12 Collapse and Damage rates for masonry buildings in Milan when local site condition is A according to Eurocode 8 classification.

| Soil Type A | | | |
|---|---|---|---|
| Regular 2-story structures | | | |
| UR | Structure ID | Collapse Rate | Damage Rate |
| *UniGe* | *Mi_A_2_C1* | 1.00E-05 | 1.90E-05 |
| *UniGe* | *Mi_A_2_C4* | 1.00E-05 | 1.90E-05 |
| *Eucentre* | *Mi_A_2_E2* | 1.00E-05 | 1.00E-05 |
| Irregular 2-story structures | | | |
| *Eucentre* | *Mi_A_2_E5* | 1.00E-05 | 1.00E-05 |
| Regular 3-story structures | | | |
| *UniGe* | *Mi_A_3_C2* | 1.00E-05 | 7.41E-05 |
| *UniGe* | *Mi_A_3_C6* | 1.00E-05 | 4.16E-05 |
| *Eucentre* | *Mi_A_3_E2* | 1.00E-05 | 1.04E-05 |
| Irregular 3-story structures | | | |
| *Eucentre* | *Mi_A_3_E5* | 1.00E-05 | 3.53E-04 |
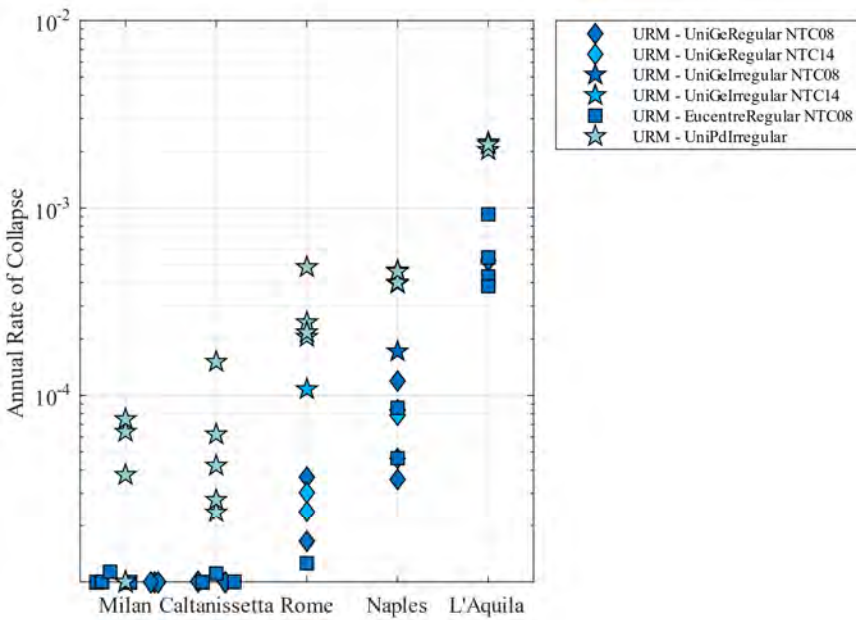
Figure 7.2.1 Failure rates for masonry case studies, when local site condition is C according to Eurocode 8 classification.
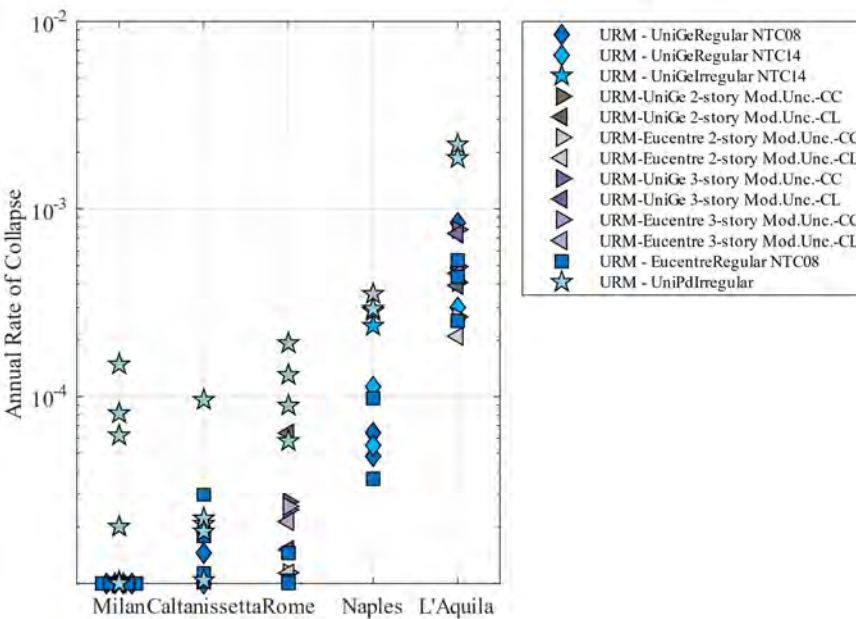


Figure 7.2.2 Failure rates for masonry case studies, when local site condition is A according to Eurocode 8 classification.
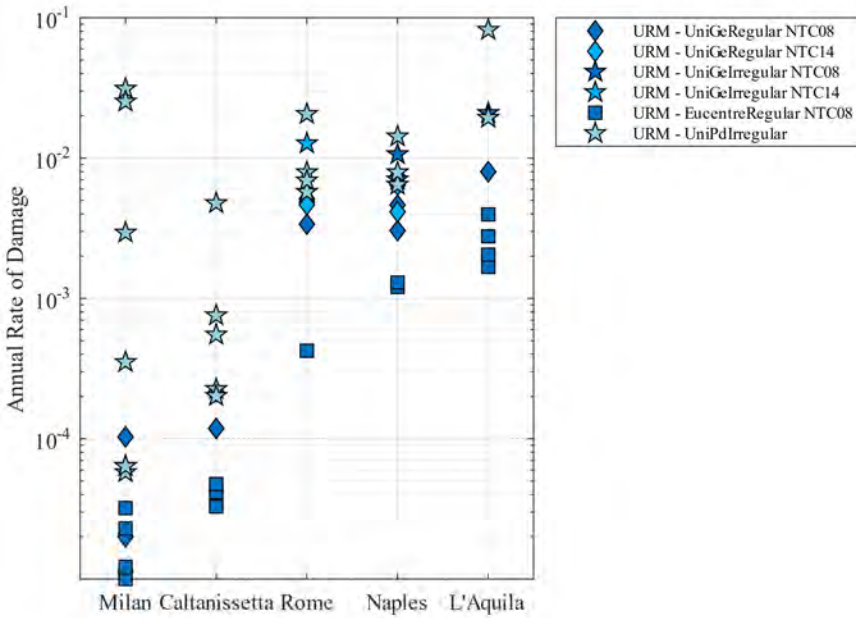
Figure 7.2.3 Damage rates for masonry case studies, when local site condition is C according to Eurocode 8 classification.
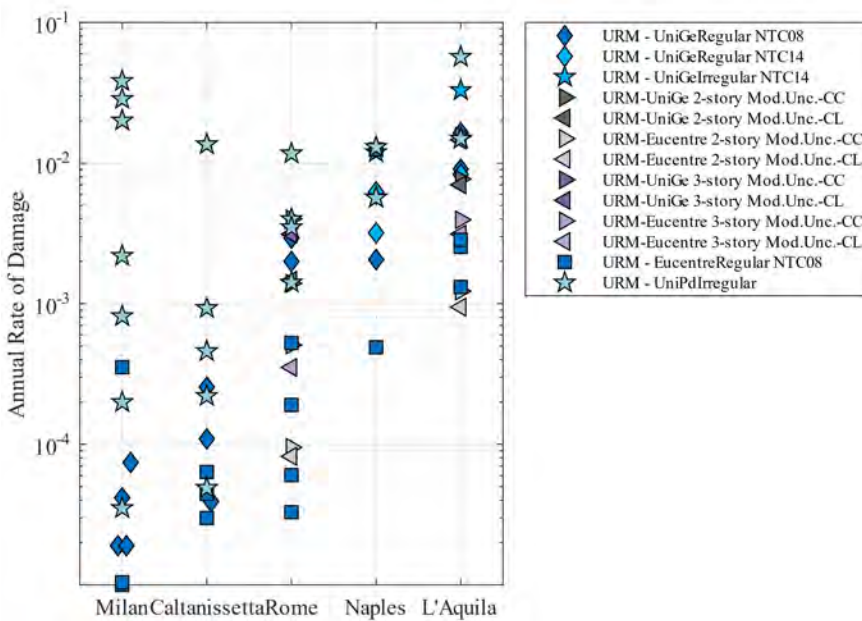


Figure 7.2.4 Damage rates for masonry case studies, when local site condition is A according to Eurocode 8 classification.

## 7.3   Nominal failure rates of precast case studies

The rates of the analyzed precast buildings in the considered cities and for both Soil Types A and C are summarized from Table 7.3.1 to Table 7.3.6. The failure rates for the precast structures are given in Figure 7.3.1 and Figure 7.3.2, while Figure 7.3.3 and Figure 7.3.4 show the rates associated to the onset of damage, both for soil A and C. It may be seen that the failure rates are significantly higher than those computed in the previous year of project, above all in the most hazardous site, i.e., L'Aquila. Indeed, while the collapse caused by excessive rotation at the column base was the only possible failure considered in the previous study, now the beam-column connections are also checked against possible collapses. This increase in collapse rate confirms what observed in real events (e.g., the Emilia 2012 earthquake), that is to say that the connections are the most critical component of precast structure, even though the structures are designed according to current seismic provisions.

Table 7.3.1 Collapse and Damage rates for precast structures in L'Aquila when local site condition is C according to Eurocode 8 classification.

**Soil Type C**

| UR | Structure Name | Collapse Rate | Damage Rate |
|---|---|---|---|
| UniNaM | *Aq_SoilC_Geom3_2sec* | 8.80E-05 | 1.12E-03 |
| UniNaM | *Aq_SoilC_Geom4_2sec* | 1.32E-04 | 1.32E-03 |
| Eucentre | *Aq_SoilC_Geom1_2sec* | 1.35E-03 | 1.03E-02 |
| Eucentre | *Aq_SoilC_Geom2_2sec* | 1.42E-04 | 1.13E-02 |

Table 7.3.2 Collapse and Damage rates for precast structures in L'Aquila when local site condition is A according to Eurocode 8 classification.

**Soil Type A**

| UR | Structure Name | Collapse Rate | Damage Rate |
|---|---|---|---|
| UniNaM | *Aq_SoilA_Geom3_2sec* | 9.70E-05 | 8.10E-04 |
| UniNaM | *Aq_SoilA_Geom4_2sec* | 7.80E-05 | 8.10E-04 |
| Eucentre | *Aq_soilA_Geom1_2sec* | 7.90E-04 | 4.90E-03 |
| Eucentre | *Aq_SoilA_Geom2_2sec* | 6.90E-04 | 4.80E-03 |

Table 7.3.3 Collapse and Damage rates for precast structures in Naples when local site condition is C according to Eurocode 8 classification.

**Soil Type C**

| UR | Structure Name | Collapse Rate | Damage Rate |
|---|---|---|---|
| UniNaM | *Na_SoilC_Geom3_2sec* | 3.70E-05 | 3.46E-04 |
| UniNaM | *Na_SoilC_Geom4_2sec* | 2.80E-05 | 2.77E-04 |
| Eucentre | *Na_SoilC_Geom1_2sec* | 5.40E-04 | 6.40E-03 |
| Eucentre | *Na_SoilC_Geom2_2sec* | 1.12E-04 | 5.90E-03 |

Table 7.3.4 Collapse and Damage rates for precast structures in Naples when local site condition is A according to Eurocode 8 classification.

**Soil Type A**

| UR | Structure Name | Collapse Rate | Damage Rate |
|---|---|---|---|
| UniNaM | *Na_SoilA_Geom3_2sec* | 2.80E-05 | 1.44E-04 |
| UniNaM | *Na_SoilA_Geom4_2sec* | 1.00E-05 | 1.44E-04 |
| Eucentre | *Na_SoilA_Geom1_2sec* | 5.60E-04 | 2.22E-03 |
| Eucentre | *Na_SoilA_Geom2_2sec* | 1.95E-04 | 2.53E-03 |

Table 7.3.5 Collapse and Damage rates for precast structures in Milan when local site
condition is C according to Eurocode 8 classification.

| Soil Type C | | | |
|---|---|---|---|
| UR | Structure Name | Collapse Rate | Damage Rate |
| UniNaM | *Mi_SoilC_Geom3_2sec* | 1.00E-05 | 1.45E-05 |
| UniNaM | *Mi_SoilC_Geom4_2sec* | 1.00E-05 | 1.45E-05 |
| Eucentre | *Mi_SoilC_Geom1_2sec* | 1.90E-05 | 2.50E-04 |
| Eucentre | *Mi_SoilC_Geom2_2sec* | 3.25E-05 | 2.23E-04 |

Table 7.3.6 Collapse and Damage rates for precast structures in Milan when local site
condition is A according to Eurocode 8 classification.

| Soil Type A | | | |
|---|---|---|---|
| UR | Structure Name | Collapse Rate | Damage Rate |
| UniNaM | *Mi_SoilA_Geom3_2sec* | 1.00E-05 | 1.00E-05 |
| UniNaM | *Mi_SoilA_Geom4_2sec* | 1.00E-05 | 1.00E-05 |
| Eucentre | *Mi_SoilA_Geom1_2sec* | 1.00E-05 | 1.06E-04 |
| Eucentre | *Mi_SoilA_Geom2_2sec* | 1.00E-05 | 7.15E-05 |
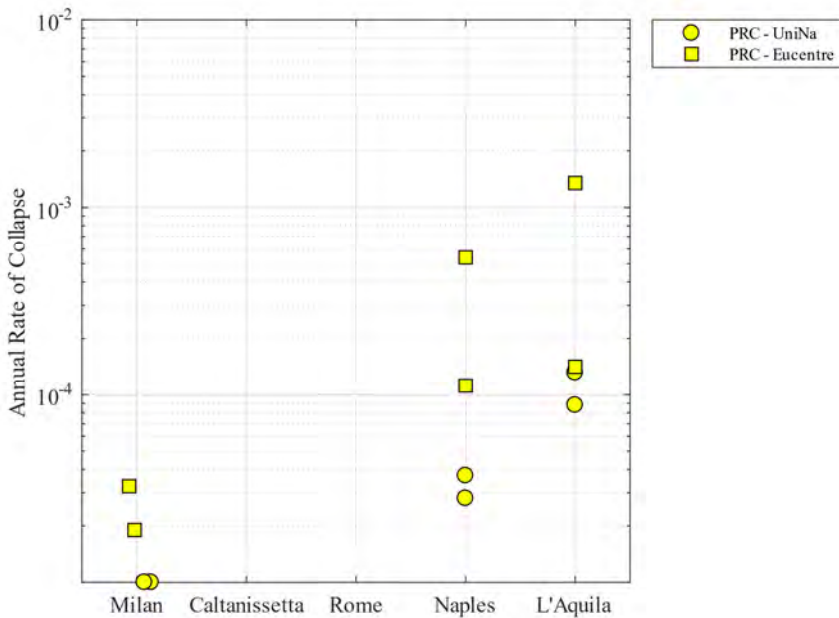


Figure 7.3.1 Failure rates for precast structures, when local site condition is C according to
Eurocode 8 classification.
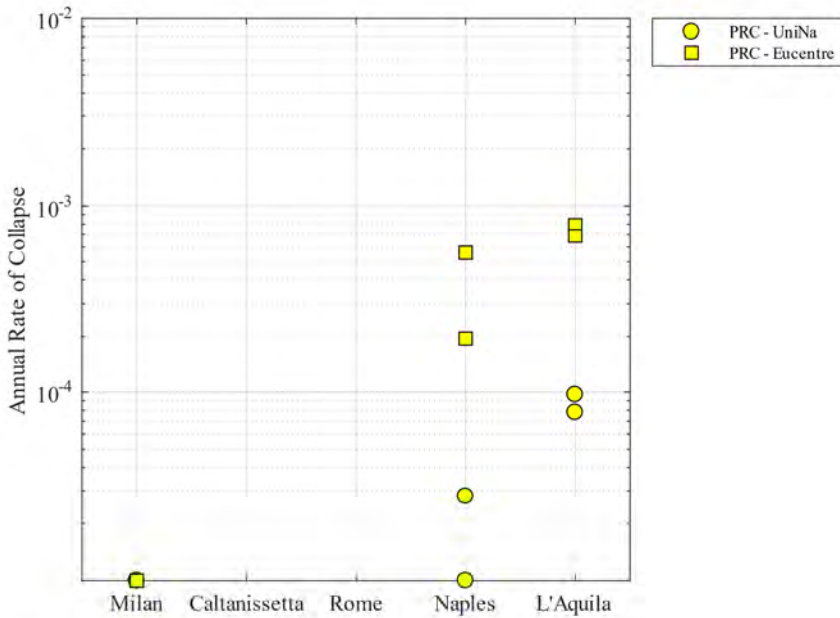
Figure 7.3.2 Failure rates for precast structures, when local site condition is A according to Eurocode 8 classification.
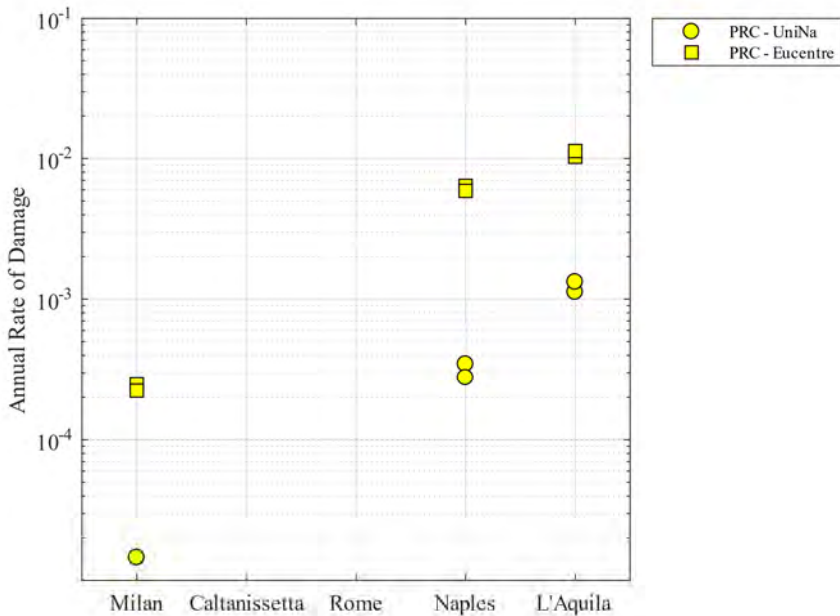


Figure 7.3.3 Damage rates for precast structures, when local site condition is C according to Eurocode 8 classification.
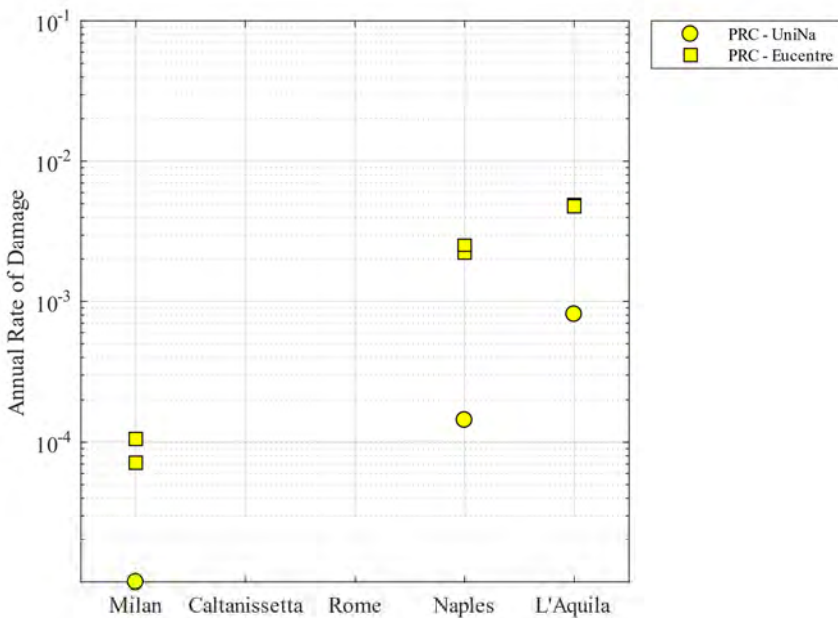
Figure 7.3.4 Damage rates for precast structures, when local site condition is A according to Eurocode 8 classification.

## 7.4   Nominal failure rates of reinforced concrete case studies

The rates of Collapse and Damage associated to Reinforced Concrete buildings in the considered cities for Soil Type C and for Soil Type A (just one case), are summarized below from Table 7.4.1 to Table 7.4.7. Figure 7.4.1 shows the failure rates while the damage rates are represented in Figure 7.4.2. In this year, also the case of nine-story shear wall structure was designed and analyzed for the cities of L'Aquila, Naples and Milan. In particular, the case of Naples was modelled also accounting for soil structure interaction in order to verify its impact in risk calculation. It may be seen that the failure rates are bounded by $10^{-5}$ for most of the cases except for the most seismically hazardous site considered (L'Aquila). The six-story buildings located in Caltanissetta and one three-story in Milan observed collapse rates higher than $10^{-5}$. The damage rates increase with the site hazard even though they seem to show higher dispersion, among diverse configurations, in Milan with respect to L'Aquila. The adoption of shear walls clearly help to strengthen the structure and decrease its vulnerability (mainly in terms of collapse). The influence of SSI seems not so important for collapse while it influences more (even though not much remarkable) for damage limit state.

Table 7.4.1 Collapse and Damage rates for reinforced concrete buildings in L'Aquila when local site condition is C according to Eurocode 8 classification.

**Soil Type C**

| UR | Structure Name | Collapse Rate | Damage Rate |
|---|---|---|---|
| 6-story frames | | | |
| UniBas | *Aq_C_6_BF* | 8.47E-05 | 1.08E-02 |
| UniBas | *Aq_C_6_IF* | 2.02E-04 | 3.93E-03 |
| UniBas | *Aq_C_6_PF* | 2.08E-04 | 3.67E-03 |
| 9-story frames | | | |
| UniCh | *Aq_C_9_BF* | 6.21E-05 | 1.16E-02 |
| UniCh | *Aq_C_9_IF* | 7.64E-05 | 1.06E-02 |
| UniCh | *Aq_C_9_PF* | 7.40E-05 | 1.21E-02 |
| 3-story frames | | | |
| UniNaM | *Aq_C_3_BF* | 3.10E-05 | 1.17E-02 |
| UniNaM | *Aq_C_3_IF* | 6.07E-05 | 2.66E-02 |
| UniNaM | *Aq_C_3_PF* | 1.06E-04 | 2.35E-03 |
| 9-story shear walls | | | |
| UniCh | *Aq_C_9_SW_BF* | 2.85E-05 | 1.03E-02 |
| UniCh | *Aq_C_9_SW_IF* | 5.40E-05 | 8.19E-03 |
| UniCh | *Aq_C_9_SW_PF* | 4.03E-05 | 1.12E-02 |

Table 7.4.2 Collapse and Damage rates for reinforced concrete 9-story frame buildings in L'Aquila when local site condition is A according to Eurocode 8 classification.

**Soil Type A**

| UR | Structure Name | Collapse Rate | Damage Rate |
|---|---|---|---|
| UniBas | *Aq_A_9_BF* | 7.91E-05 | 4.63E-03 |
| UniBas | *Aq_A_9_IF* | 8.19E-05 | 2.51E-03 |
| UniBas | *Aq_A_9_PF* | 7.98E-05 | 2.82E-03 |

Table 7.4.3 Collapse and Damage rates for reinforced concrete buildings in Naples when local site condition is C according to Eurocode 8 classification.

**Soil Type C**

| UR | Structure Name | Collapse Rate | Damage Rate |
|---|---|---|---|
| 6-story frames | | | |
| UniCh | *Na_C_6_BF* | 1.00E-05 | 5.97E-03 |
| UniCh | *Na_C_6_IF* | 1.07E-05 | 3.09E-03 |
| UniCh | *Na_C_6_PF* | 1.02E-05 | 3.03E-03 |
| 9-story frames | | | |
| UniNaV | *Na_C_9_BF* | 2.00E-05 | 7.12E-03 |
| UniNaV | *Na_C_9_IF* | 1.58E-05 | 3.29E-03 |
| UniNaV | *Na_C_9_PF* | 3.85E-05 | 3.16E-03 |
| 3-story frames | | | |
| UniNaM | *Na_C_3_BF* | 1.00E-05 | 8.28E-03 |
| UniNaM | *Na_C_3_IF* | 1.00E-05 | 2.87E-03 |
| UniNaM | *Na_C_3_PF* | 1.01E-05 | 2.58E-03 |
| 9-story shear walls | | | |

| UniNaV | *Na_C_9_SW_BF* | 1.00E-05 | 3.55E-03 |
| UniNaV | *Na_C_9_SW_IF* | 1.00E-05 | 1.28E-03 |
| UniNaV | *Na_C_9_SW_PF* | 1.00E-05 | 1.58E-03 |
| 9-story shear walls with Soil-Structure Interaction (SSI) | | | |
| UniRm | *Na_Cssi_9_setti_BF* | 1.01E-05 | 2.06E-02 |
| UniRm | *Na_Cssi_9_setti_IF* | 1.01E-05 | 5.81E-03 |
| UniRm | *Na_Cssi_9_setti_PF* | 1.01E-05 | 7.51E-03 |

Table 7.4.4 Collapse and Damage rates for reinforced concrete buildings in Naples when local site condition is C according to Eurocode 8 classification, including model uncertainty.

**Soil Type C**

| UR | Structure Name | Collapse Rate | Damage Rate |
|---|---|---|---|
| Modelling Uncertainty | | | |
| UniBas | *Aq_C_6_BF_ModUnc* | 1.12E-04 | --- |
| UniBas | *Aq_C_6_IF_ModUnc* | 2.40E-04 | --- |
| UniBas | *Aq_C_6_PF_ModUnc* | 2.03E-04 | --- |
| UniRm | *Na_C_6_BF_ModUnc* | 1.00E-05 | 5.76E-03 |
| UniRm | *Na_C_6_IF_ModUnc* | 1.33E-05 | 6.69E-03 |
| UniRm | *Na_C_6_PF_ModUnc* | 2.78E-05 | 1.78E-02 |
| Modelling Uncertainty – 20 Models | | | |
| UniRm | *Na_C_6_BF_ModUnc20* | 1.00E-05 | 5.79E-03 |
| UniRm | *Na_C_6_IF_ModUnc20* | 1.09E-05 | 8.25E-03 |
| UniRm | *Na_C_6_PF_ModUnc20* | 1.11E-05 | 1.92E-02 |

Table 7.4.5 Collapse and Damage rates for reinforced concrete buildings in Rome when local site condition is C according to Eurocode 8 classification.

**Soil Type C**

| UR | Structure Name | Collapse Rate | Damage Rate |
|---|---|---|---|
| UniNaM | *Ro_C_6_BF* | 1.00E-05 | 3.61E-03 |
| UniNaM | *Ro_C_6_IF* | 2.38E-05 | 1.12E-03 |
| UniNaM | *Ro_C_6_PF* | 3.92E-05 | 1.19E-03 |

Table 7.4.6 Collapse and Damage rates for reinforced concrete buildings in Caltanissetta when local site condition is C according to Eurocode 8 classification.

**Soil Type C**

| UR | Structure Name | Collapse Rate | Damage Rate |
|---|---|---|---|
| UniNaV | *Ca_C_6_BF* | 1.83E-05 | 2.59E-03 |
| UniNaV | *Ca_C_6_IF* | 3.21E-05 | 1.54E-03 |
| UniNaV | *Ca_C_6_PF* | 7.23E-05 | 1.47E-03 |

Table 7.4.7 Collapse and Damage rates for reinforced concrete buildings in Milan when local site condition is C according to Eurocode 8 classification.

| Soil Type C | | | |
|---|---|---|---|
| UR | Structure Name | Collapse Rate | Damage Rate |
| 6-story frames | | | |
| UniRm | *Mi_C_6_BF* | 1.00E-05 | 1.86E-04 |
| UniRm | *Mi_C_6_IF* | 1.00E-05 | 5.06E-05 |
| UniRm | *Mi_C_6_PF* | 1.00E-05 | 1.26E-04 |
| 9-story frames | | | |
| UniRm | *Mi_C_9_BF* | 1.00E-05 | 1.28E-04 |
| UniRm | *Mi_C_9_IF* | 1.00E-05 | 6.77E-05 |
| UniRm | *Mi_C_9_PF* | 1.00E-05 | 6.72E-05 |
| 3-story frames | | | |
| UniNaM | *Mi_C_3_BF* | 2.00E-05 | 3.58E-04 |
| UniNaM | *Mi_C_3_IF* | 1.00E-05 | 1.82E-05 |
| UniNaM | *Mi_C_3_PF* | 1.00E-05 | 5.46E-05 |
| 9-story shear walls | | | |
| UniBas | *Mi_C_9_SW_BF* | 1.00E-05 | 9.64E-05 |
| UniBas | *Mi_C_9_SW_IF* | 1.00E-05 | 3.28E-05 |
| UniBas | *Mi_C_9_SW_PF* | 1.00E-05 | 3.91E-05 |
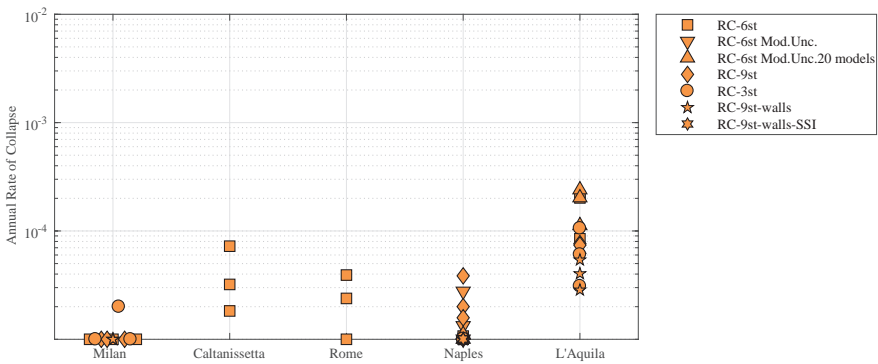


Figure 7.4.1 Failure rates for reinforced concrete buildings, when local site condition is C according to Eurocode 8 classification.
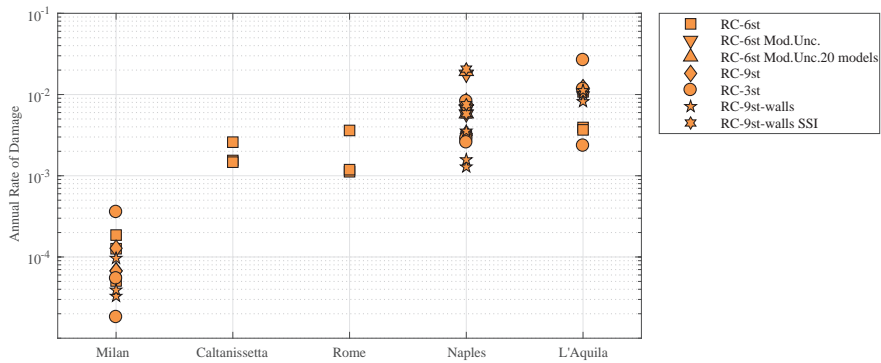
Figure 7.4.2 Damage rates for reinforced concrete buildings, when local site condition is C according to Eurocode 8 classification.

## 7.5   Nominal failure rates of steel case studies

The rates of Collapse and Damage associated to steel buildings in the considered sites (Soil Type C and Soil Type A), are summarized below from Table 7.5.1 up to Table 7.5.8. Figure 7.5.1 and Figure 7.5.2 show the failure rates for Soil C and Soil A, respectively, while the damage rates are represented in Figure 7.5.3 and Figure 7.5.4. Since this structural typology was included from the second year of project, the structures were located solely in the cities of Milan, Naples and L'Aquila. It may be seen that the failure rates are bounded by $10^{-5}$ in Milan for both soil types and in Naples for Soil Type A. The sites where higher seismic actions are expected (e.g., L'Aquila and Naples- Soil Type C) observe collapse rates higher than $10^{-5}$. Over the course of the project, the database of model was enlarged including also structures with panels and evaluating the impact of modelling uncertainty. The presence of panels helps to decrease both the damage and collapse rates.

Table 7.5.1 Collapse and Damage rates for steel buildings in L'Aquila when local site condition is C according to Eurocode 8 classification.

**Soil Type C**

| UR | Structure Name | Collapse Rate | Damage Rate |
|---|---|---|---|
| UniNaDc+UniCamZ | *AQ_C_1_Lx20Ly6* | 2.16E-04 | 1.15E-02 |
| UniNaDc+UniCamZ | *AQ_C_1_Lx20Ly8* | 1.13E-04 | 1.18E-02 |
| UniNaDc+UniCamZ | *AQ_C_1_Lx30Ly6* | 1.25E-04 | 5.76E-03 |
| UniNaDc+UniCamZ | *AQ_C_1_Lx30Ly8* | 1.46E-04 | 6.34E-03 |
| UniNaDc+UniCamZ | *AQ_C_1_Lx20Ly6_panels* | 6.01E-05 | 1.17E-03 |
| UniNaDc+UniCamZ | *AQ_C_1_Lx20Ly8_panels* | 7.39E-05 | 1.43E-03 |
| UniNaDc+UniCamZ | *AQ_C_1_Lx30Ly6_panels* | 9.38E-05 | 1.21E-03 |
| UniNaDc+UniCamZ | *AQ_C_1_Lx30Ly8_panels* | 6.49E-05 | 1.11E-03 |

Table 7.5.2 Collapse and Damage rates including modelling uncertainties for steel buildings in L'Aquila when local site condition is C according to Eurocode 8 classification.

**Soil Type C**

| UR | Structure Name | Collapse Rate | Damage Rate |
|---|---|---|---|
| UniNaDc+UniCamZ | *AQ_C_1_Lx20Ly6_panels_ModUnc* | 9.26E-05 | 1.13E-03 |
| UniNaDc+UniCamZ | *AQ_C_1_Lx20Ly8_panels_ModUnc* | 9.40E-05 | 1.31E-03 |
| UniNaDc+UniCamZ | *AQ_C_1_Lx30Ly6_panels_ModUnc* | 4.62E-05 | 1.16E-03 |
| UniNaDc+UniCamZ | *AQ_C_1_Lx30Ly8_panels_ModUnc* | 7.04E-05 | 1.18E-03 |

Table 7.5.3 Collapse and Damage rates for steel buildings in L'Aquila when local site condition is A according to Eurocode 8 classification.

**Soil Type A**

| UR | Structure Name | Collapse Rate | Damage Rate |
|---|---|---|---|
| UniNaDc+UniCamZ | *AQ_A_1_Lx20Ly6* | 9.17E-05 | 4.43E-03 |
| UniNaDc+UniCamZ | *AQ_A_1_Lx20Ly8* | 3.38E-05 | 5.83E-03 |
| UniNaDc+UniCamZ | *AQ_A_1_Lx30Ly6* | 5.86E-05 | 2.48E-03 |
| UniNaDc+UniCamZ | *AQ_A_1_Lx30Ly8* | 5.30E-05 | 2.82E-03 |
| UniNaDc+UniCamZ | *AQ_A_1_Lx20Ly6_panels* | 5.45E-05 | 4.32E-04 |
| UniNaDc+UniCamZ | *AQ_A_1_Lx20Ly8_panels* | 1.31E-05 | 4.73E-04 |
| UniNaDc+UniCamZ | *AQ_A_1_Lx30Ly6_panels* | 2.85E-05 | 4.30E-04 |
| UniNaDc+UniCamZ | *AQ_A_1_Lx30Ly8_panels* | 2.69E-05 | 4.80E-04 |

Table 7.5.4 Collapse and Damage rates including modelling uncertainties for steel buildings in L'Aquila when local site condition is A according to Eurocode 8 classification.

**Soil Type A**

| UR | Structure Name | Collapse Rate | Damage Rate |
|---|---|---|---|
| UniNaDc+UniCamZ | *AQ_A_1_Lx20Ly6_panels_ModUnc* | 4.11E-05 | 4.11E-04 |
| UniNaDc+UniCamZ | *AQ_A_1_Lx20Ly8_panels_ModUnc* | 2.21E-05 | 4.20E-04 |
| UniNaDc+UniCamZ | *AQ_A_1_Lx30Ly6_panels_ModUnc* | 2.85E-05 | 4.65E-04 |
| UniNaDc+UniCamZ | *AQ_A_1_Lx30Ly8_panels_ModUnc* | 1.85E-05 | 5.12E-04 |

Table 7.5.5 Collapse and Damage rates for steel buildings in Naples when local site condition is C according to Eurocode 8 classification.

**Soil Type C**

| UR | Structure Name | Collapse Rate | Damage Rate |
|---|---|---|---|
| UniNaDc+UniCamZ | *NA_C_1_Lx20Ly6* | 1.03E-05 | 6.53E-03 |
| UniNaDc+UniCamZ | *NA_C_1_Lx20Ly8* | 1.00E-05 | 5.79E-03 |
| UniNaDc+UniCamZ | *NA_C_1_Lx30Ly6* | 1.19E-05 | 1.67E-03 |
| UniNaDc+UniCamZ | *NA_C_1_Lx30Ly8* | 1.00E-05 | 1.82E-03 |
| UniNaDc+UniCamZ | *NA_C_1_Lx20Ly6_panels* | 1.15E-05 | 3.31E-04 |
| UniNaDc+UniCamZ | *NA_C_1_Lx20Ly8_panels* | 1.00E-05 | 3.44E-04 |
| UniNaDc+UniCamZ | *NA_C_1_Lx30Ly6_panels* | 1.00E-05 | 1.36E-04 |
| UniNaDc+UniCamZ | *NA_C_1_Lx30Ly8_panels* | 1.02E-05 | 1.42E-04 |

Table 7.5.6 Collapse and Damage rates for steel buildings in Naples when local site condition is A according to Eurocode 8 classification.

**Soil Type A**

| UR | Structure Name | Collapse Rate | Damage Rate |
|---|---|---|---|
| UniNaDc+UniCamZ | *NA_A_1_Lx20Ly6* | 1.00E-05 | 1.56E-03 |
| UniNaDc+UniCamZ | *NA_A_1_Lx20Ly8* | 1.00E-05 | 1.29E-03 |
| UniNaDc+UniCamZ | *NA_A_1_Lx30Ly6* | 1.00E-05 | 6.40E-04 |
| UniNaDc+UniCamZ | *NA_A_1_Lx30Ly8* | 1.00E-05 | 7.02E-04 |
| UniNaDc+UniCamZ | *NA_A_1_Lx20Ly6_panels* | 1.00E-05 | 5.13E-05 |
| UniNaDc+UniCamZ | *NA_A_1_Lx20Ly8_panels* | 1.00E-05 | 4.75E-05 |
| UniNaDc+UniCamZ | *NA_A_1_Lx30Ly6_panels* | 1.00E-05 | 3.86E-05 |
| UniNaDc+UniCamZ | *NA_A_1_Lx30Ly8_panels* | 1.00E-05 | 7.76E-05 |

Table 7.5.7 Collapse and Damage rates for steel buildings in Milan when local site condition is C according to Eurocode 8 classification.

**Soil Type C**

| UR | Structure Name | Collapse Rate | Damage Rate |
|---|---|---|---|
| UniNaDc+UniCamZ | *MI_C_1_Lx20Ly6* | 1.00E-05 | 1.36E-04 |
| UniNaDc+UniCamZ | *MI_C_1_Lx20Ly8* | 1.00E-05 | 1.15E-04 |
| UniNaDc+UniCamZ | *MI_C_1_Lx30Ly6* | 1.00E-05 | 2.39E-05 |
| UniNaDc+UniCamZ | *MI_C_1_Lx30Ly8* | 1.00E-05 | 2.77E-05 |
| UniNaDc+UniCamZ | *MI_C_1_Lx20Ly6_panels* | 1.00E-05 | 1.00E-05 |
| UniNaDc+UniCamZ | *MI_C_1_Lx20Ly8_panels* | 1.00E-05 | 1.00E-05 |
| UniNaDc+UniCamZ | *MI_C_1_Lx30Ly6_panels* | 1.00E-05 | 1.01E-05 |
| UniNaDc+UniCamZ | *MI_C_1_Lx30Ly8_panels* | 1.00E-05 | 1.03E-05 |

Table 7.5.8 Collapse and Damage rates for steel buildings in Milan when local site condition is A according to Eurocode 8 classification.

**Soil Type A**

| UR | Structure Name | Collapse Rate | Damage Rate |
|---|---|---|---|
| UniNaDc+UniCamZ | *MI_A_1_Lx20Ly6* | 1.00E-05 | 3.06E-05 |
| UniNaDc+UniCamZ | *MI_A_1_Lx20Ly8* | 1.00E-05 | 2.58E-05 |
| UniNaDc+UniCamZ | *MI_A_1_Lx30Ly6* | 1.00E-05 | 1.54E-05 |
| UniNaDc+UniCamZ | *MI_A_1_Lx30Ly8* | 1.00E-05 | 1.71E-05 |
| UniNaDc+UniCamZ | *MI_A_1_Lx20Ly6_panels* | 1.00E-05 | 1.00E-05 |
| UniNaDc+UniCamZ | *MI_A_1_Lx20Ly8_panels* | 1.00E-05 | 1.00E-05 |
| UniNaDc+UniCamZ | *MI_A_1_Lx30Ly6_panels* | 1.00E-05 | 1.00E-05 |
| UniNaDc+UniCamZ | *MI_A_1_Lx30Ly8_panels* | 1.00E-05 | 1.00E-05 |
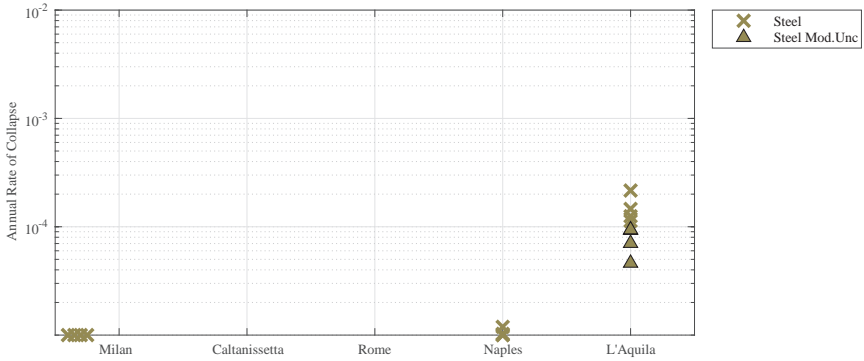
Figure 7.5.1 Failure rates for steel buildings, when local site condition is C according to Eurocode 8 classification.
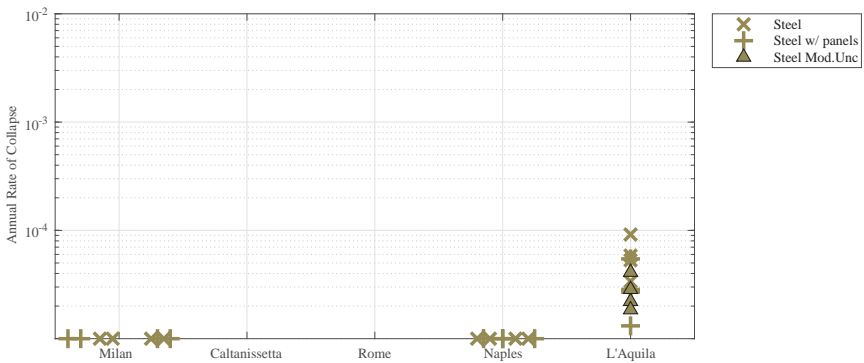


Figure 7.5.2 Failure rates for steel buildings, when local site condition is A according to Eurocode 8 classification.
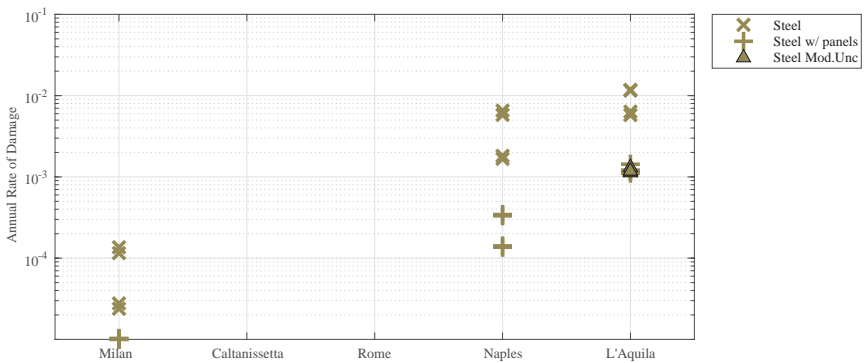


Figure 7.5.3 Damage rates for steel buildings, when local site condition is C according to Eurocode 8 classification.
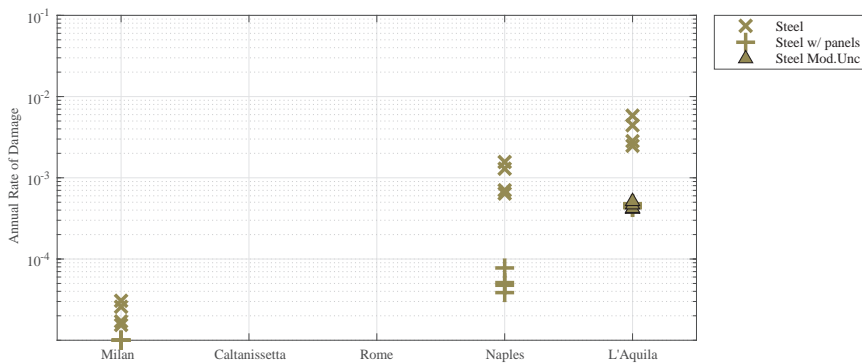
Figure 7.5.4 Damage rates for steel buildings, when local site condition is A according to Eurocode 8 classification.

## 7.6 Nominal failure rates of base-isolated case studies

The rates of Collapse and Damage associated to base-isolated buildings in three different configurations located in the site of L'Aquila - Soil Type C, are summarized below in Table 7.6.1. The collapse and damage rates are given, respectively, in Figure 7.6.1 and Figure 7.6.2. It may be seen that the failure rates are quite high if compared to the other structural typologies, while the damage rates are significantly lower. The model designed with rubber devices was subjected to both 2.0 s and 3.0 s record sets, since the natural period (2.5 s) was exactly in the middle, showing quite diverse rates. During the final year of project we included also modelling uncertainties and developed some additional configurations located in Naples.

Table 7.6.1 Collapse and Damage rates for base-isolated buildings in L'Aquila when local site condition is C according to Eurocode 8 classification.

| Soil Type C | | | |
|---|---|---|---|
| UR | Structure Name | Collapse Rate | Damage Rate |
| Isolation system: Rubber + Slider devices | | | |
| UniBasC | *BI_Rubber+Slider_Aq_C_6_c1* | 7.00E-04 | 1.60E-03 |
| UniBasC | *BI_Rubber+Slider_Aq_C_6_c2* | 7.20E-04 | 1.24E-03 |
| UniBasC | *BI_Rubber+Slider_Aq_C_6_c3* | 8.70E-04 | 9.91E-04 |
| UniBasC | *BI_Rubber+Slider_Aq_C_6_c4* | 7.10E-04 | 1.65E-03 |
| UniBasC | *BI_Rubber+Slider_Aq_C_6_c4_GAP* | 6.45E-04 | --- |
| Isolation system: DCFP devices | | | |
| UniBasP | *BI_DCFP_Aq_SLC* | 1.11E-03 | 7.00E-04 |
| UniBasP | *BI_DCFP_Aq_SLC_GAP* | 8.60E-04 | 1.13E-03 |
| UniBasP | *BI_DCFP_Aq_SLV* | 2.15E-04 | --- |
| UniBasP | *BI_DCFP_Aq_SLV_GAP* | 6.60E-04 | --- |
| Isolation system: Rubber devices | | | |
| UniCamD | *BI_Rubber_Aq_C_c1_2sec* | 1.55E-04 | 1.41E-03 |
| UniCamD | *BI_Rubber_Aq_C_c2_2sec* | 1.65E-04 | 9.50E-04 |
| UniCamD | *BI_Rubber_Aq_C_c2b_3sec* | 8.50E-04 | 2.47E-03 |
| UniCamD | *BI_Rubber_Aq_C_c2b_3sec_GAP* | 6.80E-04 | --- |
| UniCamD | *BI_Rubber_Aq_C_c2b_3sec_GAP* | 8.50E-04 | --- |

Table 7.6.2 Collapse and Damage rates for base-isolated buildings including modelling uncertainties in L'Aquila when local site condition is C according to Eurocode 8 classification.

**Soil Type C**

| UR | Structure Name | Collapse Rate | Damage Rate |
|---|---|---|---|
| Isolation system: Rubber + Slider devices | | | |
| UniBasC | *BI_Rubber+Slider_Aq_C_6_c3_ModUnc* | 6.90E-04 | 1.42E-03 |
| Isolation system: DCFP devices | | | |
| UniBasP | *BI_DCFP_Aq_ModUnc_SLC* | 1.15E-03 | 6.10E-04 |
| UniBasP | *BI_DCFP_Aq_ModUnc_SLV* | 1.60E-04 | --- |
| Isolation system: Rubber devices | | | |
| UniCamD | *BI_Rubber_Aq_C_c2b_ModUnc* | 8.00E-04 | 1.86E-03 |

Table 7.6.3 Collapse and Damage rates for base-isolated buildings in Naples when local site condition is C according to Eurocode 8 classification.

**Soil Type C**

| UR | Structure Name | Collapse Rate | Damage Rate |
|---|---|---|---|
| Isolation system: Rubber + Slider devices | | | |
| UniBasC | *BI_Rubber+Slider_Na_C_6_c1* | 1.66E-04 | 1.93E-04 |
| UniBasC | *BI_Rubber+Slider_Na_C_6_c2* | 2.95E-05 | 2.17E-04 |
| Isolation system: DCFP devices | | | |
| UniBasP | *BI_DCFP_Na_SLC* | 1.80E-04 | 8.20E-05 |
| UniBasP | *BI_DCFP_Na_SLV* | 3.70E-05 | --- |
| Isolation system: Rubber devices | | | |
| UniCamD | *BI_Rubber_Na_C_c1_2sec* | 1.00E-05 | 1.96E-04 |
| UniCamD | *BI_Rubber_Na_C_c1_2sec* | 2.45E-05 | 1.32E-04 |
| UniCamD | *BI_Rubber_Na_C_c2b_3sec* | 1.06E-04 | 1.80E-04 |
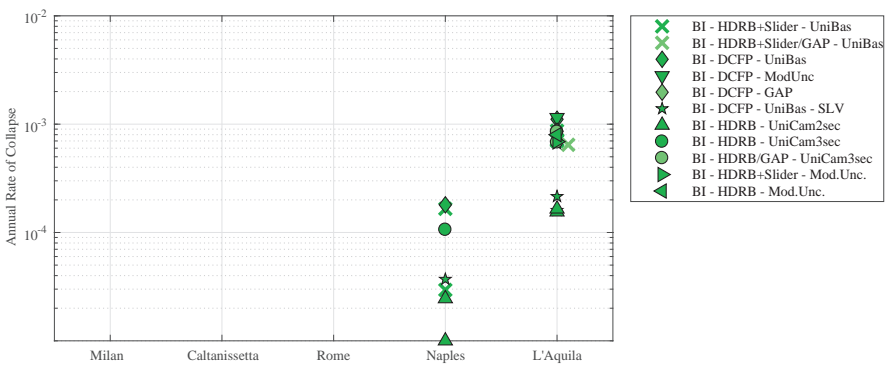


Figure 7.6.1 Failure rates for base-isolated buildings, when local site condition is C according to Eurocode 8 classification.
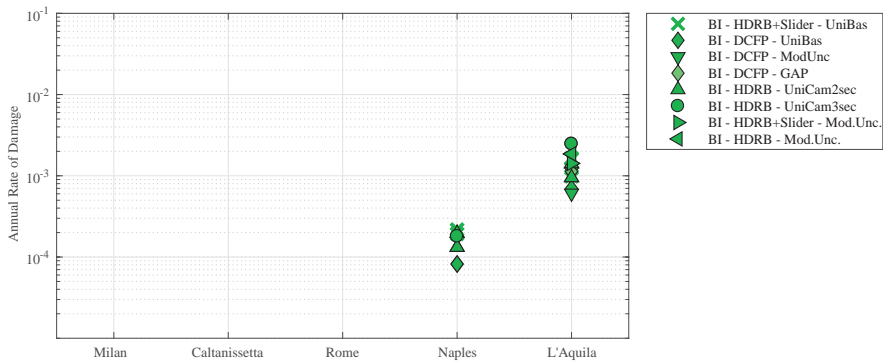
Figure 7.6.2 Damage rates for base-isolated buildings, when local site condition is C according to Eurocode 8 classification.

## 7.7   Site-to-site and structure-to-structure risk variations

All failure and damage rates shown so far are compared across structures for both Soil Types, A and C. It is important to recall, however, that for the different structural typologies different design procedures were followed, which could have had a significant contribution in determining the differences observed among the various structures.
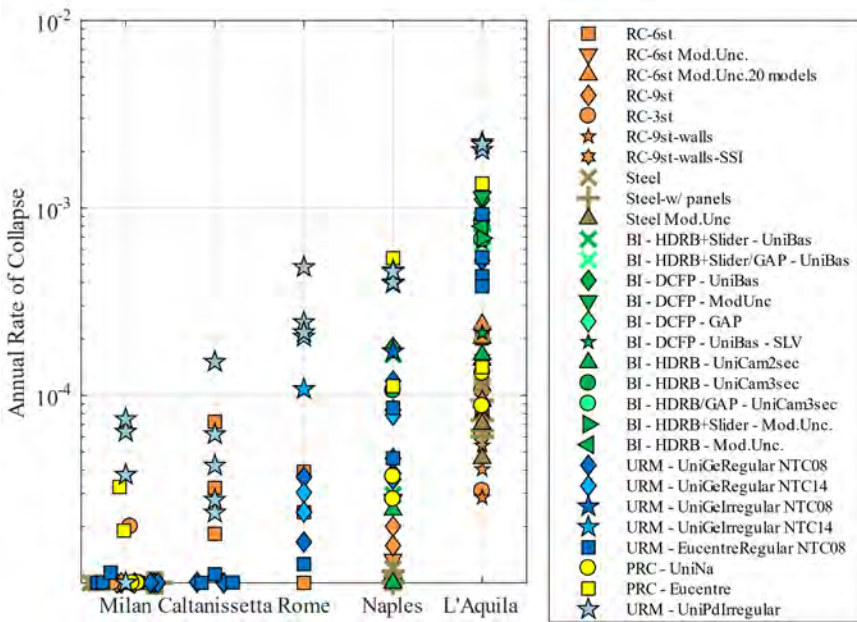


Figure 7.7.1 Annual collapse rates for different structural typologies and sites, soil C.
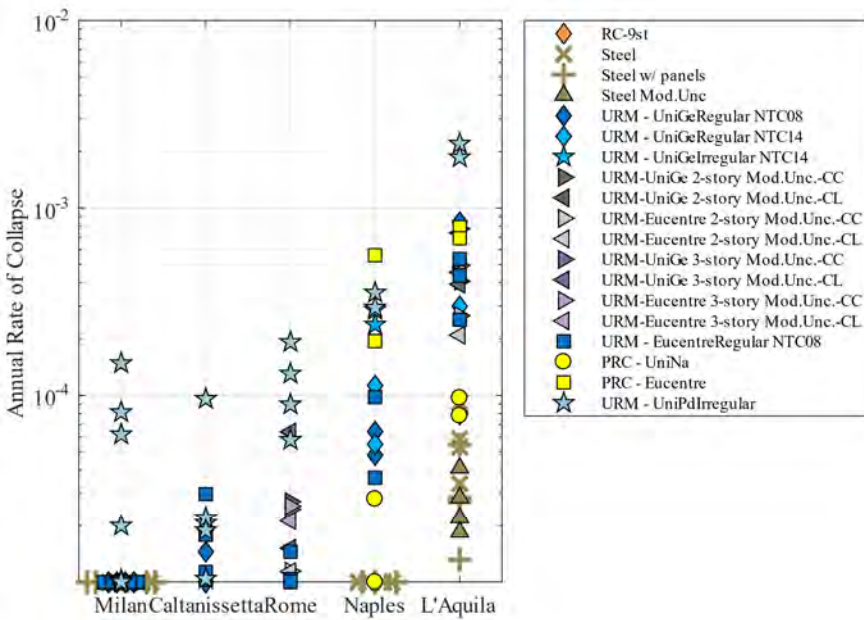
Figure 7.7.2 Annual collapse rates for different structural typologies and sites, soil A.
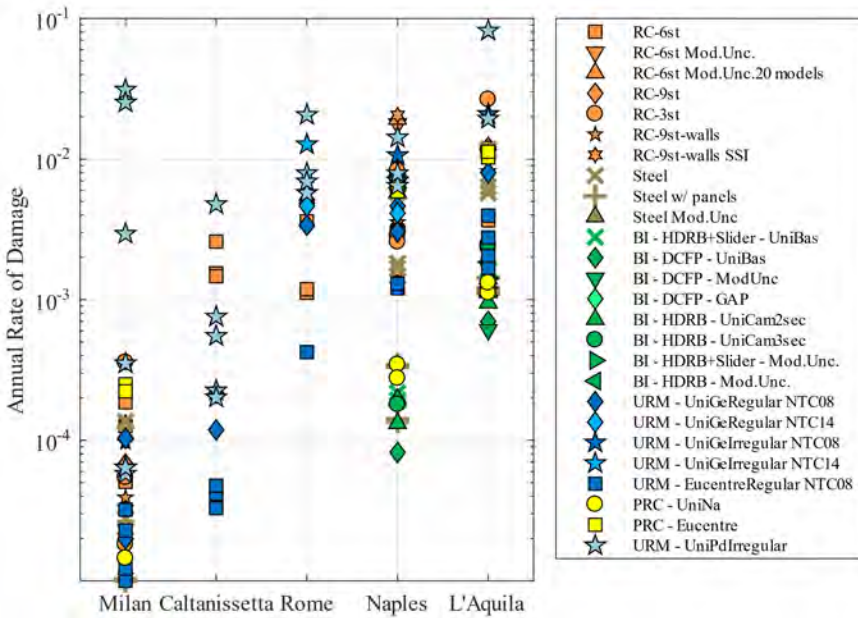


Figure 7.7.3 Annual rates associated to the onset of damage for different structural typologies and sites, soil C.
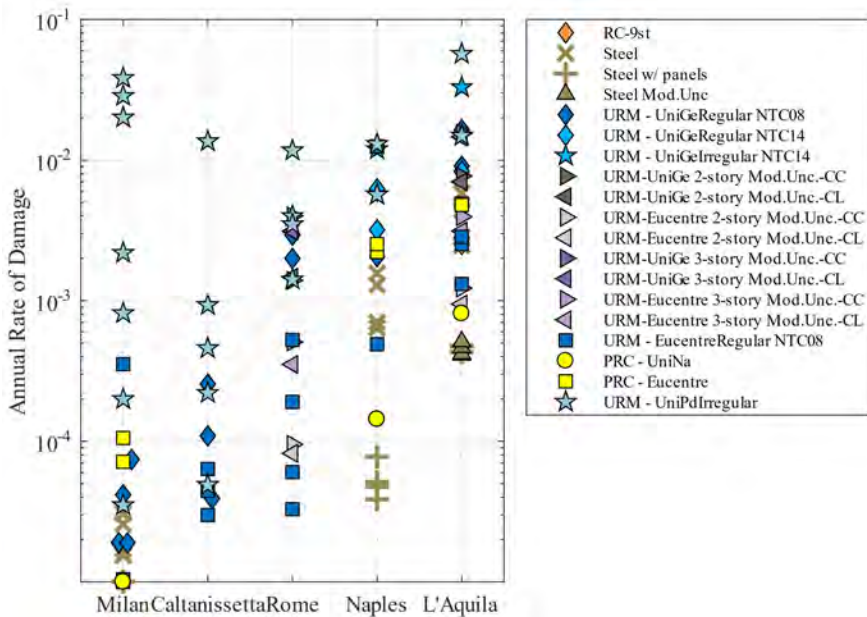
Figure 7.7.4 Annual rates associated to the onset of damage for different structural typologies and sites, soil A.

## 7.8   Conclusions

This document briefly presented the failure (global collapse and onset of usability preventing damage) rates for a set of structures belonging to the most common types in Italy. These structures were designed for life-safety and damage-limitation for several sites characterized by different seismicity levels and for two soil conditions. Nonlinear dynamic analysis, in the form of multiple stripe analysis, was the method chosen to perform structural fragility assessment for two damage states: onset of damage and collapse. The fragility curves were integrated with the site hazard curves to compute the annual failure rates for both damage states, which were shown above. The uncertainty was accounted for in the hazard, in the record-to-record variability of structural response, and, for a few cases, also in the structural modeling. The results of the project indicate the following:

1.  in some cases, the collapse failure rates are so low that only an upper bound to the actual failure rate can be provided; i.e., 0.00001;

2.  the collapse failure rates tend to increase with the site hazard;

3.  failure rates for usability preventing damage show a general trend similar to the global collapse failure rates;

4.  the comparatively high collapse failure rates of base-isolated structure may be due to their more controlled behavior during design and the lower margin of safety with respect to collapse beyond the maximum design displacement; conversely, base-isolated structures show comparatively lower usability-preventing damage failure rates;

5.  some irregular masonry configurations show failure rates much larger than others and comparable or larger than the exceedance rate of desing actions; these results are not considered fully consolidated yet;

6.  the precast reinforced concrete results are significantly different from those presented in the previous years and from preliminary literature derived from this project; this is because design has been revised for these structures during the project;

7.  the effects of modeling uncertainty and soil-structure interaction on the failure rates seem to be minor, at least in the considered examples and under the taken working hypotheses;

8.  the results' consolidation process might be continuing even after the end of the project; in general, all computed annual structural failure rates closely reflect specific assumptions on design, modeling and analysis of the considered structures, and this has to be always taken into account when discussing the results of this project.

# APPENDIX A – USABILITY-PREVENTING LIMIT STATE

A1.    **Background**

Different definitions of the Damage Limit State (DLS) for the design/assessment of buildings are provided in current seismic codes.

According to the Italian seismic code (NTC 2008), for instance, the DLS is attained when, after an earthquake, the entire building suffers damage which does not endanger the occupants' safety and the building remains immediately usable, although the interruption of use of some equipment may occur. In other words, the requirements associated to the Damage Limit State are related to the limitation of economic losses (structural and non-structural) due to frequent (low-intensity) earthquakes, keeping the building immediately operational after a seismic event. The structure should not have permanent deformations and its elements should retain the original strength and stiffness with no need for structural repair. On the other hand, non-structural damage should be repairable economically.

The Eurocode 8 states that at the DLS the occurrence of non-structural damage and the associated limitations of use (whose costs can be disproportionately high compared to the costs of the structure itself), should be prevented.

According to the CNR DT 212 (2013) guidelines, the DLS is identified by negligible damage in structural elements and slight damage in non-structural elements. Furthermore, FEMA 273 states that most operations and functions can resume immediately. Buildings ensuring the safety level according to the DLS will be safe for occupancy. Essential operations will be protected while only non-essential operations will be disrupted. Repair may be required to restore some non-essential services only.

Further examples can be made, however, it is clear that most of the current seismic codes based on performance-based design provide a qualitative (rather than operative) description of the Damage Limit State. Another observation is that most of the current seismic codes relate the attainment of the DLS to the extension and severity of damage to non-structural elements.

In this context, a general multi-criteria approach for the definition of the Damage Limit State, combining the following aspects, can be assumed:

- easy reparability of the whole building (from an economic point of view),
- no service interruption,
- the main structure maintains its ability to withstand lateral forces, while accepting a moderate decrease of stiffness (structure slightly degraded in stiffness but not in resistance).

A2.    **Multi-criteria approach for the definition of Damage Limit State**

The multi-criteria approach adopted in the present study to define the Damage Limit State is based on following three main conditions (whichever occurs first):

- Attainment of a light-widespread damage condition for no more than 50% of the main non-structural elements.
- Attainment of a severe damage condition for the first non-structural element, leading to significant interruption of use.
- Attainment of a limit value of base-shear (e.g., 95% of the maximum lateral strength for RC buildings and masonry buildings), corresponding to a condition where the structure retains its original strength and mostly its original stiffness (no need for structural repair).

It should be noted that, in the case of masonry buildings, the final threshold should be associated to a value of the base-shear not lower than 85% of the peak resistance. This lower bound is in particular justified by the fact that URM buildings may show slight but widespread damage even for values of the base-shear far from the peak value.

From a practical point of view, the step-by-step methodology for the definition of the Damage Limit State can be summarized as follows:

Pushover analysis (POA) of the structure in the two principal directions (masonry infills shall be included in the numerical model for POA) (Figure A 1a),

i.     The top displacement (or maximum Inter-storey Drift Ratio IDR) associated with the first of the aforesaid limit conditions is determined for each principal direction,

ii.    Nonlinear Time History Analyses (NTHAs) are performed, and the maximum top displacement (or IDR) is recorded for each pair of ground motion record (Figure A 1b),

iii.   For each pair of ground motion record, the Damage Limit State is deemed to be achieved if the EDP value derived from NTHA is greater than or equal to the limit value derived from POA in that direction,. (Figure A 1c).
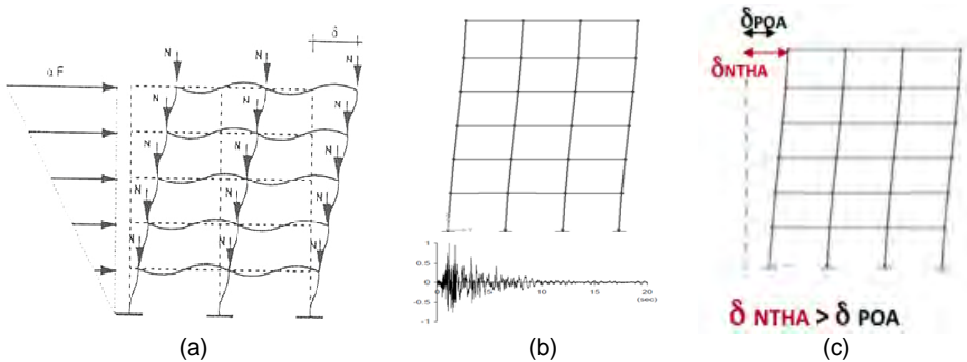


Figure A 1 Main steps for the definition of the Damage Limit State (DLS).
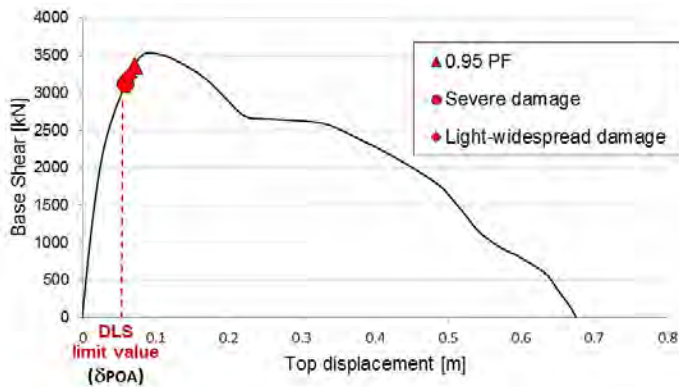


Figure A 2 Limit value of top displacement (from POA) associated with the attainment of DLS.

For the application of the above mentioned multi-criteria approach, it is fundamental that the main non-structural elements (different for each typology) are taken into account in the model.

In order to detect the aforesaid performance points on the pushover curve (see Figure A 2), a slight/moderate damage condition and a severe damage condition must be operationally defined for each non-structural elements (on the relevant force-displacement skeleton curve).

It must be pointed out that the proposed multi-criteria approach depends on the building characteristics. For instance, the limit threshold values in terms of percentages of damage infill panels vary with the number of stories of the building (e.g., in buildings with a large number of stories, the DLS could be reached at a value lower than those established for buildings with a lower number of stories) or with the collapse mechanism (e.g., in case of soft story mechanism a lower threshold percentage should be used).

## A3.     Remarks on different structural types
### A3.1.     Fixed-base and base-isolated reinforced concrete buildings

In reinforced concrete buildings the main non-structural elements considered for the definition of the Damage Limit State are masonry infills and partitions.

In the current practice, masonry infills are realized in complete contact with the surrounding RC frame without the provision of any gap or connection around the boundaries. Given this construction practice with an assumption that the infills are placed just after the surrounding RC frame is hardened, the infills are assumed as non-load bearing elements and commonly treated as non-structural elements.

It is worth noting that, although masonry infills are commonly considered as non-structural elements, damage to masonry infills can represent a threat to life (due to falling mass or hampering safe evacuation of a building). Repairing infills and partitions (and those elements affected by damage to infills, such as electrical wiring and windows) may require a lot of labors and costs.

All things considered, in this study the focus was on the in-plane response of hollow clay bricks masonry infill, constructed to be in contact within reinforced concrete frame, because they are representative of the current construction practice in Italy (and other European countries). Herein, hollow clay bricks masonry single-layer walls with a 30 cm thickness were considered.

According to Cardone et al. (2015), the damage states for the masonry panels mentioned above, can be described as follows (see Figure A 3):

- DS1 (Light Cracking): At DS1, damage results in detachment of the masonry panel from the RC frame, at the intrados of the top beam and along the upper half-height of the columns. Light diagonal cracking of the infill (one or two cracks with width <1 mm) in both directions may also occur.
- DS2 (Extensive cracking): At DS2, the cracks developed at DS1 widen (1 mm<width<2 mm). In addition, new diagonal cracks are expected to form in both directions (25-35% of the panel area is assumed to be affected by cracks at DS2). Possible failure of some brick units, located on the upper corners and top edge of the infill (corresponding to 10% of the panel area), is expected.
- DS3 (Corner crushing): At DS3, detachment of large plaster area and significant sliding in the mortar joints are expected to occur. In addition, crushing and spalling of brick units are more widespread on the panel (30% of the panel area is assumed to be affected by crushing/spalling of bricks). The wall is not repairable at reasonable costs (it is more convenient to demolish and reconstruct the entire wall). Frames (if any) are not damaged and can be retrieved and re-installed.
- DS4 (Collapse): DS4 corresponds to the in-plane or out-of-plane (whichever occurs first) global collapse of the wall. Frames (if any) are damaged and cannot be retrieved and used again.
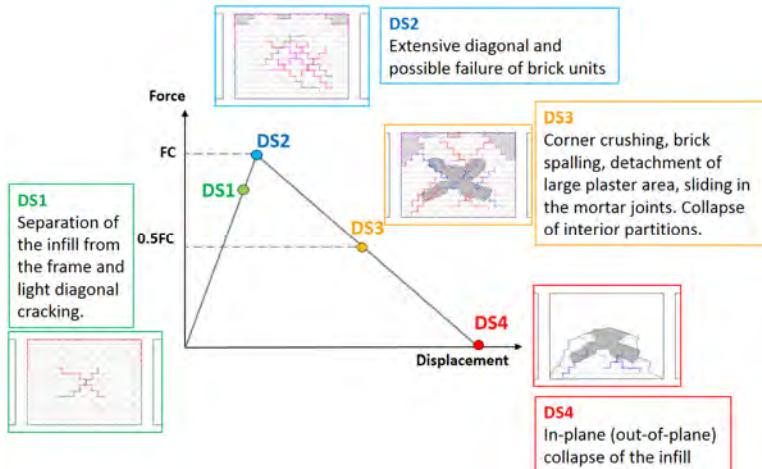
Figure A 3 Damage states for masonry panels.

All things considered, the three conditions for the definition of the DLS for fixed-base and base-isolated buildings can be rewritten as follows:

 a) Attainment of a light-widespread damage condition, corresponding to the attainment of a maximum lateral force around the peak strength in the relevant skeleton curve with no more than 50% of masonry infills in each main direction (see Figure A 4).
 b) Attainment of a severe damage condition, corresponding to the attainment of 50% strength drop from the peak strength in the relevant skeleton curve for the first masonry infill, (see Figure A 5).
 c) Attainment of a limit value of base-shear (corresponding to 95% of the peak strength from POA, as shown in Figure A 6), corresponding to a condition where the structure still retains its original strength and most of its original stiffness (no need for structural repair).
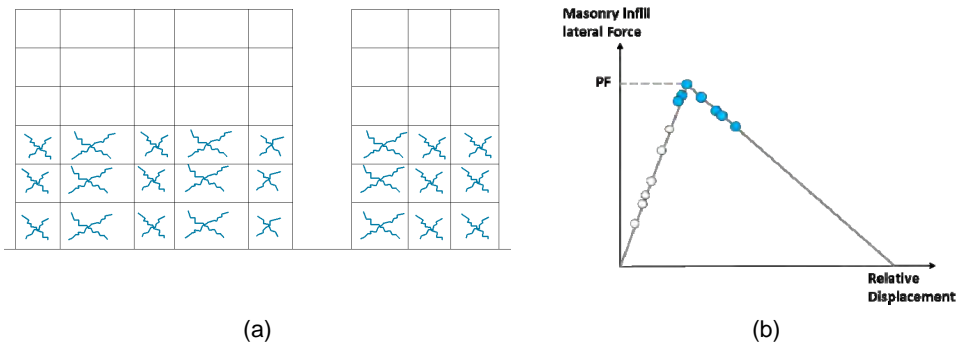


(a)                                                                 (b)

Figure A 4 Light-widespread damage condition for RC frame buildings
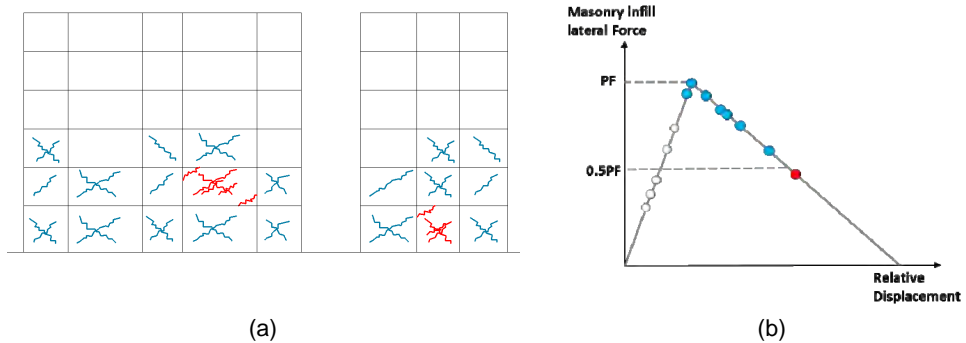
(a)                                                    (b)

Figure A 5 Severe damage condition for RC frame buildings
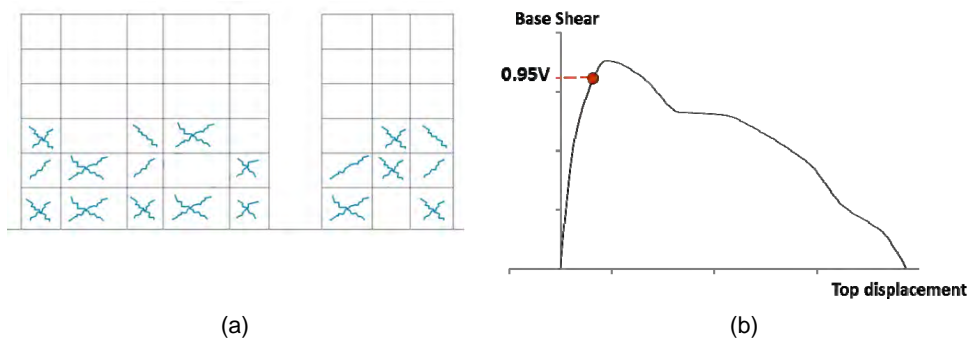


(a)                                                    (b)

Figure A 6 Attainment of a limit value of base-shear for RC frame buildings.

The limit values of top displacement obtained in this study for each case study of fixed-base and base-isolated buildings are described in Section 4.4.4 and Section 6.5.2 (Table 6.5.5), respectively.

### A3.2.    Masonry buildings

For masonry buildings, the non-structural elements (i.e., masonry infills and partitions) coincide, except a few irrelevant cases, with the structural elements themselves. Therefore, the damage states for masonry walls as well as the three conditions for the definition of the SLD are similar to those assumed for reinforced concrete buildings, however, they are particularly referred to the structural elements:

a)  The 50% of the masonry piers (in terms of resistant area) has reached the condition of light/moderate damage;
b)  A masonry pier has reached a severe damage condition (drift threshold corresponding to the DL3, as indicated in Table 2.3.3, in the case of the phenomenological nonlinear beam or attainment of the toe-crushing condition in the case of the macroelement mechanical model);
c)  The base-shear has reached the 95% of the peak resistance.

In any case the final threshold should be associated to a value of the base-shear not lower than 85% of the peak resistance. This lower bound is in particular justified by the fact that URM

buildings may show slight but widespread damage even for values of the base-shear far from the peak value.

For each case study of masonry buildings, the limit values of maximum inter-story drift, computed among all masonry walls, are listed in Sections 2.4.3 – 2.4.5.

### A3.3.    Precast industrial structures

For precast structures, the main non-structural elements are represented by precast claddings which are connected to the main structure as shown in Figure A 7.
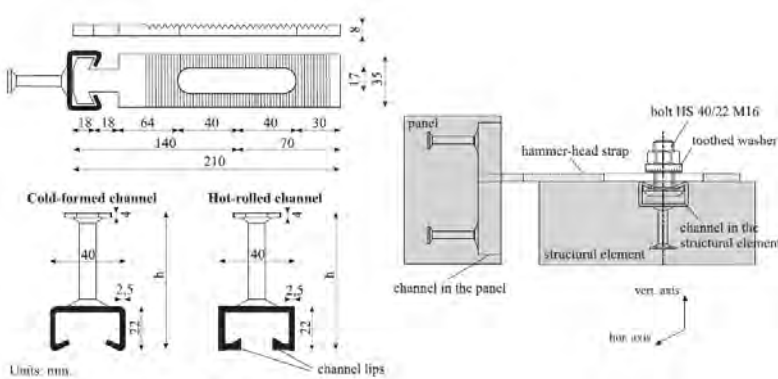


Figure A 7 Typical connection between precast claddings and main structure.

Precast panels are connected to the structure in such a way as to avoid interactions due to the deformations of the main structure under service working conditions. This is possible thanks to the type of connections used (see Figure A 7). Indeed, it allows relative displacements between the panel and the primary structure by sliding the hammer-head screw or the hammer-head bolt into the corresponding channel profile.

Figure A 8 shows the damage states of a cladding-structure connection, which theoretically should allow relative vertical and horizontal displacements, however, during a dynamic cyclic loading (or under a seismic event), the nut (or the bolt) gets stuck causing the yielding and then shear failure of the nut/bolt (or opening of the channel lips due to excessive plastic deformation), follows with consequent falling of the cladding.
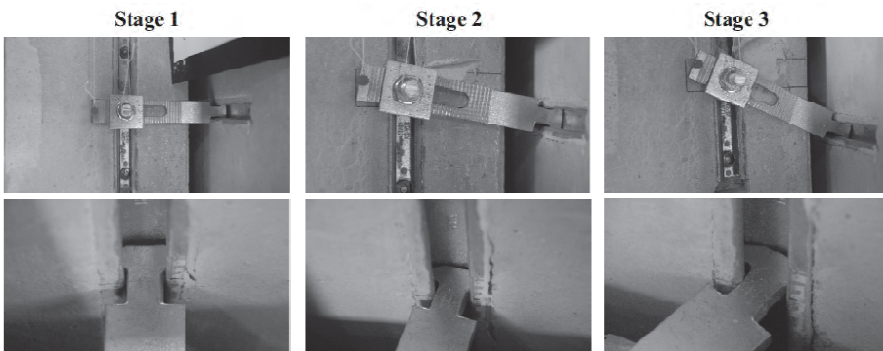


Figure A 8 Damage of hammer-head strap cladding connections

The multi-criteria for precast industrial structures can be rearranged as follows:

a) Attainment of a light-widespread damage condition, corresponding to the attainment of 50% of the peak shear strength in the cladding-structure connection (corresponding to the yielding of the bolt/nut) with no more than 50% of the claddings in each main direction (point A in Figure A 9).

b) Attainment of a severe damage condition, corresponding to the attainment of the peak strength in the connection (failure of the bolt or opening of the channel lips) for the first panel (point B in Figure A 9).

c) The third condition does not apply in this case. Indeed, it has to be noted that the collapse of the panel-structure connection occurs at very low drift values compared to the values corresponding to the attainment of the maximum lateral force of the structure.

It is worth noting that, due to the symmetry of the selected precast building, the condition a) implies the damage in all the claddings at the same time. Furthermore, there is always one critical direction.
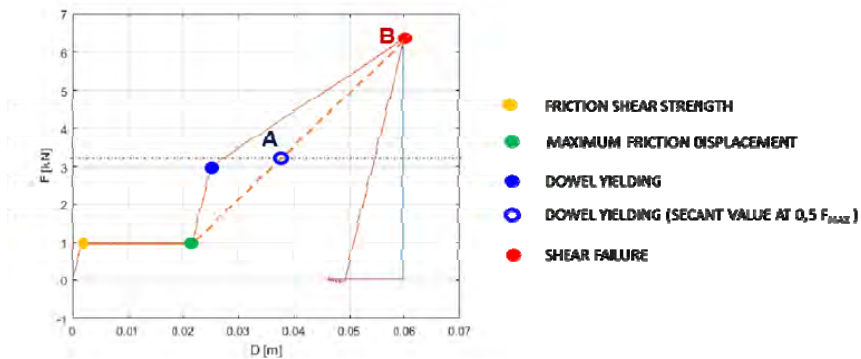


Figure A 9 Hammer-head strap cladding connection skeleton curve and associated damage states

The limit values of top displacement obtained in this study for each case study of precast buildings are discussed in Section 3.6.

### A3.4.  Steel industrial buildings

The non-structural elements considered for steel industrial buildings are sandwich panels used for lateral enclosures and horizontal roofs. Sandwich panels are usually modeled by means of two equivalent diagonal struts (see Figure A 10) whose responses account for the actual hysteretic behavior of the panel. The main responsible of such behavior is the panel-to-panel and panel-to-frame connection systems.

The behavior of such connection systems shows a low dissipative capacity under cyclic loading (De Matteis and Landolfo, 1999), essentially due to the large ovalization of the holes of the connection.
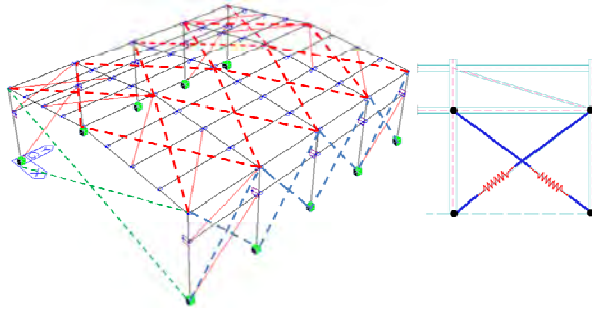
Figure A 10 Modeling of sandwich panels through equivalent struts.

The multi-criteria for steel industrial structures can be rewritten as follows:

a) Attainment of a light-widespread damage condition, corresponding to the attainment of point A on the skeleton curve of the connection system (Figure A 11a) with no more than 50% of the panels in each main direction.
b) Attainment of a severe damage condition, corresponding to the attainment of the peak strength of the skeleton curve of the connection system (point B in Figure A 11a) for the first panel.
c) Attainment of a limit value of base-shear, corresponding to 95% of the peak strength, as shown in Figure A 11b and Figure A 11c.

As can be seen, in the example shown in Figure A 11, the attainment of the DLS is due to the occurrence of the first criterion in both directions. Moreover, it should be observed that the sandwich panels of the horizontal roofs never exceed the point A, meaning that the DLS is never attained because of the roof panels.

Finally, it is worth noting that, due to the symmetry of the selected precast building, the condition a) implies the damage in all the cladding panels at the same time. Furthermore, there is always one critical direction.
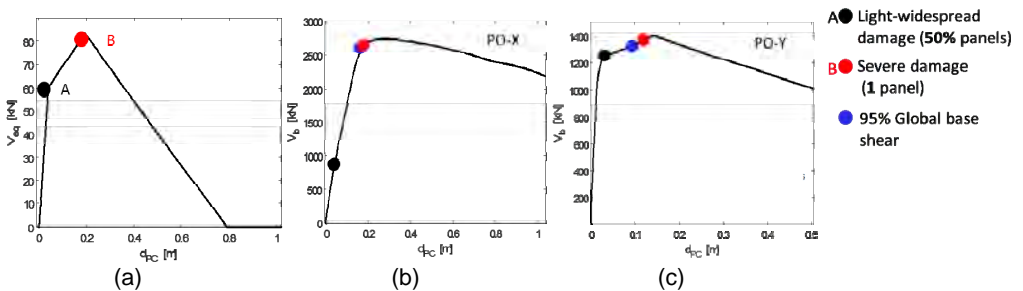


Figure A 11 (a) Damage states of panel-to-frame connections; Performance points on the Pushover curves in the (b) X-direction and (c) Y-direction.

The limit values of top displacement obtained in this study for each case study of steel buildings are listed in Table 5.5.6 (see Section 5.5.5).

## A4.  **References**

DM. LL. PP. 14/01/2008. Norme Tecniche per le Costruzioni (NTC2008), Rome (in italian).

Eurocode 8, EC8 (2004). Design of structures for earthquake resistance, part 1: general rules, seismic actions and rules for buildings, European Standard EN 1998-1, Stage 51 Draft, European Committee for Standardization (CEN), Brussels.

CNR-DT212 (2013). "Recommendations for the probabilistic seismic assessment of existing buildings". Consiglio Nazionale delle Ricerche, Rome 2013, Italy (in Italian).

Federal Emergency Management Agency, FEMA (1997), NEHRP Guidelines for the Seismic Rehabilitation of Buildings, (Report FEMA-273. Washington (DC)).

Sassun K, Sullivan TJ, Morandi P, Cardone D. (2016). Characterising the in-plane seismic performance of infill masonry. Bulletin of the New Zealand Society for Earthquake Engineering. 49AD(1):100-117.

D. Cardone, and G. Perrone, (2015) ''Developing fragility curves and loss functions for masonry infill walls'', Earthquakes and Structures, 9(1), 257-279.

G. De Matteis, R. Landolfo, (1999). "Structural behaviour of sandwich panel shear walls: an experimental analysis" Materials and Structures, 32(5), 331-341.

# APPENDIX B – SOIL-STRUCTURE INTERACTION

# B1. Introduction

Amongst the reinforced concrete (RC) building structures considered within WP4, the structure chosen as the first case study to consider dynamic Soil-Structure Interaction (SSI) is the nine-story wall-frame building in Naples founded on deformable soils (soil C).

The building has the same architectural plan as the three- and six- story frame buildings analyzed in previous years (Figure B 1a), but the lateral load-bearing system is a mixed wall-frame one (Figure B 1b) to achieve higher stiffness. Four shear walls of constant cross-section have been placed on the perimeter frame in each direction in a double symmetrical arrangement (green cross-section in the figure).
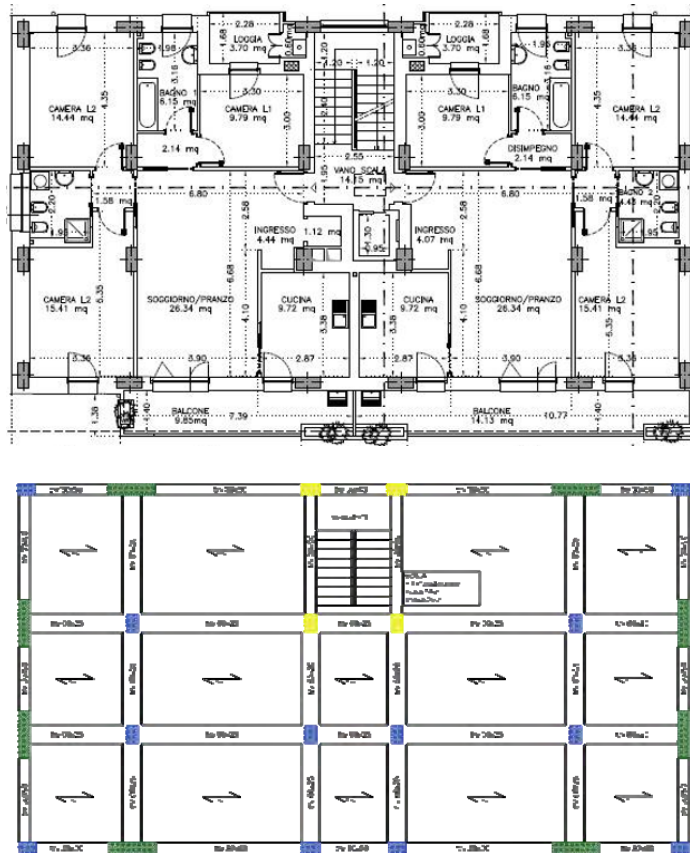


Figure B 1 (a) Architectural plan of three- and six- story buildings; (b) Structural plan of the nine-story building.

The details of the structure were designed based on linear dynamic analysis with force reduction by a behavior factor of 3.0 using the commercial software MIDAS-Gen (see Chapter 4). Here some basics of the structural characteristics are briefly overviewed. In particular, the system is classified as mixed wall-frame one, since columns were designed for seismic action as primary elements according to the code, given that their stiffness is not lower than the limiting value of 15%. While the walls, as already mentioned, have constant cross section dimensions, the columns have variable sections tapering every three floors (Table B.1). The corresponding ratio of floor area is 1.34% for walls (as compared to 1.15% and 1.63% in Milan and L'Aquila, respectively) and 1.15% for columns (at first floor). Flat beams are used within the floor and deep beams on the perimeter. The first mode vibration periods in the X (long) and Y (short)

directions were designed to be 1.25 and 1.07 seconds, respectively (regardless of the building configurations, i.e., bare-, infilled-, and pilotis-frames, since infills were modelled only as loads/masses at the design stage).

Table B.1 Summary of cross-section dimensions for vertical load-bearing members.

| Level | Walls | Columns | Staircase columns |
|-------|-------|---------|-------------------|
| 1-3 | $300 \times 1700$ | $300 \times 600$ | $300 \times 750$ |
| 4-6 | $300 \times 1700$ | $300 \times 550$ | $300 \times 650$ |
| 7-9 | $300 \times 1700$ | $300 \times 500$ | $300 \times 600$ |

The building was supposed to be on the subsoil of the central business district of Naples (so-called Centro Direzionale di Napoli, CDN), located in the eastern area of the city. The dynamic SSI analysis was performed based on the preliminarily developed site-specific evaluations of seismic hazard and associated hazard-consistent ground motions (Section 1.3). The analysis of this case study was carried out by means of the substructure method (Kausel et al. 1978) through the so-called Lumped Parameter Models, LPMs (Wolf, 1991; Ciampoli e Pinto, 2005; Carbonari et al. 2012). It is well-known that impedance functions of soil foundation system show frequency dependent characteristics. On the other hand, in order to account for non-linearity of structural members, the structural analysis cannot be but performed in time domain. Thus the frequency dependency of the impedance functions makes complicated the numerical computation. The best alternative to a fully 3D analysis involving the complete pile-soil-superstructure interaction is represented by the LPMs. They are capable to account for the frequency dependency of impedance functions and can be easily incorporated into a non-linear analysis of the structure. A large number of 3D FEM in the frequency domain have been therefore carried out to assess the impedance functions of the building's foundation. The above functions were then incorporated in the non-linear analysis of the seismic response of the building under examination.

## B2.    **Seismic site response analysis**

The reconstruction of the subsoil layering was based on the results of boreholes and cone penetration tests (CPTs) carried out in the area of the New Law Court building of Naples (Vinale, 1988). The schematic EW stratigraphic section (Figure B 2a) shows that the foundation subsoil profile consists of made ground (R), laying above volcanic ash (C), and pyroclastic silty sand (cohesionless pozzolana, Ps), alternating with alluvial materials (peat, T, and sand, S). Underneath, the Neapolitan Yellow Tuff (NYT) is replaced in some zones by weakly cemented pozzolana (Pc). This formation rests on stiff alternating layers of ash, sand and pozzolana (A) with uncertain depth. The groundwater table (GWT) is located at a depth of 1 m from the soil surface.

The shear modulus profile at small strains, $G_0$, shown in Figure B 2b, was determined based on the cross-hole and down-hole tests, which were carried out in the same area down to 60 m (Vinale, 1988). Below such a depth, no direct measurements of shear-wave velocity, $V_s$, were available and the profile was extrapolated to about 100 m on the basis of a deep CPT. According to the Italian Building Code (NTC, 2008), adopting similar soil classification criteria as Eurocode 8 (CEN, 2003), the ground type might be classifiable between C and D, given that the equivalent velocity $V_{s,30}$ is about 180 m/s.

Ground motions records were selected according to a modified conditional spectrum procedure, as explained in detail in Section 1.3. The records were selected for both soil A and C. The selected site for this analysis considering dynamic SSI effects is attributed to a category C. Thus fixed-base multiple-stripe analyses reported in Chapter 4 were carried out with soil C motions. The multiple-stripe analyses reported in this Appendix were instead carried out using the same ground motion record set obtained by seismic-soil response (SSR) analysis starting from soil A records, for both the compliant-base and the fixed-base cases. The fixed-base results from this

Appendix and Chapter 4 are thus not comparable, because the latter solely considered ground motions on a generic soil C. On the contrary, ground motions used in this Appendix are those recorded on soil A, deconvoluted to the SSR model boundary, and amplified through the layered soil model described below. The total number of ground motion records is, as for all other cases within the project, equal to 200 records, i.e., 10 intensity measure levels × 20 (bi-component) records per level.



Figure B 2 (a) Subsoil conditions; (b) Initial and mobilized stiffness profile.
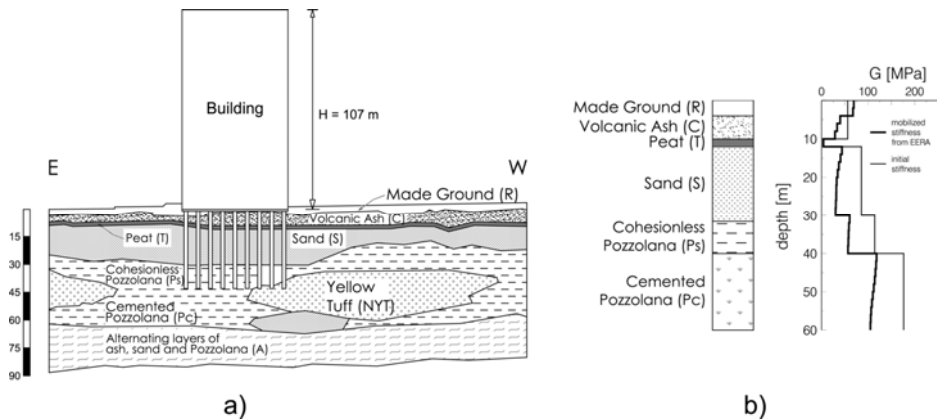
On the basis of the available geotechnical investigation, a regular layering, characterised as shown in Figure B 2b, was adopted to carry out the one-dimensional SSR analysis with the equivalent linear approach in the frequency domain, by using the STRATA code.

The decay of normalized shear modulus, $G/G_0$, and the variation of the damping ratio, D, with the shear strain, $\gamma$, (Figure B 3) were defined either by the resonant column test carried out on undisturbed specimens of pozzolana (Vinale, 1988) or based on the literature for other soils. Peat behavior was characterised following the experimental data reported by Wehling et al. (2003).

A viscoelastic bedrock was assumed at 60 m depth, with shear-wave velocity $V_{sb}$ = 800 m/s and damping ratio D = 0.5%, based on the preliminary analyses (Bilotta et al. 2013) showing that the amplification function of the subsoil was stable with respect to any reasonable assumption about the variability of $V_s$ below 60 m.



Figure B 3 (a) Normalised shear modulus and (b) Damping ratio plotted against shear strain.
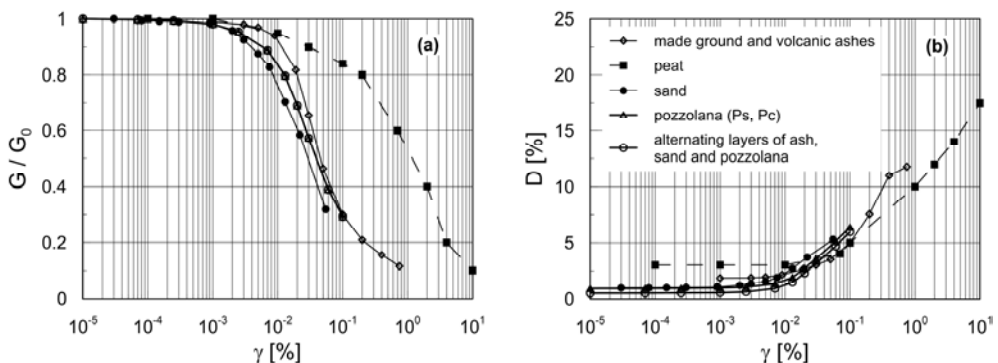
Figure B 4 shows the results of the SSR analyses for Intensity-Measure Level (IML) 2, characterized by the return period of 50 years (20 motions per level × 2 components = 40 signals) in terms of: mobilized shear strain, maximum acceleration, maximum shear stress, mobilized shear modulus and damping ratio (shown in the left-to-right order in the figure). The mobilized shear modulus and damping ratio were evaluated by entering the resultant shear strain, defined as the vector sum of the components along x- and y-directions, in curves plotted in Figure B 3. Noticeably, the mobilized shear stress is always below the limiting values $\tau_{lim1}$ and $\tau_{lim2}$, corresponding to the extreme values of the shear strength parameters (c', $\varphi$') coming from the geotechnical characterization of the subsoil under examination. If the attention is shifted to IML9 (Figure B 5), the picture is different, in the sense that the mobilized shear modulus and damping ratio decrease and increase, respectively, to a much larger extent, while the mobilized shear stress exceeds its limiting values $\tau_{lim1}$ and $\tau_{lim2}$ (dashed in the figure). With regard to this point, a recent comparison between the results of L (Linear), LE (Linear Equivalent) and NL (Non-Linear) SSR analyses and the recordings carried out through the KiK-net in Japan (Kaklamanos et al. 2013) have shown that the LE approach is accurate enough, provided that the structural period of the building at hand is larger than 0.5 s. Therefore, the exceedance of the limiting shear stress shown in Figure B 5 can be considered acceptable for the scope of this work.
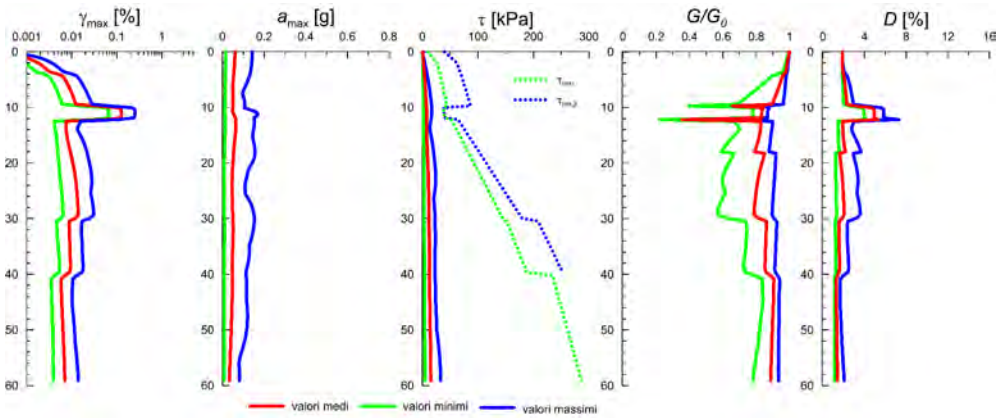


Figure B 4 Results of SSR analyses for IML2 (return period 50 years, see see Table 1.3.1).
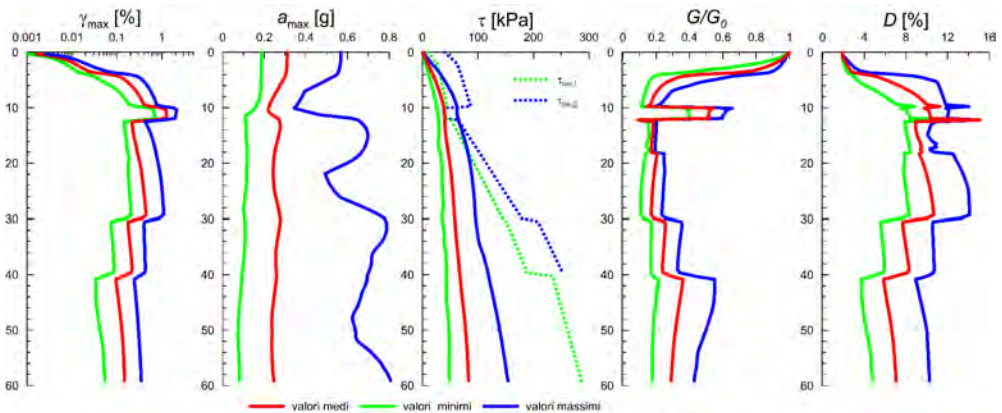


Figure B 5 Results of SSR analyses for IML9 (return period 10 000 years, see Table 1.3.1).

The average mobilized shear modulus and soil damping ratio profiles, as those represented in Figure B 4 and Figure B 5 will be considered as the basis of the frequency domain analyses

aiming at the evaluation of the impedance functions of the piled-foundation, as explained in the following.

## B3.    **Foundation design**

The first estimation of the behavior of a mat foundation gave rise to adequate safety margins against a bearing capacity failure (ULS), with a ratio of capacity and demand $R_d/E_d$ between 5 and 10 for short and long term conditions, respectively. However, such design choice might not guarantee a satisfactory behavior under working loads, as the first estimation of the average settlement resulted in about 30 cm, which is not acceptable for serviceability conditions. It was therefore decided to add piles underneath the raft with the sole aim of reducing settlement, provided that acceptable safety margins against collapse were already guaranteed by the shallow foundation. 24 CFA piles, 60 cm in diameter and 14 m in length, were adopted. The nominal bearing capacity and axial initial stiffness of the single pile were estimated as 1180 kN and 685 MN/m, respectively, thereby leading to bearing capacity and stiffness of the pile group (evaluated through a Boundary Element Method code) of 28 MN and 6301 MN/m. The initial stiffness of the raft was calculated as 619 MN/m. Such values were employed to calculate the response of the combined foundation (piled raft) by means of a method proposed by Mandolini et al. (2017) accounting for nonlinear behavior of both pile group and raft. The results of the interaction analysis are shown in Figure B 6, where it is possible to derive a settlement of about 2 cm under the working load, equal to 38 MN. Such value was deemed as acceptable for the serviceability of the superstructure.
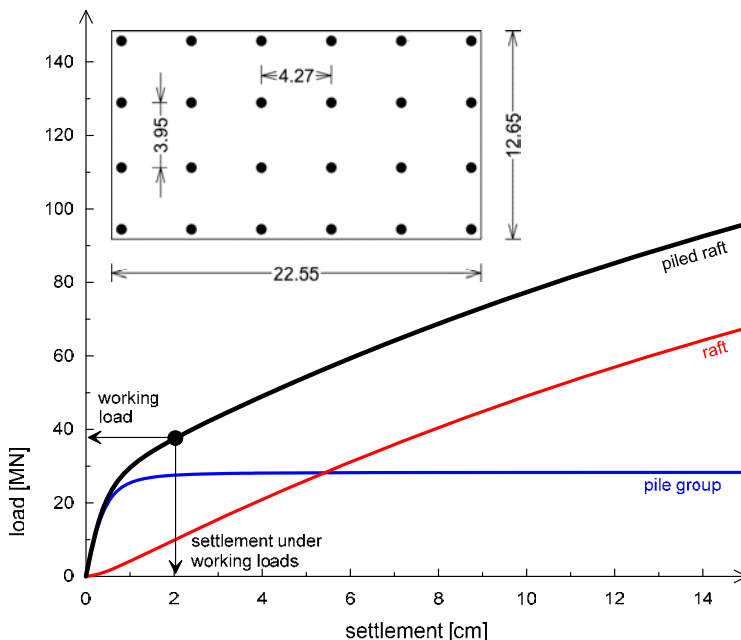


Figure B 6 Load-settlement curve of the combined foundation.

## B4.    **Foundation impedances**

The dynamic response of a building founded on piles embedded in a deformable soil may be different from that of a similarly excited, identical structure resting on a rigid ground. The factors

responsible for such a different behavior are: (i) the flexibility of the pile-foundation system; (ii) the vibrational energy dissipated by the wave radiation and by the internal soil damping.

The factors mentioned above can be incorporated in the inertial analysis of the nine-story building through the preliminary evaluation of the complete set of complex (frequency-dependent) impedance functions of the piled foundation shown in Figure B 7. The real part of the dynamic impedance represents the real stiffness, whereas the imaginary part represents the coefficient of equivalent viscous damping. This last quantity is strongly affected by the excitation frequency; usually, the imaginary part exhibits a cut-off frequency, below which there is no radiation damping (Novak and Nogami, 1977; Gazetas and Dobry, 1984). In addition, the coupled swaying-rocking stiffness may affect significantly the overall dynamic response (Velestos, 1971; Bu and Lin, 1999).

The translational, rotational and cross swaying-rotational stiffness components of the dynamic compliance were evaluated by means of Dynapile 3.0 (ENSOFT, INC. 2016), based on the consistent boundary matrix method (Blaney et al. 1976), in which group effects are incorporated through frequency dependent pile-to-pile interaction factors for all the vibration modes of the foundation, i.e., swaying, rocking and cross swaying-rocking modes, while the boundaries of the soil domain are correctly positioned at infinity. Also, the raft was considered to have a clearance to the soil.

Specifically, for each IML, the analysis in Dynapile were performed by referring to the foundation layout shown in Figure B 6, assuming the average profiles of the mobilized soil stiffness and damping ratio coming from the free-field analysis (as those shown in Figure B 4 and Figure B 5). In fact, while the shear modulus and damping ratio of the soil are strain-dependent, the studies (Kausel et al. 1978) showed that most of non-linearity occurs not due to soil-structure interaction but due to earthquake excitation. Thus, the soil properties consistent with the levels of strain mobilized in the free-field soil response can be also used without further modification for inertial interaction analysis of the compliant-base structure.

Figure B 7 shows the real and imaginary parts of the impedance functions of the pile group associated to the horizontal modes of vibration along x-axis ($K_{XX}$) and y-axis ($K_{YY}$) and rocking modes of vibration about y-axis ($K_{\theta Y}$) and x-axis ($K_{\theta X}$), for the three intensity levels IML 2, 6, and 9.

Figure B 7 Impedance functions of the piled raft.
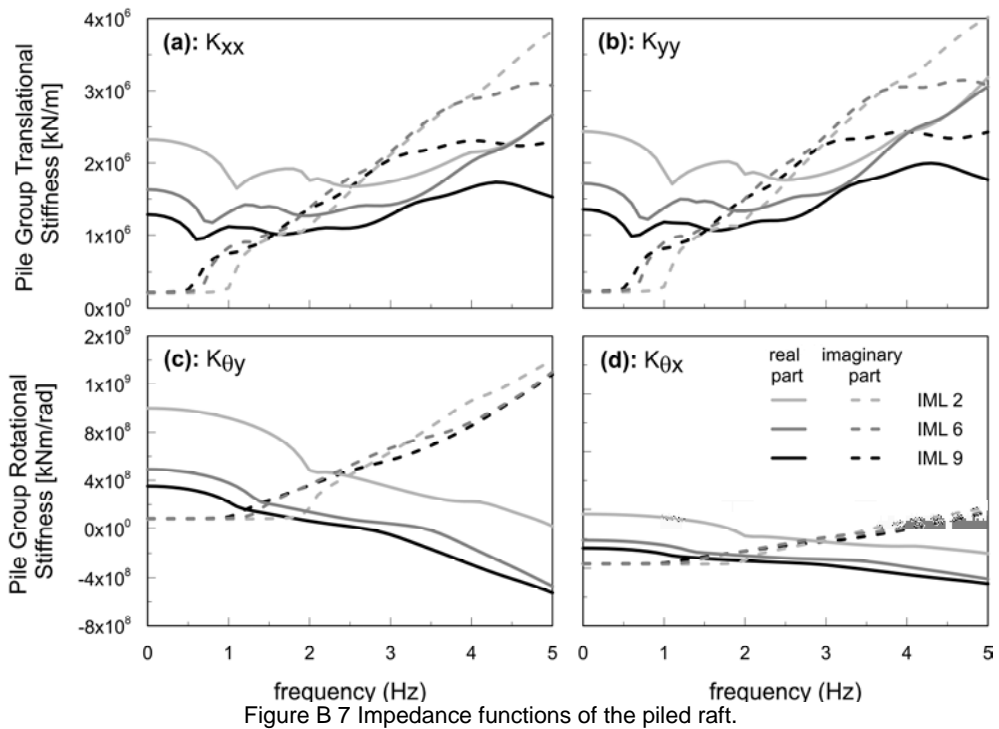
## B5.    **Calibration of lumped parameter models for time domain analysis**

Figure B 8 reports a graphical summary of the intensity-dependent dynamic impedance functions, arranged in a matrix of plots (each showing stiffness and damping versus frequency on the abscissa) with as many columns as there are IM levels (ten) and six rows: translation, rotation, cross-term, for the XZ and YZ planes, respectively, from top to bottom. By comparing the values between different intensity measures (to the same scale at all intensity levels, distinct for stiffness in light blue and damping in light red fill), it is apparent how the increase in average peak deformation of the soil layers is reflected in decreasing stiffness of the soil-foundation system. It is also clear how the coupling between sway and rocking degrees of freedom is significant. The relatively large rocking stiffness, however, suggests that overall, the effect of rotation and of coupling between rotation and translation may be of higher order. In any case, before running the analyses, the presence of the coupling term requires the adoption of a LPM that can account for such coupling. Further, in the frequency range of interest, the stiffness is decreasing with the frequency, while damping is (almost linearly) increasing. These feature led to the choice of the LPM form described below.
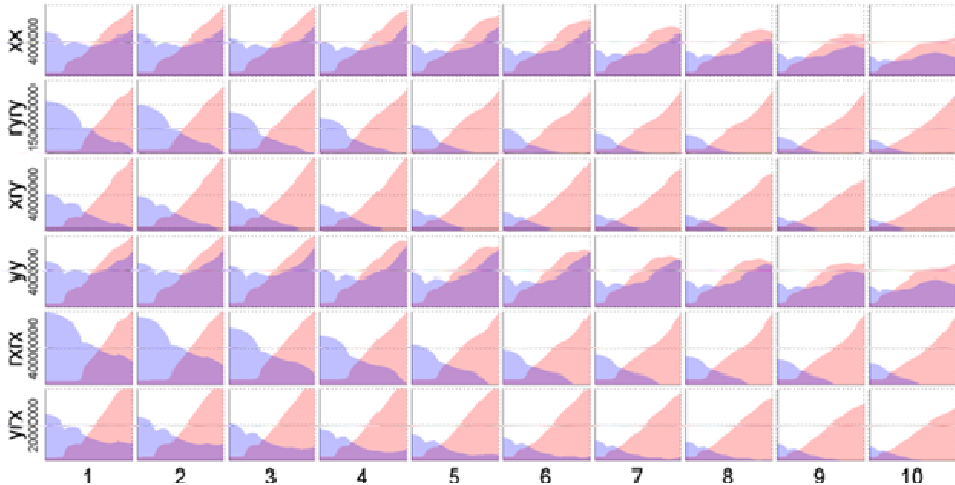
Figure B 8 Dynamic impedance functions. Blue and red denote stiffness and damping, respectively. The abscissa is frequency in each plot. The letters "x" and "y" denote translation (or sway) while "ry" and "rx" denote the corresponding rotation (or rocking) values. The plots show that there is also significant cross sway-rocking coupling.
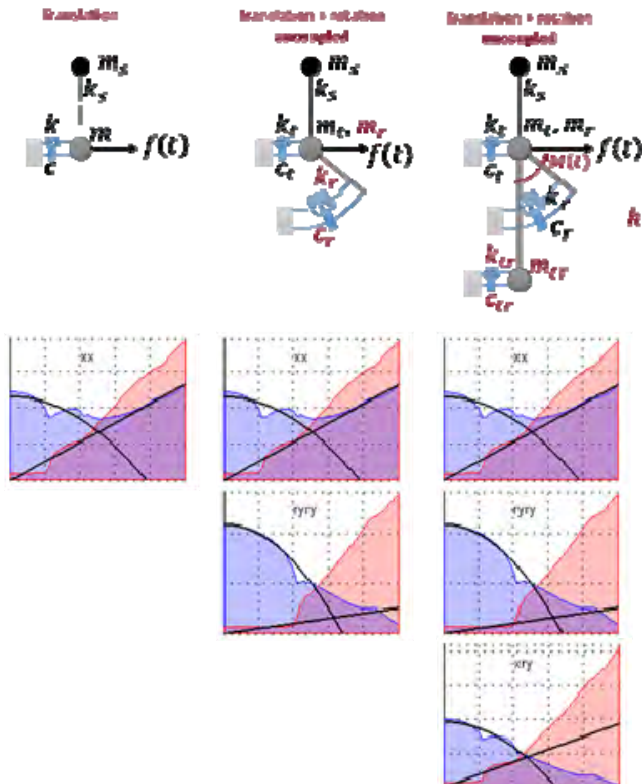


Figure B 9 LPM of increasing complexity: from left to right, translation-only model, uncoupled translation-rotation model and coupled model. Blue and red denote stiffness and damping, versus frequency in the abscissa, as in the previous figure. Black solid lines represent the fitted stiffness and damping, i.e. the stiffness and damping corresponding to the above LPM.

Even though techniques are available to describe frequency dependence of any type through a generalized LPM whose form is not known in advance (Lesgidis et al. 2015), herein a choice has been made to adopt the simplest LPM capable of describing approximately the features of the impedances in Figure B 8 over the frequency range of interest. The candidate model is the one described by (Dezi et al. 2009), and shown in the left column of Figure B 9.

The simple model on the right side, through the inclusion of a fictitious (non-physical) mass $m$ in the interface node, allows for an approximate description of frequency dependence in the stiffness term. This can be easily seen by considering the equation of motion of the system without the superstructure (shown on the left of Figure B 10):

$$m\ddot{u}(t) + c\dot{u}(t) + ku(t) = f(t) \tag{B.1}$$

where $m, c$ and $k$ are the mass, damping coefficient and stiffness, respectively, while $u(t)$ and $f(t)$ are the displacement and force functions. The dynamic impedance can be obtained by casting the equation in the frequency domain and rearranging terms:

$$[-m\Omega^2 U(\Omega) + i\Omega c U(\Omega) + kU(\Omega)]e^{i\Omega t} = F(\Omega)e^{i\Omega t} \tag{B.2}$$

$$K_{dyn}(\Omega) = F(\Omega)/U(\Omega) = [k - m\Omega^2] + ic\Omega = \Re(K_{dyn}) + i\Im(K_{dyn}) \tag{B.3}$$

where $U(\Omega)$ and $F(\Omega)$ are the Fourier transform of the displacement and force functions $u(t)$ and $f(t)$, $\Omega$ is the frequency and $K_{dyn}(\Omega)$ the dynamic impedance. The real (stiffness) and imaginary (damping) parts, $\Re(K_{dyn})$ and $\Im(K_{dyn})$, are plotted in Figure B 10. They are parabolic and linear with frequency, respectively. This is also shown with black solid lines denoting the fit of the LPM to the numerical impedances from the previous section, in Figure B 9.
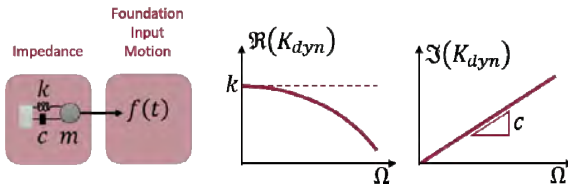


Figure B 10 Basic translation-only LPM: variation of real and imaginary parts of the dynamic impedance.

The central case in Figure B 9 is simply the extension of the previous case to two independent degrees of freedom, with the introduction of a rotational mass $m_r$ alongside the translational one, denoted now $m_t$. Coupling is achieved with left-hand model by introducing a rigid arm of height $h$ at the end of which coupling spring, dashpot and mass are located.

A comment is now due about the actual implementation of the LPM within the chosen analysis software. While some commercial softwares allow for direct specification of a linear visco-elastic coupled element, through direct assignment of the terms (including cross-terms for coupling) of the stiffness and damping matrices, Opensees does not provide this feature. This was the reason why it was necessary to use an assembly such as that shown on the left column of Figure B 9. This assembly, however, is characterized by three degrees of freedom (translation $u$ and rotation $\theta$ of the upper node, plus translation of the lower node $u'$), rather than two (translation $u$ and rotation $\theta$ of the upper node only), thus a mapping of the numerical impedances provided for two dof's onto the LPM is needed. This is done by the kinematic transformation below (only two out of three dof's are independent, due to the infinite stiffness of the arm of length $h$):

$$\boldsymbol{u_3} = \boldsymbol{Tu_2} = \begin{Bmatrix} u \\ \theta \\ u' \end{Bmatrix} = \begin{bmatrix} 1 & 0 \\ 0 & 1 \\ 1 & h \end{bmatrix} \begin{Bmatrix} u \\ \theta \end{Bmatrix} \tag{B.4}$$

Introducing this transformation, the mass matrix is obtained as:

$$\boldsymbol{M}_2 = \boldsymbol{T'M_3T} = \begin{bmatrix} 1 & 0 & 1 \\ 0 & 1 & h \end{bmatrix} \begin{bmatrix} m_t & 0 & 0 \\ 0 & m_r & 0 \\ 0 & 0 & m_{tr} \end{bmatrix} \begin{bmatrix} 1 & 0 \\ 0 & 1 \\ 1 & h \end{bmatrix} = \begin{bmatrix} m_t + m_{tr} & hm_{tr} \\ hm_{tr} & m_r + h^2 m_{tr} \end{bmatrix} \quad \text{(B.5)}$$

$$= \begin{bmatrix} M_{11} & M_{12} \\ M_{12} & M_{22} \end{bmatrix}$$

and similarly for the other matrices. Relations are thus obtained between mass, stiffness and damping terms of the two systems:

$$m_{tr} = M_{12}/h \qquad m_t = M_{11} - M_{12}/h \qquad m_r = M_{22} - hM_{12} \qquad \text{(B.6a)}$$

$$k_{tr} = K_{12}/h \qquad k_t = K_{11} - K_{12}/h \qquad k_r = K_{22} - hK_{12} \qquad \text{(B.6b)}$$

$$c_{tr} = C_{12}/h \qquad c_t = C_{11} - C_{12}/h \qquad c_r = C_{22} - hC_{12} \qquad \text{(B.6c)}$$

The above nine equations have ten unknowns, thus, the height $h$ must be assigned arbitrarily. Since all matrices must be positive definite, nine inequalities must be satisfied, similar the following ones for the masses:

$$M_{11} > 0, M_{22} > 0, M_{12}^2 < M_{11}M_{22} \qquad \text{(B.7)}$$

Also the LPM parameters must be positive definite, resulting in further conditions (here reported only for the masses):

$$m_{tr} > 0, m_t > 0, \ m_r > 0, h > M_{12}/M_{11}, h < M_{12}/M_{22} \qquad \text{(B.8)}$$

As a result, if the Dezi et al. (2009) model is adopted without modifications, there are conditions under which it is not possible to find a set of parameters satisfying all inequalities. For this reason, the final LPM adopted is the one shown in Figure B 11, modified to have different heights for the location of coupling terms for mass, stiffness and damping.
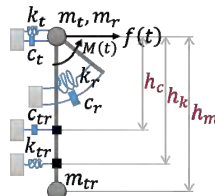


Figure B 11. Final extended LPM.

The model parameters have been determined by first performing a least-square fit in the frequency range from 0 to 2 Hz to determine the nine parameters, $M_{11}$, $M_{22}$, $M_{12}$, $K_{11}$, $K_{22}$, $K_{12}$, $C_{11}$, $C_{22}$, and $C_{12}$. Then, the obtained values were projected in Figure B 12 on the modified Dezi model independently for each stripe (intensity level) and for the X and Y plan directions.
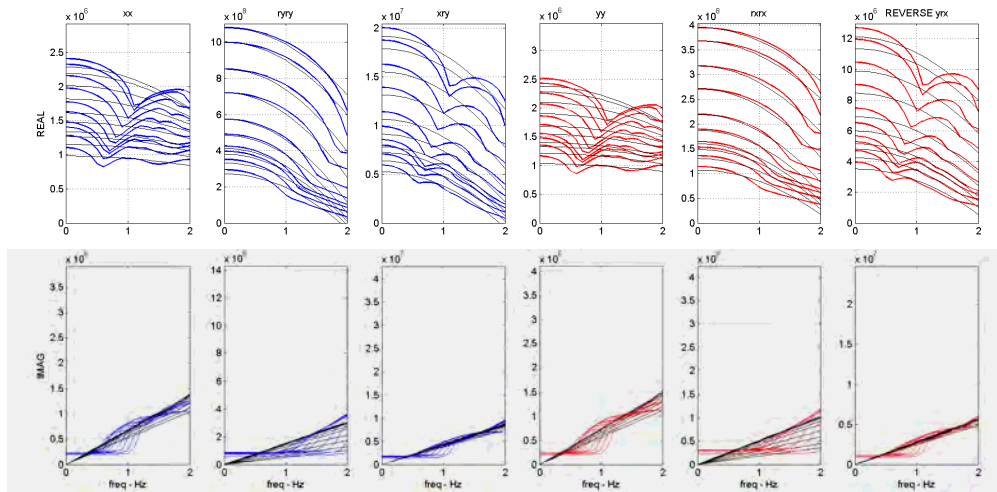
Figure B 12 Intensity and direction dependent fit to the numerical impedances.

## B6.     **Compliant base vs. fixed-base seismic response**

Numerical response results for the compliant base model (where the 3D model of each building structure is rigidly constrained at its base to a master node connected to the support through the LPM described in the previous section) were obtained for the BF, IF and PF cases. Only the BF case was compared with  the fixed-base case studied within the project. The comparison is shown for three selected intensity levels in Figure B 13. It can be preliminarily concluded that, for this specific case, even though the site is a soft soil one, the designed piled foundation, with its settlement reduction piles, ensures a very high stiffness that leads to negligible influence on the structural response. For this reason the next step will be to examine the six-story building frame with a shallow foundation, where non negligible differences are expected in response when including the dynamic SSI into the model.
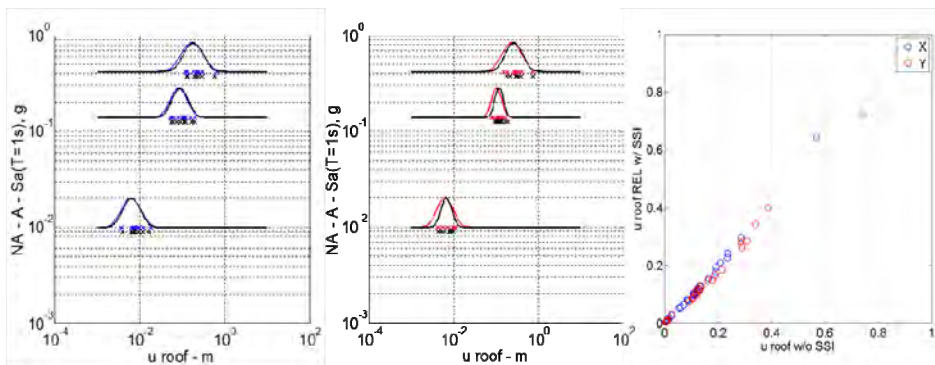


Figure B 13 Intensity and direction dependent fir to the numerical impedances.

## B7.   **References**

Bilotta E., de Sanctis L., Di Laora R., d'Onofrio A., Silvestri F. (2013). Importance of seismic site response and soil–structure interaction in dynamic behaviour of a tall building. Géotechnique 65(5), 391-400.

Blaney G.W., Kausel E., Roesset J.M. (1976). Dynamic stiffness of piles. Proc. 2nd International Conference on Numerical Methods in Geomechanics. Balcksburg, Virginia.

Bu S., Lin C.H. (1999). Coupled horizontal-rocking impedance functions for embedded square foundations at high frequency factors. Journal of earthquake engineering 3.04: 561-587.

Carbonari S., Dezi F., Leoni G. (2012). Non-linear seismic behaviour of wall–frame dual system accounting for soil–structure interaction. Earthquake Engineering and Structural Dynamics; 41(12):1651–72.

CEN/TC 250. Eurocode 8: Design of structures for earthquake resistance Part 5: Foundations, retaining structures and geotechnical aspects. European Committee for Standarization Technical Committee 250, Brussels, Belgium, Standard EN1998-5, 2003.

Ciampoli M., Pinto P.E. (2005). Effects of soil–structure interaction on inelastic seismic response of bridge piers. Journal of Structural Engineering;121(5), 806–14.

Dezi, F., Carbonari, S., Leoni, G. (2009). A model for the 3D kinematic interaction analysis of pile groups in layered soils. Earthquake Engineering & Structural Dynamics, 38(11), 1281-1305.

DM 14.01 (2008) – Approvazione delle nuove norme tecniche per le costruzioni. Gazzetta Ufficiale della Repubblica Italiana, n. 29 del 4/2/08 (Suppl. Ord. N°30).

DYNAPILE 3.0 (2016). A Program for the Analysis of Piles and Drilled Shafts Under Dynamic Loads. Ensoft Inc., Austin, Texas.

Gazetas G., Dobry R. (1984). Horizontal response of piles in layered soils. Journal of Geotechnical engineering 110.1: 20-40.

Kaklamanos J, Bradley BA, Thompson EM, Baise LG (2013). Critical parameters affecting bias and variability in site-response analyses using KiK-net downhole array data. Bulletin of the Seismological Society of America, 103(3), 1733–1749.

Kausel E., Whitman R.V., Morray J.P., Elsabee F. (1978). The spring method for embedded foundations. Nuclear Engineering Design, 48, 377-392.

Lesgidis, N., Kwon, O. S., & Sextos, A. (2015). A time‐domain seismic SSI analysis method for inelastic bridge structures through the use of a frequency‐dependent lumped parameter model. Earthquake Engineering & Structural Dynamics, 44(13), 2137-2156.

Mancuso C., Viggiani C., Mandolini A., Silvestri F. (1999). Prediction and performance of axially loaded piles under working loads. In Pre-failure Deformation Characteristics of Geomaterials (Jamiolkowski, Lancellotta & Lo Presti eds). Balkema, Rotterdam. 801-808.

Mandolini A., Di Laora R., Iodice C. (2017) Simple Approach to Static and Seismic Design of Piled Rafts. In 3rd Bolivian International Conference on Deep Foundations, 1, 107-124. Omnipress.

Novak M., Nogami T. (1977). Soil-pile interaction in horizontal vibration. Earthquake Engineering & Structural Dynamics, 5(3), 263-281.

STRATA (2013). Geotechnical Engineering Center Department of Civil, Architectural, and Environmental Engineering. University of Texas.

Veletsos A.S., Meek J.W. (1974). Dynamic Behaviour of Building Foundation Systems, Earthquake Engineering and Structural Dynamics, 3, 121-138.

Veletsos A.S., Wei Y.T. (1971). Lateral and rocking vibration of footings. Journal of Soil Mechanics & Foundations.

Viggiani C., Vinale F. (1983). Comportamento di pali trivellati di grande diametro in terreni piroclastici. Rivista Italiana di Geotecnica, 17(2), 59-84.

Vinale F. (1988). Caratterizzazione del sottosuolo di un'area campione di Napoli ai fini di una microzonazione sismica. Rivista Italiana di Geotecnica, 22(2), 77-100.

Wehling T.M., Boulanger R.W., Arulnathan R., Harder L.F., Driller M.W. (2003). Nonlinear dynamic properties of a fibrous organic soil. J Geotech Geoenviron Eng 129(10):929–939.

Wolf J.P. (1991). Consistent lumped-parameter models for unbounded soil: frequency-independent stiffness, damping and mass matrices. Earthquake Engineering and Structural Dynamics 20, 33-41.

# APPENDIX C – MODEL-UNCERTAINTY

C1. **Scope**

The effect of so-called model uncertainty was explored with reference to a subset of the structures analyzed within the project. This Appendix presents the general model developed to quantify the structure-related uncertainty, consisting of material properties, strictly speaking of aleatoric type, and uncertainty in the response models' parameters, and results for the RC typology. Amongst the building structures considered within WP4, the structures chosen were the 6-story and the 9 story frame buildings at the sites of Naples and L'Aquila.

C2. **Introduction**

Most of the work to date devoted to the development of methods for probabilistic seismic performance assessment of structures and their application has focused on the uncertainty associated with the input, rather than on that associated with the system. Few notable exceptions are represented by Veneziano et al. (1983), Schotanus et al. (2004), Lupoi et al. (2006), Kwon and Elnashai (2006), Liel et al. (2009), Dolsek (2009), Celic and Ellingwood (2010), Celarec et al. (2012), and more recently, Gokkaya et al. (2016) and O'Reilly and Sullivan (2017).

The aforementioned uncertainties can be classified as aleatoric or epistemic. The former term is often used to denote record-to-record variability, while the latter is associated with uncertainties related to material properties and response or capacity models. It has also become quite common to call the latter model (or modelling) uncertainties. In fact, uncertainty of both aleatoric and epistemic nature characterize both the input and the system. For instance, the geometry of seismic sources, seismic activity rate, and the maximum magnitude of earthquakes are all examples of quantities affected by epistemic uncertainty and are incorporated into seismic hazard evaluation, while the variability of material properties is an example of aleatoric uncertainty affecting the structure.

Epistemic or model uncertainties can be classified in two types:

- Type I: uncertainty in the choice of a model among different candidate models
- Type II: uncertainty in the parameters of the chosen model

Dealing with Type I epistemic uncertainty requires parallel models arranged in a logic tree, with weights attached to branches to reflect subjective degrees of belief of the analyst in each model. This approach, which is common practice in probabilistic seismic hazard analysis, is not used, to the best knowledge of the authors, in the structural engineering domain. As a result, when epistemic uncertainty is considered, what is really meant is Type II, i.e., the uncertainty in model parameters. Besides, it should also be noted, in most cases, that the uncertainty in model parameters is considered only in a partial manner. Typically, a hysteretic model, e.g., a trilinear backbone model for the moment-rotation curve of a RC member (e.g., Ibarra et al., 2005), has parameters which should be modelled as statistically dependent, in order to yield physically feasible realizations, but predictive equations have statistically independent error terms, i.e., the model is a collection of marginal models, rather than a multi-variate one. This is the case of the model used within the project (Haselton et al., 2007). In order to be used in risk analysis this model needs to be complemented by a number of assumptions on statistical dependence, as done, for instance, in Liel et al. (2009).

With the above in mind, it was decided within the RINTC project to explore, with reference to a subset of the considered code-conforming buildings, the relevance of structure-related uncertainty, which includes Type II modelling uncertainties and the inherent randomness in material properties. It should be noted, as also recently highlighted in O'Reilly and Sullivan (2017), there is no consensus yet on whether this "model uncertainty" is really relevant or not. Some researchers regard it as significant (e.g., Gokkaya et al., 2016), while others do not (e.g., Ellingwood et al., 2007). Arguably, it must be judged based on a careful consideration on the model uncertainties before reliable indications can be derived, in the words of Liel et al. (2009):

"Whichever procedure is utilized, correlations between the input random variables may significantly affect the extent to which modelling uncertainties impact the performance assessment." Possibly, even given a good model of modelling uncertainties, their importance will be case-dependent.

## C3. **Approaches to the treatment of model uncertainty**

Uncertainty in the structure is partly aleatoric (mainly material properties) and partly epistemic. It is useful to recall the possible approaches to the treatment of the epistemic component, which vary depending on their Type:

(1)       Type I: as already mentioned, parallel models arranged in a logic tree are used, yielding multiple results (e.g. mean annual frequency of exceedance of an EDP or of a limit state). The output takes the form of mean over the logic tree, complemented by either upper/lower fractiles or a confidence interval of the mean, giving a clear measure of the effect of epistemic uncertainty on the result. Sensitivity to each component of the epistemic uncertainty can be also obtained, e.g., according to Visser et al. (2000) or Merz and Thieken (2009).

(2)       Type II: each model parameter is modelled with a random variable.

　　a.　These variables can be arranged in a hierarchical model together with aleatoric uncertainty, such as random variables describing the variability in material properties or a series of measured time-series responses describing the variability in ground motion records. In this case the analysis yields a single result, incorporating the effect of both aleatoric and epistemic uncertainty (e.g., Veneziano et al., 1983, Schotanus et al., 2004, Lupoi et al., 2006, Dolsek, 2009, and Liel et al., 2009). Schemes for the combination of uncertainties vary from the simple one-to-one association between ground motion records and sample realizations of the structure (i.e., minimum computational effort for the consideration of the epistemic uncertainty), to the complete set of combinations of ground motion records and realization of the structure, possibly sampled according to Latin Hypercube or similar schemes (i.e., maximum computational effort).

　　b.　Alternatively, the risk analysis can be repeated for discrete values of each parameter (e.g., the 16%, 50% and 84% fractiles), keeping all remaining parameters fixed at their central value. This approach provides first-order sensitivities to epistemic uncertainty, usually represented as tornado plots (Celic and Ellingwood, 2010 and Celarec et al., 2012).

(3)       Type I and Type II:

　　a.　One possibility is to adopt approach 1 for Type I and approach 2a for Type II uncertainties. This should be done only as a way to carry out the expectation over all sources of uncertainty, presenting the result as the mean over the logic tree. This approach should not be used to compute confidence intervals or fractiles, because they would refer only to a certain part of the total structure-related epistemic uncertainty.

　　b.　The second approach consists in considering discrete values of the model parameters and associate each of them to a branch in an expanded logic tree combining both Type I and II uncertainties. Weights for the branches corresponding to model parameters could be assigned, e.g., according to Miller and Rice (1983).

The problem with approaches (2)b and (3)b is that, rigorously speaking, they can only be applied when all parameters are statistically independent. If there is statistical dependence, variation in one parameter changes the (conditional) distribution of the others. This is a problem already recognized with reference to logic trees employed in seismic hazard assessment (Bommer et al., 2005), and remains still unsolved. Therefore, in the project it was decided to consider only Type II epistemic uncertainties, alongside (aleatoric) material properties, and to adopt approach (2)a.

## C4.   **Joint distribution model of modelling uncertainties**

Complex 3D structural models of buildings, such as those constructed within the RINTC project, generally consist of the assembly of elements of multiple typologies. For example, the structural models of the base-isolated buildings include components with at least three different hysteretic models, corresponding to RC members, infill panels and isolation devices, respectively. Each of these hysteretic models is characterized by its own set of model parameter of generally different size $n_e$.

Let $\boldsymbol{y}$ denote the global vector collecting the uncertain parameters of all elements in the structural model. Vector $\boldsymbol{y}$ is the assembly of vectors $\boldsymbol{y}_{jk}^e = \{y_{ijk}^e\}$ with $i = 1, \dots, n_e$, representing uncertainty in the j-th element of e-th type, within the k–th sub-group. Sub-groups are introduced to model block effects for some parameters within each element type. A typical example is the difference of concrete strength in within-floor and between-floor correlations due to floor-wise casting.

Model parameters are generally positive-definite quantities. In some cases, for example when they represent error terms of predictive equations, they are assumed to have lognormal marginal distribution (e.g., Haselton et al., 2007). Given the typical values for their coefficient of variation, the lognormal distribution is also appropriate as a marginal model for material properties. It is thus common to adopt it for all parameters, and to postulate joint lognormality for the vector $\boldsymbol{y}$. Specification of the multi-variate model thus amounts to providing a vector of medians, or of the logarithmic means $\boldsymbol{\mu}_{lny}$, plus a matrix of covariances of the logarithms $\boldsymbol{C}_{lny,lny}$. The latter matrix can be decomposed in the matrix product:

$$\boldsymbol{C}_{lny,lny} = \boldsymbol{D}_{lny,lny}\boldsymbol{R}_{lny,lny}\boldsymbol{D}_{lny,lny} \tag{C.1}$$

where $\boldsymbol{D}_{lny,lny}$ and $\boldsymbol{R}_{lny,lny}$ denote the diagonal matrix of logarithmic standard deviations and the correlation matrix, respectively. The latter encodes the statistical dependence structure among the uncertain parameters. It cannot be built arbitrarily. Herein, it is built starting from the following considerations:

(i)     The intra- or within-element correlation matrix $\boldsymbol{R}_{j,j}$ of size $n_e \times n_e$ is known for each element type *e*, based on experimental data or, partially, on engineering judgement, which will be shown later in the typology-specific sections;

(ii)    The correlation among same variables in different elements of the same type *e* (e.g. concrete strength in two different RC members), belonging to the inter- or between element correlation matrix of size $n_{e1} \times n_{e2}$, can be established, again, based on judgement and sometimes on data;

(iii)   The latter correlation can vary with inter-element distance and, as a first approximation, can be differentiated by blocking, grouping elements within a certain distance or believed to share common factors (such as casting at the same time already mentioned for concrete strength).

(iv)    Correlation among different variables in different elements of the same type is unknown, but constraints exist on its value, based on the known or assumed correlation between the same variables within an element, and the inter-element correlation for each of the variables, in order to get valid correlation matrices (Budden et al., 2007).

(v)     In general, correlation among variables of elements of different type can be safely assumed to be zero.

Based on the above considerations the logarithm of vector $\boldsymbol{y}$ can be written as:

$$lny = \boldsymbol{\mu}_{lny} + \boldsymbol{D}_{lny,lny}\boldsymbol{\epsilon} = \boldsymbol{\mu}_{lny} + \boldsymbol{D}_{lny,lny}(\boldsymbol{A}\boldsymbol{\epsilon}_A + \boldsymbol{B}\boldsymbol{\epsilon}_B + \boldsymbol{C}\boldsymbol{\epsilon}_C) \qquad \text{(C.2)}$$

where the matrices $\boldsymbol{A}, \boldsymbol{B}$ and $\boldsymbol{C}$ are Boolean collocation matrices that sum the corresponding vectors $\boldsymbol{\epsilon}$ and are made up of $n_e \times n_e$ identity $\boldsymbol{I}$ or null $\boldsymbol{0}$ matrices, depending on whether an element belongs to the corresponding group or not. The vectors $\boldsymbol{\epsilon}$, statistically independent of each other, are made up of $n_b$ vectors of length $n_e \times 1$, where $n_b$ is the number of blocks, each being zero-mean unit-variance Gaussian with $n_e \times n_e$ correlation matrix $\boldsymbol{R}_A, \boldsymbol{R}_B$ or $\boldsymbol{R}_C$, respectively. This is more easily understood with reference to the element numbering in Figure C 1, showing a simple plane structure with two isolation devices, six RC members in two floors and two infill panels. Both isolators and infill panels belong to a single block, while RC members are grouped into $n_b = 2$ blocks, each corresponding to a floor. It should therefore be clear that there are as many sets of $\boldsymbol{R}_A, \boldsymbol{R}_B$ or $\boldsymbol{R}_C$ correlation matrices, as there are element types (i.e., the matrices for RC members will have different sizes and values from those for the other element types, e.g., isolation devices).



Figure C 1 Schematic representation of an infilled RC structure with seismic isolation.

The figure shows some of the sub-matrices of the global correlation matrix. Correlation between, e.g., element 4 (a RC column) and element 2 (an isolator device) is zero. Correlation matrix $\boldsymbol{R}_{4,4}$ is the column intra-element correlation, which is known. Correlation matrices $\boldsymbol{R}'_{4,5}$ and $\boldsymbol{R}''_{4,7}$ are the inter-element correlation matrices, of column 4 with beam 5 within its floor and with column 7 on another floor.

For the case in the figure $\boldsymbol{A}$ is the identity matrix of size $10n_e \times 10n_e$ (where 10 is the number of elements and, for the sake of illustration, it is assumed that all element types have the same number of uncertain parameters $n_e$), and $\boldsymbol{B}$ and $\boldsymbol{C}$ are expressed with:

$$\boldsymbol{B}^T = \begin{bmatrix} \boldsymbol{I} & \boldsymbol{I} & \boldsymbol{0} & \boldsymbol{0} & \boldsymbol{0} & \boldsymbol{0} & \boldsymbol{0} & \boldsymbol{0} & \boldsymbol{0} & \boldsymbol{0} \\ \boldsymbol{0} & \boldsymbol{0} & \boldsymbol{I} & \boldsymbol{I} & \boldsymbol{I} & \boldsymbol{0} & \boldsymbol{0} & \boldsymbol{0} & \boldsymbol{0} & \boldsymbol{0} \\ \boldsymbol{0} & \boldsymbol{0} & \boldsymbol{0} & \boldsymbol{0} & \boldsymbol{0} & \boldsymbol{I} & \boldsymbol{I} & \boldsymbol{I} & \boldsymbol{0} & \boldsymbol{0} \\ \boldsymbol{0} & \boldsymbol{0} & \boldsymbol{0} & \boldsymbol{0} & \boldsymbol{0} & \boldsymbol{0} & \boldsymbol{0} & \boldsymbol{0} & \boldsymbol{I} & \boldsymbol{I} \end{bmatrix} \qquad \text{(C.3)}$$

$$\boldsymbol{C}^T = \begin{bmatrix} \boldsymbol{I} & \boldsymbol{I} & \boldsymbol{0} & \boldsymbol{0} & \boldsymbol{0} & \boldsymbol{0} & \boldsymbol{0} & \boldsymbol{0} & \boldsymbol{0} & \boldsymbol{0} \\ \boldsymbol{0} & \boldsymbol{0} & \boldsymbol{I} & \boldsymbol{I} & \boldsymbol{I} & \boldsymbol{I} & \boldsymbol{I} & \boldsymbol{I} & \boldsymbol{0} & \boldsymbol{0} \\ \boldsymbol{0} & \boldsymbol{0} & \boldsymbol{0} & \boldsymbol{0} & \boldsymbol{0} & \boldsymbol{0} & \boldsymbol{0} & \boldsymbol{0} & \boldsymbol{I} & \boldsymbol{I} \end{bmatrix} \qquad \text{(C.4)}$$

The resulting correlation matrix is given by:

$$
\mathbf{R} =
\begin{bmatrix}
\overbrace{\begin{matrix} \mathbf{R}_{1,1} & \mathbf{R}'_{2,1} \\ & \mathbf{R}_{2,2} \end{matrix}}^{e=1} & \mathbf{0} & \mathbf{0} \\[2em]
& \overbrace{\begin{matrix} \overbrace{\begin{matrix} \mathbf{R}_{3,3} & \mathbf{R}'_{3,4} & \mathbf{R}'_{3,5} \end{matrix}}^{k=1} & \overbrace{\begin{matrix} \mathbf{R}''_{3,6} & \mathbf{R}''_{3,7} & \mathbf{R}''_{3,8} \end{matrix}}^{k=2} \\ \mathbf{R}_{4,4} & \mathbf{R}'_{4,5} & \mathbf{R}''_{4,6} & \mathbf{R}''_{4,7} & \mathbf{R}''_{4,8} \\ \mathbf{R}_{5,5} & \mathbf{R}''_{5,6} & \mathbf{R}''_{5,7} & \mathbf{R}''_{5,8} \\ \mathbf{R}_{6,6} & \mathbf{R}'_{6,7} & \mathbf{R}'_{6,8} \\ sym & \mathbf{R}_{7,7} & \mathbf{R}'_{7,8} \\ & \mathbf{R}_{8,8} \end{matrix}}^{e=2} & \mathbf{0} \\[2em]
& & \overbrace{\begin{matrix} \mathbf{R}_{9,9} & \mathbf{R}'_{9,10} \\ & \mathbf{R}_{10,10} \end{matrix}}^{e=3}
\end{bmatrix}
\tag{C.5}
$$

where:

- $\mathbf{R}_{j1,j2} = \mathbf{0}$ when elements $j_1$ and $j_2$ belong to different element types $e_1$ and $e_2$, which satisfies (v). from the previous list;
- $\mathbf{R}_{j,j} = \mathbf{R}_A + \mathbf{R}_B + \mathbf{R}_C$ when $j_1 = j_2$ (highest non-zero correlation), which is known according to (i). in the previous list;
- $\mathbf{R}'_{j1,j2} = \mathbf{R}_B + \mathbf{R}_C$ when elements $j_1$ and $j_2$ belong to the same element type $e$ and block $k$ (intermediate non-zero correlation);
- $\mathbf{R}''_{j1,j2} = \mathbf{R}_C$ when elements $j_1$ and $j_2$ belong to the same element type $e$, but to different blocks $k_1$ and $k_2$ (lowest non-zero correlation).

The above relations are generic, until $\mathbf{R}_A, \mathbf{R}_B$ and $\mathbf{R}_C$ are assigned. This has been done so that matrices $\mathbf{R}'$ and $\mathbf{R}''$ are based on the only available knowledge of $\mathbf{R}$ and of the "same variable" inter-element correlation, differentiated by blocking (items (ii), (iii) and (iv) in the previous list).

If the inter-element correlation coefficients for the generic $i$-th variable within a block (wb) and between blocks (bb) are denoted by $\rho_{ii}^{wb}$ and $\rho_{ii}^{bb}$, respectively, it is easy to show that, if the $j$-th sub-vector of $\boldsymbol{\epsilon}_A$ is obtained as $c_a \boldsymbol{\epsilon}_{aj}$, the $k$-th sub-vector of $\boldsymbol{\epsilon}_B$ is obtained as $c_b \boldsymbol{\epsilon}_{bk}$, and $\boldsymbol{\epsilon}_C$ is obtained as $c_c \boldsymbol{\epsilon}_c$, where $\mathbf{b}$ and $\mathbf{c}$ are the diagonal matrices given by:

$$
\mathbf{c} =
\begin{bmatrix}
\sqrt{\rho_{11}^{bb}} & \cdots & 0 \\
\vdots & \ddots & \vdots \\
0 & \cdots & \sqrt{\rho_{n_e n_e}^{bb}}
\end{bmatrix}
\tag{C.6}
$$

$$\mathbf{b} = \begin{bmatrix} \sqrt{\rho_{11}^{wb} - \rho_{11}^{bb}} & \cdots & 0 \\ \vdots & \ddots & \vdots \\ 0 & \cdots & \sqrt{\rho_{n_e n_e}^{wb} - \rho_{n_e n_e}^{bb}} \end{bmatrix} \tag{C.7}$$

and $\epsilon_{aj}$, $\epsilon_{bk}$ and $\epsilon_c$ are independent zero-mean unit-variance Gaussian vectors of size $n_e \times 1$, with the same correlation matrix $\mathbf{R}_{j,j}$, then:

$$\mathbf{R}_C = \mathbf{c}\mathbf{R}_{j,j}\mathbf{c} \tag{C.8}$$

$$\mathbf{R}_B = \mathbf{b}\mathbf{R}_{j,j}\mathbf{b} \tag{C.9}$$

and:

$$\mathbf{R}_A = \mathbf{a}\mathbf{R}_{j,j}\mathbf{a} \tag{C.10}$$

Matrix $\mathbf{a}$ can be obtained by noting that:

$$\mathbf{R}_{j,j} = \mathbf{L}_{jj}\mathbf{L}_{jj}^T = \mathbf{a}\mathbf{R}_{j,j}\mathbf{a} + \mathbf{b}\mathbf{R}_{j,j}\mathbf{b} + \mathbf{c}\mathbf{R}_{j,j}\mathbf{c} \tag{C.11}$$

from which it follows:

$$\mathbf{a} = \left(\mathbf{L}_{jj}^T\right)^{-1} \sqrt{\mathbf{L}_{jj}^T\left(\mathbf{R}_{jj} - \mathbf{b}\mathbf{R}_{j,j}\mathbf{b} - \mathbf{c}\mathbf{R}_{j,j}\mathbf{c}\right)\mathbf{L}_{jj}} \, \mathbf{L}_{jj}^{-1} \tag{C.12}$$

It should be noted that the particular choice made for the shape of $\mathbf{R}_A, \mathbf{R}_B$ and $\mathbf{R}_C$ allows direct control only of the inter-element correlation values on the diagonal of $\mathbf{R}'$ and $\mathbf{R}''$, i.e. of the correlation among same variables in different elements of the same type, which are given by:

$$R''_{ii} = \rho_{ii}\rho_{ii}^{bb} \tag{C.13}$$

$$R'_{ii} = \rho_{ii}\rho_{ii}^{wb} \tag{C.14}$$

Off-diagonal elements are not controlled and given by:

$$R''_{i_1 i_2} = \rho_{i_1 i_2}\sqrt{\rho_{i_1 i_1}^{bb}\rho_{i_2 i_2}^{bb}} \tag{C.15}$$

$$R'_{i_1 i_2} = \rho_{i_1 i_2} \left[ \sqrt{\left( \rho_{i_1 i_1}^{wb} - \rho_{i_1 i_1}^{bb} \right)\left( \rho_{i_2 i_2}^{wb} - \rho_{i_2 i_2}^{bb} \right)} + \sqrt{\rho_{i_1 i_1}^{bb} \rho_{i_2 i_2}^{bb}} \right] \tag{C.16}$$

Finally, it can be observed that the particular structure of the correlation matrix allows also a very efficient sampling procedure to be employed. While direct sampling is still feasible according to the expression:

$$\boldsymbol{y} = \exp\left( \boldsymbol{\mu}_{lny} + \boldsymbol{D}_{lny,lny} \boldsymbol{L}_{lny,lny} \boldsymbol{u} \right) \tag{C.17}$$

with $\boldsymbol{R}_{lny,lny} = \boldsymbol{L}_{lny,lny} \boldsymbol{L}_{lny,lny}^T$ and $\boldsymbol{u}$ is a vector of independent standard Gaussian variables, a more effective procedure uses the sums of independently generated short independent zero-mean unit-variance Gaussian vectors $\boldsymbol{\epsilon}_{aj}$ (as many as there elements in the model), $\boldsymbol{\epsilon}_{bk}$ (as many as there are blocks) and $\boldsymbol{\epsilon}_c$ (only one) to reproduce the target covariance structure:

$$lny_{jk} = \boldsymbol{\mu}_{lny_{jk}} + \boldsymbol{D}_{jk} \boldsymbol{\epsilon}_{jk} = \boldsymbol{\mu}_{lny_{jk}} + \boldsymbol{D}_{jk}\left( \boldsymbol{a}\boldsymbol{\epsilon}_{aj} + \boldsymbol{b}\boldsymbol{\epsilon}_{bk} + \boldsymbol{c}\boldsymbol{\epsilon}_c \right) \tag{C.18}$$

Thus, rather than forming and decomposing the full correlation matrix $\boldsymbol{R}_{lny,lny}$, it is only necessary to form much smaller matrices $\boldsymbol{a}, \boldsymbol{b}$ and $\boldsymbol{c}$ for each element type.

## C5.   **Specific aspects of reinforced concrete structures**

Two types of hysteretic models are implemented in the modelling of RC buildings within the RINTC project: the IMK response model (Ibarra et al., 2005), for the RC members, and an equivalent single strut (concentric) model for the infill panels. The details are given in Chapter 4.

The former is a trilinear model, characterized by a total of five parameters: the stiffness at 40% of the yield moment, $K_{0.4}$, the ultimate to yield moment ratio $M_u/M_y$, the incremental cap rotation (difference between the cap rotation and the yield rotation), $\Delta\theta_u$, the incremental collapse rotation (difference between the collapse rotation and the cap rotation), $\Delta\theta_c$, and the cyclic degradation parameter $\gamma$. The yield and ultimate moments are computed through basic mechanics and are random through the random material properties (see below).

Marginal predictive equations were derived for these parameters by Haselton et al. (2007). The equations are based on the assumption that parameters have a lognormal distribution, characterized with the two parameters for median and dispersion values. The model is marginal in the sense that no measure of statistical dependence among the parameters is provided. In the project, the model parameters are modelled as lognormal variables based on the equations proposed by Haselton et al. (2007), except the ultimate to yield moment ratio, that is taken deterministically equal to the median value of 1.13. Two additional lognormal variables are used to describe material variability in RC members, in particular concrete strength $f_c$ and steel yield stress $f_y$, thus, in total, 4+2=6 random variables are considered for the hysteretic model of RC members (see Figure C 2).

The parameters of the infill model are five, i.e., peak strength, cracking, peak and residual strength displacements, and the strength reduction factor for openings. Thus, five random variables are needed for each equivalent strut (Figure C.3).
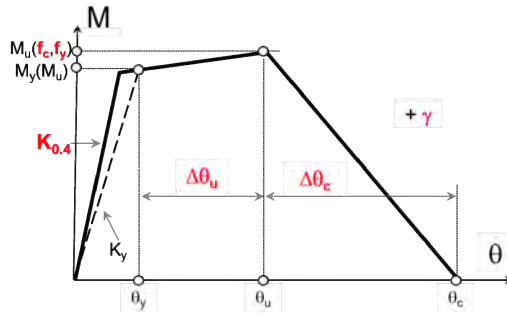
Figure C 2 Trilinear IMK model used for hinges in RC member modeling: identification of random variables.
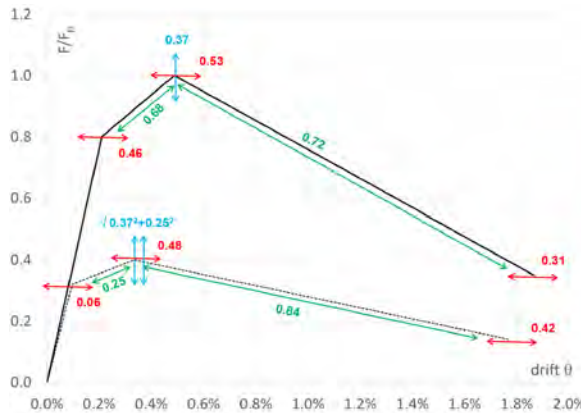


Figure C 3 Diagonal strut model: dispersion (red for displacement, blue for forces) and correlation coefficients (green), assessed from the Sassun et al data base. Note that force for both full panels and panels with openings are normalized to full panel strength $F_p$.

Table C 1 and Table C 2 summarize the logarithmic standard deviations (dispersions), intra-member, intra-floor ($\rho_{ii}^{wb} = \rho_{ii}^{sf}$) and inter-floor ($\rho_{ii}^{bb} = \rho_{ii}^{df}$) correlation coefficients, for the RC members and the infill panels (IP), respectively. The bolded values are based on experimental evidence, either provided by Haselton et al. (2007) or assessed for the purpose of this work (Table C 1). The correlation and dispersion values for the IP equivalent strut model reported in Table C 2 are rounded with respect to those in Figure C 3. The other assumed values merely reflect the common-sense fact that, both in RC and masonry buildings, increasing resistance capacity goes along with decreasing ductility capacity.

Table C 1 Dispersion and intra-member correlation coefficients for the RC member model (values in bold typeface are based on data, the remaining ones are based on expert judgement).

| Variable | $\sigma_{ln}$ | $\rho_{x,f_c}$ | $\rho_{x,f_y}$ | $\rho_{x,\lambda}$ | $\rho_{x,k_{40}}$ | $\rho_{x,\Delta\theta_u}$ | $\rho_{x,\Delta\theta_c}$ | $\rho_{x,x}^{sf}$ | $\rho_{x,x}^{df}$ |
|---|---|---|---|---|---|---|---|---|---|
| $f_c$ | **0.20** | 1.0 | 0.0 | 0.0 | 0.0 | 0.0 | 0.0 | 0.6 | 0.0 |
| $f_y$ | **0.10** | 0.0 | 1.0 | 0.0 | 0.0 | 0.0 | 0.0 | 0.9 | 0.9 |
| $\lambda$ | **0.50** | 0.0 | 0.0 | 1.0 | 0.0 | 0.0 | 0.0 | 0.8 | 0.8 |
| $k_{40}$ | **0.38** | 0.0 | 0.0 | 0.0 | 1.0 | -0.5 | -0.5 | 0.8 | 0.8 |
| $\Delta\theta_u$ | **0.61** | 0.0 | 0.0 | 0.0 | -0.5 | 1.0 | 0.8 | 0.8 | 0.8 |
| $\Delta\theta_c$ | **0.72** | 0.0 | 0.0 | 0.0 | -0.5 | 0.8 | 1.0 | 0.8 | 0.8 |

Table C 2 Dispersion and intra-member correlation coefficients for the infill model (values in bold typeface are based on data, the remaining ones are based on expert judgement).

| Variable | $\sigma_{ln}$ | $\rho_{x,f_p}$ | $\rho_{x,u_{cr}}$ | $\rho_{x,u_p}$ | $\rho_{x,u_r}$ | $\rho_{x,\rho_{op}}$ | $\rho_{x,x}^{sf}$ | $\rho_{x,x}^{df}$ |
|---|---|---|---|---|---|---|---|---|
| $f_p$ | **0.40** | 1.0 | -0.5 | -0.5 | -0.5 | 0.0 | 0.8 | 0.8 |
| $u_{cr}$ | **0.50** | -0.5 | 1.0 | **0.7** | **0.7** | 0.0 | 0.8 | 0.8 |
| $u_p$ | **0.50** | -0.5 | **0.7** | 1.0 | **0.7** | 0.0 | 0.8 | 0.8 |
| $u_r$ | **0.50** | -0.5 | **0.7** | **0.7** | 1.0 | 0.0 | 0.8 | 0.8 |
| $\rho_{op}$ | **0.25** | 0.0 | 0.0 | 0.0 | 0.0 | 1.0 | 0.8 | 0.8 |

The final random vector, based on the previous assumptions, is joint lognormal, with the median values (specified in Section 4.3) and variances and correlation matrices given by Table C 1 and by Table C 2 for RC members and infill panels, respectively.

## C6. **Results for RC structures**
### C6.1. **Six-story building in Naples**

#### C6.1.1. Sensitivity to assumed inter-element correlation values through nonlinear static analysis

Nonlinear static analysis (NLSA) was employed to quantify the sensitivity of the model parameters presented in the previous section. In particular, NLSAs were performed in both X and Y directions, for 20 samples drawn from:

- A joint distribution with zero inter-member correlation
- A joint distribution with perfect inter-member correlation
- The joint distribution described in the previous section

The results are reported, with reference to the BF configuration only, for the sake of illustration, in Figure C 4, where each row contains the results for one of the three distribution models above, arranged in the same order from the top to the bottom, while the left and right columns present the results for the X and Y directions, respectively. Similar results were obtained also for the IF and PF configurations.

In the figure, the thin lines represent individual NLSA runs, while green, blue and red dots denote the yield, peak and collapse (at 50% drop from the maximum resistance according to the adopted simplified global collapse criterion, see Section 4.4.1) points on the trilinear fit to the curve (not shown in the plots, for clarity). On the axes, lognormal probability density functions (PDFs) fitted to both the displacement and force values obtained from these clouds of points are reported, indicating the numerical values of median and dispersion by the markers with the same colors. A bold line with three different colors denotes the capacity curve obtained with the median model.

It is shown that a model with relatively high intra-floor and inter-floor correlation, like the one described in the previous section, yields results similar to those of the perfect correlation model. Also, the median model is providing an approximation of the median response of the analyses with consideration of structure-related uncertainties in the two cases of "high" and "perfect" correlation, while it represents an upper bound for the "zero" inter-member correlation case. The latter is consistent and easily explained, because with high correlation, variations towards larger or smaller values (of strength, deformability, etc.) happen to most members together, resulting in larger global variability reflected in the capacity curve. With independent members, it is highly likely that in each simulation one or more weak members are sampled, thus resulting in a premature failure.
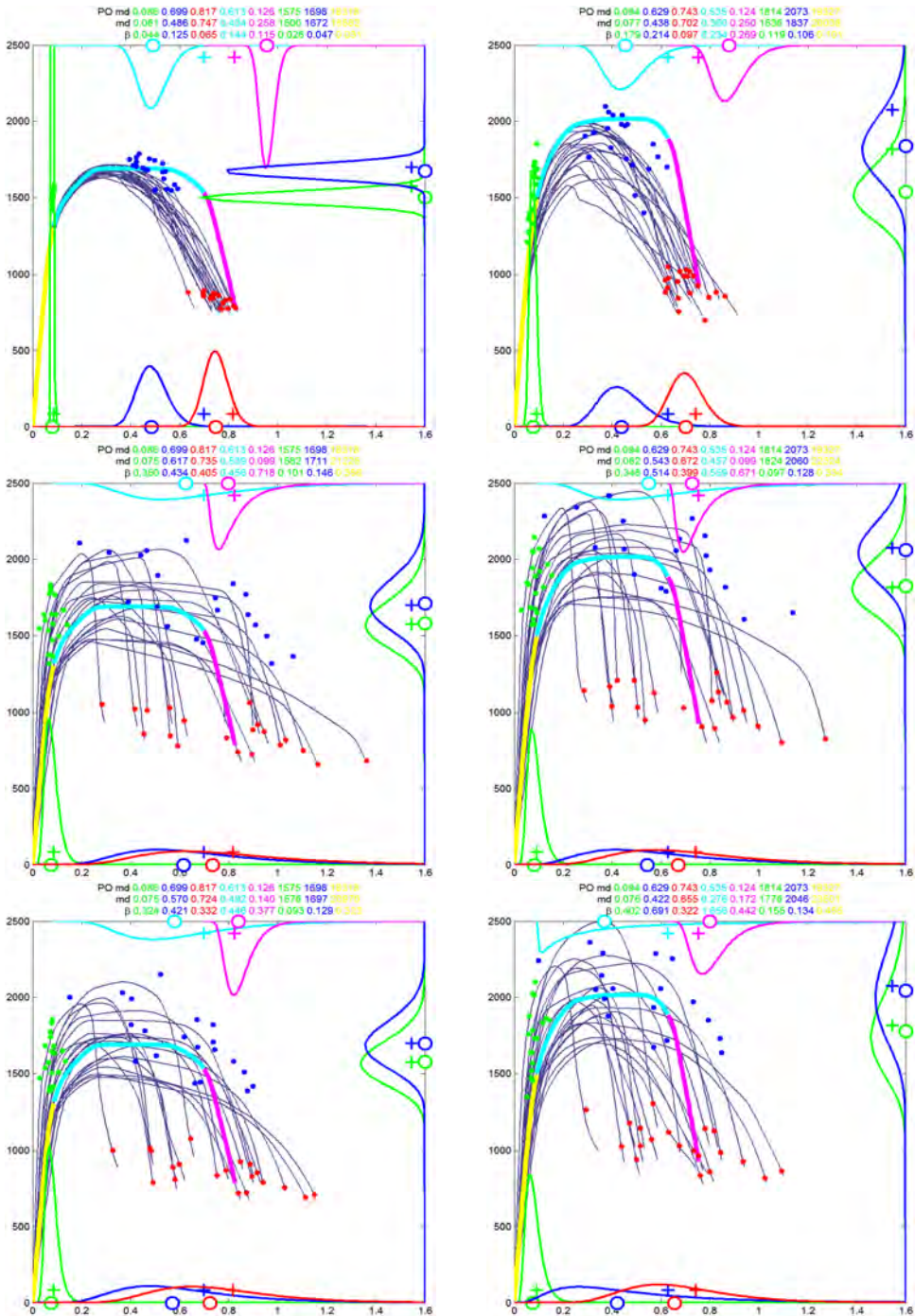
Figure C 4 NLSA results (first mode distribution) in X (left) and Y (right) directions, BF configuration, under the three inter-member correlation assumptions ("zero", "perfect" and "assumed", from top to bottom).

Finally, Figure C 5 shows a comparison of the results (fitted distribution and parameters) obtained with 20 or 200 samples, again only for the BF configuration for the sake of illustration. The figure shows that 20 samples provide an acceptable approximation of the distribution

provided by the larger sets of 200 samples, thus supporting the approach of associating one-to-one a realization of the structure to each ground motion of a stripe (i.e., using 20 models) and using the same 20 random models for all the stripes (changing only the ground motion records).
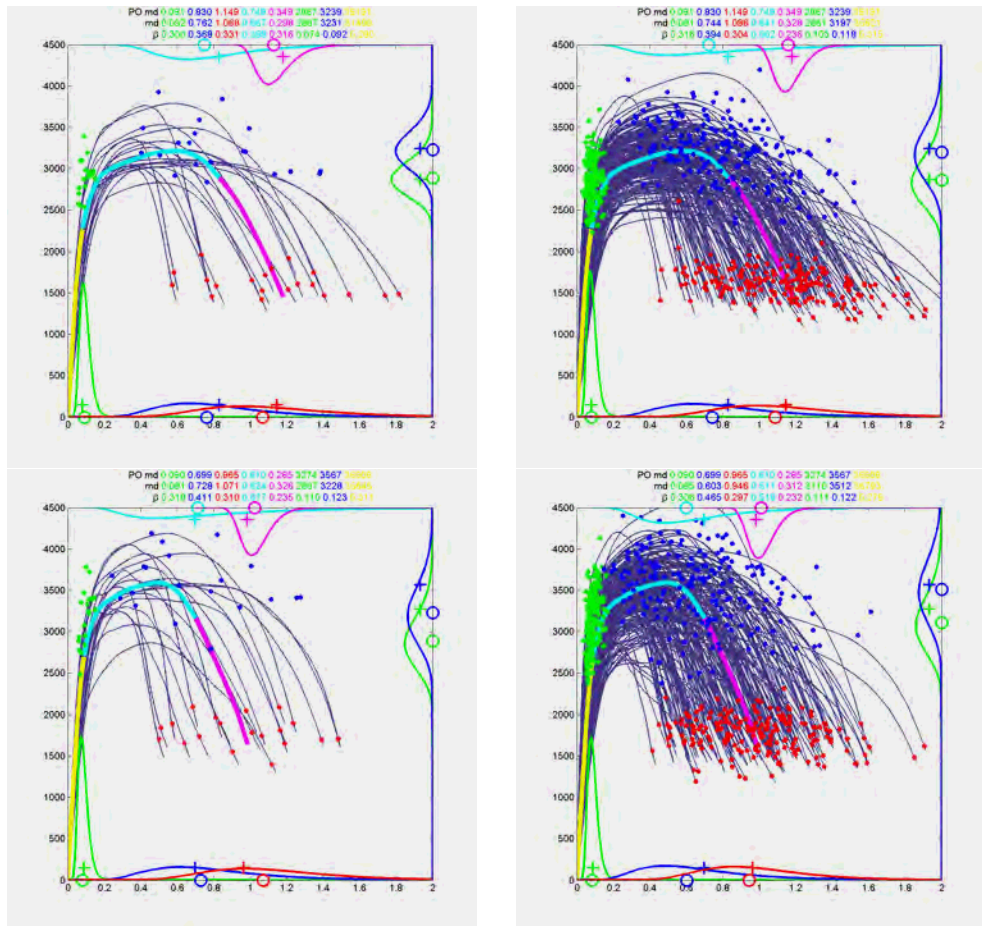


Figure C 5 NLSA results (first mode distribution) in X (top) and Y (bottom) directions, BF configuration, under the two inter-member correlation assumptions: effect of sample size on collapse capacity (20 vs 200 samples, left and right, respectively).

**C6.1.2. Inelastic response history analysis**

Figure C 6 reports the D/C ratios (in terms of top floor displacement) for the BF configuration, for the X (left) and Y (right) directions, for both limit states. In particular, the collapse limit is at the top while the damage limit state is at the bottom. The plots report both the individual run results, with markers aligned at each stripe intensity level and the fitted conditional distributions. The blue markers and shaded PDFs are those for the median model analyses (Section 4.4.2), shown for reference, while the red markers denote the results accounting for structure-related uncertainty. Figure C 7 reports similar results for the IF configuration.

The results confirm that again the collapse D/C ratios are well below 1.0 and those for the Damage Limit State are way above 1.0. It is reminded that the latter is defined in the NTC08 as maximum Inter-story Drift Ratios (IDRs) of 0.003 and 0.005 for the cases of buildings with infills (as in the IF and PF cases) and for those without infills (as in the BF case), respectively. Even

though the order of magnitude does not change, as expected, the dispersion of the D/C ratios is quite heavily affected by the additional structure-related uncertainty, leading to a significant increase in the risk (Iervolino et al., 2017). A better assessment of the induced change in terms of response can be obtained by inspecting the plots in Figure C 8 (for collapse limit state) and Figure C 9 (for damage limit state). The figures report, for all configurations (BF, IF and PF, from left to right), the scatters of D/C ratios without structure-related uncertainty in the horizontal axis against the D/C ratios with this uncertainty in the vertical axis. In all cases the median is only slightly affected, with the possible exception of the IF configuration at collapse, and dispersions are quite large, ranging from 0.3 (BF) to 0.6 (IF and PF, where infill panels also play a role and total uncertainty increases) at collapse, and from 0.2 (BF) to 0.4 (IF) at the damage limit state.
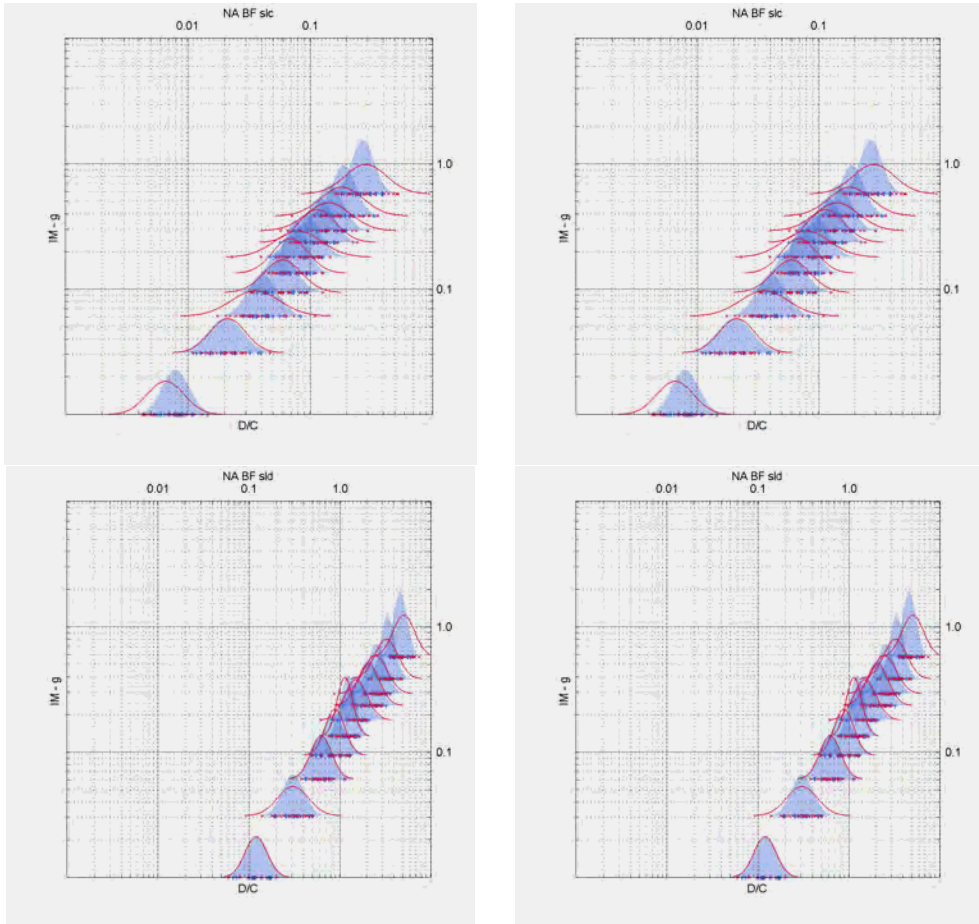


Figure C 6 D/C ratios for the BF configuration (the six-story building in Naples, soil C): at the top, collapse limit state, damage limit state at the bottom, X direction in the left column, Y direction in the right column. Blue markers and light blue shades indicate individual run results and lognormal fit for the analyses with the median model, respectively. Red markers and lines indicate the corresponding results for the analysis with structure-related uncertainty.
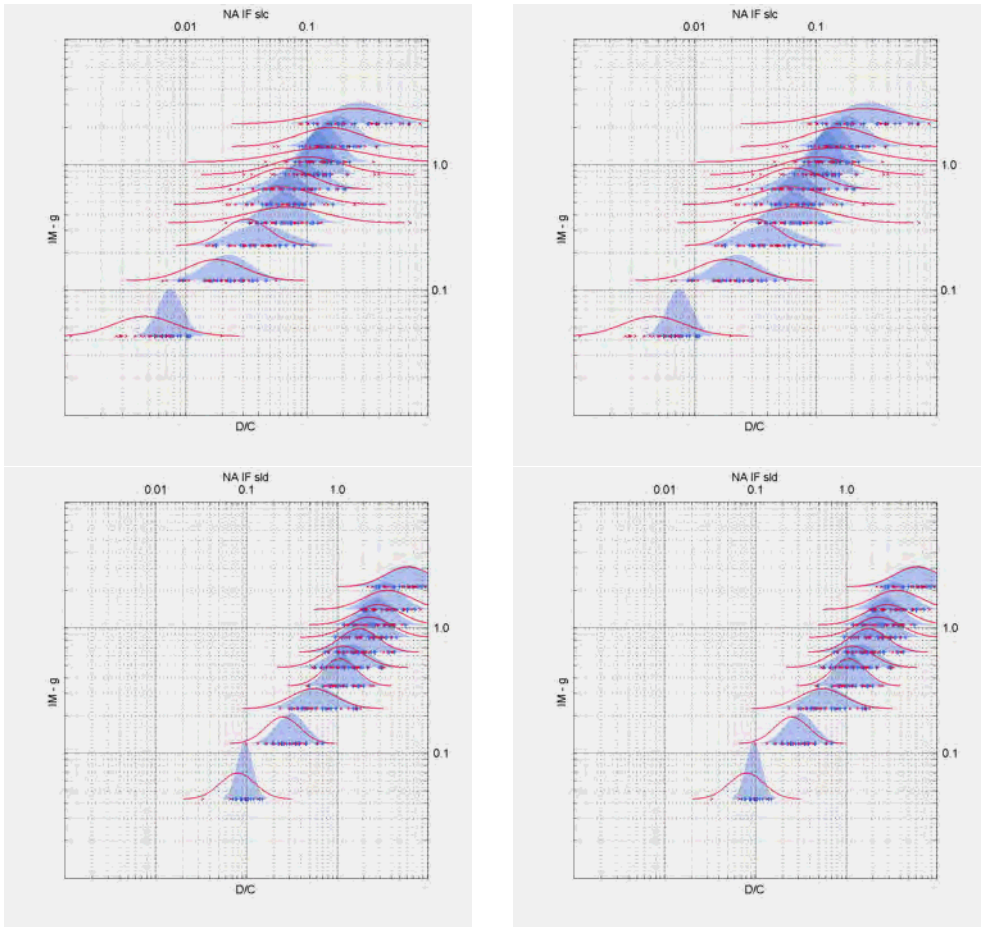
Figure C 7 D/C ratios for the IF configuration (the sic-story building in Naples, soil C): at the top, collapse limit state, damage limit state at the bottom, X direction in the left column, Y direction in the right column. Blue markers and light blue shades indicate individual run results and lognormal fit for the analyses with the median model, respectively. Red markers and lines indicate corresponding results for the analysis with structure-related uncertainty.
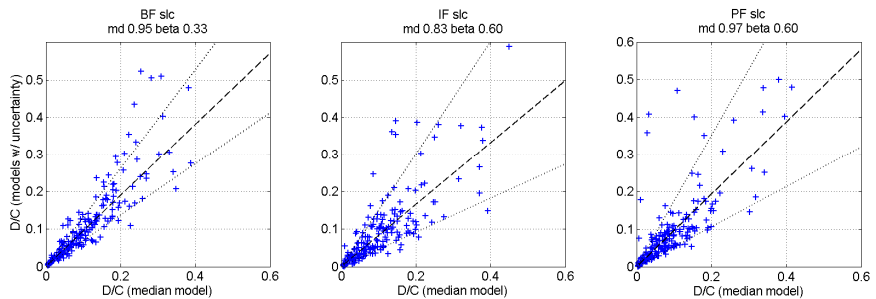


Figure C 8 Collapse Limit State: D/C ratios of model with structure-related uncertainty versus model without it, under the same ground motion excitation and for all configurations (BF, IF and PF).
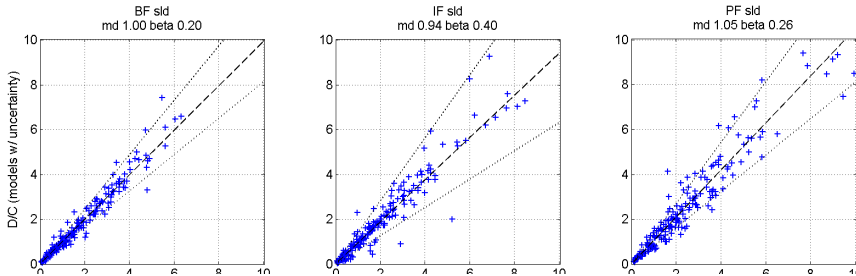
Figure C 9 Damage Limit State: D/C ratios of model with structure-related uncertainty versus model without it, under the same ground motion excitation and for all configurations (BF, IF and PF).

## C6.2.    Six-story building in L'Aquila

In this section, the results obtained for the six-story buildings designed for the site of L'Aquila (soil type C according to NTC2008) by considering the structure-related uncertainty following the joint distribution model described previously, are reported. Specifically, the results of nonlinear static pushover analyses (carried out to define the adopted simplified global collapse criterion, see Section 4.4.1) and nonlinear time history analyses (carried out to calculate the seismic demand parameter), are described in the following.

### C6.2.1. Nonlinear static analyses

Figure C 10 displays the pushover curves (20 models) for the considered building configurations (i.e., BF, IF, PF) along the two in-plane directions (i.e., X and Y) obtained by considering the structure-related uncertainty (blue lines). In the figure, the pushover curves obtained with the median model (red line) are also displayed.

To better highlight the differences, in Figure C 11 the roof displacement values (median values) at 50% decrease in base-shear evaluated for the models with (bar in blue) and without (bar in red) structure-related uncertainty are compared. In all cases, the roof displacement value relevant to the model with structure-related uncertainty is lower than the results obtained from the "deterministic" model.
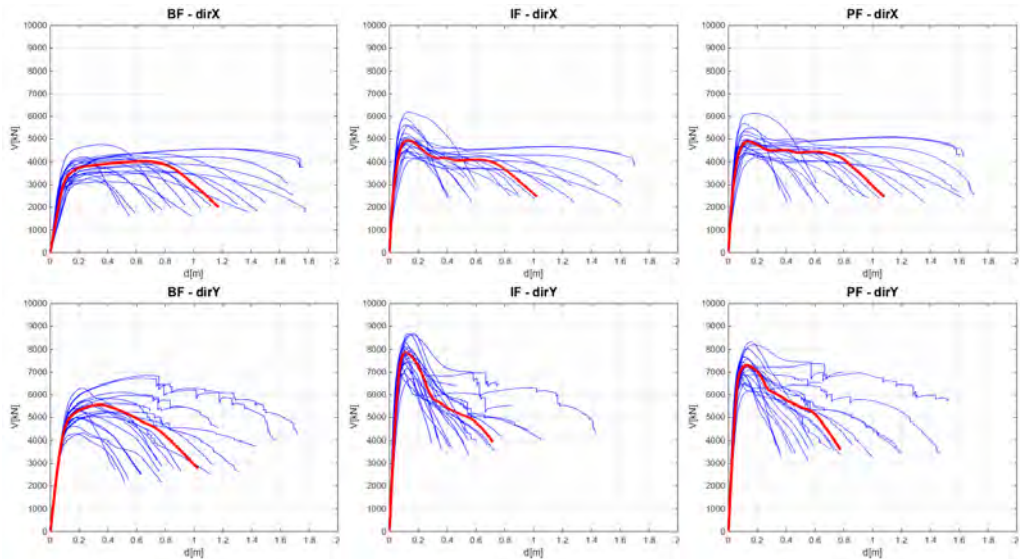
Figure C 10 NLSA results (first mode distribution) in the X (top row) and Y (bottom row) directions, for the three configurations (BF, IF and PF from left to right). Blue and red lines refer to models with and without model uncertainty, respectively.
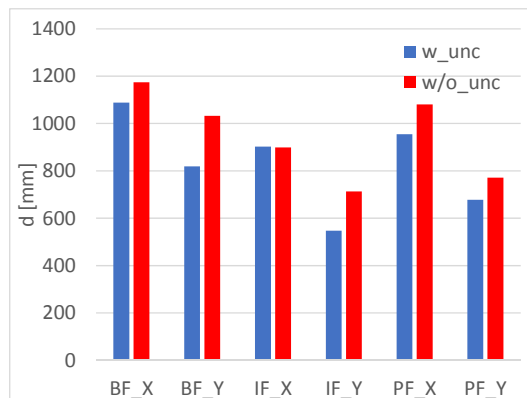


Figure C 11 Comparison between top roof displacement values obtained from model with (bars in blue) and without (bars in red) structural-related uncertainty for the considered building types.

## C6.2.2. Nonlinear dynamic analyses

Figure C.12 displays the demand on capacity ratio values (in terms of roof displacement) at the collapse limit state for all configurations, computed through nonlinear time history analyses for ten stripes with increasing intensity. Blue circles refer to analyses in which structure-related uncertainty has been considered, while red ones denote results for the deterministic model. At the top of each figure, the numbers of the global dynamic instability are also reported. As can be seen, a greater number of collapses has been found in the analyses with the model uncertainty with respect to the median model. For example, for IF type and stripe 9, the number of collapse cases is 11 with the model accounting for structure-related uncertainty, while a lower number (8) was observed for the median model.
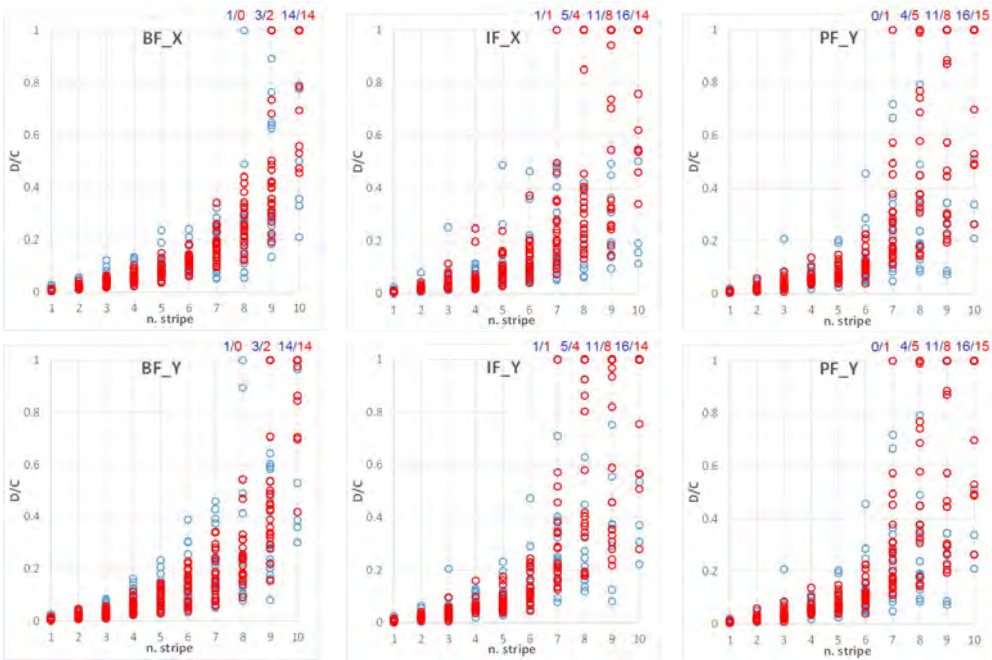
Figure C 12 D/C ratios for all considered configurations (BF, IF and PF) in the X (top row) and Y directions (bottom row) evaluated for model with (in blue) and without structure-related uncertainty (in red).
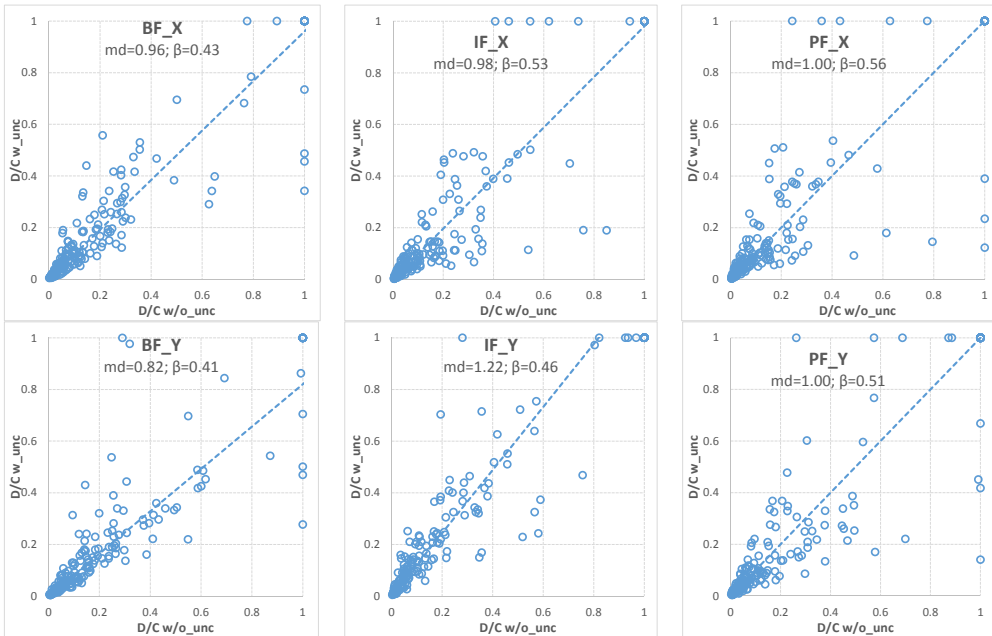


Figure C 13 D/C ratios at the collapse limit state of model with structure-related uncertainty versus model without it, for all configurations (BF, IF and PF).

Figure C 13 shows for all configurations (BF, IF and PF type) the cloud of D/C ratio values plotted according to two orthogonal axes having the abscissa equal to the D/C ratio without structure-related uncertainty and the ordinate equal to the D/C ratio with uncertainty. As shown

in the previous section with reference to the site of Naples, the model uncertainty has a slight influence on the median, with the exception of the results related to the Y direction for the BF and IF configurations. Nevertheless, the dispersion values are very large, ranging from 0.41 (BF in Y direction) to 0.56 (PF in X direction). These dispersion values, however, are mostly related to the higher intensity stripes, whose influence on the risk is lower.

## C7.    References

Bommer, J. J., Scherbaum, F., Bungum, H., Cotton, F., Sabetta, F., & Abrahamson, N. A. (2005). On the use of logic trees for ground-motion prediction equations in seismic-hazard analysis. Bulletin of the Seismological Society of America, 95(2), 377-389.

Budden, M., Hadavas, P., Hoffman, L., & Pretz, C. (2007). Generating valid 4× 4 correlation matrices. Applied Mathematics E-Notes, 7, 53-59.

Celarec, D., Ricci, P., & Dolšek, M. (2012). The sensitivity of seismic response parameters to the uncertain modelling variables of masonry-infilled reinforced concrete frames. Engineering Structures, 35, 165-177.

Celik, O. C., & Ellingwood, B. R. (2010). Seismic fragilities for non-ductile reinforced concrete frames–Role of aleatoric and epistemic uncertainties. Structural Safety, 32(1), 1-12.

Decanini, L. D., & Fantin, G. E. (1986). Modelos simplificados de la mamposteria incluida en porticos. Caracteristicas de rigidez y resistencia lateral en estado limite, Jornadas Argentinas de Ingenieria Estructural, Buenos Aires, Argentina, 2, 817-836 (in Spanish).

Decanini, L., Mollaioli, F., Mura, A., & Saragoni R. (2004). Seismic performance of masonry infilled R/C frames, Proc.13th WCEE, Paper 165, Vancouver, B.C., Canada, August 1-6.

Decanini L., Liberatore L., & Mollaioli F. (2014). Strength and stiffness reduction factors for infilled frames with openings, Earthquake Engineering and Engineering Vibration, 13(3), 437-454.

Dolsek, M. (2009). Incremental dynamic analysis with consideration of modeling uncertainties. Earthquake Engineering & Structural Dynamics, 38(6), 805-825.

Ellingwood, B. R., Celik, O. C., & Kinali, K. (2007). Fragility assessment of building structural systems in Mid‐America. Earthquake Engineering & Structural Dynamics, 36(13), 1935-1952.

Gokkaya, B. U., Baker, J. W., & Deierlein, G. G. (2016). Quantifying the impacts of modeling uncertainties on the seismic drift demands and collapse risk of buildings with implications on seismic design checks. Earthquake Engineering & Structural Dynamics, 45(10), 1661-1683.

Haselton, C.B., Liel, A.B., Taylor Lange, S. & Deierlein, G.G. (2008). Beam-Column Element Model Calibrated for Predicting Flexural Response Leading to Global Collapse of RC Frame Buildings, PEER report 2007/03.

Ibarra, L. F., Medina, R. A., & Krawinkler, H. (2005) Hysteretic models that incorporate strength and stiffness deterioration. Earthquake engineering & structural dynamics, 34(12), 1489-1511.

Iervolino, I., Spillatura, A., & Bazzurro, P. (2017). RINTC Project - Assessing the (implicit) seismic risk of code-conforming structures in Italy. COMPDYN 2017 - 6th ECCOMAS Thematic Conference on Computational Methods in Structural Dynamics and Earthquake Engineering M. Papadrakakis, M. Fragiadakis (eds.) Rhodes Island, Greece, 15–17 June 2017.

Jalayer, F., Franchin, P., & Pinto, P. E. (2007). A scalar damage measure for seismic reliability analysis of RC frames. Earthquake Engineering & Structural Dynamics, 36(13), 2059-2079.

Kwon, O. S., & Elnashai, A. (2006). The effect of material and ground motion uncertainty on the seismic vulnerability curves of RC structure. Engineering structures, 28(2), 289-303.

Liberatore, L., Noto, F., Mollaioli, F., & Franchin, P. (2018). In-Plane Response Of Masonry Infill Walls: Comprehensive Experimentally-Based Equivalent Strut Model For Deterministic And Probabilistic Analysis, Engineering Structures (accepted)

Liel, A. B., Haselton, C. B., Deierlein, G. G., & Baker, J. W. (2009). Incorporating modeling uncertainties in the assessment of seismic collapse risk of buildings. Structural Safety, 31(2), 197-211.

Lupoi, G., Franchin, P., Lupoi, A., & Pinto, P. E. (2006). Seismic fragility analysis of structural systems. Journal of Engineering Mechanics, 132(4), 385-395.

McKenna, F. (2011). OpenSees: a framework for earthquake engineering simulation, Computing in Science & Engineering 13(4), 58-66 (http://opensees.berkeley.edu).

Merz, B., & Thieken, A. H. (2009). Flood risk curves and uncertainty bounds. Natural hazards, 51(3), 437-458.

Miller III, A. C., & Rice, T. R. (1983). Discrete approximations of probability distributions. Management science, 29(3), 352-362.

O'Reilly, G. J., & Sullivan, T. J. (2017). Quantification of modelling uncertainty in existing Italian RC frames. Earthquake Engineering & Structural Dynamics.

Sassun, K., Sullivan, T. J., Morandi, P., Cardone, D. (2016). Characterising the in-plane seismic performance of infill masonry. Bulletin of the New Zealand Society for Earthquake Engineering, 49(1),100-117,.

Schotanus, M. I. J., Franchin, P., Lupoi, A., & Pinto, P. E. (2004). Seismic fragility analysis of 3D structures. Structural Safety, 26(4), 421-441.

Veneziano, D., Casciati, F., & Faravelli, L. (1983). Method of seismic fragility for complicated systems. Probabilistic methods in seismic risk assessment for nuclear power plants.

Visser, H., Folkert, R. J. M., Hoekstra, J., & De Wolff, J. J. (2000). Identifying key sources of uncertainty in climate change projections. Climatic Change, 45(3-4), 421-457.